

**A MODELLING FRAMEWORK TO DETERMINE
THE VALUE PROPOSITION OF MICROWAVE
TREATMENT OF MINERAL ORES**

by

Edson Charikinya

Thesis submitted in partial fulfillment
of the requirements for the Degree



**MASTER OF SCIENCE IN ENGINEERING
(EXTRACTIVE METALLURGICAL ENGINEERING)**

in the Faculty of Engineering
at Stellenbosch University

Supervised by

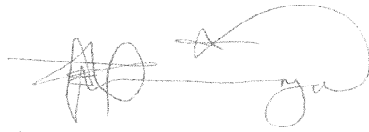
S.M. Bradshaw

MARCH 2011

Declaration

By submitting this thesis electronically, I declare that the entirety of the work contained therein is my own, original work, that I am the sole author thereof (save to the extent explicitly otherwise stated), that reproduction and publication thereof by Stellenbosch University will not infringe any third party rights and that I have not previously in its entirety or in part submitted it for obtaining any qualification.

Signature:

A handwritten signature in black ink, consisting of several loops and a long horizontal stroke.

Date: 28/02/2011

ABSTRACT

The extraction of mineral values from ore requires liberation of the minerals followed by separation. Liberation is achieved by size reduction operations which are inefficient processes typically accounting for up to 70% of the energy consumption in a mineral concentrator (Tromans, 2008). As the grade of ores reserves declines, future viability of mineral operations will be determined by the costs of comminution. Recent work has shown that microwave treatment of secondary crusher product at specific microwave energy consumption of the order of 1 kWh/t reduces the work index of the ore and increases grade and recovery in batch flotation tests. Improved liberation at coarse sizes was also demonstrated (Kingman, 2006). Based on these findings work is ongoing to commercialise the technology.

The objective of this study is to develop a modelling framework to determine the value proposition of microwave treatment of ore. It was noted that various models exist in literature for modelling of mineral processing flotation flow sheets, but these models do not incorporate the feed ore liberation property as an input variable in their calculations. Thus, a fundamentally derived property based model was identified as appropriate for flow sheet modelling of microwave treated ore, as it utilised liberation as an indirect variable in calculating the flotation rate constant through the use of contact angle to describe particle surface hydrophobicity.

The model was successfully incorporated into the flotation flow sheet units developed in HSC Chemistry and used with Mineral Liberation Analyser (MLA) data to investigate the effects of changes in feed ore liberation on rougher cell flotation recovery. Different liberation scenarios based around modification of porphyry copper flotation feed were created. A sensitivity analysis of the various feed stream liberation scenarios was carried out to test the ability of the model to effectively model the differences in downstream processing of microwave treated and untreated ores. For a single flotation cell of size 85 m³ with a solids feed flow rate of 890 tph, it was observed that below a certain size (120 µm in the case of the porphyry copper ore) changes in flotation feed liberation had no significant effect on value mineral recovery. Significant differences in value mineral

recovery were observed only at coarser sizes above 120 μm . The results indicated that improvement in recovery of value minerals due to improved liberation from applying microwave technology has size limits and is significantly dependent on the feed grind size.

Feed grind size sensitivity analysis was then carried on the same single cell flow sheet utilising feeds with the same mineralogy but with different grind sizes. The results indicated that maximum benefits from the application of microwave technology would be best obtained by utilising coarse grinding at sizes between $P_{70} = 200 \mu\text{m}$ and $P_{70} = 300 \mu\text{m}$ for the porphyry copper ores considered in this study. Coarse grinding appears to be the best way to exploit improved liberation in downstream processing of microwave treated ores.

Investigations similar to those carried out on the single cell flotation flow sheet were then carried out on a continuous plant rougher flotation flow sheet. The flow sheet consisted of nine rougher cells in series each with a volume of 85 m^3 with a solids feed flow rate of 890 tph into the bank of rougher cells. The results indicated that there was no significant difference in final rougher bank overall cumulative recovery at fine grind sizes below a P_{70} grind size of 120 μm with improvements in feed ore liberation. Feed grind size sensitivity analysis showed a significant variation in cumulative recovery at coarse grind sizes of above $P_{70} = 129 \mu\text{m}$. This variation was attributed to improvements in flotation feed ore value mineral liberation from locked composite particles to the maximum possible theoretical liberation scenario of fully liberated value mineral particles. A 7.2 percentage point improvement in cumulative value mineral overall recovery and a 2 to 3 percentage point improvement in enrichment ratio was also observed above the $P_{70} = 250 \mu\text{m}$ grind sizes after improving the flotation feed ore value mineral particle liberation of a typical flotation plant feed to a maximum. The increases in grade and cumulative recovery at coarse sizes were attributed to improvements to the flotation plant feed ore value mineral particle liberation. From the results, it was concluded that microwave technology application will offer greater benefits in downstream processing of coarse ground ores.

OPSOMMING

Die ekstraksie van mineraalwaardes uit erts vereis bevryding van die minerale gevolg deur skeiding. Bevryding word bereik deur verkleiningsprosedures wat ondoeltreffende prosesse is en wat gewoonlik vir tot 70% van die energieverbruik in 'n mineraalkonsentreerder verantwoordelik is (Tromans, 2008). Algaande die graad van ertsreserwes afneem, sal toekomstige lewensvatbaarheid van mineraalprosesse bepaal word deur die koste van vergruising. Onlangse werk het getoon dat mikrogolfbehandeling van sekondêre vergruiserprodukt by spesifieke mikrogolf-energieverbruik van ongeveer 1 kWh/t die werk-indeks van die erts verminder en die graad en opbrengs in lotflottasietoetse verhoog. Verbeterde bevryding by growwer groottes is ook aangetoon (Kingman, 2006). Werk gaan voort op grond van hierdie bevindinge ten einde die tegnologie te kommersialiseer.

Die doel van hierdie navorsing is om 'n modelleringsraamwerk te ontwikkel om die waardeproposisie van mikrogolfbehandeling van erts te bepaal. Daar is in die literatuur afgekom op verskeie modelle vir die modellering van vloeidiagramme vir flottasie van mineraalverwerking, maar hierdie modelle inkorporeer nie die voerertsbevrydingseienskap as 'n insetveranderlike in hulle berekeninge nie. 'n Fundamentele afgeleide eienskapgebaseerde model is geïdentifiseer as geskik vir vloeidiagrammodellering van mikrogolfbehandelde erts, aangesien dit bevryding as 'n indirekte veranderlike by die berekening van die floteertempokonstante aangewend het deur die gebruik van kontakhoek om hidrofobisiteit van die deeltjieoppervlak te beskryf.

Die model is suksesvol in eenhede van die flottasievloeidiagram wat in HSC Chemistry ontwikkel is, geïnkorporeer en tesame met data van die mineraalbevrydingsontleder (MBO) gebruik om die gevolge van veranderinge in voerertsbevryding op die opbrengs van voorskieselflottasie te ondersoek. Verskillende bevrydingsscenario's is geskep wat óm die modifisering van porfierkoperflotterings toevoer heen gebaseer is. 'n Sensitiwiteitsontleding van die verskillende voerstroombevrydingsscenario's is uitgevoer om die vermoë van die model om die verskille in stroomaf-verwerking van mikrogolfbehandelde en onbehandelde ertse te toets, doeltreffend te modelleer. In die geval van 'n enkele flottasiesel van 85 m³ groot met 'n vastestof-toevoervloeiempo van 890 tph, is waargeneem dat veranderinge in flottasietoever-bevryding benede 'n sekere grootte (120 µm in die geval van die porfierkopererts) geen beduidende uitwerking op die opbrengs van die waardemineraal gehad het nie. Beduidende verskille in die opbrengs van die waardemineraal is slegs by growwer

groottes bo 120 μm waargeneem. Die resultate het daarop gedui dat verbetering in die opbrengs van waardeminerale as gevolg van verbeterde bevryding ná die toepassing van mikrogolftegnologie beperkinge ten opsigte van grootte het en opvallend afhanklik is van die toevoermaalgrootte.

Sensitiwiteitstoetsing van toevoermaalgrootte is daarna op dieselfde enkele selvloeiagram wat voerders met dieselfde mineralogie gebruik uitgevoer, maar met verskillende maalgroottes. Die resultate het daarop gedui dat maksimum voordele van die toepassing van mikrogolftegnologie die beste verkry sou word deur gebruik van growwe maling by groottes tussen $P_{70} = 200 \mu\text{m}$ en $P_{70} = 300 \mu\text{m}$ vir die porfierkoperertse wat in hierdie navorsing in oorweging geneem is. Growwe maling skyn die beste manier te wees om verbeterde bevryding in stroomaf-verwerking van mikrogolfbehandelde ertse te eksploiteer.

Ondersoeke soortgelyk aan dié wat op die vloeiagram van die enkelselflottasie uitgevoer is, is toe op 'n deurlopende vloeiagram van die aanlegvoorskeierflottasie uitgevoer. Die vloeiagram het bestaan uit nege voorskeiselle in serie elk met 'n volume van 85 m^3 met 'n vastestof-toevoervloeiempo van 890 tph in die ry voorskeiselle. Die resultate het daarop gedui dat daar geen aanmerklike verskil in algemene kumulatiewe opbrengs van die finale voorskeiry by fyn maalgroottes benede 'n P_{70} -maalgrootte van $120 \mu\text{m}$ met verbetering in voerertsbevryding was nie. Sensitiwiteitsontleding van voermaalgrootte het 'n beduidende variasie in kumulatiewe opbrengs by growwe maalgroottes van bo $P_{70} = 129 \mu\text{m}$ getoon. Hierdie variasie is toegeskryf aan verbetering in waardemineraalbevryding van flottasietoevererts uit geslote saamgestelde deeltjies tot die maksimum moontlike teoretiese bevrydingsscenario van ten volle bevryde waardemineraaldeeltjies. 'n Persentasiepuntverbetering van 7.2 in die kumulatiewe algemene opbrengs van waardemineraal en 'n persentasiepuntverbetering van 2 tot 3 in die verrykingsratio is ook bo die $P_{70} = 250 \mu\text{m}$ -maalgroottes waargeneem ná verbetering van die bevryding van die waardemineraaldeeltjies van die flottasietoevererts van 'n tipiese flottasieaanlegtoevoer tot die maksimum. Die toenames in graad en kumulatiewe opbrengs by growwe groottes is toegeskryf aan verbetering in die bevryding van die waardemineraaldeeltjies van die flottasietoevererts. Op grond van die resultate is daar tot die gevolgtrekking gekom dat toepassing van mikrogolftegnologie groter voordele in stroomaf-verwerking van grofgemaalde ertse sal bied.

i. ACKNOWLEDGEMENTS

The author wishes to acknowledge the following people and organizations that made this project possible. Prof Steven Bradshaw who supervised this research and provided all the necessary support that was required to complete the research. The author would also like to thank Dr Ali Abubeker for his help. Lastly the author would like thank his family and friends for all of their encouragement and support.

ii. TABLE OF CONTENTS

ABSTRACT.....	ii
OPSOMMING.....	iv
i. ACKNOWLEDGEMENTS.....	vi
ii. TABLE OF CONTENTS.....	vii
iii. NOMENCLATURE.....	xvii
1. INTRODUCTION.....	1
2. LITERATURE REVIEW.....	4
2.1. Comminution process optimisation.....	4
2.1.1. Developments in microwave heating of ores.....	5
2.1.2. Microwave assisted comminution in mineral processing.....	6
2.2. Flotation.....	9
2.2.1. Flotation Sub-processes.....	9
2.3. Flotation modelling.....	10
2.3.1. Collection zone modelling.....	10
2.3.2. Kinetic theory rate expression.....	11
2.3.2.1. Measurement of pulp flotation kinetics of minerals in flotation cells.....	11
2.4. Probability theory approach.....	17
2.4.1. Bubble-particle interaction theory.....	17
2.4.2. Determining overall collection zone efficiency.....	17
2.4.3. Fundamental model for calculating collection zone efficiency.....	18
2.4.3.1. Collision Efficiency.....	19
2.4.3.2. Attachment efficiency.....	23
2.4.3.3. Bubble-particle stability Efficiency.....	27
2.5. Calculating collection zone overall mineral recovery.....	28
2.5.1. Froth zone value mineral recovery.....	29
2.5.2. Studies into the factors that affect froth zone recovery.....	29
2.5.2.1. Froth structure.....	30
2.5.2.2. Froth zone sub-processes.....	30
2.6. Entrainment.....	31
2.6.1. Mechanisms of entrained material drainage.....	31
2.6.2. Main Factors that affect entrainment.....	31
2.6.3. Entrainment modelling.....	32
2.7. Froth recovery.....	34
2.7.1. Methods for obtaining the froth zone recovery.....	34

2.8.	Water recovery	36
2.8.1.	Modelling water recovery	36
3.	METHODOLOGY	39
3.1.	The fundamental property based flotation model	39
3.1.1.	The bubble-particle collision frequency	40
3.1.2.	Calculation of the elementary processes.....	45
3.1.2.1.	Collision efficiency determined by the Generalised Sutherland equation (GSE) 46	
3.1.2.2.	Attachment Efficiency determined by the Dobby-Finch attachment model 47	
3.1.2.3.	Particle-bubble stability efficiency determined by Schulze model	49
3.2.	General flotation model parameter determination for model calibration.....	50
3.2.1.	Determination of particle Contact angle	50
3.2.1.1.	Composite particles contact angle calculation.....	51
3.2.2.	Energy dissipation.....	52
3.2.3.	Bubble diameter	53
3.2.3.1.	McGill bubble viewer	53
3.2.3.2.	UCT bubble size analyser.....	53
3.2.4.	Bubble rise velocity	54
3.3.	HSC Chemistry 7 simulation software.....	54
3.3.1.	Particle tracking in HSC Chemistry Simulation software	54
3.3.2.	Particles (Mineral) mode.....	54
3.3.2.1.	True particle modelling in HSC Chemistry Simulation software using MLA data 55	
3.4.	Integrating the Fundamental model into HSC Chemistry 7	55
3.5.	Conclusion.....	57
4.	CREATION OF ARTIFICIAL FEED ORES.....	58
4.1.	Introduction	58
4.2.	Copper 1 and Copper 2 base case feed ore (BC).....	58
4.2.1.	Copper 1 mineralogy ($P_{70} = 120 \mu\text{m}$)	60
4.2.2.	Copper 2 mineralogy.....	62
4.3.	Artificial flotation feed ores	64
4.3.1.	Methodology	64
4.3.2.	Copper 1 group artificial ores	66
4.3.2.1.	Fully liberated ore (FL)	67
4.3.2.2.	Fully locked ore (LC)	69

4.3.2.3.	Ore 1	72
4.3.2.4.	Ore 2	74
4.3.2.5.	Ore 3	77
4.3.3.	Copper 2 artificial ores.....	79
4.3.3.1.	Fully liberated ore.....	79
4.3.3.2.	Fully locked ore (LC)	80
4.3.3.3.	Ore 1	81
4.3.3.4.	Ore 2	82
4.3.3.5.	Ore 3	83
4.4.	Contact angle calculations Method	84
4.4.1.	Contact angle calculation results and discussion	84
4.5.	Conclusion.....	86
5.	SINGLE CELL FLOWSHEET SIMULATION.....	87
5.1.	Comparison of simulated recovery trends with experimental trends	87
5.2.	Continuous single cell flow sheet simulation.....	90
5.3.	Analysis of simulation results using the Particle analysis tool in HSC Chemistry Simulation Software.....	92
5.4.	Effects of changes in feed ore liberation on single Cell recovery.....	97
5.4.1.	Methodology	98
5.4.2.	Copper 1 feed ore ($P_{70} = 120 \mu\text{m}$): Results and discussion	99
5.4.2.1.	Sub-process bubble-particle interaction efficiency values	103
5.4.3.	Copper 2 feed ore ($P_{70} = 180 \mu\text{m}$): Results and discussion	107
5.4.3.1.	Sub-process efficiency values	109
5.4.3.2.	Feed ore Particle size sensitivity analysis.....	110
5.5.	The effects of feed ore particle size distribution on value mineral recovery	113
5.5.1.	Methodology	113
5.5.2.	Grind size sensitivity analysis results	116
5.6.	Conclusion.....	118
6.	SIMULATION OF FLOTATION PLANTS	119
6.1.	Rougher bank in series configuration simulation.....	119
6.2.	Effect of Feed ore liberation.....	123
6.2.1.	Methodology	123
6.2.2.	Copper 1 feed ore ($P_{70} = 120 \mu\text{m}$): Simulation results and discussion.....	124
6.2.3.	Copper 2 feed ore ($P_{70} = 180 \mu\text{m}$): Results and discussion	129
6.3.	Effect of Particle size distribution of the feed.....	135
6.3.1.	Methodology	135

6.3.2.	Operating plant Grind size sensitivity analysis results	136
6.4.	Conclusion.....	146
7.	CONCLUSIONS AND FUTURE WORK	147
8.	REFERENCES	150
	APPENDIX A MINERAL MODE OF OCCURRENCE FOR COPPER 2 ORE FEED	161
	APPENDIX B CALCULATED PARTICLE CONTACT ANGLE VALUES IN FEED ORE PER SIZE FRACTION	169
	APPENDIX C : MINERAL GROUPS IN COPPER FEED ORE	171
	APPENDIX D : ROUGHER CELLS IN SERIES PLANT FLOWSHEET CONFIGARATION	172
	APPENDIX E : FILE STRUCTURE IN HSC CHEMISTRY 7	173
	APPENDIX F : COPPER 1 BATCH FLOTATION EXPERIMENTAL PROCEDURE	174
	APPENDIX G : FLOTATION CELL SIMULATION INPUT VARIABLES....	175
	APPENDIX H : COPPER 1 AND COPPER 2 FLOTATION FEED ORE BULK PARTICLE WEIGHT DISTRIBUTION.....	176
	APPENDIX I SAMPLE MODEL WIZARD SCREEN CAPTURE IN HSC CHEMISTRY 7.....	182

Figure 2-1:	Mineral transport system in a flotation cell	9
Figure 4-1:	Base case feed ore cumulative particle size distribution.....	59
Figure 4-2:	Chalcopyrite mineral mode of occurrence in Copper 1 feed ore ($P_{70}=120 \mu\text{m}$) used as base case in the simulations.	61
Figure 4-3:	Pyrite mineral mode of occurrence in Copper 1 feed ore ($P_{70}=120 \mu\text{m}$) used as base case in the simulations.	61
Figure 4-4:	NSG mineral mode of occurrence in Copper 1 feed ore ($P_{70}=120 \mu\text{m}$) used as base case in the simulations.	62
Figure 4-5:	Chalcopyrite mineral mode of occurrence in Copper 2 feed ore ($P_{70}=180 \mu\text{m}$) used as base case in the simulations	63
Figure 4-6:	Pyrite mineral mode of occurrence in Copper 2 feed ore ($P_{70}=180 \mu\text{m}$) used as base case in the simulations.	63
Figure 4-7:	NSG mineral mode of occurrence in Copper 2 feed ore ($P_{70}=180 \mu\text{m}$) used as base case in the simulations.	64
Figure 4-8:	Chalcopyrite mineral mode of occurrence in fictional FL artificial feed ore with a P_{70} grind size of $120 \mu\text{m}$	68
Figure 4-9:	Pyrite mineral mode of occurrence in fictional FL artificial feed ore with a P_{70} grind size of $120 \mu\text{m}$	68
Figure 4-10:	NSG mineral mode of occurrence in fictional FL artificial feed ore with a P_{70} grind size of $120 \mu\text{m}$	69
Figure 4-11:	Chalcopyrite mineral mode of occurrence in LC artificial feed ore with a P_{70} grind size of $120 \mu\text{m}$	70

Figure 4-12: Pyrite mineral mode of occurrence in LC artificial feed ore with a P ₇₀ grind size of 120µm.....	71
Figure 4-13: NSG mineral mode of occurrence in LC artificial feed ore with a P ₇₀ grind size of 120 µm.....	71
Figure 4-14: Chalcopyrite mineral mode of occurrence in Ore 1 artificial feed ore with a P ₇₀ grind size of 120 µm.....	73
Figure 4-15: Pyrite mineral mode of occurrence in Ore 1 artificial feed ore with a P ₇₀ grind size of 120 µm.....	73
Figure 4-16: NSG mineral mode of occurrence in Ore 1 artificial feed ore with a P ₇₀ grind size of 120 µm.....	74
Figure 4-17: Chalcopyrite mineral mode of occurrence in fictional Ore 2 artificial feed ore with a P ₇₀ grind size of 120 µm.....	75
Figure 4-18: Pyrite mineral mode of occurrence in fictional Ore 2 artificial feed ore with a P ₇₀ grind size of 120 µm.....	76
Figure 4-19: NSG mineral mode of occurrence in fictional Ore artificial feed ore with a P ₇₀ grind size of 120 µm.....	76
Figure 4-20: Chalcopyrite mineral mode of occurrence in Ore 3 artificial feed ore with a P ₇₀ grind size of 120 µm.....	78
Figure 4-21: Pyrite mineral mode of occurrence in Ore 3 artificial feed ore with a P ₇₀ grind size of 120 µm.....	78
Figure 4-22: NSG mineral mode of occurrence in Ore 3 artificial feed ore with a P ₇₀ grind size of 120 µm.....	79
Figure 4-23: Comparison of contact angle values calculated using the weight composition % against those calculated utilising the surface area %.....	85
Figure 4-24: Contact angle variation with mineral particles liberation class for all feed particle size fractions.....	85
Figure 4-25: Comparison mineral recovery values obtained using the weight composition % calculated contact angles in the flotation model against those calculated utilising the surface area % calculated contact angles.....	86
Figure 5-1: Simulated batch flotation mineral recovery for Copper 1 BC feed.....	88
Figure 5-2: Experimentally determined batch flotation cell mineral recovery for Copper 1.....	89
Figure 5-3: Single unit flotation cell flow sheet simulation layout in HSC Chemistry 7 Simulation software.....	91
Figure 5-4: Chalcopyrite mineral mode of occurrence in Copper 1 base case feed ore stream to the single flotation cell flow sheet simulation. From Figure 5-4 it can be observed that most of the fully liberated Chalcopyrite in the Copper 1 ground ore feed is found between the 0 to 75 µm size fractions.....	92
Figure 5-5: Chalcopyrite mineral mode of occurrence in Copper 1 base case concentrate product stream from the single flotation cell flow sheet simulation.....	93
Figure 5-6: Chalcopyrite mineral mode of occurrence in Copper 1 base case ore tails product stream from the Single flotation cell flow sheet simulation.....	93
Figure 5-7: Mineral recovery against particle size for a Single flotation Cell simulation (Copper 1 BC feed).....	94
Figure 5-8: Particle class recovery per size fraction in the concentrate stream against Cpy wt %.....	95
Figure 5-9: Particle class recovery per size fraction in the tails stream against Chalcopyrite wt % range in particle classes.....	95
Figure 5-10: Cumulative liberation of Chalcopyrite in feed stream to the Single Unit flotation Cell flow sheet simulation.....	96

Figure 5-11: Cumulative liberation of Chalcopyrite in the output tail stream from the Single Unit flotation Cell flow sheet simulation.....	96
Figure 5-12: Cumulative liberation of Chalcopyrite in the output concentrate stream from the Single Unit flotation Cell flow sheet simulation.....	97
Figure 5-13: Chalcopyrite recovery against particle size for a single flotation Cell simulation for all the feed ore liberation scenarios considered in the simulations ($P_{70}=120\ \mu\text{m}$).....	100
Figure 5-14: Pyrite recovery against particle size for a Single flotation Cell simulation for all the feed ore liberation scenarios considered in the simulations, ($P_{70}=120\ \mu\text{m}$).	101
Figure 5-15: Pyrite recovery against particle size for a Single flotation Cell simulation for all the feed ore liberation scenarios considered in the simulations, ($P_{70}=120\ \mu\text{m}$).	102
Figure 5-16: Mean Stability efficiency against mean particle size for feed ore with a $P_{70} = 120\ \mu\text{m}$	104
Figure 5-17: Mean Stability efficiency against mean particle size for Base Case ore and the two extreme liberation cases (FL and LC), for feed ore with a $P_{70} = 120\ \mu\text{m}$	105
Figure 5-18: Mean attachment efficiency against mean particle size for feed ore with a $P_{70} = 120\ \mu\text{m}$	105
Figure 5-19: Mean Attachment efficiency against mean particle size for Base Case ore and the two extreme liberation cases (FL and LC), for feed ore with a $P_{70} = 120\ \mu\text{m}$	106
Figure 5-20: Chalcopyrite recovery against particle size for a Single flotation Cell simulation for all the feed ore liberation scenarios considered in the simulations, ($P_{70}=180\ \mu\text{m}$).....	107
Figure 5-21: Pyrite recovery against particle size for a Single flotation Cell simulation for all the feed ore liberation scenarios considered in the simulations, ($P_{70}=180\ \mu\text{m}$).	108
Figure 5-22: Mean Stability efficiency against mean particle size for feed ore with a $P_{70} = 180\ \mu\text{m}$	109
Figure 5-23: Mean attachment efficiency against mean particle size for feed ore with a $P_{70} = 180\ \mu\text{m}$	110
Figure 5-24: Chalcopyrite recovery against particle size for a Single flotation Cell ($P_{70}=63\ \mu\text{m}$).....	111
Figure 5-25 : Chalcopyrite recovery against particle size for a Single flotation Cell simulation ($P_{70}=250\ \mu\text{m}$).	112
Figure 5-26: Cumulative particle weight distribution plot of the various P_{70} grind sizes that were considered in the simulations.	114
Figure 5-27: Overall single cell unit recovery against particle size for feed ore with varying size distributions.	116
Figure 5-28: Concentrate mass recovery in a Single cell plotted against feed ore into the cell with varying size distributions.	117
Figure 5-29: Enrichment ration in a Single cell plotted against feed ore into the cell with varying size distributions.	117
Figure 6-1: Cumulative value Copper recovery as a function of cell number in the rougher flotation section of a Simulated fictional plant.	120
Figure 6-2: Cumulative value Copper recovery as a function of cell number in the rougher flotation section of an operating plant (Yianatos et al., 2006).....	121
Figure 6-3: Concentrate mass recovery as a function of cell number in the rougher flotation section of simulated fictional plant.	121
Figure 6-4: Concentrate mass recovery as a function of cell number in the rougher flotation section of an operating plant (Yianatos et al., 2006)	122
Figure 6-5: Local and cumulative copper grade profile as a function of cell number for a fictional copper plant	122
Figure 6-6: Comparison of Cu cumulative recovery per cell in a Rougher bank for different feed ore scenarios.....	125

Figure 6-7: Comparison of Cu cumulative recovery per cell in a Rougher bank for the base case and extreme feed ore scenarios.	125
Figure 6-8: Comparison of Pyrite cumulative recovery per cell in a Rougher bank for the base case and extreme feed ore scenarios.	126
Figure 6-9: Comparison of concentrate mass recovery per unit cell in a Rougher bank for different feed ore scenarios.	127
Figure 6-10: Comparison of Cu local grade per unit cell in a Rougher bank for different feed ore scenarios.	128
Figure 6-11: Comparison of Cu cumulative grade per unit cell in a Rougher bank for different feed ore scenarios.	128
Figure 6-12: Comparison of overall rougher bank value mineral enrichment ratio for different feed ore scenarios.	129
Figure 6-13: Comparison of Cu cumulative recovery per cell in a Rougher bank for different feed ore scenarios.	130
Figure 6-14: Comparison of Cu cumulative recovery per cell in a rougher bank for the base case and extreme feed ore scenarios.	131
Figure 6-15: Comparison of Pyrite cumulative recovery per cell in a Rougher bank for the base case and extreme feed ore scenarios.	132
Figure 6-16: Comparison of concentrate mass recovery per unit cell in a Rougher bank for different feed ore scenarios.	133
Figure 6-17: Comparison of Cu local grade per unit cell in a Rougher bank for different feed ore scenarios.	133
Figure 6-18 : Comparison of Cu Cumulative grade per unit cell in a Rougher bank for different feed ore scenarios ($P_{70} = 180 \mu\text{m}$).	134
Figure 6-19: Comparison of overall rougher bank value mineral enrichment ratio for different feed ore scenarios.	134
Figure 6-20: Overall a nine cell in series rougher bank recovery against particle size for feed ore grind size.	136
Figure 6-21: Concentrate mass recovery for a nine cell in series Rougher bank plotted against feed ore into the rougher section with varying feed grind size.	137
Figure 6-22: Enrichment ratio for a nine cell in series rougher bank plotted against feed ore into the rougher section with varying size distributions.	138
Figure 6-23: Cumulative Cu value mineral recovery as a function of cell number for a rougher bank processing BC, FL and LC feed ores.	139
Figure 6-24: Cumulative copper grade profiles as a function of cell for a rougher bank processing BC, FL and LC feed ores.	139
Figure 6-25: Cumulative Cu value mineral recovery as a function of cell number for a rougher bank processing BC, FL and LC feed ores.	140
Figure 6-26: Cumulative copper grade profiles as a function of cell number for a rougher bank processing BC, FL and LC feed ores.	140
Figure 6-27: Cumulative Cu value mineral recovery as a function of cell number in the rougher section of a fictional simulated nine cell in series flotation plant processing BC, FL and LC feed ore with a P_{70} grind size of $252\mu\text{m}$	142
Figure 6-28: Cumulative copper grade profiles as a function of cell for a rougher bank processing BC, FL and LC feed ores.	142
Figure 6-29: Cumulative Cu value mineral recovery as a function of cell number for a rougher bank processing BC, FL and LC feed ores.	143
Figure 6-30: Cumulative copper grade profiles as a function of cell number for a rougher bank processing BC, FL and LC feed ore.	144

Figure 6-31: Cumulative Cu value mineral recovery as a function of cell number for a rougher bank processing BC, FL and LC feed ores.....	144
Figure 6-32: Local and cumulative copper grade profiles as a function of cell number for a rougher bank processing BC, FL and LC feed ores.....	145
Figure A.1-1: Chalcopyrite mineral mode of occurrence in FL feed ore ($P_{70}=180\ \mu\text{m}$) used in the simulations.	161
Figure A.1-2: Pyrite mineral mode of occurrence in FL feed ore ($P_{70}=180\ \mu\text{m}$) used in the simulations.	161
Figure A.1-3: NSG mineral mode of occurrence in FL feed ore ($P_{70}=180\ \mu\text{m}$) in the simulations.	162
Figure A.1-4: Chalcopyrite mineral mode of occurrence in LC feed ore ($P_{70}=180\ \mu\text{m}$) used in the simulations.	162
Figure A.1-5: Pyrite mineral mode of occurrence in LC feed ore ($P_{70}=180\ \mu\text{m}$) used in the simulations.	163
Figure A.1-6: NSG mineral mode of occurrence in LC feed ore ($P_{70}=180\ \mu\text{m}$) used in the simulations.	163
Figure A.1-7: Chalcopyrite mineral mode of occurrence in Ore 1 feed ore ($P_{70}=180\ \mu\text{m}$)...	164
Figure A.1-8: Pyrite mineral mode of occurrence in Ore 1 feed ore ($P_{70}=180\ \mu\text{m}$).....	164
Figure A.1-9: NSG mineral mode of occurrence in Ore 1 feed ore ($P_{70}=180\ \mu\text{m}$).	165
Figure A.1-10: Chalcopyrite mineral mode of occurrence in Ore 2 feed ore ($P_{70}=180\ \mu\text{m}$).	165
Figure A.1-11: Pyrite mineral mode of occurrence in Ore 2 feed ore ($P_{70}=180\ \mu\text{m}$).....	166
Figure A.1-12: NSG mineral mode of occurrence in Ore 2 feed ore ($P_{70}=180\ \mu\text{m}$).	166
Figure A.1-13: Chalcopyrite mineral mode of occurrence in Ore 3 feed ore ($P_{70}=180\ \mu\text{m}$).	167
Figure A.1-14: Pyrite mineral mode of occurrence in Ore 3 feed ore ($P_{70}=180\ \mu\text{m}$).....	167
Figure A.1-15: NSG mineral mode of occurrence in Ore 3 feed ore ($P_{70}=180\ \mu\text{m}$).	168
Figure B.1-1: Contact angle variation with particle liberation class for liberation particle classes in the 0-38 μm size fraction.	169
Figure B.1-2: Contact angle variation with particle liberation class for liberation particle classes in the 106-150 μm size fractions.	169
Figure B.1-3: Contact angle variation with particle liberation class for liberation particle classes in the 300-425 micron size fraction.	170
Figure D.1-1: Rougher cell flow sheet configuration that was used in the study.....	172
Figure E.1-1: File structure in HSC Sim in the Particle (Minerals) Mode adapted from HSC Chemistry 7 manual (Roine, 2010).....	173
Figure I.1-1: Sample screen capture of model wizard screen as it would appear in HSC Chemistry 7.....	182
Figure I.1-2: Sample HSC Chemistry Simulation macro commands in HSC Chemistry 7 that form part of the model wizard.	183
Table 2-1: Summary of expressions describing the floatability component method.....	15
Table 2-2: Summary of expressions for obtaining pulp kinetics utilising the MFT test procedure.....	16
Table 2-3: Summary of collision efficiency models found in literature.....	20
Table 2-4: Summary of sliding models found in literature.....	25
Table 2-5: Summary of factors that affect entrainment.....	32
Table 2-6: Summary of methods for obtaining froth zone recovery	35
Table 2-7: Summary of water recovery models found in literature.....	37
Table 3-1: Summary of the mechanical and primary turbulence terms expressions.....	44
Table 3-2: Model calibration parameters from a study carried out by (Ralston et al., 2007)..	50

Table 4-1: Base case feed ore particle size distribution of Copper 1 ($P_{70}=120 \mu\text{m}$) and Copper 2 ($P_{70}=180 \mu\text{m}$).....	59
Table 4-2 : Mineral composition by size fraction of Copper 1 base case feed ore $P_{70}=120 \mu\text{m}$	60
Table 4-3: Mineral composition by size fraction of Copper 2 base case feed ore $P_{70}=180 \mu\text{m}$	62
Table 4-4: HSC Chemistry 7 feed ore stream file showing liberation profile for particle liberation classes in the 0-38 μm size fraction.....	65
Table 4-5: A summary of the feed ore scenarios that were used in investigating the effects of feed ore liberation changes on the downstream flotation process.	66
Table 4-6: Differences in liberation classes' weights in FL artificial ore expressed as a percentage of Copper 1 base case feed ore liberation classes.....	67
Table 4-7: Differences in liberation classes' weights in LC artificial ore expressed as a percentage of Copper 1 base case feed ore liberation classes.....	70
Table 4-8: Differences in liberation classes' weights in Ore 1 artificial ore expressed as a percentage of Copper 1 base case feed ore liberation classes.....	72
Table 4-9: Differences in liberation classes weights in Ore 2 artificial ore expressed as a percentage of Copper 1 base case feed ore liberation classes.....	75
Table 4-10: Differences in liberation classes' weights in Ore 3 artificial ore expressed as a percentage of Copper 1 base case feed ore liberation classes.....	77
Table 4-11: Differences in liberation classes' weights in FL liberated artificial ore expressed as a percentage of Copper 2 base case feed ore liberation classes	80
Table 4-12: Differences in liberation classes' weights in LC liberated artificial ore expressed as a percentage of Copper 2 base case feed ore liberation classes	81
Table 4-13: Differences in liberation classes' weights in Ore 1 liberated artificial ore expressed as a percentage of Copper 2 base case feed ore liberation classes.....	82
Table 4-14: Differences in liberation classes' weights in Ore 2 liberated artificial ore expressed as a percentage of Copper 2 base case feed ore liberation classes	82
Table 4-15: Differences in liberation classes' weights in Ore 3 liberated artificial ore expressed as a percentage of Cu 2 base case feed ore liberation	83
Table 5-1: Summary of input parameter values used in simulating experimental batch flotation test carried out on the Copper 1BC feed	88
Table 5-2: Feed and literature hydrodynamic variables that were used in simulating a Single flotation cell flow sheet operation.....	90
Table 5-3: Summary of Single flotation cell flow sheet simulation grade recovery and mass full performance indicators results.....	91
Table 5-4: Feed and literature hydrodynamic variables that were used in simulating a Single flotation cell flow sheet operation.....	99
Table 5-5: Simulated flotation process key performance parameters for the six feed ore scenarios that were considered for the base case grind size $P_{70}=120$ microns	103
Table 5-6: Simulated flotation process key performance parameters for the six feed ore scenarios that were considered for the base case grind size $P_{70}=180$ microns	109
Table 5-7: Fictional average fine particle sizes and used in the sensitivity analysis investigations ($P_{70} = 63 \mu\text{m}$)	111
Table 5-8: Fictional average coarse particle size distribution ($P_{70} = 250\mu\text{m}$).....	112
Table 5-9: Particle cumulative weight distribution of the different feed ores considered in carrying out the feed particle weight distribution sensitivity analysis.....	114
Table 5-10: Cu% feed grades at different feed grind sizes	115
Table C.1-1: Main mineral groups in feed ores and their grouping.....	171
Table C.1-2: Mineral groups in feed ores	171

Table G.1-1: Input variables used in calibrating the fundamental property based model in simulating the flotation process.	175
Table H.1-1: 0-38 μm bulk particle size class weight % for Copper 1 flotation feed ores ($P_{70} = 120 \mu\text{m}$).....	176
Table H.1-2: 38-53 μm bulk particle size class weight % for Copper 1 flotation feed ores ($P_{70} = 120 \mu\text{m}$).....	176
Table H.1-3: 53-75 μm bulk particle size class weight % for Copper 1 flotation feed ores ($P_{70} = 120 \mu\text{m}$).....	176
Table H.1-4: 75-106 μm bulk particle size class weight % for Copper 1 flotation feed ores ($P_{70} = 120 \mu\text{m}$)	177
Table H.1-5: 106-150 μm bulk particle size class weight % for Copper 1 flotation feed ores ($P_{70} = 120 \mu\text{m}$)	177
Table H.1-6: 150-212 μm bulk particle size class weight % for Copper 1 flotation feed ores ($P_{70} = 120 \mu\text{m}$)	177
Table H.1-7: 212-300 μm bulk particle size class weight % for Copper 1 flotation feed ores ($P_{70} = 120 \mu\text{m}$)	178
Table H.1-8: 300-425 μm bulk particle size class weight % for Copper 1 flotation feed ores ($P_{70} = 120 \mu\text{m}$)	178
Table H.2-1: 0-38 μm bulk particle size class weight % for Copper 2 flotation feed ores ($P_{70} = 180 \mu\text{m}$).....	179
Table H.2-2: 38-53 μm bulk particle size class weight % for Copper 1 flotation feed ores ($P_{70} = 180 \mu\text{m}$).....	179
Table H.2-3: 53-75 μm bulk particle size class weight % for Copper 1 flotation feed ores ($P_{70} = 180 \mu\text{m}$).....	179
Table H.2-4: 75-106 μm bulk particle size class weight % for Copper 1 flotation feed ores ($P_{70} = 180 \mu\text{m}$)	180
Table H.2-5: 106-150 μm bulk particle size class weight % for Copper 1 flotation feed ores ($P_{70} = 180 \mu\text{m}$)	180
Table H.2-6: 150-212 μm bulk particle size class weight % for Copper 1 flotation feed ores ($P_{70} = 180 \mu\text{m}$)	180
Table H.2-7: 212-300 μm bulk particle size class weight % for Copper 1 flotation feed ores ($P_{70} = 180 \mu\text{m}$)	181
Table H.2-8: 300-425 μm bulk particle size class weight % for Copper 1 flotation feed ores ($P_{70} = 180 \mu\text{m}$)	181
Table H.2-9: 425-850 μm bulk particle size class weight % for Copper 1 flotation feed ores ($P_{70} = 180 \mu\text{m}$)	181

iii. NOMENCLATURE

Alphabetic Symbols

- A - cross sectional area of the pulp-froth interface [m^2]
a - empirically fitted parameter in the water recovery model
 A_s - is an empirical dimensionless constant with a value of 0.5
b - empirically fitted parameter
 C_a - Concentration of mineral A [$tons/m^3$]
 CF_i - classification function
 C_{Water} - Amount of water in the concentrate [tons]
 d_{32} - Sauter mean bubble diameter [m]
 d_b - Bubble size [m]
 d_p - is the particle size [m]
 d_{pb} - is the bubble-particle aggregate diameter [m]
 E_1 - the potential energy barrier of a particle approaching a bubble [J]
 E' - is the volumetric flow of entrained material [$tons/ m^3$]
 E_a - Attachment efficiency
 E_c - Collision efficiency
 E_{coll} - collection efficiency
 E_{C-PL}^{in} -inertial effect
 E_{C-WP}^g - gravitational effects
 E_K -kinetic energy of a particle approaching a bubble [J]
 ENT_i -degree of entrainment
 E_s - Stability efficiencies efficiency
 E_{Sc}^{ic} -Interceptional effect
 F_{att} -attachment forces
 F_b -Buoyancy of the particle volume immersed in the liquid phase [N]
 F_c -capillary force [N]
 F_d -is the additional detaching forces [N]
 F_{det} -Detachment forces [N]
 F_g -gravitational force [N]
 F_h -Hydrostatic pressure force on the area enclosed by the three-phase contact [N]
 F_S -is the mass flow rate of the solid [N]

F_{Water} -Water contained in the feed [N]
 F_{σ} - is the capillary pressure in the bubble [N]
 g -Acceleration due to gravity [m/s^2]-
 G_{fr} -gas flow rate and the [m^3/min]
 J_g -Superficial gas velocity [m/s]
 k -Overall first order rate constant [min^{-1}]
 k_{avg} -the weighted average flotation rate, excluding un-floatable particles [min^{-1}]
 k_c -Collection zone first order rate constant [min^{-1}]
 K_i -is the flotation is rate constant of particles of diameter I [min^{-1}]
 k_{ij} -rate parameter for jth mineral phase from in ith size fraction [min^{-1}]
 k_j -rate parameter for jth mineral phase [min^{-1}]
 k_n - nth order rate constant [min^{-1}]
 k_{wd} -drainage rate constant of the water [min^{-1}]
 L -half the impeller blade width [m]
 M_{conc} -Mass of solids suspended in the water in the concentrate [tons]
 M_{pulp} -Mass of solids suspended in the water in the pulp phase [tons]
 n -order of reaction
 N_b -bubble number density [m^{-3}]
 N_p -number of particles per unit volume [m^{-3}]
 P_{ij} -Ore floatability for component j in the ith size fraction
 $P(k_j)$ -Cumulative weight per cent
 P_w -constant for a given flotation system
 q -turbulent kinetic energy [J]
 Q_w -is the volumetric flow rate of water [tons/s]
 r_b -bubble radius [m]
 R_{cw} -is the recovery of the water from the pulp
 R_{eb} - reynolds number
 $R_{\text{entrainment},i}$ -determining recovery by entrainment
 R_f -Froth recovery
 R_{ij} -Recovery of jth mineral phase from ith size fraction
 $R_{\text{max},i}$ - is the flotation recovery at an infinite time
 r_p -are the particle radius [m]

- R_w - water recovery
 $R_{\infty i,j}$ -Ultimate recovery of jth mineral phase from ith size fraction
 S_b -bubble surface area flux [s^{-1}]
 SG_p -is the specific gravity of the slurry
 SG_s - is the specific gravity of the solids
 SG_w -is the specific gravity of the water
 t - Flotation time [s]
 t_{fl} -film drainage time [s]
 t_{fr} -bubble-particle film rupture time [s]
 (t_{ind}) - induction time [s]
 t_r - residence time of bubbles in the unit volume [s]
 t_{TPLC} -three-phase contact line expansion and stabilization time [s]
 $\bar{U}_x, \bar{U}_y, \bar{U}_z$ -root mean square of fluctuations of the turbulent fluid velocities [m/s]
 V - is the froth volume [m^3]
 v_b -Bubble rising velocity [m/s]
 v_p -Bubble rising velocity [m/s]
 V_{fl} -average fluid velocity [m/s]
 V_x^2, V_y^2, V_z^2 -Velocity measurements in the x,y,z direction [m/s]
 Z_{pb} -is the collision frequency per unit volume between particles and bubbles

Greek Symbols

- α -a measurement of the spread in the k-distribution
 α -fraction of the froth on the surface that eventually reports to the concentrate
 α_a -fraction of air leaving the cell as un-burst bubbles
 β -dimensionless number in the Generalised Sutherland Equation
 β_w -constant in water recovery model [s^{-1}]
 $\gamma_{s/a}, \gamma_{s/l}, \gamma_{l/a}$ -solid-vapour, solid-liquid, and liquid-vapour interfacial tensions [N/m]
 ε -turbulent dissipation energy [m^2/s]
 η -water dynamic viscosity [m^2/s]
 θ -contact angle [rad]
 θ_a -adhesion angle [rad]
 θ_c -collision angle [rad]

θ_t	-is the maximum collision angle [rad]
ρ_i	-refers to the density of the bubble or particle [kg/m ³]
ρ_w	-water density [kg/m ³]
$\Delta\rho$	-is the density difference between the solid and liquid [kg/m ³]
$\Delta\rho_b$	-particle and fluid density diff [kg/m ³]
ρ_{fl}	-fluid density [kg/m ³]
ρ_p	-particle density [kg/m ³]
ψ_c^0	-value of stream function of the bubble equator [-]
ψ_c	- value of streamline stream function that coincides with the grazing trajectory [-]
ω_{top}	-is the solids mass fraction below the pulp-froth interface [-]
τ	-residence time in the unit [s]
τ_f	-mean froth residence time [s]
μ_s	-is the interstitial slurry viscosity [m ² /s]
Ω ,	-constant value in first order water recovery model [-]
q	-constant values in first order water recovery model [m ⁻³]
χ	-constant value in first order water recovery model [s ⁻¹]
δ	-the volume of water per surface area of the air bubbles [m]
ϑ	-is the kinematic viscosity [m ² /s]
Θ	-kinematic viscosity [m ² /s]
γ	-Surface tension [N/m]

CHAPTER ONE

1. INTRODUCTION

Microwave assisted comminution has been recommended as a possible commercially viable thermal treatment method for reducing comminution energy and improving value mineral liberation in the ores (Haque, 1999; Kingman and Rowson, 1998). Recent work has shown that microwave treatment of secondary crusher product at specific microwave energy consumption of the order of 1 kWh/t reduces the work index of the ore and increases grade and recovery in batch flotation tests (Kobusheshe, 2010). Improved liberation at coarse sizes was also demonstrated (Scott et al., 2008). Based on these findings work is ongoing to commercialise the technology. However, before the technology can be commercialised, key issues surrounding the industrial scale application of microwave assisted comminution need to be addressed. One of these issues is assessing the benefits of microwave treatment on downstream processing of ores.

The study of the downstream processing benefits of microwave treated ore on an operating plant is an area that has not been well researched (Kingman, 2006). This is in contrast to investigations into the benefits relating to reduced comminution energy due to microwave treatment which have been reported by a number of authors (Kingman et al., 2000a; Kingman et al., 2004b; Jones et al., 2005). The limited research has been the result of the technical and operational difficulties associated with assessing the improvement in feed ore liberation properties due to microwave treatment on an operating plant and quantifying the downstream processing benefits. Further, appropriate microwave applicators with the ability to treat continuous feed ore input on a plant scale have not been designed yet (Kobusheshe, 2010; AMIRA:P879A, 2009). To overcome such challenges, ideally, modelling techniques could offer a solution to these problems (Scott et al., 2008). There is therefore a need to develop a modelling framework for investigating the value proposition of microwave treated ore.

Current available models for describing flotation mineral processing operations do not include feed ore particle liberation as an input parameter. This is because most of the models were developed to simulate the behaviour of feeds derived from comminution processes which resulted from random fracture of the ore particles (Ali and Bradshaw, 2009). The use of microwave treatment has been observed to result in non random fracture of feed ore particles, preferentially along the grain boundaries during crushing hence resulting in a more

liberated comminution product to the flotation section (Kingman et al., 2000a). Thus, when modelling the downstream processing of microwave treated ore in a mineral processing flow sheet, feed liberation is an important variable. It is therefore necessary to develop a modelling framework for quantifying the benefits of microwave treated ore that captures this important variable.

The development of Mineral Liberation Analysers and simulation software that utilises MLA data as input in modelling mineral processes presents an opportunity for investigating the downstream processing effects of microwave treated ore through the use of process modelling and simulation techniques. These software packages such as HSC Chemistry 7.0 Simulation Software utilise what is termed as true particle modelling for simulating mineral processing operations. True particle modelling allows for the use of algorithms for tracking feed ore particles as represented in the MLA feed data to the software through the flotation circuit (Roine, 2010). This allows for liberation properties of the streams around the circuit to be analysed and for the use of liberation as an input variable in the flow sheet units modelling. However, models for unit operations that capture the effects of liberation property of the feed are in general yet to be integrated into these software packages. Of particular importance in establishing the value proposition for microwave treatment of ore would be the ability to model the effects of liberation explicitly in a flow sheet simulator. At present such models exist, e.g. the fundamental property based model for describing the flotation process (Pyke et al., 2003). However their incorporation into a flow sheet modelling package to utilise particle class tracking behaviour has not yet been achieved. The incorporation of such a model into an appropriate simulation package would allow for the simulation of a flotation plant flow sheet for investigating the value proposition of microwave treated ore.

Fundamental property based models offers the possibility of predicting flotation rate constants and hence flotation cell recovery of the particles from hydrodynamic and particle based properties. The model factors in mineral liberation as an input variable in the calculations (Pyke et al., 2003). The inclusion of the mineral liberation property is essential as liberation is the main difference between microwave treated and untreated ores. The model allows for the prediction of the flotation behaviour of each individual particle unlike the traditional methods that calculate recovery on a size fraction basis. Such models have not yet been adapted in most commercial modelling software. This thesis applies the fundamental property based model to MLA data. There is no reported work that has attempted to apply the model in true particle modelling.

Study aims and objectives

The aim of the study was to develop a modelling framework to determine the value proposition of microwave treatment of ore. This was to be done by incorporating a fundamental property based model into a flow sheet simulator. Using the framework it was the further objective of this work to investigate the effects of flotation feed ore liberation and grind size variation on a simulated single flotation cell and rougher bank flow sheet. By utilizing MLA data for real flotation feeds, various feed ore liberation scenarios and grind sizes were to be artificially generated by manipulating the liberation and grind size characteristics of typical industrial flotation feed ores. These generated artificial feed ores along with the typical flotation feed ores were then to be used in investigating the downstream flotation processing behavior of microwave enhanced liberated flotation feed ore. The work carried out in the study is presented as follows:

- Chapter 2 - A literature review of work performed in the field of microwave assisted comminution is presented in this chapter. This is followed by a literature review of flotation modelling in mineral processing.
- Chapter 3 - A description of the fundamental property model used in this study is presented in this chapter along with a presentation of the parameters that were used to calibrate the model. A review of HSC Chemistry Software and its operation is presented along with the method that was used to integrate the fundamental property based model into the software.
- Chapter 4 - A description of the feed ores used in this study is detailed in this chapter. The method that was used in creating artificial feed ore is discussed in this chapter.
- Chapter 5 - The results of simulations carried out on a Single Rougher flotation cell flow sheet utilising various ore feeds is presented in this chapter along with a discussion of these results.
- Chapter 6 - The results of simulations carried out on a fictional Rougher bank flotation cell flow sheet utilising various ore feeds is presented in this chapter along with a discussion of these results.
- Chapter 7 - This chapter presents the conclusions drawn from this study along with recommendations for future studies.

CHAPTER TWO

2. LITERATURE REVIEW

2.1. Comminution process optimisation

The extraction of mineral values from ore requires liberation of the minerals followed by separation. Liberation is achieved by size reduction operations which are inefficient processes, typically accounting for up to 70% of the energy consumption in a mineral concentrator (Tromans, 2008). The major cause of the inefficiency of the comminution process is the transformation of some of the mechanical energy into heat and noise in transmissions and friction processes among particles that do not result in their breakage. As the grade of ore reserves declines future viability of mineral operations will be determined by the costs of comminution. Research over the years has focused developing technologies that reduce the energy of comminution in the process resulting in increased liberation of value minerals. The extra revenue realised from increased value mineral recovery due to improved liberation, will be the trade off to the capital required to implement and install these methods (Haque, 1999; Kingman et al., 2004c; Kingman and Rowson, 1998; King, 1993).

Thermal pre-treatment has been an option that has been considered as a possible way of improving mineral liberation and reducing mineral ore strength hence energy of comminution (King, 1993; Haque, 1999). This is because different mineral phases in an ore have different microwave absorption and varying thermal expansion rates. Thus, thermal heating of mineral ores results in micro cracks in the ore matrix due to the difference in microwave absorption and thermal expansion rates. These micro cracks are induced around the grain boundaries resulting in reduced fracture strength of the ores and greater liberation of value mineral. Over years thermal treatment has not been a viable option due to inefficient heating methods which resulted in more energy being used during heating thereby cancelling any gains in strength reduction during comminution (Kingman and Rowson, 1998).

The benefits associated with microwave heating over conventional heating methods such as selective heating , faster heating rates and no direct contact between heating source and the heated material has resulted in renewed interest in thermally assisted comminution. Research has shown that microwave assisted comminution is possibly a commercially viable thermal treatment method for reducing comminution energy and improving value mineral liberation in the ores (Kingman, 2006).

2.1.1. Developments in microwave heating of ores

The first attempt at applying microwave technology in mineral processing reported in literature by Ford and Pei (1967) cited in Kobusheshe (2010) was in 1967. In this study microwave energy was used to heat reagent grade metal oxides and sulphides at energy inputs of between 50-200W and at a frequency of 2.45GHz. Findings from these studies were that dark coloured compounds heated rapidly compared to light coloured compounds that heated at slower rates. The results although not comprehensive, paved the way for further studies on possible applications of microwaves in mineral processing (Haque, 1999).

Several preliminary investigations on microwave heating of mineral were reported between the late 60s and late 90s. Wong (1975) cited in Haque (1999) reported on the microwave heating behaviour of metal oxides. The results indicated that microwave energy was an effective heating method for heating minerals. Chen et al. (1984) cited in Kingman and Rowson (1998) investigated the heating behaviour of forty minerals individually with microwaves in a waveguide applicator. The major findings from this study were that silicates, carbonates and sulphates were transparent to microwave heating in contrast to metal sulphides and some oxides that were easily heated by microwave energy. These results indicated the selective nature of microwave heating and the potential application of this selective heating in mineral processing as a means of reducing required energy of comminution (Kingman and Rowson, 1998).

The US Bureau of mines carried out detailed and qualitative studies on the characteristics of microwave heating of minerals and reagent grade inorganic compounds. Results similar to those obtained by Chen et al. (1984) were reported (Walkiewicz et al., 1988). The results further confirmed that microwave heating was dependent on the mineral composition with gangue minerals such as quartz, calcite and feldspar being transparent to microwave heating. Rapid heating of ore minerals within a non heating matrix was observed which resulted in the generation of thermal stresses that led to cracks along the mineral boundaries. The studies gave initial indication of the application of microwave pre-treatment of ores in mineral processing as a means of reducing the energy of comminution and improving value mineral liberation. Results similar to those obtained by the US Bureau of mines were reported by a number of authors during the same period and became the basis of subsequent studies that focused on microwave assisted comminution (Kingman and Rowson, 1998).

2.1.2. Microwave assisted comminution in mineral processing

Kingman (2000) carried out studies on commercially exploited ores. After conducting mineralogical analysis on the ores and establishing the textural relationship between the ore phases, each ore was then microwave treated with varying exposure times for each sample. The results showed an increase in grindability of the ores after microwave treatment. This increase in grindability was related to the specific mineral present in the ores that is microwave absorber and non absorber and the grain size of the phase. The results showed improvements in grindability at high microwave energy inputs of 14.3 kWh/t. This input was less than the grinding energy required input of 20 kWh/t. These results highlighted the possibility of carrying microwave assisted comminution at potentially viable microwave energy inputs (Kingman et al., 2000b).

In the same year, Kingman et al. (2000) reported results of investigations on the effects of microwave treatment on the processing of Palabora ore. The studies not only showed enhanced grindability due to microwave treatment but also demonstrated that increases in recovery of copper after froth flotation could be obtained. Scanning Electron Microscopy analysis showed significant intergranular fracture in the ore. At long exposure times reduction in copper grades were observed which suggested surface oxidation of the sulphides owing to high temperatures. The potential benefit of reduced bond work index due to microwave treatment on a grinding circuit was also investigated in the same study. This was done by simulating a closed circuit ball mill grinding plant and reducing the bond work index of the ore to a value less than the typical operating plant's value. The impact of the reduced work index value on the circulating load was then analysed. The simulations showed that microwave assisted comminution had the potential to reduce the grindability by as much as 2 kWh/t. These studies further showed that the technical feasibility of microwave assisted comminution. The influences of microwave variables such as power density and heating time on the process however were still not well understood (Kingman et al., 2004c).

Whittles et al. (2003) conducted studies to predict the influence of power density on strength reduction by applying numerical modelling methods. In the study, a binary phase ore was simulated which consisted of an absorbing phase and transparent host represented by pyrite and calcite respectively. Numerical simulations were then applied to assess the influence of applied power density on the strength of the simulated ore. The results showed that at higher power density and shorter exposure time heat lost by conduction was minimised.

The major findings from this study was that by increasing the power density, significantly greater thermally induced stresses and strain were induced at lower microwave energy input. (Whittles et al., 2003)

Experimental studies to investigate the effects of high electric field strength on a copper carbonatite ore were carried out in order to validate results of the numerical simulations. Using point load test it was shown that short microwave exposure times (0.1 to 1s) at high power density (10^{11} W m^{-3}) could lead to significant reductions in ore strength (Kingman et al., 2004a). The studies further showed that a 30% reduction in required energy of comminution was possible at microwave energy inputs less than 1kWh/t (Kingman et al., 2004a; Kingman, 2006). A significant increase in grindability at larger particle sizes was also shown at low microwave energy input values of around 0.83 kW h t^{-1} . Using quantitative analysis of materials with Scanning Electron Microscopy analysis it was shown that microwave treatment resulted in coarse liberation of value mineral in the ore. It was concluded from the study that microwave assisted comminution resulted in significant changes in ore breakage behaviour and liberation characteristics at economically feasible microwave power inputs (Kingman et al., 2004a). Similar results supporting these conclusions were obtained on further studies that were carried out on samples of Lead-Zinc ore (Kingman et al., 2004b).

Having established the benefits of microwave treatment of ore on the grinding process work was then carried out to investigate the downstream effects of microwave treatment of ore (Kingman et al., 2004c). Kingman et al. (2004c) reported a significant increase in chalcopyrite liberation at coarser sizes ($+500 \mu\text{m}$). From these findings microwave treatment of ore was suspected to increase value mineral liberation and hence overall recovery. Amankwah, Pickles and Yen (2005) reported an increase in gold recovery of microwave treated refractory gold ores. Wang et al. (2000) also reported an increase in liberation of low Copper grades after microwave treatment.

Groves et al. (2007) investigated the potential for improved liberation of low grade copper ore through microwave treatment. Microwave power of 3 kW at 2.45 GHz was used to treat the ore sample for 120 s. The tests showed a shift from transgranular fracture to intergranular fracture in copper ore. A significant increase in the degree of liberation of the value mineral, chalcopyrite was reported (Groves, 2007).

Studies on the effect of microwave treatment on the liberation spectrum of a Rod milled low grade copper carbonatite ore were reported by Scott et al. (2008). Ore samples were microwave treated at an energy level of 10.5 kW for 0.5 seconds. Grinding of both treated and untreated ore was carried out in a laboratory scale Rod mill at a d_{80} grind size of 800 μm . QEMSCAN was then used for liberation analysis of the particle size ranges between 25 μm to 850 μm . A general trend in deportment of liberated minerals to coarser size classes was observed. No significant change in liberation was observed between the treated and untreated ore. However an induced fracture after microwave treatment along the grain boundaries of microwave susceptible mineral phases was suggested from the results. From these findings it was concluded that microwave assisted comminution had the potential to increase the liberation at coarser sizes hence resulting in savings on both time and energy required for fine grinding (Scott et al., 2008).

Ali and Bradshaw (2009, 2010) carried out investigations into the mechanism of microwave induced micro fracture. Numerical simulations were carried out using finite difference method and bonded-particle modelling. Computational simulations of microwave heating and thermal damage were carried out using two phase conceptual ores. The results showed that microwave treatment at high power density offered the possibility of localizing induced damage around the grain boundaries. This followed on previous numerical modelling work by the author which had shown that the most efficient method of maximising grain boundary damage was operating at high microwave power density and decreasing exposure time. These results further showed the feasibility of microwave treatment (Ali and Bradshaw, 2009; Ali and Bradshaw, 2010).

Kobusheshe (2010) studied the downstream flotation benefits of microwave treated porphyry copper ores. The results showed improved liberation of secondary crusher product of up to 20% at typical flotation grind sizes. The ore was treated at energy input of about 2 kWh/t. Improvements in liberation were reported at coarser sizes between 212 μm to 425 μm . An increase in value mineral recovery of between 8 to 10% in coarse sizes and an overall grade increase of 1-2% were reported. These results showed the possible economic benefits of microwave pre-treatment of ore. Although the investigations were carried out in batch flotation tests, the results represent the first attempts at quantifying the benefits of microwave assisted comminution. The benefits of microwave treatment on a traditional Copper beneficiation flow sheet are still to be investigated (Kobusheshe, 2010).

2.2. Flotation

Flotation is a widely used separation process in the mineral processing industry. Flotation machines perform the task of separating hydrophobic minerals from hydrophilic ones.

The froth flotation process is made up of two separate and distinctly different zones; the collection zone and the froth zone. The collection zone is responsible for the formation of the bubble aggregates, while the froth zone is responsible for the separation of these aggregates (Banford et al., 1998; Bulatovic, 2007).

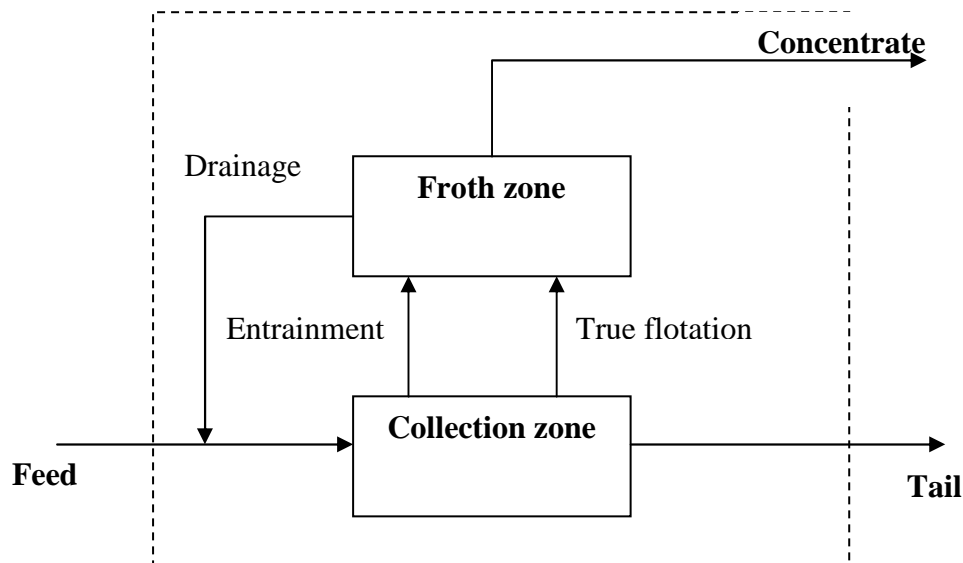


Figure 2-1: Mineral transport system in a flotation cell

Figure 2-1 is a flow chart showing mineral transport in a flotation cell. This section will present a literature review of the theory of flotation and the various models that have been developed to describe the process of flotation in flotation cells. A background summary of all the flotation sub-processes and the development of the various models to describe these processes reported in literature will be presented.

2.2.1. Flotation Sub-processes

Mineral recovery in flotation cells is a result of the combined interaction between two distinct zones in the cell, the collection and the froth zone (Yianatos et al., 1998; Honaker et al., 2006; Yianatos et al., 2008). The pulp or collection zone is responsible for the formation of the bubble-particle aggregates whilst the froth phase is responsible for separation of the aggregates from surrounding hydrophobic particles (Seaman et al., 2004; Yianatos, 2007; Honaker and Ozsever, 2003). There are two mechanisms by which concentrate is collected during flotation.

These are hydrophobic particle adhesion to the rising air bubbles commonly termed true flotation and mechanical transportation of hydrophilic gangue minerals in floated water by either particle entrainment or entrapment (Çilek and Umucu, 2001; Kirjavainen, 1996; Savassi, 2005).

The first mechanism is the most important one as it is a selective process and is the mechanism by which the bulk of the concentrate is collected (Savassi et al., 1998). This mechanism has been a focus of research into flotation (Bulatovic, 2007; Ralston and Ian, 2000). It has generally been concluded by many authors that it consists of a number of sub-processes that take place simultaneously during flotation (Bulatovic, 2007; Ralston et al., 1999). These sub-processes lead to the recovery of the value mineral particle in the concentrate and occur as follows (Bulatovic, 2007; Yoon and Mao, 1996),

- i. The mineral particle is rendered hydrophic, hydrophobicity varying from particle to particle. This allows for the preferential adhesion of mineral particles to the rising air bubbles.
- ii. Mineral particle is suspended in pulp phase.
- iii. The mineral particle collides with the rising bubble.
- iv. The particle adheres to the air bubble.
- v. Particle must not detach from the bubble during passage through the pulp phase.
- vi. Particle must detach when entering the froth phase.
- vii. Particle must not detach and drain from the froth during passage of froth to the weir.

2.3. Flotation modelling

As has been mentioned, the flotation process can be divided into two distinct zones; the pulp or collection zone and the froth phase. Flotation models have been developed to describe these two phases and their interaction (Yianatos, 2007). In this section a review of the available models for modelling the collection and the froth phase in flotation processes will be discussed. A review of models for modelling overall value mineral recovery in industrial flotation cells will be provided at the end.

2.3.1. Collection zone modelling

The pulp or collection zone is responsible for the formation of hydrophobic particle-bubble aggregates (Seaman et al., 2004). The particle-bubble aggregate is a product of the collision of the bubbles with the hydrophobic particles (Yianatos, 2007). The product aggregate is less dense than the medium and moves upwards against gravity to the froth phase.

There are two common approaches that are usually applied to flotation modelling. These are the rate expression approach and the probability theory approach. The collection zone has been extensively studied and first order kinetic models are broadly used to describe it (Alexander et al., 2003; Ferreira and Loveday, 2000).

2.3.2. Kinetic theory rate expression approach

From the knowledge of flotation sub-processes it has been concluded that flotation can best be modelled by assuming a first order rate expression for the rate of collection of value minerals to the concentrate (Alexander and Morrison, 1998; Mendez et al., 2009; Ferreira and Loveday, 2000). This rate, commonly referred to as the rate of flotation, is quantified in terms of some of the many chemical and physical factors that define the environment inside the flotation cell (Bulatovic, 2007). In this approach flotation is represented by chemical analogy, with the following differential equation being used to represent the process equation 2.1 (Alexander and Morrison, 1998; Suazo et al., 2009).

$$\frac{-dC_a}{dt} = k_n \cdot C_a^n \quad 2.1$$

Where: C_a = Concentration of mineral A

t = flotation time

k_n = nth order rate constant

n = order of reaction.

In most cases $n = 1$, i.e the process can be assumed to follow first order rate kinetics (Alexander and Morrison, 1998). In some special cases when dealing with complex ores a non first order rate approximation has been used. The order of the equation is mainly determined by the available bubble surface (Alexander and Morrison, 1998). There are many forms of the first order rate kinetics expressions that has been proposed in literature. Polat and Chander (2000) provide a comprehensive review of these models.

2.3.2.1. Measurement of pulp flotation kinetics of minerals in flotation cells

The kinetic theory has proven to be the most preferred approach in determining collection zone flotation kinetics giving acceptable results when simulating flotation recovery in the collection zone of a flotation cell. Various methods have been developed and are used in the determination of the flotation cell collection zone kinetics that describes the flotation process taking place in the pulp phase. Discussion will focus on three major methods that are in common use in industry.

These are;

1. Standard batch flotation method.
2. Floatability Component method.
3. MFT Batch flotation test method.

Standard Laboratory batch flotation method

Laboratory batch flotation tests are usually carried out in determining the flotation rate constant in an industrial or laboratory set up. A pulp sample of ore from the process being investigated is floated in a laboratory batch flotation cell. Applying the rate expression approach a first order rate equation is assumed to describe the value mineral recovery from the batch flotation cells. Equation 2.2 is the classical form of the first order rate expression which is commonly assumed for batch floatation processes (Napier-Munn, 2005).

$$R_{t,i} = R_{max,i}(1 - \exp(-k_i t)) \quad 2.2$$

Where: k_i , is the flotation is rate constant of particles of diameter i , ; $R_{max,i}$, is the flotation recovery at an infinite time. The equation is fitted to experimental data of recovery versus time for each particle size class to obtain the rate constant $R_{max,i}$ and rate constant k_i . This is done by using nonlinear least square regression. Adjustments to the obtained experimental value mineral recovery values are normally made in order to eliminate contributions to recovery due to entrainment (George et al., 2004). This is done before curve fitting in order to obtain a rate constant that describes recovery in the collection zone (Bradshaw et al., 2005). The batch flotation cell is also operated with shallow froths depths so as to remove the effects of froth zone to final concentrate grade recovered (Duan et al., 2003; Savassi, 2005). The model that has been found to give the best fit to experimental data is the modified Kelsall's model equation 2.3 (Wills and Napier-Munn, 2005). In each size class the particles are assumed to consist of two fractions, the fast floating, R_f , and the slow floating fraction, R_s , (Napier-Munn, 2005).

$$R_{t,i} = R_f [1 - (\exp(-k_{fi} t))] + R_s [1 - (\exp(-k_{si} t))] \quad 2.3$$

Where : k_{fi} and k_{si} flotation rte constant of the fast floating and slow floating fractions.

Floatability component method

Alexander and Morrison, (1998) describe a floatability component method for predicting the flotation rate constant of a particular process. In this method, the characteristics of each of the mineral phases in the streams around the circuit are determined. The specific flotation rate constant of each floatable mineral phase is determined from either batch flotation data or plant operation data. A linearising technique is used in estimating the number of floatability components within a distribution (Alexander and Morrison, 1998). The mineral fraction that is represented by a specific flotation rate is termed a floatability component. This method assumes that the floatability components corresponding to a specific flotation rate are conserved throughout the flotation circuit. Table 2-1 summarises the model expressions used in evaluating the floatability components and hence determining the pulp kinetics.

MFT Batch flotation test method

Dobby and Savassi (2005) describe the MinnovEx Flotation method. This method is a standard bench-scale test that is used to measure primary floatability characteristics of an ore. Pulp kinetics of each mineral species in the ore are determined using a batch flotation cell designed to minimise froth phase effects. The obtained kinetics of each mineral phase are then modelled by a frequency distribution of rate constants, with each class in the k-distribution containing particles of different size and liberation. Mineral recovery per size interval is assumed to remain constant with changes in size distribution of the feed affecting only the proportion of the mass in each size interval. This allows for the prediction of changes in k-distribution as the particle size distribution of the feed ore changes. This eliminates the need to carry out batch flotation test at different grinds. Table 2-2 summarises the model expressions used in applying the MFT method and hence determining the pulp kinetics.

Limitations of batch flotation methods in determining pulp kinetics.

1. Despite the batch cell being operated at shallow froth depth, the shallow froth layer still has an effect on final concentrate grade recovered (Savassi, 2005).
2. Flotation rate constant is obtained without any specific association to particle size or mineral liberation (Ralston et al., 2007).
3. The mineral hydrophobicity and particle distribution is assumed to be constant throughout the flotation circuit, which is not the case for circuits where there is addition of collectors downstream and a regrind circuit (Alexander et al., 2003).

4. Due to differences in cell characteristics and operating conditions between batch and plant operation, kinetic data obtained from batch flotation needs to be scaled up before it is applied for modelling plant operations (Yianatos et al., 2003; Yianatos et al., 2006; Yianatos et al., 2010).
5. Particle recovery by entrainment has a considerable effect on final concentrate grade and hence on flotation kinetics deduced from batch flotation test (Bradshaw et al., 2005; Savassi et al., 1998).
6. Changes in feed ore mineral liberation properties require a separate set of kinetic data to be obtained from batch experiments; this increases the cost of investigating the effects feed ore property changes to the flotation process (Dobby and Savassi, 2005).

Table 2-1: Summary of expressions describing the floatability component method

Term	Expression	Parameters	Model Input parameters required	Method for obtaining parameter
Ore floatability	$k_{i,j} = P_{ij} \cdot S_b$ $S_b = \frac{6J_g}{d_{32}}$	P_{ij} -Ore floatability for component j in the ith size fraction.	P_{ij}	Batch flotation experiment and floatability technique (Alexander and Morrison, 1998)
		S_b -bubble surface area flux	S_b	Calculated parameter describing gas dispersion in the pulp phase.
		$k_{i,j}$ -rate parameter for jth mineral phase from in ith size fraction.	$k_{i,j}$	Product of floatability component and bubble surface area
		J_g -Superficial gas velocity	J_g	J_g probe
		d_{32} -Sauter mean bubble diameter	d_{32}	UCT bubble size analyser

Table 2-2: Summary of expressions for obtaining pulp kinetics utilising the MFT test procedure

Term	Expression	Parameters	Model Input parameters required	Method for obtaining parameter
First order rate expression	$R_{ij} = R_{\infty i,j}(1 - \exp(-k_{i,j}t))$	R_{ij} -Recovery of jth mineral phase from ith size fraction.	R_{ij}	Batch flotation experiments or plant data
		$R_{\infty i,j}$ -Ultimate recovery of jth mineral phase from ith size fraction.	$R_{\infty i,j}$	Calculated from least squares regression analysis
		$k_{i,j}$ -rate parameter for jth mineral phase from in ith size fraction. t -time	$k_{i,j}$	Calculated from least squares regression analysis
K-distribution of a mineral	$P(k_j) = 1 - \exp\left[-\left(\frac{k_j}{k_{avg}}\right)^\alpha\right]$	$P(k_j)$ -Cumulative weight per cent k_{avg} -the weighted average flotation rate, excluding un-floatable particles k_j -rate parameter for jth mineral phase α -a measurement of the spread in the k-distribution	$P(k_j)$ k_{avg} k_j α	Calculated from batch flotation experiment results

2.4. Probability theory approach

Research has established that the rate of recovery in the collection zone depends on the probabilities of all the flotation sub-processes and is a function of grain size (Niemi, 1995). This has culminated in the development of the probability theory approach to collection zone flotation rate constant modelling and the study of bubble-particle interaction in order to identify the sub-processes that are involved in the formation of bubble-particle aggregates (Nguyen et al., 1997a; Ralston and Dukhin, 1999)

2.4.1. Bubble-particle interaction theory

There are three elementary processes that are essential for bubble-particle interaction (Schulze et al., 1989b; Bloom and Heindel, 1997). These are:

1. Approach of bubble and particle forming a thin liquid film.
2. Rupture of the thin film forming a three-phase bubble-particle contact interface. The angle at the three-phase line of contact between the solid mineral surface, aqueous phase and air bubble is called the contact angle (Crawford and Ralston, 1988; Prestidge and Ralston, 1996). It is a measure of solid surface wet ability and gives an indication of particle surface hydrophobicity (Chau, 2009; Chau et al., 2009). A higher contact angle indicates that the mineral surface is readily wetted by air and thus more hydrophobic (Crawford and Ralston, 1988; Prestidge and Ralston, 1996).
3. The stabilization of the bubble-particle aggregates formed against external forces.

2.4.2. Determining overall collection zone efficiency

The probability of transfer of a mineral particle from the pulp phase to the froth phase has been proposed to be the product of the probabilities of these three elementary processes (Alexander and Morrison, 1998; Ralston et al., 1999). The elementary processes (sub-processes) are evaluated separately. The probability of a particle entering the froth phase is then as the product of the following probabilities,

1. Probability of particle-bubble collision sub-process, P_c .
2. Probability of particle- bubble attachment sub-process, P_a .
3. Probability of the particle-bubble stability sub-process, $(1 - P_d)$.

The overall probability of particle collection becomes, (Alexander and Morrison, 1998; Shahbazi et al., 2009)

$$P = P_c \cdot P_a \cdot (1 - P_d) \quad 2.4$$

The major short coming of this model has been ascribing quantitative values to these probabilities. However fundamental models to evaluate these probabilities have been developed (Ralston et al., 1999; Dai et al., 2000). This has led to the development of the fundamental property based model for predicting the flotation rate constant (Pyke et al., 2003). The probabilities can also be expressed in terms of the product of the efficiency of particle-bubble; collision, attachment and stability sub-processes (Grano, 2006; Duan et al., 2003; Koh and Schwarz, 2006; Dai et al., 1998). The overall probability is equivalent to the overall collection zone efficiency equation 2.5.

$$E_{coll} = E_c \cdot E_a \cdot E_s \quad 2.5$$

Where E_{coll} is the collection efficiency and E_c, E_a, E_s are the collision, attachment and stability efficiencies respectively. If the collision frequency per unit volume between particles and bubbles is evaluated, the rate of removal of particles by bubbles in a flotation cell can be expressed as,

$$\frac{dN_p}{dt} = kN_p = -Z_{pb}E_{coll} \quad 2.6$$

Where: N_p is the number density of floatable particles, and Z_{pb} is the collision frequency per unit volume between particles and bubbles, k is the flotation rate constant. The above equation can be rearranged in order to come up with an expression for determining the flotation rate constant as a function of the collection efficiency resulting in the following expression(Newell and Grano, 2006).

$$k = \frac{Z_{pb}E_{coll}}{N_p} \quad 2.7$$

2.4.3. Fundamental model for calculating collection zone efficiency

Determination of the value of the bubble-particle interaction efficiencies is the most important step in predicting the rate constant of flotation kinetics (Nguyen et al., 1998). A lot of work has been to derive models for describing the main flotation sub-process efficiencies of collision, attachment and stability (Dai et al., 1999; Dai et al., 2000; Ralston et al., 1999). This gives a summary of the available models for evaluating the three flotation sub-processes that make up the flotation collection efficiency in equation 2.5. For each sub-process the following aspects of the models will be covered in the review:

1. An analysis of the principal theory behind the formulation and function of the models.
2. The parameters required to calibrate the models.

3. The experiments and experimental work required in obtaining parameters required for model calibration.

2.4.3.1. Collision Efficiency

For a particle to attach to a bubble collision, must take place first. The collision efficiency can be affected by many factors. Some of the factors that affect the efficiency of the bubble-particle collision sub-process will be discussed below.

Factors influencing bubble-particle collision

1. Particle size, d_p . Generally all the collision efficiency models predict an increase in collision efficiency with particle size, but the dependence of the models on particle size varies due to differences in assumptions and hydrodynamic conditions that are used in the models (Dai et al., 2000; Miettinen et al., 2009; Ralston and Ian, 2000).
2. Particle density ρ_p . Particle density has an effect on the Stokes and Reynolds numbers. Increasing particle density results in an increase in the Stokes number thus leading to a change in the bubble-particle collision mechanism from interception to inertial (Miettinen et al., 2009; Dai et al., 2000; Nguyen and Nguyen, 2009; Sarrot et al., 2005).
3. Bubble size d_b . All the collision efficiency models predict that the collision efficiency decreases with increasing bubble size although this has not yet been observed in experiments (Dai et al., 2000; Nguyen et al., 2006).
4. Bubble rising velocity v_b . At higher bubble rising velocity potential conditions apply which favour bubble-particle collision than Stokes flow conditions (Miettinen et al., 2009; Sarrot et al., 2005; Ralston and Ian, 2000).
5. Bubble surface mobility. Small amounts of surface active material in the liquid render small bubbles fully retarded (Sam et al., 1996). This affects the flow conditions at the bubble surface and the rate of liquid drainage between the bubble and the particle (Miettinen et al., 2009; Liu and Schwarz, 2009a; Phan et al., 2003). The retarded bubble surface forces the fluid streamlines away from the bubble liquid interface, hindering thin film thinning consequently resulting in lower bubble-particle collision and attachment efficiencies (Schulze, 1992; Dai et al., 2000; Ralston and Ian, 2000).

A comprehensive review of available bubble-particle collision efficiency models has been provided by Dai et al.,(2000). Some of the bubble-particle collision models that are available in literature are presented in Table 2-3.

Table 2-3: Summary of collision efficiency models found in literature.

Expression	Model description
$E_{C-LB} = \left(\frac{K}{K + 0.2} \right)^2$ $K = \frac{\rho_p \cdot v_b \cdot d_p^2}{9 \cdot \eta \cdot d_b}$	The Langmuir-Blodgett model (E_{C-LB}) was developed for the inertial hydrodynamic interaction between a stationary and falling droplet. The model is valid only for particles with large Stokes number. Mobile surface effects have an insignificant effect on (E_{C-LB}). Model is not applicable where collision occurs due to interceptional effects (Dai et al., 2000).
$E_{C-Su} = \frac{3d_p}{d_b}$	The Sutherland model (E_{C-Su}) was developed for collision between a single particle and bubble assuming mobile bubble surface, negligible particle inertia and potential flow conditions. Model caters for collision due to interceptional effects (Nguyen et al., 2006; Nguyen and Nguyen, 2009; Dai et al., 1998)
$E_{C-GA} = \frac{3}{2} \left(\frac{d_p}{d_b} \right)^2$	The Gaudin model (E_{C-GA}) was developed assuming a Stokes flow regime and ignoring inertial forces. Model is useful for bubble sizes less than 100 μ m (Miettinen et al., 2009; Dai et al., 2000).
$E_{C-FH} = \frac{v_p}{(v_p + v_b)}$	The Flint-Howarth model (E_{C-FH}) was developed for bubble-particle collisions taking place under hydrodynamic conditions in the Stokes number range between 0.001 and 0.1. Inertial forces were neglected.
$E_{C-AK} = \frac{\left(1 + \frac{d_p}{d_b}\right)^2 \left[\frac{v_p}{v_b} + \frac{2\psi_c^0}{\left(1 + \frac{d_p}{d_b}\right)^2} \right]}{\left(1 + \frac{v_p}{v_b}\right)}$	Only gravitational and viscous forces were considered in developing the Anfruns-Kitchener model (E_{C-AK}). Fluid drag and particle inertial forces were neglected. The model is valid under the following conditions; small bubbles, Stokes flow conditions and inertia less flotation (Dai et al., 2000).
$E_{C-WP} = \left[1 + \frac{2}{1 + \left(37/R_{eb}\right)^{0.85}} \right] \left(\frac{d_p}{d_b} \right)$	The Weber-Paddock model (E_{C-WP}) describes collision due to interceptional effects for a mobile bubble surface $R_{eb} < 200$. The effects of particle inertia were neglected in developing the model. Hydrodynamic interaction between the particles and the fluid was neglected as the particles were assumed to be very small. Stokes flow hydrodynamic conditions were assumed (Weber and Paddock, 1983).

$E_{C-WP} = \frac{3}{2} \left[1 + \frac{(3/16)R_{eb}}{1 + 0.24R_{eb}^{0.56}} \right] \left(\frac{d_p}{d_b} \right)^2$	<p>Weber-Paddock flow (E_{C-WP}) model for describing collision due to interceptional effects for an immobile bubble surface in the Reynolds number range $200 < R_{eb} < 300$ (Weber and Paddock, 1983) .</p>
$E_{C-YL} = \left[\frac{3}{2} + \frac{4Re^{0.72}}{15} \right] \left(\frac{d_p}{d_b} \right)^2$	<p>The Yoon and Luttrell flow (E_{C-YL}) model is valid for intermediate flow conditions. It is applicable for bubble Reynolds number between $0 < R_{eb} < 100$. Similar assumptions to those made in developing the Sutherland model were made (Mao and Yoon, 1997; Fan et al., 2010b; Fan et al., 2010a).</p>
$E_{C-Sc} = E_{Sc}^{ic} + E_{C-WP}^g + \left[1 - \frac{E_{C-Sc}^{ic}}{\left(1 + \frac{d_p}{d_b} \right)^2} \right] E_{C-PL}^{in}$ $E_{Sc}^{ic} = \frac{2\psi_c}{\left(\left(1 + \frac{v_p}{v_b} \right) v_b \right) Re_b^2}$ $E_{C-PL}^{in} = \left(\frac{1}{1 + \frac{v_p}{v_b}} \right) \left(1 + \frac{d_p}{d_p} \right)^2 \left(\frac{K}{K + a} \right)^b$ $E_{C-WP}^g = (\sin \theta_c)^2 \left(1 + \frac{d_p}{d_b} \right)^2 \left(\frac{v_p}{v_b} \right)$	<p>The Schulze model (E_{C-Sc}) considers particle-bubble collision to be the result three different effects. Interceptional effect, E_{Sc}^{ic}, gravitational effects, E_{C-WP}^g, and inertial effect, E_{C-PL}^{in}. E_{C-WP}^g is the Weber-Paddock collision model for collision due to gravitational effect. E_{C-PL}^{in} is the model reported by Plate for inertial collision efficiency. The model neglects the negative effects of the inertial forces thus over estimating the collision efficiency. The model is however superior to most of the other collision models available in literature (Schulze et al., 1989a; Dai et al., 2000).</p>

$E_{C-GSE} = E_{C-SU} \cdot \sin^2 \theta_t \cdot \exp \left\{ \left[3K_3 \left(\ln \frac{3}{E_{C-SU}} - 1.8 \right) - \frac{4 \left(\frac{2}{3} + \frac{\cos^2 \theta_t}{3} - \cos \theta_t \right)}{\sin^4 \theta_t} \right] \cos \theta_t \right\}$	<p>The GSE (Generalised Sutherland equation) model is applicable to potential flow conditions for mobile surface and for Stokes conditions that are less than 0.1. It couples the interception effects of the Sutherland model to the positive and negative effects of hydrodynamic pressing force and the centrifugal force respectively. It is a reasonable description of bubble-particle collision under potential flow conditions for both large and small particles (Dai et al., 1998; Miettinen et al., 2009)</p>
$E_{C-NV} = \frac{2D}{9Y \left(1 + v_p/v_b \right)} \left(d_p/d_b \right)^2 \left\{ [(X + Y)^2 + 3Y^2]^{1/2} \right\} + 2(X + C)^2$ $X = \frac{3}{2} + \frac{9R_{eb}}{32 + 9.88R_{eb}^{0.694}} ; \quad Y = \frac{3R_{eb}}{8 + 1.736R_{eb}^{0.518}}$ $C = \frac{v_p/v_b}{\left(d_p/d_b \right)^2} ; D = \frac{[(X + C)^2 + 3Y^2]^{1/2} - (X + C)}{3Y}$	<p>The Nguyen-Van model (E_{C-NV}) was developed by assuming that hydrodynamic and gravitational forces were the only forces controlling the collision process with the distance between the bubble and particle during collision being negligible compared to their sizes. The bubble surface was also assumed to be immobile, the motion of the bubble being unaffected by particles as the particle size was assumed to be much smaller compared to the bubble size. Particle inertial forces were neglected (Nguyen Van and Kmet, 1992; Nguyen-Van and Kmet, 1994).</p>

2.4.3.2. Attachment efficiency

Not all particles colliding with bubbles attach to the bubbles. As the bubble and particle come closer the influence of intermolecular and interfacial forces increases, consequently the liquid film between the bubble and particle draining away causing the film to rupture (Nguyen et al., 1997a; Albijanic et al., 2010). A three-phase contact line is then formed, the ability of this contact line to extend and stabilise is essential for the formation of a stable bubble-particle aggregate thus completing successful attachment of particle to bubble (Phan et al., 2003; Dobby and Finch, 1986; Zawala et al., 2008).

Induction time

The induction time (t_{ind}) is the sum of the film drainage time t_{fl} , the three-phase contact line expansion and stabilisation time t_{TPLC} and the film rupture time t_{fr} (Nguyen et al., 1997a). It is the time required by the particle to completely attach to the bubble forming a stable bubble-particle aggregate, equation 2.8 (Albijanic et al., 2010).

$$t_{ind} = t_{fl} + t_{fr} + t_{TPLC} \quad 2.8$$

The induction time has been reported to vary with particle size according to a power function, equation 2.9 (Miettinen et al., 2009).

$$t_{ind} = Ad_p^B \quad 2.9$$

Parameters A and B in the equation are independent of particle size. Parameter B has been reported to be constant with a value of 0.6 (Dai et al., 1999). An inverse relationship has been suggested for parameter A with contact angle (Koh and Schwarz, 2008; Shahbazi et al., 2010; Shahbazi et al., 2009; Koh and Schwarz, 2006).

$$A = \frac{75}{\varphi} \quad 2.10$$

d_p is the particle size in meters and φ is the contact angle in degrees. For attachment to occur the induction time must be less than the contact time.

Determination of particle Contact angle

The contact angle, φ , is described thermodynamically by Young's equation given below (see equation 2.11).

$$\gamma_{s/a} = \gamma_{s/l} + \gamma_{l/a} \cos \phi_Y \quad 2.11$$

Where $\gamma_{s/a}$, $\gamma_{s/l}$, and $\gamma_{l/a}$ represent the solid-vapour, solid-liquid, and liquid-vapour interfacial tensions, respectively (Chebbi, 2003; Chibowski, 2007; Iveson et al., 2004). For Young's equation to be valid, the solid surface should be ideal, i.e. smooth, flat, homogenous, inert, insoluble, non reactive, non porous and of non deformable quality (Chau, 2009; Chau et al., 2009). This is not the case with real mineral surfaces, hence there is a variation in contact angles measured on real surfaces (Keller et al., 2007; Lam et al., 2001; Lam et al., 2002). This leads to two definitions of contact angles, intrinsic contact angle which is the contact angle measured for flat surfaces and apparent contact angle which is the contact angle measured for rough surfaces (Chau, 2009; Chau et al., 2009). Since most mineral surfaces are rough the discussion will focus on the determination of the apparent contact angle only. The apparent contact angle is obtained by utilising optical methods that measure the contact angle as the angle between the direction to the tangent of the smoothed solid surface and the direction of the tangent to the air water interfaces (Chebbi, 2003; Chibowski, 2007; Iveson et al., 2004; Keller et al., 2007; Lam et al., 2001; Lam et al., 2002; Yang et al., 1999). A range of apparent contact angles is normally obtained, with the upper limit of the range being termed advancing contact angle and the lower limit of the range being termed receding contact angles (Chebbi, 2003; Chibowski, 2007; Iveson et al., 2004; Keller et al., 2007; Lam et al., 2001; Lam et al., 2002; Yang et al., 1999; Chau, 2009; Chau et al., 2009). The difference between the two limits being termed contact angle hysteresis (Chibowski, 2007; Lam et al., 2002).

Contact time and Sliding time

The contact time refers to the time for which the bubble and a particle are in contact after their collision (Nguyen et al., 1997b). After bubble particle collision the particle either rebounds or slides along the bubble surface (Phan et al., 2003; Albijanic et al., 2010). Where the particle simply rebounds from the bubble surface after collision the contact time is equivalent to the impact time (Schulze et al., 1989a). If particle sliding takes place after collision, the contact time is the sum of the impact and sliding time. For particles less than 100 μm the contact times are typically very small, about 10 ms or less (Miettinen et al., 2009; Dai et al., 1999). There is no rebound with particle deformation (Schulze et al., 1989a). Various models exist in literature for predicting the sliding time (Dobby and Finch, 1986). Particle impact provides kinetic energy while particle sliding provides contact time; both are

beneficial to the drainage and rupture of the film and to the expansion of three-phase contact line (TPCL) (Dai et al., 1999; Dobby and Finch, 1987; Ralston and Dukhin, 1999). From the kinetic viewpoint, the sliding time is more important than the impact time. A review of sliding time models available in literature will be given below.

Sliding time models

Table 2-4 provides is a summary of some of the models for predicting the sliding time available in literature. r_p and r_b are the particle and bubble radius respectively, θ refers to the contact angle. The Sutherland model is one of the earliest sliding time models that was proposed Sutherland in 1948. The model had some mistakes and most of the models that have been derived so far have been aimed at correct that mistake. Dai et al. (1998) presented a corrected form of the Sutherland sliding time model. For potential flow conditions both the Dobby and Finch (1986) and Yoon and Luttrell (1992) assume a maximum particle contact angle $\theta_m = 90^\circ$. This assumption is incorrect as the maximum particle contact angle is less than 90° (Dai, 1998).

Table 2-4: Summary of sliding models found in literature

Sliding time model	Reference
$t_{sl-SU} = \frac{2(r_p + r_b)}{2(v_p + v_b) + (v_p + v_b) \left(\frac{r_b}{r_p + r_b}\right)^3} \cdot \ln \left(\cot \frac{\theta}{2} \right)$	Dai et al., 1998
$t_{sl-DF} = \frac{2(r_p + r_b)}{2(v_p + v_b) + v_b \left(\frac{r_b}{r_p + r_b}\right)^3} \ln \left(\cot \frac{\theta}{2} \right)$	Dobby and Finch, 1986
$t_{sl-YL} = \frac{d_p + d_b}{3v_b} \ln \left(\cot \frac{\theta}{2} \right)$	Luttrell and Yoon, 1992

Attachment Efficiency models

The bubble-particle attachment efficiency can be modelled in terms of the contact time and sliding time (Dai et al., 1999; Hewitt et al., 1994). Another approach to modelling attachment efficiency is the energy barrier approach (Luttrell and Yoon, 1992). This approach is based on the principle that for bubble-particle attachment to take place the kinetic energy of the particle should be higher than the energy barrier between the bubble and the particle (Fan et al., 2010b; Fan et al., 2010a; Yoon and Mao, 1996; Schubert and Bischofberger, 1998). Due to the variation in sliding time models there is a corresponding variation in attachment efficiency models that are based on the sliding time approach.

The Dobby-finch attachment model

There is a collision angle, θ_a , termed the attachment angle at which the sliding time equals the induction time. Particles with collision angles less than the attachment angle will attach to the bubble (Ralston et al., 1999). The number of attached particles to the bubble can be related to the projected area defined by attachment angle while the number of particles that have collided with the bubble can be related to the projected area defined by the maximum collision angle θ_t (Dobby and Finch, 1987; Ralston et al., 1999). Thus Dobby and Finch (1987) proposed that the attachment efficiency is a ratio of these two areas.

$$E_a = \frac{\sin^2 \theta_a}{\sin^2 \theta_t} \quad 2.12$$

The attachment angle is obtained by replacing the sliding time with the calculated induction time in the sliding time model expression and rearranging the equation to obtain a value of θ which in that case is the attachment angle θ_a (Dobby and Finch, 1987).

$$\theta_a = 2 \arccos \tan \exp \left[-t_{ind} \frac{2(v_p + v_b) + v_b \left(\frac{d_p}{d_p + d_b} \right)^3}{d_p + d_b} \right] \quad 2.13$$

The Yoon-Luttrell model

Yoon-Luttrell used an approach similar to the Dobby and Finch (1987) projected area approach in deriving their attachment efficiency model (Luttrell and Yoon, 1992; Ralston and Ian, 2000). In deriving their model they assumed a maximum collision angle value of 90° .

$$E_a = \frac{\sin^2 \theta_a}{\sin^2 90^\circ} \quad 2.14$$

The Yoon-Mao Model

The model is an exponential function containing the ration of the potential energy barrier E_1 and the kinetic energy of a particle approaching a bubble E_K (Yoon and Mao, 1996; Mao and Yoon, 1997; Luttrell and Yoon, 1992). The particles must possess sufficient kinetic energy to overcome the energy barrier between the bubble and particle so that the thin film ruptures and attachment occurs.

$$E_{a-YM} = \exp\left(-\frac{E_1}{E_K}\right) \quad 2.15$$

2.4.3.3. Bubble-particle stability Efficiency

When bubble-particle stability is discussed, it is assumed that particle attachment has already taken place. There are strong detachment forces that act on the TPCL between a particle and a bubble (Zawala et al., 2008). The ability of the TPCL to resist these forces determines bubble-particle stability (Schulze, 1977). Inertia, gravity and viscous forces are some of the forces that reduce the bubble-particle stability (Ralston et al., 1999). The bubble-particle stability efficiency is strongly dependent on the adhesion forces between bubble and particle. These adhesion forces are (Phan et al., 2003; Schulze et al., 1989a);

- capillary force, F_c ,
- Hydrostatic pressure force, F_h , on the area enclosed by the three-phase contact, and
- Buoyancy, F_b , of the particle volume immersed in the liquid phase

This adhesion force has a direct relationship with contact angle and is inversely related to particle size (Yoon and Mao, 1996). Forces of adhesion must exceed detachment forces for a particle to continue being attached to the bubble surface in a static system (Yoon and Mao, 1996; Schulze et al., 1989a). Under turbulent conditions, detachment forces other than those associated with the particle weight become important (Ralston et al., 1999).

Bubble-particle stability models

Under turbulent conditions when the detaching forces are in equilibrium with the adhesive forces the following expression, equation 2.16, represents the force balance (Schulze, 1992; Pyke et al., 2003).

$$F_c + F_h + F_b - F_g - F_d - F_\sigma = 0 \quad 2.16$$

Where F_{σ} is the capillary pressure force in the bubble, F_g gravitational force and F_d is the additional detaching forces. It has been proposed that the bubble-particle stability efficiency is exponentially distributed and can be expressed as follows, (Pyke et al., 2003; Miettinen et al., 2009; Bloom and Heindel, 2003)

$$E_s = 1 - \exp\left(1 - \frac{1}{Bo^*}\right) \quad 2.17$$

The Bond number describes the stability of the bubble-particle and is defined as the ration of the detachment, F_{det} , and attachment forces, F_{att} below (Pyke et al., 2003; Miettinen et al., 2009; Schulze, 1992),

$$Bo^* = \frac{F_{att}}{F_{det}} \quad 2.18$$

Bloom and Heindel (2003) carried out experiments to validate Schulze's model. They suggested a modified expression of the model as follows:

$$E_s = 1 - \exp\left[A_s \left(1 - \frac{1}{Bo^*}\right)\right] \quad 2.19$$

where A_s is an empirical dimensionless constant with a value of 0.5 (Bloom and Heindel, 2003).

2.5. Calculating collection zone overall mineral recovery

When evaluating the performance of the flotation unit, overall collection zone mineral recovery and concentrate grade are the two key parameters used for evaluation. Various models have been proposed to describe collection zone flotation recovery. Depending on the slurry flow pattern equations 2.18 and 2.19 are used to calculate true mineral recovery for plug-flow and perfect mixing pulp flows in a flotation cell. Of key importance in calculating the mineral recoveries is the first order collection zone rate constant k . The recovery (R) is calculated as follows (Napier-Munn, 2005; Alexander and Morrison, 1998):

$$R = 1 - \exp(-k\tau) \quad \text{Plug flow} \quad 2.20$$

$$R = \frac{k\tau}{(1+k\tau)} \quad \text{Perfect Mixing} \quad 2.21$$

Where: k is the first order collection zone rate constant and τ is the residence time in the unit. For batch flotation tests plug-flow conditions are normally assumed. Single continuous plant flotation cells are assumed to follow perfect mixing characteristics (Alexander and Morrison, 1998).

The first order rate constant can be determined by kinetic or probabilistic approaches. When applying the probabilistic approach the particles are assumed to be perfectly mixed in the collection zone. Equation 2.19 is then used to calculate recovery by bubble-particle collection. The froth phase is however crucial in determining the final overall flotation cell recovery. Flotation models aimed at predicting overall flotation cell recovery attempt to incorporate the various froth phase sub-process into the final model expressions by use of froth recovery, degree of entrainment and water recovery parameters. The approaches commonly used in characterising the overall recovery in flotation cell equipment can be classified as follows (Yianatos et al., 2008). These are:

- Single stage process and overall flotation model,
- Two stage process (pulp and froth) and overall flotation rate constant,
- Two stage process (pulp and froth) and mass balance.
- Three zone flotation cell description (pulp zone, pulp-froth interface and froth zone).

The next section will provide a review on froth phase sub-processes models and the parameters for describing the froth phase effects on overall flotation recovery.

2.5.1. Froth zone value mineral recovery

The froth phase is responsible for the separation of bubble-particle aggregates from surrounding suspended hydrophobic and hydrophilic particles from the pulp zone (Honaker et al., 2006). Research has shown that the froth phase is the grade determining phase in flotation (Tsatouhas et al., 2006; Cutting et al., 1986; Vera et al., 1999b; Seaman et al., 2004). The existence of the froth phase is therefore of great importance during mineral separation (Yianatos, 2007). Industrial flotation cells are operated with the specific aim of maintaining a pulp- froth interface (Seaman et al., 2006). The froth phase phenomena has generally not been well understood in the past (Ata et al., 2002; Mathe et al., 1998). This has resulted in lack of adequate models to describe the froth phase in literature, consequently first order kinetic equation were usually imposed on the overall process (Mathe et al., 1998).

2.5.2. Studies into the factors that affect froth zone recovery

Focus has shifted towards studying the phenomena which take place in the froth zone (Moys, 1978). The outcome of the research has been the identification of the important factors that affect mineral recovery and grade in the froth zone which are; Froth structure, Froth Stability, Froth mobility, Entrainment , Particle drainage and water recovery in froths (Banford et al., 1998) (Mathe et al., 1998; Schwarz and Grano, 2005).

2.5.2.1. Froth structure

The structure of mineralized froths is the product of the interaction between two main factors: Froth drainage and froth mobility (Cutting et al., 1986; Subrahmanyam and Forssberg, 1988). Froth drainage mechanisms govern the grade of the final concentrate (Mathe et al., 1998; Honaker et al., 2006; Subrahmanyam and Forssberg, 1988). Froth mobility is described as the flow stream profile occurring in the froth between the pulp-froth interface and the froth discharge (Cutting et al., 1986). Research has confirmed the cleaning and selectivity actions of froths through the use of data on solids and grade profiles in the froth along with residence time distribution data (Massinaei et al., 2009a; Honaker et al., 2006). The solids and grade profile showed that froth zone upgrading occurred just above the pulp-froth interface (Massinaei et al., 2009a). The effect of froth depth and bubble loading on overall rate constant and froth recovery has been examined extensively in literature (Yianatos et al., 2008; Schwarz and Grano, 2005). To achieve maximum froth recovery the bubble surface area should be sufficient to carry all the particles from the collection zone including particles draining back into the pulp through particle re-attachment (Honaker and Ozsever, 2003). Increasing froth depth increases the probability of particle re-attachment (Mathe et al., 1998). Therefore increasing the bubble loading and froth depth has been found to have a positive effect on the overall rate constant (Massinaei et al., 2009a; Banford et al., 1998; Aktas et al., 2008).

2.5.2.2. Froth zone sub-processes

Detachment of mineral particles in the froths has been shown to be selective with the weakest hydrophobic particles being rejected first (Honaker et al., 2006; Honaker and Ozsever, 2003; Moys, 1978; Yianatos et al., 1988). This selectivity in detachment in the froth phase accounts for the cleaning action of the froth phase (van Deventer et al., 2004b). The probability of particle re-attachment is higher in deep froths as compared to shallow froths (Banford et al., 1998; Mathe et al., 1998). As the particle laden bubbles travel upward and cross the surface of the pulp, the particle-bubble aggregate entrains water and the hydrophobic minerals as well (Çilek and Umucu, 2001; Banford et al., 1998; Kirjavainen, 1996). As the bubble-particle aggregates continue to rise through the froth zone, the water layer surrounding the bubbles becomes thinner and coalescence (Banford et al., 1998; Meloy et al., 2007). This reduces the bubble surface area resulting in the rupture of the bubbles (Ross, 1991a; Ross, 1991b).

2.6. Entrainment

Entrainment is defined as the process where minerals are carried over with the water phase to the froth phase by mechanical transportation. Different authors agree that entrainment is a result of either one of the following mechanisms (Stevenson et al., 2007; Savassi et al., 1998; Yianatos and Contreras, 2009; Zheng et al., 2005)

1. Entrained material is transported upwards in the bubble lamella or,
2. Entrained material is transported in the wake of an air bubble

Research has shown that the mechanisms for entrainment mentioned above do not explain the water content found in flotation froths. A bubble swarm theory has been proposed in which the water in the froth is said to be as a result of ascending swarms of air bubbles mechanically pushing the water into the froth phase (Kirjavainen, 1996; Cilek, 2009; Çilek and Umucu, 2001; Çilek and Yilmazer, 2003). The flow of entrained particles can be described to be a resultant of the following two opposing transport mechanisms (Savassi et al., 1998),

- a. Upward velocity of entrained particles through the froth.
- b. Settling velocity or drainage of entrained material down towards the pulp-froth interface.

2.6.1. Mechanisms of entrained material drainage

There is a general agreement that the main methods of entrained material drainage are film water drainage, column drainage, mobility induced drainage and subduction drainage (Savassi et al., 1998; Ireland et al., 2007; Ireland and Jameson, 2007; Subrahmanyam and Forssberg, 1988; van Deventer et al., 2004b). Savassi et al. (1998) and Ireland et al. (2007) in summing up these methods of drainage cite the extensive work that was done by Cutting et al. (1989) in investigating drainage methods in froths. The extent to which each of the drainage mechanisms occurs is not only a function of the froth structure but also of the characteristics of the gangue (Ata et al., 2004). The result of entrained particle drainage from the froth is their rejection from the froth and this mostly occurs just above the pulp-froth interface (Ata et al., 2006; van Deventer et al., 2004b).

2.6.2. Main Factors that affect entrainment

The main factors that affect entrainment reported in literature have been summarised and are presented in Table 2-5. Each of the factors is stated along with a brief description of how that factor affects entrainment.

Table 2-5: Summary of factors that affect entrainment

Factor	Description	Reference
Water recovery	A strong correlation exists between water recovery and entrainment. At high water recoveries the relationship is linear .At low recoveries it is parabolic.	Subrahmanyam and Forssberg, 1988; Yianatos and Contreras, 2009; Savassi, 2005; Savassi et al., 1998
Particle size	At high water recoveries the linear plot of entrainment against water recovery shows a decreasing gradient with increasing particle size. The relationship is linear at fine particle sizes. Entrainment is insignificant at coarser sizes.	Zheng et al., 2005; Stevenson et al., 2007; Yianatos and Contreras, 2009; Neethling and Cilliers, 2009
Feed solids percentage	High solids percent reduce particle entrainment.	Subrahmanyam and Forssberg, 1988; Savassi et al., 1998; Zheng et al., 2005
Froth characteristics	Factors such as specific airflow rate, residence time, and height of froth phase determine the amount of entrained particles that enter the froth phase.	Cilek, 2009; Çilek and Yilmazer, 2003; Zheng et al., 2005; Yianatos et al., 2009
Mineral specific gravity	The probability of particle drainage from the froth of entrained particles is higher for particles with large specific gravity values.	Honaker and Ozsever, 2003; Honaker et al., 2006; Yianatos et al., 2009

2.6.3. Entrainment modelling

Many empirical models for modelling recovery by entrainment exist in literature (Zheng et al., 2006b; Savassi et al., 1998; Kirjavainen, 1996; Çilek and Umucu, 2001). These models express recovery by entrainment as a function of many variables. Some of these variables required in the model expressions are very difficult to measure (Zheng et al., 2005).

$$R_{entrainment,i} = (R_W, \mu_S, d_p, \omega_{top}, \Delta\rho) \quad 2.22$$

Where; $R_{entrainment,i}$ is the recovery of entrained material by size , R_w is water recovery, $\Delta\rho$ is the density difference between the solid and liquid, d_p is the particle size, ω_{top} is the solids mass fraction below the pulp-froth interface, and μ_s is the interstitial slurry viscosity. Most of these models only consider the effect of particle size on the degree of entrainment (Neethling and Cilliers, 2009; Zheng et al., 2005). This is because experimental results obtained so far show that particle size has a significant effect on the degree of entrainment (Zheng et al., 2006b; Kirjavainen, 1996). Zheng et al. (2006b) proposed empirical expressions for determining entrainment that tried to incorporate more variables such as particle shape and slurry viscosity. These models have been shown to be dimensionally inconsistent (Stevenson et al., 2007). Dimensionless factors per size class such as the degree of entrainment and the classification function have also been defined in modelling entrainment recovery (Yianatos and Contreras, 2009; Zheng et al., 2005).

$$ENT_i = \frac{M_{conc}^{ENT}}{M_{pulp}^{ENT}} \quad 2.23$$

$$CF_i = \frac{M_{pulp}^{ENT}}{M_{tail}^{ENT}} \quad 2.24$$

Where: ENT_i =The degree of entrainment, CF_i = The classification function, M_{conc} =Mass of solids suspended in the water in the concentrate, M_{pulp} =Mass of solids suspended in the water in the pulp phase. These dimensionless expressions are used in models that express the size recovery by entrainment as a function of water recovery. This reduces the problem of determining recovery by entrainment, $R_{entrainment,i}$, to that of obtaining the dimensionless factors as water recovery can easily be obtained from a mass balance of the system (Yianatos et al., 2009).

$$R_{entrainment,i} = ENT_i \cdot R_w \quad 2.25$$

A method proposed by Zheng et al. (2006b) for estimating the degree of entrainment is to use a fully liberated portion of the non sulphur gangue especially in the coarse size fractions. The entrainment calculation can be based on the total mass of NSG (Non sulphide gangue) in the individual size fractions with marginal error (Zheng et al., 2006b)

$$ENT_i = \frac{\left(\frac{\text{Mass of suspended non floating solid}_i}{\text{Mass of water}} \right)_{Pulp}}{\left(\frac{\text{Mass of suspended non floating solid}_i}{\text{Mass of water}} \right)_{Tail}} \quad 2.26$$

Where; i, denotes a particular size class.

2.7. Froth recovery

It is difficult to interpret the overall flotation rate constant in terms of the froth sub-processes (Ross, 1991b). The processes occurring within the froth phase are collectively represented by the froth recovery term. Froth recovery is therefore a useful parameter for measuring the performance of the froth zone (Falutsu and Dobby, 1992; Ata et al., 2002; Neethling, 2008). Neethling (2008) defined froth recovery as the fraction of the material that enters the froth attached to the bubbles that reports to the concentrate, rather than dropping back into the pulp. Froth recovery can be expressed as (Savassi et al., 1998; Yianatos et al., 2008; Neethling, 2008),

$$R_f = \frac{k}{k_c} \quad 2.27$$

Where: R_f = Froth recovery, k = Overall first order rate constant (min^{-1}), k_c = Collection zone first order rate constant (min^{-1}).

Froth recovery has a significant effect on overall recovery, it provides a measure of the loss of recovery in the froth zone (Vera et al., 2002; Massinaei et al., 2009a). Froth recovery of attached particles is a non selective process (Vera et al., 1999a).

2.7.1. Methods for obtaining the froth zone recovery

Due to its importance, several methods have been reported in literature for estimating froth phase recovery. Table 2-6 below gives a summary of the froth recovery determination methods that have been reported so far in literature.

Table 2-6: Summary of methods for obtaining froth zone recovery

Method	Description of method	References
Modified flotation column method	Method utilises a modified laboratory flotation column that allows simultaneous sampling of both the pulp and froth phase	Ata et al., 2002; Ata et al., 2006; Schwarz and Grano, 2005; Honaker and Ozsever, 2003
Mass transfer method	The method involves the measurement of a wide range of variables culminating in the development of a model that allows for the determination of flow rates into the froth.	van Deventer et al., 2001; van Deventer et al., 2004b; van Deventer et al., 2004a
Froth depth changing method	Based on the assumption that as R_f tends to one the froth depth h_f tends to zero. The froth depth is changed; concentrate flow measured at each depth and extrapolation is carried out to determine concentrate flow at zero froth depth.	Feteris et al., 1987; Vera et al., 1999b; Vera et al., 2002; Schwarz and Grano, 2005; Tsatouhas et al., 2006
Direct measurement of loading on bubbles method	This method relates to the direct measurement of bubble loading of particles at the froth pulp interface by utilising various devices designed for this purpose. Having obtained the bubble load froth recovery is then determined by carrying out calculation described below.	Falutsu and Dobby, 1992; Bradshaw and Connor, 1996; Seaman et al., 2004; Moys et al., 2009; Yianatos et al., 2008
Use of plug-flow model	The grade profiles along the froth phase are fit to a plug-flow model.	Yianatos et al., 1988; Yianatos et al., 1998; Moys, 1978; Cutting et al., 1986
Indirect measurement of loading on bubbles	The method refers to a mass balancing technique which indirectly derives the rate of attached particles entering the froth zone through the collection of pulp samples containing different portions of attached and suspended particles.	Savassi et al., 1998; Savassi, 2005; Alexander et al., 2003

2.8. Water recovery

Water recovery may be defined as the fraction of the water entering the flotation cell that is recovered in the concentrate (Yianatos et al., 2009).

$$R_{water} = \frac{C_{Water}}{F_{Water}} \quad 2.28$$

Where: C_{Water} is the Amount of water in the concentrate; F_{Water} -Water contained in the feed;
 R_{water} -Water recovery

Water recovery is strongly associated with entrainment and froth recovery (Cilek, 2009; Zheng et al., 2006a). It influences both mineral recovery and concentrate grade (Neethling and Cilliers, 2009; Cilek, 2009). This makes it a very important parameter in flotation plant design and operation. By including the solids percentage of the streams around a flotation cell the water recovery can easily be established. In cases where modelling is being carried out so as to design a flotation plant or for process control purposes the mass balance method is not appropriate for determining water recovery. Water recovery models are often used to predict the water recovery in such cases.

2.8.1. Modelling water recovery

There is lack of agreement in literature on which water recovery model is appropriate for modelling water recovery in Industrial flotation cell (Stevenson, 2007; Zheng et al., 2006a). Fundamental models have been shown to perform better than empirical models when applied to experimental data (Zheng et al., 2006a). The work carried out so far in developing fundamental models has produced models that are only for application in control purposes; no satisfactory fundamental predictive model is available in literature (Neethling et al., 2003; Neethling and Cilliers, 2003; Stevenson et al., 2007). Empirical models fit experimental data reasonably well for a given flotation system hence they offer a reasonable solution for modelling water recovery in Industrial flotation cells (Zheng et al., 2006a). Table 2.7 provides a summary of most of the models available in literature and gives a brief description of each of the models.

Table 2-7: Summary of water recovery models found in literature

Category	Expression	Model description
<p>Water recovery as a function of solids recovery models</p>	$Q_w = \frac{SG_S - SG_P}{SG_P - SG_W} \times \frac{1}{SG_S} \times F_S$ $Q_w = a \cdot F_S^b$	<p>Relates concentrate water flow rate to the solid concentration flow rate (Zheng et al., 2006a).</p> <p>Expresses concentrate water as a power function of the concentrate solids flow rate. Inappropriate for modelling flotation columns of small size diameter (Zheng et al., 2006a).</p> <p>Modified expression of the power model for water recovery in flotation columns of any size (Uribe et al., 1999). Inappropriate for application to systems where the SG and the concentrate slurry are sensitive to the process variables (Zheng et al., 2006a; Uribe et al., 1999).</p>
<p>Water recovery as a function of froth residence time</p>	$R_w = c \cdot \tau_f^d$ $\tau_f = \frac{V}{E'}$ $\frac{R_w}{1 - R_w} = \frac{R_{cw}}{1 - R_{cw}} \cdot \exp(-\beta_w \cdot \tau_f)$	<p>Savassi et al. (1998) developed an empirical expression relating froth recovery to the froth residence time based on industrial data from a lead rougher circuit. Model is unable to distinguish the effects of froth height and air rate on water recovery (Zheng et al., 2006a). The use of a single mean froth residence time does not adequately represent froth transportation and hence it cannot be used to determine water recovery (Zheng et al., 2006a).</p> <p>Water recovery is assumed to be a two step process i.e recovery of water from pulp to the froth followed by the recovery of water from the froth to the concentrate (Gorain et al., 1998). Model has the same limitations as the Savassi et al. (1998) model due to the use of a single value of mean froth residence time</p>

First order water recovery model	$R_w = 1 - \frac{1}{1 + P_w \cdot S_b \cdot \tau \cdot \Omega \cdot \exp(\rho \cdot V_f - \chi \cdot \tau_f)}$	Based on the assumption that the transfer of water from the pulp phase to the froth phase follows first order kinetic expression. First order assumption was merely a method to improve on the water recovery model by Gorain et al. (1998) and was not a reflection of the true observed mechanism of transfer of water from pulp to the froth. Model gave similar results to Savassi et al. (1998) and Gorain et al. (1998) when was applied (Zheng et al., 2006a).
Drainage model for water recovery models	$Q_w = A \cdot S_b \cdot \delta \cdot \alpha \cdot \exp(-k_{wd} \cdot \tau_f)$	Water recovery considered a two step process (Moys, 1984). Model gives god fit to the experimental data for overall water recovery. The physical significance of the model parameter e.g the water film thickness of air bubbles, may not reflect true water recovery mechanisms (Zheng et al., 2006a).
	$Q_w = \alpha_a Q_a \left(\frac{1}{1 - \frac{255.6}{r_b^2} \cdot J_g \cdot (1 - \alpha_a) \cdot \frac{\eta}{\rho_w \cdot g}} - 1 \right)$	The variables in the model have a physical meaning and can be experimentally determined (Neethling and Cilliers, 2003; Neethling et al., 2003; Neethling et al., 2000). When applied to experimental data the model gave a good fit even at different operating conditions and perfomed better than empirical models (Zheng et al., 2006a). However the model expressions used by Zheng (2006a) are unrecognizable from those in Neethling's et al. (2003) paper(Stevenson, 2007). The model is limited to application in process control and cannot be used in its present form for predictive purposes (Neethling et al., 2003). Stevenson proposes an alternative liquid recovery model and argues against that developed by Neethling et al. (2003) (Stevenson, 2007; Stevenson et al., 2007). He points out fundamental flows in developing a water recovery model based on the equations by Neethling et al. (2003) (Stevenson, 2007). The model is in excellent agreement with experimental data (Stevenson et al., 2007). However experimental tests conducted so far were carried out on de-mineralized foam.

CHAPTER THREE

3. METHODOLOGY

This Chapter describes the fundamental property based model that was used to model the flotation process in the flow sheet simulations that were used to investigate the effects of feed ore variation on flotation. Model parameter values from literature that were used in calibrating the model are presented along with methods for obtaining these parameters. Lastly, a description of HSC Chemistry 7 flow sheet simulation modelling software will be discussed along with the method that was followed in integrating the fundamental property based model into the simulation software. Each step that was carried out in developing the fundamental property based model simulation wizard in HSC Chemistry 7 simulation software during the model integration phase will be discussed in detail.

3.1. The fundamental property based flotation model

A fundamentally derived property based model was selected for determining the flotation rate constant of microwave treated ore over experimental methods because fundamental models utilise liberation as an indirect variable in calculating the flotation rate constant through the use of contact angle to describe particle surface hydrophobicity. This is in contrast to experimental methods where there is no specific association of the flotation rate to particle size or mineral liberation (Ralston et al., 2007). For this study it was important that the chosen method for determining the flotation rate constant be sensitive to changes in feed ore mineral liberation and particle size as these were variable properties in the simulations. Other major limitations of experimental methods that made them unattractive for use in this study were the costs associated with the method. This is because changes in feed ore mineral liberation properties require a separate set of kinetic data to be obtained from the experimental methods; this increases the cost of investigating the effects feed ore liberation changes to the flotation process (Dobby and Savassi, 2005).

Development of the fundamental property based model for the prediction of flotation cell recovery represents a major step in flotation modelling. The property based model, unlike first order methods, offers a great opportunity in the investigation of the effects of various cell conditions on flotation recovery and scale up processes. The expression for the rate of removal of particles per unit volume, N_p , in a flotation cell described in Chapter 2 section 2.4.2, equation 2.6 may be written as follows (Bloom and Heindel, 2002; Grano, 2006):

$$\frac{dN_P}{dt} = -k = -Z_{pb} \cdot E_{coll} / N_P \quad 3.1$$

This rate expression supports the first order rate approach to modelling flotation (Bulatovic, 2007; Mao and Yoon, 1997; Pyke et al., 2003). It was shown Chapter 2 section 2.4.2 that this rate can be expressed as the product of the collection efficiency E_{coll} and the bubble-particle collision frequency Z_{pb} equation 2.7 (Pyke et al., 2003; Mao and Yoon, 1997; Duan et al., 2003). The negative sign indicates the population density of the particles in the cell is decreasing. The flotation rate constant can thus be described as a function of appropriate bubble-particle collision frequency per unit volume Z_{pb} and the collection efficiency E_{coll} models for turbulent hydrodynamic conditions found in flotation cells (Yoon and Mao, 1996; Mao and Yoon, 1997; Bloom and Heindel, 2002).

$$k = Z_{pb} / N_P \cdot E_{coll} \quad 3.2$$

Extensive work has been carried out for developing a general turbulent flotation rate model from first principle; one such model was developed by Pyke et al. (2003) (see equation 3.3).

$$k = \overbrace{\underbrace{2.39 \frac{G_{fr}}{d_b \cdot V_{cell}}}_{\text{Mechanical term}} \left[\underbrace{\frac{0.33 \varepsilon^{\frac{4}{9}} d_b^{7/9}}{\vartheta^{\frac{1}{3}}} \left(\frac{\Delta \rho_b}{\rho_{fl}} \right)^{\frac{2}{3}} \cdot \frac{1}{v_b}}_{\text{Primary turbulence term}} \right]}_{\text{Collision frequency}} \underbrace{E_c \cdot E_a \cdot E_s}_{\text{Elementary process}}}_{\text{Flotation rate constant (time}^{-1}\text{)}} \quad 3.3$$

In equation 3.3 above the elementary flotation sub-processes are represented by relevant bubble-particle collision, attachment and stability efficiency models. The remainder of the expression represents the collision frequency per unit volume. Below the derivation of the form of the general flotation model used in this study will be given.

3.1.1. The bubble-particle collision frequency

Abrahamson (1975) derived an expression for describing the collision frequency for turbulent-flow (see equation 3.4). In the expression collision frequency is modelled in terms of the fluctuations of bubbles and particles. The bubble and particle fluctuations can be related to the character of the turbulent-flow that drives them (Brady et al., 2006).

$$Z_{pb} = 5N_p N_b d_{pb}^2 \sqrt{(\bar{V}_p^2 + \bar{V}_b^2)} \quad 3.4$$

- N_p and N_b are the number densities of floatable particles and bubbles respectively,
- \bar{V}_p and \bar{V}_b are the turbulent fluctuating velocity of the particles and bubbles respectively relative to the fluid.
-

$$d_{pb} = \left(\frac{d_p + d_b}{2} \right) \quad 3.5$$

- d_p and d_b are the particle and bubble diameters. For a fine disperse suspension the particle diameter, d_p is much smaller than the bubble diameter d_b (Schubert, 2008)

In typical flotation processes the turbulent fluctuating velocities \bar{V}_p and \bar{V}_b have been found to be a function of the local turbulent dissipation energy and are approximately given by the following empirical expression proposed by Liepe and Mockel (1976), equation (Schubert and Bischofberger, 1998; Schubert, 2008; Abrahamson, 1975; Koh and Schwarz, 2006; Liu and Schwarz, 2009b):

$$\bar{V}_i = \frac{0.33 \varepsilon^{4/9} d_i^{7/9}}{\nu^{1/3}} \left(\frac{\rho_i - \rho_f}{\rho_f} \right)^{2/3} \quad 3.6$$

where the subscript i refers to the particle or bubble,

ε is the turbulent dissipation energy

ν is the kinematic viscosity

ρ_i refers to the density of the bubble or particle

Liepe and Mockel's equation is used to describe the turbulent velocities in Abrahamson's model. This model, which is developed by dimensional analysis and least squares fitting methods over experimental data, is valid at intermediate Stokes numbers typical of flotation processes (Schubert, 1999; Brady et al., 2006). Although the model is appropriate in determining the relative particle turbulent velocity, its use for predicting the bubble turbulent velocity has been questioned in literature (Brady et al., 2006; Sherrell, 2004). An alternative model equation 3.7 has been developed specifically for determining bubble root mean square (rms) (Suazo et al., 2009; Brady et al., 2006) .

$$\bar{V}_b^2 = 2(\varepsilon d_b)^{2/3} \quad 3.7$$

Equation 3.7 was however not used for determining the fluctuating bubble velocity in this study. This was mainly because in developing the general flotation model expression shown in equation 3.3, Pyke (2003) used Liepe and Mockel's model equation 3.6 for determining the bubble fluctuating velocity.

$$\sqrt{\bar{V}_b^2 + \bar{V}_p^2} = \left[\left[\frac{0.33\varepsilon^{4/9}d_b^{7/9}}{\vartheta^{1/3}} \left(\frac{\rho_b - \rho_f}{\rho_f} \right)^{2/3} \right]^2 + \left[\frac{0.33\varepsilon^{4/9}d_p^{7/9}}{\vartheta^{1/3}} \left(\frac{\rho_p - \rho_f}{\rho_f} \right)^{2/3} \right]^2 \right]^{1/2} \quad 3.8$$

To arrive at the final expression of the collision frequency per unit volume, Pyke et al. (2003) assumed that the particle rms velocity $\sqrt{\bar{V}_p^2}$ and the particle diameter d_p could be neglected (Duan et al., 2003; Pyke et al., 2003). After making these assumptions the final expression of collision frequency per unit volume derived by Pyke et al (2003) is presented in equation 3.9.

$$Z_{pb} \approx 5N_p N_b \left(\frac{d_b}{2} \right)^2 \left[\frac{0.33\varepsilon^{4/9}d_b^{7/9}}{\vartheta^{1/3}} \left(\frac{\rho_b - \rho_f}{\rho_f} \right)^{2/3} \right] \quad 3.9$$

$$d_{pb} \approx \frac{d_b}{2} \quad 3.10$$

The assumptions made by Pyke et al. (2003) stated above, are only valid for fine particles sizes below 100 μm where the particle diameter can be considered to be much smaller than the bubble diameter. In this study the particle fluctuating velocity was considered in the final expression of the collision frequency. Thus the collision frequency per unit volume Z_{pb} used in this study is expressed as (Suazo et al., 2009);

$$Z_{pb} \approx 5 \left(\frac{d_p + d_b}{2} \right)^2 N_b N_p \left[\left[\frac{0.33\varepsilon^{4/9}d_b^{7/9}}{\vartheta^{1/3}} \left(\frac{\rho_b - \rho_f}{\rho_f} \right)^{2/3} \right]^2 + \left[\frac{0.33\varepsilon^{4/9}d_p^{7/9}}{\vartheta^{1/3}} \left(\frac{\rho_p - \rho_f}{\rho_f} \right)^{2/3} \right]^2 \right]^{1/2} \quad 3.11$$

The bubble number density N_b can be related to the gas flow rate G_{fr} and the residence time of bubbles in the unit volume t_r by the following expression (Pyke et al., 2003; Duan et al., 2003):

$$N_b = \frac{6G_{fr}}{\pi d_b^3 V_{cell}} t_r \quad 3.12$$

where V_{cell} is the flotation cell volume. The residence time of the bubbles can be expressed as the time that bubbles of velocity v_b remain in a unit volume.

$$t_r = \frac{1 \text{ unit length}}{v_b} \quad 3.13$$

Where the superficial gas velocity, J_g , is used instead of the gas flow rate, G_{fr} , the bubble number density, N_b is expressed as,

$$N_b = \frac{6J_g(L_c \times W_c)}{\pi d_b^3 \cdot V_{cell}} t_r \quad 3.14$$

where L_c and W_c are the length and width of the flotation cell (Grano, 2006).

Equation 3.15 represents the final form of the general flotation model that was used in this study for predicting the kinetic flotation rate constant, k , under turbulent flotation conditions.

$$k = 2.39 \frac{G_{fr}}{d_b^3 \cdot V_{cell}} (d_p + d_b)^2 \sqrt{\bar{V}_b^2 + \bar{V}_p^2} \left(\frac{1}{v_b} \right) \cdot E_{coll} \quad 3.15$$

Table 3-1: Summary of the mechanical and primary turbulence terms expressions

Term	Expression	Model input Parameters	Parameters required	Method for obtaining parameter
Mechanical term	$2.39 \frac{G_{fr}}{d_b \cdot V_{cell}}$	<p>G_{fr}-Gas flow rate</p> <p>d_b-bubble diameter</p> <p>V_{cell}-Volume of cell</p>	G_{fr}	Set operating variable
			d_b	UCT bubble size analyser/McGill bubble viewer
Primary turbulence Term	$\frac{0.33 \varepsilon^{\frac{4}{9}} d_i}{\vartheta^{\frac{1}{3}}} \left(\frac{\Delta \rho_i}{\rho_{fl}} \right)^{\frac{2}{3}} \cdot \frac{1}{v_b}$ $V_{fl} = \sqrt{V_x^2 + V_y^2 + V_z^2}$ $q = \frac{1}{2} [\bar{U}_x^2 + \bar{U}_y^2 + \bar{U}_z^2]$ $\varepsilon = 0.85 \frac{q^{3/2}}{L}$ <p>i = subscript- refers to bubble or particles</p>	<p>ε -turbulent dissipation energy</p> <p>V_{fl}-average fluid velocity</p> <p>V_x^2, V_y^2, V_z^2-Velocity measurements in the x,y,z direction.</p> <p>q -turbulent kinetic energy</p> <p>$\bar{U}_x, \bar{U}_y, \bar{U}_z$ -root mean square of fluctuations of the turbulent fluid velocities</p> <p>L -half the impeller blade width</p> <p>ν -kinematic viscosity</p> <p>v_b-bubble velocity</p> <p>$\Delta \rho_i$-particle and fluid density difference or bubble fluid density</p>	<p>V_{fl}</p> <p>ϑ</p> <p>v_b</p> <p>$\Delta \rho_i = \rho_i - \rho_{fl}$</p>	<p>Laser Doppler velocimetry measurements(LDV), V_{fl}</p> <p>Property of fluid</p> <p>Drag coefficient method for calculating the bubble velocity(Lapple and Shepherd 1940)</p>

Table 3-1 above is a summary of the mechanical and primary turbulence terms expressions the product of which gives bubble-particle collision frequency a value that is required in the fundamental property based model equation 3.1. The various model input parameters required to calculate each term are given in the table along with a brief description of the method that is used in obtaining the parameters.

3.1.2. Calculation of the elementary processes

The elementary processes in equation 3.1 are described by the collection efficiency; which is a product of the flotation sub-process of collision, attachment and stability (equation 3.16).

$$E_{Coll} = E_c \cdot E_a \cdot E_s \quad 3.16$$

The various models for determining the collision, attachment and stability efficiencies have been discussed in Chapter two. In deriving a general flotation model it is important to capture the turbulent characteristics of the flow in the flotation as well as the hydrodynamic and surface forces. Models that capture all three of these factors have not been fully developed. The following elementary sub-process models are used in the general flotation model for determining the collection zone efficiency,

1. GSE model for determining the Collision efficiency
2. Modified Dobby and Finch attachment model
3. Schulze stability efficiency model

These models capture the particle surface chemistry in the flotation process. The parameters required to calibrate these models can be obtained through application of different experimental methods described in literature making them useful tools in flotation modelling.

3.1.2.1. Collision efficiency determined by the Generalised Sutherland equation (GSE)

Collision efficiency has been predicted based on potential flow conditions by Sutherland and others, leading to the development of the GSE (Nguyen et al., 2006; Nguyen and Nguyen, 2009). The GSE model (Miettinen et al., 2009; Dai et al., 1998), E_{C-GSE} , incorporates the interceptional mechanism of the Sutherland model with the positive effect of hydrodynamic pressing force and the negative effect of centrifugal acceleration (equation 3.17).

$$E_{C-GSE} = E_{C-SU} \cdot \sin^2 \theta_t \cdot \exp(I_1 + I_2) \quad 3.17$$

Where $E_{C-SU} = \frac{3d_p}{d_b}$

E_{C-SU} is the Sutherland collision efficiency accounting only for the interception mechanism, I_1 is the positive effect of the hydrodynamic pressing force (equation 3.18) and I_2 is the negative effect of centrifugal acceleration (see equation 3.19).

$$I_1 = 3K_3 \left(\ln \frac{3}{E_{C-SU}} - 1.8 \right) \quad 3.18$$

$$I_2 = - \frac{4 \left(\frac{2}{3} + \frac{\cos^2 \theta_t}{3} - \cos \theta_t \right)}{\sin^4 \theta_t} \quad 3.19$$

The maximum angle of tangency θ_t is the maximum collision angle of the particle to the bubble beyond which collision is prevented (Dai et al., 1998; Dai et al., 2000; Miettinen et al., 2009). When the angle of collision $\theta_c < \theta_t$ the hydrodynamic pressing force is dominant thereby improving the chances of particle deposition, at $\theta_c > \theta_t$ the negative centrifugal force prevents collision (Dai et al., 1998; Dai et al., 2000; Miettinen et al., 2009). The maximum angle of tangency θ_t is defined as,

$$\theta_t = \sin^{-1} \left\{ 2\beta \left[(1 + \beta^2)^{1/2} - \beta \right] \right\} \quad 3.20$$

where β is a dimensionless number defined as,

$$\beta = \frac{4E_{C-SU}}{9K_3} \quad 3.21$$

K_3 is defined as,

$$K_3 = \frac{v_b(\rho_p - \rho_{fl})d_p^2}{9\mu_f d_b} \quad 3.22$$

Where; μ_f is the fluid viscosity. For large β values ($\beta \geq 1$), θ_t approaches 90° and inertial forces do not interfere with the interception mechanism; under these conditions the Sutherland collision model is valid. When $\beta \leq 1$, the θ_t values shift significantly away from 90° due to inertial forces and interceptional effects that are both at play. Thus β represents the measure of the relative importance of the interceptional and inertial effects contribution to the collision process in the GSE (Dai et al., 2000; Duan et al., 2003). The GSE model is thus capable of taking into account both the inertial and gravity effects that are present when the particle size is larger than the limit size for the Sutherlands' model ($0.1 \mu\text{m}$) (Dai et al., 2000; Pyke et al., 2003).

3.1.2.2. Attachment Efficiency determined by the Dobby-Finch attachment model

The modified Dobby-Finch attachment model is used to determine the bubble-particle attachment sub-process efficiency. The model is based on the relative magnitudes of the induction time and sliding time (Dobby and Finch, 1987). The induction and sliding time have been discussed in Chapter two, section 2.4.3.2 which offers a review of attachment models. The model assumes that particle-bubble collision occurs evenly over the section of the bubble surface between the following angles $\theta = 0$ and $\theta = \theta_t$ where θ is measured from the stagnation point or upper surface of the rising bubble (Ralston et al., 1999; Pyke et al., 2003; Duan et al., 2003). θ_t . Dobby and Finch then defined the attachment efficiency as the ratio of the area corresponding to θ_a to the area corresponding to θ_t , where θ_a is the adhesion angle.

$$E_a = \frac{\sin^2 \theta_a}{\sin^2 \theta_t} \quad 3.23$$

Where E_a Attachment efficiency, θ_a -adhesion angle, θ_t is the maximum possible collision angle.

The adhesion angle is defined as the specific contact angle where if a particle collides at this angle, its sliding time will be equivalent to the induction time. The adhesion angle relates the sliding and induction times to the attachment efficiency.

$$\theta_a = 2 \arctan \exp \left[-t_{ind} \frac{2(v_p + v_b) + v_b \left(\frac{d_p}{d_p + d_b} \right)^3}{d_p + d_b} \right] \quad 3.24$$

Where: θ_a -adhesion angle, v_p -particle velocity, v_b -bubble velocity, d_p -particle diameter, d_b -bubble diameter, t_{ind} -induction time. The induction time is a function of contact angle and particle size and can be determined experimentally. It can be correlated by the following empirical equation (Dai et al., 1999; Koh and Schwarz, 2006; Ralston et al., 1999; Pyke et al., 2003; Duan et al., 2003; Miettinen et al., 2009),

$$t_{ind} = Ad_p^{0.6} \quad 3.25$$

Where; A, constant parameter and d_p is the particle diameter. Based on the work carried out by (Dai et al., 1999), parameter A was observed to be inversely proportional to the particle contact angle φ . Using these results, Koh et al., (2006) later developed the following empirical equation for determining the induction time.

$$A = \frac{75}{\varphi} \quad 3.26$$

Where; d_p -particle diameter (m), φ -contact angle (degrees) and t_{ind} -induction time is obtained in (seconds). This expression has subsequently been successfully applied in the determination of parameter A by other authors (Shahbazi et al., 2009).

The particle settling velocity under the turbulent cell conditions, v_p , is obtained using the following expression (Bruce, 2003),

$$v_p = \frac{20.52}{d_p \rho_f} \left(\left[\left(\frac{d_p^3 (\rho_s - \rho_f) \rho_f g}{0.75 \vartheta^2} \right)^{0.5} \right]^{0.5} - 1 \right)^2 \quad 3.27$$

The modified Dobby and Finch model essentially expresses attachment efficiency as a ratio of particle attached to a bubble over the maximum possible particles that can be attached to a bubble. It does not fully capture the effects of the electrostatic, van der Waals, and hydrophobic surface forces.

However the model has been validated and has been shown to be suitable for describing the bubble-particle attachment sub-process efficiency. Models have been developed based on the DVLO theory that captures surface forces effects on the attachment process (Yoon and Mao, 1996). Comprehensive validation of these models has not been reported in literature (Ralston et al., 1999).

3.1.2.3. Particle-bubble stability efficiency determined by Schulze model

Particle-bubble stability efficiency depends on the attachment force between the bubble and the particle in relation to detachment forces, in the environment (Ralston et al., 1999; Duan et al., 2003). Schulze (2009) proposed that the bubble-particle stability efficiency could be expressed as follows,

$$E_s = 1 - \exp\left(1 - \frac{F_{att}}{F_{det}}\right) \quad 3.28$$

The modified bond number Bo^* is defined as the ratio of the attachment and detachment forces and is given by (Bloom and Heindel, 1997).

$$Bo^* = \frac{F_{att}}{F_{det}} = \frac{d_p^2(\Delta\rho g + \rho_p a_c) + 1.5d_p(\sin^2 \omega)f(d_b)}{|6\gamma \sin \omega \sin(\omega + \varphi)|} \quad 3.29$$

with,

$$f(d_b) = \left(\frac{4\gamma}{d_b} - d_b \rho_{fl} g\right) \quad 3.30$$

where; $\omega = 180^\circ - \varphi/2$ refers to the location of the particle at the liquid-vapour interface, φ -contact angle, γ -liquid-vapour surface tension, g -gravitational constant, and a_c -particle centrifugal acceleration. The particle centrifugal acceleration a_c can be related to the turbulent-flow field and the dissipation energy, ε (Schulze, 1977). Assuming that the aggregates are moved mainly by the centrifugal acceleration present in the vortex and the turbulent radius is equal to the aggregate radius the particle centrifugal acceleration can be described by equation 3.31 for large eddies. (Miettinen et al., 2009; Bloom and Heindel, 1997)

$$a_c = 1.9 \frac{\varepsilon^{2/3}}{\left(\frac{d_p}{2} + \frac{d_b}{2}\right)^{1/3}} \quad 3.31$$

3.2. General flotation model parameter determination for model calibration

In calculating the flotation rate constant using the general flotation model the following are some of the required parameters (see equation 3.15).

1. Energy dissipation
2. Bubble diameter
3. Bubble rise velocity
4. Contact angle of liberated particle.

These parameters are not commonly available from flotation cell operations plant data as they are not routinely measured. In this study values for these parameters that were used in the simulations were obtained from a previous study that was carried out by Ralston et al. (2007) on a Copper flotation concentrator plant. Table 3-2 is a summary of values of these parameters from the work carried out by Ralston et al. (2007). The methods that were used by Ralston et al (2007) to come up with these value and other methods for determining these values available in literature will be discussed and presented in this section. A list of all the fundamental property based model input parameter values that were used in calibrating the fundamental property based model in this study is given in Appendix G, Table G.1.1

Table 3-2: Model calibration parameters from a study carried out by (Ralston et al., 2007)

Variable	Literature Parameter (Ralston et al., 2007)
Sulphide mineral contact angle (φ)	78°
Energy dissipation (ϵ)	11 m ² /s ³
Bubble diameter (d_b)	0.0013 m
Bubble rise velocity (v_b)	0.18 m/s

3.2.1. Determination of particle Contact angle

The contact angle φ is described thermodynamically by Young's equation,

$$\gamma_{s/a} = \gamma_{s/l} + \gamma_{l/a} \cos \varphi \quad 3.32$$

Where $\gamma_{s/a}$, $\gamma_{s/l}$, $\gamma_{l/a}$ are the solid-vapour, solid-liquid, and liquid-vapour interfacial tensions respectively. Duan et al. (2003) used the relationship between advancing contact angle and Time of Flight Secondary ion Mass spectroscopy (ToF-Sims) analysis results, to determine the sulphide particles single phase contact angle.

Ralston et al (2007) using the same method reported a sulphide contact angle value of 78°. In this study a value for the contact angle of fully liberated sulphide minerals of 78° was used, while fully liberated NSG was assumed to have a zero contact angle as was the case in Ralston's study (Ralston et al., 2007). Contact angle values for sulphide minerals that are reported in literature range between 68° to 85° (Duan et al., 2003; Pyke et al., 2003; Ralston et al., 2007). Most mineral particle exists as composites while current contact angle measurement methods report contact angle values for single phase minerals. To overcome this problem the Cassie equation has been found to be appropriate for determining the composite particle contact angle (Ralston et al., 2007). A description of composite particle contact angle calculation method utilising the Cassie equation as used in this study is given below.

3.2.1.1. Composite particles contact angle calculation

Cassie equation is often applied in determining the contact angle ore particles (Ralston et al., 2007; Chau et al., 2009). The individual ideal mineral contact angles are used to relate the apparent contact angle of the ore particle through Cassie's equation as follows (see equation 3.33) (Bormashenko, 2008; Iwamatsu, 2006; Rodríguez-Valverde, 2008; Whyman et al., 2008; Zhang and Kwok, 2005; Chau et al., 2009),

$$\cos \varphi = f_1 \cos \varphi_1 + f_2 \cos \varphi_2 \quad 3.33$$

where; f_1 and f_2 -fractional areas of mineral surfaces on a single particle with contact angle φ_1 and φ_2 . The Cassie's equation was initially proposed for describing contact angle changes for two component porous surfaces (Iwamatsu, 2006; Zhang and Kwok, 2005). It can be used for predicting the contact angle of rough heterogeneous hydrophobic surfaces (Bormashenko, 2008). There are some concerns regarding the validity of Cassie's equation especially its application to mineral systems (Iwamatsu, 2006; Zhang and Kwok, 2005; Rodríguez-Valverde, 2008). However no alternative models have been developed yet that adequately capture the physical surface properties (Ralston et al., 2007).

3.2.2. Energy dissipation

The main source of energy in a mechanical flotation cell is derived from the motion of the impeller which produces the turbulent conditions within the cell. It has been shown that energy dissipation affects both the particle-bubble collision frequency and the bubble-particle aggregate stability (Newell and Grano, 2006; Newell and Grano, 2007). Direct calculation of energy dissipation rate requires evaluation of the strain rate at a spatial resolution less than the Kolmogorov length scale (Newell and Grano, 2006; Newell and Grano, 2007; Brady et al., 2006). There are no methods available in literature that can fully resolve the instantaneous spatial derivatives at such small scales (Brady et al., 2006). However there are methods that have been reported in literature for calculating dissipation energy based on different techniques for measuring velocity fluctuations in a stirred tank. Some of these methods are; Digital particle image velocimetry, Laser-Doppler velocimetry, and hot wire velocimetry methods (Wu and Patterson, 1989; Brady et al., 2006; Newell and Grano, 2006; Newell and Grano, 2007). Wu and Patterson (1989) proposed the following equation for calculating the turbulent dissipation energy,

$$\varepsilon = \frac{Aq^3}{L} \quad 3.34$$

where, A is a constant, L is a measure of the turbulent length macro scale and q is the turbulent kinetic energy. A has been found to be equal to 0.85 and L is generally assumed to be constant and equal to half the turbine length (Wu and Patterson, 1989). The turbulent kinetic energy can be obtained as follows (Duan et al., 2003; Pyke et al., 2003),

$$q = \frac{1}{2} [\bar{U}_x^2 + \bar{U}_y^2 + \bar{U}_z^2] \quad 3.35$$

where; \bar{U}_x^2 , \bar{U}_y^2 , \bar{U}_z^2 are the root mean square of fluctuations of the measured turbulent fluid velocities (Pyke et al., 2003; Duan et al., 2003). In this study a local energy dissipation value of 11W/kg for a 85 m³ mechanical flotation cell as reported by Ralston et al.(2007) was used to calibrate the fundamental based model along with other parameters from the same study by Ralston et al.(2007).

3.2.3. Bubble diameter

There are two well established techniques for measuring bubble size in flotation cells; capillary and imaging techniques (Hernandez-Aguilar et al., 2004). The McGill bubble viewer and the UCT bubble size analyser have been tested under both laboratory and plant conditions and they have been shown to give satisfactory estimates of bubble size in flotation cells (Hernandez-Aguilar et al., 2004; Ralston et al., 2007; Grau and Heiskanen, 2002; Grau and Heiskanen, 2003). Typical bubble diameter sizes range between 0.8 mm to 2 mm (Schwarz and Alexander, 2006; Grano, 2006; Massinaei et al., 2009b). A Sauter mean bubble diameter of 1.3 mm reported in the work done by Ralston et al. (2007) was used in the model calibration. Various methods are available in literature for obtaining this value for a typical operating flotation cell. These methods will be described briefly below.

3.2.3.1. McGill bubble viewer

The McGill bubble viewer utilises imaging techniques for bubble size measurement. It is designed to measure bubble sizes by directing a sample of bubbles into a specially design viewing chamber (Hernandez-Aguilar et al., 2004). The bubbles in the chamber are then exposed to light and photographed with a digital camera as they impact on a sloped glass plane (Grau and Heiskanen, 2002; Leiva et al., 2010). An image analysis procedure is then used to size the collected bubbles and hence determine the Sauter mean bubble diameter (Grau and Heiskanen, 2002; Hernandez-Aguilar et al., 2004).

3.2.3.2. UCT bubble size analyser

The UCT bubble size analyser utilises capillary methods for measuring the bubble size. It operates by capturing the bubbles and drawing them through a capillary tube (Hernandez-Aguilar et al., 2004). A sampling tube is attached to a water reservoir where the capillary tube is placed (Grau and Heiskanen, 2002). Captured bubbles ascend through the sampling tube to the reservoir where they are suctioned into the capillary tube (Grau and Heiskanen, 2002; Hernandez-Aguilar et al., 2004). In the capillary tube the bubble length and velocities are measured by using optical detectors (Ralston et al., 2007). From these reading the bubble sizes are then determined (Grau and Heiskanen, 2002).

3.2.4. Bubble rise velocity

Bubble rise velocity is assumed to be equivalent to the fluid velocity that is measured by utilising velocimetry techniques (Pyke et al., 2003). In this study a bubble rise velocity value of 1 cm/s from the work by Ralston et al. (2007) was used in calibrating the model.

3.3. HSC Chemistry 7 simulation software

HSC Chemistry 7 simulation software has a function that allows for true particle modelling. True particle modelling refers to the highest level of modelling in HSC Chemistry Simulation software where the mineral particles that are treated in the simulation processes have been measured using MLA. The Mineral Liberation Analysis data files are used directly to represent the feed ore particles in the simulations. Particles are then generated based on the mineralogical information from the MLA data. The program then utilises particle tracking algorithms which allows for the liberation data for each of the streams in the simulation to be reported during the simulations. This is an important function as the actual individual particle liberation data can be used in the simulation.

3.3.1. Particle tracking in HSC Chemistry Simulation software

HSC Chemistry 7 simulation module has four calculation modes.

1. Particles (Minerals)
2. Reactions (Hydro)
3. Distribution (Pyro)
4. Experimental

Discussion will focus on the particle mode as it is the appropriate mode for carrying out simulation in minerals processing operations.

3.3.2. Particles (Mineral) mode

The liquid phase is assumed to be inert and no reactions take place in the system. This mode is appropriate for modelling grinding and flotation circuit processes. In this mode the variables are particles; these can in the simplest case be un-sized liberated particles. The most complex case is where the particles are real measured particles from Mineral Liberation Analysis data (MLA) (Roine, 2010).

3.3.2.1. True particle modelling in HSC Chemistry Simulation software using MLA data

The minerals based models that are used in simulating mineral processing flow sheets in HSC Chemistry 7 simulation module treat mineral particles from MLA data which have the following properties.

1. Size Diameter
2. Mineral Composition as wt%
3. Composition by volume
4. Mineral composition by surface area %

In generating particles in HSC Chemistry 7 Simulation software, mineralogical data are required. This data can be subdivided into two categories.

1. Global set up data which constitutes of general global mineral properties which do not change in the process such as chemical composition and specific gravity. These are calculated in HSC Chemistry 7 Simulation software for each particle and stream.
2. Input stream set up data which is obtained from the MLA analysis data. It consists of the main particle properties such as particle mineral composition and size. The following mineralogical information which is presented as a feed stream set up file in HSC Chemistry Simulation software is obtained from MLA data.
 - a. Weight percentage of each size class
 - b. Weight percentage of each mineral in each size class and bulk feed stream
 - c. Chemical composition of the fractions and the bulk feed

Appendix E is a summary of the file structure in HSC Chemistry 7 simulation software package.

3.4. Integrating the Fundamental model into HSC Chemistry 7

The fundamental property based flotation model was integrated into HSC Sim program so as to facilitate its use in flotation modelling.

A general flotation model wizard was created in HSC Chemistry Simulation 7 module utilising HSC Chemistry 7 Excel Macro commands in order to allow for the use of the

fundamental property based model in HSC Chemistry 7 during modelling. The model calculation steps were applied to individual particles, this allowed for the calculation of the flotation rate constant of individual particle based on the individual particle's liberation, density and size properties. The particle's liberation was related to particle hydrophobicity through the particle contact angle.

The model calculation steps programmed in the wizard were as follows.

1. Utilising the Cassie's equation, contact angles for all particles in each size class were calculated. This was done taking into account the individual single mineral contact angles of the mineral groups making up the particles and their composition.
2. The sub-process efficiencies for each particle were then calculated by taking into account the particle and fluid properties and contact angles.
3. Using the cell hydrodynamic information, the Mechanical and turbulent terms in the general flotation model expression were calculated.
4. A flotation rate constant, k_{Coll} , for each particle was then evaluated.
5. Perfect mixing in pulp zone was assumed in calculating the overall collection zone recovery, R_{Coll} , for each particle.

$$R_{Coll} = \frac{k_{Coll} \cdot t}{(1 + k_{Coll} \cdot t)} \quad 3.36$$

6. The flotation cell was assumed to consists of two distinct phases the pulp and the froth phase. The froth recovery term, R_f , was used to describe the contribution of the froth phase to the bubble-particle recovery to the concentrate, $R_{attached}$. The bubble-particle recovery is expressed as a product of the froth phase recovery and the collection zone recovery.

$$R_{attached,i} = R_f \cdot R_{Coll} \quad 3.37$$

7. The contribution of entrainment, R_{ent} , to overall recovery was calculated using flotation cell water recovery, R_w , and the degree of entrainment ENT for each particle (Yianatos et al., 2009; Zheng et al., 2006b; Zheng et al., 2005).

$$R_{ent} = R_w \cdot ENT \quad 3.38$$

The degree of entrainment, ENT , was calculated per particle size using an empirical model as follows (Savassi et al., 1998; Zheng et al., 2006b),

$$ENT = \frac{2}{\exp\left(2.292\left(\frac{d_i}{\xi}\right)^{adj}\right) + \exp\left(-2.292\left(\frac{d_i}{\xi}\right)^{adj}\right)} \quad 3.39$$

$$adj = \frac{\ln(1/\delta)}{\exp(d_i/\xi)} \quad 3.40$$

Where; d_i is particle size (μm), ξ is the entrainment parameter, or the particle size for which the degree of entrainment is 20%, δ is the drainage parameter, related to the preferential drainage of coarse particles.

8. The overall recovery across the flotation cell (R_{ovr}) for each individual particle was calculated using the following expression,

$$R_{ovr} = \frac{R_{attached}(100 - R_{ent})}{100 + R_{ent}} \quad 3.41$$

Appendix I shows an example of model wizard screen captures as they would appear in HSC Chemistry 7.

3.5. Conclusion

In this Chapter the parameters used in flotation modelling and the method used in incorporating the fundamental property based model in HSC Chemistry 7 have been described in detail. After integrating, the model in HSC Chemistry 7 and obtaining all the parameters required for model calibration from literature a modelling framework for investigating the effect of feed ore liberation variation on recovery was developed and is now ready for use. In order to carry out preliminary investigations on the effect of liberation variation on flotation recovery, different artificial ores with varying liberation profiles should be prepared. By investigating the downstream processing flotation recovery of these ores it is hoped to get an indication of the expected benefits of improved liberation due to microwave treatment on flotation recovery. The next Chapter will discuss the creation of these different flotation feeds.

CHAPTER FOUR

4. CREATION OF ARTIFICIAL FEED ORES

Laboratory Rod milled flotation feed MLA data for porphyry copper ore at two grind sizes ($P_{70}=120\ \mu\text{m}$ and $P_{70}=180\ \mu\text{m}$) from a previous study, was available for use as a flotation feed in this study (AMIRA:P879A, 2009). This MLA data was manipulated to create different flotation feeds with different mineral particle liberation spectrum. Thus additional floatation feed ores termed artificial flotation feed ores in this study, were created for use in investigating the effects of feed ore liberation change on value mineral recovery. These ores were supposed to represent various possible liberation scenarios of ground flotation feed ores. Their liberation profiles ranged from well liberated to poorly liberated ores. Thus allowing for the investigation of the effects of enhanced liberation expected from the application of microwave technology to be investigated using these ores.

4.1. Introduction

A detailed discussion of the methodology that was used in creating different flotation feeds will be given below along with a description of the base case feed ores that were used in creating artificial ores in this study. This will be followed by a detailed analysis of the key differences between the created artificial ores and the base case feed ores. Lastly the method that was used in calculating contact angles from the MLA data will be discussed briefly.

4.2. Copper 1 and Copper 2 base case feed ore (BC)

The particle size distribution and the MLA data of the two base case Rod milled flotation feed ores Copper 1 ($P_{70} = 120\ \mu\text{m}$ ground feed) and Copper 2 ($P_{70} = 180\ \mu\text{m}$ ground feed) was obtained from previous experimental analysis carried out on the ores (AMIRA:P879A, 2009). In creating a stream file in HSC Geo, the ore feed in the simulations was grouped into the following three main mineral groups as is instructed when creating a stream file in HSC Chemistry 7 simulation software: Chalcopyrite (Cpy), NSG and Pyrite (Py). Chalcopyrite was selected as it represents the average composition of the copper sulphides in the feed. Appendix C, Table C.1-1 and Table C.1-2 shows the

mineral grouping that was carried out in creating the stream files and all the minerals groups that were in the feed ore before grouping respectively. The particle size distribution for Copper 1 and Copper 2 feed ore is presented in Table 4-1 below. Copper 1 BC feed ore contains 312 particle liberation classes while Copper 2 BC feed ore contains on average 357 particle liberation classes.

Table 4-1: Base case feed ore particle size distribution of Copper 1 ($P_{70}=120 \mu\text{m}$) and Copper 2 ($P_{70}=180 \mu\text{m}$)

Grind size weight distribution (wt. %)		
Size class (μm)	Copper 1	Copper 2
-600+425		4.87
-425+300	2.63	13.48
-300+212	12.25	12.71
-212+150	13.72	8.83
-150+106	10.82	7.01
-106+75	8.09	5.46
-75+53	6.67	4.83
-53+38	6.30	4.64
-38	39.52	38.17

From the cumulative particle size distribution curve in Figure 4-1 it can be seen that for the two feed ores there is a high weight percentage of fines in the feed which constitutes at least 38% of the bulk feed weight.

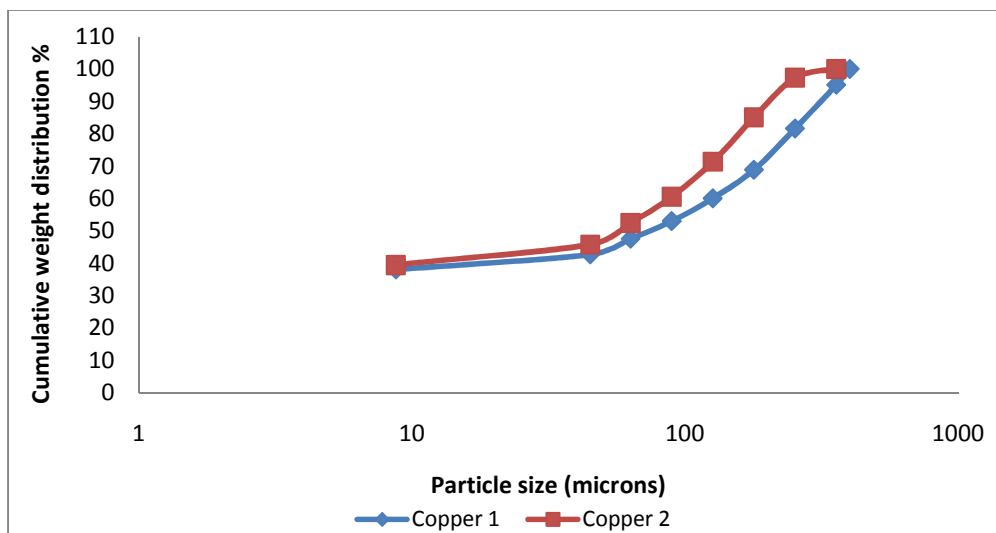


Figure 4-1: Base case feed ore cumulative particle size distribution.

The feed ore mineral composition by size for Copper 1 ore is shown in Table 4-2. Copper 1 feed ore had a Copper grade of 1.12%, while Copper 2 had a feed Copper grade of 1.08%. The mineral composition and mineral particle mode of occurrence for Copper 1 will be discussed first followed by a similar discussion of Copper 2 mineralogy.

4.2.1. Copper 1 mineralogy ($P_{70} = 120 \mu\text{m}$)

The bulk mineral composition by size for Copper 1 shows a low Chalcopyrite grade for the coarser size fractions (see Table 4-2).

Table 4-2 : Bulk mineral composition by size fraction of Copper 1 base case feed ore
 $P_{70}=120 \mu\text{m}$.

Size Class(μm)	0-38	38-53	53-75	75-106	106-150	150-212	212-300	300-425
Cpy wt%	4.24	3.55	3.19	3.09	2.76	2.17	1.78	1.33
Py wt%	4.32	5.92	7.88	7.59	10.39	9.47	8.00	7.19
NSG wt%	91.44	90.53	88.93	89.32	86.85	88.37	90.21	91.48

Figure 4-2 to Figure 4-4 is a graphical presentation of the mineral mode of occurrence of Chalcopyrite, Pyrite and NSG in Copper 1 base case feed ore. The mineral mode of occurrence for Chalcopyrite in Copper 1 feed ore shows that most of the chalcopyrite particles appear in fine size class range (0-38 μm) as fully liberated particles, (see Figure 4-2). The second most significant mode of occurrence for Chalcopyrite is as an associated binary particle with NSG predominantly in the 0 to 38 μm size class. Pyrite appears mostly as fully liberated particle in all size classes (see Figure 4-3). The second most significant mode of occurrence for Pyrite is as a binary liberated particle with Chalcopyrite. NSG appears in the feed largely as fully liberated particles although it is also associated with Chalcopyrite and Pyrite value minerals (see Figure 4-4).

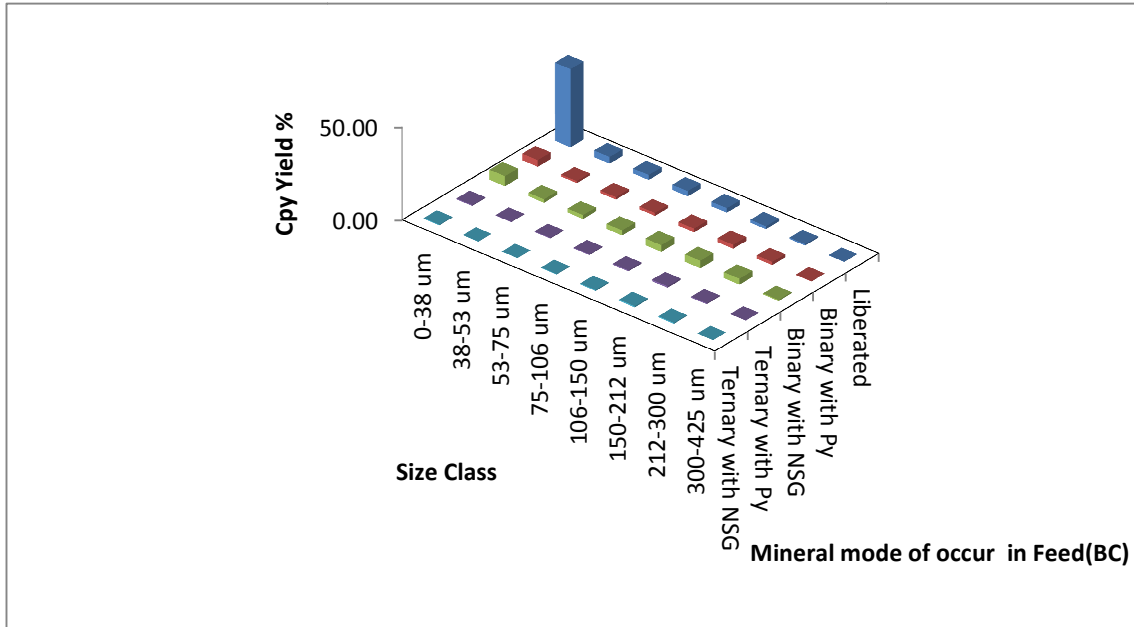


Figure 4-2: Chalcopyrite mineral mode of occurrence in Copper 1 feed ore ($P_{70}=120 \mu\text{m}$) used as base case in the simulations.

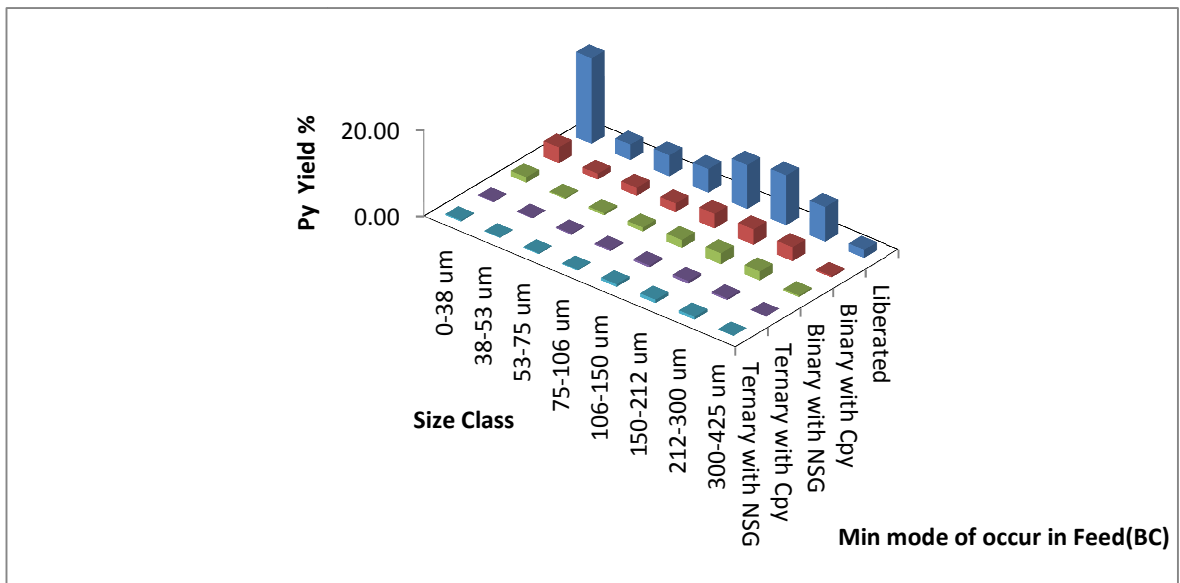


Figure 4-3: Pyrite mineral mode of occurrence in Copper 1 feed ore ($P_{70}=120 \mu\text{m}$) used as base case in the simulations.

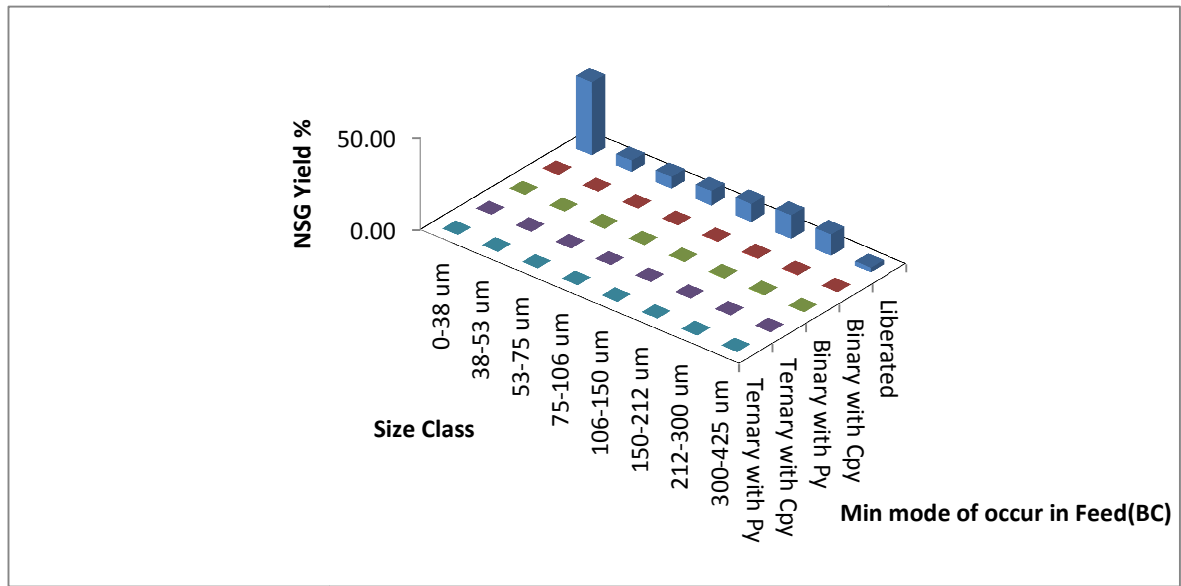


Figure 4-4: NSG mineral mode of occurrence in Copper 1 feed ore ($P_{70}=120 \mu\text{m}$) used as base case in the simulations.

4.2.2. Copper 2 mineralogy

The feed ore mineral composition by size for Copper 2 ore is shown in Table 4-3 below. Copper 2 ore feed has a Cu grade of 1.08%. Figure 4-5 to Figure 4-7 are graphical presentations of the mineral mode of occurrence of Chalcopyrite, Pyrite and NSG in Copper 2 base case feed ore. The mineral composition by size for Copper 2 also shows a low Chalcopyrite grade for the coarser size fractions, (see Table 4-3).

Table 4-3: Bulk mineral composition by size fraction of Copper 2 base case feed ore $P_{70}=180 \mu\text{m}$.

Size Class(μm)	0-38	38-53	53-75	75-106	106-150	150-212	212-300	300-425	425-600
Cpy wt%	4.05	3.74	3.75	2.97	3.17	2.69	2.30	1.44	1.32
Py wt%	3.23	6.81	7.63	7.89	9.26	10.67	9.20	8.03	6.34
NSG wt%	92.71	89.46	88.62	89.14	87.57	86.64	88.51	90.53	92.35

The mineral mode of occurrence for Chalcopyrite in Copper 2 feed ore is similar to that of Copper 1 ore feed, (see Figure 4-5). Pyrite appears mostly as fully liberated particles in all particle size classes, with second most significant mode of occurrence of Pyrite being as binary particles with Chalcopyrite (see Figure 4-6). NSG appears in the feed largely as fully liberated particles although it is also significantly associated with Chalcopyrite and Pyrite value minerals (see Figure 4-7).

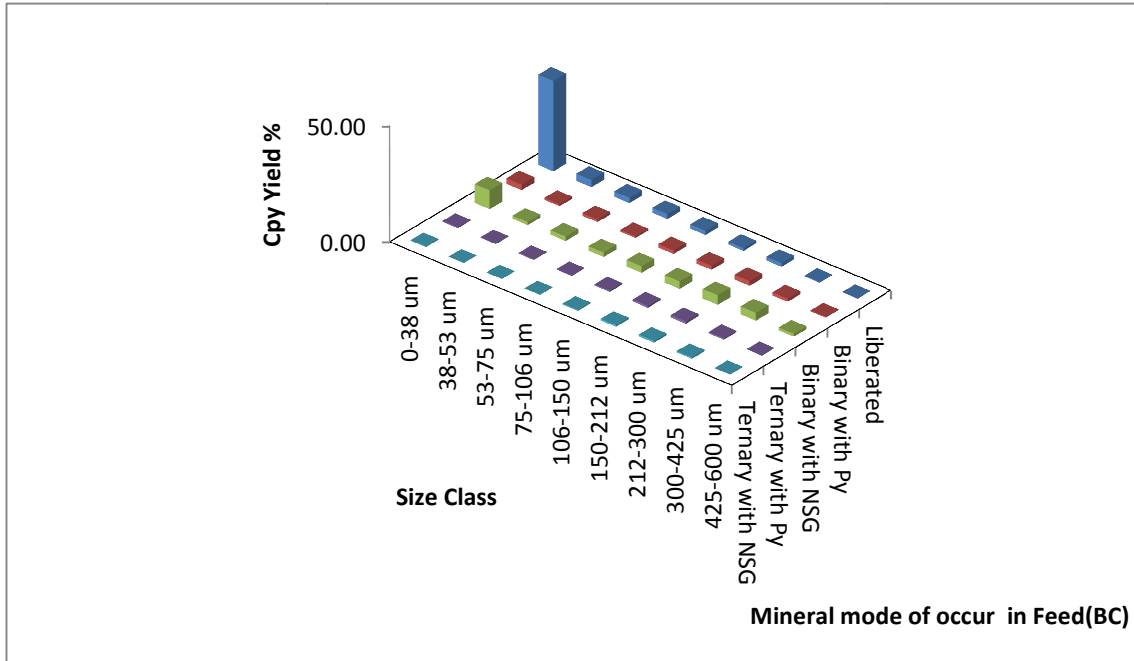


Figure 4-5: Chalcopyrite mineral mode of occurrence in Copper 2 feed ore ($P_{70}=180 \mu\text{m}$) used as base case in the simulations

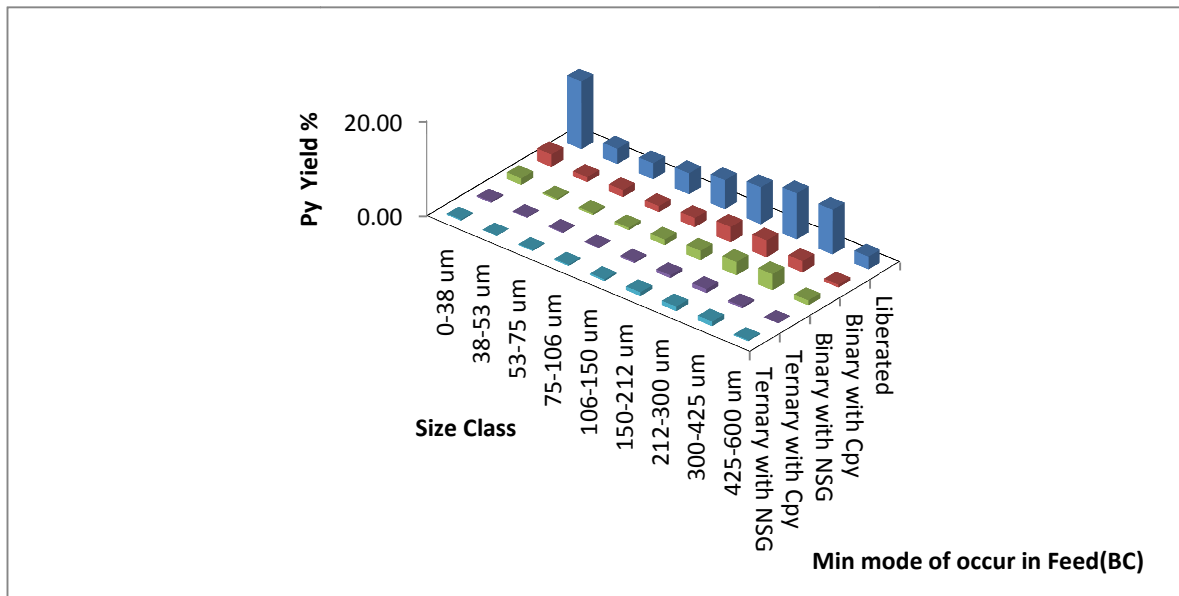


Figure 4-6: Pyrite mineral mode of occurrence in Copper 2 feed ore ($P_{70}=180 \mu\text{m}$) used as base case in the simulations.

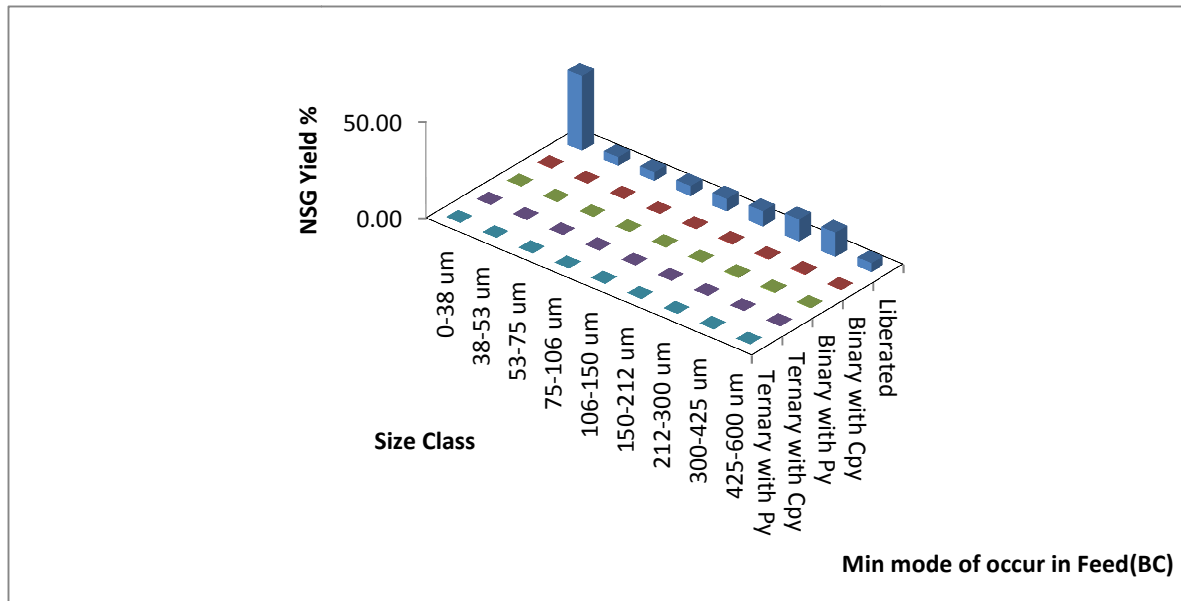


Figure 4-7: NSG mineral mode of occurrence in Copper 2 feed ore (P₇₀=180 µm) used as base case in the simulations.

4.3. Artificial flotation feed ores

Liberation in HSC is expressed as particle mineral composition. Table 4-4 shows the size class liberation profile as it appears in a stream file in HSC Chemistry for Copper 1 ore in the 0-38 micron size fraction. By redistributing the weights between the particle liberation classes in each size fraction and recalculating the particle liberation class composition, a new feed HSC Chemistry stream file is created which has a different liberation profile compared with the original starting base feed case ore, but with the same mineral composition.

4.3.1. Methodology

Artificial flotation feed ore was created by manipulating ball milled porphyry copper feed ore MLA data that were available from a previous study, which was aimed at investigating the effects of microwave treatment on flotation (AMIRA:P879A, 2009). These feed ores consisted of Copper 1 and Copper 2 flotation feed ore at P₇₀ grind sizes of 120 µm and 180 µm, respectively. These flotation feeds were selected to be the base case feed ores.

Changing the stream file liberation profile of the base case feed ores allowed for different liberation scenarios of these ores to be considered, thus creating artificial ores. These artificial ores were created based on HSC Chemistry 7 feed ore stream data for the base case ores. These different artificial feed ores had the same mineral composition and particle size distribution as the base case feed ores with the only difference between them being the particle liberation spectrum.

Table 4-4: HSC Chemistry 7 feed ore stream file showing liberation profile for particle liberation classes in the 0-38 μm size fraction.

Mineral mode of occurrence	Liberation particle class	Particle class composition			Particle class weight in tons			Bulk wt% of flotation feed	Fraction wt% of class
		Cpy %	Py %	NSG %	Cpy tph	Py tph	NSG tph		
Fully liberated	Cpy	100.0	0.0	0.0	12.0	0.0	0.0	1.3	3.4
Fully liberated	Py	0.0	100.0	0.0	0.0	11.1	0.0	1.2	3.1
Fully liberated	NSG	0.0	0.0	100.0	0.0	0.0	325.0	36.1	91.6
Binary	CpyPy	93.1	6.9	0.0	0.2	0.0	0.0	0.8	1.7
Binary	CpyNSG	69.8	30.2	0.0	0.0	0.0	0.0	0.0	0.0
Binary	PyNSG	57.5	42.5	0.0	0.0	0.2	0.06	0.0	0.0
Ternary	CpyPyNSG	50.7	47.5	1.8	0.1	0.1	0.0	0.0	0.1
Fraction Total					12.3	11.4	325.0	40.0	100

Table 4-4 above is an example of a feed ore size fraction liberation profile (0-38 μm) for Copper 1 ore. In this example the 0 to 38 μm size fraction constituted 40% of the bulk 890 tph feed stream solids weight fraction.

The following underlying principles describing well liberated ore and poorly liberated ore were used as guidelines in creating the various liberated ore scenarios. It is generally understood that improved value mineral recovery is expected from a feed ore that has the following properties;

- Most of the value mineral exists as fully liberated particles.
- Most of the NSG is fully liberated.

Poor value mineral recovery is expected from feed ores that have the following properties;

- Most of the value mineral exist as ternary composite
- Most of the value mineral groups exist as binary composite particles with NSG.

Table 4-5 below summarises the feed ore liberation scenarios that were used as flotation feeds in this study as well as the number of particle liberation classes in each of the feed ores in the simulations. Two extreme fictional liberation profile scenarios were first considered. These were fully liberated (FL) feed ore where the three value mineral groups exist as fully liberated particles in the feed ore, and fully locked where all three mineral groups in the feed stream exist as binary and ternary composite particles in the feed stream. Three other fictional feed ore liberation profile scenarios that lay between the fully locked and the fully liberated ore profile were also considered, these will referred to as Ore 1, Ore 2 and Ore 3 in this study.

Table 4-5: A summary of the feed ore scenarios that were used in investigating the effects of feed ore liberation changes on the downstream flotation process.

Feed ore scenario	Liberation characterisation	Number of particle liberation classes	
		Copper 1 (120 µm)	Copper 2 (180 µm)
BC	Base Case Porphyry Copper ore	312	351
FL	Fully liberated ore (Artificial ore)	24	27
Ore 1	Well liberated ore (Artificial ore)	312	324
Ore 2	Highly liberated ore (Artificial ore)	312	351
Ore 3	Poorly liberated ore (Artificial ore)	312	351
LC	Completely locked ore (Artificial ore)	312	351

4.3.2. Copper 1 group artificial ores

The major variations between the BC feeds and the artificial feeds that were created will be discussed below, starting with variations between Copper 1 base case feed and the five artificial feeds that were created from it. Appendix H shows the bulk particle weight for all the particle liberation classes in a size class, for Copper 1 flotation feed ores (see Table H.1-1 to Table H.1-8).

4.3.2.1. Fully liberated ore (FL)

In creating fully liberated feed, mineral group weights that exist in other mineral liberation classes per individual size fractions were summed up into the fully liberated class of each mineral group in the ore. The result was a flotation feed consisting of only fully liberated mineral particle class in each size class fraction. Table 4-6 below shows the increase in fully liberated value mineral particle class in fully liberated ore compared with the base case after assuming that all the other liberation classes in the base case are fully liberated classes. Appendix H shows the bulk particle weight for BC compared with FL for all the particle liberation classes in a size class (see Table H.1-1 to Table H.1-8). Figure 4-8 below shows the mineral mode of occurrence of Cpy in the FL feed ore while Figure 4-9 and Figure 4-10 shows the mineral mode of occurrence for Py and NSG in the ore.

Table 4-6: Differences in liberation classes' weights in FL artificial ore expressed as a percentage of Copper 1 base case feed ore liberation classes.

Relative weight % of minerals in fully liberated class of FL ore compared to that of BC ore			
Size Class	Cpy	Py	NSG
0-38 µm	118%	125%	101%
38-53 µm	184%	162%	102%
53-75 µm	269%	159%	102%
75-106 µm	286%	159%	103%
106-150 µm	383%	169%	105%
150-212 µm	636%	168%	106%
212-300 µm	649%	170%	106%
300-425 µm	708%	151%	106%

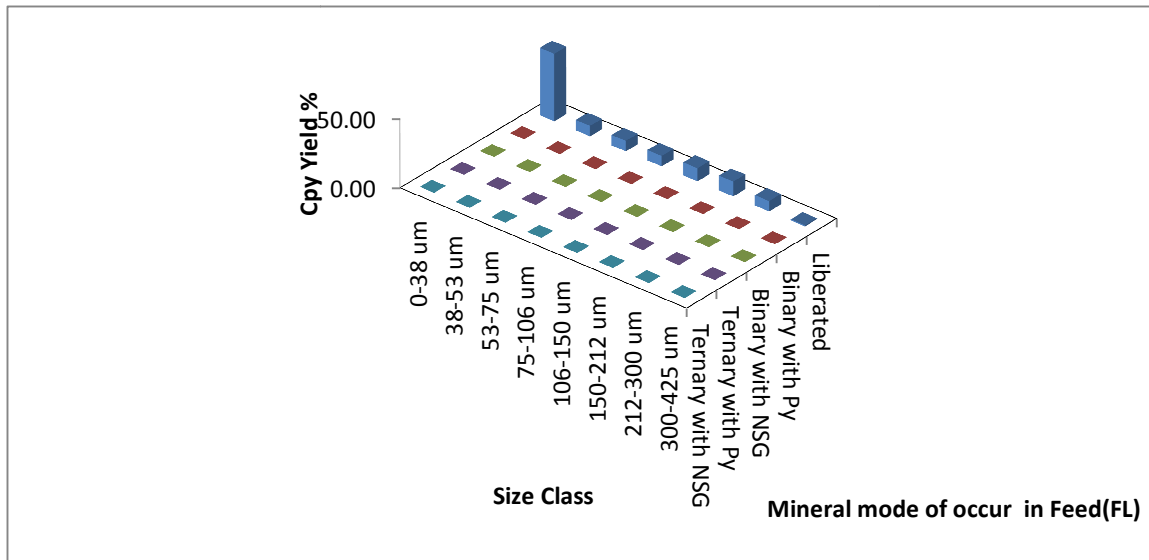


Figure 4-8: Chalcopyrite mineral mode of occurrence in fictional FL artificial feed ore with a P₇₀ grind size of 120 µm.

Figure 4-8 shows that the Chalcopyrite mode of occurrence is as fully liberated particles only. Significant fully liberated Chalcopyrite particles appear in the fine size class range.

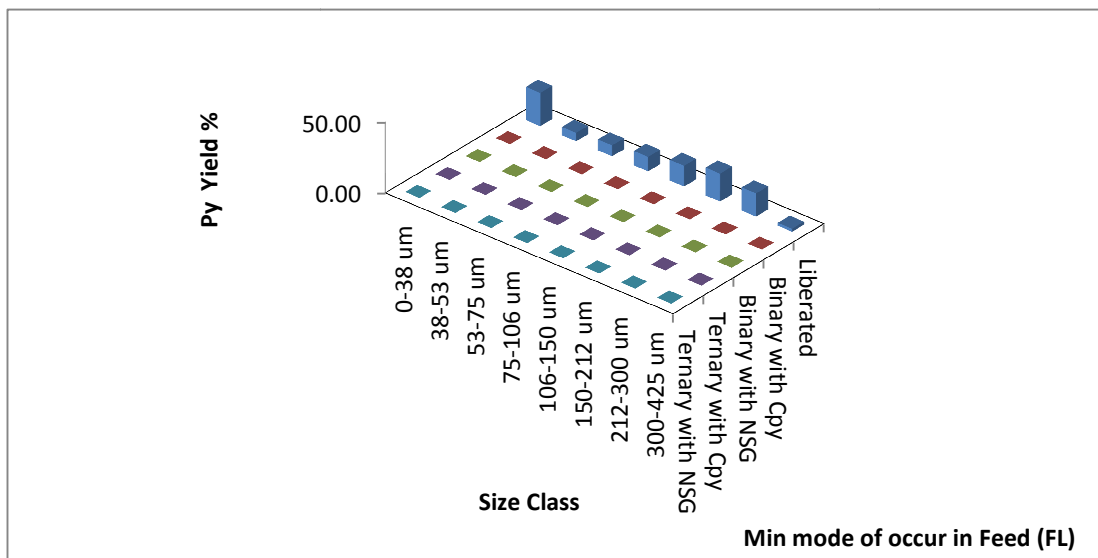


Figure 4-9: Pyrite mineral mode of occurrence in fictional FL artificial feed ore with a P₇₀ grind size of 120 µm.

Figure 4-9 and Figure 4-10 show that Pyrite and NSG occurred as fully liberated particles as well. The fully liberated Pyrite particles are spread well over the fine and coarse size

classes in contrast to NSG fully liberated particles which appear mostly in the fine size class.

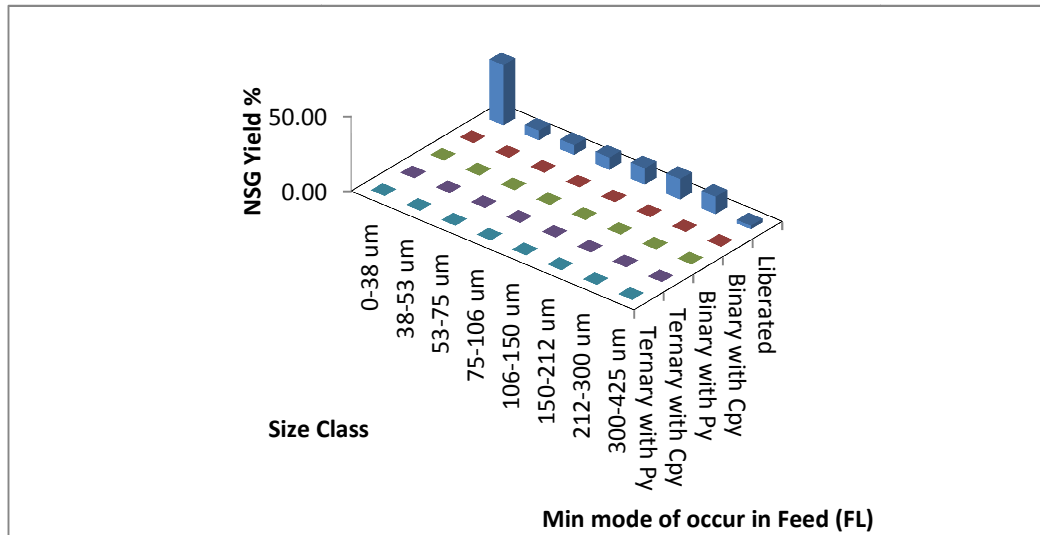


Figure 4-10: NSG mineral mode of occurrence in fictional FL artificial feed ore with a P₇₀ grind size of 120 μm.

4.3.2.2. Fully locked ore (LC)

In creating the fully locked ore, 100% of the weights of fully liberated Chalcopyrite, Pyrite and NSG mineral in each size class were redistributed evenly between the existing binary liberation classes in that size fraction for each mineral group. New values of the particle liberation classes were recalculated. The major difference between the base case ore and the fully locked ore was the absence of any fully liberated particle class in the fully locked ore. Table 4-7 expresses the differences in particle liberation class weights between the base case and the fully locked ore as a percentage after redistributing the fully liberated mineral class weights into the binary and ternary liberation classes. . Appendix H shows the bulk particle weight for BC compared with LC for all the particle liberation classes in a size class (see Table H.1-1 to Table H.1-8).Figure 4-11 below shows the mineral mode of occurrence of Chalcopyrite in the LC feed. Figure 4-12 and Figure 4-13 show the mineral mode of occurrence of Pyrite and NSG in the ore.

Table 4-7: Differences in liberation classes' weights in LC artificial ore expressed as a percentage of Copper 1 base case feed ore liberation classes.

Relative weight % of binary and ternary particles in Fully locked ore(LC) compared to that of BC ore				
Size Class	CpyPy	CpyNSG	PyNSG	CpyPyNSG
0-38 μm	511%	6153%	14044%	100%
38-53 μm	234%	1968%	5384%	100%
53-75 μm	235%	1790%	4650%	100%
75-106 μm	240%	1741%	3297%	100%
106-150 μm	222%	1415%	2231%	100%
150-212 μm	233%	1280%	1729%	100%
212-300 μm	247%	1354%	1405%	100%
300-425 μm	309%	1739%	1483%	100%

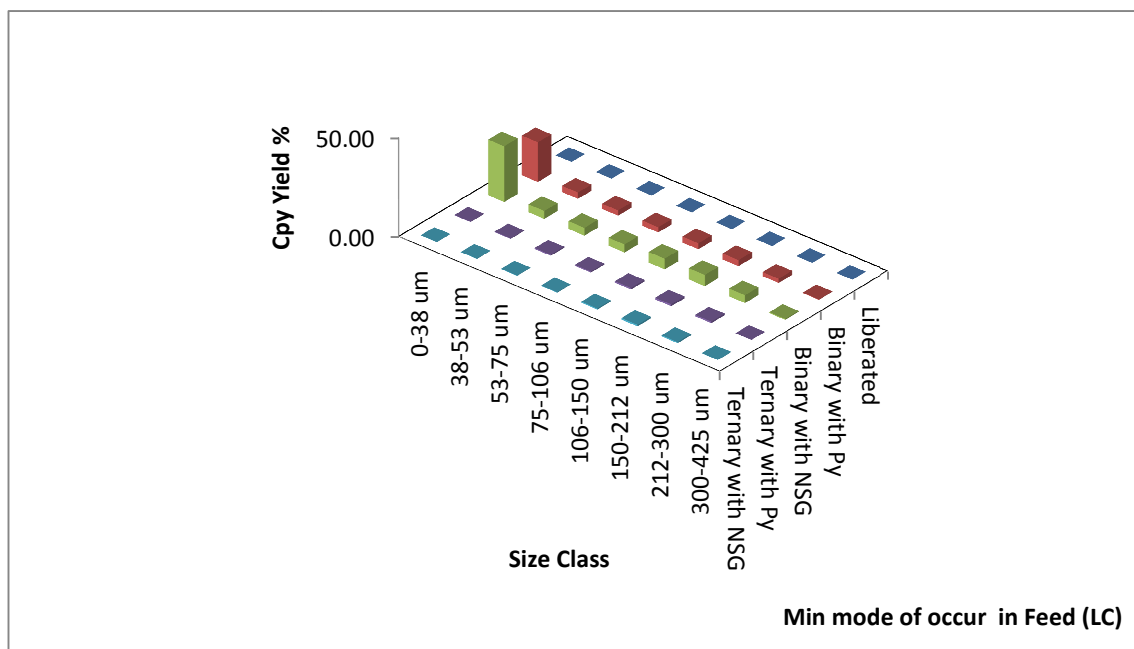


Figure 4-11: Chalcopyrite mineral mode of occurrence in LC artificial feed ore with a P₇₀ grind size of 120 μm .

Most of Chalcopyrite in the LC feed ore appears as binary particles with NSG with a considerable fraction appearing in the 0 to 38 μm size class, Figure 4-11.

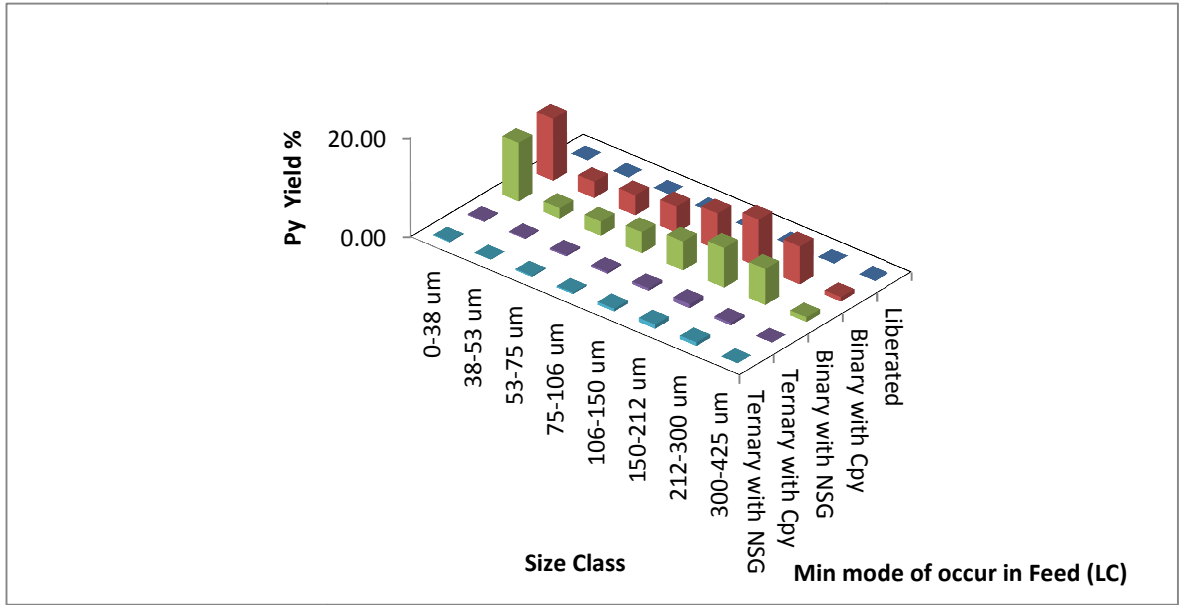


Figure 4-12: Pyrite mineral mode of occurrence in LC artificial feed ore with a P₇₀ grind size of 120µm.

Most of Pyrite in the LC feed ore appears as binary particles with NSG and Chalcopyrite over a range of size fractions, Figure 4-12.

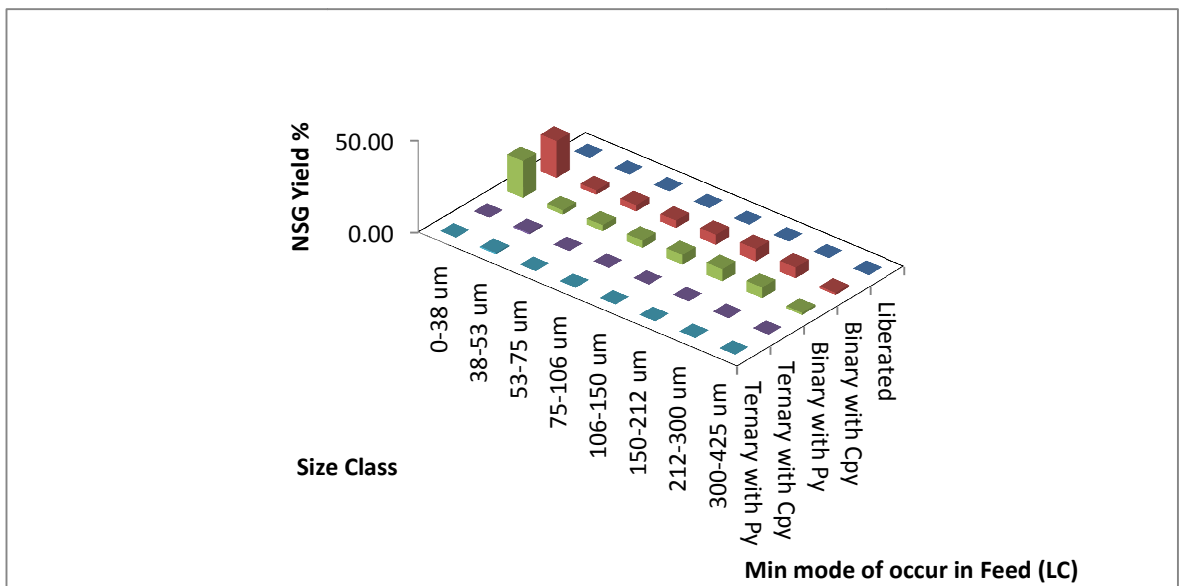


Figure 4-13: NSG mineral mode of occurrence in LC artificial feed ore with a P₇₀ grind size of 120 µm.

Most of NSG in the LC feed ore appears as binary particles with Chalcopyrite and Pyrite. A considerable fraction of these binary particles appears in the 0 to 38 μm fine size class, Figure 4-13.

4.3.2.3. Ore 1

Ore 1 was created by redistributing 100% of the ternary liberated particle class weights in the BC to the existing BC fully liberated classes. The major difference between the BC ore and Ore 1 was the absence of ternary particle liberation classes in the Ore 1 and an increase in fully liberated class weight due to the redistribution of the ternaries (see Table 4-8). Appendix H shows the bulk particle weight for BC compared with Ore 1 for all the particle liberation classes in a size class (see Table H.1-1 to Table H.1-8).

Figure 4-14 below shows the mineral mode of occurrence of Chalcopyrite in Ore 1 feed ore while Figure 4-15 and Figure 4-16 shows the mineral mode of occurrence of Py and NSG in the ore.

Table 4-8: Differences in liberation classes' weights in Ore 1 artificial ore expressed as a percentage of Copper 1 base case feed ore liberation classes.

Relative weight % of minerals in fully liberated class of Ore 1 compared to that of BC ore			
Size class	Cpy	Py	NSG
0-38 μm	101%	102%	100%
38-53 μm	110%	110%	101%
53-75 μm	127%	112%	100%
75-106 μm	130%	111%	100%
106-150 μm	155%	114%	101%
150-212 μm	207%	115%	101%
212-300 μm	225%	113%	101%
300-425 μm	192%	108%	100%

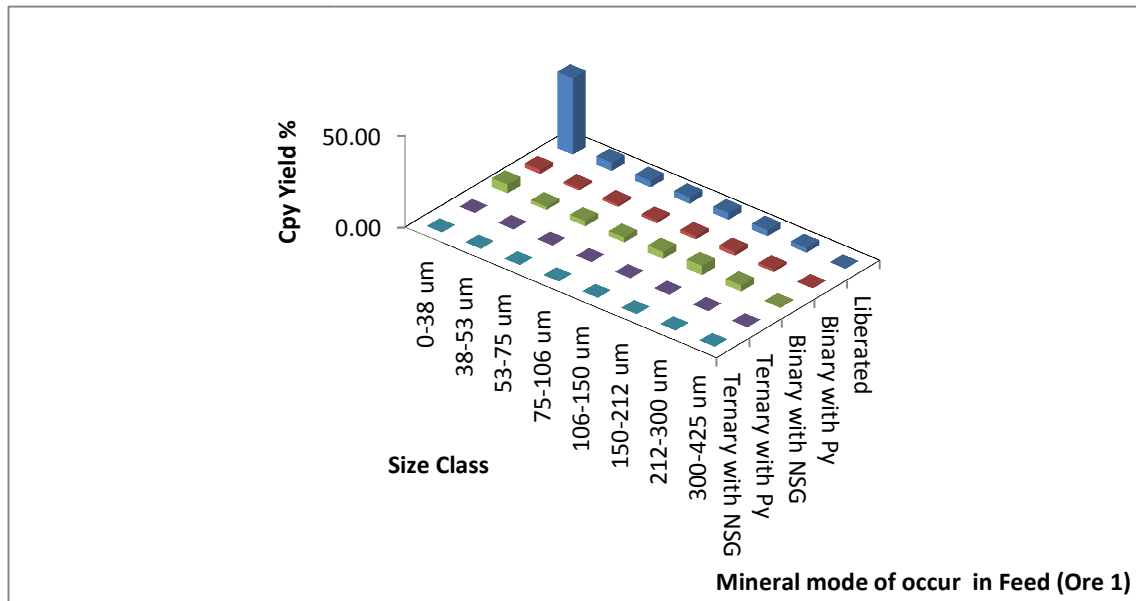


Figure 4-14: Chalcopyrite mineral mode of occurrence in Ore 1 artificial feed ore with a P₇₀ grind size of 120 µm.

Compared with the base case feed ore, Ore 1 had more fully liberated Chalcopyrite particles especially in the coarse size classes, Figure 4-14.

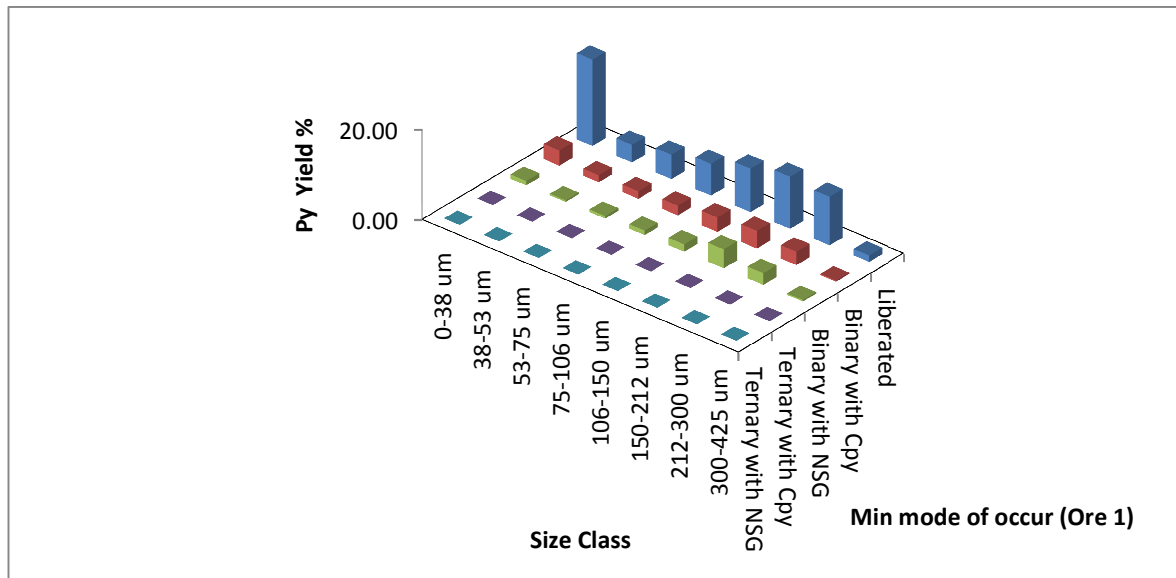


Figure 4-15: Pyrite mineral mode of occurrence in Ore 1 artificial feed ore with a P₇₀ grind size of 120 µm.

The Pyrite and NSG mode of occurrence in Ore 1 feed were closely similar to their mode of occurrence in the base case feed ore, Figure 4-15 and Figure 4-16.

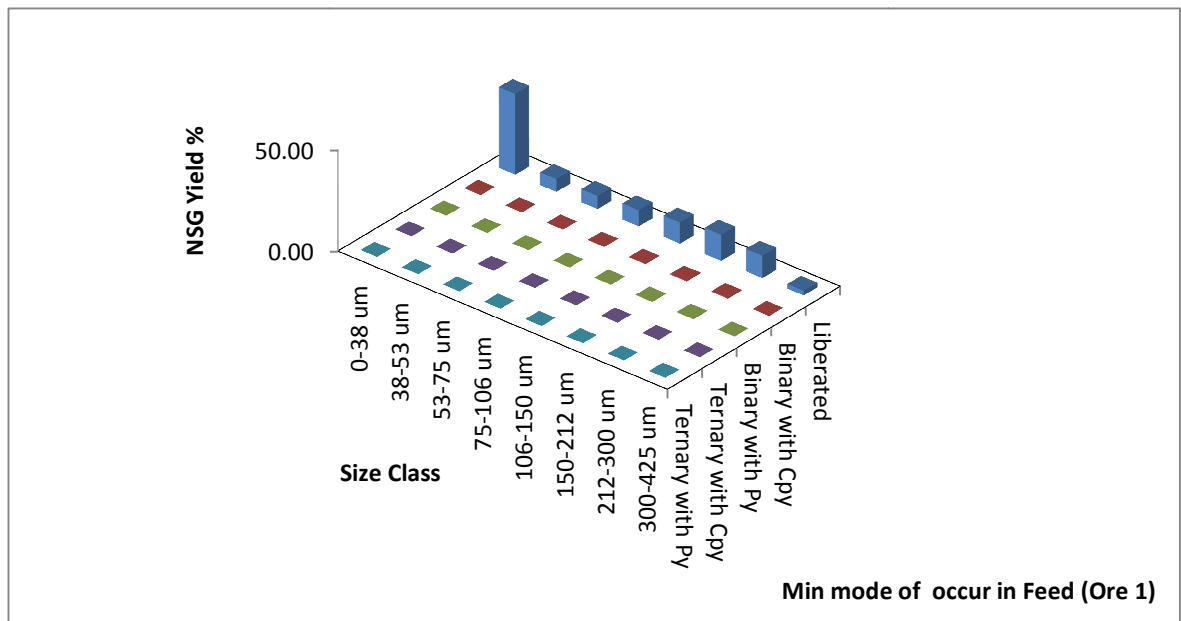


Figure 4-16: NSG mineral mode of occurrence in Ore 1 artificial feed ore with a P₇₀ grind size of 120 μm.

4.3.2.4. Ore 2

Ore 2 was created by redistributing 100% of the fully liberated Cpy and Py classes in the BC to the existing binary classes in each size fraction for the two mineral groups. Thus, the major difference between the BC and Ore 2 was the absence of fully liberated Cpy and Py classes in Ore 2. The percentage difference in binary liberated particle class weight in Ore 2 compared to the BC is presented in Table 4-9 below. Appendix H shows the bulk particle weight for BC compared with Ore 2 for all the particle liberation classes in a size class (see Table H.1-1 to Table H.1-8).

Table 4-9: Differences in liberation classes weights in Ore 2 artificial ore expressed as a percentage of Copper 1 base case feed ore liberation classes.

Relative weight % of binary particles in Ore 2 compared to that of BC ore			
Size class	PyCpy	CpyNSG	PyNSG
0-38 μm	486%	341%	609%
38-53 μm	234%	157%	373%
53-75 μm	235%	126%	328%
75-106 μm	240%	120%	274%
106-150 μm	222%	113%	218%
150-212 μm	232%	107%	199%
212-300 μm	246%	108%	176%
300-425 μm	308%	108%	160%

Ore 2 is expected to behave fairly similar to the extreme FL case due to the presence of fully liberated NSG and the higher percentage of CpyPy binary composites in the ore compared to the amount presented in the base case (see Figure 4-17). This is because Cpy and Py have the same contact angle although their densities are different.

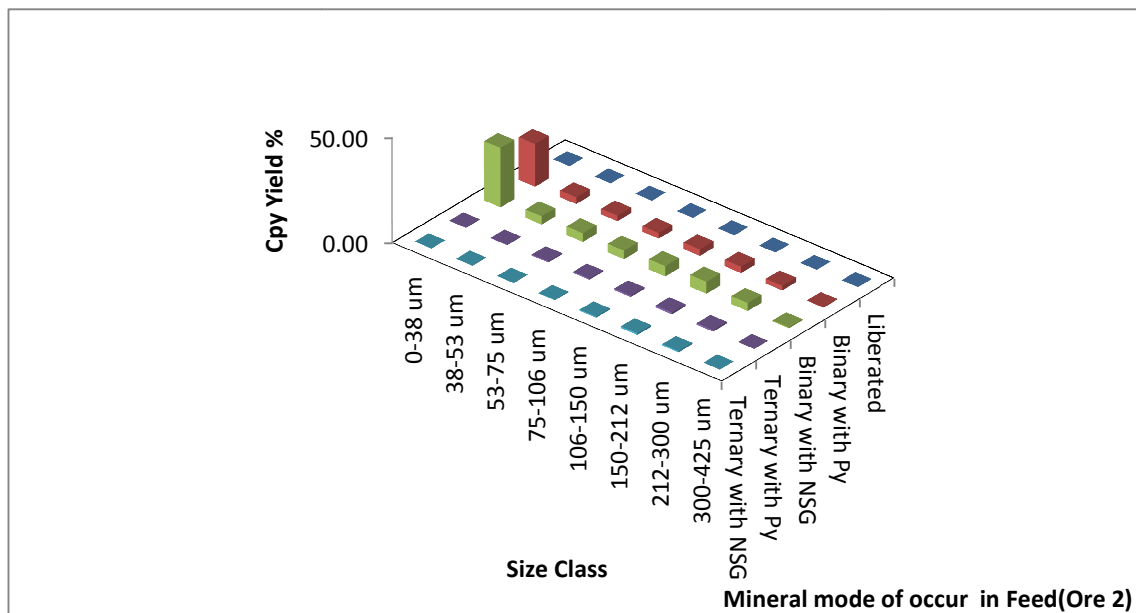


Figure 4-17: Chalcopyrite mineral mode of occurrence in fictional Ore 2 artificial feed ore with a P₇₀ grind size of 120 μm .

Figure 4-18 and Figure 4-19 below show the mineral mode of occurrence for Py and NSG in the Ore 2.

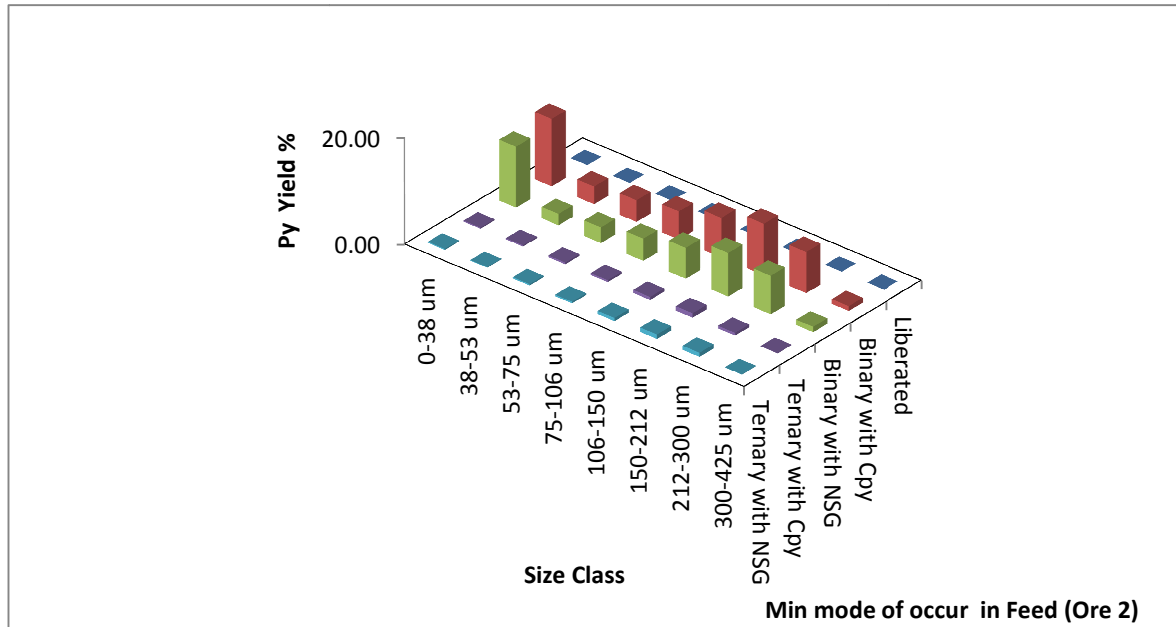


Figure 4-18: Pyrite mineral mode of occurrence in fictional Ore 2 artificial feed ore with a P₇₀ grind size of 120 µm.

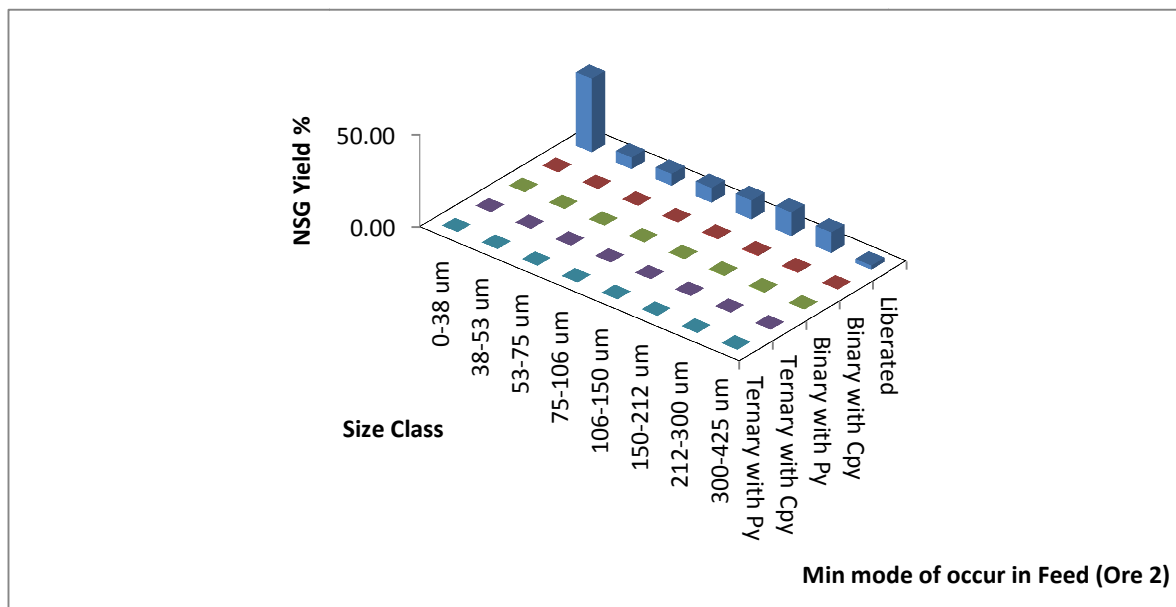


Figure 4-19: NSG mineral mode of occurrence in fictional Ore artificial feed ore with a P₇₀ grind size of 120 µm.

4.3.2.5. Ore 3

Ore 3 was created by redistributing 100% of the fully liberated NSG classes in the BC to the existing NSg+Py and NSG+Cpy binary liberated classes in each size fraction.

Table 4-10: Differences in liberation classes' weights in Ore 3 artificial ore expressed as a percentage of Copper 1 base case feed ore liberation classes.

Relative weight % of binary and ternary particles in Ore 3 compared to that of BC ore			
Size class	CpyNSG	PyNSG	CpyPyNSG
0-38 μm	5938%	13592%	100%
38-53 μm	1911%	5111%	100%
53-75 μm	1764%	4422%	100%
75-106 μm	1721%	3123%	100%
106-150 μm	1402%	2113%	100%
150-212 μm	1273%	1630%	100%
212-300 μm	1347%	1328%	100%
300-425 μm	1732%	1423%	100%

The major difference between the BC and Ore 1 was the absence of fully liberated NSG mineral classes in Ore 3. The relative percentage of binary and ternary liberated particle classes weight in Ore 3 compared to the BC is presented in Table 4-10 above. Appendix H shows the bulk particle weight for BC compared with Ore 3 for all the particle liberation classes in a size class (see Table H.1-1 to Table H.1-8). Ore 3 is expected to give less recovery of the value mineral than the BC ore due to the greater occurrence of the value mineral in association with NSG in the binary liberation class (see Figure 4-20).

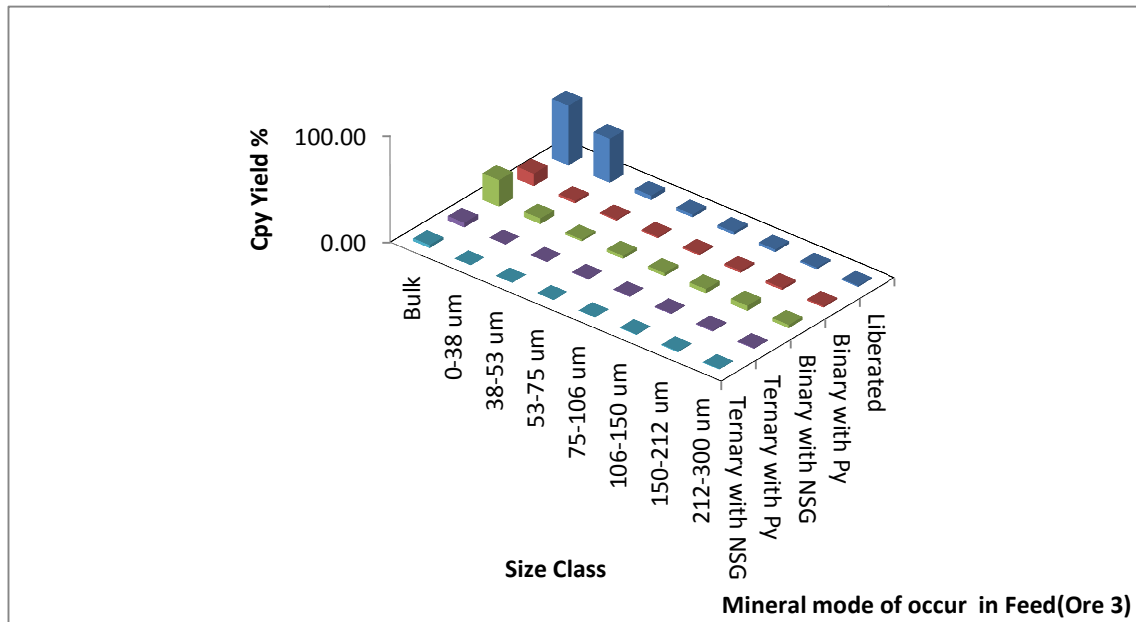


Figure 4-20: Chalcopyrite mineral mode of occurrence in Ore 3 artificial feed ore with a P₇₀ grind size of 120 µm.

Figure 4-21 and Figure 4-22 shows the mineral mode of occurrence of Py and NSG in the ore.

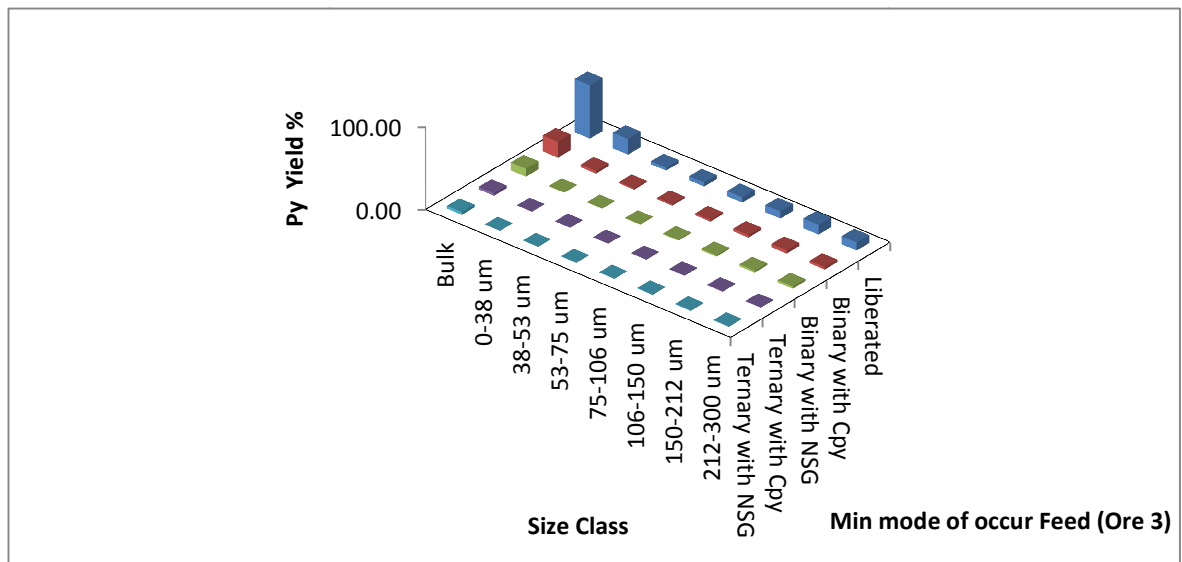


Figure 4-21: Pyrite mineral mode of occurrence in Ore 3 artificial feed ore with a P₇₀ grind size of 120 µm.

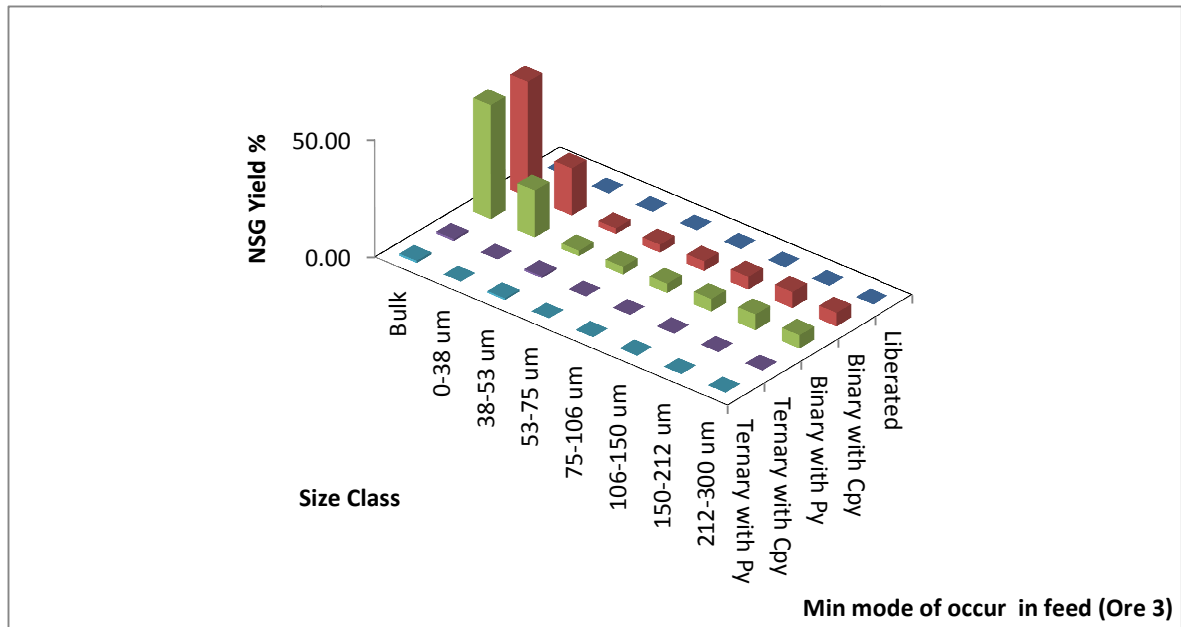


Figure 4-22: NSG mineral mode of occurrence in Ore 3 artificial feed ore with a P₇₀ grind size of 120 μm.

4.3.3. Copper 2 artificial ores

Similar artificial ores were created utilising Copper 2 base case feed with a P₇₀ grind size of 180μm, thus creating two groups of artificial feeds at different grind sizes. Methods similar to those described above in creating Copper 1 artificial ores were also applied in creating Copper 2 artificial ores. The resulting artificial feeds are presented below. The mineral modes of occurrence graphs for each ore are presented in Appendix A. Appendix H shows the bulk particle weight for all the particle liberation classes in a size class, for Copper 2 flotation feed ores (see Table H.2-1 to Table H.2-9).

4.3.3.1. Fully liberated ore

The differences between the base case and fully liberated ore were similar to those obtained for FL ore created from Copper 1 ore with a P₇₀ grind size of 120 μm (see Table 4-11). Appendix H shows the bulk particle weight for BC compared with FL for all the particle liberation classes in a size class (see Table H.2-1 to Table H.2-9).

Similar methods for creating FL liberated ore as described in section 4.3.2.1 were used in creating FL artificial ore from Copper 2 base case feed ore. Graphs of the mineral mode of occurrence for Chalcopyrite, Pyrite and NSG in FL liberated ore at a P₇₀ grind size of 180 µm are shown in Appendix A Figure A.1-1 to Figure A.1-3.

Table 4-11: Differences in liberation classes' weights in FL liberated artificial ore expressed as a percentage of Copper 2 base case feed ore liberation classes .

Relative weight % of minerals in fully liberated class of FL ore compared to that of BC ore			
Size Class	Cpy	Py	NSG
0-38 µm	129%	585%	101%
38-53 µm	181%	148%	101%
53-75 µm	254%	168%	102%
75-106 µm	249%	149%	103%
106-150 µm	394%	160%	105%
150-212 µm	632%	182%	106%
212-300 µm	600%	182%	107%
300-425 µm	2130%	174%	108%
425-600 µm	1160%	172%	108%

4.3.3.2. Fully locked ore (LC)

Similar methods for creating LC liberated ore as described in section 4.3.2.2 for LC created from Copper 1 base case feed were applied in creating LC artificial ore from Copper 2 base case feed ore. The differences between the base case and LC liberated ore at a P₇₀ grind size of 180 µm were similar to those obtained for LC ore created from Copper 1 ore with a P₇₀ grind size of 120µm (see Table 4-12). Appendix H shows the bulk particle weight for BC compared with LC for all the particle liberation classes in a size class (see Table H.2-1 to Table H.2-9). Graphs of the mineral mode of occurrence for Chalcopyrite, Pyrite and NSG in LC liberated ore at a P₇₀ grind size of 180 µm are shown in Appendix A, Figure A.1-4 to Figure A.1-6.

Table 4-12: Differences in liberation classes' weights in LC liberated artificial ore expressed as a percentage of Copper 2 base case feed ore liberation classes .

Relative weight % of binary particles in Fully locked ore(LC) compared to that of BC ore			
Size Class	CpyPy	CpyNSG	PyNSG
0-38 µm	526%	3849%	9029%
38-53 µm	263%	2702%	7080%
53-75 µm	212%	1899%	4653%
75-106 µm	271%	1752%	3668%
106-150 µm	239%	1321%	2154%
150-212 µm	210%	1226%	1564%
212-300 µm	225%	1199%	1269%
300-425 µm	275%	1262%	1089%
425-600 µm	304%	1499%	985%

4.3.3.3. Ore 1

Similar methods for creating Ore 1 artificial ore as described in section 4.3.2.3 for Ore artificial feed ore created from Copper 1 base case feed were applied in creating Ore 1 artificial ore from Copper 2 base case feed ore. The differences between the base case and Ore 1 liberated ore at a P₇₀ grind size of 180 µm were also similar to those obtained for Ore 1 artificial ore created from Copper 1 ore with a P₇₀ grind size of 120 µm (see Table 4-13). Appendix H shows the bulk particle weight for BC compared with Ore 1 for all the particle liberation classes in a size class (see Table H.2-1 to Table H.2-9). Graphs of the mineral mode of occurrence for Chalcopyrite, Pyrite and NSG in Ore 1 artificial ore at a P₇₀ grind size of 180µm are shown in Appendix A Figure A.1-7 to Figure A.1-9

Table 4-13: Differences in liberation classes' weights in Ore 1 liberated artificial ore expressed as a percentage of Copper 2 base case feed ore liberation classes.

Relative weight % of minerals in Ore 1 compared to that of BC ore			
Size Class	Cpy	Py	NSG
0-38 μm	129%	585%	101%
38-53 μm	181%	148%	101%
53-75 μm	254%	168%	102%
75-106 μm	249%	149%	103%
106-150 μm	394%	160%	105%
150-212 μm	632%	182%	106%
212-300 μm	600%	182%	107%
300-425 μm	2130%	174%	108%
425-600 μm	1160%	172%	108%

4.3.3.4. Ore 2

Similar methods for creating Ore 2 artificial ore as described in section 4.3.2.4 for Ore artificial feed ore created from Copper 1 base case feed were applied in creating Ore 2 artificial ore from Copper 2 base case feed ore.

Table 4-14: Differences in liberation classes' weights in Ore 2 liberated artificial ore expressed as a percentage of Copper 2 base case feed ore liberation classes .

Relative weight % of binary particles in Ore 2 compared to that of BC ore			
Size Class	CpyPy	CpyNSG	PyNSG
0-38 μm	526%	224%	331%
38-53 μm	263%	160%	444%
53-75 μm	212%	131%	325%
75-106 μm	271%	124%	305%
106-150 μm	239%	113%	232%
150-212 μm	210%	108%	197%
212-300 μm	225%	108%	168%
300-425 μm	275%	103%	152%
425-600 μm	304%	107%	137%

The differences between the Base case and Ore 2 liberated ore at a P₇₀ grind size of 180 µm were also similar to those obtained for Ore 2 artificial ore created from Copper 1 ore with a P₇₀ grind size of 120 µm (see Table 4-14). Appendix H shows the bulk particle weight for BC compared with Ore 2 for all the particle liberation classes in a size class (see Table H.2-1 to Table H.2-9). Graphs of the mineral mode of occurrence for Chalcopyrite, Pyrite and NSG in Ore 2 artificial ore at a P₇₀ grind size of 180 µm are shown in Appendix A, Figure A.1-10 to Figure A.1-12.

4.3.3.5. Ore 3

Similar methods for creating Ore 3 artificial ore as described in section 4.3.2.5 for Ore 3 artificial feed ore created from Copper 1 base case feed were applied in creating Ore 3 artificial ore from Copper 2 base case feed ore. The differences between the Base case and Ore 3 liberated ore at a P₇₀ grind size of 180µm were also similar to those obtained for Ore 3 artificial ore created from Copper 1 ore with a P₇₀ grind size of 120 µm (see Table 4-15). Appendix H shows the bulk particle weight for Ore 3 compared with FL for all the particle liberation classes in a size class (see Table H.2-1 to Table H.2-9). Graphs of the mineral mode of occurrence for Chalcopyrite, Pyrite and NSG in Ore 3 artificial ore at a P₇₀ grind size of 180µm are shown in Appendix A, Figure A.1-13 to Figure A.1-15.

Table 4-15: Differences in liberation classes' weights in Ore 3 liberated artificial ore expressed as a percentage of Cu 2 base case feed ore liberation

Relative weight % of binary particles in Ore 3 compared to that of BC ore		
Size Class	CpyNSG	PyNSG
0-38 µm	3725%	8798%
38-53 µm	2642%	6736%
53-75 µm	1868%	4427%
75-106 µm	1728%	3463%
106-150 µm	1308%	2022%
150-212 µm	1218%	1467%
212-300 µm	1191%	1201%
300-425 µm	1258%	1037%
425-600 µm	1492%	948%

4.4. Contact angle calculations Method

Mineral particle liberation in HSC Chemistry 7 is defined as either mineral weight composition percent or as surface area percent, of mineral as a fraction of other minerals that constitute the particle. In calculating the particle contact angle utilising the Cassie's equation for composite particles, surface area values of each mineral phase should be used according to the definition of the Cassie's equation (see equation 3.33). However, Ralston et al. (2007) utilised the weight composition percent definition of liberation in predicting the contact angle of composite particles in his work. Due to the methodology used in producing artificial ore feed in this work, where liberation was defined as weight composition percentage, the mineral weight composition definition of liberation was therefore used in calculating the contact angle.

Before this could be done, investigations had to be carried out to determine the relative error associated with utilising the weight percentage definition of liberation in calculating the composite particle contact angle utilising the Cassie's equation. Using the base case Copper 1 ore feed liberation data, contact angle values were calculated for each particle utilising both definitions of particle liberations in HSC Chemistry 7. The values of the contact angles that were obtained were then used in the general flotation model to predict flotation recovery in a single unit flotation cell. The recovery results obtained from the use of each contact angle definition were then compared in order to determine the differences in the values. A pure sulphide mineral contact angle value of 78° was used in the calculations.

4.4.1. Contact angle calculation results and discussion

Figure 4-23 shows a comparison of contact angle values calculated using surface area and weight % definitions of particle liberation in HSC Chemistry simulations in a single size class (0-38 μm). Appendix B Figure B.1-1 to Figure B.1-3 represent typical values of the contact angles for each particle in a specific size fraction calculated utilising Cassie's equation in the simulations.

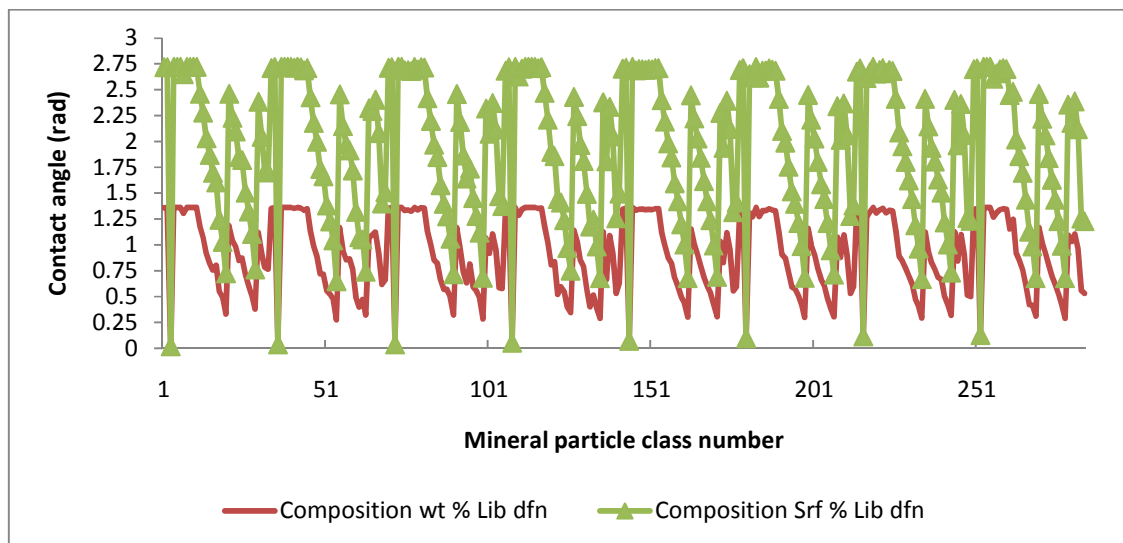


Figure 4-23: Comparison of contact angle values calculated using the weight composition % against those calculated utilising the surface area %.

It can be seen from Figure 4-24 that there is similar trends of contact angle values for particles in different size fractions.

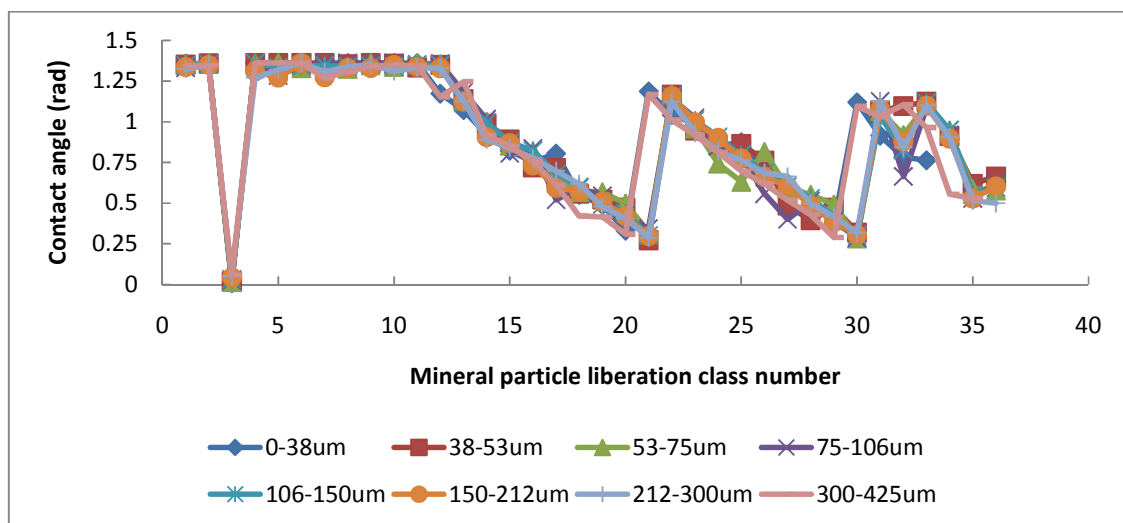


Figure 4-24: Contact angle variation with mineral particles liberation class for all feed particle size fractions

The recovery results in Figure 4-25 show a large difference in recovery at coarse sizes for chalcopyrite between simulated mineral recovery values obtained utilising liberation wt% calculated contact angles and that obtained by utilising surface area %.

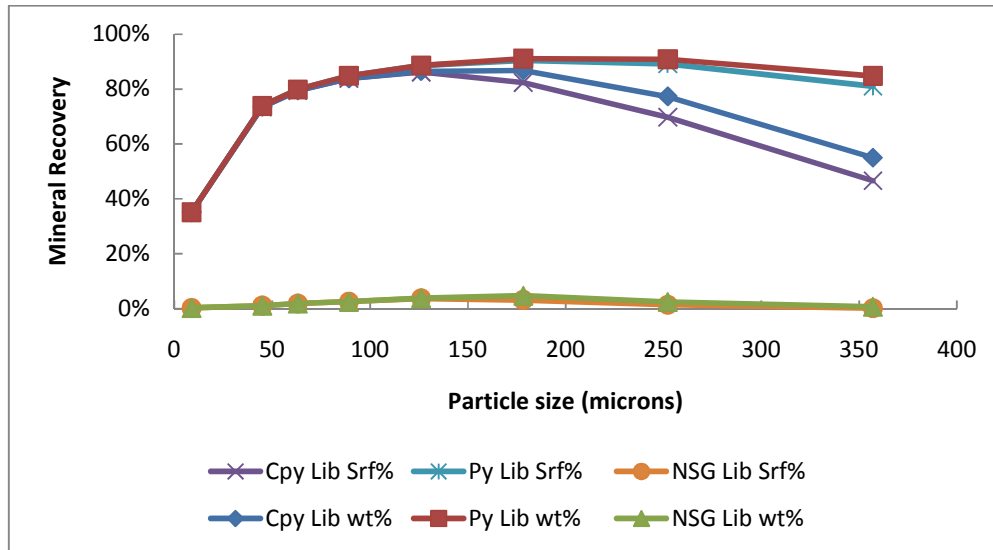


Figure 4-25: Comparison mineral recovery values obtained using the weight composition % calculated contact angles in the flotation model against those calculated utilising the surface area % calculated contact angles.

The weight percentage definition of liberation was used throughout this study in calculating particle contact angles.

4.5. Conclusion

This Chapter has provided a detailed description of the feed ores that were used in this study. A detailed methodology of how artificial ores were created from the two base case feed ore feeds MLA data that was available in this study has been given. These artificial ores are appropriate for use in carrying out investigations on the effect of feed ore liberation variation on flotation recovery. These artificial ores have varying liberation profiles which could represent the potential changes in feed ore liberation expected from microwave assisted comminution. The next Chapter will discuss the simulation studies that were carried utilising these artificial ores.

CHAPTER FIVE

5. SINGLE CELL FLOWSHEET SIMULATION

This Chapter will present and discuss the results of single cell flotation simulations that were carried out by incorporating the fundamental property based model into HSC Chemistry 7 simulation software. Firstly, preliminary flotation cell simulation results that were carried out in order to compare the general trend predicted by the fundamental flotation model with results obtained from experimental batch flotation tests will be presented. This will be followed by a presentation of the results of simulations of a continuous single flotation cell that were carried out in order to explore HSC Chemistry 7 simulation software particle tracking capability and to further test the flotation model's suitability for use in true particle modelling in HSC Chemistry 7. A description of the investigations that were carried out in order to determine the effects of feed ore liberation on single cell flotation value mineral recovery will be given. Lastly details of simulation results from investigations into the effect of grind size variation on value mineral recovery and their analysis will be given.

5.1. Comparison of simulated recovery trends with experimental trends

The mineral recovery values obtained from batch flotation experiments carried out on Copper 1 BC feed in a previous study (AMIRA:P879A, 2009), were compared with those calculated using the fundamental property based model. Details of the batch experimental flotation tests procedures from the previous study on Copper 1 BC feed are provided in Appendix F. No attempt was made to fit the actual experimental recovery values with model values due to lack of some of the hydrodynamic parameter values that characterised the experimental batch flotation conditions when the study was carried out. Where such values were not available, suitable values from literature were substituted into the model. This analysis was done as a way of determining the model's appropriateness for use in true particle modelling.

Table 5-1 shows the input parameter values that were used in simulating the experimental batch flotation test carried out on the Copper 1 BC feed, along with literature values of parameters that were not measured in the experiments.

Table 5-1: Summary of input parameter values used in simulating experimental batch flotation test carried out on the Copper 1BC feed .

Operating Parameter	Batch Experiments	Literature Data (Pyke et al., 2003)
Cell volume	0.004 m ³	
Energy dissipation (ϵ)	n.m	20 m ² /s ³
Bubble diameter (d _b)	n.m	0.0012 m
Bubble rise velocity (v _b)	n.m	0.18 m/s
Apparent viscosity of slurry (ϑ)	n.m	0.000891 kg/ms
Gas flow rate (G _{fr})	0.004 m ³ /min	
Sulphide mineral contact angle (θ)	n.m	78° (Ralston et al., 2007)
NSG contact angle (θ)	n.m	0° (Ralston et al., 2007)

Note that n.a refers to values that were not measured.

From Figures 5-1 and 5-2, it can be seen that the general trends in mineral recovery obtained from the model were fairly similar to those obtained experimentally.

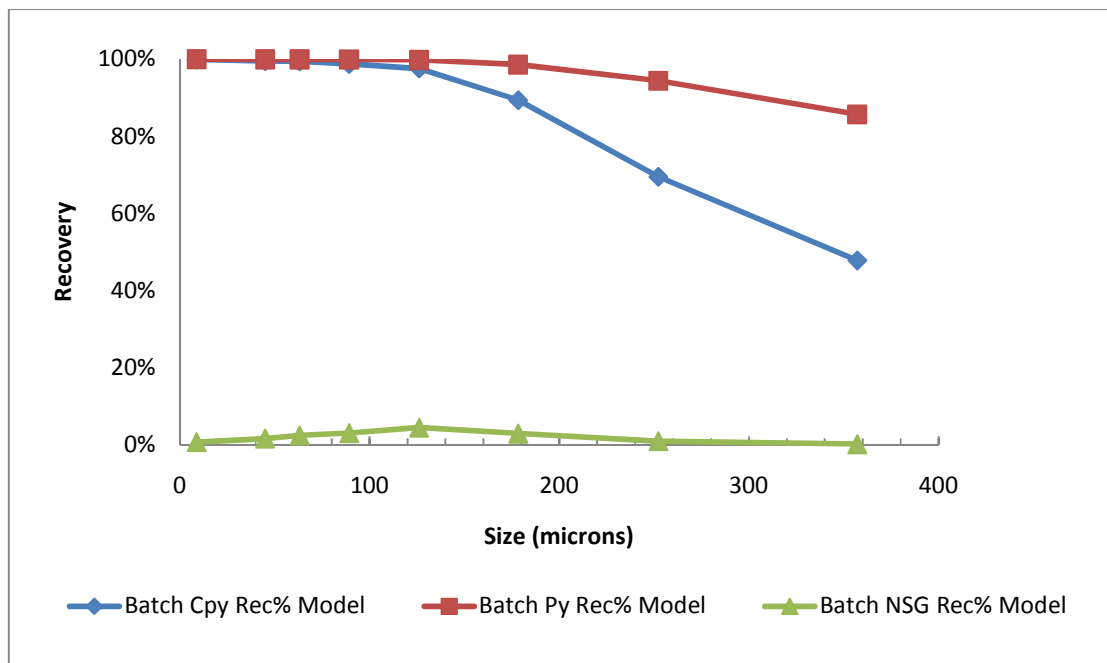


Figure 5-1: Simulated batch flotation mineral recovery for Copper 1 BC feed

The recovery values obtained from the model were higher than the experimental values, (see Figure 5-1). The higher simulated recovery values (see Figure 5-1) as compared to experimentally determined recovery values (Figure 5-2) were attributed to the first order rate expression model that was used in simulating the recovery values which assumes an ultimate recovery of 100%. This assumption, although widely used, is generally accepted to be an overestimation of the flotation ultimate recovery value (Wills and Napier-Munn, 2005). Greater recovery of NSG was observed from the experimental results compared to the flotation model prediction. This difference can be attributed to the effects of entrainment during the batch flotation experimental runs which contributed to high experimental NSG recovery. This high degree of entrainment observed during the batch experiments was higher than the entrainment values predicted by the flotation model. The results showed that the model could predict batch flotation recovery trends similar to those obtained experimentally. It was concluded that the model was appropriate for use in true particle modelling in HSC Chemistry 7 simulation software.

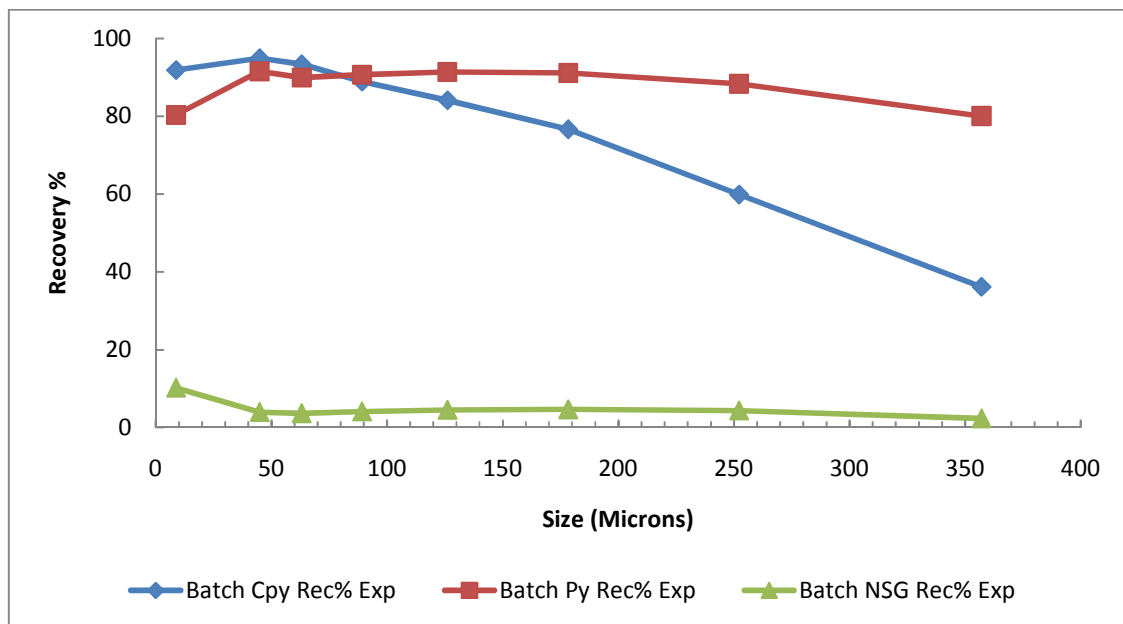


Figure 5-2: Experimentally determined batch flotation cell mineral recovery for Copper 1.

5.2. Continuous single cell flow sheet simulation

Single cell flotation simulation utilising Copper 1 base case feed data with a $P_{70} = 120 \mu\text{m}$ was carried out, after which the trends in flotation rate constant and mineral recovery were analysed. This was done in order to test the modelling framework developed in this study utilising HSC Chemistry 7 simulation software for the purpose of investigating the effects of feed ore liberation on value mineral recovery. These single cell simulation runs allowed for the various flotation simulation outputs to be analysed and for the particle tracking capability of HSC Chemistry 7 software to be explored. Table 5-2 is summary of the variables that were used in simulating a single flotation cell. The single cell flotation flow sheet designed in HSC Chemistry 7, consisted of a 85 m^3 flotation cell with feed solids input feed rate of 890 tph. These values that were used are equivalent to those that appear in a similar study by Ralston et al. (2007) for which flotation cell hydrodynamic parameter values required for model calibration used in this study were adapted from.

Table 5-2: Feed and literature hydrodynamic variables that were used in simulating a Single flotation cell flow sheet operation.

Variable	Parameter	Literature Parameter (Ralston et al.,2007)
Feed Ore	Porphyry Copper Ore	
P_{70}	120 μm	
Cell volume	85 m^3	85 m^3
Solids feed rate	890 tph	890tph
Solids weight % in feed		40.8%
Sulphide mineral contact angle (θ)		78°
NSG contact angle (θ)		0°
Energy dissipation (ϵ)		11 m^2/s^3
Bubble diameter (d_b)		0.0013 m
Bubble rise velocity (v_b)		0.18 m/s
Apparent viscosity of slurry (ϑ)		0.2 kg/ms
Gas flow rate (G_{fr})		4 m^3/min

Figure 5-3 shows the single cell flow sheet that was created in HSC Chemistry Simulation software and used for the simulations.

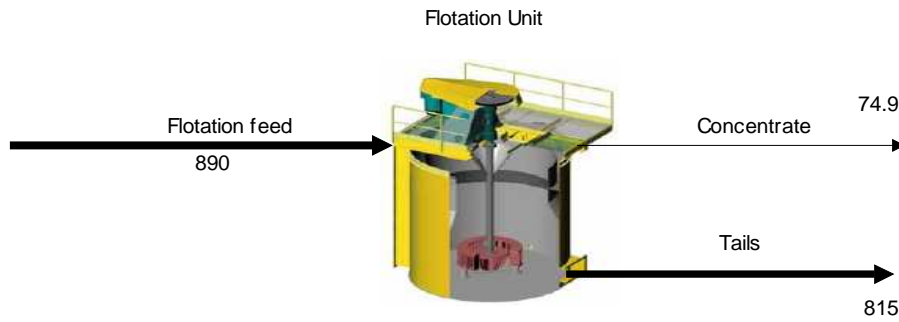


Figure 5-3: Single unit flotation cell flow sheet simulation layout in HSC Chemistry 7 Simulation software.

The following variables were selected to be indicators of the measure of the performance of the flotation cell; Cu recovery (%), Cu grade in the concentrate, mass pull and the enrichment ratio. Values of these variables from the simulations were compared with those from literature, as shown in Table 5-3.

Simulation results obtained were comparable with those reported in literature for a single cell operation, Table 5-3. The results show that the simulated flotation cell recovery values are within range of literature values for typical industrial single copper flotation cells. It can be concluded from the results that the fundamental property based flotation model has been successfully integrated into HSC Chemistry 7 simulation software.

Table 5-3: Summary of Single flotation cell flow sheet simulation grade recovery and mass full performance indicators results.

Parameter	Simulated value	Typical literature value (Yianatos et al., 2006)
Cu Recovery	56.3%	54.9%
Cu% grade in concentrate	7.43%	n.a ¹
Mass pull	8.00%	n.a
Enrichment ratio	6.69	7.20

¹ Note that the abbreviation n.a was used to indicate data that was not available for a single cell operation in literature

5.3. Analysis of simulation results using the Particle analysis tool in HSC Chemistry Simulation Software

The following stream properties and performance parameters of the single flotation cell were analysed using HSC Chemistry 7 simulation software particle tracking tool;

- I. Mineral mode of occurrence in the streams around the cell
- II. Value mineral recovery in concentrate and tail streams
- III. Cumulative liberation of minerals in the streams
- IV. Particle recovery in each stream

The following sections will present and discuss the results of each of the stream properties that were analysed.

Mineral mode of occurrence in the streams around the cell

Figures 5-4 to 5-6 are graphs showing the mineral mode of occurrence of Chalcopyrite in the feed concentrate and tail streams around the simulated single cell flotation unit flow sheet.

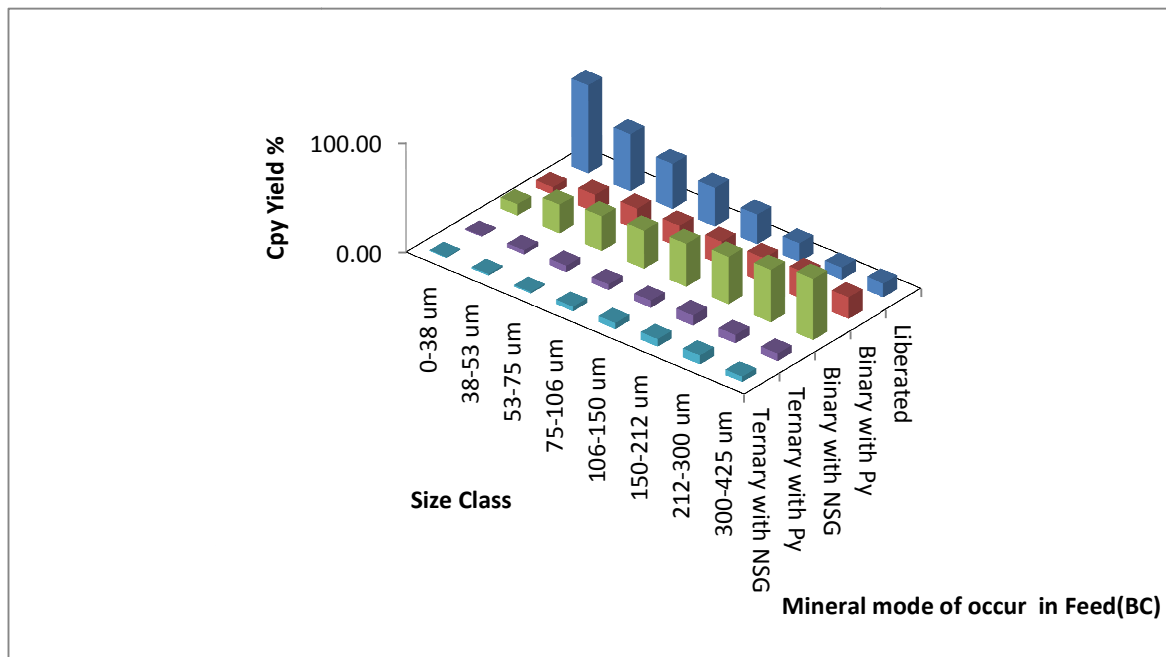


Figure 5-4: Chalcopyrite mineral mode of occurrence in Copper 1 base case feed ore stream to the single flotation cell flow sheet simulation. From Figure 5-4 it can be observed that most of the fully liberated Chalcopyrite in the Copper 1 ground ore feed is found between the 0 to 75 μm size fractions.

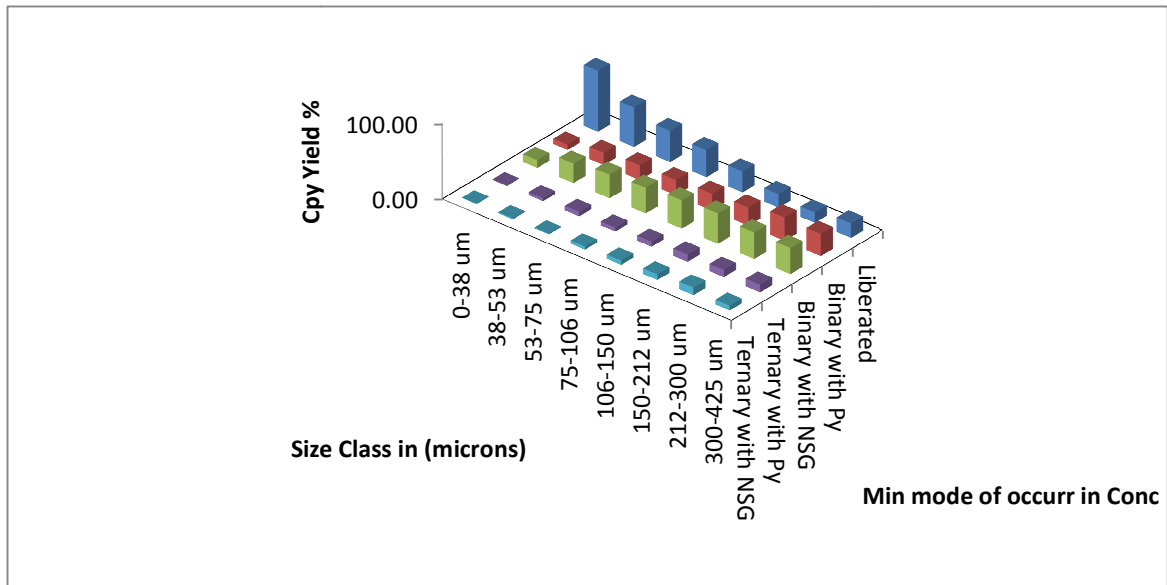


Figure 5-5: Chalcopyrite mineral mode of occurrence in Copper 1 base case concentrate product stream from the single flotation cell flow sheet simulation.

The mode of occurrence of mineral particles in the 0 to 75 μm fine size fraction range that report to the tails (see Figure 5-6), can be seen to be similar to mineral particles in the same size fraction range that report to the concentrate (see Figure 5-5).

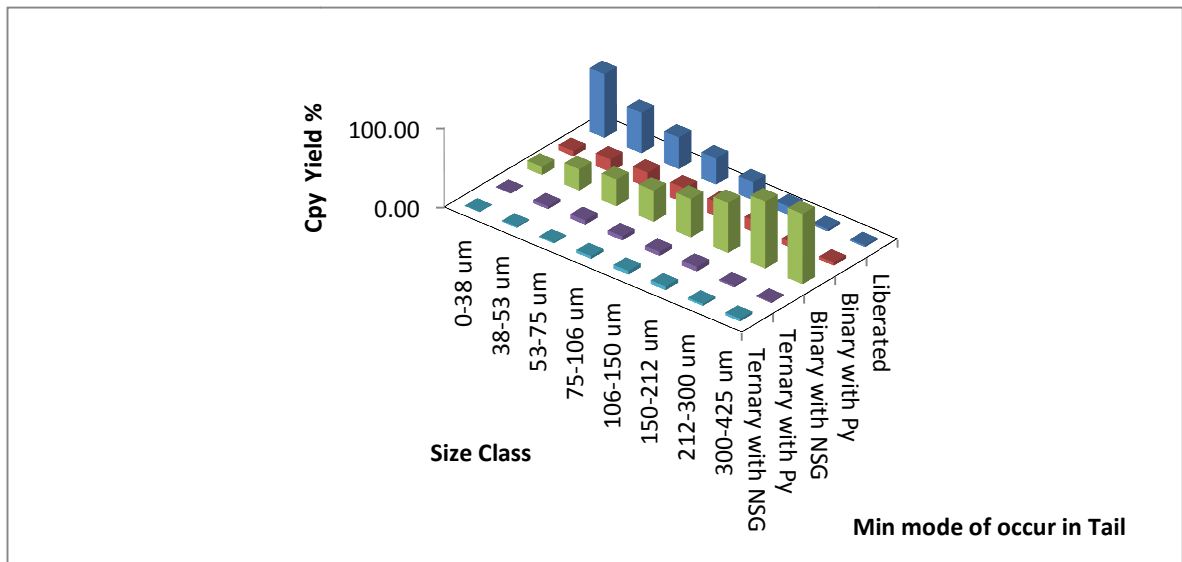


Figure 5-6: Chalcopyrite mineral mode of occurrence in Copper 1 base case ore tails product stream from the Single flotation cell flow sheet simulation.

Value mineral recovery in concentrate and tail streams

Analysis of the value mineral recovery against particle size shows a decrease in mineral recovery with increasing particle size above the 100 μm particle size, Figure 5-7. This trend compares well with that found in literature for the variation of mineral recovery with particle size (Pyke et al., 2003). As particle size increases the stability and attachment efficiencies also decrease, resulting in the value mineral particles detaching from the bubbles in the froth zone back into the pulp (see equation 3.28). A lower recovery is observed for fine particles below 100 μm particle size, as they have smaller size compared to the bubbles hence lower collection zone efficiency. Most of the NSG reports to the tails stream due to low floatability.

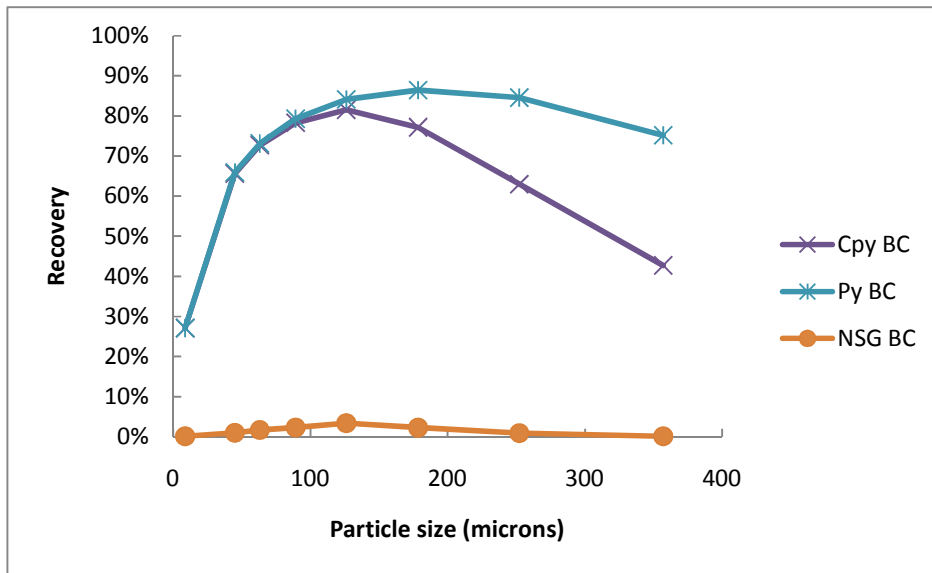


Figure 5-7: Mineral recovery against particle size for a Single flotation Cell simulation (Copper 1 BC feed).

Analysis of Particle recovery in streams around the Single cell flow sheet

Analysis of mineral particle recovery into the concentrate and tail streams of the simulated flotation cell operation showed a high recovery of coarse Chalcopyrite associated particles into the concentrate stream (see Figure 5-8). The fine sized particles in the 0 to 38 μm size fraction are poorly recovered into the concentrate stream despite being more liberated as compared to the coarser sized fractions (see Figure 5-9).

In practice the flotation rate of hydrophobic value minerals decreases with decreasing particle size due to the fact that as the particle size decreases the lower collision efficiency decreases as well (Ralston et al., 2007). This explains the poor recovery of fully liberated fine sized value mineral particles observed in the simulations (see Figure 5-8 and Figure 5-9).

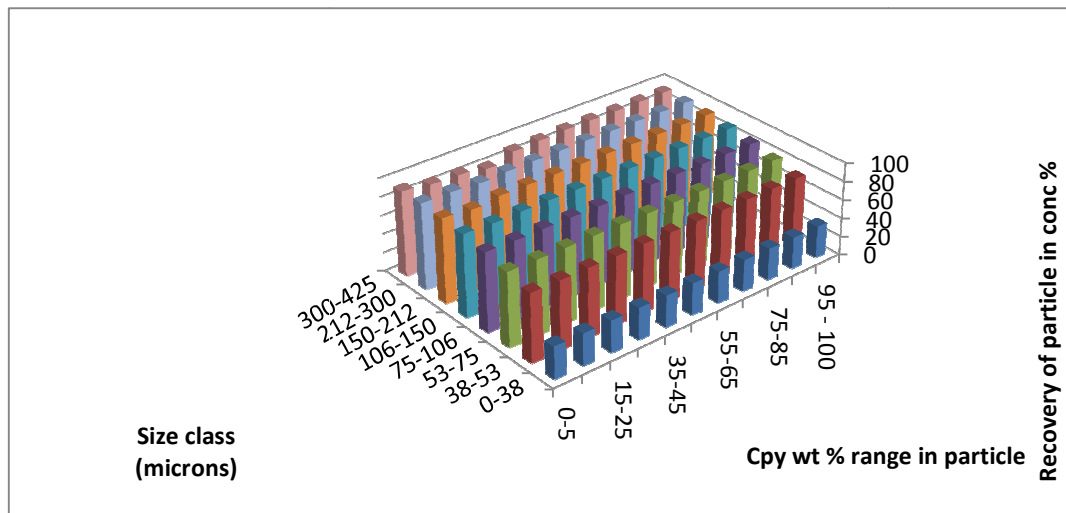


Figure5-8: Particle class recovery per size fraction in the concentrate stream against Cpy wt %.

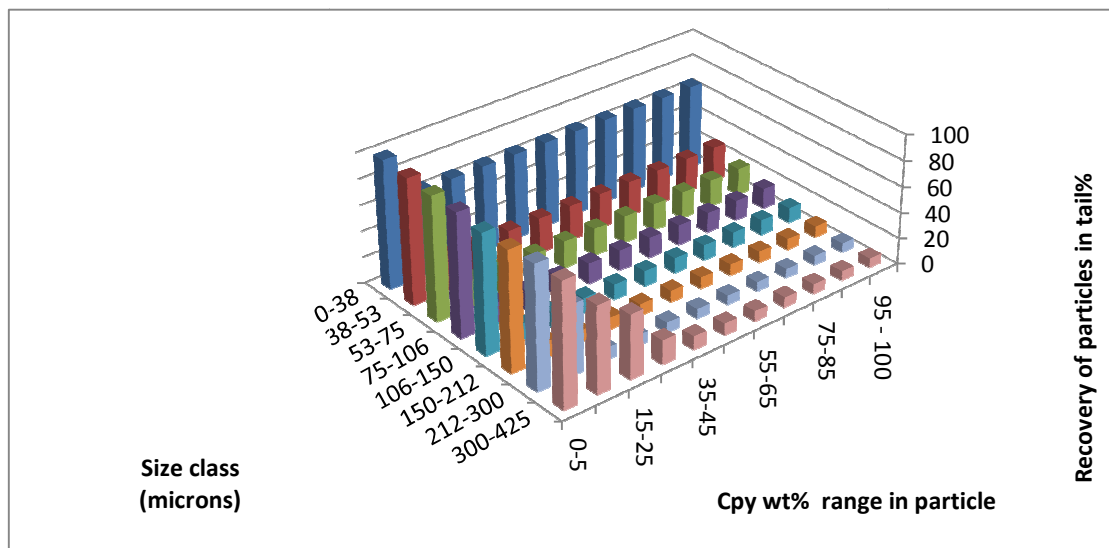


Figure 5-9: Particle class recovery per size fraction in the tails stream against Chalcopyrite wt % range in particle classes.

Analysis of Cumulative liberation of minerals in the flow streams

The feed stream liberation profile shows a greater liberation of particles in the 0 to 38 μm size fraction Figure 5-10.

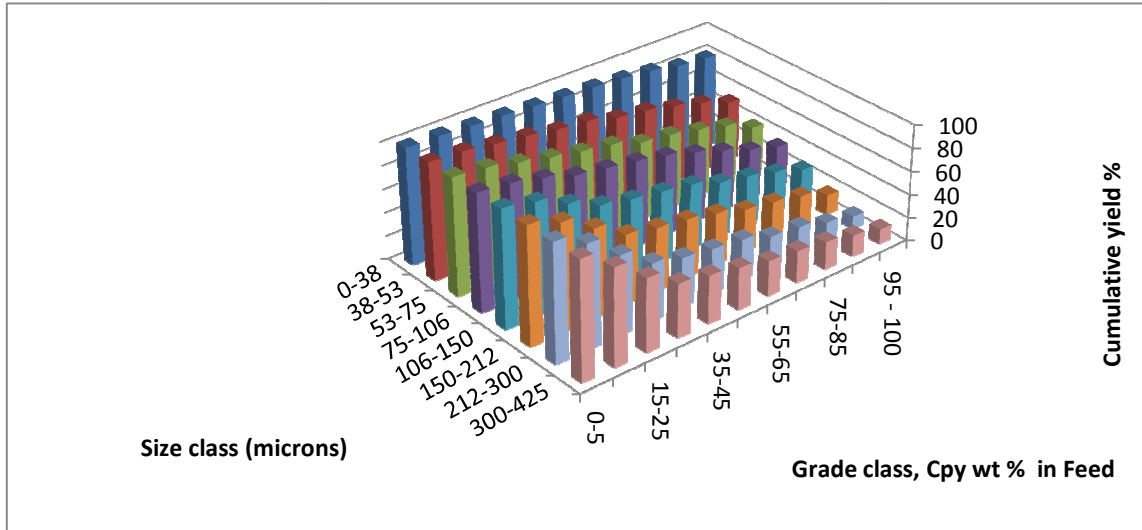


Figure 5-10: Cumulative liberation of Chalcopyrite in feed stream to the Single Unit flotation Cell flow sheet simulation.

There is a decrease in the cumulative liberation of particles from the fine sized fractions (0-38 μm) to the coarse sizes (300-425 μm) (see Figure 5-10).

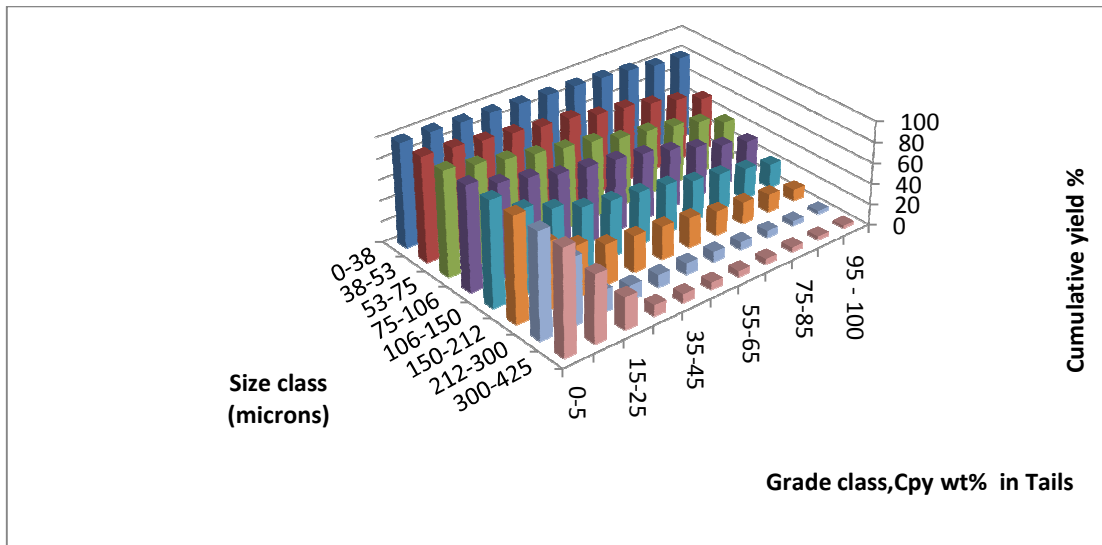


Figure 5-11: Cumulative liberation of Chalcopyrite in the output tail stream from the Single Unit flotation Cell flow sheet simulation.

Figures 5-11 and 5-12 show that fully liberated Chalcopyrite in the fine sized fractions (0-75 μm) mostly reported to the tails as was explained earlier fine sized particles have a lower probability of colliding with bubble hence they recover poorly.

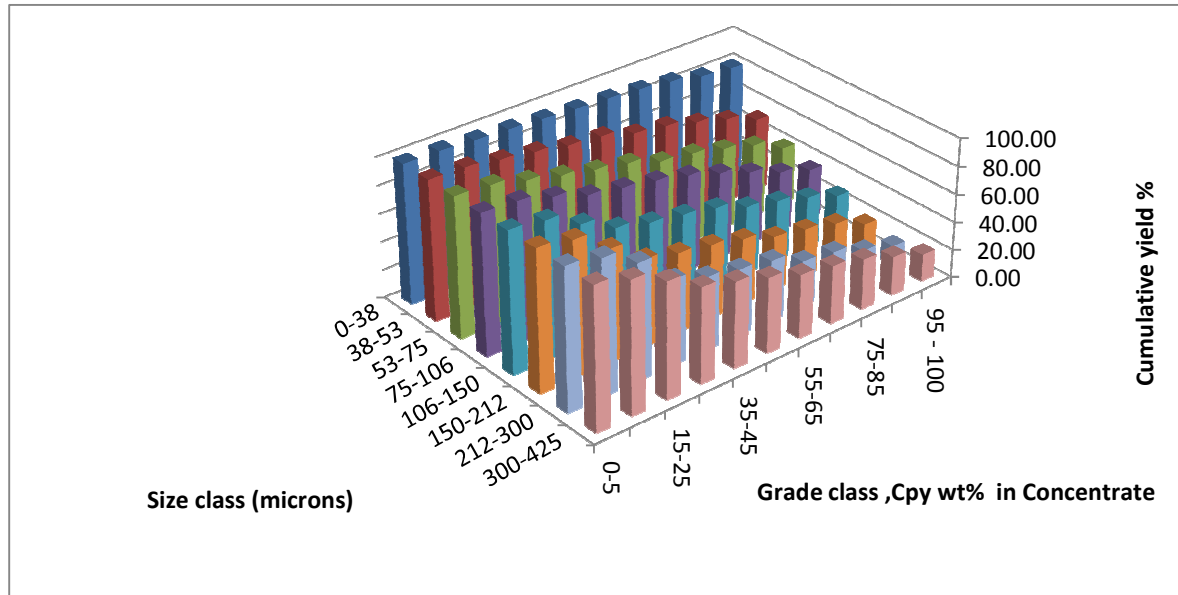


Figure 5-12: Cumulative liberation of Chalcopyrite in the output concentrate stream from the Single Unit flotation Cell flow sheet simulation.

5.4. Effects of changes in feed ore liberation on single Cell recovery

In order to understand fully the effects of microwave treatment on the downstream processing of ores, there is first a need to study the effects of feed ore liberation variation on the flotation process. This section presents the results of single flotation cell operation simulation work that was carried out to investigate the effects of feed ore liberation on value mineral recovery. The feed ore scenarios that were considered in the investigation are summarised in Table 4-5 Chapter 4. A detailed description of the feed ores has been provided in Chapter 4, section 4.3. Two ore groups representing flotation feeds at different grind sizes were utilised in the investigations, namely Copper 1 ($P_{70}=120 \mu\text{m}$) and Copper 2 ($P_{70}=180 \mu\text{m}$) flotation feed ores. A brief description of the method that was used in obtaining the simulation results for Copper 1 base case ore and artificial ores derived from it will be presented first followed by Copper 2 base case ore and its associated artificial ores. This will be followed by the presentation and discussion of the simulation results that were obtained for each feed ore group.

5.4.1. Methodology

A single flotation cell flow sheet was created in HSC Chemistry simulation software. A fundamental property based model wizard created for the purpose of this study and described in Chapter 3, section 3.3 was used to model the flotation process on the simulated flow sheet. The simulated flotation cell hydrodynamic conditions were described by utilising literature data from a previous study carried out by Ralston et al. (2007) on an industrial copper plant (see Table 5-4 and Appendix G Table G.1-1). These literature operating and hydrodynamic conditions were used to calibrate the fundamental property based model in all the simulations that were carried out. Six single cell flow sheet simulations representing the six different feed ore liberation scenarios considered in the study were carried out. The following flotation performance measurement parameters that are calculated from the model simulation output values were selected as key output parameters for investigating the effects of feed ore liberation changes;

1. Value mineral recovery by size (Chalcopyrite),
2. Cell enrichment ratio per feed ore
3. Cell mass pull per feed ore

Results that were obtained for both Copper 1 and Copper 2 feed ore groups were then analysed in order to determine the values of the key output parameters that have been listed above.

Table 5-4: Feed and literature hydrodynamic variables that were used in simulating a Single flotation cell flow sheet operation.

Variable	Parameter	Literature Parameter (Ralston et al., 2007)
Feed ore Type	Copper 1/ Copper 2 feeds	
P ₇₀	120 μm/180μm	
Cell volume	85 m ³	85 m ³
Feed rate	890 tph	890 tph
Sulphide mineral contact angle (θ)		78°
NSG contact angle (θ)		0°
Energy dissipation (ε)		11 m ² /s ³
Bubble diameter (d _b)		0.0013 m
Bubble rise velocity (v _b)		0.18 m/s
Apparent viscosity of slurry (ϑ)		0.2 kg/ms
Gas flow rate (G _{fr})		4 m ³ /min
Surface tension (γ)		70 N/m

5.4.2. Copper 1 feed ore (P₇₀ = 120 μm): Results and discussion

Figures 5-13 to 5-15 are graphical representation of the flotation simulation model's mineral recovery against particle size for all the feed ore scenarios that were considered. The differences in mineral recovery between the ores can be attributed to the differences in liberation profiles of the feed ore and hence the mineral particle hydrophobicity as described by the particle surface contact angle.

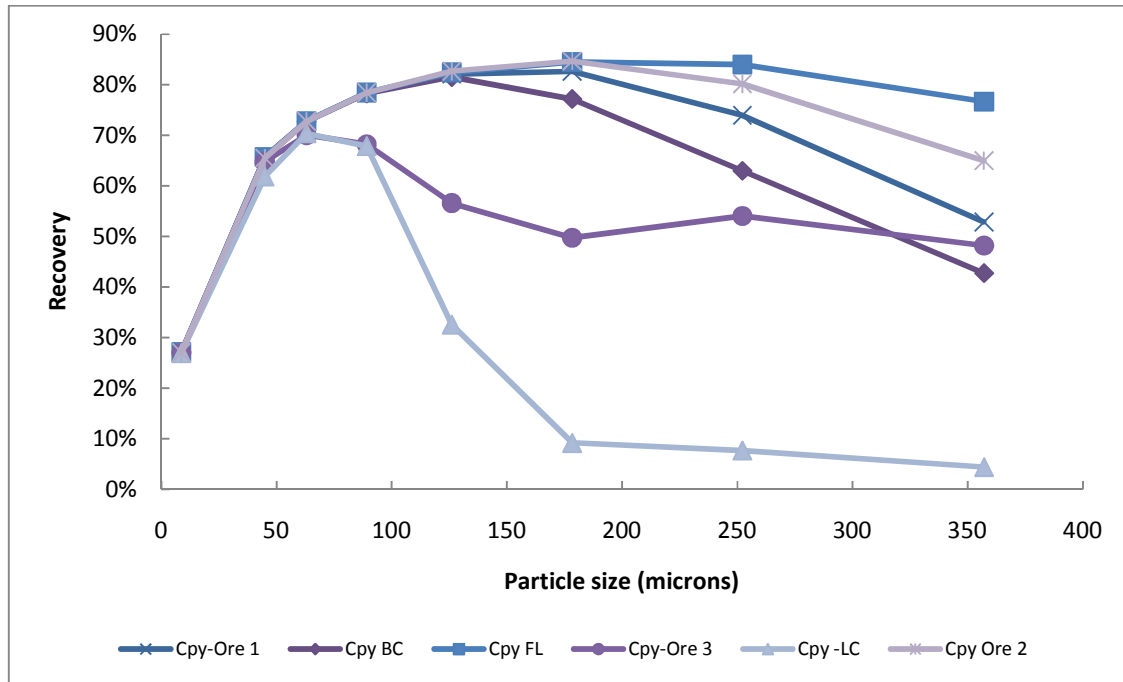


Figure 5-13: Chalcopyrite recovery against particle size for a single flotation Cell simulation for all the feed ore liberation scenarios considered in the simulations ($P_{70}=120 \mu\text{m}$).

Figure 5-13 and 5-14 show a decrease in value mineral recovery with increasing particle size. It is understood from literature that value mineral recovery decreases with increasing particle size (Pyke et al., 2003). There is no significant difference in value mineral recovery between the ores in the fine particle size classes Figure 5-13 and 5-14. As particle sizes increases there is a drop in recovery of the poorly liberated ores first (LC and Ore 3). As size increases and especially between the 120 μm to 150 μm particle size fractions, a significant difference in value mineral recovery is observed between the four well liberated ore feeds, which becomes quite pronounced at the very coarse particle sizes (see Figure 5-13 and Figure 5-14) .

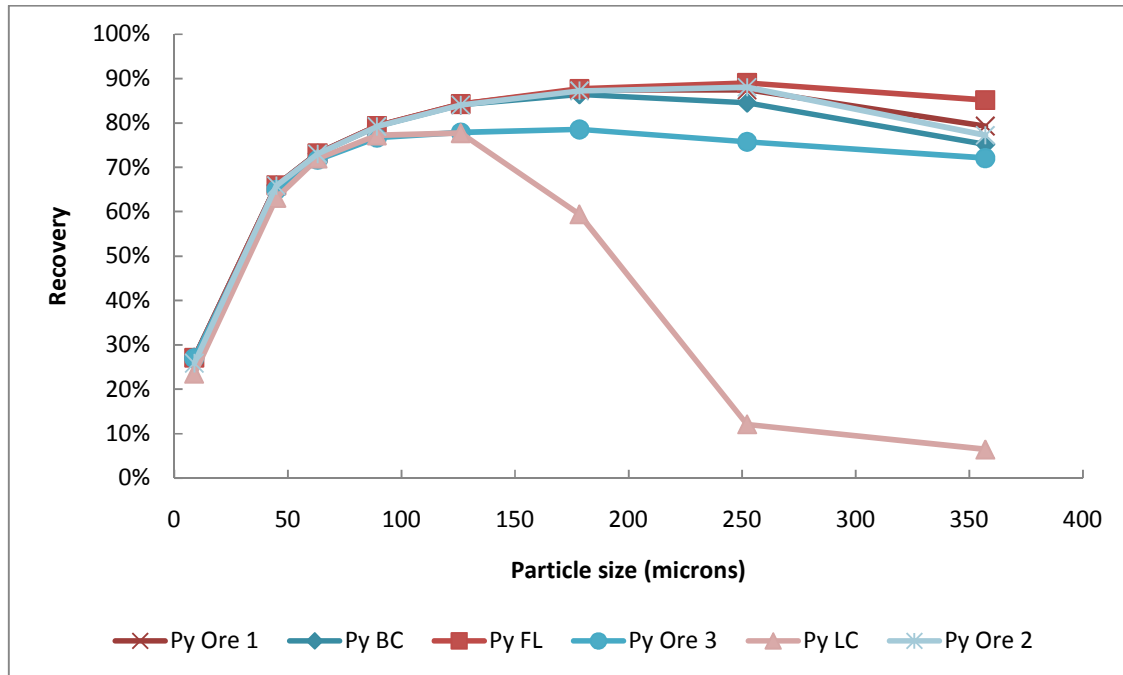


Figure 5-14: Pyrite recovery against particle size for a Single flotation Cell simulation for all the feed ore liberation scenarios considered in the simulations, ($P_{70}=120\mu\text{m}$).

Figure 5-14 shows similar Pyrite mineral recovery trend as that observed for Chalcopyrite. This can be attributed to the fact that a fully liberated Pyrite mineral particle was assumed to have the same hydrophobicity (contact angle) as a fully liberated Chalcopyrite value mineral in the simulations. For Pyrite value mineral recovery above the 150 μm particle size the percentage Pyrite recovery values for BC, Ore 1 and Ore 2 feed are of similar magnitude. This is mostly due to the fact that Pyrite in the BC feed is well liberated (see Figure 4-3). Thus the improvement in the recovery of Pyrite in FL, Ore 1 and Ore 2 feed compared with the BC feed Pyrite recovery is smaller than that observed for Cpy recovery (see Figure 5-13 and Figure 5-14).

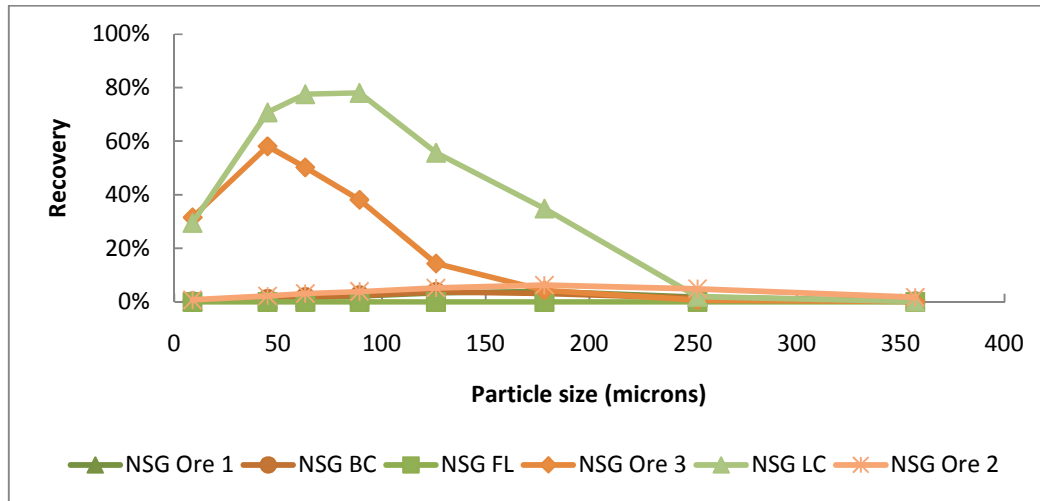


Figure 5-15: Pyrite recovery against particle size for a Single flotation Cell simulation for all the feed ore liberation scenarios considered in the simulations, ($P_{70}=120 \mu\text{m}$).

The high NSG recovery reported for LC and Ore 3 feed ore shown in Figure 5-15 was due to the bulk of the NSG in these feed ores occurring in association with Chalcopyrite and Pyrite minerals as binary or ternary composite particles. Most of the NSG associated with the floating mineral therefore reported to the concentrate, hence high NSG recovery values were obtained for these ores.

Table 5-5 below summarises the results of the simulated flotation process key performance parameters for the six feed ore scenarios that were considered for Copper 1 group ores with a grind size P_{70} of $120 \mu\text{m}$. From the table it can be observed that the FL and LC feed ore are the two extreme feed ore liberation scenarios in this study. FL ore describes an ideal fully liberated ore which gives maximum value mineral recovery, enrichment ratio and a very low mass pull as shown in Table 5-5. LC on the other hand is the complete opposite of FL feed ore as can be seen from the results in Table 5-5 below. Ore 1 and 2 feed ores have flotation performance values that are better than the BC feed ore (see Table 5-5). This is because Ore 1 has more fully liberated value minerals per size fraction compared to the BC feed; hence it gives better value mineral recovery (see Table 4-8). Ore 2 feed has more ChalcopyritePyrite (CpyPy) binary particles per size fraction compared with the BC feed and Ore 1 (see Figure 4-5, Figure 4-14 and Figure 4-17).

The CpyPy binary particles have composite contact angle values that are equivalent to fully liberated sulphide value mineral particles. Therefore Ore 2 feed ore recovers better than the BC and Ore 1 feed ores (Table 5-5).

Table 5-5: Simulated flotation process key performance parameters for the six feed ore scenarios that were considered for the base case grind size $P_{70}=120$ microns

Feed ore type	Mass pull %	Enrichment ratio	Cu Rec %	Cu % grade
BC	7.4	6.2	46.2	6.9
FL	6.2	7.9	48.8	8.8
Ore 1	7.2	6.8	47.0	7.2
Ore 2	7.4	6.3	46.3	6.7
Ore 3	13.8	2.8	38.4	3.0
LC	28.6	1.3	35.9	1.4

The simulation results above indicate the existence of maximum particle size below which changes in feed ore liberation have no effect on mineral recovery. An improvement in BC feed Cu recovery of 5.6% and an improvement in concentrate Cu grade of 27.5% can be achieved by improving the BC feed value mineral liberation to that of FL feed (see Table 5-5). Following on these results a further analysis of the sub-process bubble-particle interaction efficiency values for the different ores used in the simulations was carried out.

5.4.2.1. Sub-process bubble-particle interaction efficiency values

From the simulation results only an analysis of the trend in the stability and attachment sub-process efficiency was carried out, as the collision efficiency is not dependent on particle liberation. The following calculation steps were carried out in order to obtain the weighted mean sub-process efficiency values. For each feed ore within a given size class the product of the sub-process efficiency value and chalcopyrite weight percent of each particle class in the size class was summed up to determine the weighted sub-process efficiency. Equation 5.1 below summarises the calculation steps that were used in calculating the weighted mean sub-process efficiency per size fraction in the study.

$$\sum_{i=1}^n E_{zi} \times \text{Cpy wt\%}_{ij} = E_{zj} \quad 5.1$$

E_{zj} - weighted mean sub-process efficiency for size fraction j

Cpy wt% -chalcopyrite composition in each particle class i in size fraction j

z - Stability or attachment sub-process

n -number of particle liberation classes in j size fraction

i -particle liberation class

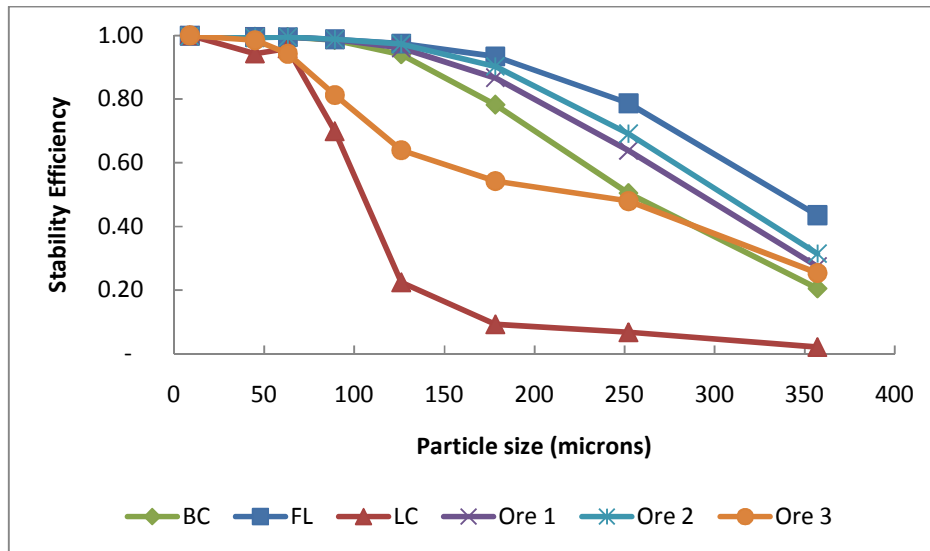


Figure 5-16: Mean Stability efficiency against mean particle size for feed ore with a $P_{70} = 120\mu\text{m}$

Figure 5-16 shows a decreasing trend in stability efficiency with increasing particle size. This is due to the effects of detachment forces acting on the bubble-particle aggregate which become predominantly large with increasing particle size (see equation 3.28). As particle size increases a higher particle contact angle value is required to float mineral particles with large particles sizes. There is no significant difference in stability efficiency at fine particle sizes below $75\mu\text{m}$, Figure 5-16. This explains the trend in mineral recovery that was observed in the simulations.

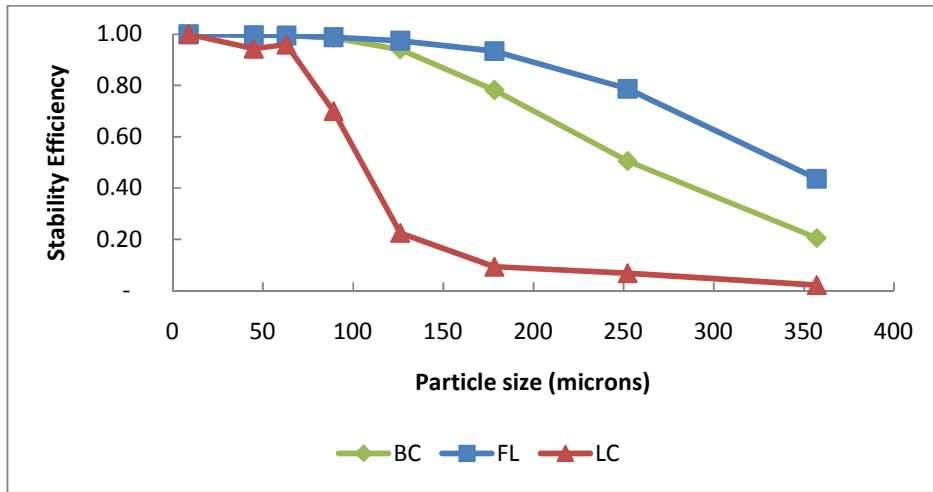


Figure 5-17: Mean Stability efficiency against mean particle size for Base Case ore and the two extreme liberation cases (FL and LC), for feed ore with a $P_{70} = 120 \mu\text{m}$.

Analysing the stability efficiency of the extreme liberated feed ore cases (i.e. LC and FL feed ores) clearly shows that there is a maximum particle size above which stability efficiency becomes a strong function of feed ore liberation profile (see Figure 5-17). This maximum particle size is greater for well-liberated feed ores for example BC and FL feed ores compared with poorly liberated ores such as LC feed ore (see Figure 5-17). This trend in particle stability efficiency with varying feed ore liberation explains the trends observed in mineral recovery.

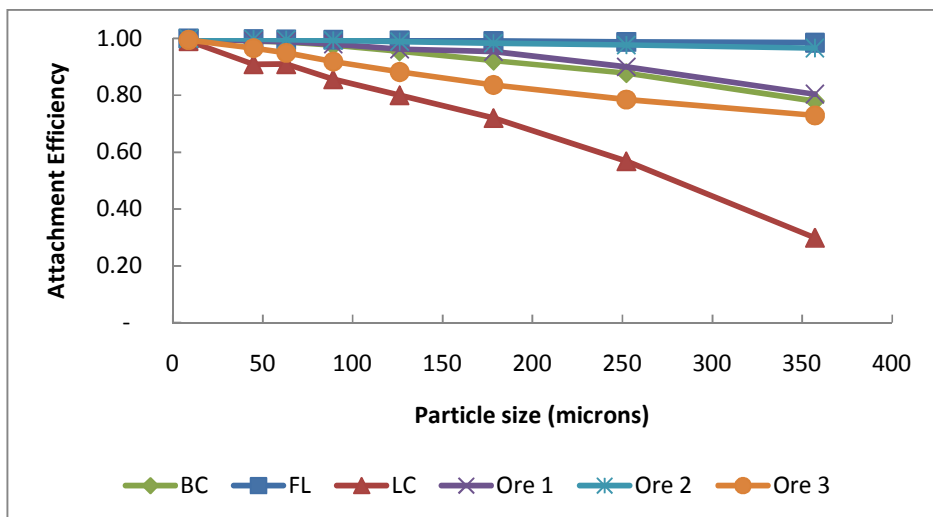


Figure 5-18: Mean attachment efficiency against mean particle size for feed ore with a $P_{70} = 120 \mu\text{m}$.

Figure 5-18 shows a decreasing trend in attachment efficiency with increasing particle size. This is because an increase in particle size results in a decrease in sliding time and an increase in the induction time hence decreases the attachment efficiency (see equation 3.24 and 3.25). Figure 5-19 below shows that the difference in stability efficiency is more pronounced at coarse particle sizes.

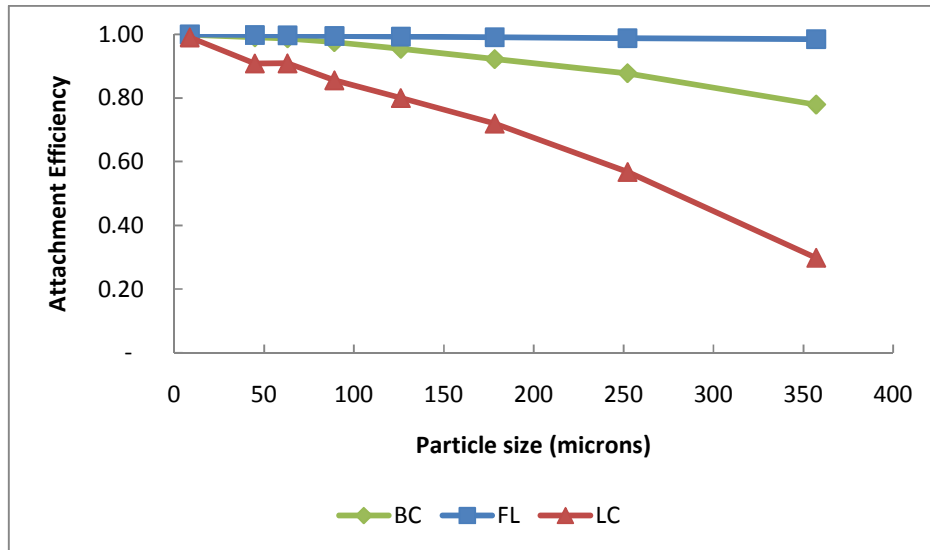


Figure 5-19: Mean Attachment efficiency against mean particle size for Base Case ore and the two extreme liberation cases (FL and LC), for feed ore with a $P_{70} = 120 \mu\text{m}$.

The differences in recovery, which were mostly observed at coarse particle sizes, with varying feed ore liberation can be attributed to the variation of stability and attachment efficiency values at coarse sizes. Since the feed ores used in the simulation have similar mineralogy, the differences in stability and attachment efficiency trends are due to a variation in particle contact angle, hence feed ore particles liberation properties. The results indicate the existence of a maximum particle size below which any improvement in mineral liberation as expected from the application of microwave technology does not result in an increase in value mineral recovery and that this maximum particle size is a strong function of the flotation feed ore liberation profile.

5.4.3. Copper 2 feed ore ($P_{70} = 180 \mu\text{m}$): Results and discussion

Copper 2 group feed ores with a grind size of $P_{70} = 180 \mu\text{m}$ represented coarse feed ore in the study. Figure 5-20 shows a decreasing trend in Chalcopyrite mineral recovery with increasing particle size above $120 \mu\text{m}$ particle size and a significant difference in mineral recovery at coarse sizes for the different ores mostly for FL feed above the $180 \mu\text{m}$ particle size.

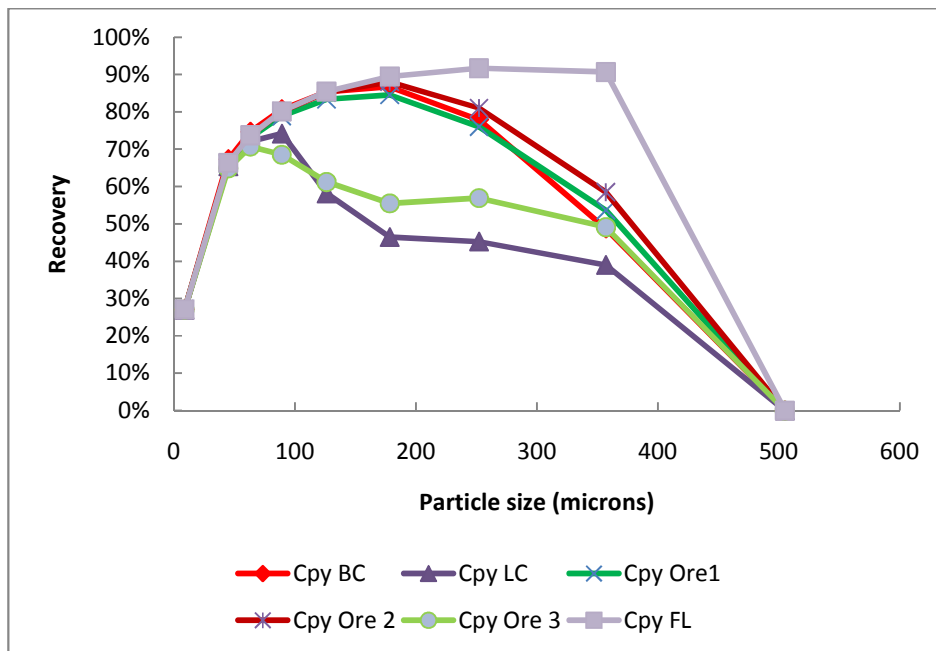


Figure 5-20: Chalcopyrite recovery against particle size for a Single flotation Cell simulation for all the feed ore liberation scenarios considered in the simulations, ($P_{70}=180 \mu\text{m}$).

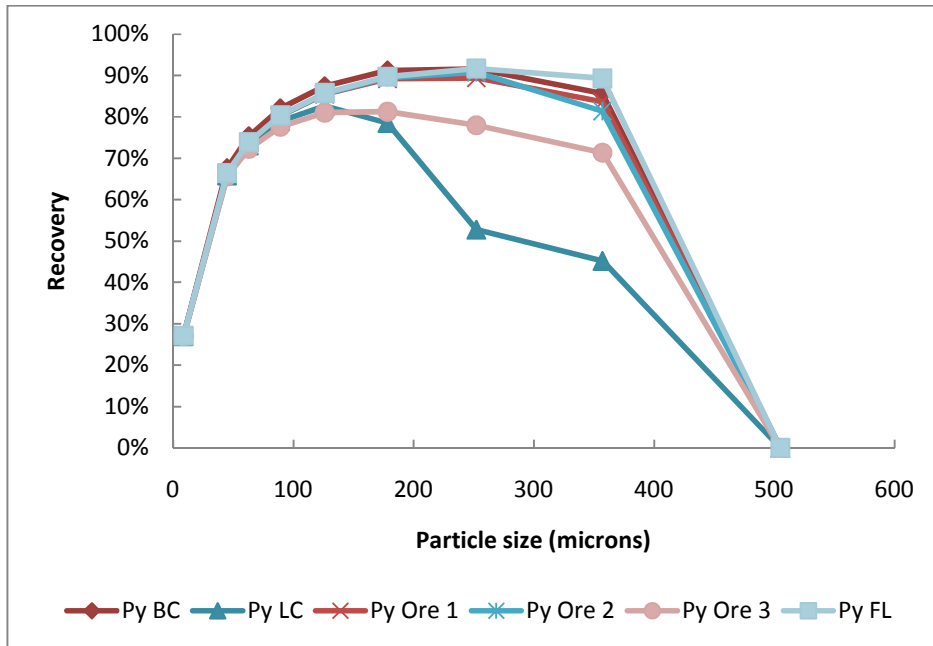


Figure 5-21: Pyrite recovery against particle size for a Single flotation Cell simulation for all the feed ore liberation scenarios considered in the simulations, ($P_{70}=180 \mu\text{m}$).

Figure 5-21 shows a decreasing trend in Pyrite mineral recovery with increasing particle size. There is little difference in mineral recovery at coarse sizes between the BC, Ore 1, Ore 2 and FL feed. Little improvement in pyrite recovery was observed between the BC and fully liberated feed ores in (see Figure 5-21). This was due to high pyrite liberation in the base case feed that was used in creating the fully liberated artificial ore (see Figure 4-6). Consequently further improvements in liberation of the BC feed yielded small improvements in Pyrite recovery (see Figure 5-21).

Table 5-6 below summarises the results of the simulated flotation process key performance parameters for the six feed ore scenarios that were considered for this ore. Better results were obtained for Copper 2 ore compared to those obtained for Copper 1 ore Table 5-6. An improvement in BC feed Cu recovery of 11.0% and an improvement in concentrate Cu grade of 31.3% can be achieved by improving the BC feed value mineral liberation to that of FL feed (see Table 5-6).

Table 5-6: Simulated flotation process key performance parameters for the six feed ore scenarios that were considered for the base case grind size $P_{70}=180$ microns

Feed ore type	Mass pull %	Enrichment ratio	Cu Rec %	Cu % grade
BC	7.0	6.3	44.5	6.7
FL	6.0	8.2	49.4	8.8
Ore 1	6.8	6.7	46.0	7.1
Ore 2	7.4	6.3	46.3	6.7
Ore 3	13.8	2.8	38.4	3.0
LC	24.1	1.5	35.7	1.6

5.4.3.1. Sub-process efficiency values

The stability and attachment efficiency values that were calculated in the simulation for the various feed ores in the simulations are shown to below in Figure 5-22 and Figure 5-23.

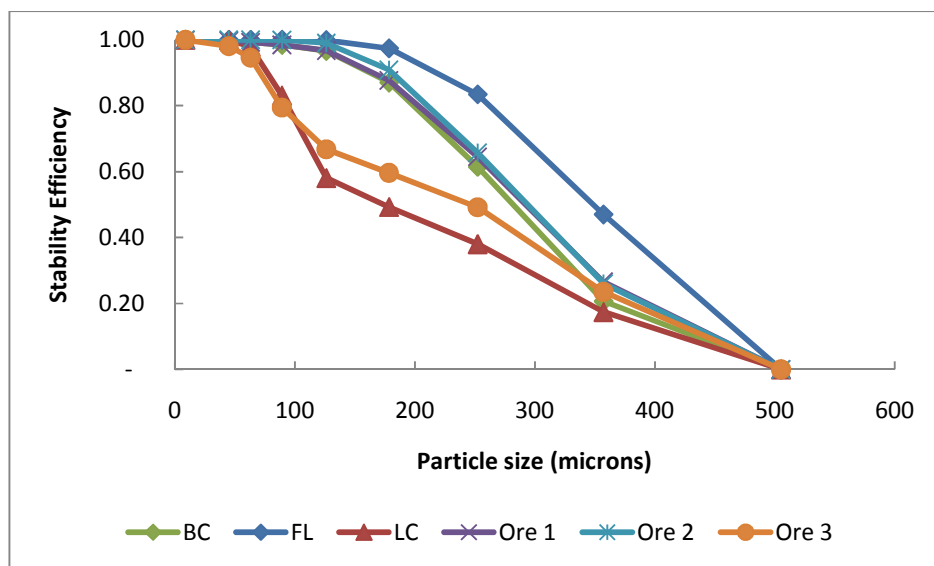


Figure 5-22: Mean Stability efficiency against mean particle size for feed ore with a $P_{70} = 180\mu\text{m}$.

Figure 5-22 shows a similar decreasing trend in stability efficiency with increasing particles size as was observed earlier for Copper 1 feed ores.

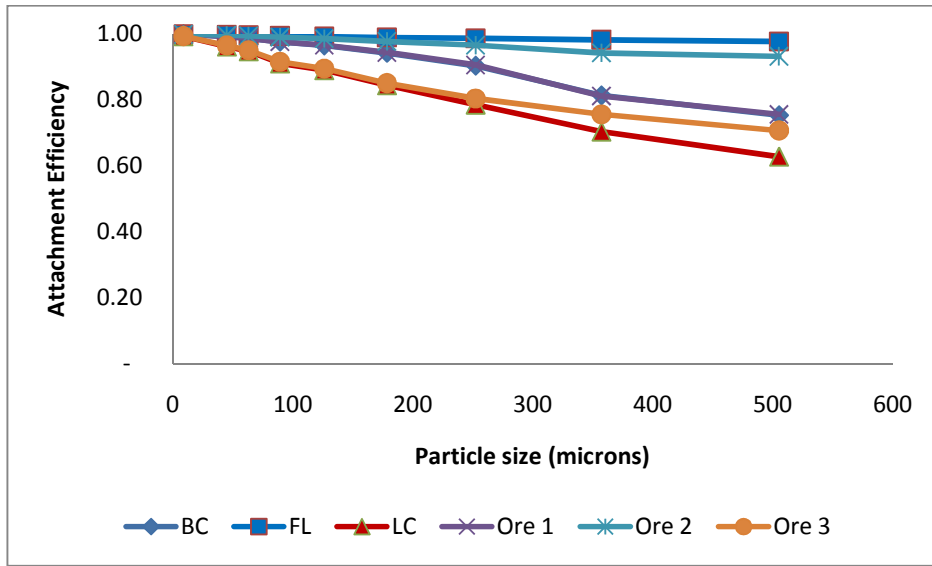


Figure 5-23: Mean attachment efficiency against mean particle size for feed ore with a $P_{70} = 180 \mu\text{m}$

Figure 5-23 shows decreasing attachment efficiency with increasing particle size. The results that were obtained for coarse ground feed ores stability and attachment efficiency further confirmed the significant variation in sub-process efficiency values at coarse size.

5.4.3.2. Feed ore Particle size sensitivity analysis

A particle size sensitivity analysis study was carried out on the Copper 2 group ores to verify the sensitivity of the flotation process as described by the fundamental property based model to particle size, for feed ores with the same mineralogy but with different particle size distributions. This was aimed at showing that there is a maximum particle size below which mineral recovery was not a strong function of feed ore liberation. Two sets of fictional mean particle size fractions were used describing very fine feed ores ($P_{70} = 63 \mu\text{m}$) and a very coarse ground ore ($P_{70} = 250 \mu\text{m}$). No changes were made to the feed ore particle weight distribution per size class of the original Copper 2 group ores described in Table 4-1, Chapter 4, section 4.2. Simulations similar to the ones described above were then carried out. Table 5-7 shows the fictional average mean particle sizes that were considered in investigating the fundamental property based model sensitivity in simulating flotation recovery for a very fine ground ore.

Table 5-7: Fictional average fine particle sizes and used in the sensitivity analysis investigations ($P_{70} = 63 \mu\text{m}$)

Average Size (μm)	Particle weight distribution, wt%
8.72	38.17
19.16	4.64
26.10	4.83
48.33	5.46
55.00	7.01
65.00	8.83
85.00	12.71
110.00	13.48
126.10	4.87

Figure 5-24 is the value mineral recovery results that were obtained using the particle size classes shown in Table 5-7. The results confirm the existence of a maximum particle size above which mineral recovery begins to drop in response to differences in feed ore liberation properties. This maximum particle size is lower for poorly liberated ores such as Ore 3 and LC (see Figure 5-24). This point is very important in the application of microwave technology in mineral processing as it indicates that little benefit from microwave enhanced liberation will be realised at fine flotation feed grind sizes.

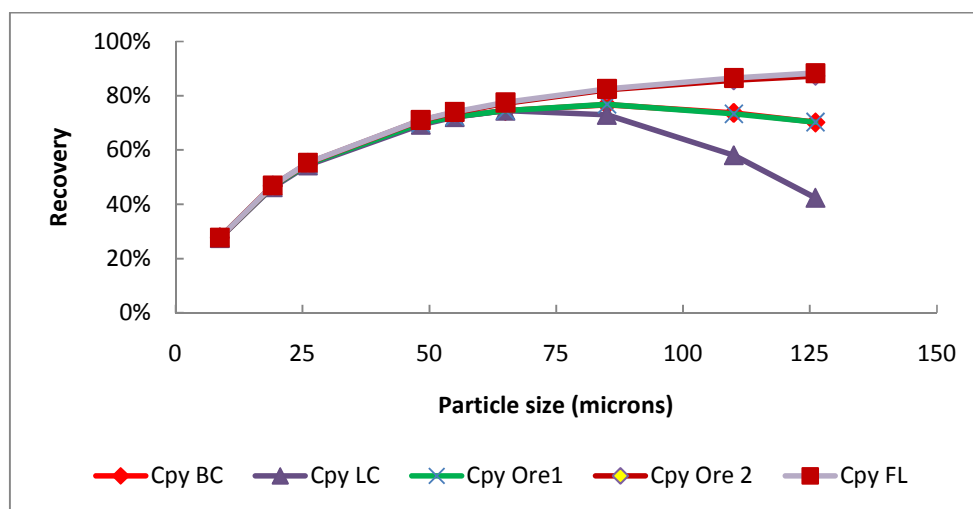


Figure 5-24: Chalcopyrite recovery against particle size for a Single flotation Cell ($P_{70}=63 \mu\text{m}$).

Table 5-8 shows the fictional average mean coarse particle sizes that were considered in investigating the fundamental property based model sensitivity in simulating flotation recovery for a very coarse ground ore along with the original bulk particle weight distribution for Copper 2 ores.

Table 5-8: Fictional average coarse particle size distribution ($P_{70} = 250\mu\text{m}$)

Average Size (μm)	Particle weight distribution, wt%
63.05	38.17
89.16	4.64
126.10	4.83
178.33	5.46
200.00	7.01
252.19	8.83
300.00	12.71
357.07	13.48
504.98	4.87

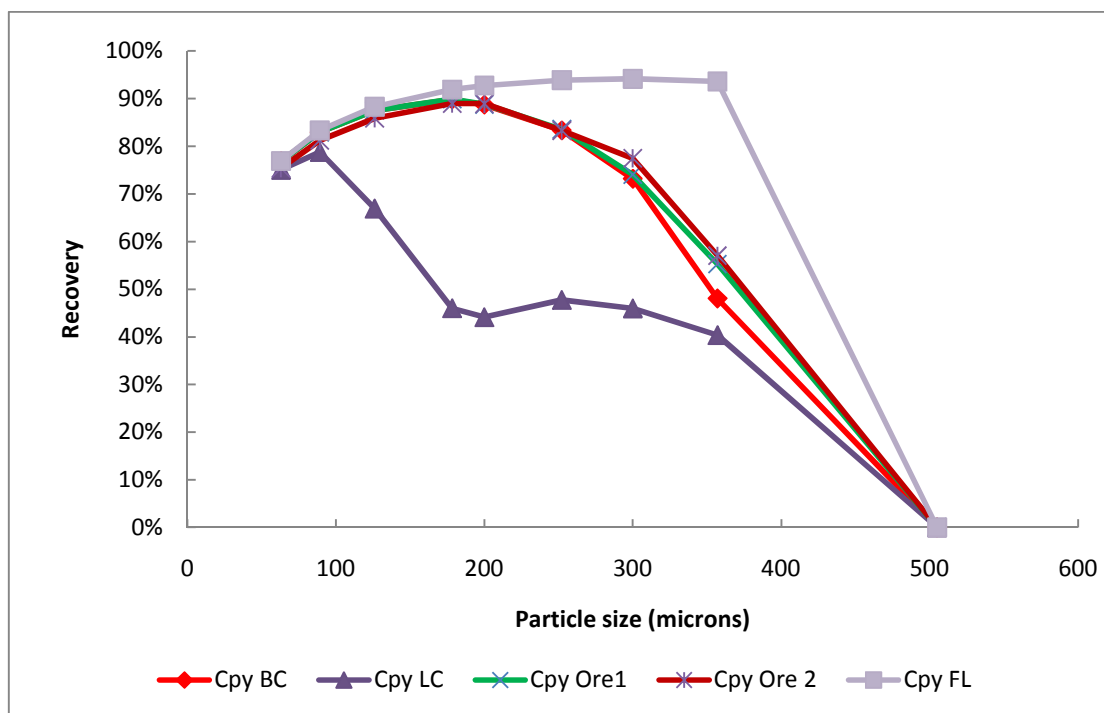


Figure 5-25 : Chalcopyrite recovery against particle size for a Single flotation Cell simulation ($P_{70}=250\mu\text{m}$).

Figure 5-25 further supports the results observed so far, which indicate that at coarse particle sizes the variation in feed ore liberation has a significant effect on value mineral recovery. From the sensitivity analysis results it appears that feed ore particle recovery is not a strong function of particle liberation at fine particle sizes, as shown in Figure 5-24. Maximum benefits from enhanced liberation due to microwave assisted comminution can thus be achieved by optimising feed ore grinding, Figure 5-25.

5.5. The effects of feed ore particle size distribution on value mineral recovery

Based on the results of investigations into the effects of varying feed ore liberation on value mineral recovery presented above, where a significant difference in value mineral recovery at coarser grind sizes with variation in liberation was observed, a feed ore grind size sensitivity study was carried out in order to investigate further the effects of grind size variation on value mineral recovery. The study was undertaken by using three feed ore liberation scenarios. These were LC feed ore representing the worst liberation case scenario, FL feed ore representing the maximum possible feed ore particle liberation scenario and a base case scenario, representing feed ore with a liberation spectrum from experimentally ground flotation feed. A brief outline of the methodology that was used will be described below followed by a presentation of the results and their discussion.

5.5.1. Methodology

Feed ore with varying grind size was created by varying the particle distribution of the Copper 2 group feed ores. The feed ore grind sizes that were used in the investigation are shown in (see Table 5-9).

Table 5-9: Particle cumulative weight distribution of the different feed ores considered in carrying out the feed particle weight distribution sensitivity analysis

Mean Size fraction	P ₇₀ Grind size				
	89 μm	129 μm	252 μm	300 μm	430 μm
8.72	37.17	25.6	10.17	8.12	0.87
44.88	47.71	38.14	17.81	14.76	2.42
63.05	60.54	53.65	26.64	22.59	5.25
89.16	69.99	63.1	36.1	31.05	7.39
126.10	77	70.11	46.11	43.06	10.11
178.33	85.83	78.94	57.94	51.92	17.97
252.19	93.69	86.65	70.65	62.66	26.79
357.07	97.13	95.13	89.13	79.2	44.2
504.98	100	100	100	100	100

Figure 5-26 is a cumulative weight distribution plot of the grind sizes considered in the sensitivity analysis. The graph shows a clear difference in particle weight distributions at different grind sizes.

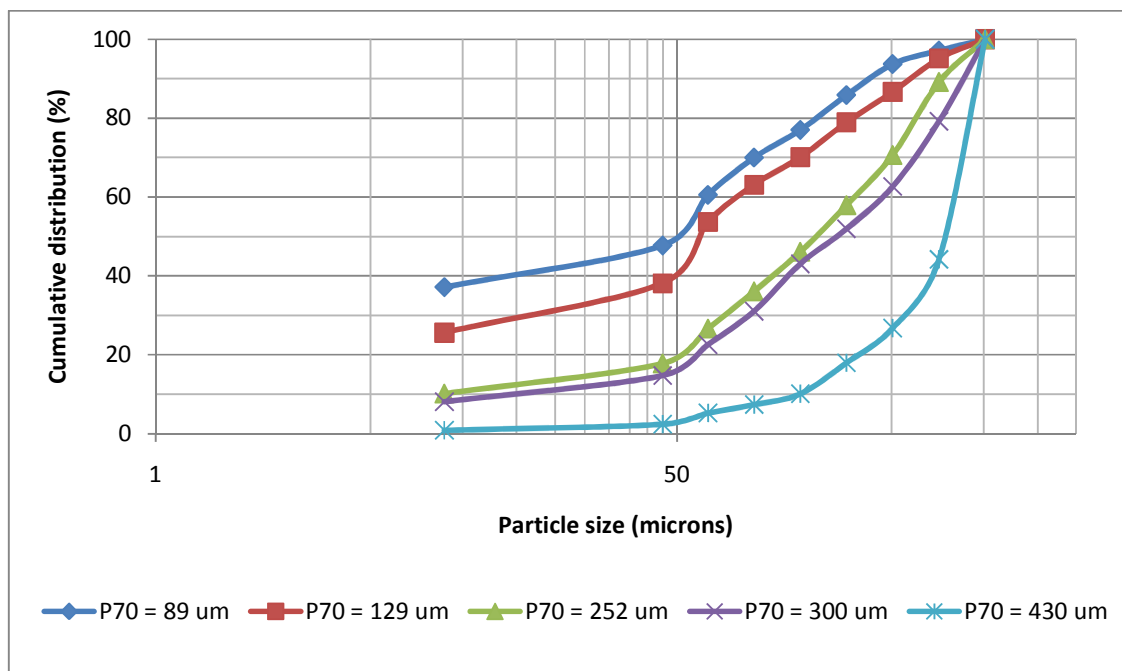


Figure 5-26: Cumulative particle weight distribution plot of the various P₇₀ grind sizes that were considered in the simulations.

Stream files were created for each particle size with the weight distribution that was considered shown in Table 5-9. By manipulating the feed particle size weight distribution in creating feeds with different grind sizes, feeds with different copper feed grades was produced (see Table 5-10). It was therefore not possible to create artificial ores with the same head grade since the liberation spectrum in each class was fixed. In practice this difference in head grade has a significant effect on feed ore recovery with feed ores with higher head grades having high value mineral recovery. However in this study the difference in final feed ore recovery due to the variation in feed ore head grade was assumed to be insignificant.

The resultant feed ores had different grind sizes and grade, but the same mineral composition per size fraction as Copper 2 BC feed which was used as a basis for creating the different grind size feeds by manipulating its size fraction weight distribution. All the feed ores had a particle liberation spectrum per size class that was the same as Copper 2 feed ores, since the mineral composition per size class for all the ores was the same. It was therefore not possible to create artificial ores with the same head grade since the liberation spectrum in each class was fixed. In practice this difference in head grade has a significant effect on feed ore recovery with feed ores with higher head grades having high value mineral recovery. However in this study the difference in final feed ore recovery due to the variation in feed ore head grade in was assumed to be insignificant (see Table 5-10).

Table 5-10: Cu% feed grades at different feed grind sizes

Mean Size fraction	P₇₀ Grind size				
	89 µm	129 µm	252 µm	300 µm	430 µm
Cu% feed grade	1.17	1.10	0.92	0.86	0.60

For each grind size shown in Table 5-9, three single cell simulations were carried out for the three feed ore liberation scenarios (i.e. BC, LC and FL) that were considered for each feed grind size. Similar cell operating and hydrodynamic conditions similar to those described in the previous simulations (see Table 5-4) were used in carrying out the simulations.

5.5.2. Grind size sensitivity analysis results

An increase in overall recovery was observed within a P_{70} feed ore grind size range of 89 to 250 μm (Figure 5-27). This trend in overall recovery is consistent with literature where an improvement in overall value mineral recovery is expected for relatively coarse ground feed ore (Gupta and Yan, 2006). Above the optimum grind size the overall recovery begins to drop with increasing particle grind size. The overall recovery for all the feeds decreased with increasing particle size over the 250 μm to 430 μm feed ore grind sizes.

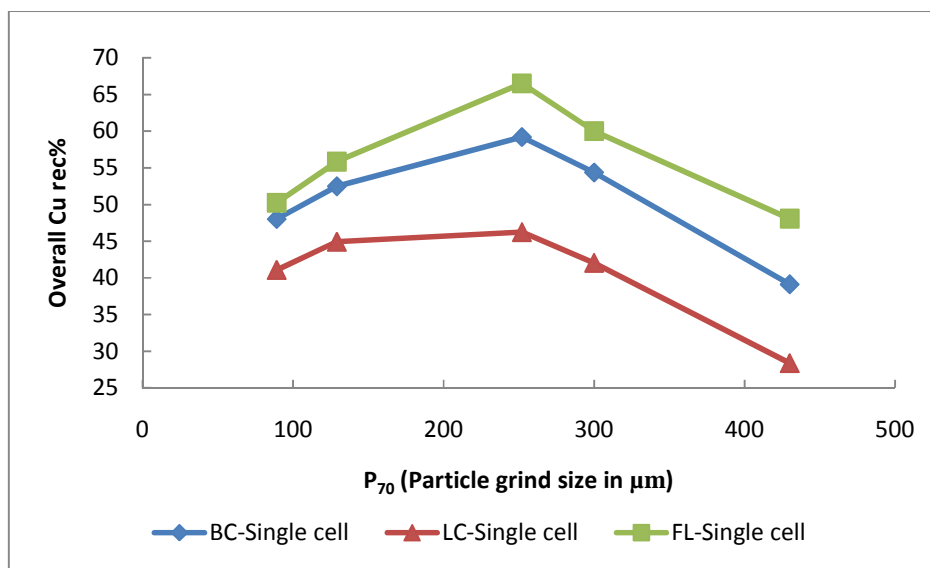


Figure 5-27: Overall single cell unit recovery against particle size for feed ore with varying size distributions.

The results indicate that there is a drop in overall copper recovery with increasing particle size above $P_{70} = 250 \mu\text{m}$.

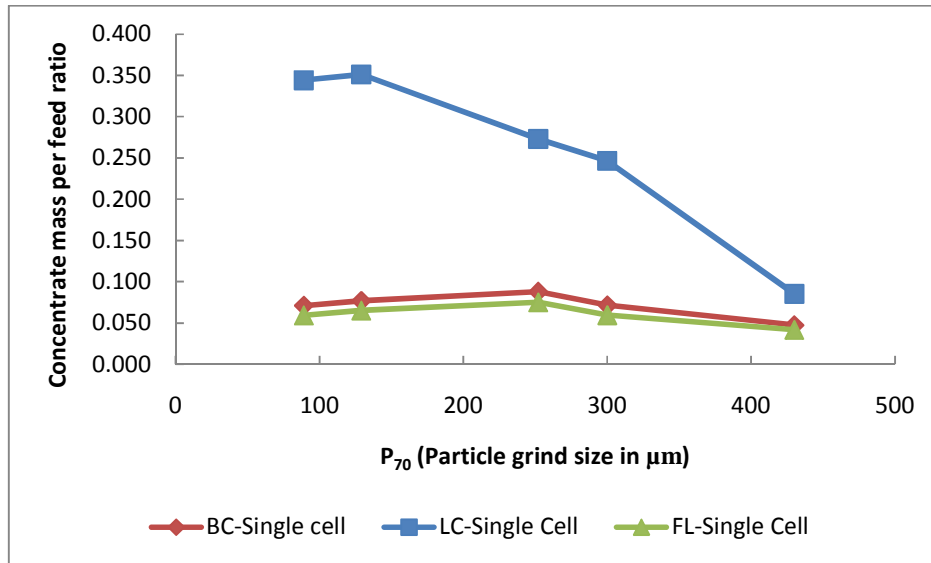


Figure 5-28: Concentrate mass recovery in a Single cell plotted against feed ore into the cell with varying size distributions.

Analysis of concentrate mass recovery as shown in Figure 5-28 indicates a low concentrate mass recovery above the 250 μm feed ore particle grind sizes for fully liberated and base case feed ores.

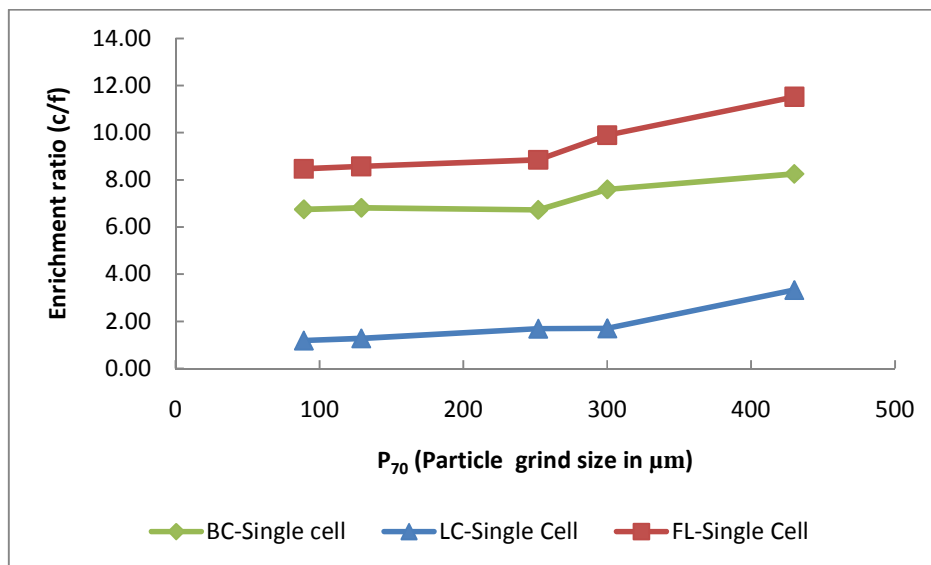


Figure 5-29: Enrichment ratio in a Single cell plotted against feed ore into the cell with varying size distributions.

Figure 5-30 shows an increase in enrichment ratio above the 250 μm P_{70} grind sizes. This increase is more pronounced for fully liberated ore. The results of the feed ore grind size sensitivity analysis study indicate that possible improvements in mineral recovery due to microwave treatment can be obtained for the particular ores considered in this study, if it is ground at size between a $P_{70} = 200 \mu\text{m}$ to $300 \mu\text{m}$. There is a limit to coarse particle flotation of $500 \mu\text{m}$ above which it becomes increasingly difficult to float coarse particles (Gontijo et al., 2007).

5.6. Conclusion

Simulations that were carried out using the fundamental property based model showed that mineral recovery trends obtained using the property based model were comparable to experimental batch flotation recovery trends obtained from a previous study for the same ore (AMIRA:P879A, 2009). The fundamental property based model has been successfully integrated into the simulation software and can be used for true particle modelling based on the results from the continuous single flotation cell simulations. Investigations into the effects of feed ore liberation variation on single cell flotation value mineral recovery showed that there exists a minimum particle size below which any variation in feed ore liberation has no effect on mineral recovery. Significant differences in value mineral recovery were only observed at coarse particle sizes. The results of the feed ore grind size sensitivity analysis indicate that maximum benefit from the application of microwave technology can best be obtained by utilising coarse grinding at sizes between $200 \mu\text{m}$ to $300 \mu\text{m}$ for the ores considered in this study

CHAPTER SIX

6. SIMULATION OF FLOTATION PLANTS

After successfully investigating the effects of feed ore liberation and particle size on value mineral recovery using a single flotation cell, work was carried out to determine these effects when a typical plant flow sheet is employed. A typical operating plant flotation flow sheet was developed for the purpose of investigating these effects in HSC Chemistry 7 simulation software. This section will describe the simulations that were carried out in investigating the effects of feed ore liberation and grind size by utilising rougher flotation section flow sheet. This will be followed by a presentation and discussion of the results from these simulations.

6.1. Rougher bank in series configuration simulation

The rougher flotation section flow sheet configuration, which was considered in this study, consisted of nine rougher cells in series with no recycle stream. Figure .D.1-1, Appendix D shows the rougher cell configuration that was used in the study. This flow sheet configuration is similar to the one at Escondida Leguna Seca copper plant (Yianatos et al., 2006). Flow sheet simulation results were compared with literature values for a similar cell configuration rougher plant. Flotation cell operating and hydrodynamic conditions that were used in the single cell simulations were also used to calibrate the fundamental property based model in each of the nine cells making up the rougher section flow sheet. The values describing the hydrodynamic conditions that were used in the model calibration were from a previous study in literature that was carried out by Ralston et al. (2007) on an industrial copper ore mineral processing plant. The values of the hydrodynamic and flotation cell operating condition parameters that were used in the investigations are shown in

Table 5-4 Chapter 5 (see also Appendix G). All flotation cells in the rougher bank were assumed to be operating at identical hydrodynamic and operating conditions, thus the froth depth in all the nine cells was assumed to be equal. Furthermore, the particle surface contact angle of the fully liberated value minerals was also assumed to be the same throughout the rougher bank.

The observed trend in simulated value mineral recovery (see Figure 6-1) was similar to that obtained from literature for a flow sheet of similar configuration treating a different copper ore feed (see Figure 6-2).

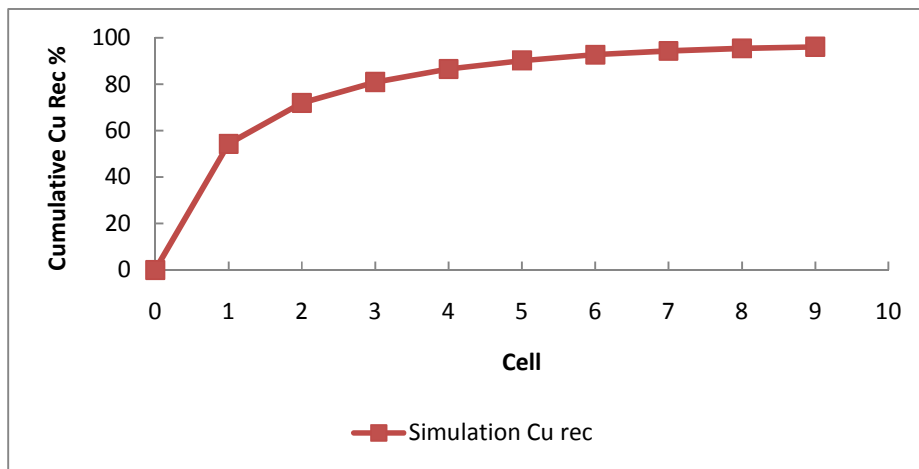


Figure 6-1: Cumulative value Copper recovery as a function of cell number in the rougher flotation section of a Simulated fictional plant.

From Figure 6-1 and Figure 6-2, it can be observed that there is a progressive decrease in local recovery per unit cell across the bank of rougher cells. A high stage recovery is observed for the first rougher cell; this is due to the presence of large amounts of floatable solids in the feed to the first rougher cell.

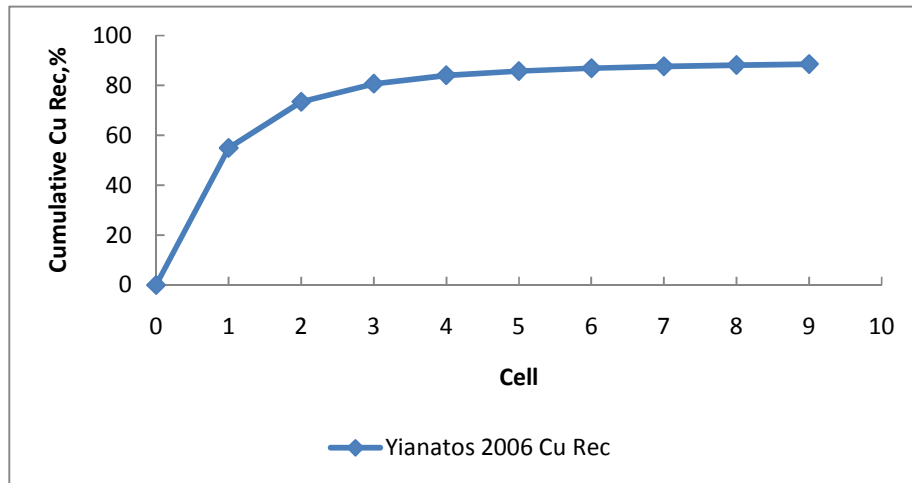


Figure 6-2: Cumulative value Copper recovery as a function of cell number in the rougher flotation section of an operating plant (Yianatos et al., 2006).

The amount of floatable solids in the feeds to subsequent cells progressively decreases along the rougher bank, as more of the floatable particles have already been recovered as concentrate.

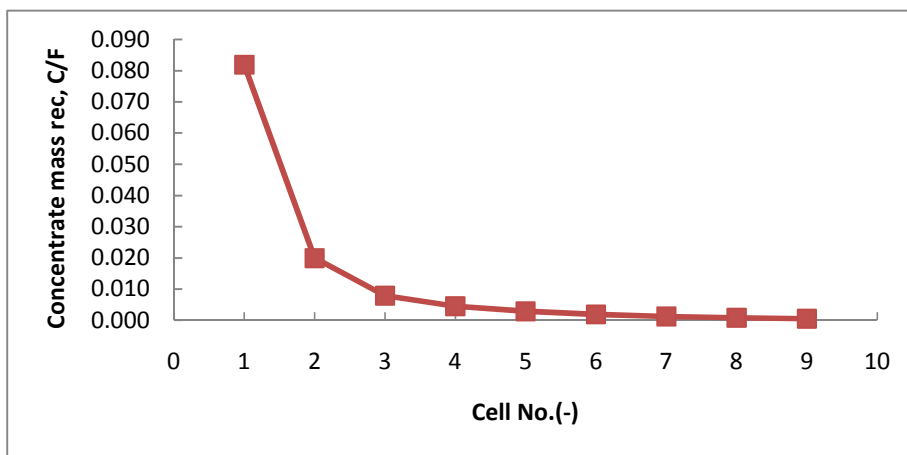


Figure 6-3: Concentrate mass recovery as a function of cell number in the rougher flotation section of simulated fictional plant.

The trends in concentrate mass recovery obtained from the simulation (see Figure 6-3) were comparable with those reported in literature for a similar rougher section flow sheet configuration (see Figure 6-4).

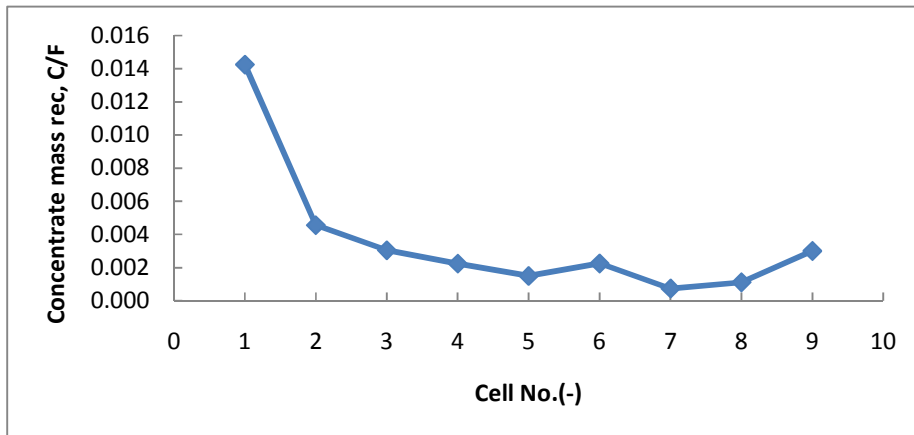


Figure 6-4: Concentrate mass recovery as a function of cell number in the rougher flotation section of an operating plant (Yianatos et al., 2006)

Lower concentrate mass recovery values were obtained for the third up to the ninth rougher cells (see Figure 6-3).

This was due to the assumptions that were made in describing the flotation process in the downstream flotation cell, where the same flotation selectivity was assumed for all the cells in the rougher bank. In typical industrial operation there is a difference in both the operational and hydrodynamic conditions that exist around each rougher flotation cell in the rougher bank (Yianatos et al., 2006).

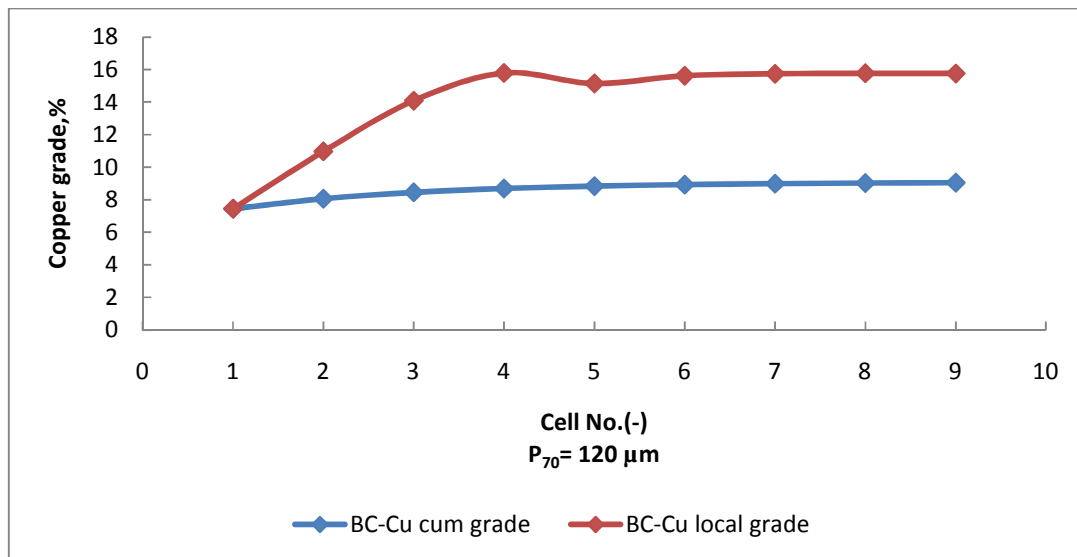


Figure 6-5: Local and cumulative copper grade profile as a function of cell number for a fictional copper plant

The local copper concentrate grade was expected to decrease downwards along the bank reaching a value closer to the feed (Wills and Napier-Munn, 2005); this was not the observed trend for the simulated grade profile (see Figure 6-5). This was due to pyrite and chalcopyrite being assumed to have similar contact angles in the simulations, because of this there was no significant difference in the chalcopyrite to pyrite ratio down the bank of rougher cells. Thus pyrite controlled the copper grade hence there was no drop in copper grade across the bank as is expected from literature. Contact angle values that were reported in literature were those for sulphide bearing mineral particles, no contact angle values were available for pyrite and chalcopyrite separately from the study by Ralston et al. (2007). In actual operations the value of the pyrite contact angle is lower than that of chalcopyrite due to the use of modifiers and depressants as the object of flotation is to recover more of the chalcopyrite.

However, for these simulations this assumption was deemed appropriate, as the cell conditions and the flotation feed ore sulphide contact angles were kept constant throughout all the simulations that were carried out, thus allowing for comparison of the various simulated results for different ore feeds.

6.2. Effect of Feed ore liberation

This section presents the results of the simulations carried out, of a nine rougher cells in series flotation flow sheet in order to investigate the effects of feed ore liberation on value mineral recovery.

6.2.1. Methodology

The feed ore scenarios that were considered for investigating the effects of feed ore liberation using a single flotation cell in Chapter 5 were also used here in this investigation. These consist of two ore groups which represent flotation feed ore at different grind sizes namely Copper 1 ($P_{70}=120\ \mu\text{m}$) and Copper 2 ($P_{70}=180\ \mu\text{m}$). The fundamental property based model was applied to model the flotation process in each individual cell. Six rougher section flow sheet simulations, representing the six different feed ore liberation scenarios (see

Table 5-4, Chapter 5), were run for each ore group. Comparative plots of the following feed ore scenario simulation results were then plotted and analysed for Copper 1 and Copper 2 feed ore groups. These were:

- I. Cumulative value mineral recovery per unit cell,
- II. Overall enrichment ratio across the bank of rougher section,
- III. Concentrate mass recovery per unit cell,
- IV. Local copper grade in concentrate per unit cell,
- V. Cumulative copper grade in concentrate per unit cell,

6.2.2. Copper 1 feed ore ($P_{70} = 120 \mu\text{m}$): Simulation results and discussion

Figure 6-6 below shows the simulation results obtained for different ores. As can be seen, a spread in cumulative recovery values of the various feed ores, which was attributed to the differences in liberation profiles between the ores, was observed.

However, there was only a slight improvement (about 2.5 percentage points) in final cumulative value mineral recovery between the BC and fully liberated ore. The improvement in recovery is even more reduced between the BC ore and Ore 1 or Ore 2 artificial ores as the number of cells increases.

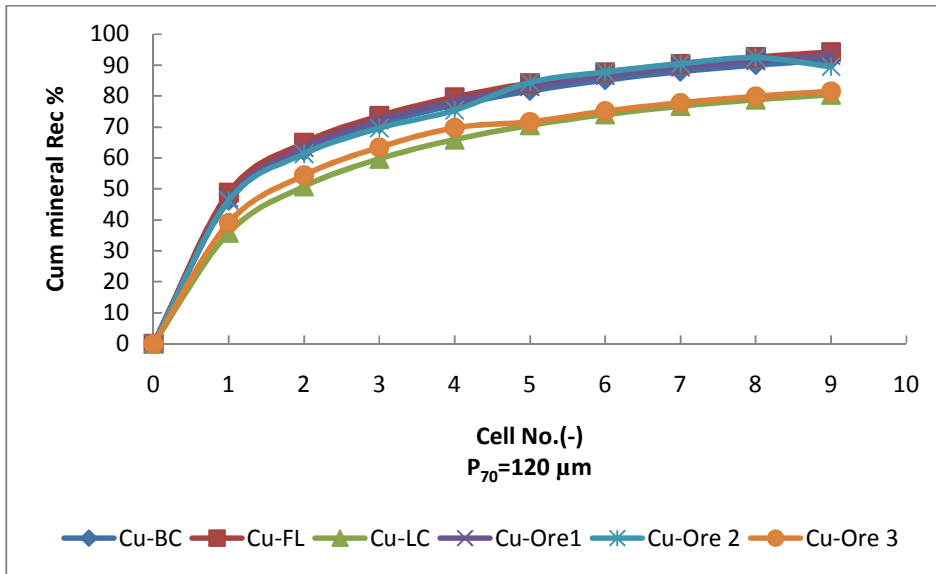


Figure 6-6: Comparison of Cu cumulative recovery per cell in a Rougher bank for different feed ore scenarios.

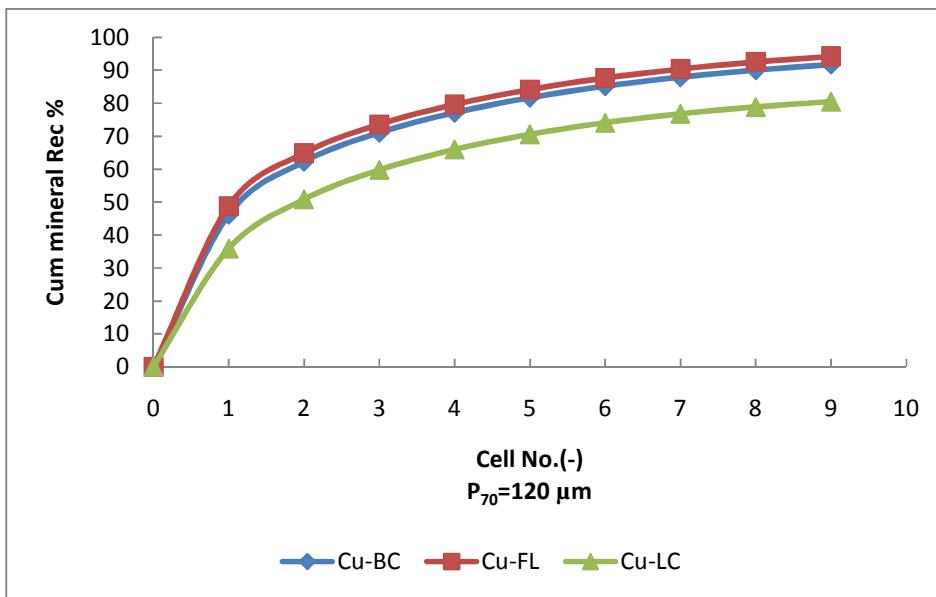


Figure 6-7: Comparison of Cu cumulative recovery per cell in a Rougher bank for the base case and extreme feed ore scenarios.

Figure 6-7 shows the cumulative recovery per unit cell values for the extreme feed ore liberation scenarios. As can be seen, a high cumulative copper recovery of about 94.2% for FL ore, 91.7% for BC and 80.4% for LC feed ore after the ninth rougher cell were obtained. There is an overall 13.8 percentage point spread in recovery between LC and

FL feed. The small difference in recovery between the BC feed ore and FL ore indicates that at a fine feed ore grind size of $P_{70} = 120 \mu\text{m}$ only a slight change in recovery would be expected from improving feed ore liberation through the application of microwave technology.

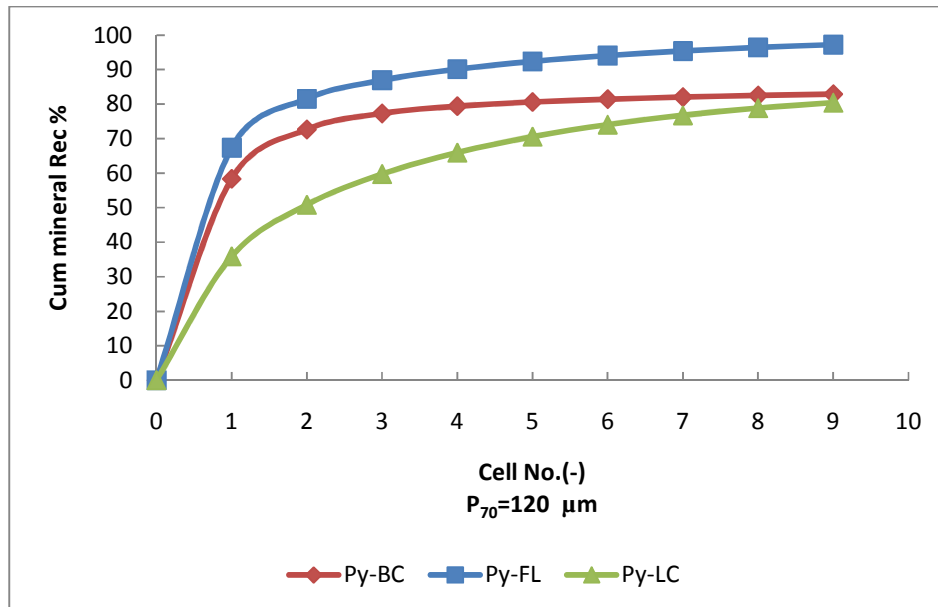


Figure 6-8: Comparison of Pyrite cumulative recovery per cell in a Rougher bank for the base case and extreme feed ore scenarios.

Figure 6-8 shows the pyrite cumulative recoveries obtained for the three cases (FL, BC, and LC). Compared with Copper cumulative recovery, significant improvement in the final cumulative mineral recovery between the BC and fully liberated ore of about 10 percentage points was observed. From analysis of the mineral mode of occurrence graphs for Pyrite in the BC feed at this grind size, Figure 4-2 (see Chapter 4, section 4.2), it can be observed that a greater amount of Pyrite exists in the binary and ternary classes in association with NSG compared with Cpy in the coarse size fractions.

When assuming that all the Pyrite exists as fully liberated particles in the FL feed, a higher improvement in recovery is expected between the BC and FL feed for Py recovery compared with that of Copper recovery after making similar assumptions for Cpy (see Figure 6-8).

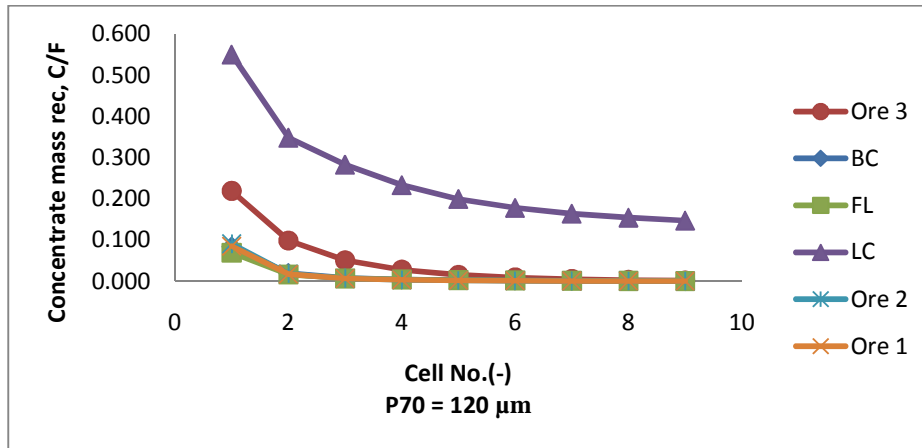


Figure 6-9: Comparison of concentrate mass recovery per unit cell in a Rougher bank for different feed ore scenarios.

It should be noted that in this study an equal froth depth was assumed for all the flotation cells in the rougher bank of cells. Thus, as shown in Figure 6-9, a progressive decrease in concentrate mass flow rates across the rougher bank was observed for all ores as expected. As can be seen, a significant variation of the concentrate mass recovery per unit cell was obtained for the different feed ores. LC feed ore has the highest concentrate mass recovery ratio per unit cell; this is followed by Ore 3 artificial ore feed. LC and Ore 3 are poorly liberated ores. The value mineral in these ores occurs as binary or ternary particles with non floating NSG which constitutes the bulk weight of the feed. Thus the bulk of the recovered concentrate contains value particles, explaining the high concentrate mass pull that was observed for the ores. There is no significant difference in concentrate mass recovery trends obtained for BC, FL, Ore 1 and Ore 2 feed ore across the rougher bank of cells. These feed ores represent relatively well liberated ore, hence there is greater amount of floatable solids in these ores.

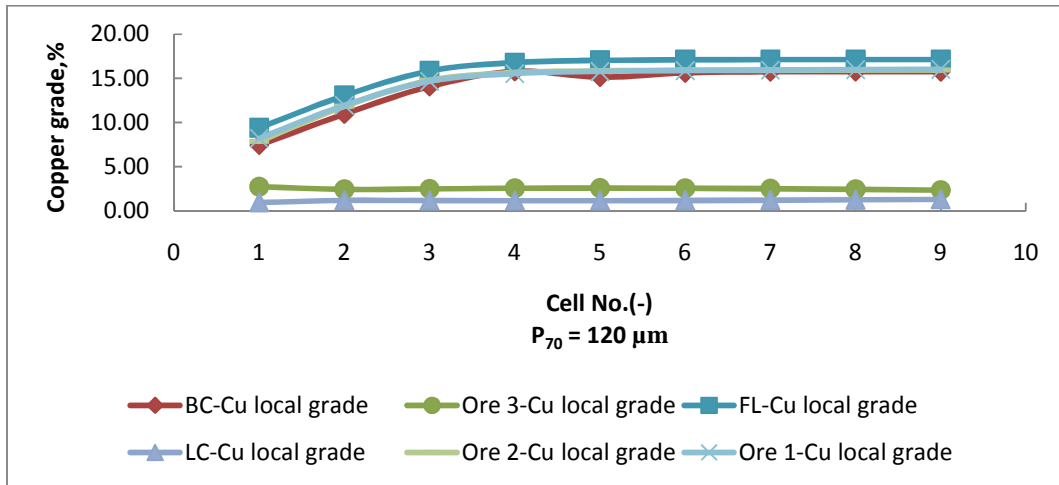


Figure 6-10: Comparison of Cu local grade per unit cell in a Rougher bank for different feed ore scenarios

Figure 6-10 shows the local copper grade obtained for each ore. The local copper concentrate grade was expected to decrease downwards along the bank, reaching a value closer to the feed (Wills and Napier-Munn, 2005). However, due to the assumption of constant flotation conditions for all the cells, all the rougher cells in the bank had high flotation selectivity. Thus, as shown in Figure 6-10, the recovered concentrate mass downwards along the bank had an increasing value mineral grade due to a decreasing concentrate mass pull (see Figure 6-9).

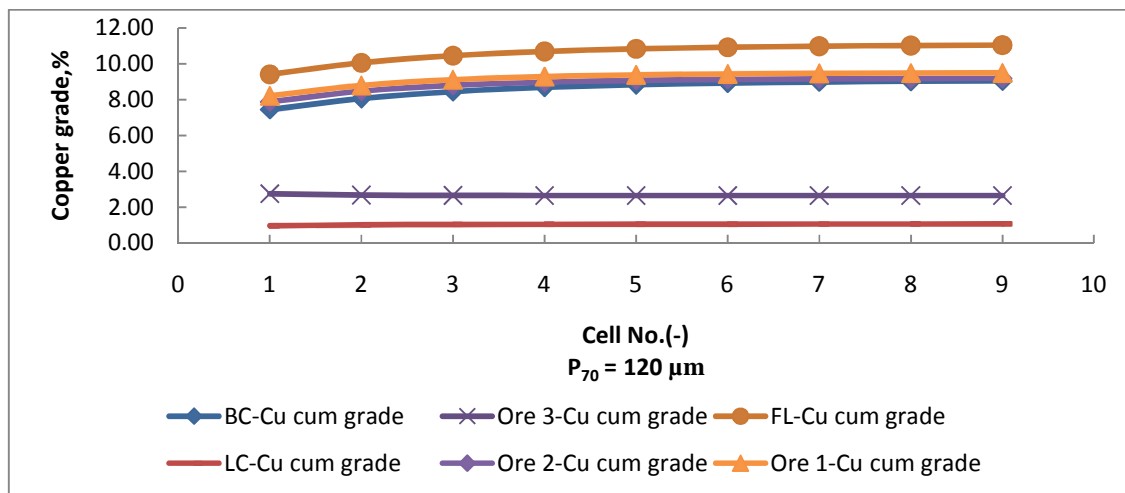


Figure 6-11: Comparison of Cu cumulative grade per unit cell in a Rougher bank for different feed ore scenarios

The cumulative copper grade plots show a low cumulative grade for LC and Ore 3 feed ores (see Figure 6-11). Similar cumulative copper grade values were observed for BC, Ore 1 and Ore 2. FL feed ore has a higher cumulative concentrate copper grade compared to the other feed ores. An increase in cumulative copper grade between the base case feed ore and the FL ore of about 1.9 percentage points was observed (see Figure 6-11). This shows that there is potential to improve final concentrate copper grade through increasing feed ore value mineral liberation.

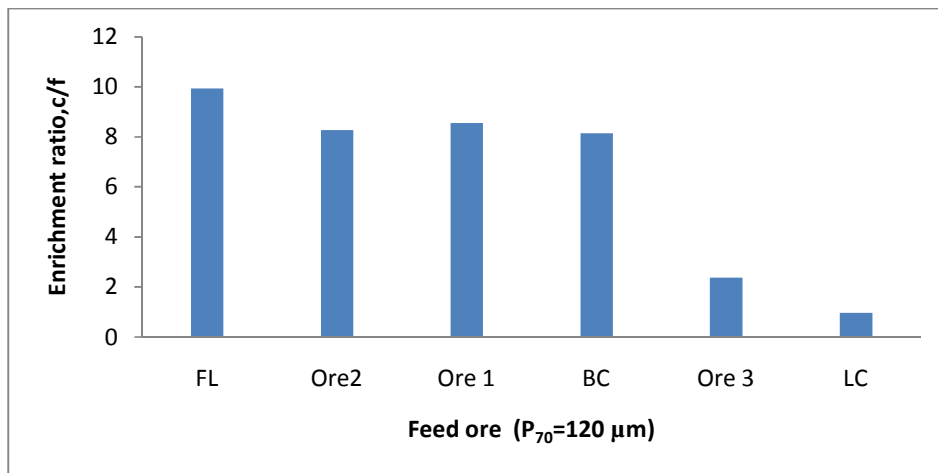


Figure 6-12: Comparison of overall rougher bank value mineral enrichment ratio for different feed ore scenarios.

Figure 6-12 shows the overall rougher bank value mineral enrichment ratio obtained for different feed ore scenarios. As can be seen, higher enrichment ratios were observed for the FL, Ore 1 and Ore 2 compared with the base case feed ore. Thus improved liberation has the effect of improving the overall rougher bank enrichment ratio. The poorly liberated ores gave very low enrichment ratio values this was due to low copper grade of the final concentrate for the two ores.

6.2.3. Copper 2 feed ore (P₇₀ = 180 μm): Results and discussion

Trends in value mineral cumulative recovery observed for various feed ores for P₇₀ grind size of 180 μm were similar to those reported in section 6.2.1 for the P₇₀ grind size of 120 μm (see Figure 6-6 and Figure 6-13).

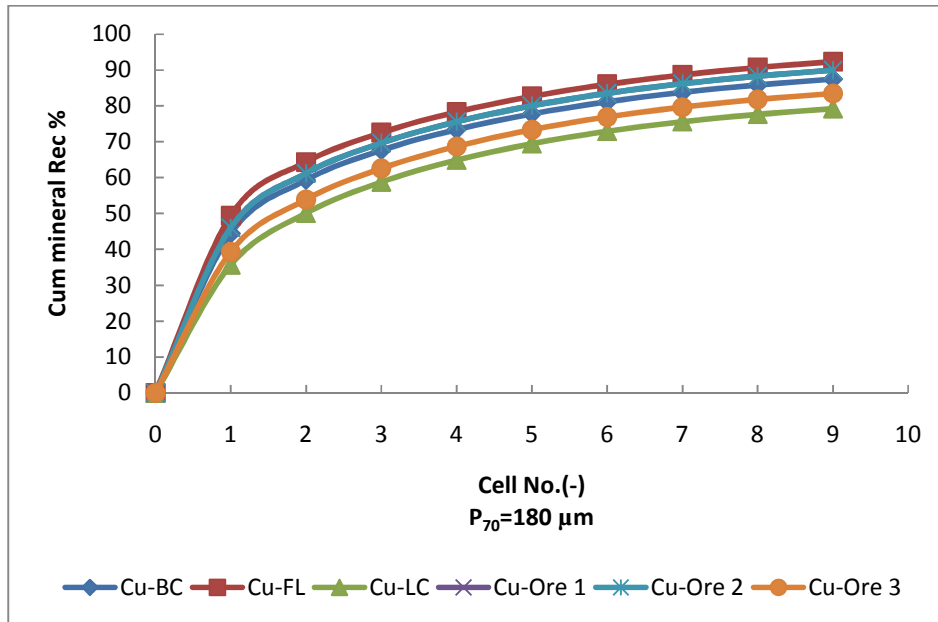


Figure 6-13: Comparison of Cu cumulative recovery per cell in a Rougher bank for different feed ore scenarios.

The cumulative recovery per unit cell values obtained for the base case and the extreme feed ore scenarios are shown in Figure 6-14. It can be seen that cumulative copper recovery of about 92.3% for FL ore ,87.5% for BC and 79.2% for LC feed ore after the ninth rougher cell were obtained. A 13.1 percentage point spread in Cu cumulative recovery after the ninth rougher cell was observed between Copper 2, LC and FL artificial feed ores, this spread in cumulative recovery is less than that which was obtained for Copper 1 LC and FL feeds. As the grind size becomes coarser, the spread in cumulative recovery becomes larger.

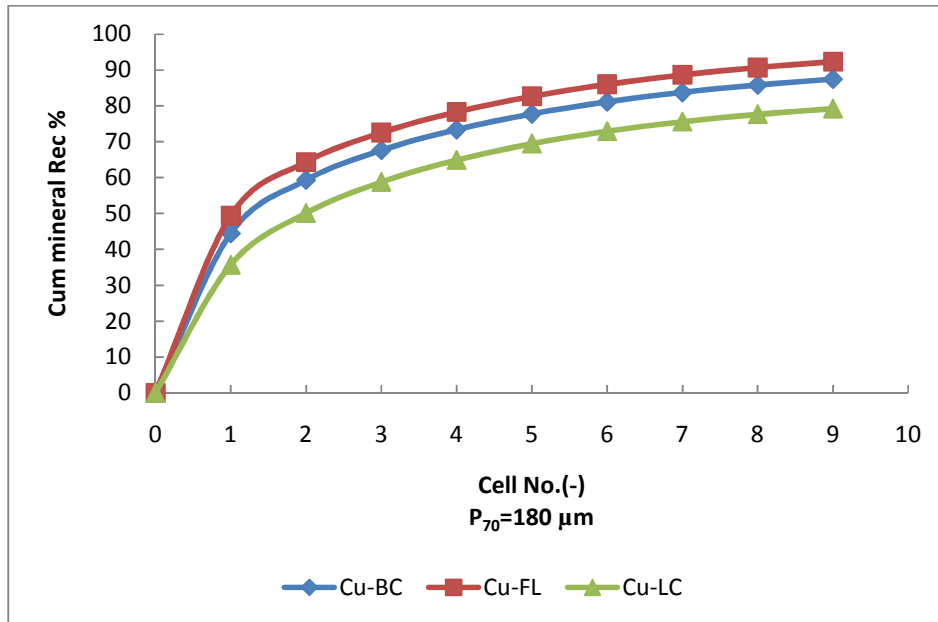


Figure 6-14: Comparison of Cu cumulative recovery per cell in a rougher bank for the base case and extreme feed ore scenarios

There was a noticeable improvement in final Cu cumulative value mineral recovery between the BC and FL ore of about 4.8 percentage points (see Figure 6-14). This improvement in Cu cumulative recovery was greater than the 2.5 percentage point improvement that was observed for a P_{70} grind size of $120\ \mu\text{m}$ (see Figure 6-7). As shown earlier in Chapter 5, section 5.4 there is a greater improvement in value mineral recovery at coarser sizes as feed ore liberation increases. Copper 2 artificial BC and FL feed ores at a P_{70} grind size of $180\ \mu\text{m}$ are coarser than Copper 1 artificial BC and FL feed ores. This explains the greater improvement in cumulative Cu recovery between the BC and FL Copper 2 feed ores compared to that between similar Copper 1 artificial feed ores.

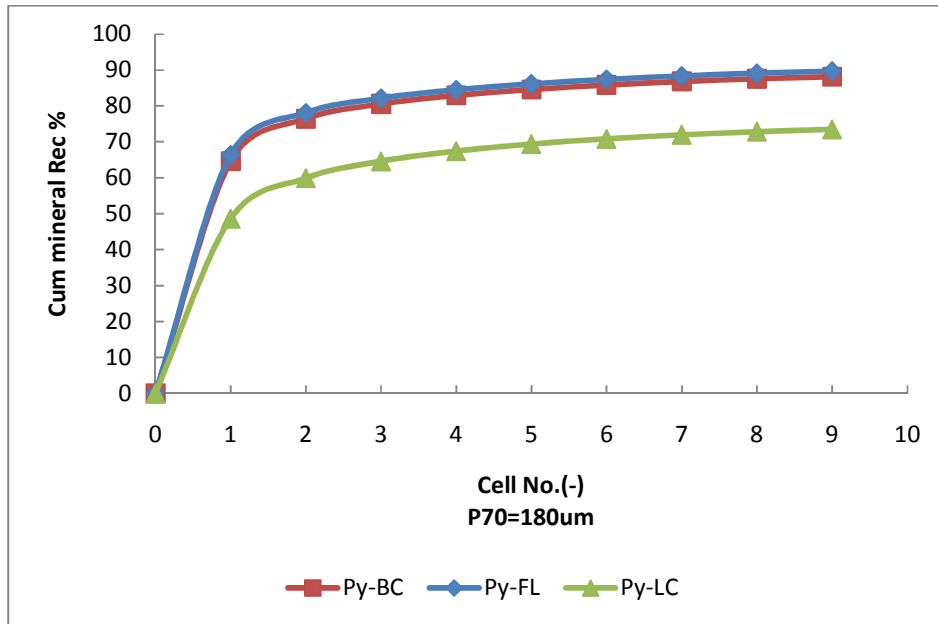


Figure 6-15: Comparison of Pyrite cumulative recovery per cell in a Rougher bank for the base case and extreme feed ore scenarios.

No significant difference in Pyrite cumulative recovery between the base case and the fully liberated case was observed, (see Figure 6-16). This might be due to the Pyrite mode of occurrence in the ore (see Figure 4-6, Chapter 4 Sections 4.2). Pyrite in the base case feed ore was observed to appear primarily as fully liberated particles or in association with Chalcopyrite. There was no room for improved liberation. Thus the cumulative recovery of BC and FL ores were similar.

The concentrate mass recovery obtained for LC feed ore with a P70 grind size of 180 μm was significantly less than that obtained at a P₇₀ grind size of 120 μm (see Figure 6-16 and Figure 6-9). At coarser feed ore grind sizes there is a particle size limit to flotation recovery. This is due to a decreasing stability and attachment efficiency at coarse sizes as was observed in Chapter 5 Section 5.2 (see

Figure 5-16 and Figure 5-18). Similar trends in concentrate mass recovery were observed for the other ores as seen at a P₇₀ grind size of 120 μm (see Figure 6-9).

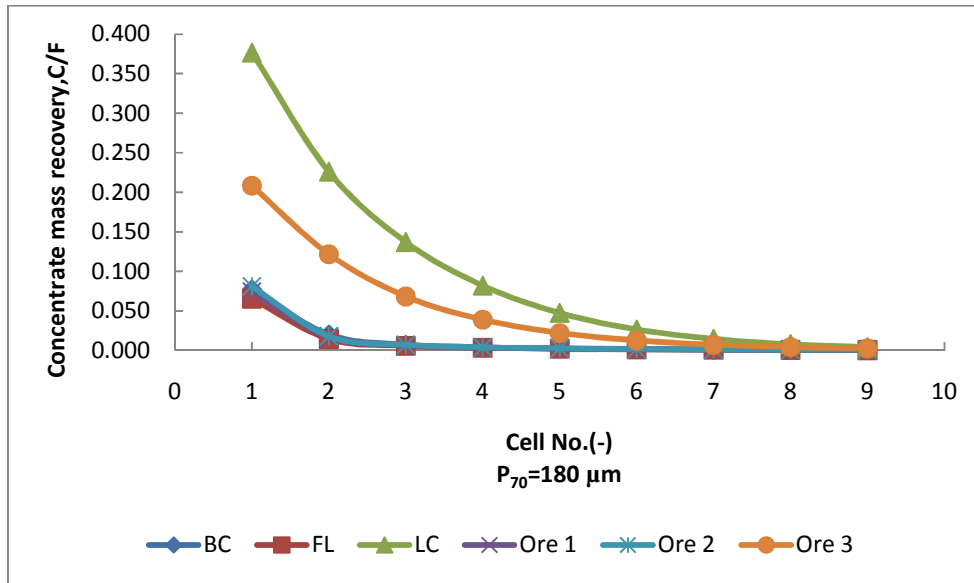


Figure 6-16: Comparison of concentrate mass recovery per unit cell in a Rougher bank for different feed ore scenarios

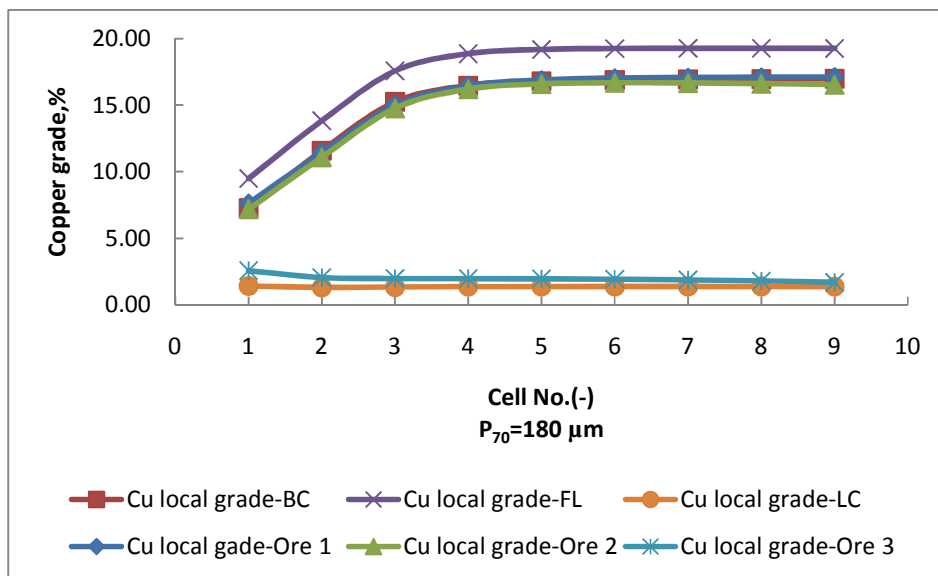


Figure 6-17: Comparison of Cu local grade per unit cell in a Rougher bank for different feed ore scenarios

Slightly higher local copper concentrate grades were observed for the FL, Ore 1, Ore 2 and BC feed ores at a P_{70} grind size of $180 \mu\text{m}$ compared with that observed at a P_{70} grind size of $120 \mu\text{m}$ (see Figure 6-11 and Figure 6-18).

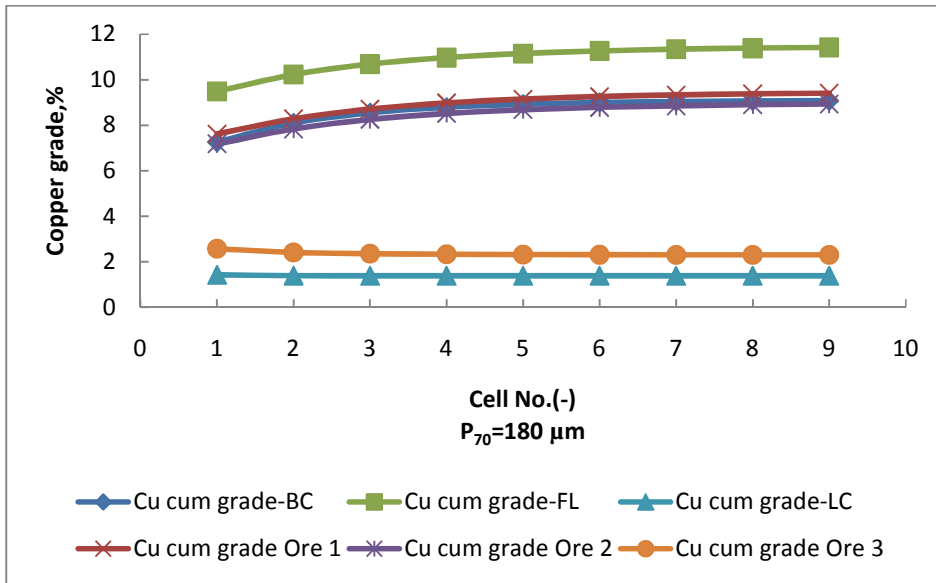


Figure 6-18 : Comparison of Cu Cumulative grade per unit cell in a Rougher bank for different feed ore scenarios (P₇₀ = 180 μm).

The trends in cumulative copper grade per unit cell were similar to those that were observed for feed ore at P₇₀ grind size of 120 μm (see Figure 6-19). An improvement in cumulative copper grade between the base case feed ore and the FL ore of about 2.35 percentage points was observed at a P₇₀ grind size of 180 μm.

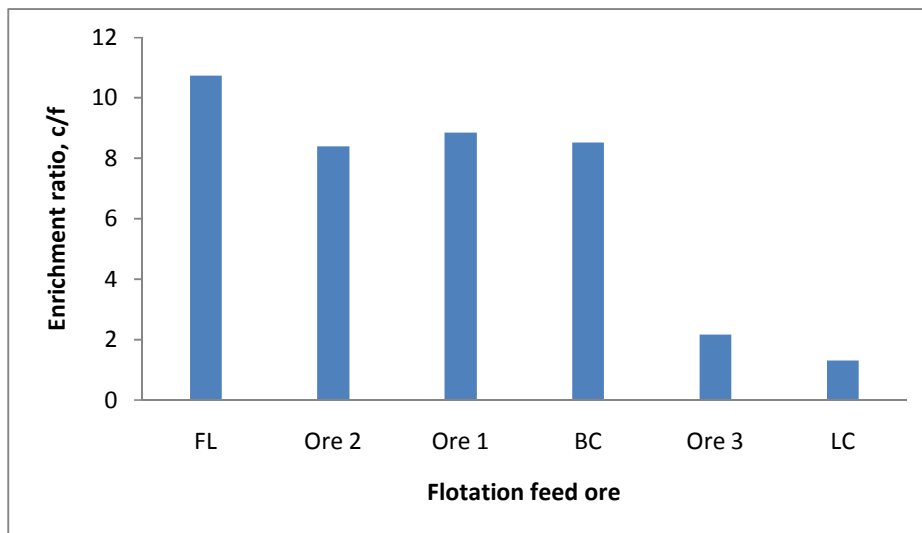


Figure 6-19: Comparison of overall rougher bank value mineral enrichment ratio for different feed ore scenarios.

The trends in overall enrichment ratio across the rougher bank flotation section for the various feed ores that were considered were similar to those observed for Copper 1 feed ore group at a P₇₀ grind size of 120 µm (see Figure 6-20).

6.3. Effect of Particle size distribution of the feed

Feed ore grind size sensitivity analysis was carried out in order to investigate further the effects of grind size of the feed on value mineral recovery for a typical operating plant rougher section. A brief outline of the methodology that was used will be described below followed by a presentation of the results and their discussion.

6.3.1. Methodology

The same feed ore grind sizes described earlier in Chapter 5, Table 5-9 were used in the investigations. For each grind size that was considered, three operating rougher concentrator section plant simulations were carried out, representing the three feed ore liberation scenarios that were considered to represent the base case and the two extreme liberation scenario cases. The LC and FL feeds represent the bounding cases. A base case scenario was included as a reference point representing the current flotation practice feed ore liberation scenario. The same flotation cell operating and hydrodynamic conditions as used in the previous simulations (see Table 5-1) were used in the investigations.

The overall rougher bank flotation section value mineral recovery, concentrate mass recovery and enrichment ratio values were analysed. This was followed by a cell by cell analysis of;

- I. Cumulative value mineral recovery per unit cell,
- II. Local copper grade in concentrate per unit cell,
- III. Concentrate mass recovery per unit cell,
- IV. Unit cell enrichment ratio per unit cell,
- V. Cumulative copper grade in concentrate per unit cell,

The results and their discussion are presented in the next section.

6.3.2. Operating plant Grind size sensitivity analysis results

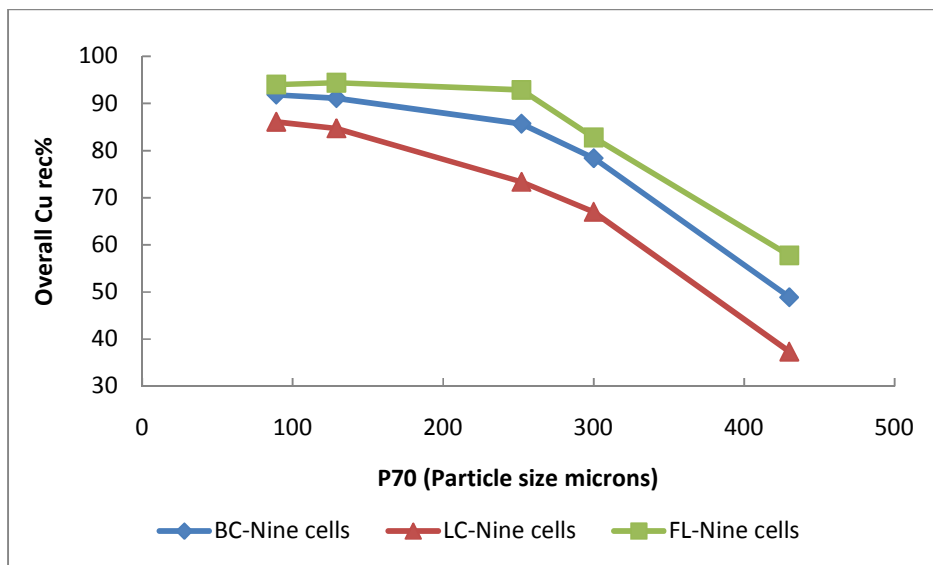


Figure 6-20: Overall a nine cell in series rougher bank recovery against particle size for feed ore grind size.

Figure 6-20 shows a decreasing trend in overall recovery for all feed ores with increasing P_{70} particle grind size. It is well known that flotation recovery decreases at very coarse sizes due to an increase in detachment forces (Gontijo et al., 2007). High contact angle values are required to float very coarse particles; fully liberated ore particles have high contact angle values hence their recovery is better than that of BC and LC feed ore. An increase in improvement in recovery between the base case and fully liberated ore feed was observed at P_{70} grind sizes greater than 250 μm .

Below a $P_{70}=120 \mu\text{m}$ grind size an improvement in overall recovery between the BC and FL liberated feed ore of around 3 percentage points is observed compared to an improvement in recovery of about 7 percentage points above the 250 μm grind size (see Figure 6-20). This shows that enhancement of feed ore value mineral liberation has more effect on value mineral recovery for coarser ground feeds.

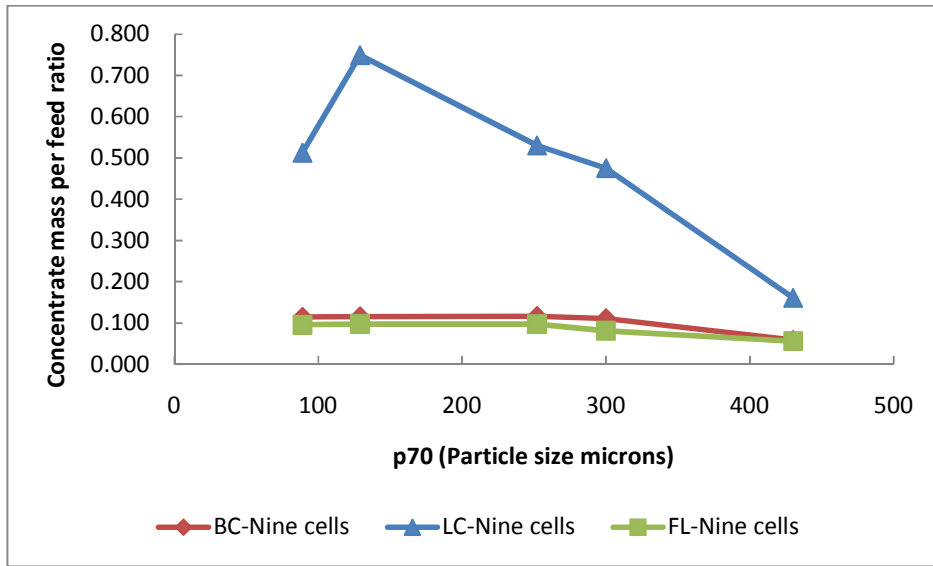


Figure 6-21: Concentrate mass recovery for a nine cell in series Rougher bank plotted against feed ore into the rougher section with varying feed grind size.

Analysis of concentrate mass recovery indicates a low concentrate mass recovery for fully liberated and base case feed ores (see Figure 6-21). The concentrate mass recovery for LC feed ore shows an increasing trend in the fine particle grind size range between 89 μm and 129 μm and decreases with particle size over a P_{70} grind size of 129 μm . Due to the composite nature of LC feed, a higher concentrate mass flow rate is observed at fine grind sizes which decrease with increasing grind size due to poor recovery of very coarse, locked particles.

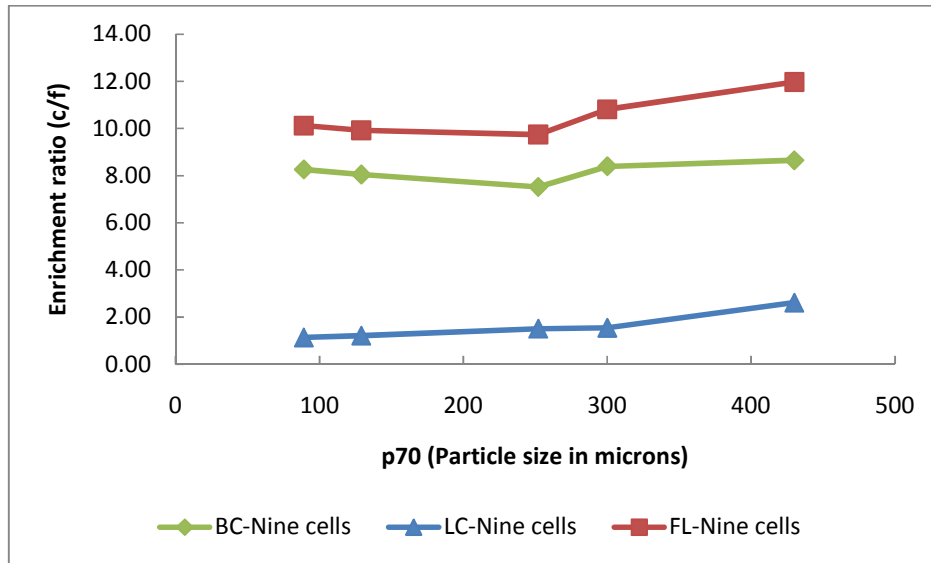


Figure 6-22: Enrichment ratio for a nine cell in series rougher bank plotted against feed ore into the rougher section with varying size distributions.

Figure 6-22 shows an increase in enrichment ratio above the 250 μm P_{70} grind sizes for all feeds. The increase is more pronounced for fully liberated ore. However, there are limits to coarse particle recovery at these coarse particle sizes especially where the particles are poorly liberated. This explains why the increase in BC and LC feed enrichment ratio is not as pronounced as that of FL feed above the 250 μm P_{70} grind sizes.

Analysis of cumulative copper value mineral recovery per unit cell for a feed ore grind size P_{70} of 89 μm showed a 2.1 percentage point improvement in cumulative copper recovery between the BC and fully liberated feed (see Figure 6-23). This improvement was observed after nine flotation cells. This supports the observation made earlier in Chapter 5 Section 5.4 that at fine grind sizes differences in value mineral liberation have no significant effect on value mineral particle flotation recovery (see Figure 5-20).

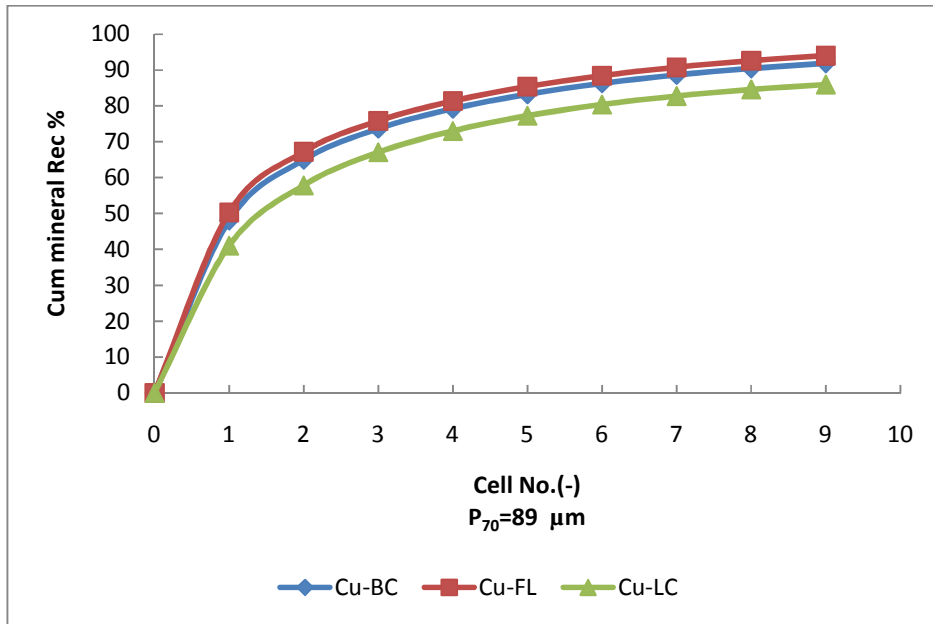


Figure 6-23: Cumulative Cu value mineral recovery as a function of cell number for a rougher bank processing BC, FL and LC feed ores.

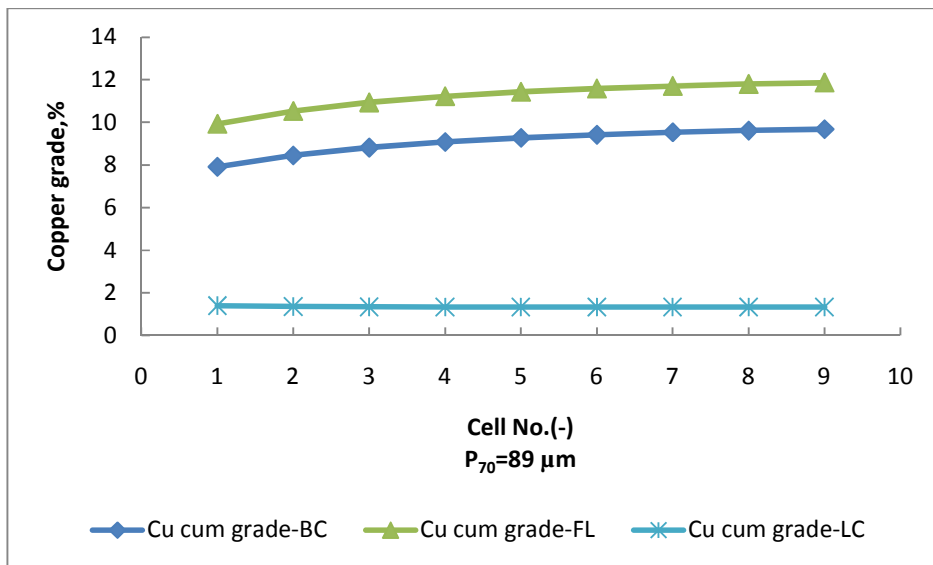


Figure 6-24: Cumulative copper grade profiles as a function of cell for a rougher bank processing BC, FL and LC feed ores.

A difference in cumulative copper grade between the base case and fully liberated ore was observed to be around 2 percentage points at grind size of $P_{70} = 89\mu\text{m}$ (see Figure 6-24).

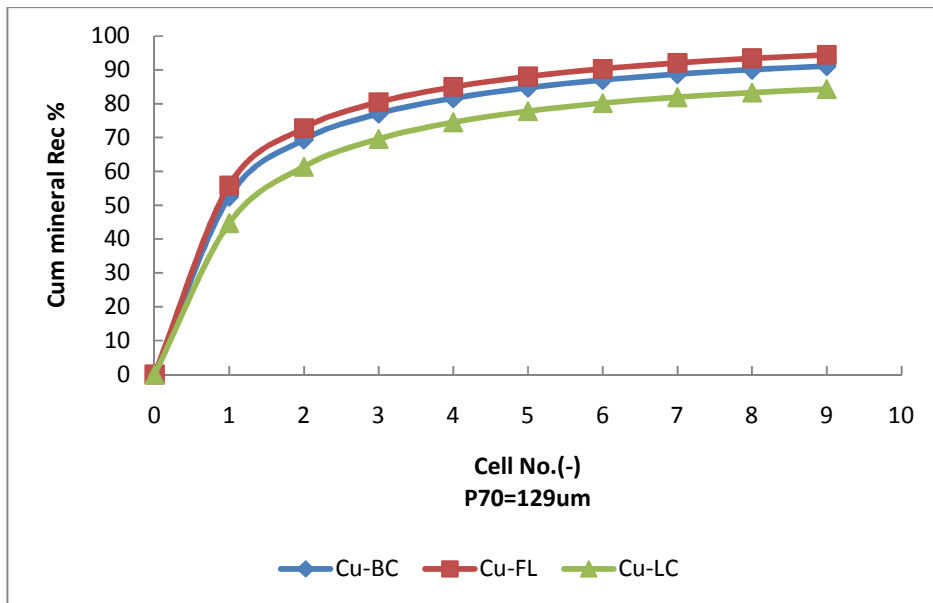


Figure 6-25: Cumulative Cu value mineral recovery as a function of cell number for a rougher bank processing BC, FL and LC feed ores.

Analysis of cumulative copper value mineral recovery per unit cell at a feed ore grind size of $P_{70}=129\mu\text{m}$ showed an improvement in cumulative copper recovery between the BC and fully liberated feed of 3.3 percentage points (see Figure 6-25).

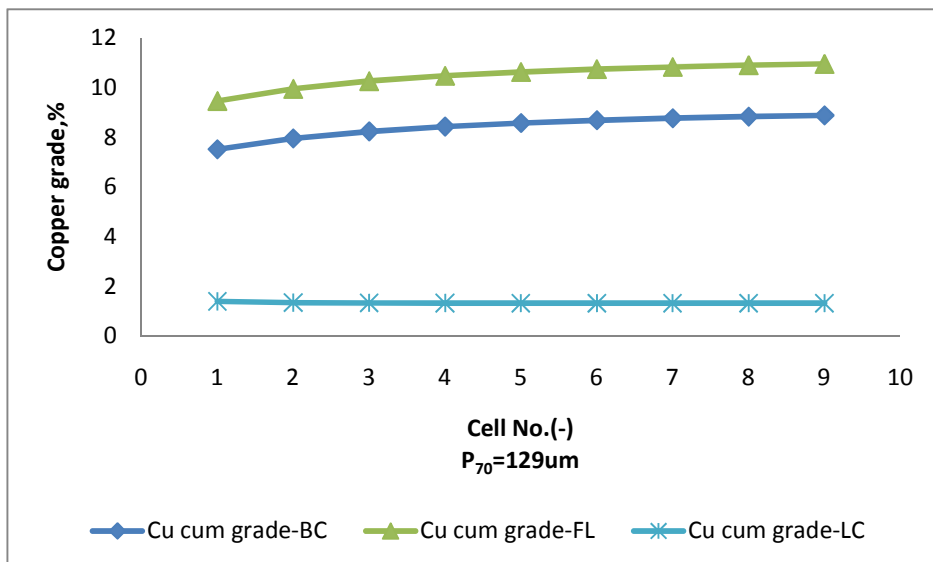


Figure 6-26: Cumulative copper grade profiles as a function of cell number for a rougher bank processing BC, FL and LC feed ores.

The difference in cumulative copper grade between the base case and fully liberated ore that was observed at a P₇₀ grind size of 89 µm was around 2 percentage points (see Figure 6-26). There was a progressive decrease in Copper grade as the particle grind size increased hence the final cumulative grade for FL ore at a P₇₀ grind size of 129 µm was lower than that at P₇₀ grind size of 89 µm.

The results indicate a high value mineral cumulative recovery at a P₇₀ grind sizes of 89 to 129 µm for the base case feed. However there are operational problems associated with fine grinding of flotation feeds such as slimes build up which would result in lower value mineral recoveries than those predicted from the simulation (Tabosa and Rubio, 2010). Grinding feed ore at P₇₀ grind sizes of 89 µm increases the probability of producing progeny feed particles with sizes below 10 µm. These ultra fine mineral particles are usually called slimes (Sondir et al., 2002). Slimes worsen the selectivity of collector reaction with the desired value mineral as the slime may coat the mineral surface (Sondir et al., 2002; Tabosa and Rubio, 2010). This in turn results in a decrease in the contact angle of the value mineral, thus reducing the value mineral recovery. The effect of slimes was not considered in this study. It is therefore possible that the recovery values predicted from the simulations could be lower in practice.

The cumulative copper value mineral recovery per unit cell obtained at a feed ore grind size P₇₀ of 252 µm showed a significant improvement in cumulative copper recovery between the BC and fully liberated ore (7.2 percentage points)(see Figure 6-27). This further supports the observation that at coarser particle sizes, a change in feed ore liberation has a significant effect on flotation recovery.

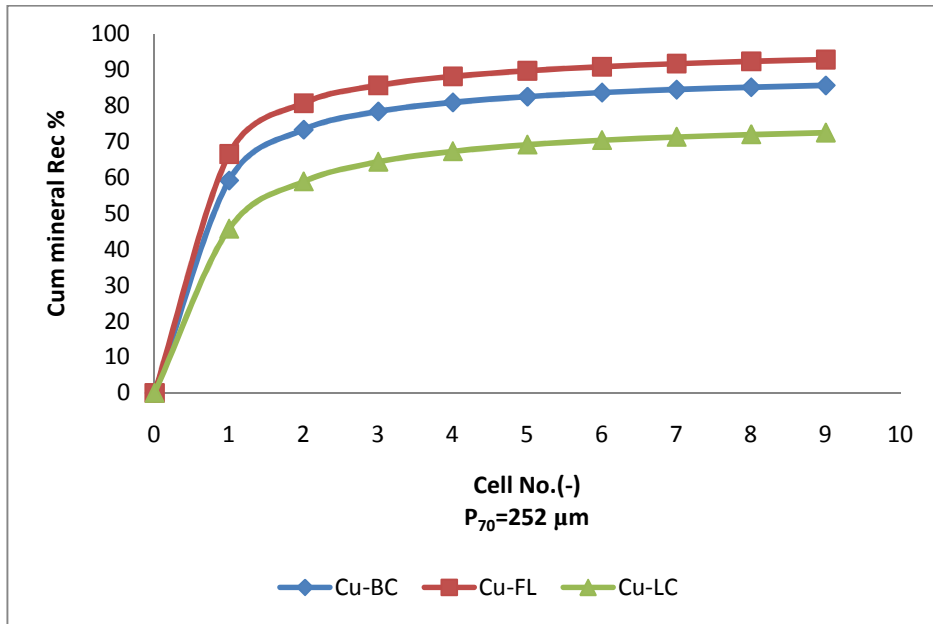


Figure 6-27: Cumulative Cu value mineral recovery as a function of cell number in the rougher section of a fictional simulated nine cell in series flotation plant processing BC, FL and LC feed ore with a P_{70} grind size of 252 μ m.

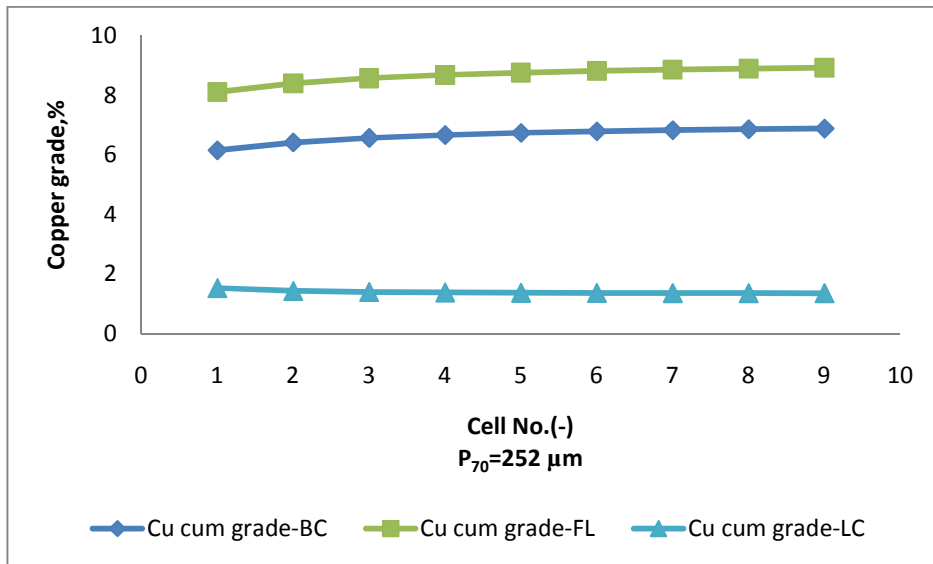


Figure 6-28: Cumulative copper grade profiles as a function of cell for a rougher bank processing BC, FL and LC feed ores.

Figure 6-28 shows a difference in cumulative copper grade of 2 percentage points between the base case and the fully liberated case at grind size of $P_{70} = 252 \mu$ m.

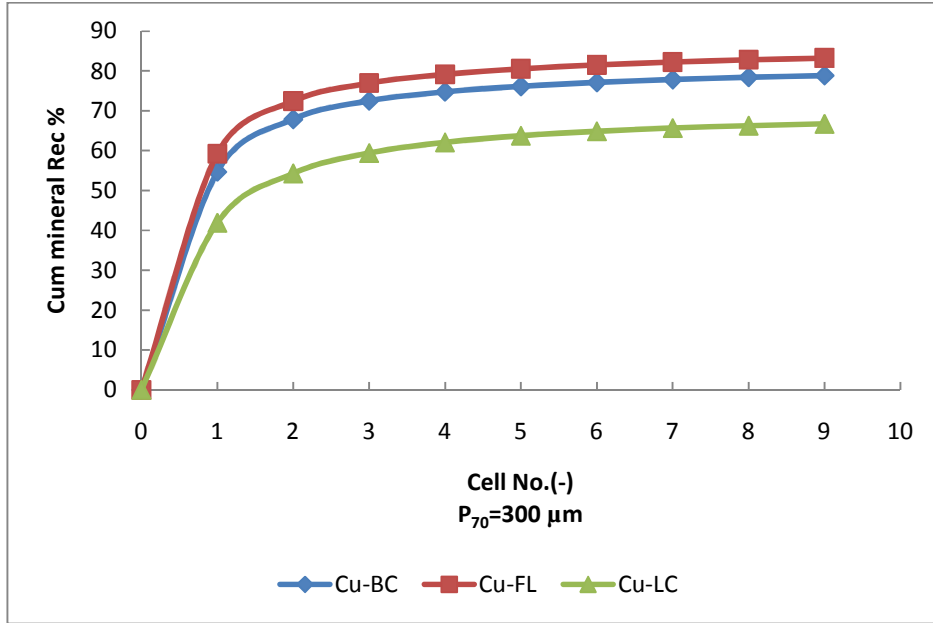


Figure 6-29: Cumulative Cu value mineral recovery as a function of cell number for a rougher bank processing BC, FL and LC feed ores.

At a feed ore grind size of $P_{70} = 300 \mu\text{m}$, the difference in value mineral recovery between the BC and fully liberated ore was less than that which was observed at a P_{70} grind size of $252 \mu\text{m}$ (see Figure 6-29). The difference was in the range of about 4.5 percentage points. A decrease in overall cumulative recovery is observed at this grind size compared with that at a P_{70} grind size of $252 \mu\text{m}$. As explained earlier overall cumulative recovery decreases with increasing particle sizes. A grind size of $252 \mu\text{m}$ is the optimum grind size where overall value mineral flotation recovery difference between the BC and FL feed is at its highest before it progressively decreases with increasing particle size.

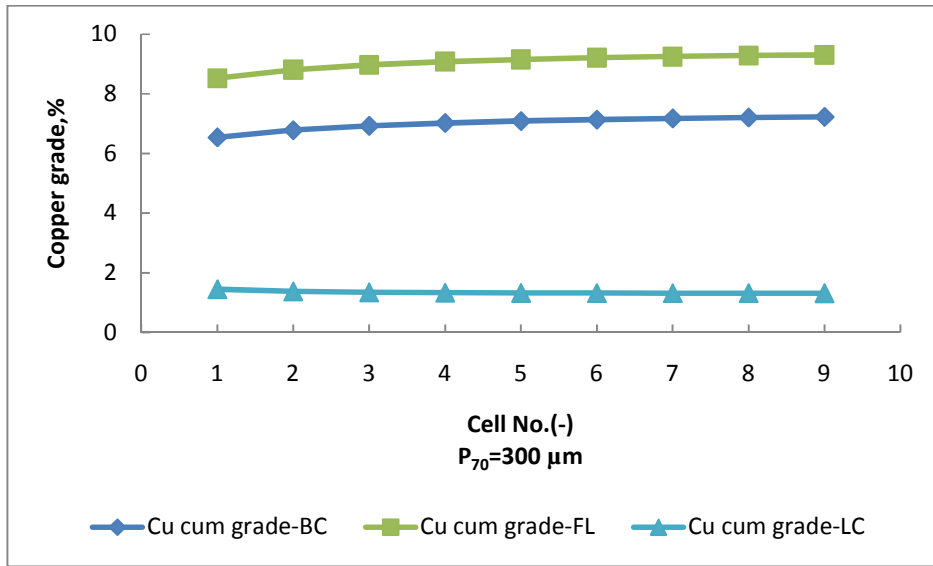


Figure 6-30: Cumulative copper grade profiles as a function of cell number for a rougher bank processing BC, FL and LC feed ore.

Figure 6-30 shows a difference in cumulative recovery of 2 percentage points for a feed ore grind size of P_{70} of 300 μm between the base case ore and fully liberated ore.

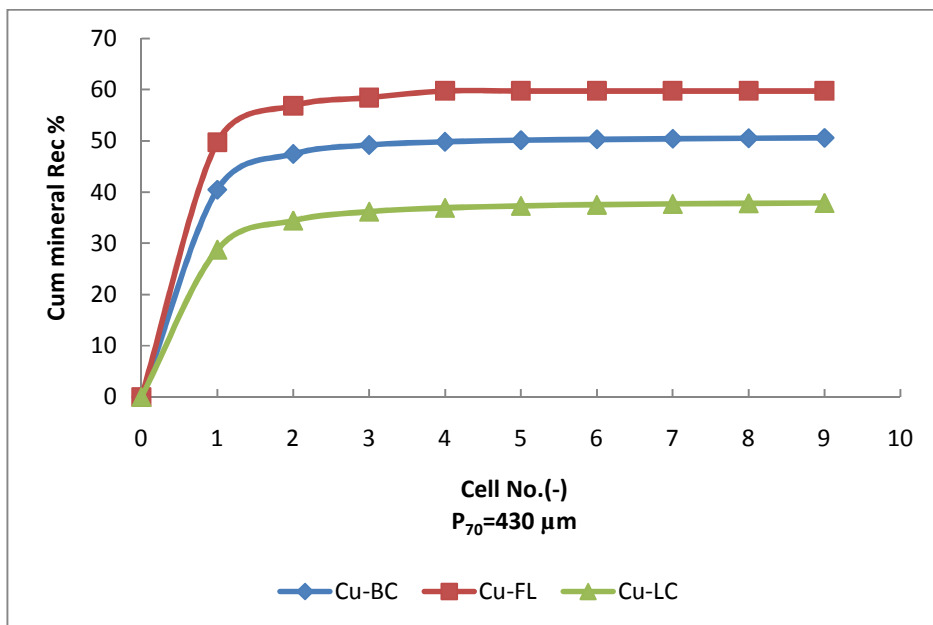


Figure 6-31: Cumulative Cu value mineral recovery as a function of cell number for a rougher bank processing BC, FL and LC feed ores.

At a coarser P_{70} grind size of $430\ \mu\text{m}$ an improvement in overall cumulative value mineral recovery of 9.4 percentage points between the BC and the fully liberated feed is observed (see Figure 6-31). Although the particle size effects of flotation recovery lowers the cumulative recovery of the all the feed ores, the high contact angle of the fully liberated ore allows for the coarse size particles to be recovered, hence a greater difference in overall cumulative recovery is observed at this grind size between the BC, FL and LC feed. Flotation circuits do not effectively recover very coarse particles (Mull and Sarich, 2002). The optimum particle size for flotation ranges between $38\ \mu\text{m}$ and $150\ \mu\text{m}$ (Sondir et al., 2002).

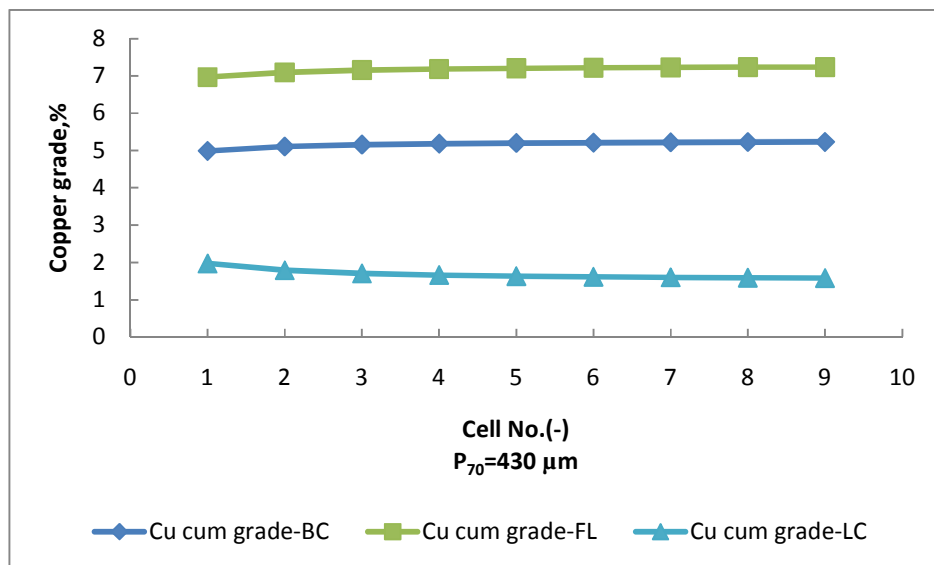


Figure 6-32: Local and cumulative copper grade profiles as a function of cell number for a rougher bank processing BC, FL and LC feed ores.

A cumulative grade difference of 2 percentage points at grind size of $P_{70} = 430\ \mu\text{m}$ was observed between the base case and fully liberated ores (see Figure 6-32). Analysis of the cumulative copper grade profile plots across the nine flotation cells for all feed grind sizes showed a 2 percentage point improvement in grade for all grind sizes. As explained earlier all the feed had similar liberation spectrum per size class, hence the same improvement in grade was observed between the BC and FL feed at different grind sizes.

6.4. Conclusion

A continuous plant rougher flotation flow sheet has been successfully developed that utilises the property based model for predicting flotation recovery. Results from applying the model in investigating the effects of feed ore liberation variation on flotation recovery indicate a greater variation in flotation recovery and final concentrate grade at coarse grind sizes of above 250 μm . The results presented in this Chapter have shown that a feed ore grind size of 252 μm gives the best value mineral recovery results for FL feed compared to the BC feed. At this grind size the overall difference in value mineral recovery between the BC and FL feed is at its highest before it progressively decreases with increasing particle size. This appears to be the best grind size result for exploiting improvements in flotation feed liberation due to microwave assisted comminution as there is a higher cumulative recovery difference between the BC and FL ore at this grind size.

CHAPTER SEVEN

7. CONCLUSIONS AND FUTURE WORK

Future commercialisation of microwave technology for mineral processing will depend on the determination and quantification of all the downstream processing benefits associated with the technology. Due to the limitations associated with such an exercise such as the costs of carrying out investigations on an operating plant, flow sheet modelling presents the best option for preliminary determination of the optimal value proposition for microwave assisted processing of ores.

In view of this, a modelling framework for investigating the downstream flotation processing effects of microwave treatment has been developed. The modelling framework is made up of a simulation flow sheet modelling tool in HSC Chemistry Software utilising MLA data and a fundamental property based flotation model that accounts for feed ore liberation in modelling flotation cell operation. The fundamental property model has been successfully integrated into the simulation software and can be used for true particle modelling based on the results from the continuous single flotation cell simulations (see Chapter 5).

A downstream flotation flow sheet simulation utilising the developed tool and MLA data from a previous study was then carried out in order to investigate the downstream processing effects of changes in feed ore liberation as expected from microwave treatment. Artificial feed with varying degrees of liberation were created and used to simulate the changes in feed ore liberation. From the single cell flotation results it has been found that below a certain size (120 μm) changes in feed ore liberation have no effect on value mineral recovery. Significant differences in value mineral recovery were only observed at sizes above 120 μm . From this result, it can be concluded that increasing recovery of value minerals due to improved liberation from applying microwave technology has size limits and is dependent on the feed ore grind size.

Feed ore grind size sensitivity analysis was then carried on the same single cell flow sheet utilising different ores with liberation properties and grind sizes. The results indicated that maximum benefits from the application of microwave technology would

best be obtained by utilising coarse grinding at sizes between $P_{70} = 200 \mu\text{m}$ and $P_{70} = 300 \mu\text{m}$ for the ores considered in this study. Coarse grinding appears to be the best way to exploit improved liberation in downstream processing of ores.

Investigations similar to those carried out on a single cell flotation flow sheet were then carried out on a continuous plant rougher flotation flow sheet. The results indicate no significant differences in final rougher bank overall cumulative recovery and grade at fine grind sizes for different flotation feeds. Feed ore grind size sensitivity analysis showed a greater difference in recovery at coarse grind sizes of above $P_{70} = 250 \mu\text{m}$ between the BC and FL feed. From the results it can be concluded that microwave technology application will offer greater benefits in downstream processing of coarse ground ores.

This study has produced a modelling framework for investigating the downstream processing effects of microwave treated flotation feed ore. Through the use of this modelling framework, it is now possible to investigate how differing degrees of mineral liberation, such as might be achieved through microwave treatment, affect the grade and recovery achieved in flotation. This is a significant contribution in the mineral processing field, particularly in the study of application of microwave assisted comminution. Most of the investigations that have been reported in literature on the study of the effects of downstream processing on microwave treated ore have been based on batch flotation results of microwave treated flotation feed. This study presents one of the few attempts at trying to determine the value proposition of microwave treated ore on an operating plant scale.

Using the development modelling framework and analysing the results from the simulations it has been shown in this study that mechanically agitated froth flotation cells can best exploit well-liberated material only if the material is coarser than a critical size. This important finding will direct investigations on how to best exploit the benefits of microwave induced grain boundary fracture towards the area of concentration of coarse flotation feeds. One possible suggestion would be to investigate the use of coarse grinding (as can be achieved in high pressure grinding rolls - HPGRs) following microwave treatment, followed by flash flotation of the coarsely liberated material.

The major limitations of such an investigation would be that no model exists in the open literature that allows prediction of liberation from coarse grinding in HPGRs. Further, no model exists in the open literature which allows fundamental modelling of particles behaviour in flash flotation. Future work should possibly look at the development of such types of models. Developing of these models and incorporating them into a flow sheet simulator such as the one used in this study will allow for a better assessment of the value proposition for microwave treatment.

The modelling framework developed in this study can be further improved on. Methods such as the creation of artificial flotation feeds and the fundamental models that have been used to describe the flotation process in this study can be developed further. It will also be essential to validate the flow sheet simulation results with experimental or plant data in the future, this will allow for a more accurate estimate of the potential benefits of microwave assisted processing of ores to be made. This study only focused on the downstream rougher bank flotation process, a study of a complete mineral processing flow sheet circuit that incorporates the comminution processes as well as the final cleaner stages will provide more information on the downstream processing benefits of microwave assisted processing of ores. Such a study would allow for the optimum grind size for microwave treated ore to be determined for a traditional processing flow sheet.

8. REFERENCES

- ABRAHAMSON, J. (1975) Collision rates of small particles in a vigorously turbulent fluid. *Chemical Engineering Science*, 30, 1371-1379.
- AKTAS, Z., CILLIERS, J. J. & BANFORD, A. W. (2008) Dynamic froth stability: Particle size, airflow rate and conditioning time effects. *International Journal of Mineral Processing*, 87, 65-71.
- ALBIJANIC, B., OZDEMIR, O., NGUYEN, A. V. & BRADSHAW, D. (2010) A review of induction and attachment times of wetting thin films between air bubbles and particles and its relevance in the separation of particles by flotation. *Advances in Colloid and Interface Science*, 159, 1-21.
- ALEXANDER, D. J., FRANZIDIS, J. P. & MANLAPIG, E. V. (2003) Froth recovery measurement in plant scale flotation cells. *Minerals Engineering*, 16, 1197-1203.
- ALEXANDER, D. J. & MORRISON, R. D. (1998) Rapid estimation of floatability components in industrial flotation plants. *Minerals Engineering*, 11, 133-143.
- ALI, A. Y. & BRADSHAW, S. M. (2009) Quantifying damage around grain boundaries in microwave treated ores. *Chemical Engineering and Processing: Process Intensification*, 48, 1566-1573.
- ALI, A. Y. & BRADSHAW, S. M. (2010) Bonded-particle modelling of microwave-induced damage in ore particles. *Minerals Engineering*, 23, 780-790.
- AMANKWAH, R. K., PICKLES, C. A. & YEN, W. T. (2005) Gold recovery by microwave augmented ashing of waste activated carbon. *Minerals Engineering*, 18, 517-526.
- AMIRA:P879A (2009) AMIRA P879A :PROGRESS REPORT.
- ATA, S., AHMED, N. & JAMESON, G. J. (2002) Collection of hydrophobic particles in the froth phase. *International Journal of Mineral Processing*, 64, 101-122.
- ATA, S., AHMED, N. & JAMESON, G. J. (2004) The effect of hydrophobicity on the drainage of gangue minerals in flotation froths. *Minerals Engineering*, 17, 897-901.
- ATA, S., PIGRAM, S. & JAMESON, G. J. (2006) Tracking of particles in the froth phase: An experimental technique. *Minerals Engineering*, 19, 824-830.
- BANFORD, A. W., AKTAS, Z. & WOODBURN, E. T. (1998) Interpretation of the effect of froth structure on the performance of froth flotation using image analysis. *Powder Technology*, 98, 61-73.
- BLOOM, F. & HEINDEL, T. J. (1997) Mathematical modelling of the flotation deinking process. *Mathematical and Computer Modelling*, 25, 13-58.
- BLOOM, F. & HEINDEL, T. J. (2002) On the structure of collision and detachment frequencies in flotation models. *Chemical Engineering Science*, 57, 2467-2473.
- BLOOM, F. & HEINDEL, T. J. (2003) Modeling flotation separation in a semi-batch process. *Chemical Engineering Science*, 58, 353-365.
- BORMASHENKO, E. (2008) Why does the Cassie-Baxter equation apply? *Colloids and Surfaces A: Physicochemical and Engineering Aspects*, 324, 47-50.
- BRADSHAW, D. J. & CONNOR, C. T. (1996) Measurement of the sub-process of bubble loadin in flotation. *Minerals Engineering*, 9, 443-448.

- BRADSHAW, D. J., OOSTENDORP, B. & HARRIS, P. J. (2005) Development of methodologies to improve the assessment of reagent behaviour in flotation with particular reference to collectors and depressants. *Minerals Engineering*, 18, 239-246.
- BRADY, M. R., TELIONIS, D. P., VLACHOS, P. P. & YOON, R.-H. (2006) Evaluation of multiphase flotation models in grid turbulence via Particle Image Velocimetry. *International Journal of Mineral Processing*, 80, 133-143.
- BULATOVIC, S. M. (2007) Summary of the Theoretical Aspects of Flotation. *Handbook of Flotation Reagents*. Amsterdam, Elsevier.
- CHAU, T. T. (2009) A review of techniques for measurement of contact angles and their applicability on mineral surfaces. *Minerals Engineering*, 22, 213-219.
- CHAU, T. T., BRUCKARD, W. J., KOH, P. T. L. & NGUYEN, A. V. (2009) A review of factors that affect contact angle and implications for flotation practice. *Advances in Colloid and Interface Science*, 150, 106-115.
- CHEBBI, R. (2003) Deformation of advancing gas-liquid interfaces in capillary tubes. *Journal of Colloid and Interface Science*, 265, 166-173.
- CHIBOWSKI, E. (2007) On some relations between advancing, receding and Young's contact angles. *Advances in Colloid and Interface Science*, 133, 51-59.
- CILEK, E. C. (2009) The effect of hydrodynamic conditions on true flotation and entrainment in flotation of a complex sulphide ore. *International Journal of Mineral Processing*, 90, 35-44.
- ÇILEK, E. C. & UMUCU, Y. (2001) A statistical model for gangue entrainment into froths in flotation of sulphide ores. *Minerals Engineering*, 14, 1055-1066.
- ÇILEK, E. C. & YILMAZER, B. Z. (2003) Effects of hydrodynamic parameters on entrainment and flotation performance. *Minerals Engineering*, 16, 745-756.
- CRAWFORD, R. & RALSTON, J. (1988) The influence of particle size and contact angle in mineral flotation. *International Journal of Mineral Processing*, 23, 1-24.
- CUTTING, G. W., BARBER, S. P. & NEWTON, S. (1986) Effects of froth structure and mobility on the performance and simulation of continuously operated flotation cells. *International Journal of Mineral Processing*, 16, 43-61.
- DAI, Z. (1998) PARTICLE-BUBBLE HETERO COAGULATION. *Ian Wark Research Institute Faculty of Health and Biomedical Science*. South Australia, University of South Australia.
- DAI, Z., DUKHIN, S., FORNASIERO, D. & RALSTON, J. (1998) The Inertial Hydrodynamic Interaction of Particles and Rising Bubbles with Mobile Surfaces. *Journal of Colloid and Interface Science*, 197, 275-292.
- DAI, Z., FORNASIERO, D. & RALSTON, J. (1999) Particle-Bubble Attachment in Mineral Flotation. *Journal of Colloid and Interface Science*, 217, 70-76.
- DAI, Z., FORNASIERO, D. & RALSTON, J. (2000) Particle-bubble collision models -- a review. *Advances in Colloid and Interface Science*, 85, 231-256.
- DOBBY, G. S. & FINCH, J. A. (1986) A model of particle sliding time for flotation size bubbles. *Journal of Colloid and Interface Science*, 109, 493-498.
- DOBBY, G. S. & FINCH, J. A. (1987) Particle size dependence in flotation derived from a fundamental model of the capture process. *International Journal of Mineral Processing*, 21, 241-260.

- DUAN, J.,FORNASIERO, D. & RALSTON, J. (2003) Calculation of the flotation rate constant of chalcopyrite particles in an ore. *International Journal of Mineral Processing*, 72, 227-237.
- FALUTSU, M. & DOBBY, G. S. (1992) Froth performance in commercial sized flotation columns. *Minerals Engineering*, 5, 1207-1223.
- FAN, M.,TAO, D.,HONAKER, R. & LUO, Z. (2010a) Nanobubble generation and its application in froth flotation (part I): nanobubble generation and its effects on properties of microbubble and millimeter scale bubble solutions. *Mining Science and Technology (China)*, 20, 1-19.
- FAN, M.,TAO, D.,HONAKER, R. & LUO, Z. (2010b) Nanobubble generation and its applications in froth flotation (part II): fundamental study and theoretical analysis. *Mining Science and Technology (China)*, 20, 159-177.
- FERREIRA, J. P. & LOVEDAY, B. K. (2000) An improved model for simulation of flotation circuits. *Minerals Engineering*, 13, 1441-1453.
- FETERIS, S. M.,FREW, J. A. & JOWETT, A. (1987) Modelling the effect of froth depth in flotation. *International Journal of Mineral Processing*, 20, 121-135.
- GEORGE, P.,NGUYEN, A. V. & JAMESON, G. J. (2004) Assessment of true flotation and entrainment in the flotation of submicron particles by fine bubbles. *Minerals Engineering*, 17, 847-853.
- GONTIJO, C.,FORNASIERO, D. & RALSTON, J. (2007) The limits of fine and coarse particle flotation. *The Canadian Journal of Chemical Engineering*, 85, 739-747.
- GORAIN, B. K.,HARRIS, M. C.,FRANZIDIS, J. P. & MANLAPIG, E. V. (1998) The effect of froth residence time on the kinetics of flotation. *Minerals Engineering*, 11, 627-638.
- GRANO, S. (2006) Effect of impeller rotational speed on the size dependent flotation rate of galena in full scale plant cells. *Minerals Engineering*, 19, 1307-1318.
- GRAU, R. A. & HEISKANEN, K. (2002) Visual technique for measuring bubble size in flotation machines. *Minerals Engineering*, 15, 507-513.
- GRAU, R. A. & HEISKANEN, K. (2003) Gas dispersion measurements in a flotation cell. *Minerals Engineering*, 16, 1081-1089.
- GROVES, L. (2007) Selective Heating of minerals and Ores using Microwave Energy. *School of Chemical and Environmental Engineering Nottingham, University of Nottingham*.
- GUPTA, A. & YAN, D. S. (2006) Flotation. *Mineral Processing Design and Operation*. Amsterdam, Elsevier Science.
- HAQUE, K. E. (1999) Microwave energy for mineral treatment processes--a brief review. *International Journal of Mineral Processing*, 57, 1-24.
- HERNANDEZ-AGUILAR, J. R.,COLEMAN, R. G.,GOMEZ, C. O. & FINCH, J. A. (2004) A comparison between capillary and imaging techniques for sizing bubbles in flotation systems. *Minerals Engineering*, 17, 53-61.
- HEWITT, D.,FORNASIERO, D. & RALSTON, J. (1994) Bubble particle attachment efficiency. *Minerals Engineering*, 7, 657-665.
- HONAKER, R. Q. & OZSEVER, A. V. (2003) Evaluation of the selective detachment process in flotation froth. *Minerals Engineering*, 16, 975-982.
- HONAKER, R. Q.,OZSEVER, A. V. & PAREKH, B. K. (2006) Selective detachment process in column flotation froth. *Minerals Engineering*, 19, 687-695.

- IRELAND, P., CUNNINGHAM, R. & JAMESON, G. J. (2007) The behaviour of wash water injected into a froth. *International Journal of Mineral Processing*, 84, 99-107.
- IRELAND, P. M. & JAMESON, G. J. (2007) Liquid transport in a multi-layer froth. *Journal of Colloid and Interface Science*, 314, 207-213.
- IVESON, S. M., HOLT, S. & BIGGS, S. (2004) Advancing contact angle of iron ores as a function of their hematite and goethite content: implications for pelletising and sintering. *International Journal of Mineral Processing*, 74, 281-287.
- IWAMATSU, M. (2006) The validity of Cassie's law: A simple exercise using a simplified model. *Journal of Colloid and Interface Science*, 294, 176-181.
- JONES, D. A., KINGMAN, S. W., WHITTLES, D. N. & LOWNDES, I. S. (2005) Understanding microwave assisted breakage. *Minerals Engineering*, 18, 659-669.
- KELLER, A. A., BROJE, V. & SETTY, K. (2007) Effect of advancing velocity and fluid viscosity on the dynamic contact angle of petroleum hydrocarbons. *Journal of Petroleum Science and Engineering*, 58, 201-206.
- KING, R. P. (1993) Comminution and liberation of minerals. *Minerals Engineering*, 7, 129-140.
- KINGMAN, S. (2006) Recent development in microwave processing of minerals. *International Materials Reviews*, 51, 1-12.
- KINGMAN, S., BRADSHAW, S., ROWSON, N. A., JACKSON, K., CUMBANE, A. & GREENWOOD, R. (2004a) Development of microwave assisted comminution. *International Journal of Mineral Processing*, 74, 71-83.
- KINGMAN, S., VORSTER, W. & ROWSON, N. A. (2000a) 'The effect of microwave radiation on the processing of Palabora copper ore'. *J. S. Afr. Inst. Min. Metall.*, 197-204.
- KINGMAN, S. W., JACKSON, K., BRADSHAW, S. M., ROWSON, N. A. & GREENWOOD, R. (2004b) An investigation into the influence of microwave treatment on mineral ore comminution. *Powder Technology*, 146, 176-184.
- KINGMAN, S. W., JACKSON, K., CUMBANE, A., BRADSHAW, S. M., ROWSON, N. A. & GREENWOOD, R. (2004c) Recent developments in microwave-assisted comminution. *International Journal of Mineral Processing*, 74, 71-83.
- KINGMAN, S. W. & ROWSON, N. A. (1998) Microwave treatment of minerals-a review. *Minerals Engineering*, 11, 1081-1087.
- KINGMAN, S. W., VORSTER, W. & ROWSON, N. A. (2000b) The influence of mineralogy on microwave assisted grinding. *Minerals Engineering*, 13, 313-327.
- KIRJAVAINEN, V. M. (1996) Review and analysis of factors controlling the mechanical flotation of gangue minerals. *International Journal of Mineral Processing*, 46, 21-34.
- KOBUSHESHE, J. (2010) Microwave enhanced processing of ores. *Department of Chemical and Environmental Engineering*. Nottingham, University of Nottingham.
- KOH, P. T. L. & SCHWARZ, M. P. (2006) CFD modelling of bubble-particle attachments in flotation cells. *Minerals Engineering*, 19, 619-626.
- KOH, P. T. L. & SCHWARZ, M. P. (2008) Modelling attachment rates of multi-sized bubbles with particles in a flotation cell. *Minerals Engineering*, 21, 989-993.

- LAM, C. N. C., KO, R. H. Y., YU, L. M. Y., NG, A., LI, D., HAIR, M. L. & NEUMANN, A. W. (2001) Dynamic Cycling Contact Angle Measurements: Study of Advancing and Receding Contact Angles. *Journal of Colloid and Interface Science*, 243, 208-218.
- LAM, C. N. C., WU, R., LI, D., HAIR, M. L. & NEUMANN, A. W. (2002) Study of the advancing and receding contact angles: liquid sorption as a cause of contact angle hysteresis. *Advances in Colloid and Interface Science*, 96, 169-191.
- LEIVA, J., VINNETT, L., CONTRERAS, F. & YIANATOS, J. (2010) Estimation of the actual bubble surface area flux in flotation. *Minerals Engineering*, In Press, Corrected Proof.
- LIU, T. Y. & SCHWARZ, M. P. (2009a) CFD-based modelling of bubble-particle collision efficiency with mobile bubble surface in a turbulent environment. *International Journal of Mineral Processing*, 90, 45-55.
- LIU, T. Y. & SCHWARZ, M. P. (2009b) CFD-based multiscale modelling of bubble-particle collision efficiency in a turbulent flotation cell. *Chemical Engineering Science*, 64, 5287-5301.
- LUTTRELL, G. H. & YOON, R. H. (1992) A hydrodynamic model for bubble--particle attachment. *Journal of Colloid and Interface Science*, 154, 129-137.
- MAO, L. & YOON, R.-H. (1997) Predicting flotation rates using a rate equation derived from first principles. *International Journal of Mineral Processing*, 51, 171-181.
- MASSINAEI, M., KOLAHDOOZAN, M., NOAPARAST, M., OLIAZADEH, M., YIANATOS, J., SHAMSADINI, R. & YARAHMADI, M. (2009a) Froth zone characterization of an industrial flotation column in rougher circuit. *Minerals Engineering*, 22, 272-278.
- MASSINAEI, M., KOLAHDOOZAN, M., NOAPARAST, M., OLIAZADEH, M., YIANATOS, J., SHAMSADINI, R. & YARAHMADI, M. (2009b) Hydrodynamic and kinetic characterization of industrial columns in rougher circuit. *Minerals Engineering*, 22, 357-365.
- MATHE, Z. T., HARRIS, M. C., O'CONNOR, C. T. & FRANZIDIS, J. P. (1998) Review of froth modelling in steady state flotation systems. *Minerals Engineering*, 11, 397-421.
- MELOY, J. R., NEETHLING, S. J. & CILLIERS, J. J. (2007) Modelling the axial dispersion of particles in froths. *International Journal of Mineral Processing*, 84, 185-191.
- MENDEZ, D. A., GÁLVEZ, E. D. & CISTERNAS, L. A. (2009) State of the art in the conceptual design of flotation circuits. *International Journal of Mineral Processing*, 90, 1-15.
- MIETTINEN, T., RALSTON, J. & FORNASIERO, D. (2009) The limits of fine particle flotation. *Minerals Engineering*, 23, 420-437.
- MOYS, M. H. (1978) A study of a plug-flow model for flotation froth behaviour. *International Journal of Mineral Processing*, 5, 21-38.
- MOYS, M. H. (1984) Residence time distributions and mass transport in the froth phase of the flotation process. *International Journal of Mineral Processing*, 13, 117-142.
- MOYS, M. H., YIANATOS, J. & LARENAS, J. (2009) Measurement of particle loading on bubbles in the flotation process. *Minerals Engineering*, 23, 131-136.

- MULL, T. & SARICH, S. (2002) Development of a mineral processing flowsheet- Case History, Batu Hijou. *Mineral processing plant design practice and control proceedings*, 12, 2211-2237.
- NAPIER-MUNN, T. (2005) Preface to 7th Edition. *Wills' Mineral Processing Technology (Seventh Edition)*. Oxford, Butterworth-Heinemann.
- NEETHLING, S. J. (2008) Simple approximations for estimating froth recovery. *International Journal of Mineral Processing*, 89, 44-52.
- NEETHLING, S. J. & CILLIERS, J. J. (2003) Modelling flotation froths. *International Journal of Mineral Processing*, 72, 267-287.
- NEETHLING, S. J. & CILLIERS, J. J. (2009) The entrainment factor in froth flotation: Model for particle size and other operating parameter effects. *International Journal of Mineral Processing*, 93, 141-148.
- NEETHLING, S. J., CILLIERS, J. J. & WOODBURN, E. T. (2000) Prediction of the water distribution in a flowing foam. *Chemical Engineering Science*, 55, 4021-4028.
- NEETHLING, S. J., LEE, H. T. & CILLIERS, J. J. (2003) Simple relationships for predicting the recovery of liquid from flowing foams and froths. *Minerals Engineering*, 16, 1123-1130.
- NEWELL, R. & GRANO, S. (2006) Hydrodynamics and scale up in Rushton turbine flotation cells: Part 2. Flotation scale-up for laboratory and pilot cells. *International Journal of Mineral Processing*, 81, 65-78.
- NEWELL, R. & GRANO, S. (2007) Hydrodynamics and scale up in Rushton turbine flotation cells: Part 1 -- Cell hydrodynamics. *International Journal of Mineral Processing*, 81, 224-236.
- NGUYEN-VAN, A. & KMET, S. (1994) Probability of collision between particles and bubbles in flotation: the theoretical inertialess model involving a swarm of bubbles in pulp phase. *International Journal of Mineral Processing*, 40, 155-169.
- NGUYEN, A. V., RALSTON, J. & SCHULZE, H. J. (1998) On modelling of bubble-particle attachment probability in flotation. *International Journal of Mineral Processing*, 53, 225-249.
- NGUYEN, A. V., SCHULZE, H. J. & RALSTON, J. (1997a) Elementary steps in particle-bubble attachment. *International Journal of Mineral Processing*, 51, 183-195.
- NGUYEN, A. V., SCHULZE, H. J., STECHEMESSER, H. & ZOBEL, G. (1997b) Contact time during impact of a spherical particle against a plane gas-liquid interface: theory. *International Journal of Mineral Processing*, 50, 97-111.
- NGUYEN, C. M., NGUYEN, A. V. & MILLER, J. D. (2006) Computational validation of the Generalized Sutherland Equation for bubble-particle encounter efficiency in flotation. *International Journal of Mineral Processing*, 81, 141-148.
- NGUYEN, P. T. & NGUYEN, A. V. (2009) Validation of the generalised Sutherland equation for bubble-particle encounter efficiency in flotation: Effect of particle density. *Minerals Engineering*, 22, 176-181.
- NGUYEN VAN, A. & KMET, S. (1992) Collision efficiency for fine mineral particles with single bubble in a countercurrent flow regime. *International Journal of Mineral Processing*, 35, 205-223.

- NIEMI, A. J. (1995) Role of kinetics in modelling and control of flotation plants. *Powder Technology*, 82, 69-77.
- PHAN, C. M., NGUYEN, A. V., MILLER, J. D., EVANS, G. M. & JAMESON, G. J. (2003) Investigations of bubble-particle interactions. *International Journal of Mineral Processing*, 72, 239-254.
- POLAT, M. & CHANDER, S. (2000) First-order flotation kinetics models and methods for estimation of the true distribution of flotation rate constants. *International Journal of Mineral Processing*, 58, 145-166.
- PRESTIDGE, C. A. & RALSTON, J. (1996) Contact angle studies of particulate sulphide minerals. *Minerals Engineering*, 9, 85-102.
- PYKE, B., FORNASIERO, D. & RALSTON, J. (2003) Bubble particle heterocoagulation under turbulent conditions. *Journal of Colloid and Interface Science*, 265, 141-151.
- RALSTON, J. & DUKHIN, S. S. (1999) The interaction between particles and bubbles. *Colloids and Surfaces A: Physicochemical and Engineering Aspects*, 151, 3-14.
- RALSTON, J., FORNASIERO, D., GRANO, S., DUAN, J. & AKROYD, T. (2007) Reducing uncertainty in mineral flotation--flotation rate constant prediction for particles in an operating plant ore. *International Journal of Mineral Processing*, 84, 89-98.
- RALSTON, J., FORNASIERO, D. & HAYES, R. (1999) Bubble-particle attachment and detachment in flotation. *International Journal of Mineral Processing*, 56, 133-164.
- RALSTON, J. & IAN, D. W. (2000) FLOTATION | Bubble-Particle Capture. *Encyclopedia of Separation Science*. Oxford, Academic Press.
- RODRÍGUEZ-VALVERDE, M. A. (2008) Mechanical derivation of the Wenzel and Cassie equations using a statistical interpretation of drop dispensation. *Journal of Colloid and Interface Science*, 327, 477-479.
- ROINE, A. (2010) *HSC Chemistry 7.0*, Outotec Research Oy.
- ROSS, V. E. (1991a) The behaviour of particles in flotation froths. *Minerals Engineering*, 4, 959-974.
- ROSS, V. E. (1991b) An investigation of sub-processes in equilibrium froths (I): the mechanisms of detachment and drainage. *International Journal of Mineral Processing*, 31, 37-50.
- SAM, A., GOMEZ, C. O. & FINCH, J. A. (1996) Axial velocity profiles of single bubbles in water/frother solutions. *International Journal of Mineral Processing*, 47, 177-196.
- SARROT, V., GUIRAUD, P. & LEGENDRE, D. (2005) Determination of the collision frequency between bubbles and particles in flotation. *Chemical Engineering Science*, 60, 6107-6117.
- SAVASSI, O. N. (2005) A compartment model for the mass transfer inside a conventional flotation cell. *International Journal of Mineral Processing*, 77, 65-79.
- SAVASSI, O. N., ALEXANDER, D. J., FRANZIDIS, J. P. & MANLAPIG, E. V. (1998) An empirical model for entrainment in industrial flotation plants. *Minerals Engineering*, 11, 243-256.

- SCHUBERT, H. (1999) On the turbulence-controlled microprocesses in flotation machines. *International Journal of Mineral Processing*, 56, 257-276.
- SCHUBERT, H. (2008) On the optimization of hydrodynamics in fine particle flotation. *Minerals Engineering*, 21, 930-936.
- SCHUBERT, H. & BISCHOFBERGER, C. (1998) On the microprocesses air dispersion and particle-bubble attachment in flotation machines as well as consequences for the scale-up of macroprocesses. *International Journal of Mineral Processing*, 52, 245-259.
- SCHULZE, H. J. (1977) New theoretical and experimental investigations on stability of bubble/particle aggregates in flotation: A theory on the upper particle size of floatability. *International Journal of Mineral Processing*, 4, 241-259.
- SCHULZE, H. J. (1992) Probability of particle attachment on gas bubbles by sliding. *Advances in Colloid and Interface Science*, 40, 283-305.
- SCHULZE, H. J., RADOEV, B., GEIDEL, T., STECHEMESSER, H. & TÖPFER, E. (1989a) Investigations of the collision process between particles and gas bubbles in flotation -- A theoretical analysis. *International Journal of Mineral Processing*, 27, 263-278.
- SCHULZE, H. J., WAHL, B. & GOTTSCHALK, G. (1989b) Determination of adhesive strength of particles within the liquid/gas interface in flotation by means of a centrifuge method. *Journal of Colloid and Interface Science*, 128, 57-65.
- SCHWARZ, S. & ALEXANDER, D. (2006) Gas dispersion measurements in industrial flotation cells. *Minerals Engineering*, 19, 554-560.
- SCHWARZ, S. & GRANO, S. (2005) Effect of particle hydrophobicity on particle and water transport across a flotation froth. *Colloids and Surfaces A: Physicochemical and Engineering Aspects*, 256, 157-164.
- SCOTT, G., BRADSHAW, S. M. & EKSTEEN, J. J. (2008) The effect of microwave pretreatment on the liberation of a copper carbonatite ore after milling. *International Journal of Mineral Processing*, 85, 121-128.
- SEAMAN, D. R., FRANZIDIS, J. P. & MANLAPIG, E. V. (2004) Bubble load measurement in the pulp zone of industrial flotation machines--a new device for determining the froth recovery of attached particles. *International Journal of Mineral Processing*, 74, 1-13.
- SEAMAN, D. R., MANLAPIG, E. V. & FRANZIDIS, J. P. (2006) Selective transport of attached particles across the pulp-froth interface. *Minerals Engineering*, 19, 841-851.
- SHAHBAZI, B., REZAI, B. & JAVAD KOLEINI, S. M. (2009) The effect of hydrodynamic parameters on probability of bubble-particle collision and attachment. *Minerals Engineering*, 22, 57-63.
- SHAHBAZI, B., REZAI, B. & JAVAD KOLEINI, S. M. (2010) Bubble-particle collision and attachment probability on fine particles flotation. *Chemical Engineering and Processing: Process Intensification*, In Press, Corrected Proof.
- SHERRELL, I. (2004) Development of a Flotation Rate Equation from First Principles under Turbulent Flow Conditions. *Mining and Minerals Engineering Department*. Blacksburg, Virginia, Virginia Polytechnic Institute and State University.
- SONDIR, I., PRAVDIC, V. & BOSKOVIC, R. (2002) Electrokinetics of clay mineral surfaces. *Encyclopedia of surface and colloid science*, 2, 1887-2241.

- STEVENSON, P. (2007) Comments on "An evaluation of different models of water recovery in flotation" by X. Zheng, J.P. Franzidis and N.W. Johnson. *Minerals Engineering*, 20, 207-209.
- STEVENSON, P.,ATA, S. & EVANS, G. M. (2007) Convective-dispersive gangue transport in flotation froth. *Chemical Engineering Science*, 62, 5736-5744.
- SUAZO, C. J.,KRACHT, W. & ALRUIZ, O. M. (2009) Geometallurgical modelling of the Collahuasi flotation circuit. *Minerals Engineering*, 23, 137-142.
- SUBRAHMANYAM, T. V. & FORSSBERG, E. (1988) Froth stability, particle entrainment and drainage in flotation -- A review. *International Journal of Mineral Processing*, 23, 33-53.
- TABOSA, E. & RUBIO, J. (2010) Flotation of copper sulphides assisted by high intensity conditioning (HIC) and concentrate recirculation. *Minerals Engineering*, 23, 1198-1206.
- TROMANS, D. (2008) Mineral comminution: Energy efficiency considerations. *Minerals Engineering*, 21, 613-620.
- TSATOUHAS, G.,GRANO, S. R. & VERA, M. (2006) Case studies on the performance and characterisation of the froth phase in industrial flotation circuits. *Minerals Engineering*, 19, 774-783.
- URIBE, S. A.,VÁZQUEZ, V. D.,PÉREZ, G. R. & NAVA, A. F. (1999) A statistical model for the concentrate water in flotation columns. *Minerals Engineering*, 12, 937-948.
- VAN DEVENTER, J. S. J.,FENG, D. & BURGER, A. J. (2001) The use of bubble loads to interpret transport phenomena at the pulp-froth interface in a flotation column. *Chemical Engineering Science*, 56, 6313-6319.
- VAN DEVENTER, J. S. J.,FENG, D. & BURGER, A. J. (2004a) Transport phenomena at the pulp-froth interface in a flotation column: I. Recovery profiles. *International Journal of Mineral Processing*, 74, 201-215.
- VAN DEVENTER, J. S. J.,FENG, D. & BURGER, A. J. (2004b) Transport phenomena at the pulp-froth interface in a flotation column: II. Detachment. *International Journal of Mineral Processing*, 74, 217-231.
- VERA, M. A.,FRANZIDIS, J. P. & MANLAPIG, E. V. (1999a) The JKMRC high bubble surface area flux flotation cell. *Minerals Engineering*, 12, 477-484.
- VERA, M. A.,FRANZIDIS, J. P. & MANLAPIG, E. V. (1999b) Simultaneous determination of collection zone rate constant and froth zone recovery in a mechanical flotation environment. *Minerals Engineering*, 12, 1163-1176.
- VERA, M. A.,MATHE, Z. T.,FRANZIDIS, J. P.,HARRIS, M. C.,MANLAPIG, E. V. & O'CONNOR, C. T. (2002) The modelling of froth zone recovery in batch and continuously operated laboratory flotation cells. *International Journal of Mineral Processing*, 64, 135-151.
- WEBER, M. E. & PADDOCK, D. (1983) Interceptional and gravitational collision efficiencies for single collectors at intermediate Reynolds numbers. *Journal of Colloid and Interface Science*, 94, 328-335.
- WHITTLES, D. N.,KINGMAN, S. W. & REDDISH, D. J. (2003) Application of numerical modelling for prediction of the influence of power density on microwave-assisted breakage. *International Journal of Mineral Processing*, 68, 71-91.

- WHYMAN, G., BORMASHENKO, E. & STEIN, T. (2008) The rigorous derivation of Young, Cassie-Baxter and Wenzel equations and the analysis of the contact angle hysteresis phenomenon. *Chemical Physics Letters*, 450, 355-359.
- WILLS, B. A. & NAPIER-MUNN, T. (2005) Froth flotation. *Wills' Mineral Processing Technology (Seventh Edition)*. Oxford, Butterworth-Heinemann.
- WU, H. & PATTERSON, G. K. (1989) Laser-Doppler measurements of turbulent-flow parameters in a stirred mixer. *Chemical Engineering Science*, 44, 2207-2221.
- YANG, S. Y., HIRASAKI, G. J., BASU, S. & VAIDYA, R. (1999) Mechanisms for contact angle hysteresis and advancing contact angles. *Journal of Petroleum Science and Engineering*, 24, 63-73.
- YIANATOS, J. & CONTRERAS, F. (2009) Particle entrainment model for industrial flotation cells. *Powder Technology*, 197, 260-267.
- YIANATOS, J., CONTRERAS, F., DÍAZ, F. & VILLANUEVA, A. (2009) Direct measurement of entrainment in large flotation cells. *Powder Technology*, 189, 42-47.
- YIANATOS, J., CONTRERAS, F., MORALES, P., CODDOU, F., ELGUETA, H. & ORTÍZ, J. (2010) A novel scale-up approach for mechanical flotation cells. *Minerals Engineering*, In Press, Corrected Proof.
- YIANATOS, J. B. (2007) Fluid Flow and Kinetic Modelling in Flotation Related Processes: Columns and Mechanically Agitated Cells--A Review. *Chemical Engineering Research and Design*, 85, 1591-1603.
- YIANATOS, J. B., BERGH, L. G. & AGUILERA, J. (2003) Flotation scale up: use of separability curves. *Minerals Engineering*, 16, 347-352.
- YIANATOS, J. B., BERGH, L. G. & CORTÉS, G. A. (1998) Froth zone modelling of an industrial flotation column. *Minerals Engineering*, 11, 423-435.
- YIANATOS, J. B., FINCH, J. A. & LAPLANTE, A. R. (1988) Selectivity in column flotation froths. *International Journal of Mineral Processing*, 23, 279-292.
- YIANATOS, J. B., HENRÍQUEZ, F. H. & OROZ, A. G. (2006) Characterization of large size flotation cells. *Minerals Engineering*, 19, 531-538.
- YIANATOS, J. B., MOYS, M. H., CONTRERAS, F. & VILLANUEVA, A. (2008) Froth recovery of industrial flotation cells. *Minerals Engineering*, 21, 817-825.
- YOON, R.-H. & MAO, L. (1996) Application of Extended DLVO Theory, IV: Derivation of Flotation Rate Equation from First Principles. *Journal of Colloid and Interface Science*, 181, 613-626.
- ZAWALA, J., DRZYMALA, J. & MALYSA, K. (2008) An investigation into the mechanism of the three-phase contact formation at fluorite surface by colliding bubble. *International Journal of Mineral Processing*, 88, 72-79.
- ZHANG, J. & KWOK, D. Y. (2005) On the validity of the Cassie equation via a mean-field free-energy lattice Boltzmann approach. *Journal of Colloid and Interface Science*, 282, 434-438.
- ZHENG, X., FRANZIDIS, J. P. & JOHNSON, N. W. (2006a) An evaluation of different models of water recovery in flotation. *Minerals Engineering*, 19, 871-882.
- ZHENG, X., FRANZIDIS, J. P., JOHNSON, N. W. & MANLAPIG, E. V. (2005) Modelling of entrainment in industrial flotation cells: the effect of solids suspension. *Minerals Engineering*, 18, 51-58.

ZHENG, X., JOHNSON, N. W. & FRANZIDIS, J. P. (2006b) Modelling of entrainment in industrial flotation cells: Water recovery and degree of entrainment. *Minerals Engineering*, 19, 1191-1203.

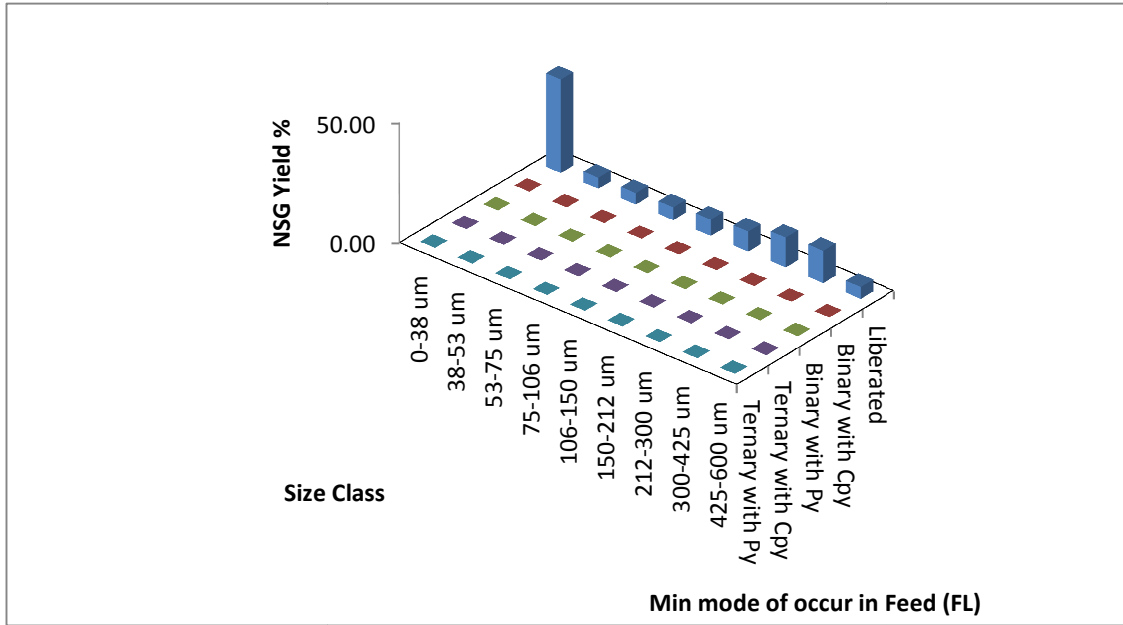


Figure A.1-3: NSG mineral mode of occurrence in FL feed ore ($P_{70}=180 \mu\text{m}$) in the simulations.

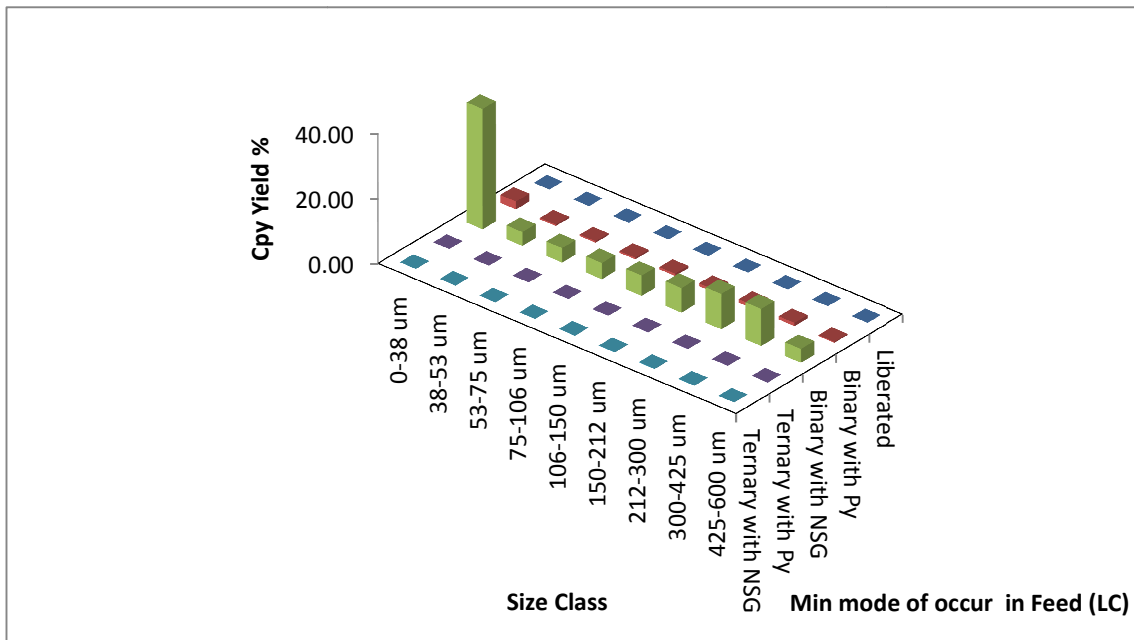


Figure A.1-4: Chalcopyrite mineral mode of occurrence in LC feed ore ($P_{70}=180 \mu\text{m}$) used in the simulations.

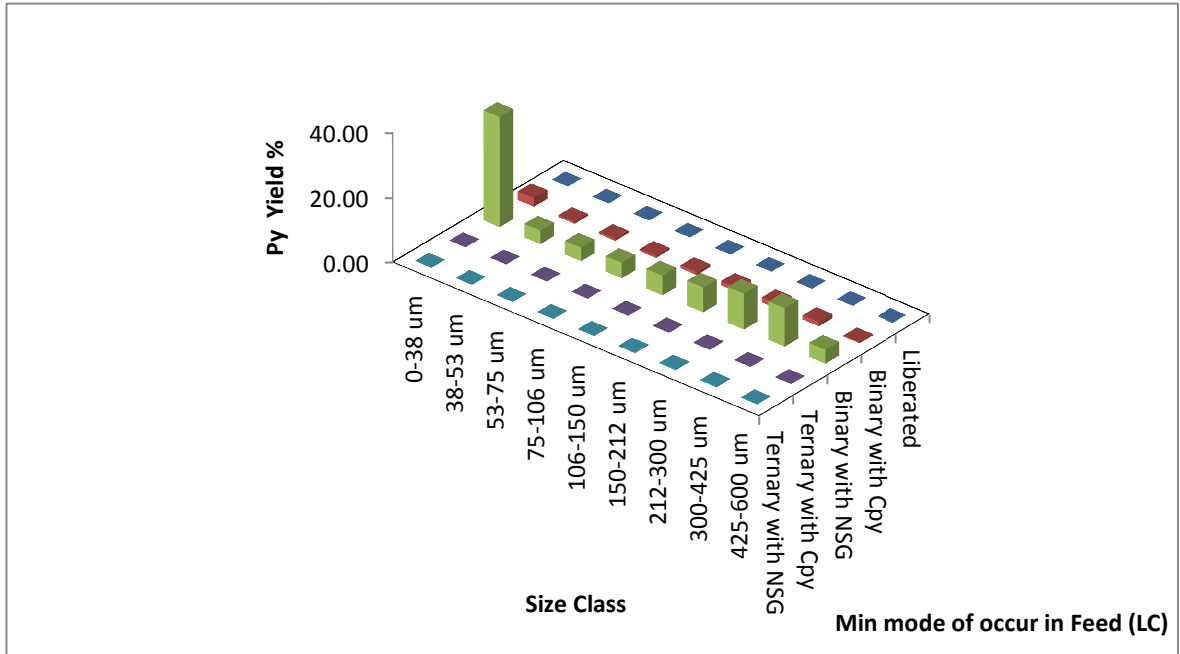


Figure A.1-5: Pyrite mineral mode of occurrence in LC feed ore ($P_{70}=180 \mu\text{m}$) used in the simulations.

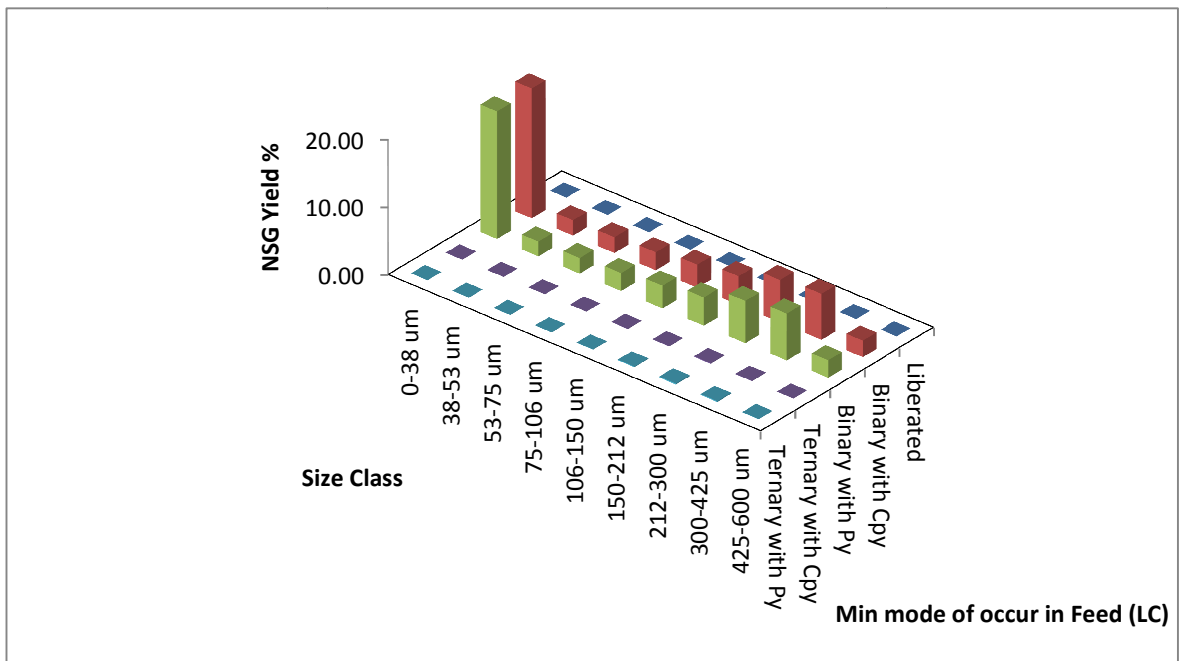


Figure A.1-6: NSG mineral mode of occurrence in LC feed ore ($P_{70}=180 \mu\text{m}$) used in the simulations.

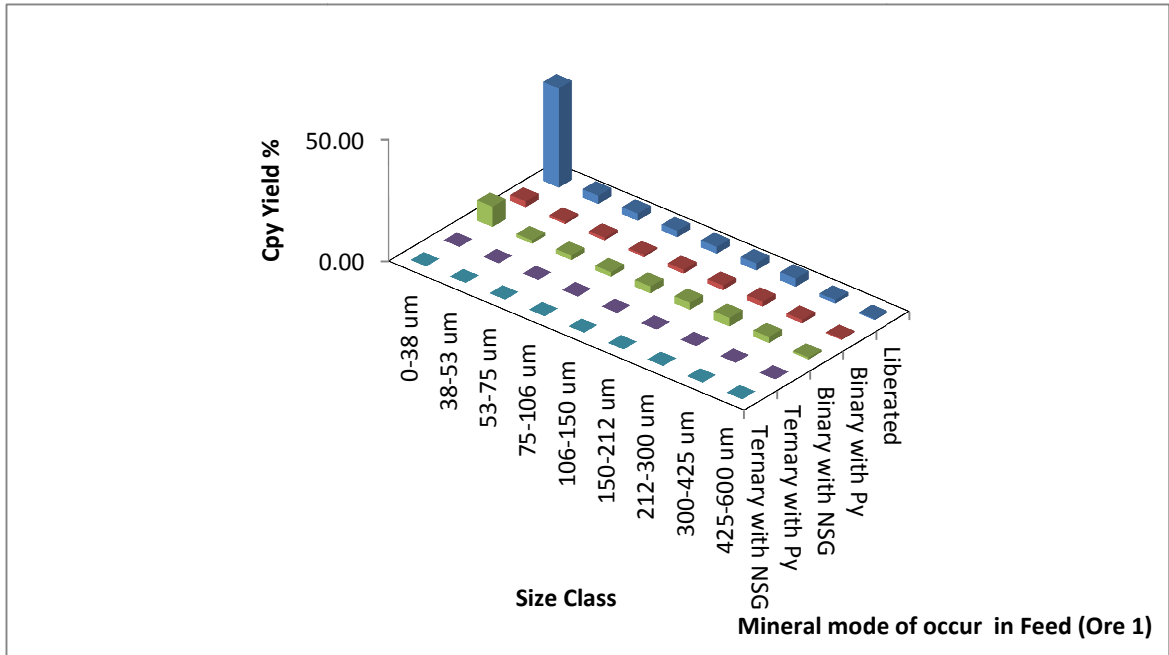


Figure A.1-7: Chalcopyrite mineral mode of occurrence in Ore 1 feed ore ($P_{70}=180 \mu\text{m}$).

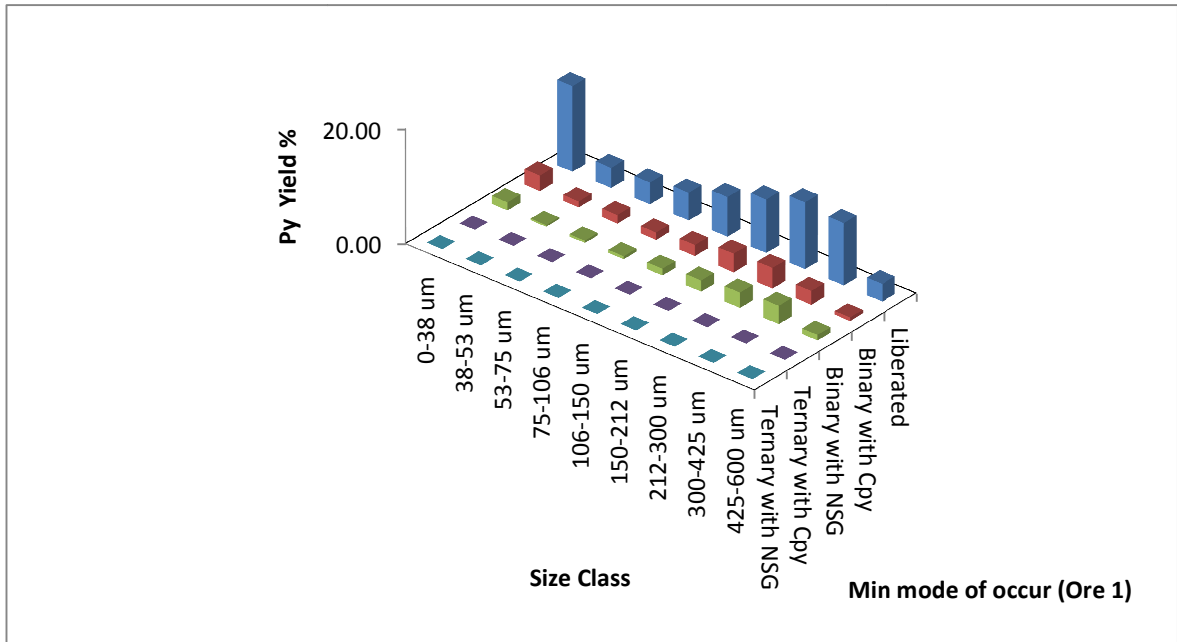


Figure A.1-8: Pyrite mineral mode of occurrence in Ore 1 feed ore ($P_{70}=180 \mu\text{m}$).

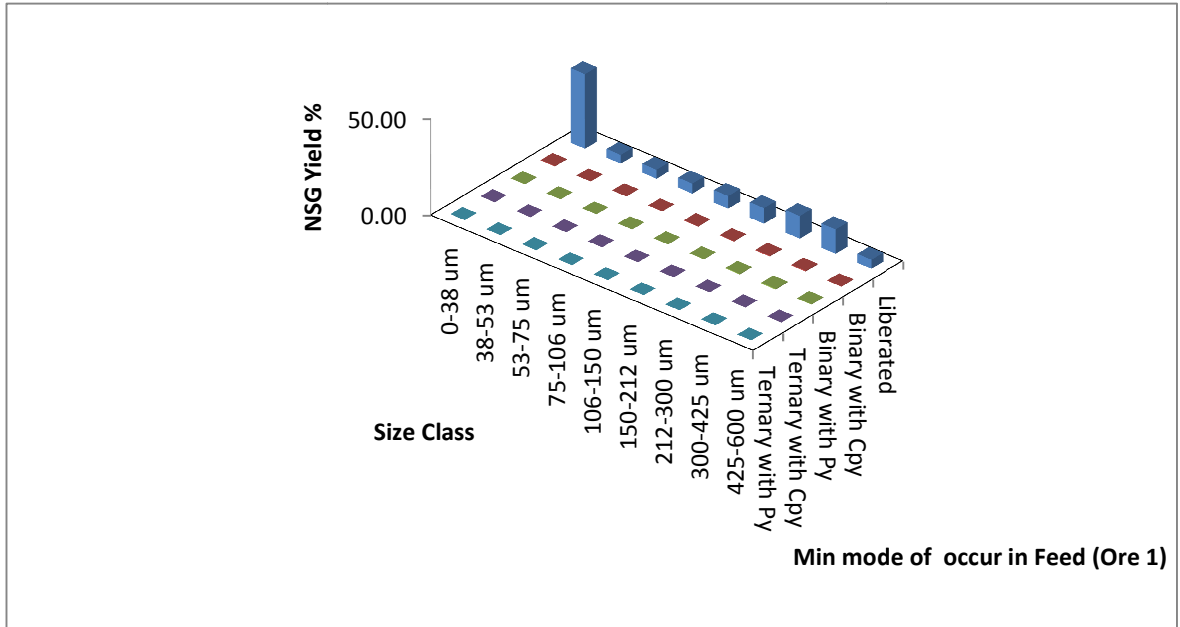


Figure A.1-9: NSG mineral mode of occurrence in Ore 1 feed ore ($P_{70}=180 \mu\text{m}$).

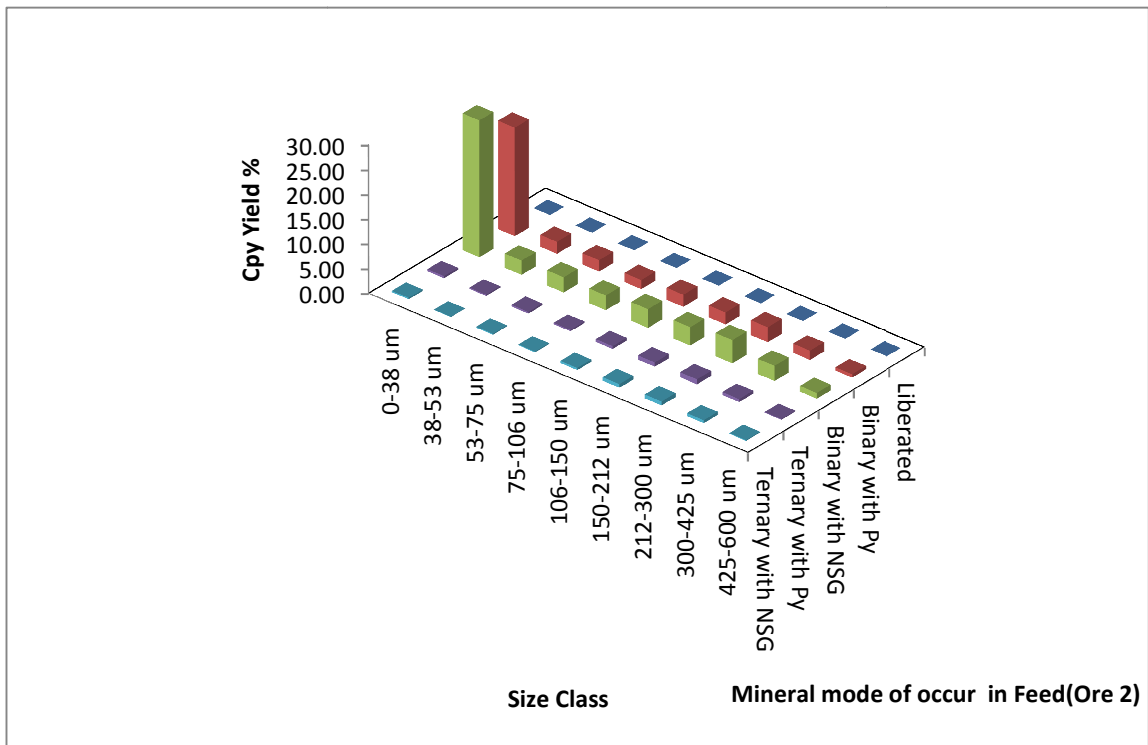


Figure A.1-10: Chalcopyrite mineral mode of occurrence in Ore 2 feed ore ($P_{70}=180 \mu\text{m}$)

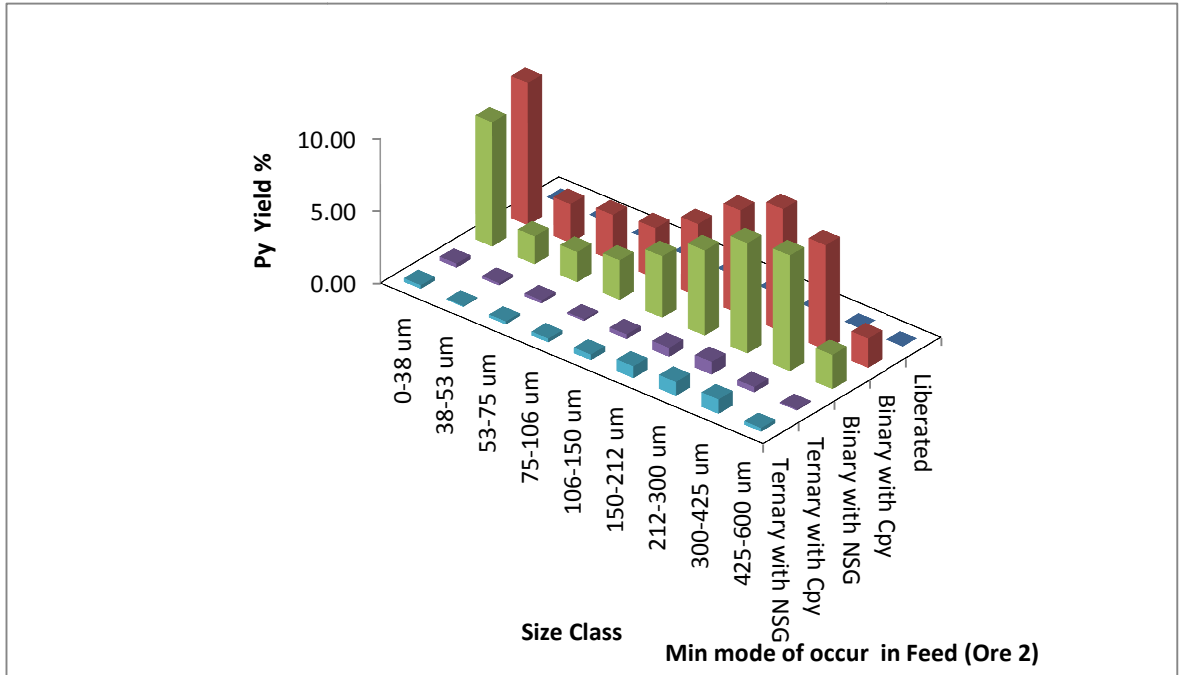


Figure A.1-11: Pyrite mineral mode of occurrence in Ore 2 feed ore ($P_{70}=180 \mu\text{m}$).

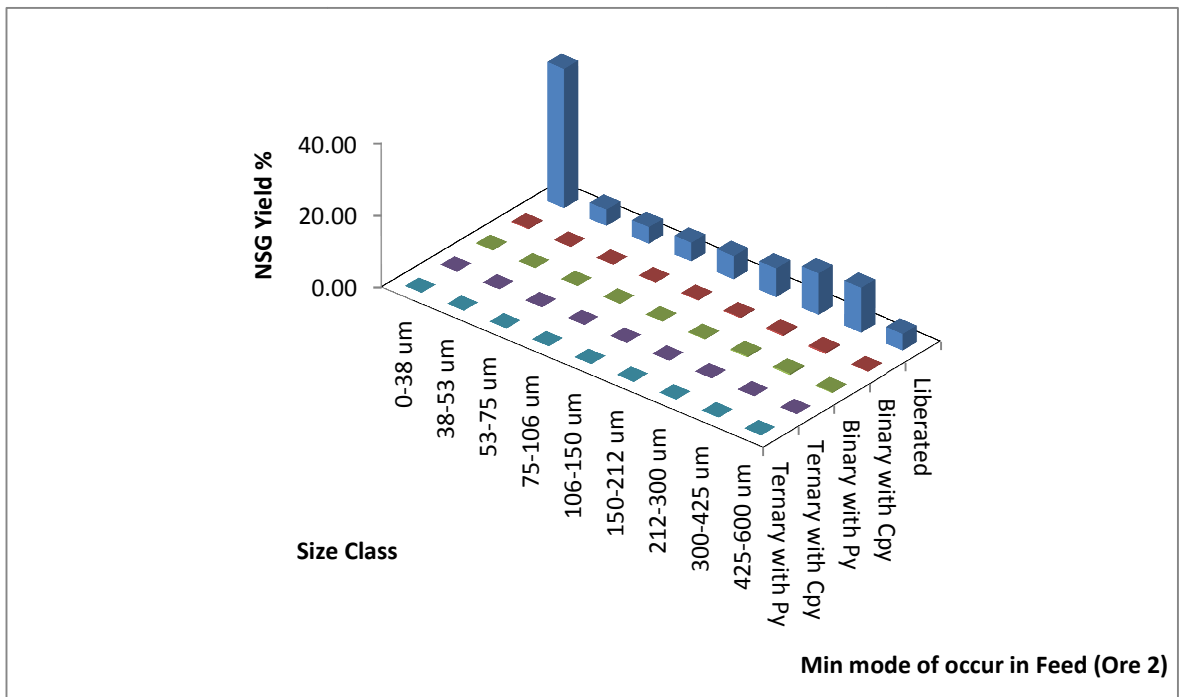


Figure A.1-12: NSG mineral mode of occurrence in Ore 2 feed ore ($P_{70}=180 \mu\text{m}$).

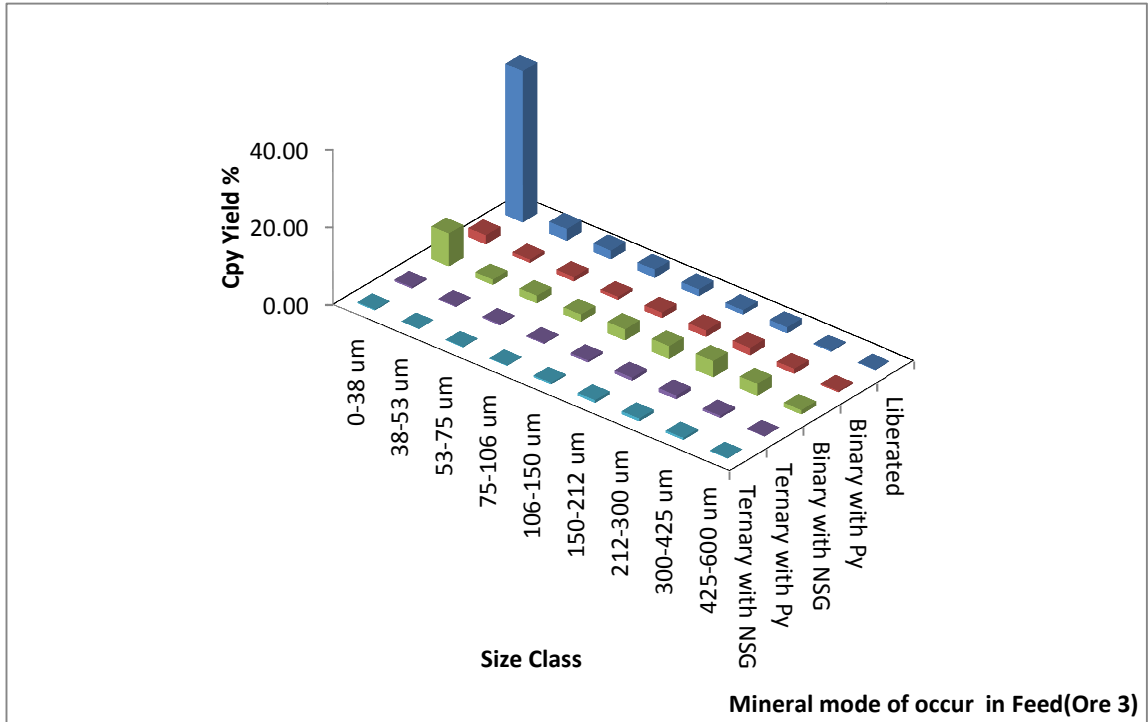


Figure A.1-13: Chalcopyrite mineral mode of occurrence in Ore 3 feed ore ($P_{70}=180 \mu\text{m}$).

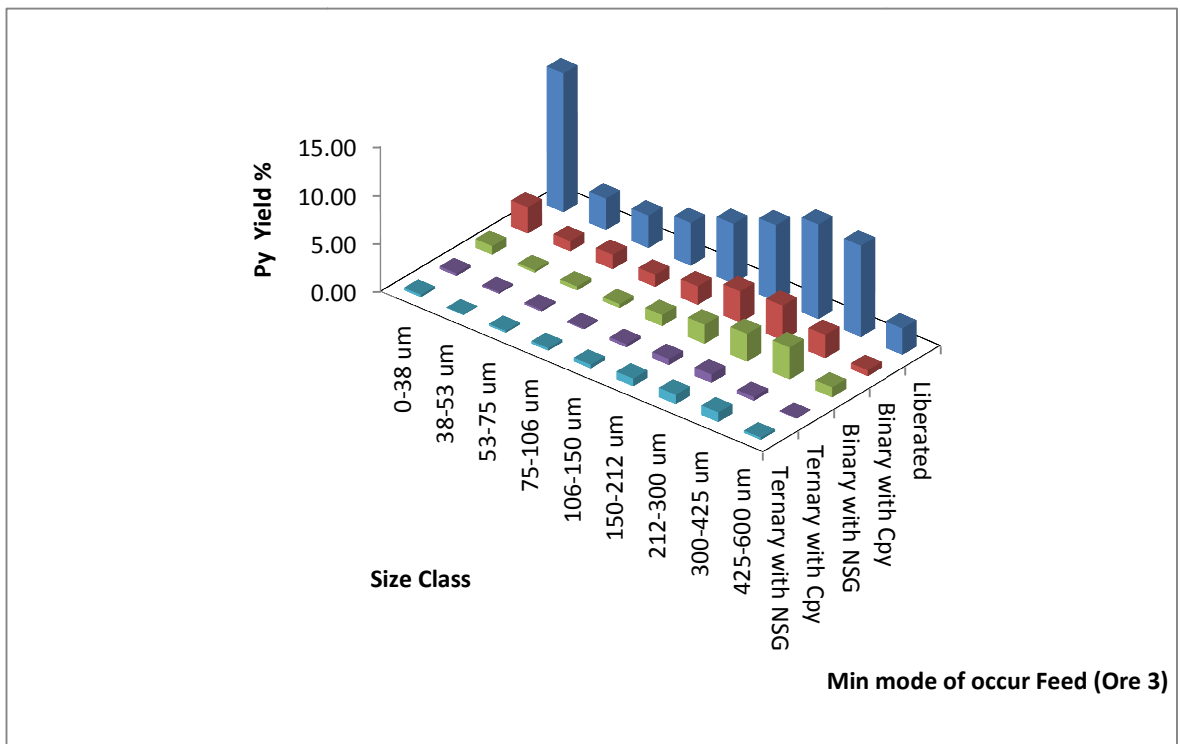


Figure A.1-14: Pyrite mineral mode of occurrence in Ore 3 feed ore ($P_{70}=180 \mu\text{m}$).

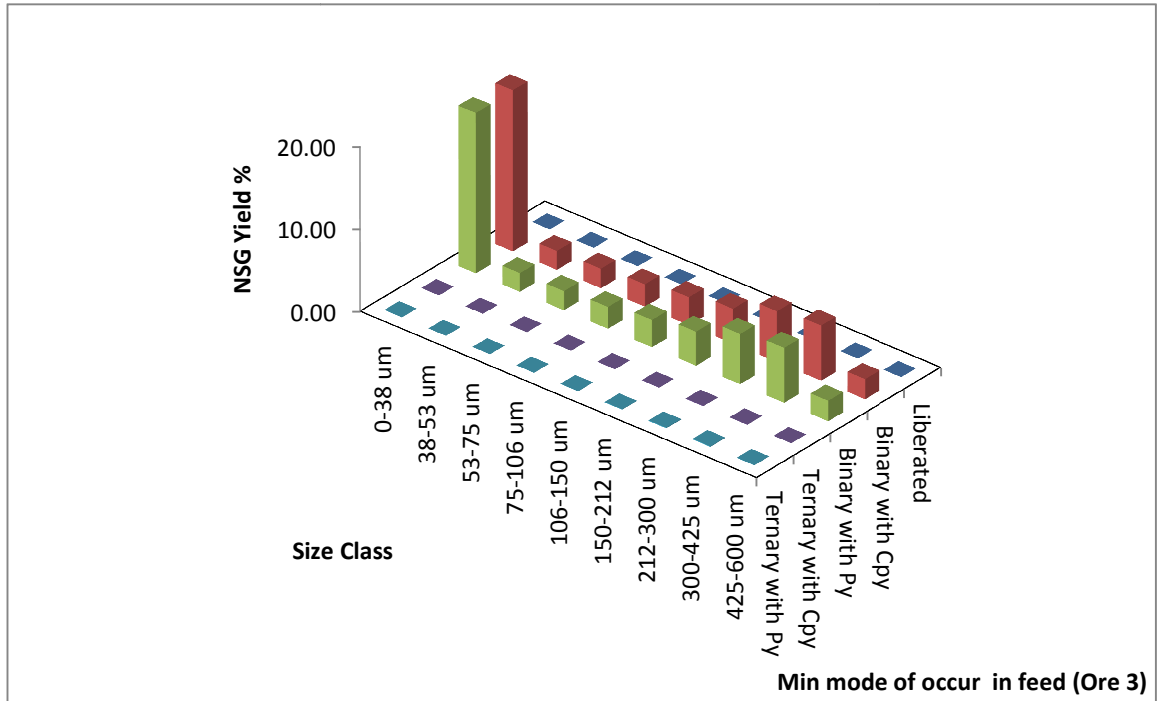


Figure A.1-15: NSG mineral mode of occurrence in Ore 3 feed ore (P₇₀=180 μm).

APPENDIX B CALCULATED PARTICLE CONTACT ANGLE VALUES IN FEED ORE PER SIZE FRACTION

B.1.

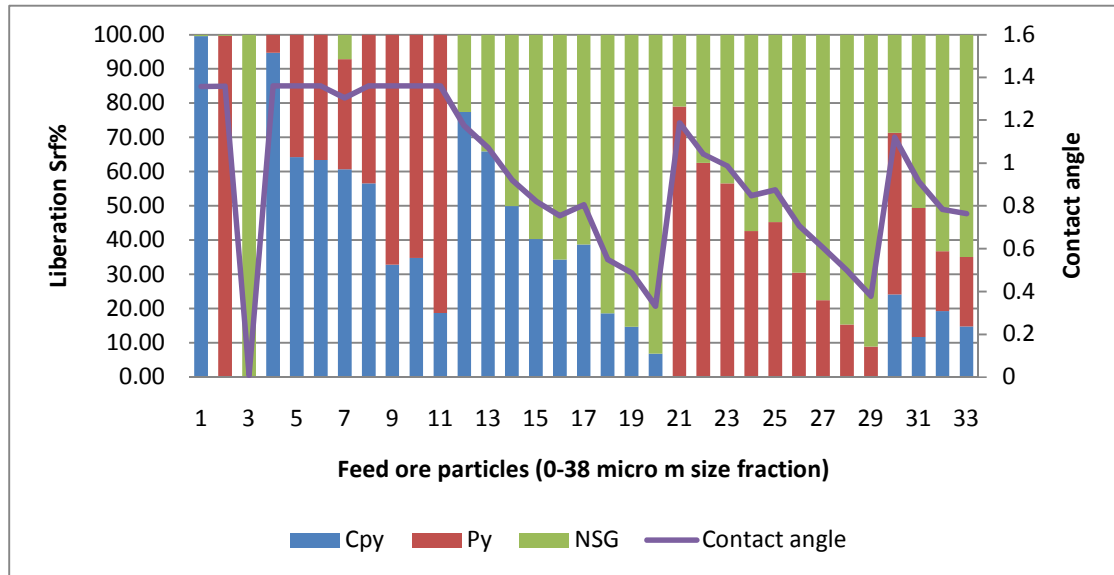


Figure B.1-1: Contact angle variation with particle liberation class for liberation particle classes in the 0-38 μm size fraction.

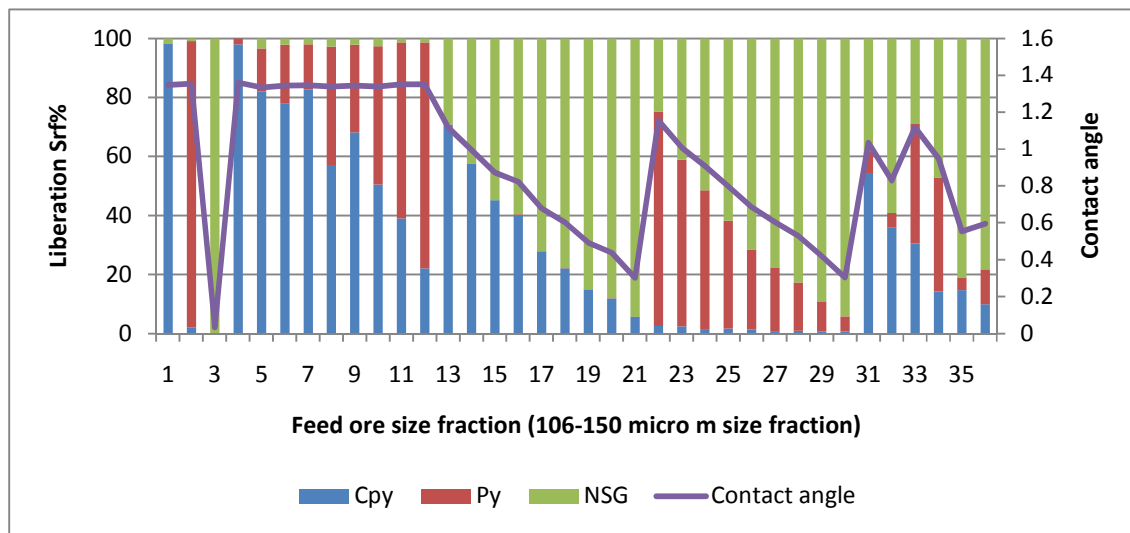


Figure B.1-2: Contact angle variation with particle liberation class for liberation particle classes in the 106-150 μm size fractions.

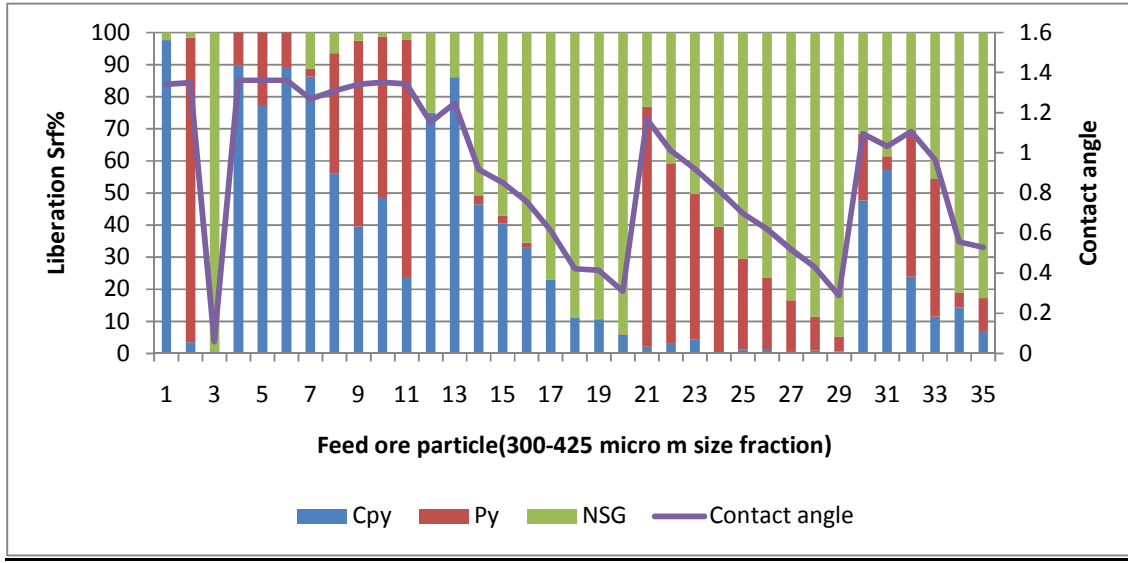


Figure B.1-3: Contact angle variation with particle liberation class for liberation particle classes in the 300-425 micron size fraction.

APPENDIX C : MINERAL GROUPS IN COPPER FEED ORE

C.1.

Table C.1-1: Main mineral groups in feed ores and their grouping

Cu bearing minerals	Non Cu bearing sulphides	Gangue minerals
<ul style="list-style-type: none"> • Chalcopyrite • Digenite • Covellite • Chalcocite • Anilite • Bornite • Enargite 	<ul style="list-style-type: none"> • Pyrite • Sphalerite 	<ul style="list-style-type: none"> • Illite (NSG) • All other minerals non sulphur minerals

Table C.1-2: Mineral groups in feed ores

	Mineral	Wt%	Formula	Mineral
1	Epi wt%	0.05	Ca ₂ (Al,Fe) ₃ Si ₃ O ₁₂ OH	Epidote
2	Titan wt%	0.05	CaTiSiO ₅	Titanite
3	Ort wt%	2.57	KAlSi ₃ O ₈	Orthoclase
4	Cal wt%	0.01	CaCO ₃	Calcite
5	Horn wt%	0.41	(Ca ₂ ,Na)(Mg ₂ FeAl)Si ₆ O ₂₂ (OH) ₂	Hornblende
6	Viv wt%	0.01	Fe ₃ (PO ₄) ₂ .8(H ₂ O)	Vivianite
7	Plum wt%	0.07	PbAl ₃ (PO ₄) ₂ (OH) ₅ .(H ₂ O)	Plumbogummite
8	Eng wt%	0.30	Cu ₃ AsS ₄	Enargite
9	Py wt%	6.25	FeS ₂	Pyrite
10	Dig wt%	0.21	Cu ₉ S ₅	Digenite
11	Iser wt%	0.06	FeTi ₂ O ₅	Iserite
12	Ilmen wt%	0.07	FeTiO ₃	Ilmenite
13	Hem wt%	0.67	Fe ₂ O ₃	Hematite
14	Cov wt%	0.04	CuS	Covellite
15	Cpy wt%	0.47	CuFeS ₂	Chalcopyrite
16	Chal wt%	0.91	Cu ₂ S	Chalcocite
17	Anil wt%	0.16	Cu ₇ S ₄	Anilite
18	Born wt%	0.77	Cu ₅ FeS ₄	Bornite
19	Mol wt%	0.01	MoS ₂	Molybdenite
20	Sph wt%	0.01	ZnS	Sphalerite
21	Alb wt%	2.31	NaAlSi ₃ O ₈	Albite
22	Chl wt%	8.59	(Mg ₃ ,Fe ₂)Al(AlSi ₃)O ₁₀ (OH) ₈	Chlorite
23	Gyp wt%	0.01	(Ca ₂ ,Na)(Mg ₂ FeAl)Si ₆ O ₂₂ (OH) ₂	Gypsum
24	Ill wt%	25.65	KAl ₂ (AlSi ₃ O ₁₀)(OH) ₂	Illite
25	Kao wt%	3.08	Al ₂ Si ₂ O ₅ (OH) ₄	Kaolinite
26	Kemm wt%	0.06	(Sr,Ce)Al ₃ (AsO ₄)(SO ₄)(OH) ₆	Kemmlitzite
27	Mon wt%	0.02	(La,Ce)PO ₄	Monazite
28	Olig wt%	0.78	(Na,Ca)(Al,Si) ₄ O ₈	Oligoclase
29	Pyro wt%	2.48	Al ₂ Si ₄ O ₁₀ (OH) ₂	Pyrophyllite
30	Qtz wt%	42.89	SiO ₂	Quartz
31	Goe wt%	0.06	FeOOH	Goethite
32	Rut wt%	0.25	TiO ₂	Rutile

APPENDIX D : ROUGHER CELLS IN SERIES PLANT FLOWSHEET CONFIGURATION

D.1.

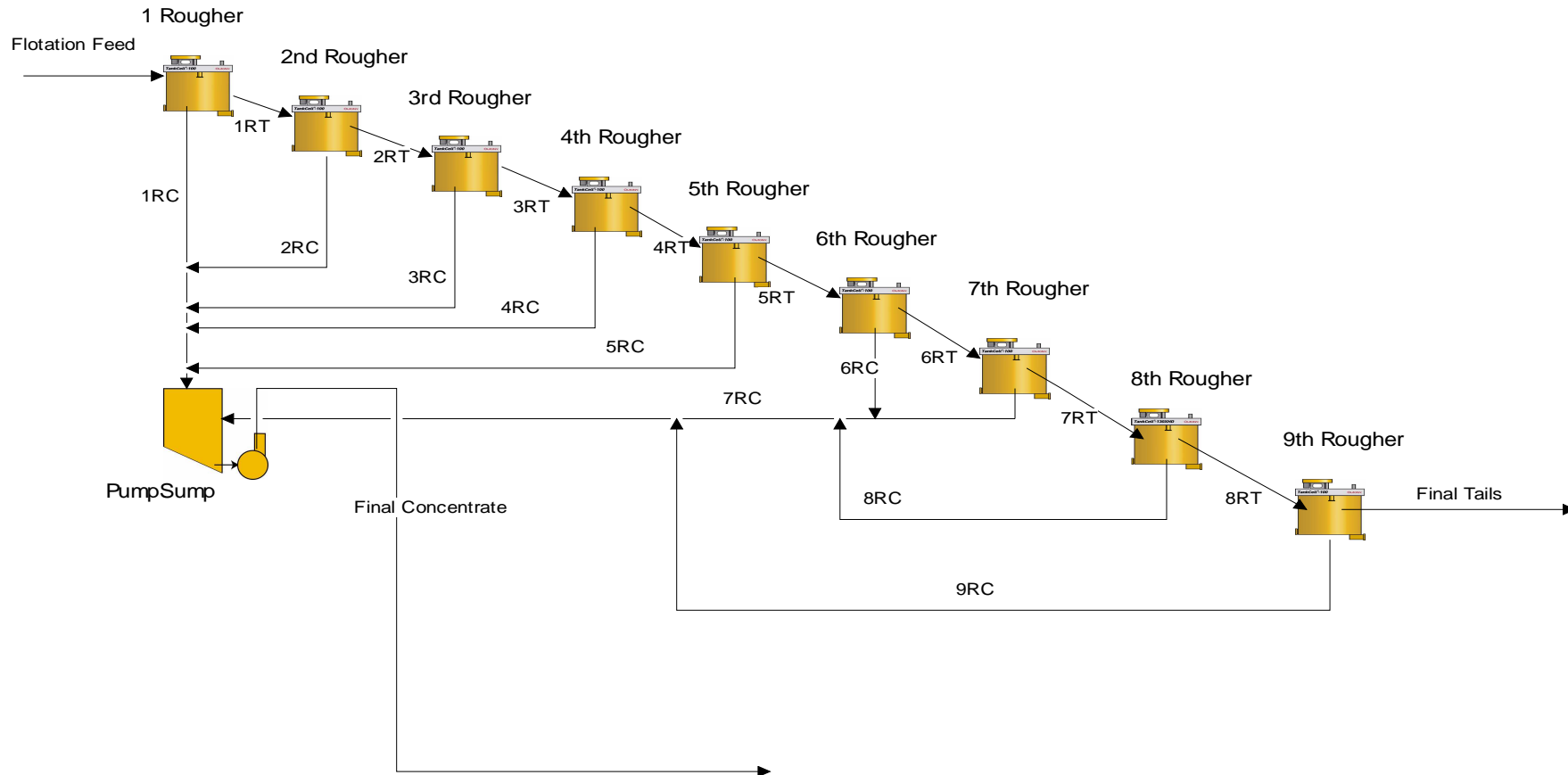


Figure D.1-1: Rougher cell flow sheet configuration that was used in the study.

APPENDIX E : FILE STRUCTURE IN HSC CHEMISTRY 7

E.1.

Global mineral settings in HSC are stored in the MinSetup.xls file while the composition of each input stream is stored in the Mineralogy_Stream.xls file. Each process unit is presented by an individual MS Excel file with the name of the unit. Figure 3-1 below summarises the file structure in HSC Sim. The properties of individual streams in HSC Sim in a mineral processing flow sheet are calculated from particle flow rates, particle composition and mineral properties. Mineral elements in the streams do not therefore behave independently in the process but with other associated mineral elements that are bound with them in the same particle (Roine, 2010).

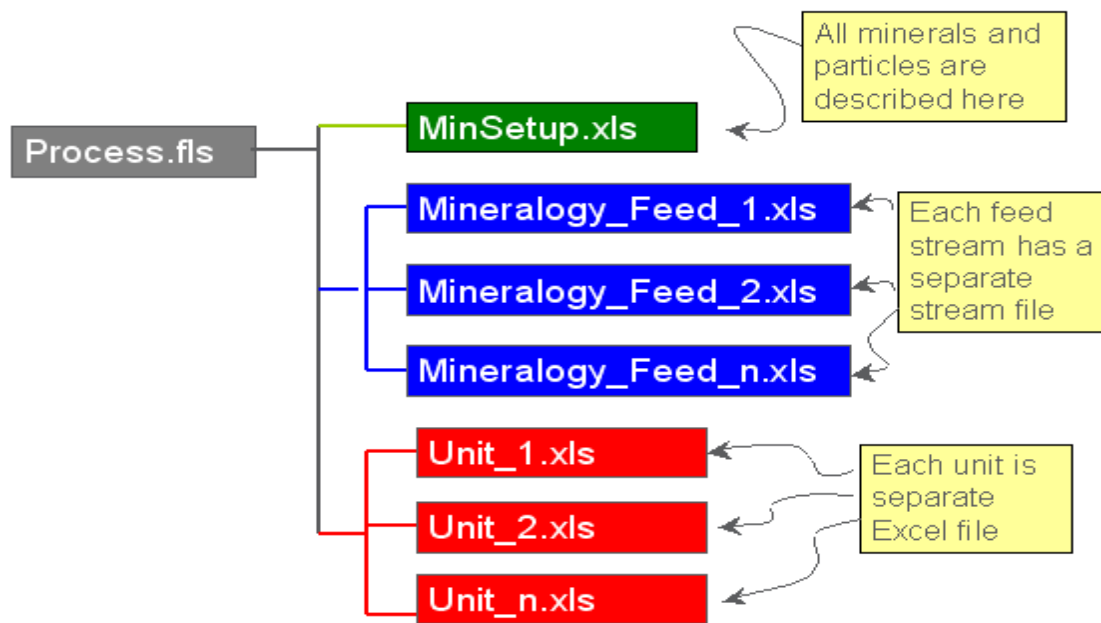


Figure E.1-1: File structure in HSC Sim in the Particle (Minerals) Mode adapted from HSC Chemistry 7 manual (Roine, 2010).

APPENDIX F : COPPER 1 BATCH FLOTATION EXPERIMENTAL PROCEDURE

F.1.

Porphyry copper ore was crushed in a Laboratory Rod mill at two grind sizes $P_{70} = 120 \mu\text{m}$ and $P_{70} = 180 \mu\text{m}$. A standard flotation procedure for obtaining flotation recovery by size data was used. The method involved floating the ore in a standard batch flotation cell designed for this purpose. Concentrate from the flotation cell was collected at timed intervals of 0.5, 1, 4, 9, 15 minutes. Flotation was carried out in a Denver D12 flotation machine was used to float the ore feed at an impeller speed of 1000 to 1100rpm. The flotation cell size was 4L and air was fed at a flow rate of 0.5L/min. In order to obtain recovery by size data the timed concentrates were combined and the following measurements were taken.

1. Solids % in the combined concentrate.
2. The size distribution of the combined concentrate.
3. Assay of each size class in the combined concentrate.

APPENDIX G : FLOTATION CELL SIMULATION INPUT VARIABLES

G.1.

Table G.1-1: Input variables used in calibrating the fundamental property based model in simulating the flotation process.

Variable	Parameter	Literature input parameter (Ralston et al., 2007)
Feed ore Type	Copper 1 base case feed	
P ₇₀ grind size	120 μm	
Cell volume (V)	85 m ³	85 m ³
Feed rate	890 tph	890 tph
Sulphide mineral contact angle (θ)		78°
NSG contact angle (θ)		0°
Energy dissipation (ε)		11 m ² /s ³
Bubble diameter (d _b)		0.0013 m
Bubble rise velocity (v _b)		0.18 m/s
Apparent viscosity of slurry (ϑ)		0.2 kg/ms
Gas flow rate (G _{fr})		4 m ³ /min
Surface tension (γ)		70 N/m
Fluid density (ρ _{fl})	1263 kg/ m ³	
Bubble density (ρ _b)	0.5 ρ _{fl} (Koh and Schwarz, 2006)	
Acceleration due to gravity	9.81 m/s ²	
Fluid velocity v _{fl}	0.1724 m/s	

APPENDIX H : COPPER 1 AND COPPER 2 FLOTATION FEED ORE BULK PARTICLE WEIGHT DISTRIBUTION.

H.1.

Table H.1-1: 0-38 μm bulk particle size class weight % for Copper 1 flotation feed ores (P_{70} = 120 μm)

Size Class	ParticleType	Bulk particle weight %					
		BC	FL	LC	Ore 1	Ore 2	Ore3
0-38 μm	Cpy	1.36	1.56	0.00	1.39	0.00	1.36
0-38 μm	Py	1.35	1.52	0.00	1.38	0.00	1.35
0-38 μm	NSG	35.87	36.34	0.00	35.90	35.87	0.00
0-38 μm	Cpy-Py	0.36	0.00	1.71	0.36	1.71	0.36
0-38 μm	Cpy-NSG	0.36	0.00	18.97	0.36	1.04	18.29
0-38 μm	Py-NSG	0.14	0.00	18.74	0.14	0.81	18.07
0-38 μm	NSG+	0.09	0.00	0.09	0.00	0.09	0.09

Table H.1-2: 38-53 μm bulk particle size class weight % for Copper 1 flotation feed ores (P_{70} = 120 μm)

Size Class	Cpy-Py	Bulk particle weight %					
		BC	FL	LC	Ore 1	Ore 2	Ore3
38-53 μm	Cpy	0.12	0.24	0.00	0.13	0.00	0.12
38-53 μm	Py	0.25	0.38	0.00	0.27	0.00	0.25
38-53 μm	NSG	5.62	5.75	0.00	5.63	5.62	0.00
38-53 μm	Cpy-Py	0.13	0.00	0.31	0.13	0.31	0.13
38-53 μm	Cpy-NSG	0.12	0.00	2.98	0.12	0.17	2.92
38-53 μm	Py-NSG	0.03	0.00	2.97	0.03	0.16	2.84
38-53 μm	NSG+	0.04	0.00	0.04	0.00	0.04	0.04

Table H.1-3: 53-75 μm bulk particle size class weight % for Copper 1 flotation feed ores (P_{70} = 120 μm)

Size Class	Cpy-NSG	Bulk particle weight %					
		BC	FL	LC	Ore 1	Ore 2	Ore3
53-75 μm	Cpy	0.09	0.24	0.00	0.10	0.00	0.09
53-75 μm	Py	0.34	0.50	0.00	0.37	0.00	0.34
53-75 μm	NSG	5.81	6.03	0.00	5.83	5.81	0.00
53-75 μm	Cpy-Py	0.17	0.00	0.38	0.17	0.38	0.17
53-75 μm	Cpy-NSG	0.13	0.00	3.09	0.13	0.18	3.04
53-75 μm	Py-NSG	0.07	0.00	3.14	0.07	0.24	2.97
53-75 μm	NSG+	0.07	0.00	0.07	0.00	0.07	0.07

Table H.1-4: 75-106 μm bulk particle size class weight % for Copper 1 flotation feed ores

($P_{70} = 120 \mu\text{m}$)

Size Class	Py-NSG	Bulk particle weight %					
		BC	FL	LC	Ore 1	Ore 2	Ore3
75-106 μm	Cpy	0.09	0.24	0.00	0.11	0.00	0.09
75-106 μm	Py	0.38	0.66	0.00	0.41	0.00	0.38
75-106 μm	NSG	7.03	7.36	0.00	7.06	7.03	0.00
75-106 μm	Cpy-Py	0.19	0.00	0.42	0.19	0.42	0.19
75-106 μm	Cpy-NSG	0.21	0.00	3.77	0.21	0.26	3.72
75-106 μm	Py-NSG	0.11	0.00	3.81	0.11	0.30	3.63
75-106 μm	NSG+	0.09	0.00	0.09	0.00	0.09	0.09

Table H.1-5: 106-150 μm bulk particle size class weight % for Copper 1 flotation feed ores

($P_{70} = 120 \mu\text{m}$)

Size Class	Cpy-Py-NSG	Bulk particle weight %					
		BC	FL	LC	Ore 1	Ore 2	Ore3
106-150 μm	Cpy	0.08	0.30	0.00	0.12	0.00	0.08
106-150 μm	Py	0.70	0.94	0.00	0.78	0.00	0.70
106-150 μm	NSG	8.99	9.82	0.00	9.05	8.98	0.01
106-150 μm	Cpy-Py	0.29	0.00	0.68	0.29	0.68	0.29
106-150 μm	Cpy-NSG	0.34	0.00	4.88	0.34	0.39	4.83
106-150 μm	Py-NSG	0.25	0.00	5.09	0.25	0.60	4.74
106-150 μm	NSG+	0.17	0.00	0.17	0.00	0.17	0.17

Table H.1-6: 150-212 μm bulk particle size class weight % for Copper 1 flotation feed ores

($P_{70} = 120 \mu\text{m}$)

Size Class	Cpy-Py	Bulk particle weight %					
		BC	FL	LC	Ore 1	Ore 2	Ore3
150-212 μm	Cpy	0.05	0.34	0.00	0.10	0.00	0.05
150-212 μm	Py	0.80	1.27	0.00	0.89	0.00	0.79
150-212 μm	NSG	11.50	12.32	0.00	11.58	11.49	0.02
150-212 μm	Cpy-Py	0.30	0.00	0.73	0.30	0.73	0.30
150-212 μm	Cpy-NSG	0.45	0.00	6.23	0.45	0.48	6.19
150-212 μm	Py-NSG	0.39	0.00	6.53	0.39	0.79	6.14
150-212 μm	NSG+	0.23	0.00	0.23	0.00	0.23	0.23

Table H.1-7: 212-300 μm bulk particle size class weight % for Copper 1 flotation feed ores
($P_{70} = 120 \mu\text{m}$)

Size Class	Cpy-NSG	Bulk particle weight %					
		BC	FL	LC	Ore 1	Ore 2	Ore3
212-300 μm	Cpy	0.02	0.24	0.00	0.06	0.00	0.02
212-300 μm	Py	0.55	1.06	0.00	0.63	0.00	0.55
212-300 μm	NSG	10.42	10.59	0.00	10.49	10.39	0.03
212-300 μm	Cpy-Py	0.27	0.00	0.57	0.27	0.57	0.27
212-300 μm	Cpy-NSG	0.40	0.00	5.62	0.40	0.43	5.60
212-300 μm	Py-NSG	0.41	0.00	5.88	0.41	0.68	5.60
212-300 μm	NSG+	0.18	0.00	0.18	0.00	0.18	0.18

Table H.1-8: 300-425 μm bulk particle size class weight % for Copper 1 flotation feed ores
($P_{70} = 120 \mu\text{m}$)

Size Class	Py-NSG	Bulk particle weight %					
		BC	FL	LC	Ore 1	Ore 2	Ore3
300-425 μm	Cpy	0.00	0.03	0.00	0.01	0.00	0.00
300-425 μm	Py	0.13	0.13	0.00	0.14	0.00	0.13
300-425 μm	NSG	2.28	2.15	0.00	2.29	2.27	0.01
300-425 μm	Cpy-Py	0.03	0.00	0.10	0.03	0.10	0.03
300-425 μm	Cpy-NSG	0.08	0.00	1.22	0.08	0.08	1.21
300-425 μm	Py-NSG	0.08	0.00	1.29	0.08	0.15	1.22
300-425 μm	NSG+	0.03	0.00	0.03	0.00	0.03	0.03

H.2.

Table H.2-1: 0-38 μm bulk particle size class weight % for Copper 2 flotation feed ores (P_{70} = 180 μm)

Size Class	ParticleType	Bulk particle weight %					
		BC	FL	LC	Ore 1	Ore 2	Ore3
0-38 μm	Cpy	1.20	1.55	0.00	1.22	0.00	1.20
0-38 μm	Py	0.93	1.23	0.00	0.97	0.00	0.93
0-38 μm	NSG	35.02	35.39	0.00	35.05	35.02	0.00
0-38 μm	Cpy-Py	0.25	0.00	1.32	0.25	1.32	0.25
0-38 μm	Cpy-NSG	0.48	0.00	18.60	0.48	1.08	18.00
0-38 μm	Py-NSG	0.20	0.00	18.18	0.20	0.67	17.71
0-38 μm	NSG+	0.08	0.00	0.08	0.00	0.08	0.08

Table H.2-2: 38-53 μm bulk particle size class weight % for Copper 1 flotation feed ores (P_{70} = 180 μm)

Size Class	Cpy-Py	Bulk particle weight %					
		BC	FL	LC	Ore 1	Ore 2	Ore3
38-53 μm	Cpy	0.10	0.17	0.00	0.11	0.00	0.10
38-53 μm	Py	0.21	0.32	0.00	0.23	0.00	0.21
38-53 μm	NSG	4.09	4.15	0.00	4.10	4.09	0.00
38-53 μm	Cpy-Py	0.09	0.00	0.25	0.09	0.25	0.09
38-53 μm	Cpy-NSG	0.08	0.00	2.18	0.08	0.13	2.13
38-53 μm	Py-NSG	0.03	0.00	2.18	0.03	0.14	2.08
38-53 μm	NSG+	0.03	0.00	0.03	0.00	0.03	0.03

Table H.2-3: 53-75 μm bulk particle size class weight % for Copper 1 flotation feed ores (P_{70} = 180 μm)

Size Class	Cpy-NSG	Bulk particle weight %					
		BC	FL	LC	Ore 1	Ore 2	Ore3
53-75 μm	Cpy	0.07	0.18	0.00	0.09	0.00	0.07
53-75 μm	Py	0.22	0.37	0.00	0.25	0.00	0.22
53-75 μm	NSG	4.18	4.28	0.00	4.20	4.18	0.00
53-75 μm	Cpy-Py	0.13	0.00	0.28	0.13	0.28	0.13
53-75 μm	Cpy-NSG	0.12	0.00	2.25	0.12	0.16	2.21
53-75 μm	Py-NSG	0.05	0.00	2.25	0.05	0.16	2.14
53-75 μm	NSG+	0.06	0.00	0.06	0.00	0.06	0.06

Table H.2-4: 75-106 µm bulk particle size class weight % for Copper 1 flotation feed ores

(P₇₀ = 180 µm)

Size Class	Py-NSG	Bulk particle weight %					
		BC	FL	LC	Ore 1	Ore 2	Ore3
75-106 um	Cpy	0.06	0.16	0.00	0.08	0.00	0.06
75-106 um	Py	0.29	0.43	0.00	0.32	0.00	0.29
75-106 um	NSG	4.73	4.87	0.00	4.74	4.72	0.00
75-106 um	Cpy-Py	0.10	0.00	0.28	0.10	0.28	0.10
75-106 um	Cpy-NSG	0.15	0.00	2.54	0.15	0.18	2.51
75-106 um	Py-NSG	0.07	0.00	2.58	0.07	0.21	2.43
75-106 um	NSG+	0.06	0.00	0.06	0.00	0.06	0.06

Table H.2-5: 106-150 µm bulk particle size class weight % for Copper 1 flotation feed ores

(P₇₀ = 180 µm)

Size Class	Cpy-Py-NSG	Bulk particle weight %					
		BC	FL	LC	Ore 1	Ore 2	Ore3
106-150 um	Cpy	0.06	0.22	0.00	0.09	0.00	0.06
106-150 um	Py	0.41	0.65	0.00	0.45	0.00	0.40
106-150 um	NSG	5.87	6.14	0.00	5.91	5.86	0.01
106-150 um	Cpy-Py	0.17	0.00	0.40	0.17	0.40	0.17
106-150 um	Cpy-NSG	0.24	0.00	3.21	0.24	0.27	3.17
106-150 um	Py-NSG	0.15	0.00	3.28	0.15	0.35	3.08
106-150 um	NSG+	0.12	0.00	0.12	0.00	0.12	0.12

Table H.2-6: 150-212 µm bulk particle size class weight % for Copper 1 flotation feed ores

(P₇₀ = 180 µm)

Size Class	Cpy-Py	Bulk particle weight %					
		BC	FL	LC	Ore 1	Ore 2	Ore3
150-212 um	Cpy	0.04	0.24	0.00	0.09	0.00	0.04
150-212 um	Py	0.52	0.94	0.00	0.61	0.00	0.52
150-212 um	NSG	7.22	7.65	0.00	7.29	7.21	0.01
150-212 um	Cpy-Py	0.26	0.00	0.54	0.26	0.54	0.26
150-212 um	Cpy-NSG	0.32	0.00	3.95	0.32	0.35	3.93
150-212 um	Py-NSG	0.26	0.00	4.13	0.26	0.52	3.87
150-212 um	NSG+	0.21	0.00	0.21	0.00	0.21	0.21

Table H.2-7: 212-300 µm bulk particle size class weight % for Copper 1 flotation feed ores

(P₇₀ = 180 µm)

Size Class	Cpy-NSG	Bulk particle weight %					
		BC	FL	LC	Ore 1	Ore 2	Ore3
212-300 um	Cpy	0.05	0.29	0.00	0.11	0.00	0.05
212-300 um	Py	0.64	1.17	0.00	0.76	0.00	0.64
212-300 um	NSG	10.48	11.25	0.00	10.60	10.46	0.03
212-300 um	Cpy-Py	0.29	0.00	0.64	0.29	0.64	0.29
212-300 um	Cpy-NSG	0.48	0.00	5.75	0.48	0.52	5.71
212-300 um	Py-NSG	0.47	0.00	6.03	0.47	0.80	5.70
212-300 um	NSG+	0.29	0.00	0.29	0.00	0.29	0.29

Table H.2-8: 300-425 µm bulk particle size class weight % for Copper 1 flotation feed ores

(P₇₀ = 180 µm)

Size Class	Py-NSG	Bulk particle weight %					
		BC	FL	LC	Ore 1	Ore 2	Ore3
300-425 um	Cpy	0.01	0.19	0.00	0.05	0.00	0.01
300-425 um	Py	0.62	1.08	0.00	0.71	0.00	0.62
300-425 um	NSG	11.35	12.20	0.00	11.44	11.31	0.04
300-425 um	Cpy-Py	0.19	0.00	0.53	0.19	0.53	0.19
300-425 um	Cpy-NSG	0.49	0.00	6.16	0.48	0.50	6.14
300-425 um	Py-NSG	0.60	0.00	6.57	0.60	0.92	6.26
300-425 um	NSG+	0.22	0.00	0.22	0.00	0.22	0.22

Table H.2-9: 425-850 µm bulk particle size class weight % for Copper 1 flotation feed ores

(P₇₀ = 180 µm)

Size Class	Cpy-Py-NSG	Bulk particle weight %					
		BC	FL	LC	Ore 1	Ore 2	Ore3
425-850 um	Cpy	0.01	0.06	0.00	0.01	0.00	0.01
425-850 um	Py	0.18	0.31	0.00	0.20	0.00	0.18
425-850 um	NSG	4.18	4.50	0.00	4.21	4.16	0.02
425-850 um	Cpy-Py	0.05	0.00	0.15	0.05	0.15	0.05
425-850 um	Cpy-NSG	0.15	0.00	2.24	0.15	0.16	2.23
425-850 um	Py-NSG	0.25	0.00	2.42	0.25	0.34	2.33
425-850 um	NSG+	0.06	0.00	0.06	0.00	0.06	0.06

APPENDIX I SAMPLE MODEL WIZARD SCREEN CAPTURE IN HSC CHEMISTRY 7

I.1.

	A	B	C	D	E	F	G	H	I	J	K	L	M	N	O	P
1	MODEL:	Fundamental Property based model				To apply wizard select 'Run Excel Wizard...' on the 'Wizard' menu										
2	WIZARD FILE:	HSC_Sim_S_1_Particle_Wizards.xls														
3	WIZARD SHEET:	Flotation property based model														
4	AUTHOR:	Edson Charikinya, Stellenbosch University				Use this model for flotation, using kinetic equation according to: <i>Causes (i.e. taking into account entrainment and both minerals)</i>										
5	VERSION:	21 May 2010 for Mineralogical Treatment of Materials Group														
6	Material divided between the products according to mineral composition and size class					Blue text indicates user check input										
7						Red text is calculated value which should not be touched, or it is an error message										
8																
9	Basic info		Guides to fill in the parameters: (check and fill all fields with blue text)													
10	Minerals	0														
11	Size fractions	1														
12	Particles															
13	Input streams															
14	Output streams															
15																
16	Cell Operating parameters		Advancing water Contact angles in Radians for fully liberated minerals													
17	Total volume m3	85														
18	Input pulp m3/h	1500														
19	Residence time, min	3.4														
20	Scale-up factor	1														
21	Eff. residence time, min	3.4														
22	σ	1.2														
23	Gas flowrate (Q) m3/min	4														
24	Mean Bubble diameter (m)	0.0013														
25	Fluid velocity (m/s)	0.01														
26	Bubble velocity (m/s)	0.01														
27	Fluid density (kg/m3)	1400														
28	Bubble density (kg/m3)	4100														
29	Density Diff (kg/m3)	2700														
30	Dissipation energy (m2/s3)	11														
31	viscosity (Pas)	0.2														
32	Kinematic Viscosity (m2/s)	0.00014208														
33	Surface tension	0.072														
34	Concentrate is	1	Stream1													
35																
36	Number of collision per unit volume		Advancing water COS(Contact angles)-contact angles in Radians for fully liberated minerals													
37	Mechanical Term(m/min)	85.52														
38	Primary turbulence term (m)	0.16														
39	Water Recovery %	1.2%														
40																
			Total cell volume													
			Input pulp volume (from the input sheet)													
			Calculated residence time													
			Scale-up factor													
			Residence time used													
			Bubble surface area flux (not used)													
			Gas flowrate													
			The measured mean bubble diameter													
			Measured Velocity of the fluid													
			The measured bubble velocity													
			Density of the pulp													
			The density of the bubble													
			Bubble pulp density difference													
			Dissipation Energy													
			Pulp viscosity													
			Kinematic viscosity													
			Surface tension													
			Give 1 or 2 (i.e. column F or F on the output sheet)													
			Entrainment calculation parameters													
			Ent Parameter													
			0.00003													
			Drainage													
			1													
			Adj													
			1													
			induction time constant													
			0.6													

Figure I.1-1: Sample screen capture of model wizard screen as it would appear in HSC Chemistry 7.

**A MODELLING FRAMEWORK TO DETERMINE
THE VALUE PROPOSITION OF MICROWAVE
TREATMENT OF MINERAL ORES**

by

Edson Charikinya

Thesis submitted in partial fulfillment
of the requirements for the Degree

of

**MASTER OF SCIENCE IN ENGINEERING
(EXTRACTIVE METALLURGICAL ENGINEERING)**

in the Faculty of Engineering
at Stellenbosch University

Supervised by

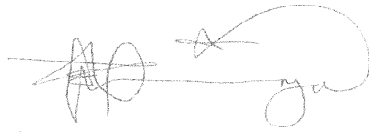
S.M. Bradshaw

MARCH 2011

Declaration

By submitting this thesis electronically, I declare that the entirety of the work contained therein is my own, original work, that I am the sole author thereof (save to the extent explicitly otherwise stated), that reproduction and publication thereof by Stellenbosch University will not infringe any third party rights and that I have not previously in its entirety or in part submitted it for obtaining any qualification.

Signature:

A handwritten signature in black ink, consisting of several loops and a long horizontal stroke.

Date: 28/02/2011

ABSTRACT

The extraction of mineral values from ore requires liberation of the minerals followed by separation. Liberation is achieved by size reduction operations which are inefficient processes typically accounting for up to 70% of the energy consumption in a mineral concentrator (Tromans, 2008). As the grade of ores reserves declines, future viability of mineral operations will be determined by the costs of comminution. Recent work has shown that microwave treatment of secondary crusher product at specific microwave energy consumption of the order of 1 kWh/t reduces the work index of the ore and increases grade and recovery in batch flotation tests. Improved liberation at coarse sizes was also demonstrated (Kingman, 2006). Based on these findings work is ongoing to commercialise the technology.

The objective of this study is to develop a modelling framework to determine the value proposition of microwave treatment of ore. It was noted that various models exist in literature for modelling of mineral processing flotation flow sheets, but these models do not incorporate the feed ore liberation property as an input variable in their calculations. Thus, a fundamentally derived property based model was identified as appropriate for flow sheet modelling of microwave treated ore, as it utilised liberation as an indirect variable in calculating the flotation rate constant through the use of contact angle to describe particle surface hydrophobicity.

The model was successfully incorporated into the flotation flow sheet units developed in HSC Chemistry and used with Mineral Liberation Analyser (MLA) data to investigate the effects of changes in feed ore liberation on rougher cell flotation recovery. Different liberation scenarios based around modification of porphyry copper flotation feed were created. A sensitivity analysis of the various feed stream liberation scenarios was carried out to test the ability of the model to effectively model the differences in downstream processing of microwave treated and untreated ores. For a single flotation cell of size 85 m³ with a solids feed flow rate of 890 tph, it was observed that below a certain size (120 µm in the case of the porphyry copper ore) changes in flotation feed liberation had no significant effect on value mineral recovery. Significant differences in value mineral

recovery were observed only at coarser sizes above 120 μm . The results indicated that improvement in recovery of value minerals due to improved liberation from applying microwave technology has size limits and is significantly dependent on the feed grind size.

Feed grind size sensitivity analysis was then carried on the same single cell flow sheet utilising feeds with the same mineralogy but with different grind sizes. The results indicated that maximum benefits from the application of microwave technology would be best obtained by utilising coarse grinding at sizes between $P_{70} = 200 \mu\text{m}$ and $P_{70} = 300 \mu\text{m}$ for the porphyry copper ores considered in this study. Coarse grinding appears to be the best way to exploit improved liberation in downstream processing of microwave treated ores.

Investigations similar to those carried out on the single cell flotation flow sheet were then carried out on a continuous plant rougher flotation flow sheet. The flow sheet consisted of nine rougher cells in series each with a volume of 85 m^3 with a solids feed flow rate of 890 tph into the bank of rougher cells. The results indicated that there was no significant difference in final rougher bank overall cumulative recovery at fine grind sizes below a P_{70} grind size of 120 μm with improvements in feed ore liberation. Feed grind size sensitivity analysis showed a significant variation in cumulative recovery at coarse grind sizes of above $P_{70} = 129 \mu\text{m}$. This variation was attributed to improvements in flotation feed ore value mineral liberation from locked composite particles to the maximum possible theoretical liberation scenario of fully liberated value mineral particles. A 7.2 percentage point improvement in cumulative value mineral overall recovery and a 2 to 3 percentage point improvement in enrichment ratio was also observed above the $P_{70} = 250 \mu\text{m}$ grind sizes after improving the flotation feed ore value mineral particle liberation of a typical flotation plant feed to a maximum. The increases in grade and cumulative recovery at coarse sizes were attributed to improvements to the flotation plant feed ore value mineral particle liberation. From the results, it was concluded that microwave technology application will offer greater benefits in downstream processing of coarse ground ores.

OPSOMMING

Die ekstraksie van mineraalwaardes uit erts vereis bevryding van die minerale gevolg deur skeiding. Bevryding word bereik deur verkleiningsprosedures wat ondoeltreffende prosesse is en wat gewoonlik vir tot 70% van die energieverbruik in 'n mineraalkonsentreerder verantwoordelik is (Tromans, 2008). Algaande die graad van ertsreserwes afneem, sal toekomstige lewensvatbaarheid van mineraalprosesse bepaal word deur die koste van vergruising. Onlangse werk het getoon dat mikrogolfbehandeling van sekondêre vergruiserprodukt by spesifieke mikrogolf-energieverbruik van ongeveer 1 kWh/t die werk-indeks van die erts verminder en die graad en opbrengs in lotflottasietoetse verhoog. Verbeterde bevryding by growwer groottes is ook aangetoon (Kingman, 2006). Werk gaan voort op grond van hierdie bevindinge ten einde die tegnologie te kommersialiseer.

Die doel van hierdie navorsing is om 'n modelleringsraamwerk te ontwikkel om die waardeproposisie van mikrogolfbehandeling van erts te bepaal. Daar is in die literatuur afgekom op verskeie modelle vir die modellering van vloeidiagramme vir flottasie van mineraalverwerking, maar hierdie modelle inkorporeer nie die voerertsbevrydingseienskap as 'n insetveranderlike in hulle berekeninge nie. 'n Fundamentele afgeleide eienskapgebaseerde model is geïdentifiseer as geskik vir vloeidiagrammodellering van mikrogolfbehandelde erts, aangesien dit bevryding as 'n indirekte veranderlike by die berekening van die floteertempokonstante aangewend het deur die gebruik van kontakhoek om hidrofobisiteit van die deeltjieoppervlak te beskryf.

Die model is suksesvol in eenhede van die flottasievloeidiagram wat in HSC Chemistry ontwikkel is, geïnkorporeer en tesame met data van die mineraalbevrydingsontleder (MBO) gebruik om die gevolge van veranderinge in voerertsbevryding op die opbrengs van voorskieselflottasie te ondersoek. Verskillende bevrydingsscenario's is geskep wat óm die modifisering van porfierkoperflotterings toevoer heen gebaseer is. 'n Sensitiwiteitsontleding van die verskillende voerstroombevrydingsscenario's is uitgevoer om die vermoë van die model om die verskille in stroomaf-verwerking van mikrogolfbehandelde en onbehandelde ertse te toets, doeltreffend te modelleer. In die geval van 'n enkele flottasiesel van 85 m³ groot met 'n vastestof-toevoervloeitempo van 890 tph, is waargeneem dat veranderinge in flottasietoever-bevryding benede 'n sekere grootte (120 µm in die geval van die porfierkopererts) geen beduidende uitwerking op die opbrengs van die waardemineraal gehad het nie. Beduidende verskille in die opbrengs van die waardemineraal is slegs by growwer

groottes bo 120 μm waargeneem. Die resultate het daarop gedui dat verbetering in die opbrengs van waardeminerale as gevolg van verbeterde bevryding ná die toepassing van mikrogolftegnologie beperkinge ten opsigte van grootte het en opvallend afhanklik is van die toevoermaalgrootte.

Sensitiwiteitstoetsing van toevoermaalgrootte is daarna op dieselfde enkele selvloeiendiagram wat voerders met dieselfde mineralogie gebruik uitgevoer, maar met verskillende maalgroottes. Die resultate het daarop gedui dat maksimum voordele van die toepassing van mikrogolftegnologie die beste verkry sou word deur gebruik van growwe maling by groottes tussen $P_{70} = 200 \mu\text{m}$ en $P_{70} = 300 \mu\text{m}$ vir die porfierkoperertse wat in hierdie navorsing in oorweging geneem is. Growwe maling skyn die beste manier te wees om verbeterde bevryding in stroomaf-verwerking van mikrogolfbehandelde ertse te eksploiteer.

Ondersoeke soortgelyk aan dié wat op die vloeiendiagram van die enkelselflottasie uitgevoer is, is toe op 'n deurlopende vloeiendiagram van die aanlegvoorskeierflottasie uitgevoer. Die vloeiendiagram het bestaan uit nege voorskeiselle in serie elk met 'n volume van 85 m^3 met 'n vastestof-toevoervloeitempo van 890 tph in die ry voorskeiselle. Die resultate het daarop gedui dat daar geen aanmerklike verskil in algemene kumulatiewe opbrengs van die finale voorskeiry by fyn maalgroottes benede 'n P_{70} -maalgrootte van $120 \mu\text{m}$ met verbetering in voerertsbevryding was nie. Sensitiwiteitsontleding van voermaalgrootte het 'n beduidende variasie in kumulatiewe opbrengs by growwe maalgroottes van bo $P_{70} = 129 \mu\text{m}$ getoon. Hierdie variasie is toegeskryf aan verbetering in waardemineraalbevryding van flottasietoevererts uit geslote saamgestelde deeltjies tot die maksimum moontlike teoretiese bevrydingsscenario van ten volle bevryde waardemineraaldeeltjies. 'n Persentasiepuntverbetering van 7.2 in die kumulatiewe algemene opbrengs van waardemineraal en 'n persentasiepuntverbetering van 2 tot 3 in die verrykingsratio is ook bo die $P_{70} = 250 \mu\text{m}$ -maalgroottes waargeneem ná verbetering van die bevryding van die waardemineraaldeeltjies van die flottasietoevererts van 'n tipiese flottasieaanlegtoevoer tot die maksimum. Die toenames in graad en kumulatiewe opbrengs by growwe groottes is toegeskryf aan verbetering in die bevryding van die waardemineraaldeeltjies van die flottasietoevererts. Op grond van die resultate is daar tot die gevolgtrekking gekom dat toepassing van mikrogolftegnologie groter voordele in stroomaf-verwerking van grofgemaalde ertse sal bied.

i. ACKNOWLEDGEMENTS

The author wishes to acknowledge the following people and organizations that made this project possible. Prof Steven Bradshaw who supervised this research and provided all the necessary support that was required to complete the research. The author would also like to thank Dr Ali Abubeker for his help. Lastly the author would like thank his family and friends for all of their encouragement and support.

ii. TABLE OF CONTENTS

ABSTRACT.....	ii
OPSOMMING.....	iv
i. ACKNOWLEDGEMENTS.....	vi
ii. TABLE OF CONTENTS.....	vii
iii. NOMENCLATURE.....	xvii
1. INTRODUCTION.....	1
2. LITERATURE REVIEW.....	4
2.1. Comminution process optimisation.....	4
2.1.1. Developments in microwave heating of ores.....	5
2.1.2. Microwave assisted comminution in mineral processing.....	6
2.2. Flotation.....	9
2.2.1. Flotation Sub-processes.....	9
2.3. Flotation modelling.....	10
2.3.1. Collection zone modelling.....	10
2.3.2. Kinetic theory rate expression.....	11
2.3.2.1. Measurement of pulp flotation kinetics of minerals in flotation cells.....	11
2.4. Probability theory approach.....	17
2.4.1. Bubble-particle interaction theory.....	17
2.4.2. Determining overall collection zone efficiency.....	17
2.4.3. Fundamental model for calculating collection zone efficiency.....	18
2.4.3.1. Collision Efficiency.....	19
2.4.3.2. Attachment efficiency.....	23
2.4.3.3. Bubble-particle stability Efficiency.....	27
2.5. Calculating collection zone overall mineral recovery.....	28
2.5.1. Froth zone value mineral recovery.....	29
2.5.2. Studies into the factors that affect froth zone recovery.....	29
2.5.2.1. Froth structure.....	30
2.5.2.2. Froth zone sub-processes.....	30
2.6. Entrainment.....	31
2.6.1. Mechanisms of entrained material drainage.....	31
2.6.2. Main Factors that affect entrainment.....	31
2.6.3. Entrainment modelling.....	32
2.7. Froth recovery.....	34
2.7.1. Methods for obtaining the froth zone recovery.....	34

2.8.	Water recovery	36
2.8.1.	Modelling water recovery	36
3.	METHODOLOGY	39
3.1.	The fundamental property based flotation model	39
3.1.1.	The bubble-particle collision frequency	40
3.1.2.	Calculation of the elementary processes.....	45
3.1.2.1.	Collision efficiency determined by the Generalised Sutherland equation (GSE)	46
3.1.2.2.	Attachment Efficiency determined by the Dobby-Finch attachment model	47
3.1.2.3.	Particle-bubble stability efficiency determined by Schulze model	49
3.2.	General flotation model parameter determination for model calibration.....	50
3.2.1.	Determination of particle Contact angle	50
3.2.1.1.	Composite particles contact angle calculation.....	51
3.2.2.	Energy dissipation.....	52
3.2.3.	Bubble diameter	53
3.2.3.1.	McGill bubble viewer	53
3.2.3.2.	UCT bubble size analyser.....	53
3.2.4.	Bubble rise velocity	54
3.3.	HSC Chemistry 7 simulation software.....	54
3.3.1.	Particle tracking in HSC Chemistry Simulation software	54
3.3.2.	Particles (Mineral) mode.....	54
3.3.2.1.	True particle modelling in HSC Chemistry Simulation software using MLA data	55
3.4.	Integrating the Fundamental model into HSC Chemistry 7	55
3.5.	Conclusion.....	57
4.	CREATION OF ARTIFICIAL FEED ORES.....	58
4.1.	Introduction	58
4.2.	Copper 1 and Copper 2 base case feed ore (BC).....	58
4.2.1.	Copper 1 mineralogy ($P_{70} = 120 \mu\text{m}$)	60
4.2.2.	Copper 2 mineralogy.....	62
4.3.	Artificial flotation feed ores	64
4.3.1.	Methodology	64
4.3.2.	Copper 1 group artificial ores	66
4.3.2.1.	Fully liberated ore (FL)	67
4.3.2.2.	Fully locked ore (LC)	69

4.3.2.3.	Ore 1	72
4.3.2.4.	Ore 2	74
4.3.2.5.	Ore 3	77
4.3.3.	Copper 2 artificial ores.....	79
4.3.3.1.	Fully liberated ore.....	79
4.3.3.2.	Fully locked ore (LC)	80
4.3.3.3.	Ore 1	81
4.3.3.4.	Ore 2	82
4.3.3.5.	Ore 3	83
4.4.	Contact angle calculations Method	84
4.4.1.	Contact angle calculation results and discussion	84
4.5.	Conclusion.....	86
5.	SINGLE CELL FLOWSHEET SIMULATION.....	87
5.1.	Comparison of simulated recovery trends with experimental trends	87
5.2.	Continuous single cell flow sheet simulation.....	90
5.3.	Analysis of simulation results using the Particle analysis tool in HSC Chemistry Simulation Software.....	92
5.4.	Effects of changes in feed ore liberation on single Cell recovery.....	97
5.4.1.	Methodology	98
5.4.2.	Copper 1 feed ore ($P_{70} = 120 \mu\text{m}$): Results and discussion	99
5.4.2.1.	Sub-process bubble-particle interaction efficiency values	103
5.4.3.	Copper 2 feed ore ($P_{70} = 180 \mu\text{m}$): Results and discussion	107
5.4.3.1.	Sub-process efficiency values	109
5.4.3.2.	Feed ore Particle size sensitivity analysis.....	110
5.5.	The effects of feed ore particle size distribution on value mineral recovery	113
5.5.1.	Methodology	113
5.5.2.	Grind size sensitivity analysis results	116
5.6.	Conclusion.....	118
6.	SIMULATION OF FLOTATION PLANTS	119
6.1.	Rougher bank in series configuration simulation.....	119
6.2.	Effect of Feed ore liberation.....	123
6.2.1.	Methodology	123
6.2.2.	Copper 1 feed ore ($P_{70} = 120 \mu\text{m}$): Simulation results and discussion.....	124
6.2.3.	Copper 2 feed ore ($P_{70} = 180 \mu\text{m}$): Results and discussion	129
6.3.	Effect of Particle size distribution of the feed.....	135
6.3.1.	Methodology	135

6.3.2.	Operating plant Grind size sensitivity analysis results	136
6.4.	Conclusion.....	146
7.	CONCLUSIONS AND FUTURE WORK	147
8.	REFERENCES	150
	APPENDIX A MINERAL MODE OF OCCURRENCE FOR COPPER 2 ORE FEED	161
	APPENDIX B CALCULATED PARTICLE CONTACT ANGLE VALUES IN FEED ORE PER SIZE FRACTION	169
	APPENDIX C : MINERAL GROUPS IN COPPER FEED ORE	171
	APPENDIX D : ROUGHER CELLS IN SERIES PLANT FLOWSHEET CONFIGARATION	172
	APPENDIX E : FILE STRUCTURE IN HSC CHEMISTRY 7	173
	APPENDIX F : COPPER 1 BATCH FLOTATION EXPERIMENTAL PROCEDURE	174
	APPENDIX G : FLOTATION CELL SIMULATION INPUT VARIABLES....	175
	APPENDIX H : COPPER 1 AND COPPER 2 FLOTATION FEED ORE BULK PARTICLE WEIGHT DISTRIBUTION.....	176
	APPENDIX I SAMPLE MODEL WIZARD SCREEN CAPTURE IN HSC CHEMISTRY 7.....	182

Figure 2-1:	Mineral transport system in a flotation cell	9
Figure 4-1:	Base case feed ore cumulative particle size distribution.....	59
Figure 4-2:	Chalcopyrite mineral mode of occurrence in Copper 1 feed ore ($P_{70}=120 \mu\text{m}$) used as base case in the simulations.	61
Figure 4-3:	Pyrite mineral mode of occurrence in Copper 1 feed ore ($P_{70}=120 \mu\text{m}$) used as base case in the simulations.	61
Figure 4-4:	NSG mineral mode of occurrence in Copper 1 feed ore ($P_{70}=120 \mu\text{m}$) used as base case in the simulations.	62
Figure 4-5:	Chalcopyrite mineral mode of occurrence in Copper 2 feed ore ($P_{70}=180 \mu\text{m}$) used as base case in the simulations	63
Figure 4-6:	Pyrite mineral mode of occurrence in Copper 2 feed ore ($P_{70}=180 \mu\text{m}$) used as base case in the simulations.	63
Figure 4-7:	NSG mineral mode of occurrence in Copper 2 feed ore ($P_{70}=180 \mu\text{m}$) used as base case in the simulations.	64
Figure 4-8:	Chalcopyrite mineral mode of occurrence in fictional FL artificial feed ore with a P_{70} grind size of $120 \mu\text{m}$	68
Figure 4-9:	Pyrite mineral mode of occurrence in fictional FL artificial feed ore with a P_{70} grind size of $120 \mu\text{m}$	68
Figure 4-10:	NSG mineral mode of occurrence in fictional FL artificial feed ore with a P_{70} grind size of $120 \mu\text{m}$	69
Figure 4-11:	Chalcopyrite mineral mode of occurrence in LC artificial feed ore with a P_{70} grind size of $120 \mu\text{m}$	70

Figure 4-12: Pyrite mineral mode of occurrence in LC artificial feed ore with a P ₇₀ grind size of 120µm.....	71
Figure 4-13: NSG mineral mode of occurrence in LC artificial feed ore with a P ₇₀ grind size of 120 µm.....	71
Figure 4-14: Chalcopyrite mineral mode of occurrence in Ore 1 artificial feed ore with a P ₇₀ grind size of 120 µm.	73
Figure 4-15: Pyrite mineral mode of occurrence in Ore 1 artificial feed ore with a P ₇₀ grind size of 120 µm.....	73
Figure 4-16: NSG mineral mode of occurrence in Ore 1 artificial feed ore with a P ₇₀ grind size of 120 µm.....	74
Figure 4-17: Chalcopyrite mineral mode of occurrence in fictional Ore 2 artificial feed ore with a P ₇₀ grind size of 120 µm.	75
Figure 4-18: Pyrite mineral mode of occurrence in fictional Ore 2 artificial feed ore with a P ₇₀ grind size of 120 µm.	76
Figure 4-19: NSG mineral mode of occurrence in fictional Ore artificial feed ore with a P ₇₀ grind size of 120 µm.	76
Figure 4-20: Chalcopyrite mineral mode of occurrence in Ore 3 artificial feed ore with a P ₇₀ grind size of 120 µm.	78
Figure 4-21: Pyrite mineral mode of occurrence in Ore 3 artificial feed ore with a P ₇₀ grind size of 120 µm.....	78
Figure 4-22: NSG mineral mode of occurrence in Ore 3 artificial feed ore with a P ₇₀ grind size of 120 µm.....	79
Figure 4-23: Comparison of contact angle values calculated using the weight composition % against those calculated utilising the surface area %.....	85
Figure 4-24: Contact angle variation with mineral particles liberation class for all feed particle size fractions	85
Figure 4-25: Comparison mineral recovery values obtained using the weight composition % calculated contact angles in the flotation model against those calculated utilising the surface area % calculated contact angles.....	86
Figure 5-1: Simulated batch flotation mineral recovery for Copper 1 BC feed	88
Figure 5-2: Experimentally determined batch flotation cell mineral recovery for Copper 1. .	89
Figure 5-3: Single unit flotation cell flow sheet simulation layout in HSC Chemistry 7 Simulation software.	91
Figure 5-4: Chalcopyrite mineral mode of occurrence in Copper 1 base case feed ore stream to the single flotation cell flow sheet simulation. From Figure 5-4 it can be observed that most of the fully liberated Chalcopyrite in the Copper 1 ground ore feed is found between the 0 to 75 µm size fractions.....	92
Figure 5-5: Chalcopyrite mineral mode of occurrence in Copper 1 base case concentrate product stream from the single flotation cell flow sheet simulation.....	93
Figure 5-6: Chalcopyrite mineral mode of occurrence in Copper 1 base case ore tails product stream from the Single flotation cell flow sheet simulation.	93
Figure 5-7: Mineral recovery against particle size for a Single flotation Cell simulation (Copper 1 BC feed).....	94
Figure5-8: Particle class recovery per size fraction in the concentrate stream against Cpy wt %	95
Figure 5-9: Particle class recovery per size fraction in the tails stream against Chalcopyrite wt % range in particle classes.	95
Figure 5-10: Cumulative liberation of Chalcopyrite in feed stream to the Single Unit flotation Cell flow sheet simulation.	96

Figure 5-11: Cumulative liberation of Chalcopyrite in the output tail stream from the Single Unit flotation Cell flow sheet simulation.	96
Figure 5-12: Cumulative liberation of Chalcopyrite in the output concentrate stream from the Single Unit flotation Cell flow sheet simulation.	97
Figure 5-13: Chalcopyrite recovery against particle size for a single flotation Cell simulation for all the feed ore liberation scenarios considered in the simulations ($P_{70}=120\ \mu\text{m}$).	100
Figure 5-14: Pyrite recovery against particle size for a Single flotation Cell simulation for all the feed ore liberation scenarios considered in the simulations, ($P_{70}=120\ \mu\text{m}$).	101
Figure 5-15: Pyrite recovery against particle size for a Single flotation Cell simulation for all the feed ore liberation scenarios considered in the simulations, ($P_{70}=120\ \mu\text{m}$).	102
Figure 5-16: Mean Stability efficiency against mean particle size for feed ore with a $P_{70} = 120\ \mu\text{m}$	104
Figure 5-17: Mean Stability efficiency against mean particle size for Base Case ore and the two extreme liberation cases (FL and LC), for feed ore with a $P_{70} = 120\ \mu\text{m}$	105
Figure 5-18: Mean attachment efficiency against mean particle size for feed ore with a $P_{70} = 120\ \mu\text{m}$	105
Figure 5-19: Mean Attachment efficiency against mean particle size for Base Case ore and the two extreme liberation cases (FL and LC), for feed ore with a $P_{70} = 120\ \mu\text{m}$	106
Figure 5-20: Chalcopyrite recovery against particle size for a Single flotation Cell simulation for all the feed ore liberation scenarios considered in the simulations, ($P_{70}=180\ \mu\text{m}$).	107
Figure 5-21: Pyrite recovery against particle size for a Single flotation Cell simulation for all the feed ore liberation scenarios considered in the simulations, ($P_{70}=180\ \mu\text{m}$).	108
Figure 5-22: Mean Stability efficiency against mean particle size for feed ore with a $P_{70} = 180\ \mu\text{m}$	109
Figure 5-23: Mean attachment efficiency against mean particle size for feed ore with a $P_{70} = 180\ \mu\text{m}$	110
Figure 5-24: Chalcopyrite recovery against particle size for a Single flotation Cell ($P_{70}=63\ \mu\text{m}$).	111
Figure 5-25 : Chalcopyrite recovery against particle size for a Single flotation Cell simulation ($P_{70}=250\ \mu\text{m}$).	112
Figure 5-26: Cumulative particle weight distribution plot of the various P_{70} grind sizes that were considered in the simulations.	114
Figure 5-27: Overall single cell unit recovery against particle size for feed ore with varying size distributions.	116
Figure 5-28: Concentrate mass recovery in a Single cell plotted against feed ore into the cell with varying size distributions.	117
Figure 5-29: Enrichment ration in a Single cell plotted against feed ore into the cell with varying size distributions.	117
Figure 6-1: Cumulative value Copper recovery as a function of cell number in the rougher flotation section of a Simulated fictional plant.	120
Figure 6-2: Cumulative value Copper recovery as a function of cell number in the rougher flotation section of an operating plant (Yianatos et al., 2006).	121
Figure 6-3: Concentrate mass recovery as a function of cell number in the rougher flotation section of simulated fictional plant.	121
Figure 6-4: Concentrate mass recovery as a function of cell number in the rougher flotation section of an operating plant (Yianatos et al., 2006)	122
Figure 6-5: Local and cumulative copper grade profile as a function of cell number for a fictional copper plant	122
Figure 6-6: Comparison of Cu cumulative recovery per cell in a Rougher bank for different feed ore scenarios.	125

Figure 6-7: Comparison of Cu cumulative recovery per cell in a Rougher bank for the base case and extreme feed ore scenarios.	125
Figure 6-8: Comparison of Pyrite cumulative recovery per cell in a Rougher bank for the base case and extreme feed ore scenarios.	126
Figure 6-9: Comparison of concentrate mass recovery per unit cell in a Rougher bank for different feed ore scenarios.	127
Figure 6-10: Comparison of Cu local grade per unit cell in a Rougher bank for different feed ore scenarios.	128
Figure 6-11: Comparison of Cu cumulative grade per unit cell in a Rougher bank for different feed ore scenarios.	128
Figure 6-12: Comparison of overall rougher bank value mineral enrichment ratio for different feed ore scenarios.	129
Figure 6-13: Comparison of Cu cumulative recovery per cell in a Rougher bank for different feed ore scenarios.	130
Figure 6-14: Comparison of Cu cumulative recovery per cell in a rougher bank for the base case and extreme feed ore scenarios.	131
Figure 6-15: Comparison of Pyrite cumulative recovery per cell in a Rougher bank for the base case and extreme feed ore scenarios.	132
Figure 6-16: Comparison of concentrate mass recovery per unit cell in a Rougher bank for different feed ore scenarios.	133
Figure 6-17: Comparison of Cu local grade per unit cell in a Rougher bank for different feed ore scenarios.	133
Figure 6-18 : Comparison of Cu Cumulative grade per unit cell in a Rougher bank for different feed ore scenarios ($P_{70} = 180 \mu\text{m}$).	134
Figure 6-19: Comparison of overall rougher bank value mineral enrichment ratio for different feed ore scenarios.	134
Figure 6-20: Overall a nine cell in series rougher bank recovery against particle size for feed ore grind size.	136
Figure 6-21: Concentrate mass recovery for a nine cell in series Rougher bank plotted against feed ore into the rougher section with varying feed grind size.	137
Figure 6-22: Enrichment ratio for a nine cell in series rougher bank plotted against feed ore into the rougher section with varying size distributions.	138
Figure 6-23: Cumulative Cu value mineral recovery as a function of cell number for a rougher bank processing BC, FL and LC feed ores.	139
Figure 6-24: Cumulative copper grade profiles as a function of cell for a rougher bank processing BC, FL and LC feed ores.	139
Figure 6-25: Cumulative Cu value mineral recovery as a function of cell number for a rougher bank processing BC, FL and LC feed ores.	140
Figure 6-26: Cumulative copper grade profiles as a function of cell number for a rougher bank processing BC, FL and LC feed ores.	140
Figure 6-27: Cumulative Cu value mineral recovery as a function of cell number in the rougher section of a fictional simulated nine cell in series flotation plant processing BC, FL and LC feed ore with a P_{70} grind size of $252\mu\text{m}$	142
Figure 6-28: Cumulative copper grade profiles as a function of cell for a rougher bank processing BC, FL and LC feed ores.	142
Figure 6-29: Cumulative Cu value mineral recovery as a function of cell number for a rougher bank processing BC, FL and LC feed ores.	143
Figure 6-30: Cumulative copper grade profiles as a function of cell number for a rougher bank processing BC, FL and LC feed ore.	144

Figure 6-31: Cumulative Cu value mineral recovery as a function of cell number for a rougher bank processing BC, FL and LC feed ores.....	144
Figure 6-32: Local and cumulative copper grade profiles as a function of cell number for a rougher bank processing BC, FL and LC feed ores.....	145
Figure A.1-1: Chalcopyrite mineral mode of occurrence in FL feed ore ($P_{70}=180\ \mu\text{m}$) used in the simulations.	161
Figure A.1-2: Pyrite mineral mode of occurrence in FL feed ore ($P_{70}=180\ \mu\text{m}$) used in the simulations.	161
Figure A.1-3: NSG mineral mode of occurrence in FL feed ore ($P_{70}=180\ \mu\text{m}$) in the simulations.	162
Figure A.1-4: Chalcopyrite mineral mode of occurrence in LC feed ore ($P_{70}=180\ \mu\text{m}$) used in the simulations.	162
Figure A.1-5: Pyrite mineral mode of occurrence in LC feed ore ($P_{70}=180\ \mu\text{m}$) used in the simulations.	163
Figure A.1-6: NSG mineral mode of occurrence in LC feed ore ($P_{70}=180\ \mu\text{m}$) used in the simulations.	163
Figure A.1-7: Chalcopyrite mineral mode of occurrence in Ore 1 feed ore ($P_{70}=180\ \mu\text{m}$)...	164
Figure A.1-8: Pyrite mineral mode of occurrence in Ore 1 feed ore ($P_{70}=180\ \mu\text{m}$).....	164
Figure A.1-9: NSG mineral mode of occurrence in Ore 1 feed ore ($P_{70}=180\ \mu\text{m}$).	165
Figure A.1-10: Chalcopyrite mineral mode of occurrence in Ore 2 feed ore ($P_{70}=180\ \mu\text{m}$).	165
Figure A.1-11: Pyrite mineral mode of occurrence in Ore 2 feed ore ($P_{70}=180\ \mu\text{m}$).....	166
Figure A.1-12: NSG mineral mode of occurrence in Ore 2 feed ore ($P_{70}=180\ \mu\text{m}$).	166
Figure A.1-13: Chalcopyrite mineral mode of occurrence in Ore 3 feed ore ($P_{70}=180\ \mu\text{m}$).	167
Figure A.1-14: Pyrite mineral mode of occurrence in Ore 3 feed ore ($P_{70}=180\ \mu\text{m}$).....	167
Figure A.1-15: NSG mineral mode of occurrence in Ore 3 feed ore ($P_{70}=180\ \mu\text{m}$).	168
Figure B.1-1: Contact angle variation with particle liberation class for liberation particle classes in the 0-38 μm size fraction.	169
Figure B.1-2: Contact angle variation with particle liberation class for liberation particle classes in the 106-150 μm size fractions.	169
Figure B.1-3: Contact angle variation with particle liberation class for liberation particle classes in the 300-425 micron size fraction.	170
Figure D.1-1: Rougher cell flow sheet configuration that was used in the study.....	172
Figure E.1-1: File structure in HSC Sim in the Particle (Minerals) Mode adapted from HSC Chemistry 7 manual (Roine, 2010).....	173
Figure I.1-1: Sample screen capture of model wizard screen as it would appear in HSC Chemistry 7.....	182
Figure I.1-2: Sample HSC Chemistry Simulation macro commands in HSC Chemistry 7 that form part of the model wizard.	183
Table 2-1: Summary of expressions describing the floatability component method.....	15
Table 2-2: Summary of expressions for obtaining pulp kinetics utilising the MFT test procedure.....	16
Table 2-3: Summary of collision efficiency models found in literature.....	20
Table 2-4: Summary of sliding models found in literature.....	25
Table 2-5: Summary of factors that affect entrainment.....	32
Table 2-6: Summary of methods for obtaining froth zone recovery	35
Table 2-7: Summary of water recovery models found in literature.....	37
Table 3-1: Summary of the mechanical and primary turbulence terms expressions.....	44
Table 3-2: Model calibration parameters from a study carried out by (Ralston et al., 2007)..	50

Table 4-1: Base case feed ore particle size distribution of Copper 1 ($P_{70}=120 \mu\text{m}$) and Copper 2 ($P_{70}=180 \mu\text{m}$).....	59
Table 4-2 : Mineral composition by size fraction of Copper 1 base case feed ore $P_{70}=120 \mu\text{m}$	60
Table 4-3: Mineral composition by size fraction of Copper 2 base case feed ore $P_{70}=180 \mu\text{m}$	62
Table 4-4: HSC Chemistry 7 feed ore stream file showing liberation profile for particle liberation classes in the 0-38 μm size fraction.....	65
Table 4-5: A summary of the feed ore scenarios that were used in investigating the effects of feed ore liberation changes on the downstream flotation process.	66
Table 4-6: Differences in liberation classes' weights in FL artificial ore expressed as a percentage of Copper 1 base case feed ore liberation classes.....	67
Table 4-7: Differences in liberation classes' weights in LC artificial ore expressed as a percentage of Copper 1 base case feed ore liberation classes.....	70
Table 4-8: Differences in liberation classes' weights in Ore 1 artificial ore expressed as a percentage of Copper 1 base case feed ore liberation classes.....	72
Table 4-9: Differences in liberation classes weights in Ore 2 artificial ore expressed as a percentage of Copper 1 base case feed ore liberation classes.....	75
Table 4-10: Differences in liberation classes' weights in Ore 3 artificial ore expressed as a percentage of Copper 1 base case feed ore liberation classes.....	77
Table 4-11: Differences in liberation classes' weights in FL liberated artificial ore expressed as a percentage of Copper 2 base case feed ore liberation classes	80
Table 4-12: Differences in liberation classes' weights in LC liberated artificial ore expressed as a percentage of Copper 2 base case feed ore liberation classes	81
Table 4-13: Differences in liberation classes' weights in Ore 1 liberated artificial ore expressed as a percentage of Copper 2 base case feed ore liberation classes.....	82
Table 4-14: Differences in liberation classes' weights in Ore 2 liberated artificial ore expressed as a percentage of Copper 2 base case feed ore liberation classes	82
Table 4-15: Differences in liberation classes' weights in Ore 3 liberated artificial ore expressed as a percentage of Cu 2 base case feed ore liberation	83
Table 5-1: Summary of input parameter values used in simulating experimental batch flotation test carried out on the Copper 1BC feed	88
Table 5-2: Feed and literature hydrodynamic variables that were used in simulating a Single flotation cell flow sheet operation.....	90
Table 5-3: Summary of Single flotation cell flow sheet simulation grade recovery and mass full performance indicators results.....	91
Table 5-4: Feed and literature hydrodynamic variables that were used in simulating a Single flotation cell flow sheet operation.....	99
Table 5-5: Simulated flotation process key performance parameters for the six feed ore scenarios that were considered for the base case grind size $P_{70}=120$ microns	103
Table 5-6: Simulated flotation process key performance parameters for the six feed ore scenarios that were considered for the base case grind size $P_{70}=180$ microns	109
Table 5-7: Fictional average fine particle sizes and used in the sensitivity analysis investigations ($P_{70} = 63 \mu\text{m}$)	111
Table 5-8: Fictional average coarse particle size distribution ($P_{70} = 250\mu\text{m}$).....	112
Table 5-9: Particle cumulative weight distribution of the different feed ores considered in carrying out the feed particle weight distribution sensitivity analysis.....	114
Table 5-10: Cu% feed grades at different feed grind sizes	115
Table C.1-1: Main mineral groups in feed ores and their grouping.....	171
Table C.1-2: Mineral groups in feed ores	171

Table G.1-1: Input variables used in calibrating the fundamental property based model in simulating the flotation process.	175
Table H.1-1: 0-38 μm bulk particle size class weight % for Copper 1 flotation feed ores ($P_{70} = 120 \mu\text{m}$).....	176
Table H.1-2: 38-53 μm bulk particle size class weight % for Copper 1 flotation feed ores ($P_{70} = 120 \mu\text{m}$).....	176
Table H.1-3: 53-75 μm bulk particle size class weight % for Copper 1 flotation feed ores ($P_{70} = 120 \mu\text{m}$).....	176
Table H.1-4: 75-106 μm bulk particle size class weight % for Copper 1 flotation feed ores ($P_{70} = 120 \mu\text{m}$)	177
Table H.1-5: 106-150 μm bulk particle size class weight % for Copper 1 flotation feed ores ($P_{70} = 120 \mu\text{m}$)	177
Table H.1-6: 150-212 μm bulk particle size class weight % for Copper 1 flotation feed ores ($P_{70} = 120 \mu\text{m}$)	177
Table H.1-7: 212-300 μm bulk particle size class weight % for Copper 1 flotation feed ores ($P_{70} = 120 \mu\text{m}$)	178
Table H.1-8: 300-425 μm bulk particle size class weight % for Copper 1 flotation feed ores ($P_{70} = 120 \mu\text{m}$)	178
Table H.2-1: 0-38 μm bulk particle size class weight % for Copper 2 flotation feed ores ($P_{70} = 180 \mu\text{m}$).....	179
Table H.2-2: 38-53 μm bulk particle size class weight % for Copper 1 flotation feed ores ($P_{70} = 180 \mu\text{m}$).....	179
Table H.2-3: 53-75 μm bulk particle size class weight % for Copper 1 flotation feed ores ($P_{70} = 180 \mu\text{m}$).....	179
Table H.2-4: 75-106 μm bulk particle size class weight % for Copper 1 flotation feed ores ($P_{70} = 180 \mu\text{m}$)	180
Table H.2-5: 106-150 μm bulk particle size class weight % for Copper 1 flotation feed ores ($P_{70} = 180 \mu\text{m}$)	180
Table H.2-6: 150-212 μm bulk particle size class weight % for Copper 1 flotation feed ores ($P_{70} = 180 \mu\text{m}$)	180
Table H.2-7: 212-300 μm bulk particle size class weight % for Copper 1 flotation feed ores ($P_{70} = 180 \mu\text{m}$)	181
Table H.2-8: 300-425 μm bulk particle size class weight % for Copper 1 flotation feed ores ($P_{70} = 180 \mu\text{m}$)	181
Table H.2-9: 425-850 μm bulk particle size class weight % for Copper 1 flotation feed ores ($P_{70} = 180 \mu\text{m}$)	181

iii. NOMENCLATURE

Alphabetic Symbols

- A - cross sectional area of the pulp-froth interface [m^2]
a - empirically fitted parameter in the water recovery model
 A_s - is an empirical dimensionless constant with a value of 0.5
b - empirically fitted parameter
 C_a - Concentration of mineral A [$tons/m^3$]
 CF_i - classification function
 C_{Water} - Amount of water in the concentrate [tons]
 d_{32} - Sauter mean bubble diameter [m]
 d_b - Bubble size [m]
 d_p - is the particle size [m]
 d_{pb} - is the bubble-particle aggregate diameter [m]
 E_1 - the potential energy barrier of a particle approaching a bubble [J]
 E' - is the volumetric flow of entrained material [$tons/ m^3$]
 E_a - Attachment efficiency
 E_c - Collision efficiency
 E_{coll} - collection efficiency
 E_{C-PL}^{in} - inertial effect
 E_{C-WP}^g - gravitational effects
 E_K - kinetic energy of a particle approaching a bubble [J]
 ENT_i - degree of entrainment
 E_s - Stability efficiencies efficiency
 E_{Sc}^{ic} - Interceptional effect
 F_{att} - attachment forces
 F_b - Buoyancy of the particle volume immersed in the liquid phase [N]
 F_c - capillary force [N]
 F_d - is the additional detaching forces [N]
 F_{det} - Detachment forces [N]
 F_g - gravitational force [N]
 F_h - Hydrostatic pressure force on the area enclosed by the three-phase contact [N]
 F_S - is the mass flow rate of the solid [N]

F_{Water} -Water contained in the feed [N]
 F_{σ} - is the capillary pressure in the bubble [N]
 g -Acceleration due to gravity [m/s^2]-
 G_{fr} -gas flow rate and the [m^3/min]
 J_g -Superficial gas velocity [m/s]
 k -Overall first order rate constant [min^{-1}]
 k_{avg} -the weighted average flotation rate, excluding un-floatable particles [min^{-1}]
 k_c -Collection zone first order rate constant [min^{-1}]
 K_i -is the flotation is rate constant of particles of diameter I [min^{-1}]
 k_{ij} -rate parameter for jth mineral phase from in ith size fraction [min^{-1}]
 k_j -rate parameter for jth mineral phase [min^{-1}]
 k_n - nth order rate constant [min^{-1}]
 k_{wd} -drainage rate constant of the water [min^{-1}]
 L -half the impeller blade width [m]
 M_{conc} -Mass of solids suspended in the water in the concentrate [tons]
 M_{pulp} -Mass of solids suspended in the water in the pulp phase [tons]
 n -order of reaction
 N_b -bubble number density [m^{-3}]
 N_p -number of particles per unit volume [m^{-3}]
 P_{ij} -Ore floatability for component j in the ith size fraction
 $P(k_j)$ -Cumulative weight per cent
 P_w -constant for a given flotation system
 q -turbulent kinetic energy [J]
 Q_w -is the volumetric flow rate of water [tons/s]
 r_b -bubble radius [m]
 R_{cw} -is the recovery of the water from the pulp
 R_{eb} - reynolds number
 $R_{\text{entrainment},i}$ -determining recovery by entrainment
 R_f -Froth recovery
 R_{ij} -Recovery of jth mineral phase from ith size fraction
 $R_{\text{max},i}$ - is the flotation recovery at an infinite time
 r_p -are the particle radius [m]

- R_w - water recovery
 $R_{\infty i,j}$ -Ultimate recovery of jth mineral phase from ith size fraction
 S_b -bubble surface area flux [s^{-1}]
 SG_p -is the specific gravity of the slurry
 SG_s - is the specific gravity of the solids
 SG_w -is the specific gravity of the water
 t - Flotation time [s]
 t_{fl} -film drainage time [s]
 t_{fr} -bubble-particle film rupture time [s]
 (t_{ind}) - induction time [s]
 t_r - residence time of bubbles in the unit volume [s]
 t_{TPLC} -three-phase contact line expansion and stabilization time [s]
 $\bar{U}_x, \bar{U}_y, \bar{U}_z$ -root mean square of fluctuations of the turbulent fluid velocities [m/s]
 V - is the froth volume [m^3]
 v_b -Bubble rising velocity [m/s]
 v_p -Bubble rising velocity [m/s]
 V_{fl} -average fluid velocity [m/s]
 V_x^2, V_y^2, V_z^2 -Velocity measurements in the x,y,z direction [m/s]
 Z_{pb} -is the collision frequency per unit volume between particles and bubbles

Greek Symbols

- α -a measurement of the spread in the k-distribution
 α -fraction of the froth on the surface that eventually reports to the concentrate
 α_a -fraction of air leaving the cell as un-burst bubbles
 β -dimensionless number in the Generalised Sutherland Equation
 β_w -constant in water recovery model [s^{-1}]
 $\gamma_{s/a}, \gamma_{s/l}, \gamma_{l/a}$ -solid-vapour, solid-liquid, and liquid-vapour interfacial tensions [N/m]
 ε -turbulent dissipation energy [m^2/s]
 η -water dynamic viscosity [m^2/s]
 θ -contact angle [rad]
 θ_a -adhesion angle [rad]
 θ_c -collision angle [rad]

θ_t	-is the maximum collision angle [rad]
ρ_i	-refers to the density of the bubble or particle [kg/m ³]
ρ_w	-water density [kg/m ³]
$\Delta\rho$	-is the density difference between the solid and liquid [kg/m ³]
$\Delta\rho_b$	-particle and fluid density diff [kg/m ³]
ρ_{fl}	-fluid density [kg/m ³]
ρ_p	-particle density [kg/m ³]
ψ_c^0	-value of stream function of the bubble equator [-]
ψ_c	- value of streamline stream function that coincides with the grazing trajectory [-]
ω_{top}	-is the solids mass fraction below the pulp-froth interface [-]
τ	-residence time in the unit [s]
τ_f	-mean froth residence time [s]
μ_s	-is the interstitial slurry viscosity [m ² /s]
Ω ,	-constant value in first order water recovery model [-]
q	-constant values in first order water recovery model [m ⁻³]
χ	-constant value in first order water recovery model [s ⁻¹]
δ	-the volume of water per surface area of the air bubbles [m]
ϑ	-is the kinematic viscosity [m ² /s]
Θ	-kinematic viscosity [m ² /s]
γ	-Surface tension [N/m]

CHAPTER ONE

1. INTRODUCTION

Microwave assisted comminution has been recommended as a possible commercially viable thermal treatment method for reducing comminution energy and improving value mineral liberation in the ores (Haque, 1999; Kingman and Rowson, 1998). Recent work has shown that microwave treatment of secondary crusher product at specific microwave energy consumption of the order of 1 kWh/t reduces the work index of the ore and increases grade and recovery in batch flotation tests (Kobusheshe, 2010). Improved liberation at coarse sizes was also demonstrated (Scott et al., 2008). Based on these findings work is ongoing to commercialise the technology. However, before the technology can be commercialised, key issues surrounding the industrial scale application of microwave assisted comminution need to be addressed. One of these issues is assessing the benefits of microwave treatment on downstream processing of ores.

The study of the downstream processing benefits of microwave treated ore on an operating plant is an area that has not been well researched (Kingman, 2006). This is in contrast to investigations into the benefits relating to reduced comminution energy due to microwave treatment which have been reported by a number of authors (Kingman et al., 2000a; Kingman et al., 2004b; Jones et al., 2005). The limited research has been the result of the technical and operational difficulties associated with assessing the improvement in feed ore liberation properties due to microwave treatment on an operating plant and quantifying the downstream processing benefits. Further, appropriate microwave applicators with the ability to treat continuous feed ore input on a plant scale have not been designed yet (Kobusheshe, 2010; AMIRA:P879A, 2009). To overcome such challenges, ideally, modelling techniques could offer a solution to these problems (Scott et al., 2008). There is therefore a need to develop a modelling framework for investigating the value proposition of microwave treated ore.

Current available models for describing flotation mineral processing operations do not include feed ore particle liberation as an input parameter. This is because most of the models were developed to simulate the behaviour of feeds derived from comminution processes which resulted from random fracture of the ore particles (Ali and Bradshaw, 2009). The use of microwave treatment has been observed to result in non random fracture of feed ore particles, preferentially along the grain boundaries during crushing hence resulting in a more

liberated comminution product to the flotation section (Kingman et al., 2000a). Thus, when modelling the downstream processing of microwave treated ore in a mineral processing flow sheet, feed liberation is an important variable. It is therefore necessary to develop a modelling framework for quantifying the benefits of microwave treated ore that captures this important variable.

The development of Mineral Liberation Analysers and simulation software that utilises MLA data as input in modelling mineral processes presents an opportunity for investigating the downstream processing effects of microwave treated ore through the use of process modelling and simulation techniques. These software packages such as HSC Chemistry 7.0 Simulation Software utilise what is termed as true particle modelling for simulating mineral processing operations. True particle modelling allows for the use of algorithms for tracking feed ore particles as represented in the MLA feed data to the software through the flotation circuit (Roine, 2010). This allows for liberation properties of the streams around the circuit to be analysed and for the use of liberation as an input variable in the flow sheet units modelling. However, models for unit operations that capture the effects of liberation property of the feed are in general yet to be integrated into these software packages. Of particular importance in establishing the value proposition for microwave treatment of ore would be the ability to model the effects of liberation explicitly in a flow sheet simulator. At present such models exist, e.g. the fundamental property based model for describing the flotation process (Pyke et al., 2003). However their incorporation into a flow sheet modelling package to utilise particle class tracking behaviour has not yet been achieved. The incorporation of such a model into an appropriate simulation package would allow for the simulation of a flotation plant flow sheet for investigating the value proposition of microwave treated ore.

Fundamental property based models offers the possibility of predicting flotation rate constants and hence flotation cell recovery of the particles from hydrodynamic and particle based properties. The model factors in mineral liberation as an input variable in the calculations (Pyke et al., 2003). The inclusion of the mineral liberation property is essential as liberation is the main difference between microwave treated and untreated ores. The model allows for the prediction of the flotation behaviour of each individual particle unlike the traditional methods that calculate recovery on a size fraction basis. Such models have not yet been adapted in most commercial modelling software. This thesis applies the fundamental property based model to MLA data. There is no reported work that has attempted to apply the model in true particle modelling.

Study aims and objectives

The aim of the study was to develop a modelling framework to determine the value proposition of microwave treatment of ore. This was to be done by incorporating a fundamental property based model into a flow sheet simulator. Using the framework it was the further objective of this work to investigate the effects of flotation feed ore liberation and grind size variation on a simulated single flotation cell and rougher bank flow sheet. By utilizing MLA data for real flotation feeds, various feed ore liberation scenarios and grind sizes were to be artificially generated by manipulating the liberation and grind size characteristics of typical industrial flotation feed ores. These generated artificial feed ores along with the typical flotation feed ores were then to be used in investigating the downstream flotation processing behavior of microwave enhanced liberated flotation feed ore. The work carried out in the study is presented as follows:

- Chapter 2 - A literature review of work performed in the field of microwave assisted comminution is presented in this chapter. This is followed by a literature review of flotation modelling in mineral processing.
- Chapter 3 - A description of the fundamental property model used in this study is presented in this chapter along with a presentation of the parameters that were used to calibrate the model. A review of HSC Chemistry Software and its operation is presented along with the method that was used to integrate the fundamental property based model into the software.
- Chapter 4 - A description of the feed ores used in this study is detailed in this chapter. The method that was used in creating artificial feed ore is discussed in this chapter.
- Chapter 5 - The results of simulations carried out on a Single Rougher flotation cell flow sheet utilising various ore feeds is presented in this chapter along with a discussion of these results.
- Chapter 6 - The results of simulations carried out on a fictional Rougher bank flotation cell flow sheet utilising various ore feeds is presented in this chapter along with a discussion of these results.
- Chapter 7 - This chapter presents the conclusions drawn from this study along with recommendations for future studies.

CHAPTER TWO

2. LITERATURE REVIEW

2.1. Comminution process optimisation

The extraction of mineral values from ore requires liberation of the minerals followed by separation. Liberation is achieved by size reduction operations which are inefficient processes, typically accounting for up to 70% of the energy consumption in a mineral concentrator (Tromans, 2008). The major cause of the inefficiency of the comminution process is the transformation of some of the mechanical energy into heat and noise in transmissions and friction processes among particles that do not result in their breakage. As the grade of ore reserves declines future viability of mineral operations will be determined by the costs of comminution. Research over the years has focused developing technologies that reduce the energy of comminution in the process resulting in increased liberation of value minerals. The extra revenue realised from increased value mineral recovery due to improved liberation, will be the trade off to the capital required to implement and install these methods (Haque, 1999; Kingman et al., 2004c; Kingman and Rowson, 1998; King, 1993).

Thermal pre-treatment has been an option that has been considered as a possible way of improving mineral liberation and reducing mineral ore strength hence energy of comminution (King, 1993; Haque, 1999). This is because different mineral phases in an ore have different microwave absorption and varying thermal expansion rates. Thus, thermal heating of mineral ores results in micro cracks in the ore matrix due to the difference in microwave absorption and thermal expansion rates. These micro cracks are induced around the grain boundaries resulting in reduced fracture strength of the ores and greater liberation of value mineral. Over years thermal treatment has not been a viable option due to inefficient heating methods which resulted in more energy being used during heating thereby cancelling any gains in strength reduction during comminution (Kingman and Rowson, 1998).

The benefits associated with microwave heating over conventional heating methods such as selective heating , faster heating rates and no direct contact between heating source and the heated material has resulted in renewed interest in thermally assisted comminution. Research has shown that microwave assisted comminution is possibly a commercially viable thermal treatment method for reducing comminution energy and improving value mineral liberation in the ores (Kingman, 2006).

2.1.1. Developments in microwave heating of ores

The first attempt at applying microwave technology in mineral processing reported in literature by Ford and Pei (1967) cited in Kobusheshe (2010) was in 1967. In this study microwave energy was used to heat reagent grade metal oxides and sulphides at energy inputs of between 50-200W and at a frequency of 2.45GHz. Findings from these studies were that dark coloured compounds heated rapidly compared to light coloured compounds that heated at slower rates. The results although not comprehensive, paved the way for further studies on possible applications of microwaves in mineral processing (Haque, 1999).

Several preliminary investigations on microwave heating of mineral were reported between the late 60s and late 90s. Wong (1975) cited in Haque (1999) reported on the microwave heating behaviour of metal oxides. The results indicated that microwave energy was an effective heating method for heating minerals. Chen et al. (1984) cited in Kingman and Rowson (1998) investigated the heating behaviour of forty minerals individually with microwaves in a waveguide applicator. The major findings from this study were that silicates, carbonates and sulphates were transparent to microwave heating in contrast to metal sulphides and some oxides that were easily heated by microwave energy. These results indicated the selective nature of microwave heating and the potential application of this selective heating in mineral processing as a means of reducing required energy of comminution (Kingman and Rowson, 1998).

The US Bureau of mines carried out detailed and qualitative studies on the characteristics of microwave heating of minerals and reagent grade inorganic compounds. Results similar to those obtained by Chen et al. (1984) were reported (Walkiewicz et al., 1988). The results further confirmed that microwave heating was dependent on the mineral composition with gangue minerals such as quartz, calcite and feldspar being transparent to microwave heating. Rapid heating of ore minerals within a non heating matrix was observed which resulted in the generation of thermal stresses that led to cracks along the mineral boundaries. The studies gave initial indication of the application of microwave pre-treatment of ores in mineral processing as a means of reducing the energy of comminution and improving value mineral liberation. Results similar to those obtained by the US Bureau of mines were reported by a number of authors during the same period and became the basis of subsequent studies that focused on microwave assisted comminution (Kingman and Rowson, 1998).

2.1.2. Microwave assisted comminution in mineral processing

Kingman (2000) carried out studies on commercially exploited ores. After conducting mineralogical analysis on the ores and establishing the textural relationship between the ore phases, each ore was then microwave treated with varying exposure times for each sample. The results showed an increase in grindability of the ores after microwave treatment. This increase in grindability was related to the specific mineral present in the ores that is microwave absorber and non absorber and the grain size of the phase. The results showed improvements in grindability at high microwave energy inputs of 14.3 kWh/t. This input was less than the grinding energy required input of 20 kWh/t. These results highlighted the possibility of carrying microwave assisted comminution at potentially viable microwave energy inputs (Kingman et al., 2000b).

In the same year, Kingman et al. (2000) reported results of investigations on the effects of microwave treatment on the processing of Palabora ore. The studies not only showed enhanced grindability due to microwave treatment but also demonstrated that increases in recovery of copper after froth flotation could be obtained. Scanning Electron Microscopy analysis showed significant intergranular fracture in the ore. At long exposure times reduction in copper grades were observed which suggested surface oxidation of the sulphides owing to high temperatures. The potential benefit of reduced bond work index due to microwave treatment on a grinding circuit was also investigated in the same study. This was done by simulating a closed circuit ball mill grinding plant and reducing the bond work index of the ore to a value less than the typical operating plant's value. The impact of the reduced work index value on the circulating load was then analysed. The simulations showed that microwave assisted comminution had the potential to reduce the grindability by as much as 2 kWh/t. These studies further showed that the technical feasibility of microwave assisted comminution. The influences of microwave variables such as power density and heating time on the process however were still not well understood (Kingman et al., 2004c).

Whittles et al. (2003) conducted studies to predict the influence of power density on strength reduction by applying numerical modelling methods. In the study, a binary phase ore was simulated which consisted of an absorbing phase and transparent host represented by pyrite and calcite respectively. Numerical simulations were then applied to assess the influence of applied power density on the strength of the simulated ore. The results showed that at higher power density and shorter exposure time heat lost by conduction was minimised.

The major findings from this study was that by increasing the power density, significantly greater thermally induced stresses and strain were induced at lower microwave energy input. (Whittles et al., 2003)

Experimental studies to investigate the effects of high electric field strength on a copper carbonatite ore were carried out in order to validate results of the numerical simulations. Using point load test it was shown that short microwave exposure times (0.1 to 1s) at high power density (10^{11} W m^{-3}) could lead to significant reductions in ore strength (Kingman et al., 2004a). The studies further showed that a 30% reduction in required energy of comminution was possible at microwave energy inputs less than 1kWh/t (Kingman et al., 2004a; Kingman, 2006). A significant increase in grindability at larger particle sizes was also shown at low microwave energy input values of around 0.83 kW h t^{-1} . Using quantitative analysis of materials with Scanning Electron Microscopy analysis it was shown that microwave treatment resulted in coarse liberation of value mineral in the ore. It was concluded from the study that microwave assisted comminution resulted in significant changes in ore breakage behaviour and liberation characteristics at economically feasible microwave power inputs (Kingman et al., 2004a). Similar results supporting these conclusions were obtained on further studies that were carried out on samples of Lead-Zinc ore (Kingman et al., 2004b).

Having established the benefits of microwave treatment of ore on the grinding process work was then carried out to investigate the downstream effects of microwave treatment of ore (Kingman et al., 2004c). Kingman et al. (2004c) reported a significant increase in chalcopyrite liberation at coarser sizes ($+500 \mu\text{m}$). From these findings microwave treatment of ore was suspected to increase value mineral liberation and hence overall recovery. Amankwah, Pickles and Yen (2005) reported an increase in gold recovery of microwave treated refractory gold ores. Wang et al. (2000) also reported an increase in liberation of low Copper grades after microwave treatment.

Groves et al. (2007) investigated the potential for improved liberation of low grade copper ore through microwave treatment. Microwave power of 3 kW at 2.45 GHz was used to treat the ore sample for 120 s. The tests showed a shift from transgranular fracture to intergranular fracture in copper ore. A significant increase in the degree of liberation of the value mineral, chalcopyrite was reported (Groves, 2007).

Studies on the effect of microwave treatment on the liberation spectrum of a Rod milled low grade copper carbonatite ore were reported by Scott et al. (2008). Ore samples were microwave treated at an energy level of 10.5 kW for 0.5 seconds. Grinding of both treated and untreated ore was carried out in a laboratory scale Rod mill at a d_{80} grind size of 800 μm . QEMSCAN was then used for liberation analysis of the particle size ranges between 25 μm to 850 μm . A general trend in deportment of liberated minerals to coarser size classes was observed. No significant change in liberation was observed between the treated and untreated ore. However an induced fracture after microwave treatment along the grain boundaries of microwave susceptible mineral phases was suggested from the results. From these findings it was concluded that microwave assisted comminution had the potential to increase the liberation at coarser sizes hence resulting in savings on both time and energy required for fine grinding (Scott et al., 2008).

Ali and Bradshaw (2009, 2010) carried out investigations into the mechanism of microwave induced micro fracture. Numerical simulations were carried out using finite difference method and bonded-particle modelling. Computational simulations of microwave heating and thermal damage were carried out using two phase conceptual ores. The results showed that microwave treatment at high power density offered the possibility of localizing induced damage around the grain boundaries. This followed on previous numerical modelling work by the author which had shown that the most efficient method of maximising grain boundary damage was operating at high microwave power density and decreasing exposure time. These results further showed the feasibility of microwave treatment (Ali and Bradshaw, 2009; Ali and Bradshaw, 2010).

Kobusheshe (2010) studied the downstream flotation benefits of microwave treated porphyry copper ores. The results showed improved liberation of secondary crusher product of up to 20% at typical flotation grind sizes. The ore was treated at energy input of about 2 kWh/t. Improvements in liberation were reported at coarser sizes between 212 μm to 425 μm . An increase in value mineral recovery of between 8 to 10% in coarse sizes and an overall grade increase of 1-2% were reported. These results showed the possible economic benefits of microwave pre-treatment of ore. Although the investigations were carried out in batch flotation tests, the results represent the first attempts at quantifying the benefits of microwave assisted comminution. The benefits of microwave treatment on a traditional Copper beneficiation flow sheet are still to be investigated (Kobusheshe, 2010).

2.2. Flotation

Flotation is a widely used separation process in the mineral processing industry. Flotation machines perform the task of separating hydrophobic minerals from hydrophilic ones.

The froth flotation process is made up of two separate and distinctly different zones; the collection zone and the froth zone. The collection zone is responsible for the formation of the bubble aggregates, while the froth zone is responsible for the separation of these aggregates (Banford et al., 1998; Bulatovic, 2007).

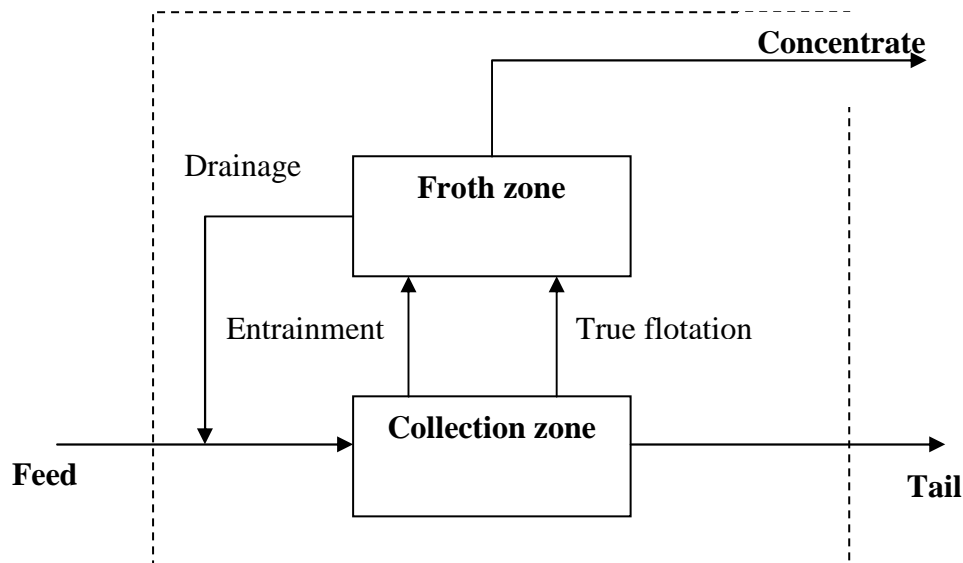


Figure 2-1: Mineral transport system in a flotation cell

Figure 2-1 is a flow chart showing mineral transport in a flotation cell. This section will present a literature review of the theory of flotation and the various models that have been developed to describe the process of flotation in flotation cells. A background summary of all the flotation sub-processes and the development of the various models to describe these processes reported in literature will be presented.

2.2.1. Flotation Sub-processes

Mineral recovery in flotation cells is a result of the combined interaction between two distinct zones in the cell, the collection and the froth zone (Yianatos et al., 1998; Honaker et al., 2006; Yianatos et al., 2008). The pulp or collection zone is responsible for the formation of the bubble-particle aggregates whilst the froth phase is responsible for separation of the aggregates from surrounding hydrophobic particles (Seaman et al., 2004; Yianatos, 2007; Honaker and Ozsever, 2003). There are two mechanisms by which concentrate is collected during flotation.

These are hydrophobic particle adhesion to the rising air bubbles commonly termed true flotation and mechanical transportation of hydrophilic gangue minerals in floated water by either particle entrainment or entrapment (Çilek and Umucu, 2001; Kirjavainen, 1996; Savassi, 2005).

The first mechanism is the most important one as it is a selective process and is the mechanism by which the bulk of the concentrate is collected (Savassi et al., 1998). This mechanism has been a focus of research into flotation (Bulatovic, 2007; Ralston and Ian, 2000). It has generally been concluded by many authors that it consists of a number of sub-processes that take place simultaneously during flotation (Bulatovic, 2007; Ralston et al., 1999). These sub-processes lead to the recovery of the value mineral particle in the concentrate and occur as follows (Bulatovic, 2007; Yoon and Mao, 1996),

- i. The mineral particle is rendered hydrophobic, hydrophobicity varying from particle to particle. This allows for the preferential adhesion of mineral particles to the rising air bubbles.
- ii. Mineral particle is suspended in pulp phase.
- iii. The mineral particle collides with the rising bubble.
- iv. The particle adheres to the air bubble.
- v. Particle must not detach from the bubble during passage through the pulp phase.
- vi. Particle must detach when entering the froth phase.
- vii. Particle must not detach and drain from the froth during passage of froth to the weir.

2.3. Flotation modelling

As has been mentioned, the flotation process can be divided into two distinct zones; the pulp or collection zone and the froth phase. Flotation models have been developed to describe these two phases and their interaction (Yianatos, 2007). In this section a review of the available models for modelling the collection and the froth phase in flotation processes will be discussed. A review of models for modelling overall value mineral recovery in industrial flotation cells will be provided at the end.

2.3.1. Collection zone modelling

The pulp or collection zone is responsible for the formation of hydrophobic particle-bubble aggregates (Seaman et al., 2004). The particle-bubble aggregate is a product of the collision of the bubbles with the hydrophobic particles (Yianatos, 2007). The product aggregate is less dense than the medium and moves upwards against gravity to the froth phase.

There are two common approaches that are usually applied to flotation modelling. These are the rate expression approach and the probability theory approach. The collection zone has been extensively studied and first order kinetic models are broadly used to describe it (Alexander et al., 2003; Ferreira and Loveday, 2000).

2.3.2. Kinetic theory rate expression approach

From the knowledge of flotation sub-processes it has been concluded that flotation can best be modelled by assuming a first order rate expression for the rate of collection of value minerals to the concentrate (Alexander and Morrison, 1998; Mendez et al., 2009; Ferreira and Loveday, 2000). This rate, commonly referred to as the rate of flotation, is quantified in terms of some of the many chemical and physical factors that define the environment inside the flotation cell (Bulatovic, 2007). In this approach flotation is represented by chemical analogy, with the following differential equation being used to represent the process equation 2.1 (Alexander and Morrison, 1998; Suazo et al., 2009).

$$\frac{-dC_a}{dt} = k_n \cdot C_a^n \quad 2.1$$

Where: C_a = Concentration of mineral A

t = flotation time

k_n = nth order rate constant

n = order of reaction.

In most cases $n = 1$, i.e the process can be assumed to follow first order rate kinetics (Alexander and Morrison, 1998). In some special cases when dealing with complex ores a non first order rate approximation has been used. The order of the equation is mainly determined by the available bubble surface (Alexander and Morrison, 1998). There are many forms of the first order rate kinetics expressions that has been proposed in literature. Polat and Chander (2000) provide a comprehensive review of these models.

2.3.2.1. Measurement of pulp flotation kinetics of minerals in flotation cells

The kinetic theory has proven to be the most preferred approach in determining collection zone flotation kinetics giving acceptable results when simulating flotation recovery in the collection zone of a flotation cell. Various methods have been developed and are used in the determination of the flotation cell collection zone kinetics that describes the flotation process taking place in the pulp phase. Discussion will focus on three major methods that are in common use in industry.

These are;

1. Standard batch flotation method.
2. Floatability Component method.
3. MFT Batch flotation test method.

Standard Laboratory batch flotation method

Laboratory batch flotation tests are usually carried out in determining the flotation rate constant in an industrial or laboratory set up. A pulp sample of ore from the process being investigated is floated in a laboratory batch flotation cell. Applying the rate expression approach a first order rate equation is assumed to describe the value mineral recovery from the batch flotation cells. Equation 2.2 is the classical form of the first order rate expression which is commonly assumed for batch floatation processes (Napier-Munn, 2005).

$$R_{t,i} = R_{max,i}(1 - \exp(-k_i t)) \quad 2.2$$

Where: k_i , is the flotation is rate constant of particles of diameter i , ; $R_{max,i}$, is the flotation recovery at an infinite time. The equation is fitted to experimental data of recovery versus time for each particle size class to obtain the rate constant $R_{max,i}$ and rate constant k_i . This is done by using nonlinear least square regression. Adjustments to the obtained experimental value mineral recovery values are normally made in order to eliminate contributions to recovery due to entrainment (George et al., 2004). This is done before curve fitting in order to obtain a rate constant that describes recovery in the collection zone (Bradshaw et al., 2005). The batch flotation cell is also operated with shallow froths depths so as to remove the effects of froth zone to final concentrate grade recovered (Duan et al., 2003; Savassi, 2005). The model that has been found to give the best fit to experimental data is the modified Kelsall's model equation 2.3 (Wills and Napier-Munn, 2005). In each size class the particles are assumed to consist of two fractions, the fast floating, R_f , and the slow floating fraction, R_s , (Napier-Munn, 2005).

$$R_{t,i} = R_f \left[1 - \left(\exp(-k_{fi} t) \right) \right] + R_s \left[1 - \left(\exp(-k_{si} t) \right) \right] \quad 2.3$$

Where : k_{fi} and k_{si} flotation rte constant of the fast floating and slow floating fractions.

Floatability component method

Alexander and Morrison, (1998) describe a floatability component method for predicting the flotation rate constant of a particular process. In this method, the characteristics of each of the mineral phases in the streams around the circuit are determined. The specific flotation rate constant of each floatable mineral phase is determined from either batch flotation data or plant operation data. A linearising technique is used in estimating the number of floatability components within a distribution (Alexander and Morrison, 1998). The mineral fraction that is represented by a specific flotation rate is termed a floatability component. This method assumes that the floatability components corresponding to a specific flotation rate are conserved throughout the flotation circuit. Table 2-1 summarises the model expressions used in evaluating the floatability components and hence determining the pulp kinetics.

MFT Batch flotation test method

Dobby and Savassi (2005) describe the MinnovEx Flotation method. This method is a standard bench-scale test that is used to measure primary floatability characteristics of an ore. Pulp kinetics of each mineral species in the ore are determined using a batch flotation cell designed to minimise froth phase effects. The obtained kinetics of each mineral phase are then modelled by a frequency distribution of rate constants, with each class in the k-distribution containing particles of different size and liberation. Mineral recovery per size interval is assumed to remain constant with changes in size distribution of the feed affecting only the proportion of the mass in each size interval. This allows for the prediction of changes in k-distribution as the particle size distribution of the feed ore changes. This eliminates the need to carry out batch flotation test at different grinds. Table 2-2 summarises the model expressions used in applying the MFT method and hence determining the pulp kinetics.

Limitations of batch flotation methods in determining pulp kinetics.

1. Despite the batch cell being operated at shallow froth depth, the shallow froth layer still has an effect on final concentrate grade recovered (Savassi, 2005).
2. Flotation rate constant is obtained without any specific association to particle size or mineral liberation (Ralston et al., 2007).
3. The mineral hydrophobicity and particle distribution is assumed to be constant throughout the flotation circuit, which is not the case for circuits where there is addition of collectors downstream and a regrind circuit (Alexander et al., 2003).

4. Due to differences in cell characteristics and operating conditions between batch and plant operation, kinetic data obtained from batch flotation needs to be scaled up before it is applied for modelling plant operations (Yianatos et al., 2003; Yianatos et al., 2006; Yianatos et al., 2010).
5. Particle recovery by entrainment has a considerable effect on final concentrate grade and hence on flotation kinetics deduced from batch flotation test (Bradshaw et al., 2005; Savassi et al., 1998).
6. Changes in feed ore mineral liberation properties require a separate set of kinetic data to be obtained from batch experiments; this increases the cost of investigating the effects feed ore property changes to the flotation process (Dobby and Savassi, 2005).

Table 2-1: Summary of expressions describing the floatability component method

Term	Expression	Parameters	Model Input parameters required	Method for obtaining parameter
Ore floatability	$k_{i,j} = P_{ij} \cdot S_b$ $S_b = \frac{6J_g}{d_{32}}$	P_{ij} -Ore floatability for component j in the ith size fraction.	P_{ij}	Batch flotation experiment and floatability technique (Alexander and Morrison, 1998)
		S_b -bubble surface area flux	S_b	Calculated parameter describing gas dispersion in the pulp phase.
		$k_{i,j}$ -rate parameter for jth mineral phase from in ith size fraction.	$k_{i,j}$	Product of floatability component and bubble surface area
		J_g -Superficial gas velocity	J_g	J_g probe
		d_{32} -Sauter mean bubble diameter	d_{32}	UCT bubble size analyser

Table 2-2: Summary of expressions for obtaining pulp kinetics utilising the MFT test procedure

Term	Expression	Parameters	Model Input parameters required	Method for obtaining parameter
First order rate expression	$R_{ij} = R_{\infty i,j}(1 - \exp(-k_{i,j}t))$	R_{ij} -Recovery of jth mineral phase from ith size fraction.	R_{ij}	Batch flotation experiments or plant data
		$R_{\infty i,j}$ -Ultimate recovery of jth mineral phase from ith size fraction.	$R_{\infty i,j}$	Calculated from least squares regression analysis
		$k_{i,j}$ -rate parameter for jth mineral phase from in ith size fraction. t -time	$k_{i,j}$	Calculated from least squares regression analysis
K-distribution of a mineral	$P(k_j) = 1 - \exp\left[-\left(\frac{k_j}{k_{avg}}\right)^\alpha\right]$	$P(k_j)$ -Cumulative weight per cent k_{avg} -the weighted average flotation rate, excluding un-floatable particles k_j -rate parameter for jth mineral phase α -a measurement of the spread in the k-distribution	$P(k_j)$ k_{avg} k_j α	Calculated from batch flotation experiment results

2.4. Probability theory approach

Research has established that the rate of recovery in the collection zone depends on the probabilities of all the flotation sub-processes and is a function of grain size (Niemi, 1995). This has culminated in the development of the probability theory approach to collection zone flotation rate constant modelling and the study of bubble-particle interaction in order to identify the sub-processes that are involved in the formation of bubble-particle aggregates (Nguyen et al., 1997a; Ralston and Dukhin, 1999)

2.4.1. Bubble-particle interaction theory

There are three elementary processes that are essential for bubble-particle interaction (Schulze et al., 1989b; Bloom and Heindel, 1997). These are:

1. Approach of bubble and particle forming a thin liquid film.
2. Rupture of the thin film forming a three-phase bubble-particle contact interface. The angle at the three-phase line of contact between the solid mineral surface, aqueous phase and air bubble is called the contact angle (Crawford and Ralston, 1988; Prestidge and Ralston, 1996). It is a measure of solid surface wet ability and gives an indication of particle surface hydrophobicity (Chau, 2009; Chau et al., 2009). A higher contact angle indicates that the mineral surface is readily wetted by air and thus more hydrophobic (Crawford and Ralston, 1988; Prestidge and Ralston, 1996).
3. The stabilization of the bubble-particle aggregates formed against external forces.

2.4.2. Determining overall collection zone efficiency

The probability of transfer of a mineral particle from the pulp phase to the froth phase has been proposed to be the product of the probabilities of these three elementary processes (Alexander and Morrison, 1998; Ralston et al., 1999). The elementary processes (sub-processes) are evaluated separately. The probability of a particle entering the froth phase is then as the product of the following probabilities,

1. Probability of particle-bubble collision sub-process, P_c .
2. Probability of particle- bubble attachment sub-process, P_a .
3. Probability of the particle-bubble stability sub-process, $(1 - P_d)$.

The overall probability of particle collection becomes, (Alexander and Morrison, 1998; Shahbazi et al., 2009)

$$P = P_c \cdot P_a \cdot (1 - P_d) \quad 2.4$$

The major short coming of this model has been ascribing quantitative values to these probabilities. However fundamental models to evaluate these probabilities have been developed (Ralston et al., 1999; Dai et al., 2000). This has led to the development of the fundamental property based model for predicting the flotation rate constant (Pyke et al., 2003). The probabilities can also be expressed in terms of the product of the efficiency of particle-bubble; collision, attachment and stability sub-processes (Grano, 2006; Duan et al., 2003; Koh and Schwarz, 2006; Dai et al., 1998). The overall probability is equivalent to the overall collection zone efficiency equation 2.5.

$$E_{Coll} = E_c \cdot E_a \cdot E_s \quad 2.5$$

Where E_{Coll} is the collection efficiency and E_c, E_a, E_s are the collision, attachment and stability efficiencies respectively. If the collision frequency per unit volume between particles and bubbles is evaluated, the rate of removal of particles by bubbles in a flotation cell can be expressed as,

$$\frac{dN_p}{dt} = kN_p = -Z_{pb}E_{Coll} \quad 2.6$$

Where: N_p is the number density of floatable particles, and Z_{pb} is the collision frequency per unit volume between particles and bubbles, k is the flotation rate constant. The above equation can be rearranged in order to come up with an expression for determining the flotation rate constant as a function of the collection efficiency resulting in the following expression(Newell and Grano, 2006).

$$k = \frac{Z_{pb}E_{Coll}}{N_p} \quad 2.7$$

2.4.3. Fundamental model for calculating collection zone efficiency

Determination of the value of the bubble-particle interaction efficiencies is the most important step in predicting the rate constant of flotation kinetics (Nguyen et al., 1998). A lot of work has been to derive models for describing the main flotation sub-process efficiencies of collision, attachment and stability (Dai et al., 1999; Dai et al., 2000; Ralston et al., 1999). This gives a summary of the available models for evaluating the three flotation sub-processes that make up the flotation collection efficiency in equation 2.5. For each sub-process the following aspects of the models will be covered in the review:

1. An analysis of the principal theory behind the formulation and function of the models.
2. The parameters required to calibrate the models.

3. The experiments and experimental work required in obtaining parameters required for model calibration.

2.4.3.1. Collision Efficiency

For a particle to attach to a bubble collision, must take place first. The collision efficiency can be affected by many factors. Some of the factors that affect the efficiency of the bubble-particle collision sub-process will be discussed below.

Factors influencing bubble-particle collision

1. Particle size, d_p . Generally all the collision efficiency models predict an increase in collision efficiency with particle size, but the dependence of the models on particle size varies due to differences in assumptions and hydrodynamic conditions that are used in the models (Dai et al., 2000; Miettinen et al., 2009; Ralston and Ian, 2000).
2. Particle density ρ_p . Particle density has an effect on the Stokes and Reynolds numbers. Increasing particle density results in an increase in the Stokes number thus leading to a change in the bubble-particle collision mechanism from interception to inertial (Miettinen et al., 2009; Dai et al., 2000; Nguyen and Nguyen, 2009; Sarrot et al., 2005).
3. Bubble size d_b . All the collision efficiency models predict that the collision efficiency decreases with increasing bubble size although this has not yet been observed in experiments (Dai et al., 2000; Nguyen et al., 2006).
4. Bubble rising velocity v_b . At higher bubble rising velocity potential conditions apply which favour bubble-particle collision than Stokes flow conditions (Miettinen et al., 2009; Sarrot et al., 2005; Ralston and Ian, 2000).
5. Bubble surface mobility. Small amounts of surface active material in the liquid render small bubbles fully retarded (Sam et al., 1996). This affects the flow conditions at the bubble surface and the rate of liquid drainage between the bubble and the particle (Miettinen et al., 2009; Liu and Schwarz, 2009a; Phan et al., 2003). The retarded bubble surface forces the fluid streamlines away from the bubble liquid interface, hindering thin film thinning consequently resulting in lower bubble-particle collision and attachment efficiencies (Schulze, 1992; Dai et al., 2000; Ralston and Ian, 2000).

A comprehensive review of available bubble-particle collision efficiency models has been provided by Dai et al.,(2000). Some of the bubble-particle collision models that are available in literature are presented in Table 2-3.

Table 2-3: Summary of collision efficiency models found in literature.

Expression	Model description
$E_{C-LB} = \left(\frac{K}{K + 0.2} \right)^2$ $K = \frac{\rho_p \cdot v_b \cdot d_p^2}{9 \cdot \eta \cdot d_b}$	The Langmuir-Blodgett model (E_{C-LB}) was developed for the inertial hydrodynamic interaction between a stationary and falling droplet. The model is valid only for particles with large Stokes number. Mobile surface effects have an insignificant effect on (E_{C-LB}). Model is not applicable where collision occurs due to interceptional effects (Dai et al., 2000).
$E_{C-Su} = \frac{3d_p}{d_b}$	The Sutherland model (E_{C-Su}) was developed for collision between a single particle and bubble assuming mobile bubble surface, negligible particle inertia and potential flow conditions. Model caters for collision due to interceptional effects (Nguyen et al., 2006; Nguyen and Nguyen, 2009; Dai et al., 1998)
$E_{C-GA} = \frac{3}{2} \left(\frac{d_p}{d_b} \right)^2$	The Gaudin model (E_{C-GA}) was developed assuming a Stokes flow regime and ignoring inertial forces. Model is useful for bubble sizes less than 100 μ m (Miettinen et al., 2009; Dai et al., 2000).
$E_{C-FH} = \frac{v_p}{(v_p + v_b)}$	The Flint-Howarth model (E_{C-FH}) was developed for bubble-particle collisions taking place under hydrodynamic conditions in the Stokes number range between 0.001 and 0.1. Inertial forces were neglected.
$E_{C-AK} = \frac{\left(1 + \frac{d_p}{d_b}\right)^2 \left[\frac{v_p}{v_b} + \frac{2\psi_c^0}{\left(1 + \frac{d_p}{d_b}\right)^2} \right]}{\left(1 + \frac{v_p}{v_b}\right)}$	Only gravitational and viscous forces were considered in developing the Anfruns-Kitchener model (E_{C-AK}). Fluid drag and particle inertial forces were neglected. The model is valid under the following conditions; small bubbles, Stokes flow conditions and inertia less flotation (Dai et al., 2000).
$E_{C-WP} = \left[1 + \frac{2}{1 + \left(37/R_{eb}\right)^{0.85}} \right] \left(\frac{d_p}{d_b} \right)$	The Weber-Paddock model (E_{C-WP}) describes collision due to interceptional effects for a mobile bubble surface $R_{eb} < 200$. The effects of particle inertia were neglected in developing the model. Hydrodynamic interaction between the particles and the fluid was neglected as the particles were assumed to be very small. Stokes flow hydrodynamic conditions were assumed (Weber and Paddock, 1983).

$E_{C-WP} = \frac{3}{2} \left[1 + \frac{(3/16)R_{eb}}{1 + 0.24R_{eb}^{0.56}} \right] \left(\frac{d_p}{d_b} \right)^2$	<p>Weber-Paddock flow (E_{C-WP}) model for describing collision due to interceptional effects for an immobile bubble surface in the Reynolds number range $200 < R_{eb} < 300$ (Weber and Paddock, 1983) .</p>
$E_{C-YL} = \left[\frac{3}{2} + \frac{4Re^{0.72}}{15} \right] \left(\frac{d_p}{d_b} \right)^2$	<p>The Yoon and Luttrell flow (E_{C-YL}) model is valid for intermediate flow conditions. It is applicable for bubble Reynolds number between $0 < R_{eb} < 100$. Similar assumptions to those made in developing the Sutherland model were made (Mao and Yoon, 1997; Fan et al., 2010b; Fan et al., 2010a).</p>
$E_{C-Sc} = E_{Sc}^{ic} + E_{C-WP}^g + \left[1 - \frac{E_{C-Sc}^{ic}}{\left(1 + \frac{d_p}{d_b} \right)^2} \right] E_{C-PL}^{in}$ $E_{Sc}^{ic} = \frac{2\psi_c}{\left(\left(1 + \frac{v_p}{v_b} \right) v_b \right) Re_b^2}$ $E_{C-PL}^{in} = \left(\frac{1}{1 + \frac{v_p}{v_b}} \right) \left(1 + \frac{d_p}{d_p} \right)^2 \left(\frac{K}{K + a} \right)^b$ $E_{C-WP}^g = (\sin \theta_c)^2 \left(1 + \frac{d_p}{d_b} \right)^2 \left(\frac{v_p}{v_b} \right)$	<p>The Schulze model (E_{C-Sc}) considers particle-bubble collision to be the result three different effects. Interceptional effect, E_{Sc}^{ic}, gravitational effects, E_{C-WP}^g, and inertial effect, E_{C-PL}^{in}. E_{C-WP}^g is the Weber-Paddock collision model for collision due to gravitational effect. E_{C-PL}^{in} is the model reported by Plate for inertial collision efficiency. The model neglects the negative effects of the inertial forces thus over estimating the collision efficiency. The model is however superior to most of the other collision models available in literature (Schulze et al., 1989a; Dai et al., 2000).</p>

$E_{C-GSE} = E_{C-SU} \cdot \sin^2 \theta_t \cdot \exp \left\{ \left[3K_3 \left(\ln \frac{3}{E_{C-SU}} - 1.8 \right) - \frac{4 \left(\frac{2}{3} + \frac{\cos^2 \theta_t}{3} - \cos \theta_t \right)}{\sin^4 \theta_t} \right] \cos \theta_t \right\}$	<p>The GSE (Generalised Sutherland equation) model is applicable to potential flow conditions for mobile surface and for Stokes conditions that are less than 0.1. It couples the interception effects of the Sutherland model to the positive and negative effects of hydrodynamic pressing force and the centrifugal force respectively. It is a reasonable description of bubble-particle collision under potential flow conditions for both large and small particles (Dai et al., 1998; Miettinen et al., 2009)</p>
$E_{C-NV} = \frac{2D}{9Y \left(1 + v_p/v_b \right)} \left(d_p/d_b \right)^2 \left\{ [(X + Y)^2 + 3Y^2]^{1/2} \right\} + 2(X + C)^2$ $X = \frac{3}{2} + \frac{9R_{eb}}{32 + 9.88R_{eb}^{0.694}} ; \quad Y = \frac{3R_{eb}}{8 + 1.736R_{eb}^{0.518}}$ $C = \frac{v_p/v_b}{\left(d_p/d_b \right)^2} ; D = \frac{[(X + C)^2 + 3Y^2]^{1/2} - (X + C)}{3Y}$	<p>The Nguyen-Van model (E_{C-NV}) was developed by assuming that hydrodynamic and gravitational forces were the only forces controlling the collision process with the distance between the bubble and particle during collision being negligible compared to their sizes. The bubble surface was also assumed to be immobile, the motion of the bubble being unaffected by particles as the particle size was assumed to be much smaller compared to the bubble size. Particle inertial forces were neglected (Nguyen Van and Kmet, 1992; Nguyen-Van and Kmet, 1994).</p>

2.4.3.2. Attachment efficiency

Not all particles colliding with bubbles attach to the bubbles. As the bubble and particle come closer the influence of intermolecular and interfacial forces increases, consequently the liquid film between the bubble and particle draining away causing the film to rupture (Nguyen et al., 1997a; Albijanic et al., 2010). A three-phase contact line is then formed, the ability of this contact line to extend and stabilise is essential for the formation of a stable bubble-particle aggregate thus completing successful attachment of particle to bubble (Phan et al., 2003; Dobby and Finch, 1986; Zawala et al., 2008).

Induction time

The induction time (t_{ind}) is the sum of the film drainage time t_{fl} , the three-phase contact line expansion and stabilisation time t_{TPLC} and the film rupture time t_{fr} (Nguyen et al., 1997a). It is the time required by the particle to completely attach to the bubble forming a stable bubble-particle aggregate, equation 2.8 (Albijanic et al., 2010).

$$t_{ind} = t_{fl} + t_{fr} + t_{TPLC} \quad 2.8$$

The induction time has been reported to vary with particle size according to a power function, equation 2.9 (Miettinen et al., 2009).

$$t_{ind} = Ad_p^B \quad 2.9$$

Parameters A and B in the equation are independent of particle size. Parameter B has been reported to be constant with a value of 0.6 (Dai et al., 1999). An inverse relationship has been suggested for parameter A with contact angle (Koh and Schwarz, 2008; Shahbazi et al., 2010; Shahbazi et al., 2009; Koh and Schwarz, 2006).

$$A = \frac{75}{\varphi} \quad 2.10$$

d_p is the particle size in meters and φ is the contact angle in degrees. For attachment to occur the induction time must be less than the contact time.

Determination of particle Contact angle

The contact angle, φ , is described thermodynamically by Young's equation given below (see equation 2.11).

$$\gamma_{s/a} = \gamma_{s/l} + \gamma_{l/a} \cos \phi_Y \quad 2.11$$

Where $\gamma_{s/a}$, $\gamma_{s/l}$, and $\gamma_{l/a}$ represent the solid-vapour, solid-liquid, and liquid-vapour interfacial tensions, respectively (Chebbi, 2003; Chibowski, 2007; Iveson et al., 2004). For Young's equation to be valid, the solid surface should be ideal, i.e. smooth, flat, homogenous, inert, insoluble, non reactive, non porous and of non deformable quality (Chau, 2009; Chau et al., 2009). This is not the case with real mineral surfaces, hence there is a variation in contact angles measured on real surfaces (Keller et al., 2007; Lam et al., 2001; Lam et al., 2002). This leads to two definitions of contact angles, intrinsic contact angle which is the contact angle measured for flat surfaces and apparent contact angle which is the contact angle measured for rough surfaces (Chau, 2009; Chau et al., 2009). Since most mineral surfaces are rough the discussion will focus on the determination of the apparent contact angle only. The apparent contact angle is obtained by utilising optical methods that measure the contact angle as the angle between the direction to the tangent of the smoothed solid surface and the direction of the tangent to the air water interfaces (Chebbi, 2003; Chibowski, 2007; Iveson et al., 2004; Keller et al., 2007; Lam et al., 2001; Lam et al., 2002; Yang et al., 1999). A range of apparent contact angles is normally obtained, with the upper limit of the range being termed advancing contact angle and the lower limit of the range being termed receding contact angles (Chebbi, 2003; Chibowski, 2007; Iveson et al., 2004; Keller et al., 2007; Lam et al., 2001; Lam et al., 2002; Yang et al., 1999; Chau, 2009; Chau et al., 2009). The difference between the two limits being termed contact angle hysteresis (Chibowski, 2007; Lam et al., 2002).

Contact time and Sliding time

The contact time refers to the time for which the bubble and a particle are in contact after their collision (Nguyen et al., 1997b). After bubble particle collision the particle either rebounds or slides along the bubble surface (Phan et al., 2003; Albijanic et al., 2010). Where the particle simply rebounds from the bubble surface after collision the contact time is equivalent to the impact time (Schulze et al., 1989a). If particle sliding takes place after collision, the contact time is the sum of the impact and sliding time. For particles less than 100 μm the contact times are typically very small, about 10 ms or less (Miettinen et al., 2009; Dai et al., 1999). There is no rebound with particle deformation (Schulze et al., 1989a). Various models exist in literature for predicting the sliding time (Dobby and Finch, 1986). Particle impact provides kinetic energy while particle sliding provides contact time; both are

beneficial to the drainage and rupture of the film and to the expansion of three-phase contact line (TPCL) (Dai et al., 1999; Dobby and Finch, 1987; Ralston and Dukhin, 1999). From the kinetic viewpoint, the sliding time is more important than the impact time. A review of sliding time models available in literature will be given below.

Sliding time models

Table 2-4 provides is a summary of some of the models for predicting the sliding time available in literature. r_p and r_b are the particle and bubble radius respectively, θ refers to the contact angle. The Sutherland model is one of the earliest sliding time models that was proposed Sutherland in 1948. The model had some mistakes and most of the models that have been derived so far have been aimed at correct that mistake. Dai et al. (1998) presented a corrected form of the Sutherland sliding time model. For potential flow conditions both the Dobby and Finch (1986) and Yoon and Luttrell (1992) assume a maximum particle contact angle $\theta_m = 90^\circ$. This assumption is incorrect as the maximum particle contact angle is less than 90° (Dai, 1998).

Table 2-4: Summary of sliding models found in literature

Sliding time model	Reference
$t_{sl-SU} = \frac{2(r_p + r_b)}{2(v_p + v_b) + (v_p + v_b) \left(\frac{r_b}{r_p + r_b}\right)^3} \cdot \ln \left(\cot \frac{\theta}{2} \right)$	Dai et al., 1998
$t_{sl-DF} = \frac{2(r_p + r_b)}{2(v_p + v_b) + v_b \left(\frac{r_b}{r_p + r_b}\right)^3} \ln \left(\cot \frac{\theta}{2} \right)$	Dobby and Finch, 1986
$t_{sl-YL} = \frac{d_p + d_b}{3v_b} \ln \left(\cot \frac{\theta}{2} \right)$	Luttrell and Yoon, 1992

Attachment Efficiency models

The bubble-particle attachment efficiency can be modelled in terms of the contact time and sliding time (Dai et al., 1999; Hewitt et al., 1994). Another approach to modelling attachment efficiency is the energy barrier approach (Luttrell and Yoon, 1992). This approach is based on the principle that for bubble-particle attachment to take place the kinetic energy of the particle should be higher than the energy barrier between the bubble and the particle (Fan et al., 2010b; Fan et al., 2010a; Yoon and Mao, 1996; Schubert and Bischofberger, 1998). Due to the variation in sliding time models there is a corresponding variation in attachment efficiency models that are based on the sliding time approach.

The Dobby-finch attachment model

There is a collision angle, θ_a , termed the attachment angle at which the sliding time equals the induction time. Particles with collision angles less than the attachment angle will attach to the bubble (Ralston et al., 1999). The number of attached particles to the bubble can be related to the projected area defined by attachment angle while the number of particles that have collided with the bubble can be related to the projected area defined by the maximum collision angle θ_t (Dobby and Finch, 1987; Ralston et al., 1999). Thus Dobby and Finch (1987) proposed that the attachment efficiency is a ratio of these two areas.

$$E_a = \frac{\sin^2 \theta_a}{\sin^2 \theta_t} \quad 2.12$$

The attachment angle is obtained by replacing the sliding time with the calculated induction time in the sliding time model expression and rearranging the equation to obtain a value of θ which in that case is the attachment angle θ_a (Dobby and Finch, 1987).

$$\theta_a = 2 \arccos \tan \exp \left[-t_{ind} \frac{2(v_p + v_b) + v_b \left(\frac{d_p}{d_p + d_b} \right)^3}{d_p + d_b} \right] \quad 2.13$$

The Yoon-Luttrell model

Yoon-Luttrell used an approach similar to the Dobby and Finch (1987) projected area approach in deriving their attachment efficiency model (Luttrell and Yoon, 1992; Ralston and Ian, 2000). In deriving their model they assumed a maximum collision angle value of 90° .

$$E_a = \frac{\sin^2 \theta_a}{\sin^2 90^\circ} \quad 2.14$$

The Yoon-Mao Model

The model is an exponential function containing the ration of the potential energy barrier E_1 and the kinetic energy of a particle approaching a bubble E_K (Yoon and Mao, 1996; Mao and Yoon, 1997; Luttrell and Yoon, 1992). The particles must possess sufficient kinetic energy to overcome the energy barrier between the bubble and particle so that the thin film ruptures and attachment occurs.

$$E_{a-YM} = \exp\left(-\frac{E_1}{E_K}\right) \quad 2.15$$

2.4.3.3. Bubble-particle stability Efficiency

When bubble-particle stability is discussed, it is assumed that particle attachment has already taken place. There are strong detachment forces that act on the TPCL between a particle and a bubble (Zawala et al., 2008). The ability of the TPCL to resist these forces determines bubble-particle stability (Schulze, 1977). Inertia, gravity and viscous forces are some of the forces that reduce the bubble-particle stability (Ralston et al., 1999). The bubble-particle stability efficiency is strongly dependent on the adhesion forces between bubble and particle. These adhesion forces are (Phan et al., 2003; Schulze et al., 1989a);

- capillary force, F_c ,
- Hydrostatic pressure force, F_h , on the area enclosed by the three-phase contact, and
- Buoyancy, F_b , of the particle volume immersed in the liquid phase

This adhesion force has a direct relationship with contact angle and is inversely related to particle size (Yoon and Mao, 1996). Forces of adhesion must exceed detachment forces for a particle to continue being attached to the bubble surface in a static system (Yoon and Mao, 1996; Schulze et al., 1989a). Under turbulent conditions, detachment forces other than those associated with the particle weight become important (Ralston et al., 1999).

Bubble-particle stability models

Under turbulent conditions when the detaching forces are in equilibrium with the adhesive forces the following expression, equation 2.16, represents the force balance (Schulze, 1992; Pyke et al., 2003).

$$F_c + F_h + F_b - F_g - F_d - F_\sigma = 0 \quad 2.16$$

Where F_{σ} is the capillary pressure force in the bubble, F_g gravitational force and F_d is the additional detaching forces. It has been proposed that the bubble-particle stability efficiency is exponentially distributed and can be expressed as follows, (Pyke et al., 2003; Miettinen et al., 2009; Bloom and Heindel, 2003)

$$E_s = 1 - \exp\left(1 - \frac{1}{Bo^*}\right) \quad 2.17$$

The Bond number describes the stability of the bubble-particle and is defined as the ration of the detachment, F_{det} , and attachment forces, F_{att} below (Pyke et al., 2003; Miettinen et al., 2009; Schulze, 1992),

$$Bo^* = \frac{F_{att}}{F_{det}} \quad 2.18$$

Bloom and Heindel (2003) carried out experiments to validate Schulze's model. They suggested a modified expression of the model as follows:

$$E_s = 1 - \exp\left[A_s \left(1 - \frac{1}{Bo^*}\right)\right] \quad 2.19$$

where A_s is an empirical dimensionless constant with a value of 0.5 (Bloom and Heindel, 2003).

2.5. Calculating collection zone overall mineral recovery

When evaluating the performance of the flotation unit, overall collection zone mineral recovery and concentrate grade are the two key parameters used for evaluation. Various models have been proposed to describe collection zone flotation recovery. Depending on the slurry flow pattern equations 2.18 and 2.19 are used to calculate true mineral recovery for plug-flow and perfect mixing pulp flows in a flotation cell. Of key importance in calculating the mineral recoveries is the first order collection zone rate constant k . The recovery (R) is calculated as follows (Napier-Munn, 2005; Alexander and Morrison, 1998):

$$R = 1 - \exp(-k\tau) \quad \text{Plug flow} \quad 2.20$$

$$R = \frac{k\tau}{(1+k\tau)} \quad \text{Perfect Mixing} \quad 2.21$$

Where: k is the first order collection zone rate constant and τ is the residence time in the unit. For batch flotation tests plug-flow conditions are normally assumed. Single continuous plant flotation cells are assumed to follow perfect mixing characteristics (Alexander and Morrison, 1998).

The first order rate constant can be determined by kinetic or probabilistic approaches. When applying the probabilistic approach the particles are assumed to be perfectly mixed in the collection zone. Equation 2.19 is then used to calculate recovery by bubble-particle collection. The froth phase is however crucial in determining the final overall flotation cell recovery. Flotation models aimed at predicting overall flotation cell recovery attempt to incorporate the various froth phase sub-process into the final model expressions by use of froth recovery, degree of entrainment and water recovery parameters. The approaches commonly used in characterising the overall recovery in flotation cell equipment can be classified as follows (Yianatos et al., 2008). These are:

- Single stage process and overall flotation model,
- Two stage process (pulp and froth) and overall flotation rate constant,
- Two stage process (pulp and froth) and mass balance.
- Three zone flotation cell description (pulp zone, pulp-froth interface and froth zone).

The next section will provide a review on froth phase sub-processes models and the parameters for describing the froth phase effects on overall flotation recovery.

2.5.1. Froth zone value mineral recovery

The froth phase is responsible for the separation of bubble-particle aggregates from surrounding suspended hydrophobic and hydrophilic particles from the pulp zone (Honaker et al., 2006). Research has shown that the froth phase is the grade determining phase in flotation (Tsatouhas et al., 2006; Cutting et al., 1986; Vera et al., 1999b; Seaman et al., 2004). The existence of the froth phase is therefore of great importance during mineral separation (Yianatos, 2007). Industrial flotation cells are operated with the specific aim of maintaining a pulp- froth interface (Seaman et al., 2006). The froth phase phenomena has generally not been well understood in the past (Ata et al., 2002; Mathe et al., 1998). This has resulted in lack of adequate models to describe the froth phase in literature, consequently first order kinetic equation were usually imposed on the overall process (Mathe et al., 1998).

2.5.2. Studies into the factors that affect froth zone recovery

Focus has shifted towards studying the phenomena which take place in the froth zone (Moys, 1978). The outcome of the research has been the identification of the important factors that affect mineral recovery and grade in the froth zone which are; Froth structure, Froth Stability, Froth mobility, Entrainment , Particle drainage and water recovery in froths (Banford et al., 1998) (Mathe et al., 1998; Schwarz and Grano, 2005).

2.5.2.1. Froth structure

The structure of mineralized froths is the product of the interaction between two main factors: Froth drainage and froth mobility (Cutting et al., 1986; Subrahmanyam and Forssberg, 1988). Froth drainage mechanisms govern the grade of the final concentrate (Mathe et al., 1998; Honaker et al., 2006; Subrahmanyam and Forssberg, 1988). Froth mobility is described as the flow stream profile occurring in the froth between the pulp-froth interface and the froth discharge (Cutting et al., 1986). Research has confirmed the cleaning and selectivity actions of froths through the use of data on solids and grade profiles in the froth along with residence time distribution data (Massinaei et al., 2009a; Honaker et al., 2006). The solids and grade profile showed that froth zone upgrading occurred just above the pulp-froth interface (Massinaei et al., 2009a). The effect of froth depth and bubble loading on overall rate constant and froth recovery has been examined extensively in literature (Yianatos et al., 2008; Schwarz and Grano, 2005). To achieve maximum froth recovery the bubble surface area should be sufficient to carry all the particles from the collection zone including particles draining back into the pulp through particle re-attachment (Honaker and Ozsever, 2003). Increasing froth depth increases the probability of particle re-attachment (Mathe et al., 1998). Therefore increasing the bubble loading and froth depth has been found to have a positive effect on the overall rate constant (Massinaei et al., 2009a; Banford et al., 1998; Aktas et al., 2008).

2.5.2.2. Froth zone sub-processes

Detachment of mineral particles in the froths has been shown to be selective with the weakest hydrophobic particles being rejected first (Honaker et al., 2006; Honaker and Ozsever, 2003; Moys, 1978; Yianatos et al., 1988). This selectivity in detachment in the froth phase accounts for the cleaning action of the froth phase (van Deventer et al., 2004b). The probability of particle re-attachment is higher in deep froths as compared to shallow froths (Banford et al., 1998; Mathe et al., 1998). As the particle laden bubbles travel upward and cross the surface of the pulp, the particle-bubble aggregate entrains water and the hydrophobic minerals as well (Çilek and Umucu, 2001; Banford et al., 1998; Kirjavainen, 1996). As the bubble-particle aggregates continue to rise through the froth zone, the water layer surrounding the bubbles becomes thinner and coalescence (Banford et al., 1998; Meloy et al., 2007). This reduces the bubble surface area resulting in the rupture of the bubbles (Ross, 1991a; Ross, 1991b).

2.6. Entrainment

Entrainment is defined as the process where minerals are carried over with the water phase to the froth phase by mechanical transportation. Different authors agree that entrainment is a result of either one of the following mechanisms (Stevenson et al., 2007; Savassi et al., 1998; Yianatos and Contreras, 2009; Zheng et al., 2005)

1. Entrained material is transported upwards in the bubble lamella or,
2. Entrained material is transported in the wake of an air bubble

Research has shown that the mechanisms for entrainment mentioned above do not explain the water content found in flotation froths. A bubble swarm theory has been proposed in which the water in the froth is said to be as a result of ascending swarms of air bubbles mechanically pushing the water into the froth phase (Kirjavainen, 1996; Cilek, 2009; Çilek and Umucu, 2001; Çilek and Yilmazer, 2003). The flow of entrained particles can be described to be a resultant of the following two opposing transport mechanisms (Savassi et al., 1998),

- a. Upward velocity of entrained particles through the froth.
- b. Settling velocity or drainage of entrained material down towards the pulp-froth interface.

2.6.1. Mechanisms of entrained material drainage

There is a general agreement that the main methods of entrained material drainage are film water drainage, column drainage, mobility induced drainage and subduction drainage (Savassi et al., 1998; Ireland et al., 2007; Ireland and Jameson, 2007; Subrahmanyam and Forssberg, 1988; van Deventer et al., 2004b). Savassi et al. (1998) and Ireland et al. (2007) in summing up these methods of drainage cite the extensive work that was done by Cutting et al. (1989) in investigating drainage methods in froths. The extent to which each of the drainage mechanisms occurs is not only a function of the froth structure but also of the characteristics of the gangue (Ata et al., 2004). The result of entrained particle drainage from the froth is their rejection from the froth and this mostly occurs just above the pulp-froth interface (Ata et al., 2006; van Deventer et al., 2004b).

2.6.2. Main Factors that affect entrainment

The main factors that affect entrainment reported in literature have been summarised and are presented in Table 2-5. Each of the factors is stated along with a brief description of how that factor affects entrainment.

Table 2-5: Summary of factors that affect entrainment

Factor	Description	Reference
Water recovery	A strong correlation exists between water recovery and entrainment. At high water recoveries the relationship is linear .At low recoveries it is parabolic.	Subrahmanyam and Forssberg, 1988; Yianatos and Contreras, 2009; Savassi, 2005; Savassi et al., 1998
Particle size	At high water recoveries the linear plot of entrainment against water recovery shows a decreasing gradient with increasing particle size. The relationship is linear at fine particle sizes. Entrainment is insignificant at coarser sizes.	Zheng et al., 2005; Stevenson et al., 2007; Yianatos and Contreras, 2009; Neethling and Cilliers, 2009
Feed solids percentage	High solids percent reduce particle entrainment.	Subrahmanyam and Forssberg, 1988; Savassi et al., 1998; Zheng et al., 2005
Froth characteristics	Factors such as specific airflow rate, residence time, and height of froth phase determine the amount of entrained particles that enter the froth phase.	Cilek, 2009; Çilek and Yilmazer, 2003; Zheng et al., 2005; Yianatos et al., 2009
Mineral specific gravity	The probability of particle drainage from the froth of entrained particles is higher for particles with large specific gravity values.	Honaker and Ozsever, 2003; Honaker et al., 2006; Yianatos et al., 2009

2.6.3. Entrainment modelling

Many empirical models for modelling recovery by entrainment exist in literature (Zheng et al., 2006b; Savassi et al., 1998; Kirjavainen, 1996; Çilek and Umucu, 2001). These models express recovery by entrainment as a function of many variables. Some of these variables required in the model expressions are very difficult to measure (Zheng et al., 2005).

$$R_{entrainment,i} = (R_W, \mu_S, d_p, \omega_{top}, \Delta\rho) \quad 2.22$$

Where; $R_{entrainment,i}$ is the recovery of entrained material by size , R_w is water recovery, $\Delta\rho$ is the density difference between the solid and liquid, d_p is the particle size, ω_{top} is the solids mass fraction below the pulp-froth interface, and μ_s is the interstitial slurry viscosity. Most of these models only consider the effect of particle size on the degree of entrainment (Neethling and Cilliers, 2009; Zheng et al., 2005). This is because experimental results obtained so far show that particle size has a significant effect on the degree of entrainment (Zheng et al., 2006b; Kirjavainen, 1996). Zheng et al. (2006b) proposed empirical expressions for determining entrainment that tried to incorporate more variables such as particle shape and slurry viscosity. These models have been shown to be dimensionally inconsistent (Stevenson et al., 2007). Dimensionless factors per size class such as the degree of entrainment and the classification function have also been defined in modelling entrainment recovery (Yianatos and Contreras, 2009; Zheng et al., 2005).

$$ENT_i = \frac{M_{conc}^{ENT}}{M_{pulp}^{ENT}} \quad 2.23$$

$$CF_i = \frac{M_{pulp}^{ENT}}{M_{tail}^{ENT}} \quad 2.24$$

Where: ENT_i =The degree of entrainment, CF_i = The classification function, M_{conc} =Mass of solids suspended in the water in the concentrate, M_{pulp} =Mass of solids suspended in the water in the pulp phase. These dimensionless expressions are used in models that express the size recovery by entrainment as a function of water recovery. This reduces the problem of determining recovery by entrainment, $R_{entrainment,i}$, to that of obtaining the dimensionless factors as water recovery can easily be obtained from a mass balance of the system (Yianatos et al., 2009).

$$R_{entrainment,i} = ENT_i \cdot R_w \quad 2.25$$

A method proposed by Zheng et al. (2006b) for estimating the degree of entrainment is to use a fully liberated portion of the non sulphur gangue especially in the coarse size fractions. The entrainment calculation can be based on the total mass of NSG (Non sulphide gangue) in the individual size fractions with marginal error (Zheng et al., 2006b)

$$ENT_i = \frac{\left(\frac{\text{Mass of suspended non floating solid}_i}{\text{Mass of water}} \right)_{Pulp}}{\left(\frac{\text{Mass of suspended non floating solid}_i}{\text{Mass of water}} \right)_{Tail}} \quad 2.26$$

Where; i, denotes a particular size class.

2.7. Froth recovery

It is difficult to interpret the overall flotation rate constant in terms of the froth sub-processes (Ross, 1991b). The processes occurring within the froth phase are collectively represented by the froth recovery term. Froth recovery is therefore a useful parameter for measuring the performance of the froth zone (Falutsu and Dobby, 1992; Ata et al., 2002; Neethling, 2008). Neethling (2008) defined froth recovery as the fraction of the material that enters the froth attached to the bubbles that reports to the concentrate, rather than dropping back into the pulp. Froth recovery can be expressed as (Savassi et al., 1998; Yianatos et al., 2008; Neethling, 2008),

$$R_f = \frac{k}{k_c} \quad 2.27$$

Where: R_f = Froth recovery, k = Overall first order rate constant (min^{-1}), k_c = Collection zone first order rate constant (min^{-1}).

Froth recovery has a significant effect on overall recovery, it provides a measure of the loss of recovery in the froth zone (Vera et al., 2002; Massinaei et al., 2009a). Froth recovery of attached particles is a non selective process (Vera et al., 1999a).

2.7.1. Methods for obtaining the froth zone recovery

Due to its importance, several methods have been reported in literature for estimating froth phase recovery. Table 2-6 below gives a summary of the froth recovery determination methods that have been reported so far in literature.

Table 2-6: Summary of methods for obtaining froth zone recovery

Method	Description of method	References
Modified flotation column method	Method utilises a modified laboratory flotation column that allows simultaneous sampling of both the pulp and froth phase	Ata et al., 2002; Ata et al., 2006; Schwarz and Grano, 2005; Honaker and Ozsever, 2003
Mass transfer method	The method involves the measurement of a wide range of variables culminating in the development of a model that allows for the determination of flow rates into the froth.	van Deventer et al., 2001; van Deventer et al., 2004b; van Deventer et al., 2004a
Froth depth changing method	Based on the assumption that as R_f tends to one the froth depth h_f tends to zero. The froth depth is changed; concentrate flow measured at each depth and extrapolation is carried out to determine concentrate flow at zero froth depth.	Feteris et al., 1987; Vera et al., 1999b; Vera et al., 2002; Schwarz and Grano, 2005; Tsatouhas et al., 2006
Direct measurement of loading on bubbles method	This method relates to the direct measurement of bubble loading of particles at the froth pulp interface by utilising various devices designed for this purpose. Having obtained the bubble load froth recovery is then determined by carrying out calculation described below.	Falutsu and Dobby, 1992; Bradshaw and Connor, 1996; Seaman et al., 2004; Moys et al., 2009; Yianatos et al., 2008
Use of plug-flow model	The grade profiles along the froth phase are fit to a plug-flow model.	Yianatos et al., 1988; Yianatos et al., 1998; Moys, 1978; Cutting et al., 1986
Indirect measurement of loading on bubbles	The method refers to a mass balancing technique which indirectly derives the rate of attached particles entering the froth zone through the collection of pulp samples containing different portions of attached and suspended particles.	Savassi et al., 1998; Savassi, 2005; Alexander et al., 2003

2.8. Water recovery

Water recovery may be defined as the fraction of the water entering the flotation cell that is recovered in the concentrate (Yianatos et al., 2009).

$$R_{water} = \frac{C_{Water}}{F_{Water}} \quad 2.28$$

Where: C_{Water} is the Amount of water in the concentrate; F_{Water} -Water contained in the feed;
 R_{water} -Water recovery

Water recovery is strongly associated with entrainment and froth recovery (Cilek, 2009; Zheng et al., 2006a). It influences both mineral recovery and concentrate grade (Neethling and Cilliers, 2009; Cilek, 2009). This makes it a very important parameter in flotation plant design and operation. By including the solids percentage of the streams around a flotation cell the water recovery can easily be established. In cases where modelling is being carried out so as to design a flotation plant or for process control purposes the mass balance method is not appropriate for determining water recovery. Water recovery models are often used to predict the water recovery in such cases.

2.8.1. Modelling water recovery

There is lack of agreement in literature on which water recovery model is appropriate for modelling water recovery in Industrial flotation cell (Stevenson, 2007; Zheng et al., 2006a). Fundamental models have been shown to perform better than empirical models when applied to experimental data (Zheng et al., 2006a). The work carried out so far in developing fundamental models has produced models that are only for application in control purposes; no satisfactory fundamental predictive model is available in literature (Neethling et al., 2003; Neethling and Cilliers, 2003; Stevenson et al., 2007). Empirical models fit experimental data reasonably well for a given flotation system hence they offer a reasonable solution for modelling water recovery in Industrial flotation cells (Zheng et al., 2006a). Table 2.7 provides a summary of most of the models available in literature and gives a brief description of each of the models.

Table 2-7: Summary of water recovery models found in literature

Category	Expression	Model description
<p>Water recovery as a function of solids recovery models</p>	$Q_w = \frac{SG_S - SG_P}{SG_P - SG_W} \times \frac{1}{SG_S} \times F_S$ $Q_w = a \cdot F_S^b$	<p>Relates concentrate water flow rate to the solid concentration flow rate (Zheng et al., 2006a).</p> <p>Expresses concentrate water as a power function of the concentrate solids flow rate. Inappropriate for modelling flotation columns of small size diameter (Zheng et al., 2006a).</p> <p>Modified expression of the power model for water recovery in flotation columns of any size (Uribe et al., 1999). Inappropriate for application to systems where the SG and the concentrate slurry are sensitive to the process variables (Zheng et al., 2006a; Uribe et al., 1999).</p>
<p>Water recovery as a function of froth residence time</p>	$R_w = c \cdot \tau_f^d$ $\tau_f = \frac{V}{E'}$ $\frac{R_w}{1 - R_w} = \frac{R_{cw}}{1 - R_{cw}} \cdot \exp(-\beta_w \cdot \tau_f)$	<p>Savassi et al. (1998) developed an empirical expression relating froth recovery to the froth residence time based on industrial data from a lead rougher circuit. Model is unable to distinguish the effects of froth height and air rate on water recovery (Zheng et al., 2006a). The use of a single mean froth residence time does not adequately represent froth transportation and hence it cannot be used to determine water recovery (Zheng et al., 2006a).</p> <p>Water recovery is assumed to be a two step process i.e recovery of water from pulp to the froth followed by the recovery of water from the froth to the concentrate (Gorain et al., 1998). Model has the same limitations as the Savassi et al. (1998) model due to the use of a single value of mean froth residence time</p>

First order water recovery model	$R_w = 1 - \frac{1}{1 + P_w \cdot S_b \cdot \tau \cdot \Omega \cdot \exp(\rho \cdot V_f - \chi \cdot \tau_f)}$	<p>Based on the assumption that the transfer of water from the pulp phase to the froth phase follows first order kinetic expression. First order assumption was merely a method to improve on the water recovery model by Gorain et al. (1998) and was not a reflection of the true observed mechanism of transfer of water from pulp to the froth. Model gave similar results to Savassi et al. (1998) and Gorain et al. (1998) when was applied (Zheng et al., 2006a).</p>
Drainage model for water recovery models	$Q_w = A \cdot S_b \cdot \delta \cdot \alpha \cdot \exp(-k_{wd} \cdot \tau_f)$	<p>Water recovery considered a two step process (Moys, 1984). Model gives god fit to the experimental data for overall water recovery. The physical significance of the model parameter e.g the water film thickness of air bubbles, may not reflect true water recovery mechanisms (Zheng et al., 2006a).</p>
	$Q_w = \alpha_a Q_a \left(\frac{1}{1 - \frac{255.6}{r_b^2} \cdot J_g \cdot (1 - \alpha_a) \cdot \frac{\eta}{\rho_w \cdot g}} - 1 \right)$	<p>The variables in the model have a physical meaning and can be experimentally determined (Neethling and Cilliers, 2003; Neethling et al., 2003; Neethling et al., 2000). When applied to experimental data the model gave a good fit even at different operating conditions and perfomed better than empirical models (Zheng et al., 2006a). However the model expressions used by Zheng (2006a) are unrecognizable from those in Neethling's et al. (2003) paper(Stevenson, 2007). The model is limited to application in process control and cannot be used in its present form for predictive purposes (Neethling et al., 2003). Stevenson proposes an alternative liquid recovery model and argues against that developed by Neethling et al. (2003) (Stevenson, 2007; Stevenson et al., 2007). He points out fundamental flows in developing a water recovery model based on the equations by Neethling et al. (2003) (Stevenson, 2007). The model is in excellent agreement with experimental data (Stevenson et al., 2007). However experimental tests conducted so far were carried out on de-mineralized foam.</p>

CHAPTER THREE

3. METHODOLOGY

This Chapter describes the fundamental property based model that was used to model the flotation process in the flow sheet simulations that were used to investigate the effects of feed ore variation on flotation. Model parameter values from literature that were used in calibrating the model are presented along with methods for obtaining these parameters. Lastly, a description of HSC Chemistry 7 flow sheet simulation modelling software will be discussed along with the method that was followed in integrating the fundamental property based model into the simulation software. Each step that was carried out in developing the fundamental property based model simulation wizard in HSC Chemistry 7 simulation software during the model integration phase will be discussed in detail.

3.1. The fundamental property based flotation model

A fundamentally derived property based model was selected for determining the flotation rate constant of microwave treated ore over experimental methods because fundamental models utilise liberation as an indirect variable in calculating the flotation rate constant through the use of contact angle to describe particle surface hydrophobicity. This is in contrast to experimental methods where there is no specific association of the flotation rate to particle size or mineral liberation (Ralston et al., 2007). For this study it was important that the chosen method for determining the flotation rate constant be sensitive to changes in feed ore mineral liberation and particle size as these were variable properties in the simulations. Other major limitations of experimental methods that made them unattractive for use in this study were the costs associated with the method. This is because changes in feed ore mineral liberation properties require a separate set of kinetic data to be obtained from the experimental methods; this increases the cost of investigating the effects feed ore liberation changes to the flotation process (Dobby and Savassi, 2005).

Development of the fundamental property based model for the prediction of flotation cell recovery represents a major step in flotation modelling. The property based model, unlike first order methods, offers a great opportunity in the investigation of the effects of various cell conditions on flotation recovery and scale up processes. The expression for the rate of removal of particles per unit volume, N_p , in a flotation cell described in Chapter 2 section 2.4.2, equation 2.6 may be written as follows (Bloom and Heindel, 2002; Grano, 2006):

$$\frac{dN_P}{dt} = -k = -Z_{pb} \cdot E_{coll} / N_P \quad 3.1$$

This rate expression supports the first order rate approach to modelling flotation (Bulatovic, 2007; Mao and Yoon, 1997; Pyke et al., 2003). It was shown Chapter 2 section 2.4.2 that this rate can be expressed as the product of the collection efficiency E_{coll} and the bubble-particle collision frequency Z_{pb} equation 2.7 (Pyke et al., 2003; Mao and Yoon, 1997; Duan et al., 2003). The negative sign indicates the population density of the particles in the cell is decreasing. The flotation rate constant can thus be described as a function of appropriate bubble-particle collision frequency per unit volume Z_{pb} and the collection efficiency E_{coll} models for turbulent hydrodynamic conditions found in flotation cells (Yoon and Mao, 1996; Mao and Yoon, 1997; Bloom and Heindel, 2002).

$$k = Z_{pb} / N_p E_{coll} \quad 3.2$$

Extensive work has been carried out for developing a general turbulent flotation rate model from first principle; one such model was developed by Pyke et al. (2003) (see equation 3.3).

$$k = \overbrace{\underbrace{2.39 \frac{G_{fr}}{d_b \cdot V_{cell}}}_{\text{Mechanical term}} \underbrace{\left[\frac{0.33 \varepsilon^{\frac{4}{9}} d_b^{7/9}}{\vartheta^{\frac{1}{3}}} \left(\frac{\Delta \rho_b}{\rho_{fl}} \right)^{\frac{2}{3}} \cdot \frac{1}{v_b} \right]}_{\text{Primary turbulence term}}}_{\text{Collision frequency}} \underbrace{E_c \cdot E_a \cdot E_s}_{\text{Elementary process}} \quad 3.3$$

Flotation rate constant (time⁻¹)

In equation 3.3 above the elementary flotation sub-processes are represented by relevant bubble-particle collision, attachment and stability efficiency models. The remainder of the expression represents the collision frequency per unit volume. Below the derivation of the form of the general flotation model used in this study will be given.

3.1.1. The bubble-particle collision frequency

Abrahamson (1975) derived an expression for describing the collision frequency for turbulent-flow (see equation 3.4). In the expression collision frequency is modelled in terms of the fluctuations of bubbles and particles. The bubble and particle fluctuations can be related to the character of the turbulent-flow that drives them (Brady et al., 2006).

$$Z_{pb} = 5N_p N_b d_{pb}^2 \sqrt{(\bar{V}_p^2 + \bar{V}_b^2)} \quad 3.4$$

- N_p and N_b are the number densities of floatable particles and bubbles respectively,
- \bar{V}_p and \bar{V}_b are the turbulent fluctuating velocity of the particles and bubbles respectively relative to the fluid.
-

$$d_{pb} = \left(\frac{d_p + d_b}{2} \right) \quad 3.5$$

- d_p and d_b are the particle and bubble diameters. For a fine disperse suspension the particle diameter, d_p is much smaller than the bubble diameter d_b (Schubert, 2008)

In typical flotation processes the turbulent fluctuating velocities \bar{V}_p and \bar{V}_b have been found to be a function of the local turbulent dissipation energy and are approximately given by the following empirical expression proposed by Liepe and Mockel (1976), equation (Schubert and Bischofberger, 1998; Schubert, 2008; Abrahamson, 1975; Koh and Schwarz, 2006; Liu and Schwarz, 2009b):

$$\bar{V}_i = \frac{0.33 \varepsilon^{4/9} d_i^{7/9}}{\nu^{1/3}} \left(\frac{\rho_i - \rho_f}{\rho_f} \right)^{2/3} \quad 3.6$$

where the subscript i refers to the particle or bubble,

ε is the turbulent dissipation energy

ν is the kinematic viscosity

ρ_i refers to the density of the bubble or particle

Liepe and Mockel's equation is used to describe the turbulent velocities in Abrahamson's model. This model, which is developed by dimensional analysis and least squares fitting methods over experimental data, is valid at intermediate Stokes numbers typical of flotation processes (Schubert, 1999; Brady et al., 2006). Although the model is appropriate in determining the relative particle turbulent velocity, its use for predicting the bubble turbulent velocity has been questioned in literature (Brady et al., 2006; Sherrell, 2004). An alternative model equation 3.7 has been developed specifically for determining bubble root mean square (rms) (Suazo et al., 2009; Brady et al., 2006) .

$$\bar{V}_b^2 = 2(\varepsilon d_2)^{2/3} \quad 3.7$$

Equation 3.7 was however not used for determining the fluctuating bubble velocity in this study. This was mainly because in developing the general flotation model expression shown in equation 3.3, Pyke (2003) used Liepe and Mockel's model equation 3.6 for determining the bubble fluctuating velocity.

$$\sqrt{\bar{V}_b^2 + \bar{V}_p^2} = \left[\left[\frac{0.33\varepsilon^{4/9}d_b^{7/9}}{\vartheta^{1/3}} \left(\frac{\rho_b - \rho_f}{\rho_f} \right)^{2/3} \right]^2 + \left[\frac{0.33\varepsilon^{4/9}d_p^{7/9}}{\vartheta^{1/3}} \left(\frac{\rho_p - \rho_f}{\rho_f} \right)^{2/3} \right]^2 \right]^{1/2} \quad 3.8$$

To arrive at the final expression of the collision frequency per unit volume, Pyke et al. (2003) assumed that the particle rms velocity $\sqrt{\bar{V}_p^2}$ and the particle diameter d_p could be neglected (Duan et al., 2003; Pyke et al., 2003). After making these assumptions the final expression of collision frequency per unit volume derived by Pyke et al (2003) is presented in equation 3.9.

$$Z_{pb} \approx 5N_p N_b \left(\frac{d_b}{2} \right)^2 \left[\frac{0.33\varepsilon^{4/9}d_b^{7/9}}{\vartheta^{1/3}} \left(\frac{\rho_b - \rho_f}{\rho_f} \right)^{2/3} \right] \quad 3.9$$

$$d_{pb} \approx \frac{d_b}{2} \quad 3.10$$

The assumptions made by Pyke et al. (2003) stated above, are only valid for fine particles sizes below 100 μm where the particle diameter can be considered to be much smaller than the bubble diameter. In this study the particle fluctuating velocity was considered in the final expression of the collision frequency. Thus the collision frequency per unit volume Z_{pb} used in this study is expressed as (Suazo et al., 2009);

$$Z_{pb} \approx 5 \left(\frac{d_p + d_b}{2} \right)^2 N_b N_p \left[\left[\frac{0.33\varepsilon^{4/9}d_b^{7/9}}{\vartheta^{1/3}} \left(\frac{\rho_b - \rho_f}{\rho_f} \right)^{2/3} \right]^2 + \left[\frac{0.33\varepsilon^{4/9}d_p^{7/9}}{\vartheta^{1/3}} \left(\frac{\rho_p - \rho_f}{\rho_f} \right)^{2/3} \right]^2 \right]^{1/2} \quad 3.11$$

The bubble number density N_b can be related to the gas flow rate G_{fr} and the residence time of bubbles in the unit volume t_r by the following expression (Pyke et al., 2003; Duan et al., 2003):

$$N_b = \frac{6G_{fr}}{\pi d_b^3 V_{cell}} t_r \quad 3.12$$

where V_{cell} is the flotation cell volume. The residence time of the bubbles can be expressed as the time that bubbles of velocity v_b remain in a unit volume.

$$t_r = \frac{1 \text{ unit length}}{v_b} \quad 3.13$$

Where the superficial gas velocity, J_g , is used instead of the gas flow rate, G_{fr} , the bubble number density, N_b is expressed as,

$$N_b = \frac{6J_g(L_c \times W_c)}{\pi d_b^3 \cdot V_{cell}} t_r \quad 3.14$$

where L_c and W_c are the length and width of the flotation cell (Grano, 2006).

Equation 3.15 represents the final form of the general flotation model that was used in this study for predicting the kinetic flotation rate constant, k , under turbulent flotation conditions.

$$k = 2.39 \frac{G_{fr}}{d_b^3 \cdot V_{cell}} (d_p + d_b)^2 \sqrt{\bar{V}_b^2 + \bar{V}_p^2} \left(\frac{1}{v_b} \right) \cdot E_{coll} \quad 3.15$$

Table 3-1 above is a summary of the mechanical and primary turbulence terms expressions the product of which gives bubble-particle collision frequency a value that is required in the fundamental property based model equation 3.1. The various model input parameters required to calculate each term are given in the table along with a brief description of the method that is used in obtaining the parameters.

3.1.2. Calculation of the elementary processes

The elementary processes in equation 3.1 are described by the collection efficiency; which is a product of the flotation sub-process of collision, attachment and stability (equation 3.16).

$$E_{Coll} = E_c \cdot E_a \cdot E_s \quad 3.16$$

The various models for determining the collision, attachment and stability efficiencies have been discussed in Chapter two. In deriving a general flotation model it is important to capture the turbulent characteristics of the flow in the flotation as well as the hydrodynamic and surface forces. Models that capture all three of these factors have not been fully developed. The following elementary sub-process models are used in the general flotation model for determining the collection zone efficiency,

1. GSE model for determining the Collision efficiency
2. Modified Dobby and Finch attachment model
3. Schulze stability efficiency model

These models capture the particle surface chemistry in the flotation process. The parameters required to calibrate these models can be obtained through application of different experimental methods described in literature making them useful tools in flotation modelling.

3.1.2.1. Collision efficiency determined by the Generalised Sutherland equation (GSE)

Collision efficiency has been predicted based on potential flow conditions by Sutherland and others, leading to the development of the GSE (Nguyen et al., 2006; Nguyen and Nguyen, 2009). The GSE model (Miettinen et al., 2009; Dai et al., 1998), E_{C-GSE} , incorporates the interceptional mechanism of the Sutherland model with the positive effect of hydrodynamic pressing force and the negative effect of centrifugal acceleration (equation 3.17).

$$E_{C-GSE} = E_{C-SU} \cdot \sin^2 \theta_t \cdot \exp(I_1 + I_2) \quad 3.17$$

Where $E_{C-SU} = \frac{3d_p}{d_b}$

E_{C-SU} is the Sutherland collision efficiency accounting only for the interception mechanism, I_1 is the positive effect of the hydrodynamic pressing force (equation 3.18) and I_2 is the negative effect of centrifugal acceleration (see equation 3.19).

$$I_1 = 3K_3 \left(\ln \frac{3}{E_{C-SU}} - 1.8 \right) \quad 3.18$$

$$I_2 = - \frac{4 \left(\frac{2}{3} + \frac{\cos^2 \theta_t}{3} - \cos \theta_t \right)}{\sin^4 \theta_t} \quad 3.19$$

The maximum angle of tangency θ_t is the maximum collision angle of the particle to the bubble beyond which collision is prevented (Dai et al., 1998; Dai et al., 2000; Miettinen et al., 2009). When the angle of collision $\theta_c < \theta_t$ the hydrodynamic pressing force is dominant thereby improving the chances of particle deposition, at $\theta_c > \theta_t$ the negative centrifugal force prevents collision (Dai et al., 1998; Dai et al., 2000; Miettinen et al., 2009). The maximum angle of tangency θ_t is defined as,

$$\theta_t = \sin^{-1} \left\{ 2\beta \left[(1 + \beta^2)^{1/2} - \beta \right] \right\} \quad 3.20$$

where β is a dimensionless number defined as,

$$\beta = \frac{4E_{C-SU}}{9K_3} \quad 3.21$$

K_3 is defined as,

$$K_3 = \frac{v_b(\rho_p - \rho_{fl})d_p^2}{9\mu_f d_b} \quad 3.22$$

Where; μ_f is the fluid viscosity. For large β values ($\beta \geq 1$), θ_t approaches 90° and inertial forces do not interfere with the interception mechanism; under these conditions the Sutherland collision model is valid. When $\beta \leq 1$, the θ_t values shift significantly away from 90° due to inertial forces and interceptional effects that are both at play. Thus β represents the measure of the relative importance of the interceptional and inertial effects contribution to the collision process in the GSE (Dai et al., 2000; Duan et al., 2003). The GSE model is thus capable of taking into account both the inertial and gravity effects that are present when the particle size is larger than the limit size for the Sutherlands' model ($0.1 \mu\text{m}$) (Dai et al., 2000; Pyke et al., 2003).

3.1.2.2. Attachment Efficiency determined by the Dobby-Finch attachment model

The modified Dobby-Finch attachment model is used to determine the bubble-particle attachment sub-process efficiency. The model is based on the relative magnitudes of the induction time and sliding time (Dobby and Finch, 1987). The induction and sliding time have been discussed in Chapter two, section 2.4.3.2 which offers a review of attachment models. The model assumes that particle-bubble collision occurs evenly over the section of the bubble surface between the following angles $\theta = 0$ and $\theta = \theta_t$ where θ is measured from the stagnation point or upper surface of the rising bubble (Ralston et al., 1999; Pyke et al., 2003; Duan et al., 2003). θ_t . Dobby and Finch then defined the attachment efficiency as the ratio of the area corresponding to θ_a to the area corresponding to θ_t , where θ_a is the adhesion angle.

$$E_a = \frac{\sin^2 \theta_a}{\sin^2 \theta_t} \quad 3.23$$

Where E_a Attachment efficiency, θ_a -adhesion angle, θ_t is the maximum possible collision angle.

The adhesion angle is defined as the specific contact angle where if a particle collides at this angle, its sliding time will be equivalent to the induction time. The adhesion angle relates the sliding and induction times to the attachment efficiency.

$$\theta_a = 2 \arctan \exp \left[-t_{ind} \frac{2(v_p + v_b) + v_b \left(\frac{d_p}{d_p + d_b} \right)^3}{d_p + d_b} \right] \quad 3.24$$

Where: θ_a -adhesion angle, v_p -particle velocity, v_b -bubble velocity, d_p -particle diameter, d_b -bubble diameter, t_{ind} -induction time. The induction time is a function of contact angle and particle size and can be determined experimentally. It can be correlated by the following empirical equation (Dai et al., 1999; Koh and Schwarz, 2006; Ralston et al., 1999; Pyke et al., 2003; Duan et al., 2003; Miettinen et al., 2009),

$$t_{ind} = Ad_p^{0.6} \quad 3.25$$

Where; A, constant parameter and d_p is the particle diameter. Based on the work carried out by (Dai et al., 1999), parameter A was observed to be inversely proportional to the particle contact angle φ . Using these results, Koh et al., (2006) later developed the following empirical equation for determining the induction time.

$$A = \frac{75}{\varphi} \quad 3.26$$

Where; d_p -particle diameter (m), φ -contact angle (degrees) and t_{ind} -induction time is obtained in (seconds). This expression has subsequently been successfully applied in the determination of parameter A by other authors (Shahbazi et al., 2009).

The particle settling velocity under the turbulent cell conditions, v_p , is obtained using the following expression (Bruce, 2003),

$$v_p = \frac{20.52}{d_p \rho_f} \left(\left[\left(\frac{d_p^3 (\rho_s - \rho_f) \rho_f g}{0.75 \vartheta^2} \right)^{0.5} \right]^{0.5} - 1 \right)^2 \quad 3.27$$

The modified Dobby and Finch model essentially expresses attachment efficiency as a ratio of particle attached to a bubble over the maximum possible particles that can be attached to a bubble. It does not fully capture the effects of the electrostatic, van der Waals, and hydrophobic surface forces.

However the model has been validated and has been shown to be suitable for describing the bubble-particle attachment sub-process efficiency. Models have been developed based on the DVLO theory that captures surface forces effects on the attachment process (Yoon and Mao, 1996). Comprehensive validation of these models has not been reported in literature (Ralston et al., 1999).

3.1.2.3. Particle-bubble stability efficiency determined by Schulze model

Particle-bubble stability efficiency depends on the attachment force between the bubble and the particle in relation to detachment forces, in the environment (Ralston et al., 1999; Duan et al., 2003). Schulze (2009) proposed that the bubble-particle stability efficiency could be expressed as follows,

$$E_s = 1 - \exp\left(1 - \frac{F_{att}}{F_{det}}\right) \quad 3.28$$

The modified bond number Bo^* is defined as the ratio of the attachment and detachment forces and is given by (Bloom and Heindel, 1997).

$$Bo^* = \frac{F_{att}}{F_{det}} = \frac{d_p^2(\Delta\rho g + \rho_p a_c) + 1.5d_p(\sin^2 \omega)f(d_b)}{|6\gamma \sin \omega \sin(\omega + \varphi)|} \quad 3.29$$

with,

$$f(d_b) = \left(\frac{4\gamma}{d_b} - d_b \rho_{fl} g\right) \quad 3.30$$

where; $\omega = 180^\circ - \varphi/2$ refers to the location of the particle at the liquid-vapour interface, φ -contact angle, γ -liquid-vapour surface tension, g -gravitational constant, and a_c -particle centrifugal acceleration. The particle centrifugal acceleration a_c can be related to the turbulent-flow field and the dissipation energy, ε (Schulze, 1977). Assuming that the aggregates are moved mainly by the centrifugal acceleration present in the vortex and the turbulent radius is equal to the aggregate radius the particle centrifugal acceleration can be described by equation 3.31 for large eddies. (Miettinen et al., 2009; Bloom and Heindel, 1997)

$$a_c = 1.9 \frac{\varepsilon^{2/3}}{\left(\frac{d_p}{2} + \frac{d_b}{2}\right)^{1/3}} \quad 3.31$$

3.2. General flotation model parameter determination for model calibration

In calculating the flotation rate constant using the general flotation model the following are some of the required parameters (see equation 3.15).

1. Energy dissipation
2. Bubble diameter
3. Bubble rise velocity
4. Contact angle of liberated particle.

These parameters are not commonly available from flotation cell operations plant data as they are not routinely measured. In this study values for these parameters that were used in the simulations were obtained from a previous study that was carried out by Ralston et al. (2007) on a Copper flotation concentrator plant. Table 3-2 is a summary of values of these parameters from the work carried out by Ralston et al. (2007). The methods that were used by Ralston et al (2007) to come up with these value and other methods for determining these values available in literature will be discussed and presented in this section. A list of all the fundamental property based model input parameter values that were used in calibrating the fundamental property based model in this study is given in Appendix G, Table G.1.1

Table 3-2: Model calibration parameters from a study carried out by (Ralston et al., 2007)

Variable	Literature Parameter (Ralston et al., 2007)
Sulphide mineral contact angle (φ)	78°
Energy dissipation (ϵ)	11 m ² /s ³
Bubble diameter (d_b)	0.0013 m
Bubble rise velocity (v_b)	0.18 m/s

3.2.1. Determination of particle Contact angle

The contact angle φ is described thermodynamically by Young's equation,

$$\gamma_{s/a} = \gamma_{s/l} + \gamma_{l/a} \cos \varphi \quad 3.32$$

Where $\gamma_{s/a}$, $\gamma_{s/l}$, $\gamma_{l/a}$ are the solid-vapour, solid-liquid, and liquid-vapour interfacial tensions respectively. Duan et al. (2003) used the relationship between advancing contact angle and Time of Flight Secondary ion Mass spectroscopy (ToF-Sims) analysis results, to determine the sulphide particles single phase contact angle.

Ralston et al (2007) using the same method reported a sulphide contact angle value of 78°. In this study a value for the contact angle of fully liberated sulphide minerals of 78° was used, while fully liberated NSG was assumed to have a zero contact angle as was the case in Ralston's study (Ralston et al., 2007). Contact angle values for sulphide minerals that are reported in literature range between 68° to 85° (Duan et al., 2003; Pyke et al., 2003; Ralston et al., 2007). Most mineral particle exists as composites while current contact angle measurement methods report contact angle values for single phase minerals. To overcome this problem the Cassie equation has been found to be appropriate for determining the composite particle contact angle (Ralston et al., 2007). A description of composite particle contact angle calculation method utilising the Cassie equation as used in this study is given below.

3.2.1.1. Composite particles contact angle calculation

Cassie equation is often applied in determining the contact angle ore particles (Ralston et al., 2007; Chau et al., 2009). The individual ideal mineral contact angles are used to relate the apparent contact angle of the ore particle through Cassie's equation as follows (see equation 3.33) (Bormashenko, 2008; Iwamatsu, 2006; Rodríguez-Valverde, 2008; Whyman et al., 2008; Zhang and Kwok, 2005; Chau et al., 2009),

$$\cos \varphi = f_1 \cos \varphi_1 + f_2 \cos \varphi_2 \quad 3.33$$

where; f_1 and f_2 -fractional areas of mineral surfaces on a single particle with contact angle φ_1 and φ_2 . The Cassie's equation was initially proposed for describing contact angle changes for two component porous surfaces (Iwamatsu, 2006; Zhang and Kwok, 2005). It can be used for predicting the contact angle of rough heterogeneous hydrophobic surfaces (Bormashenko, 2008). There are some concerns regarding the validity of Cassie's equation especially its application to mineral systems (Iwamatsu, 2006; Zhang and Kwok, 2005; Rodríguez-Valverde, 2008). However no alternative models have been developed yet that adequately capture the physical surface properties (Ralston et al., 2007).

3.2.2. Energy dissipation

The main source of energy in a mechanical flotation cell is derived from the motion of the impeller which produces the turbulent conditions within the cell. It has been shown that energy dissipation affects both the particle-bubble collision frequency and the bubble-particle aggregate stability (Newell and Grano, 2006; Newell and Grano, 2007). Direct calculation of energy dissipation rate requires evaluation of the strain rate at a spatial resolution less than the Kolmogorov length scale (Newell and Grano, 2006; Newell and Grano, 2007; Brady et al., 2006). There are no methods available in literature that can fully resolve the instantaneous spatial derivatives at such small scales (Brady et al., 2006). However there are methods that have been reported in literature for calculating dissipation energy based on different techniques for measuring velocity fluctuations in a stirred tank. Some of these methods are; Digital particle image velocimetry, Laser-Doppler velocimetry, and hot wire velocimetry methods (Wu and Patterson, 1989; Brady et al., 2006; Newell and Grano, 2006; Newell and Grano, 2007). Wu and Patterson (1989) proposed the following equation for calculating the turbulent dissipation energy,

$$\varepsilon = \frac{Aq^3}{L} \quad 3.34$$

where, A is a constant, L is a measure of the turbulent length macro scale and q is the turbulent kinetic energy. A has been found to be equal to 0.85 and L is generally assumed to be constant and equal to half the turbine length (Wu and Patterson, 1989). The turbulent kinetic energy can be obtained as follows (Duan et al., 2003; Pyke et al., 2003),

$$q = \frac{1}{2} [\bar{U}_x^2 + \bar{U}_y^2 + \bar{U}_z^2] \quad 3.35$$

where; \bar{U}_x^2 , \bar{U}_y^2 , \bar{U}_z^2 are the root mean square of fluctuations of the measured turbulent fluid velocities (Pyke et al., 2003; Duan et al., 2003). In this study a local energy dissipation value of 11W/kg for a 85 m³ mechanical flotation cell as reported by Ralston et al.(2007) was used to calibrate the fundamental based model along with other parameters from the same study by Ralston et al.(2007).

3.2.3. Bubble diameter

There are two well established techniques for measuring bubble size in flotation cells; capillary and imaging techniques (Hernandez-Aguilar et al., 2004). The McGill bubble viewer and the UCT bubble size analyser have been tested under both laboratory and plant conditions and they have been shown to give satisfactory estimates of bubble size in flotation cells (Hernandez-Aguilar et al., 2004; Ralston et al., 2007; Grau and Heiskanen, 2002; Grau and Heiskanen, 2003). Typical bubble diameter sizes range between 0.8 mm to 2 mm (Schwarz and Alexander, 2006; Grano, 2006; Massinaei et al., 2009b). A Sauter mean bubble diameter of 1.3 mm reported in the work done by Ralston et al. (2007) was used in the model calibration. Various methods are available in literature for obtaining this value for a typical operating flotation cell. These methods will be described briefly below.

3.2.3.1. McGill bubble viewer

The McGill bubble viewer utilises imaging techniques for bubble size measurement. It is designed to measure bubble sizes by directing a sample of bubbles into a specially design viewing chamber (Hernandez-Aguilar et al., 2004). The bubbles in the chamber are then exposed to light and photographed with a digital camera as they impact on a slopped glass plane (Grau and Heiskanen, 2002; Leiva et al., 2010). An image analysis procedure is then used to size the collected bubbles and hence determine the Sauter mean bubble diameter (Grau and Heiskanen, 2002; Hernandez-Aguilar et al., 2004).

3.2.3.2. UCT bubble size analyser

The UCT bubble size analyser utilises capillary methods for measuring the bubble size. It operates by capturing the bubbles and drawing them through a capillary tube (Hernandez-Aguilar et al., 2004). A sampling tube is attached to a water reservoir where the capillary tube is placed (Grau and Heiskanen, 2002). Captured bubbles ascend through the sampling tube to the reservoir where they are suctioned into the capillary tube (Grau and Heiskanen, 2002; Hernandez-Aguilar et al., 2004). In the capillary tube the bubble length and velocities are measured by using optical detectors (Ralston et al., 2007). From these reading the bubble sizes are then determined (Grau and Heiskanen, 2002).

3.2.4. Bubble rise velocity

Bubble rise velocity is assumed to be equivalent to the fluid velocity that is measured by utilising velocimetry techniques (Pyke et al., 2003). In this study a bubble rise velocity value of 1 cm/s from the work by Ralston et al. (2007) was used in calibrating the model.

3.3. HSC Chemistry 7 simulation software

HSC Chemistry 7 simulation software has a function that allows for true particle modelling. True particle modelling refers to the highest level of modelling in HSC Chemistry Simulation software where the mineral particles that are treated in the simulation processes have been measured using MLA. The Mineral Liberation Analysis data files are used directly to represent the feed ore particles in the simulations. Particles are then generated based on the mineralogical information from the MLA data. The program then utilises particle tracking algorithms which allows for the liberation data for each of the streams in the simulation to be reported during the simulations. This is an important function as the actual individual particle liberation data can be used in the simulation.

3.3.1. Particle tracking in HSC Chemistry Simulation software

HSC Chemistry 7 simulation module has four calculation modes.

1. Particles (Minerals)
2. Reactions (Hydro)
3. Distribution (Pyro)
4. Experimental

Discussion will focus on the particle mode as it is the appropriate mode for carrying out simulation in minerals processing operations.

3.3.2. Particles (Mineral) mode

The liquid phase is assumed to be inert and no reactions take place in the system. This mode is appropriate for modelling grinding and flotation circuit processes. In this mode the variables are particles; these can in the simplest case be un-sized liberated particles. The most complex case is where the particles are real measured particles from Mineral Liberation Analysis data (MLA) (Roine, 2010).

3.3.2.1. True particle modelling in HSC Chemistry Simulation software using MLA data

The minerals based models that are used in simulating mineral processing flow sheets in HSC Chemistry 7 simulation module treat mineral particles from MLA data which have the following properties.

1. Size Diameter
2. Mineral Composition as wt%
3. Composition by volume
4. Mineral composition by surface area %

In generating particles in HSC Chemistry 7 Simulation software, mineralogical data are required. This data can be subdivided into two categories.

1. Global set up data which constitutes of general global mineral properties which do not change in the process such as chemical composition and specific gravity. These are calculated in HSC Chemistry 7 Simulation software for each particle and stream.
2. Input stream set up data which is obtained from the MLA analysis data. It consists of the main particle properties such as particle mineral composition and size. The following mineralogical information which is presented as a feed stream set up file in HSC Chemistry Simulation software is obtained from MLA data.
 - a. Weight percentage of each size class
 - b. Weight percentage of each mineral in each size class and bulk feed stream
 - c. Chemical composition of the fractions and the bulk feed

Appendix E is a summary of the file structure in HSC Chemistry 7 simulation software package.

3.4. Integrating the Fundamental model into HSC Chemistry 7

The fundamental property based flotation model was integrated into HSC Sim program so as to facilitate its use in flotation modelling.

A general flotation model wizard was created in HSC Chemistry Simulation 7 module utilising HSC Chemistry 7 Excel Macro commands in order to allow for the use of the

fundamental property based model in HSC Chemistry 7 during modelling. The model calculation steps were applied to individual particles, this allowed for the calculation of the flotation rate constant of individual particle based on the individual particle's liberation, density and size properties. The particle's liberation was related to particle hydrophobicity through the particle contact angle.

The model calculation steps programmed in the wizard were as follows.

1. Utilising the Cassie's equation, contact angles for all particles in each size class were calculated. This was done taking into account the individual single mineral contact angles of the mineral groups making up the particles and their composition.
2. The sub-process efficiencies for each particle were then calculated by taking into account the particle and fluid properties and contact angles.
3. Using the cell hydrodynamic information, the Mechanical and turbulent terms in the general flotation model expression were calculated.
4. A flotation rate constant, k_{Coll} , for each particle was then evaluated.
5. Perfect mixing in pulp zone was assumed in calculating the overall collection zone recovery, R_{Coll} , for each particle.

$$R_{Coll} = \frac{k_{Coll} \cdot t}{(1 + k_{Coll} \cdot t)} \quad 3.36$$

6. The flotation cell was assumed to consists of two distinct phases the pulp and the froth phase. The froth recovery term, R_f , was used to describe the contribution of the froth phase to the bubble-particle recovery to the concentrate, $R_{attached}$. The bubble-particle recovery is expressed as a product of the froth phase recovery and the collection zone recovery.

$$R_{attached,i} = R_f \cdot R_{Coll} \quad 3.37$$

7. The contribution of entrainment, R_{ent} , to overall recovery was calculated using flotation cell water recovery, R_w , and the degree of entrainment ENT for each particle (Yianatos et al., 2009; Zheng et al., 2006b; Zheng et al., 2005).

$$R_{ent} = R_w \cdot ENT \quad 3.38$$

The degree of entrainment, ENT , was calculated per particle size using an empirical model as follows (Savassi et al., 1998; Zheng et al., 2006b),

$$ENT = \frac{2}{\exp\left(2.292\left(\frac{d_i}{\xi}\right)^{adj}\right) + \exp\left(-2.292\left(\frac{d_i}{\xi}\right)^{adj}\right)} \quad 3.39$$

$$adj = \frac{\ln\left(\frac{1}{\delta}\right)}{\exp\left(\frac{d_i}{\xi}\right)} \quad 3.40$$

Where; d_i is particle size (μm), ξ is the entrainment parameter, or the particle size for which the degree of entrainment is 20%, δ is the drainage parameter, related to the preferential drainage of coarse particles.

8. The overall recovery across the flotation cell (R_{ovr}) for each individual particle was calculated using the following expression,

$$R_{ovr} = \frac{R_{attached}(100 - R_{ent})}{100 + R_{ent}} \quad 3.41$$

Appendix I shows an example of model wizard screen captures as they would appear in HSC Chemistry 7.

3.5. Conclusion

In this Chapter the parameters used in flotation modelling and the method used in incorporating the fundamental property based model in HSC Chemistry 7 have been described in detail. After integrating, the model in HSC Chemistry 7 and obtaining all the parameters required for model calibration from literature a modelling framework for investigating the effect of feed ore liberation variation on recovery was developed and is now ready for use. In order to carry out preliminary investigations on the effect of liberation variation on flotation recovery, different artificial ores with varying liberation profiles should be prepared. By investigating the downstream processing flotation recovery of these ores it is hoped to get an indication of the expected benefits of improved liberation due to microwave treatment on flotation recovery. The next Chapter will discuss the creation of these different flotation feeds.

CHAPTER FOUR

4. CREATION OF ARTIFICIAL FEED ORES

Laboratory Rod milled flotation feed MLA data for porphyry copper ore at two grind sizes ($P_{70}=120\ \mu\text{m}$ and $P_{70}=180\ \mu\text{m}$) from a previous study, was available for use as a flotation feed in this study (AMIRA:P879A, 2009). This MLA data was manipulated to create different flotation feeds with different mineral particle liberation spectrum. Thus additional floatation feed ores termed artificial flotation feed ores in this study, were created for use in investigating the effects of feed ore liberation change on value mineral recovery. These ores were supposed to represent various possible liberation scenarios of ground flotation feed ores. Their liberation profiles ranged from well liberated to poorly liberated ores. Thus allowing for the investigation of the effects of enhanced liberation expected from the application of microwave technology to be investigated using these ores.

4.1. Introduction

A detailed discussion of the methodology that was used in creating different flotation feeds will be given below along with a description of the base case feed ores that were used in creating artificial ores in this study. This will be followed by a detailed analysis of the key differences between the created artificial ores and the base case feed ores. Lastly the method that was used in calculating contact angles from the MLA data will be discussed briefly.

4.2. Copper 1 and Copper 2 base case feed ore (BC)

The particle size distribution and the MLA data of the two base case Rod milled flotation feed ores Copper 1 ($P_{70} = 120\ \mu\text{m}$ ground feed) and Copper 2 ($P_{70} = 180\ \mu\text{m}$ ground feed) was obtained from previous experimental analysis carried out on the ores (AMIRA:P879A, 2009). In creating a stream file in HSC Geo, the ore feed in the simulations was grouped into the following three main mineral groups as is instructed when creating a stream file in HSC Chemistry 7 simulation software: Chalcopyrite (Cpy), NSG and Pyrite (Py). Chalcopyrite was selected as it represents the average composition of the copper sulphides in the feed. Appendix C, Table C.1-1 and Table C.1-2 shows the

mineral grouping that was carried out in creating the stream files and all the minerals groups that were in the feed ore before grouping respectively. The particle size distribution for Copper 1 and Copper 2 feed ore is presented in Table 4-1 below. Copper 1 BC feed ore contains 312 particle liberation classes while Copper 2 BC feed ore contains on average 357 particle liberation classes.

Table 4-1: Base case feed ore particle size distribution of Copper 1 ($P_{70}=120 \mu\text{m}$) and Copper 2 ($P_{70}=180 \mu\text{m}$)

Grind size weight distribution (wt. %)		
Size class (μm)	Copper 1	Copper 2
-600+425		4.87
-425+300	2.63	13.48
-300+212	12.25	12.71
-212+150	13.72	8.83
-150+106	10.82	7.01
-106+75	8.09	5.46
-75+53	6.67	4.83
-53+38	6.30	4.64
-38	39.52	38.17

From the cumulative particle size distribution curve in Figure 4-1 it can be seen that for the two feed ores there is a high weight percentage of fines in the feed which constitutes at least 38% of the bulk feed weight.

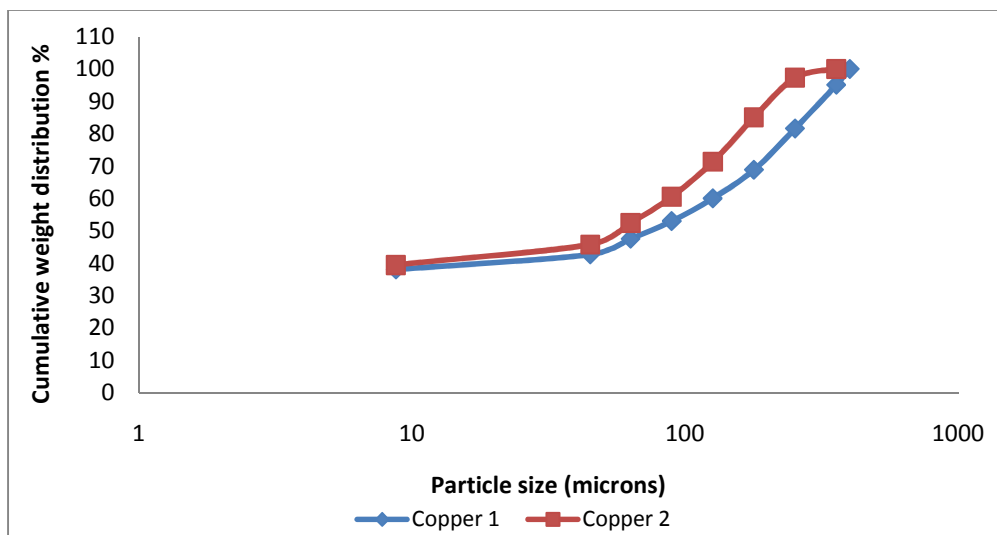


Figure 4-1: Base case feed ore cumulative particle size distribution.

The feed ore mineral composition by size for Copper 1 ore is shown in Table 4-2. Copper 1 feed ore had a Copper grade of 1.12%, while Copper 2 had a feed Copper grade of 1.08%. The mineral composition and mineral particle mode of occurrence for Copper 1 will be discussed first followed by a similar discussion of Copper 2 mineralogy.

4.2.1. Copper 1 mineralogy ($P_{70} = 120 \mu\text{m}$)

The bulk mineral composition by size for Copper 1 shows a low Chalcopyrite grade for the coarser size fractions (see Table 4-2).

Table 4-2 : Bulk mineral composition by size fraction of Copper 1 base case feed ore
 $P_{70}=120 \mu\text{m}$.

Size Class(μm)	0-38	38-53	53-75	75-106	106-150	150-212	212-300	300-425
Cpy wt%	4.24	3.55	3.19	3.09	2.76	2.17	1.78	1.33
Py wt%	4.32	5.92	7.88	7.59	10.39	9.47	8.00	7.19
NSG wt%	91.44	90.53	88.93	89.32	86.85	88.37	90.21	91.48

Figure 4-2 to Figure 4-4 is a graphical presentation of the mineral mode of occurrence of Chalcopyrite, Pyrite and NSG in Copper 1 base case feed ore. The mineral mode of occurrence for Chalcopyrite in Copper 1 feed ore shows that most of the chalcopyrite particles appear in fine size class range (0-38 μm) as fully liberated particles, (see Figure 4-2). The second most significant mode of occurrence for Chalcopyrite is as an associated binary particle with NSG predominantly in the 0 to 38 μm size class. Pyrite appears mostly as fully liberated particle in all size classes (see Figure 4-3). The second most significant mode of occurrence for Pyrite is as a binary liberated particle with Chalcopyrite. NSG appears in the feed largely as fully liberated particles although it is also associated with Chalcopyrite and Pyrite value minerals (see Figure 4-4).

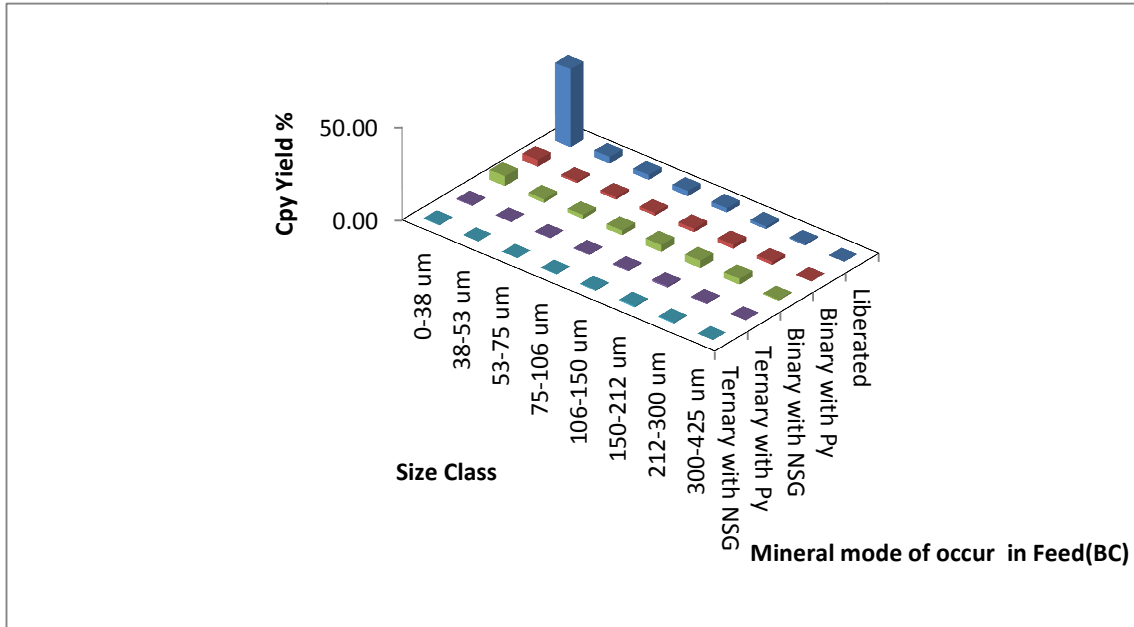


Figure 4-2: Chalcopyrite mineral mode of occurrence in Copper 1 feed ore ($P_{70}=120 \mu\text{m}$) used as base case in the simulations.

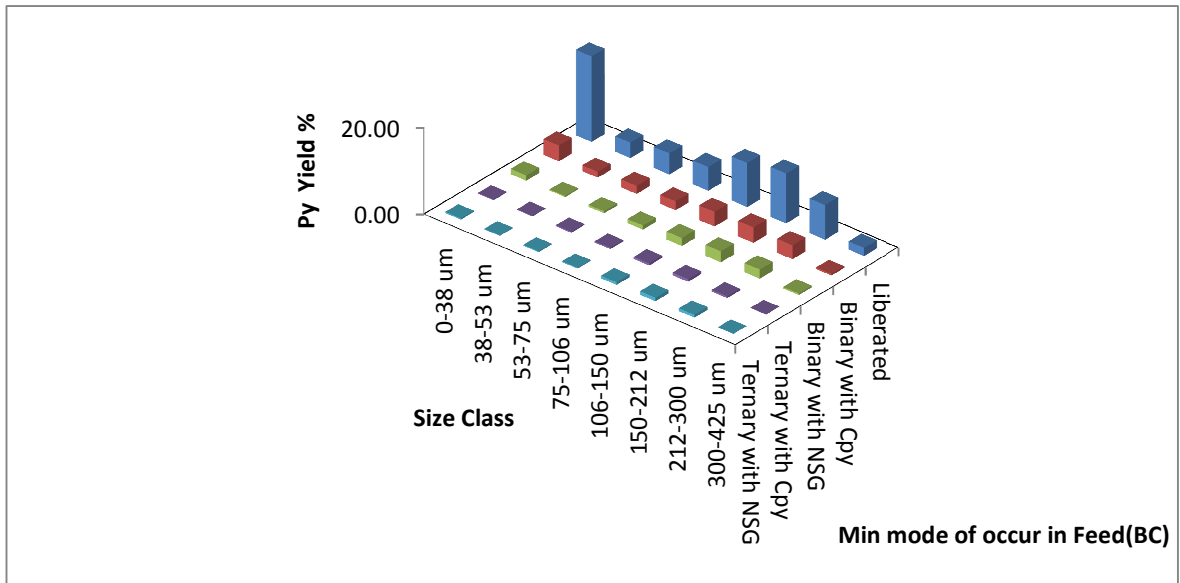


Figure 4-3: Pyrite mineral mode of occurrence in Copper 1 feed ore ($P_{70}=120 \mu\text{m}$) used as base case in the simulations.

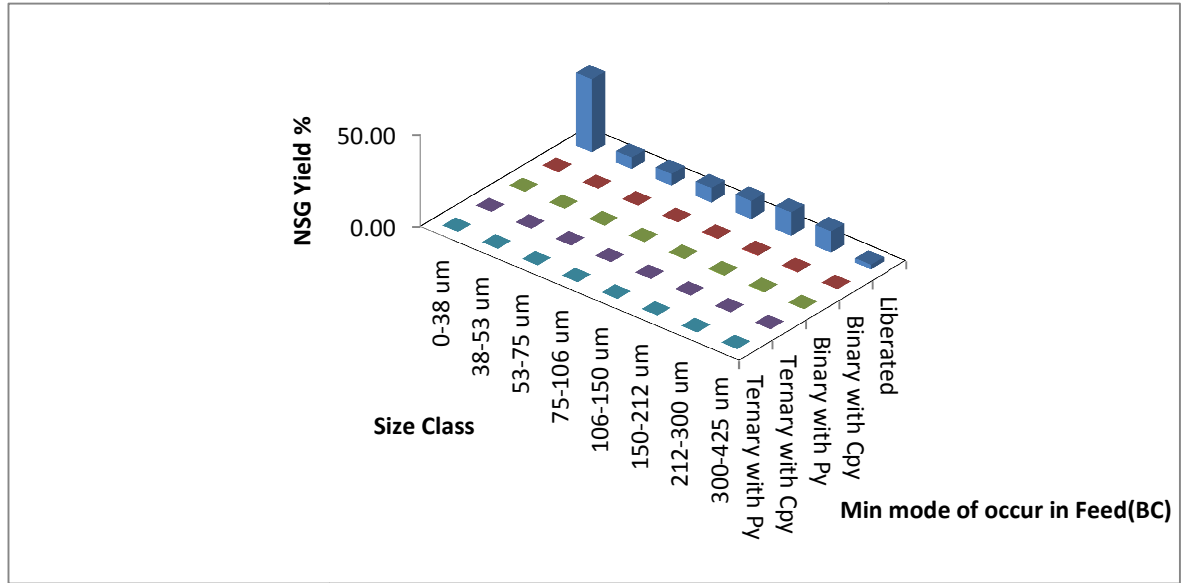


Figure 4-4: NSG mineral mode of occurrence in Copper 1 feed ore ($P_{70}=120 \mu\text{m}$) used as base case in the simulations.

4.2.2. Copper 2 mineralogy

The feed ore mineral composition by size for Copper 2 ore is shown in Table 4-3 below. Copper 2 ore feed has a Cu grade of 1.08%. Figure 4-5 to Figure 4-7 are graphical presentations of the mineral mode of occurrence of Chalcopyrite, Pyrite and NSG in Copper 2 base case feed ore. The mineral composition by size for Copper 2 also shows a low Chalcopyrite grade for the coarser size fractions, (see Table 4-3).

Table 4-3: Bulk mineral composition by size fraction of Copper 2 base case feed ore $P_{70}=180 \mu\text{m}$.

Size Class(μm)	0-38	38-53	53-75	75-106	106-150	150-212	212-300	300-425	425-600
Cpy wt%	4.05	3.74	3.75	2.97	3.17	2.69	2.30	1.44	1.32
Py wt%	3.23	6.81	7.63	7.89	9.26	10.67	9.20	8.03	6.34
NSG wt%	92.71	89.46	88.62	89.14	87.57	86.64	88.51	90.53	92.35

The mineral mode of occurrence for Chalcopyrite in Copper 2 feed ore is similar to that of Copper 1 ore feed, (see Figure 4-5). Pyrite appears mostly as fully liberated particles in all particle size classes, with second most significant mode of occurrence of Pyrite being as binary particles with Chalcopyrite (see Figure 4-6). NSG appears in the feed largely as fully liberated particles although it is also significantly associated with Chalcopyrite and Pyrite value minerals (see Figure 4-7).

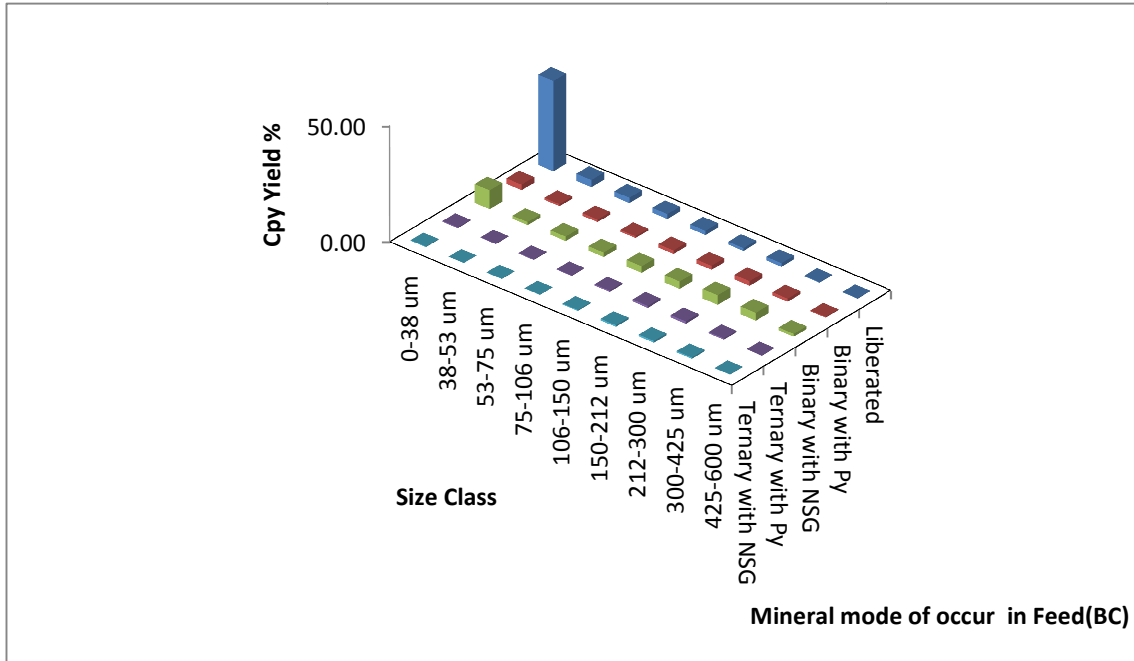


Figure 4-5: Chalcopyrite mineral mode of occurrence in Copper 2 feed ore ($P_{70}=180 \mu\text{m}$) used as base case in the simulations

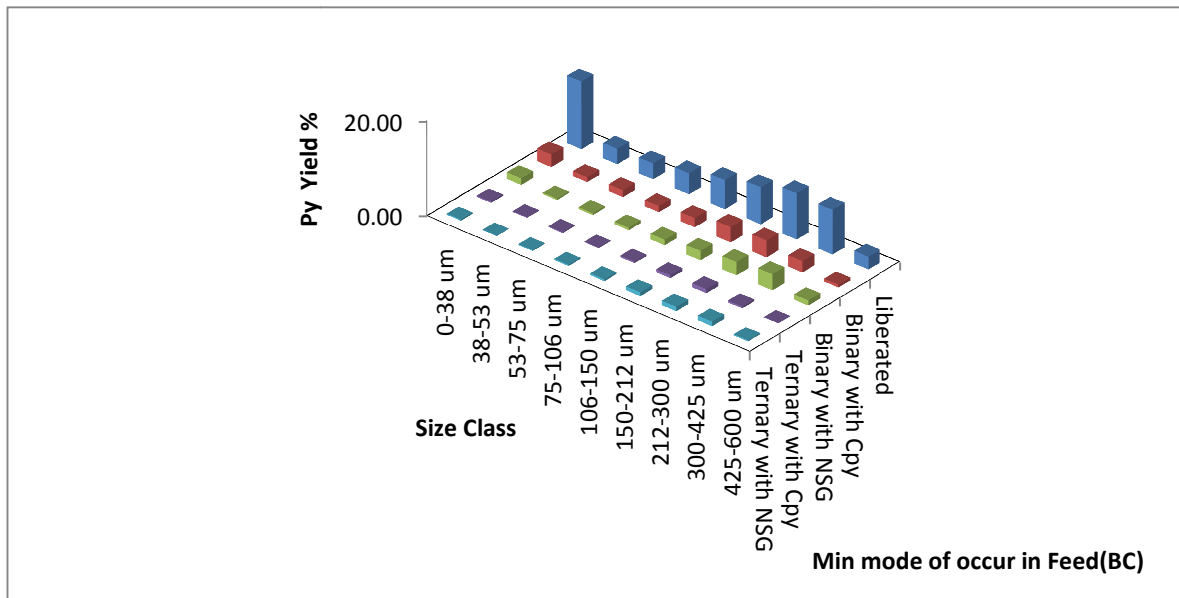


Figure 4-6: Pyrite mineral mode of occurrence in Copper 2 feed ore ($P_{70}=180 \mu\text{m}$) used as base case in the simulations.

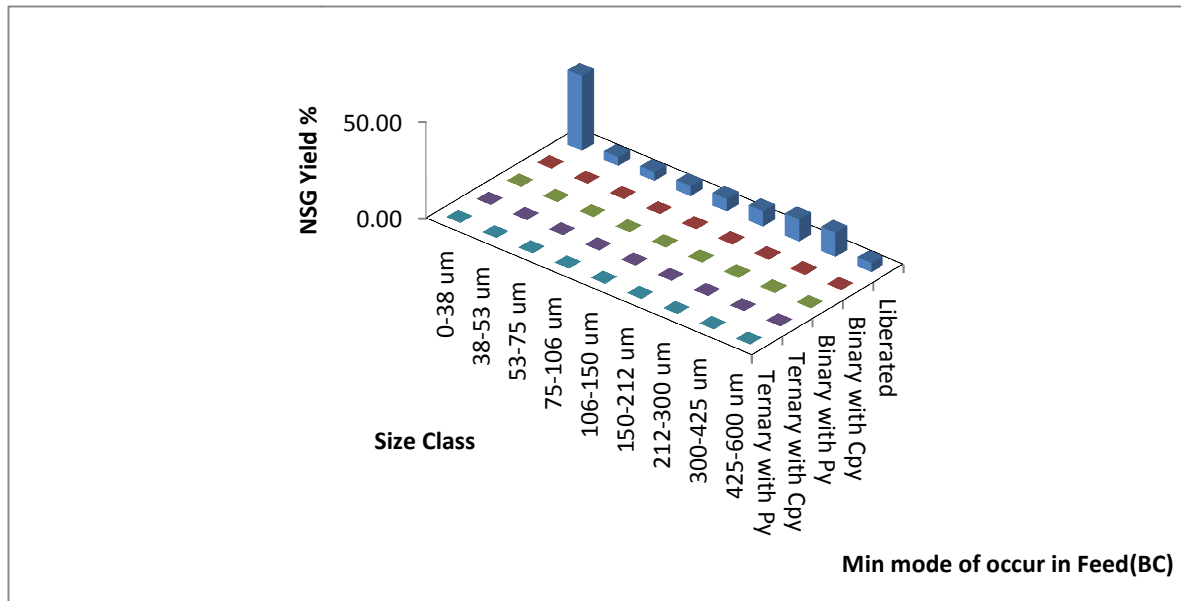


Figure 4-7: NSG mineral mode of occurrence in Copper 2 feed ore ($P_{70}=180 \mu\text{m}$) used as base case in the simulations.

4.3. Artificial flotation feed ores

Liberation in HSC is expressed as particle mineral composition. Table 4-4 shows the size class liberation profile as it appears in a stream file in HSC Chemistry for Copper 1 ore in the 0-38 micron size fraction. By redistributing the weights between the particle liberation classes in each size fraction and recalculating the particle liberation class composition, a new feed HSC Chemistry stream file is created which has a different liberation profile compared with the original starting base feed case ore, but with the same mineral composition.

4.3.1. Methodology

Artificial flotation feed ore was created by manipulating ball milled porphyry copper feed ore MLA data that were available from a previous study, which was aimed at investigating the effects of microwave treatment on flotation (AMIRA:P879A, 2009). These feed ores consisted of Copper 1 and Copper 2 flotation feed ore at P_{70} grind sizes of $120 \mu\text{m}$ and $180 \mu\text{m}$, respectively. These flotation feeds were selected to be the base case feed ores.

Changing the stream file liberation profile of the base case feed ores allowed for different liberation scenarios of these ores to be considered, thus creating artificial ores. These artificial ores were created based on HSC Chemistry 7 feed ore stream data for the base case ores. These different artificial feed ores had the same mineral composition and particle size distribution as the base case feed ores with the only difference between them being the particle liberation spectrum.

Table 4-4: HSC Chemistry 7 feed ore stream file showing liberation profile for particle liberation classes in the 0-38 μm size fraction.

Mineral mode of occurrence	Liberation particle class	Particle class composition			Particle class weight in tons			Bulk wt% of flotation feed	Fraction wt% of class
		Cpy %	Py %	NSG %	Cpy tph	Py tph	NSG tph		
Fully liberated	Cpy	100.0	0.0	0.0	12.0	0.0	0.0	1.3	3.4
Fully liberated	Py	0.0	100.0	0.0	0.0	11.1	0.0	1.2	3.1
Fully liberated	NSG	0.0	0.0	100.0	0.0	0.0	325.0	36.1	91.6
Binary	CpyPy	93.1	6.9	0.0	0.2	0.0	0.0	0.8	1.7
Binary	CpyNSG	69.8	30.2	0.0	0.0	0.0	0.0	0.0	0.0
Binary	PyNSG	57.5	42.5	0.0	0.0	0.2	0.06	0.0	0.0
Ternary	CpyPyNSG	50.7	47.5	1.8	0.1	0.1	0.0	0.0	0.1
Fraction Total					12.3	11.4	325.0	40.0	100

Table 4-4 above is an example of a feed ore size fraction liberation profile (0-38 μm) for Copper 1 ore. In this example the 0 to 38 μm size fraction constituted 40% of the bulk 890 tph feed stream solids weight fraction.

The following underlying principles describing well liberated ore and poorly liberated ore were used as guidelines in creating the various liberated ore scenarios. It is generally understood that improved value mineral recovery is expected from a feed ore that has the following properties;

- Most of the value mineral exists as fully liberated particles.
- Most of the NSG is fully liberated.

Poor value mineral recovery is expected from feed ores that have the following properties;

- Most of the value mineral exist as ternary composite
- Most of the value mineral groups exist as binary composite particles with NSG.

Table 4-5 below summarises the feed ore liberation scenarios that were used as flotation feeds in this study as well as the number of particle liberation classes in each of the feed ores in the simulations. Two extreme fictional liberation profile scenarios were first considered. These were fully liberated (FL) feed ore where the three value mineral groups exist as fully liberated particles in the feed ore, and fully locked where all three mineral groups in the feed stream exist as binary and ternary composite particles in the feed stream. Three other fictional feed ore liberation profile scenarios that lay between the fully locked and the fully liberated ore profile were also considered, these will referred to as Ore 1, Ore 2 and Ore 3 in this study.

Table 4-5: A summary of the feed ore scenarios that were used in investigating the effects of feed ore liberation changes on the downstream flotation process.

Feed ore scenario	Liberation characterisation	Number of particle liberation classes	
		Copper 1 (120 µm)	Copper 2 (180 µm)
BC	Base Case Porphyry Copper ore	312	351
FL	Fully liberated ore (Artificial ore)	24	27
Ore 1	Well liberated ore (Artificial ore)	312	324
Ore 2	Highly liberated ore (Artificial ore)	312	351
Ore 3	Poorly liberated ore (Artificial ore)	312	351
LC	Completely locked ore (Artificial ore)	312	351

4.3.2. Copper 1 group artificial ores

The major variations between the BC feeds and the artificial feeds that were created will be discussed below, starting with variations between Copper 1 base case feed and the five artificial feeds that were created from it. Appendix H shows the bulk particle weight for all the particle liberation classes in a size class, for Copper 1 flotation feed ores (see Table H.1-1 to Table H.1-8).

4.3.2.1. Fully liberated ore (FL)

In creating fully liberated feed, mineral group weights that exist in other mineral liberation classes per individual size fractions were summed up into the fully liberated class of each mineral group in the ore. The result was a flotation feed consisting of only fully liberated mineral particle class in each size class fraction. Table 4-6 below shows the increase in fully liberated value mineral particle class in fully liberated ore compared with the base case after assuming that all the other liberation classes in the base case are fully liberated classes. Appendix H shows the bulk particle weight for BC compared with FL for all the particle liberation classes in a size class (see Table H.1-1 to Table H.1-8). Figure 4-8 below shows the mineral mode of occurrence of Cpy in the FL feed ore while Figure 4-9 and Figure 4-10 shows the mineral mode of occurrence for Py and NSG in the ore.

Table 4-6: Differences in liberation classes' weights in FL artificial ore expressed as a percentage of Copper 1 base case feed ore liberation classes.

Relative weight % of minerals in fully liberated class of FL ore compared to that of BC ore			
Size Class	Cpy	Py	NSG
0-38 µm	118%	125%	101%
38-53 µm	184%	162%	102%
53-75 µm	269%	159%	102%
75-106 µm	286%	159%	103%
106-150 µm	383%	169%	105%
150-212 µm	636%	168%	106%
212-300 µm	649%	170%	106%
300-425 µm	708%	151%	106%

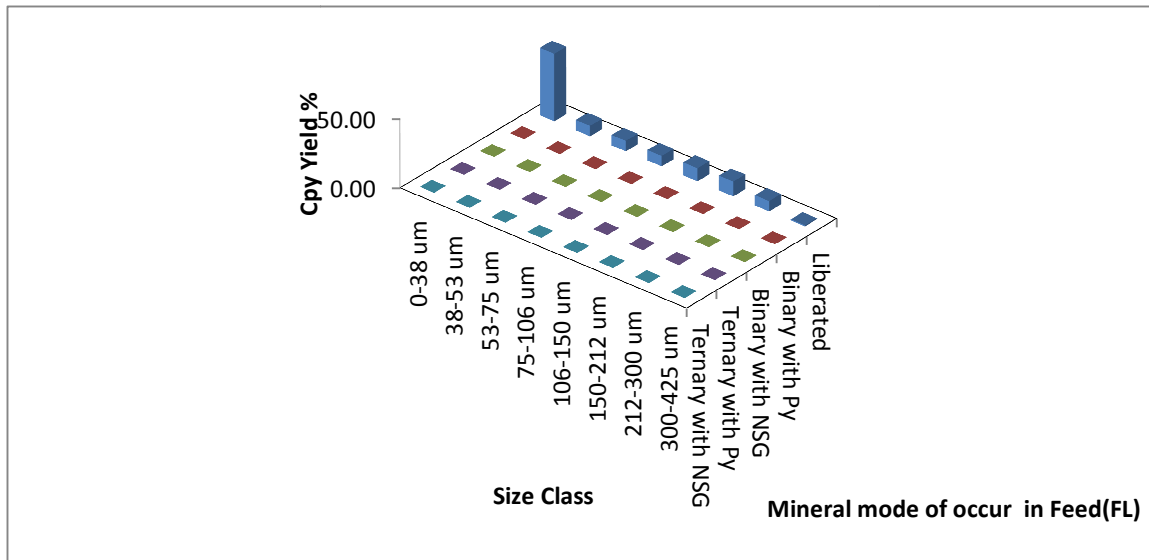


Figure 4-8: Chalcopyrite mineral mode of occurrence in fictional FL artificial feed ore with a P₇₀ grind size of 120 µm.

Figure 4-8 shows that the Chalcopyrite mode of occurrence is as fully liberated particles only. Significant fully liberated Chalcopyrite particles appear in the fine size class range.

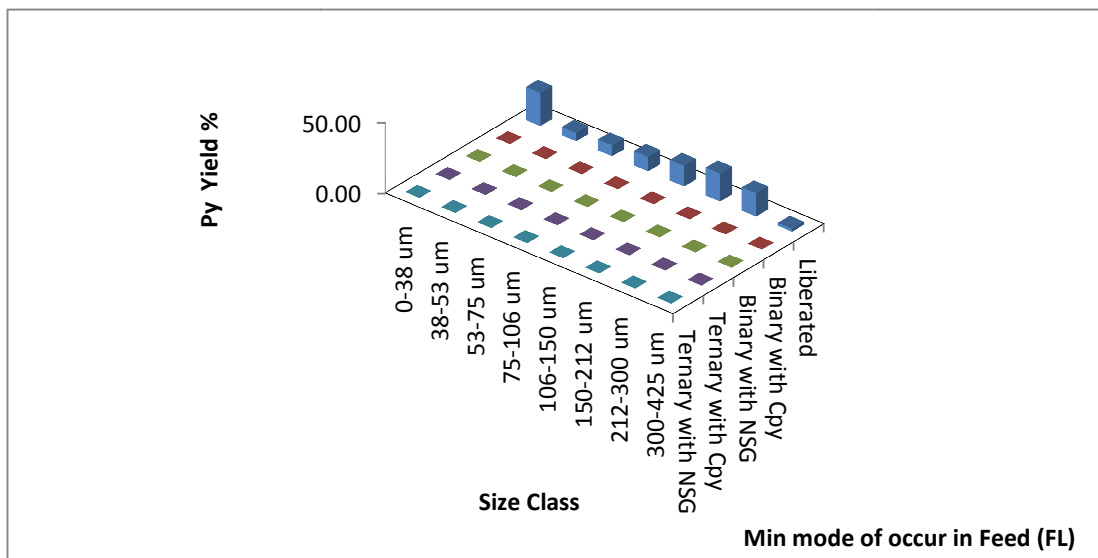


Figure 4-9: Pyrite mineral mode of occurrence in fictional FL artificial feed ore with a P₇₀ grind size of 120 µm.

Figure 4-9 and Figure 4-10 show that Pyrite and NSG occurred as fully liberated particles as well. The fully liberated Pyrite particles are spread well over the fine and coarse size

classes in contrast to NSG fully liberated particles which appear mostly in the fine size class.

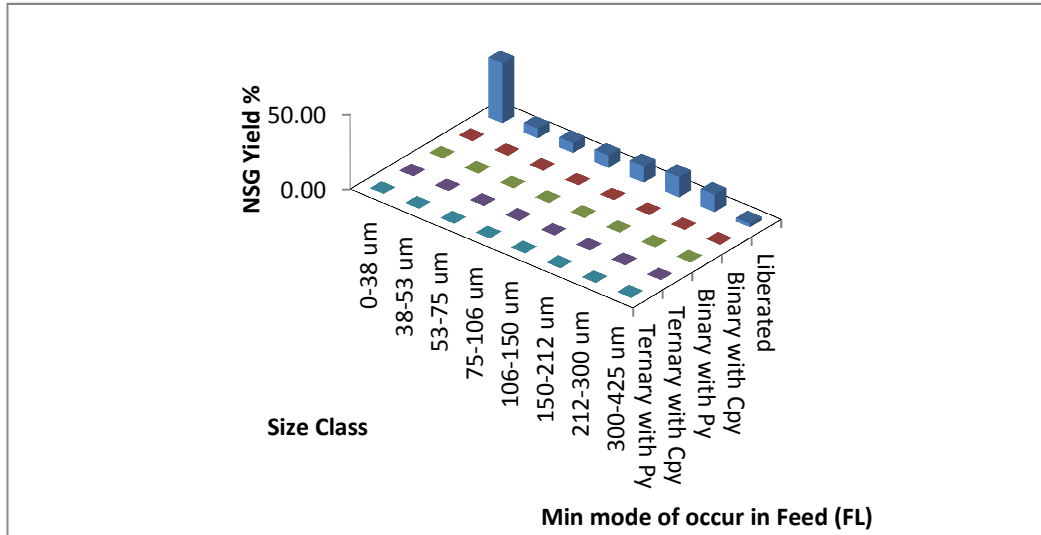


Figure 4-10: NSG mineral mode of occurrence in fictional FL artificial feed ore with a P₇₀ grind size of 120 μm.

4.3.2.2. Fully locked ore (LC)

In creating the fully locked ore, 100% of the weights of fully liberated Chalcopyrite, Pyrite and NSG mineral in each size class were redistributed evenly between the existing binary liberation classes in that size fraction for each mineral group. New values of the particle liberation classes were recalculated. The major difference between the base case ore and the fully locked ore was the absence of any fully liberated particle class in the fully locked ore. Table 4-7 expresses the differences in particle liberation class weights between the base case and the fully locked ore as a percentage after redistributing the fully liberated mineral class weights into the binary and ternary liberation classes. . Appendix H shows the bulk particle weight for BC compared with LC for all the particle liberation classes in a size class (see Table H.1-1 to Table H.1-8).Figure 4-11 below shows the mineral mode of occurrence of Chalcopyrite in the LC feed. Figure 4-12 and Figure 4-13 show the mineral mode of occurrence of Pyrite and NSG in the ore.

Table 4-7: Differences in liberation classes' weights in LC artificial ore expressed as a percentage of Copper 1 base case feed ore liberation classes.

Relative weight % of binary and ternary particles in Fully locked ore(LC) compared to that of BC ore				
Size Class	CpyPy	CpyNSG	PyNSG	CpyPyNSG
0-38 μm	511%	6153%	14044%	100%
38-53 μm	234%	1968%	5384%	100%
53-75 μm	235%	1790%	4650%	100%
75-106 μm	240%	1741%	3297%	100%
106-150 μm	222%	1415%	2231%	100%
150-212 μm	233%	1280%	1729%	100%
212-300 μm	247%	1354%	1405%	100%
300-425 μm	309%	1739%	1483%	100%

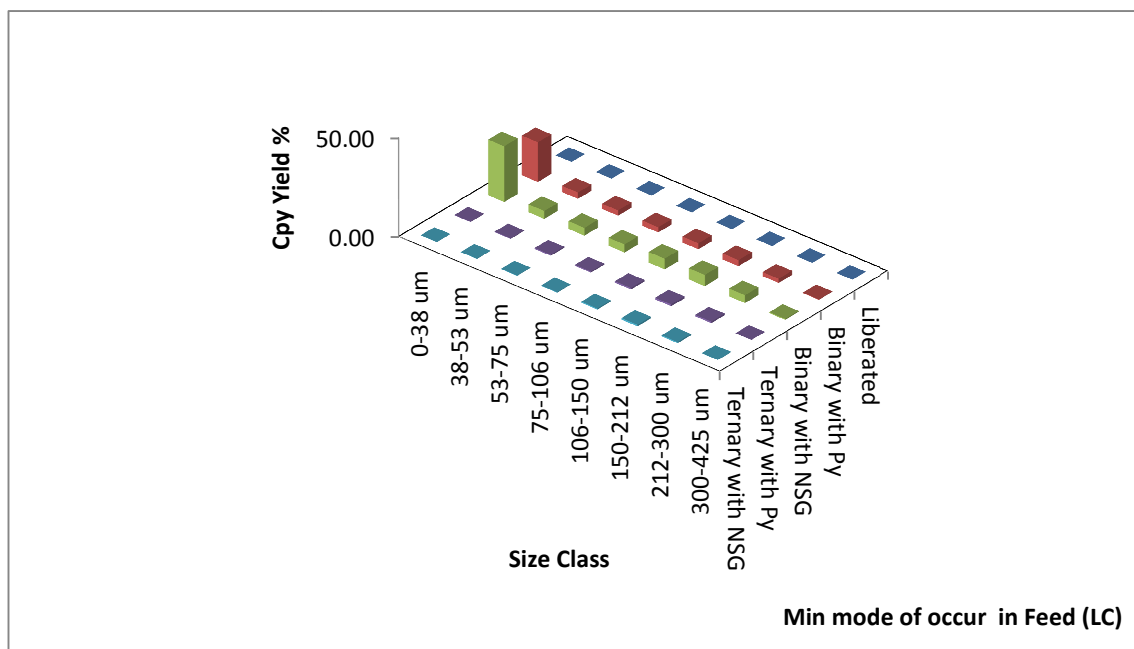


Figure 4-11: Chalcopyrite mineral mode of occurrence in LC artificial feed ore with a P_{70} grind size of 120 μm .

Most of Chalcopyrite in the LC feed ore appears as binary particles with NSG with a considerable fraction appearing in the 0 to 38 μm size class, Figure 4-11.

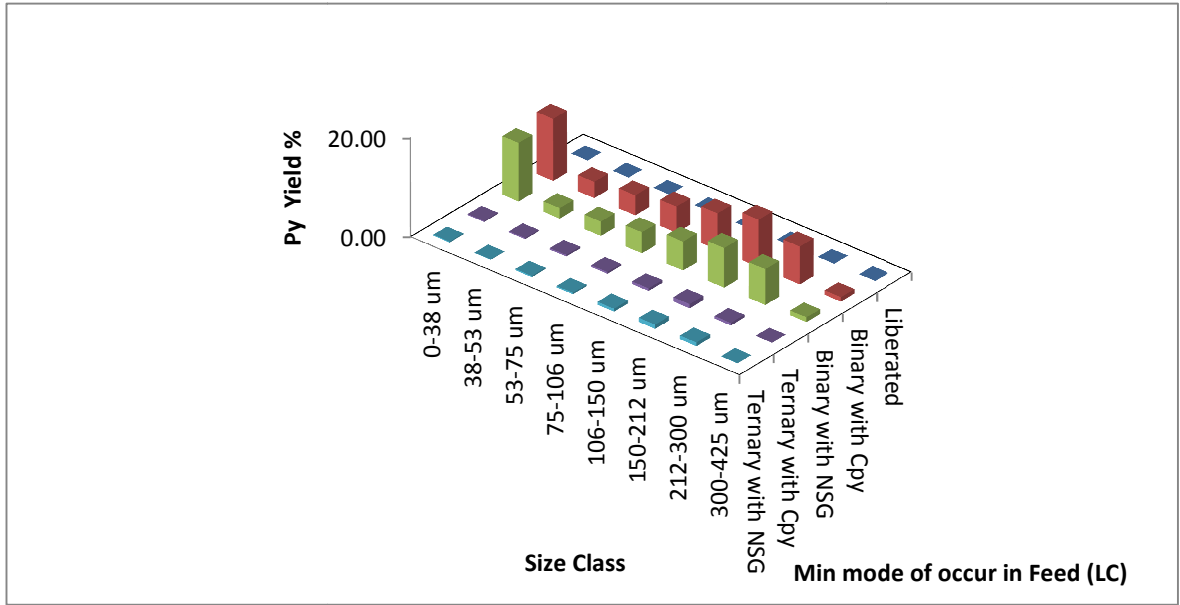


Figure 4-12: Pyrite mineral mode of occurrence in LC artificial feed ore with a P₇₀ grind size of 120µm.

Most of Pyrite in the LC feed ore appears as binary particles with NSG and Chalcopyrite over a range of size fractions, Figure 4-12.

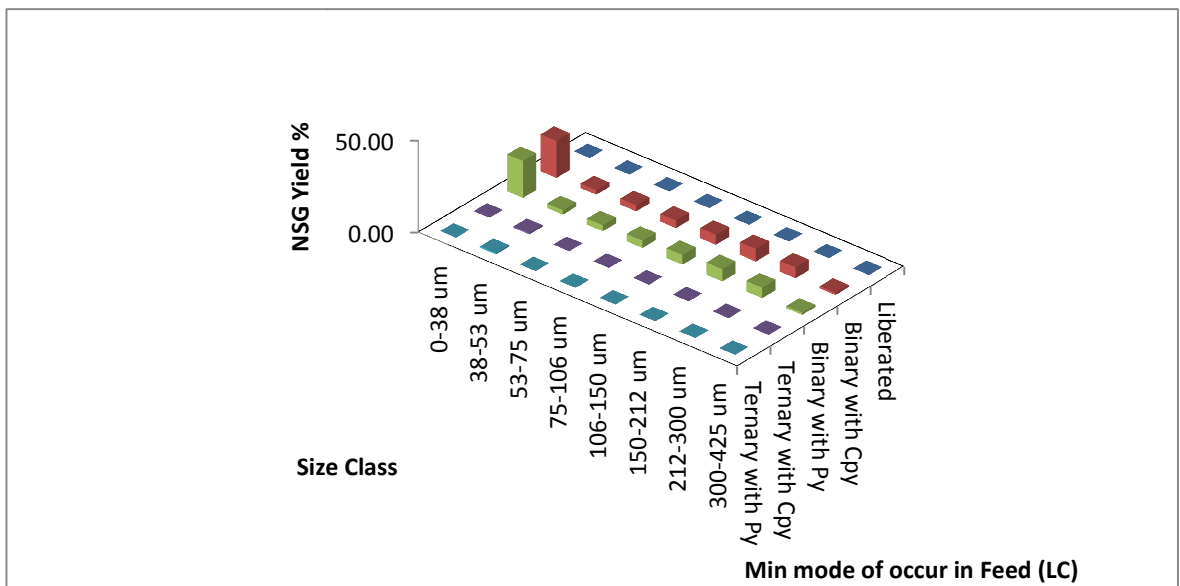


Figure 4-13: NSG mineral mode of occurrence in LC artificial feed ore with a P₇₀ grind size of 120 µm.

Most of NSG in the LC feed ore appears as binary particles with Chalcopyrite and Pyrite. A considerable fraction of these binary particles appears in the 0 to 38 μm fine size class, Figure 4-13.

4.3.2.3. Ore 1

Ore 1 was created by redistributing 100% of the ternary liberated particle class weights in the BC to the existing BC fully liberated classes. The major difference between the BC ore and Ore 1 was the absence of ternary particle liberation classes in the Ore 1 and an increase in fully liberated class weight due to the redistribution of the ternaries (see Table 4-8). Appendix H shows the bulk particle weight for BC compared with Ore 1 for all the particle liberation classes in a size class (see Table H.1-1 to Table H.1-8).

Figure 4-14 below shows the mineral mode of occurrence of Chalcopyrite in Ore 1 feed ore while Figure 4-15 and Figure 4-16 shows the mineral mode of occurrence of Py and NSG in the ore.

Table 4-8: Differences in liberation classes' weights in Ore 1 artificial ore expressed as a percentage of Copper 1 base case feed ore liberation classes.

Relative weight % of minerals in fully liberated class of Ore 1 compared to that of BC ore			
Size class	Cpy	Py	NSG
0-38 μm	101%	102%	100%
38-53 μm	110%	110%	101%
53-75 μm	127%	112%	100%
75-106 μm	130%	111%	100%
106-150 μm	155%	114%	101%
150-212 μm	207%	115%	101%
212-300 μm	225%	113%	101%
300-425 μm	192%	108%	100%

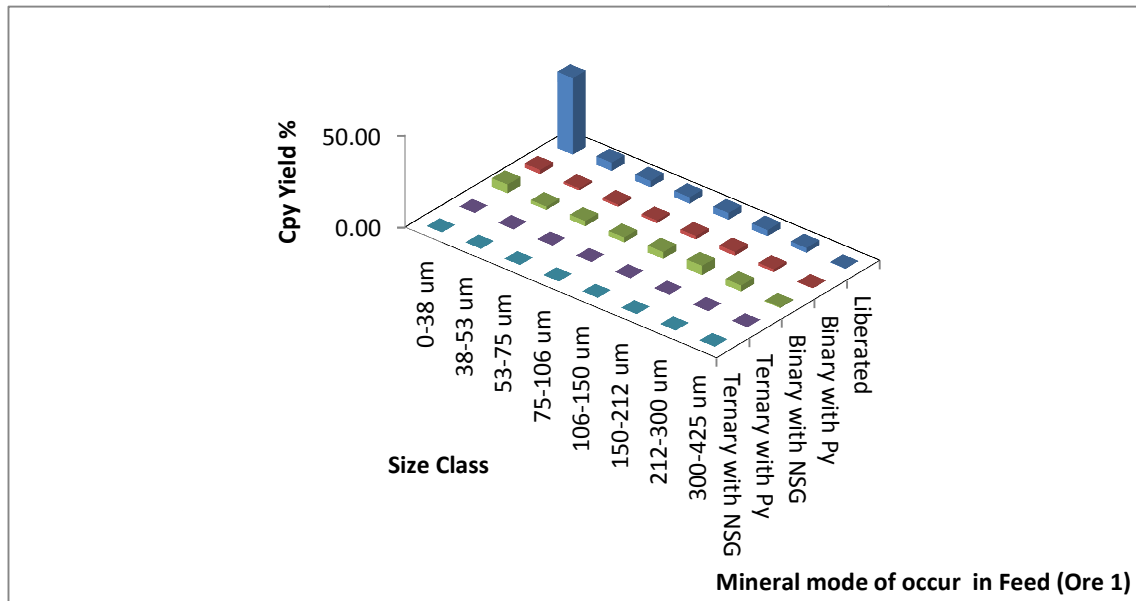


Figure 4-14: Chalcopyrite mineral mode of occurrence in Ore 1 artificial feed ore with a P₇₀ grind size of 120 µm.

Compared with the base case feed ore, Ore 1 had more fully liberated Chalcopyrite particles especially in the coarse size classes, Figure 4-14.

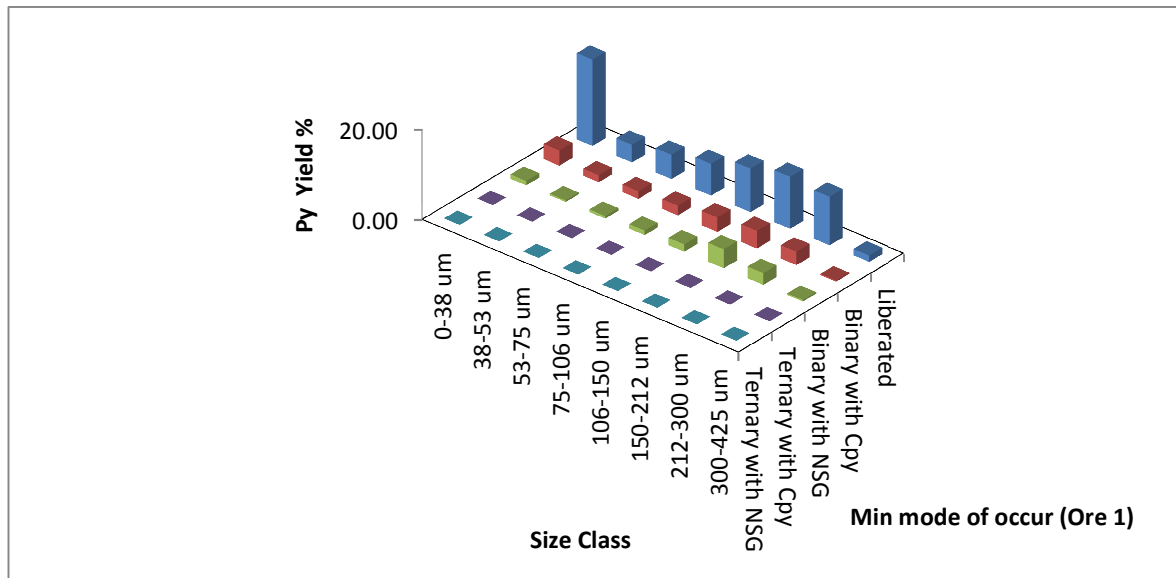


Figure 4-15: Pyrite mineral mode of occurrence in Ore 1 artificial feed ore with a P₇₀ grind size of 120 µm.

The Pyrite and NSG mode of occurrence in Ore 1 feed were closely similar to their mode of occurrence in the base case feed ore, Figure 4-15 and Figure 4-16.

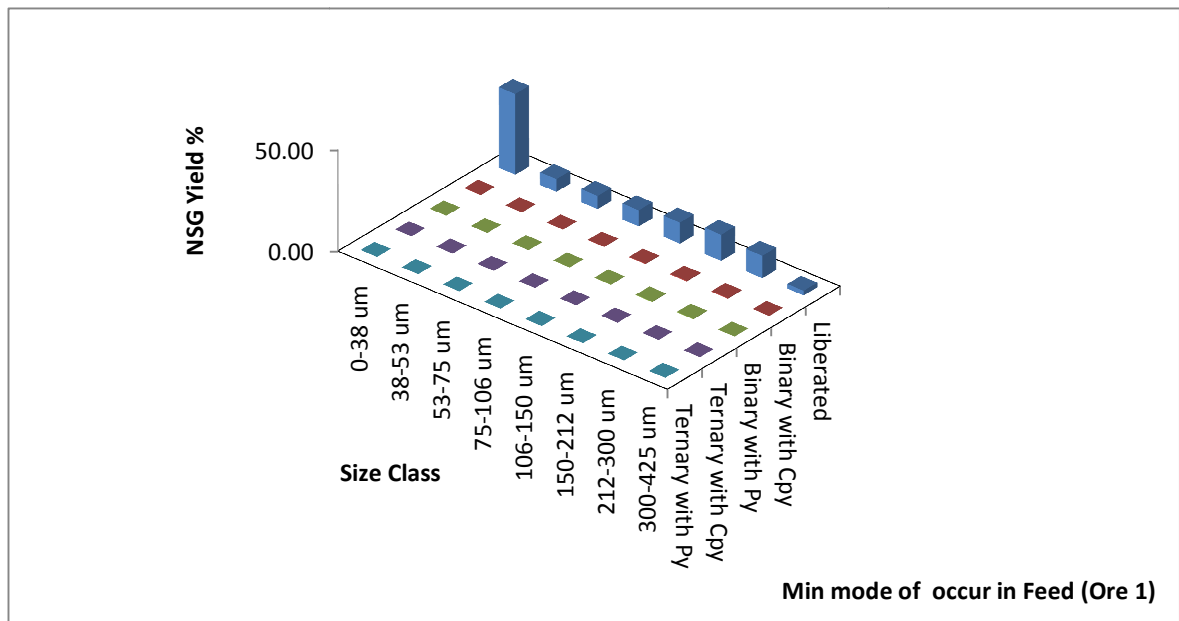


Figure 4-16: NSG mineral mode of occurrence in Ore 1 artificial feed ore with a P₇₀ grind size of 120 μm.

4.3.2.4. Ore 2

Ore 2 was created by redistributing 100% of the fully liberated Cpy and Py classes in the BC to the existing binary classes in each size fraction for the two mineral groups. Thus, the major difference between the BC and Ore 2 was the absence of fully liberated Cpy and Py classes in Ore 2. The percentage difference in binary liberated particle class weight in Ore 2 compared to the BC is presented in Table 4-9 below. Appendix H shows the bulk particle weight for BC compared with Ore 2 for all the particle liberation classes in a size class (see Table H.1-1 to Table H.1-8).

Table 4-9: Differences in liberation classes weights in Ore 2 artificial ore expressed as a percentage of Copper 1 base case feed ore liberation classes.

Relative weight % of binary particles in Ore 2 compared to that of BC ore			
Size class	PyCpy	CpyNSG	PyNSG
0-38 μm	486%	341%	609%
38-53 μm	234%	157%	373%
53-75 μm	235%	126%	328%
75-106 μm	240%	120%	274%
106-150 μm	222%	113%	218%
150-212 μm	232%	107%	199%
212-300 μm	246%	108%	176%
300-425 μm	308%	108%	160%

Ore 2 is expected to behave fairly similar to the extreme FL case due to the presence of fully liberated NSG and the higher percentage of CpyPy binary composites in the ore compared to the amount presented in the base case (see Figure 4-17). This is because Cpy and Py have the same contact angle although their densities are different.

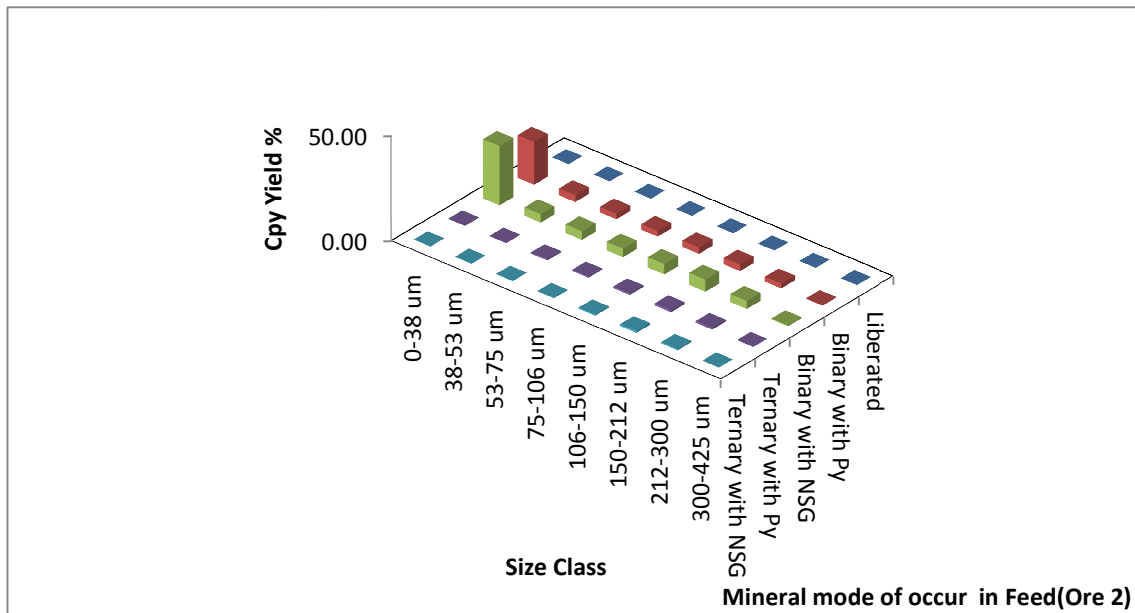


Figure 4-17: Chalcopyrite mineral mode of occurrence in fictional Ore 2 artificial feed ore with a P₇₀ grind size of 120 μm .

Figure 4-18 and Figure 4-19 below show the mineral mode of occurrence for Py and NSG in the Ore 2.

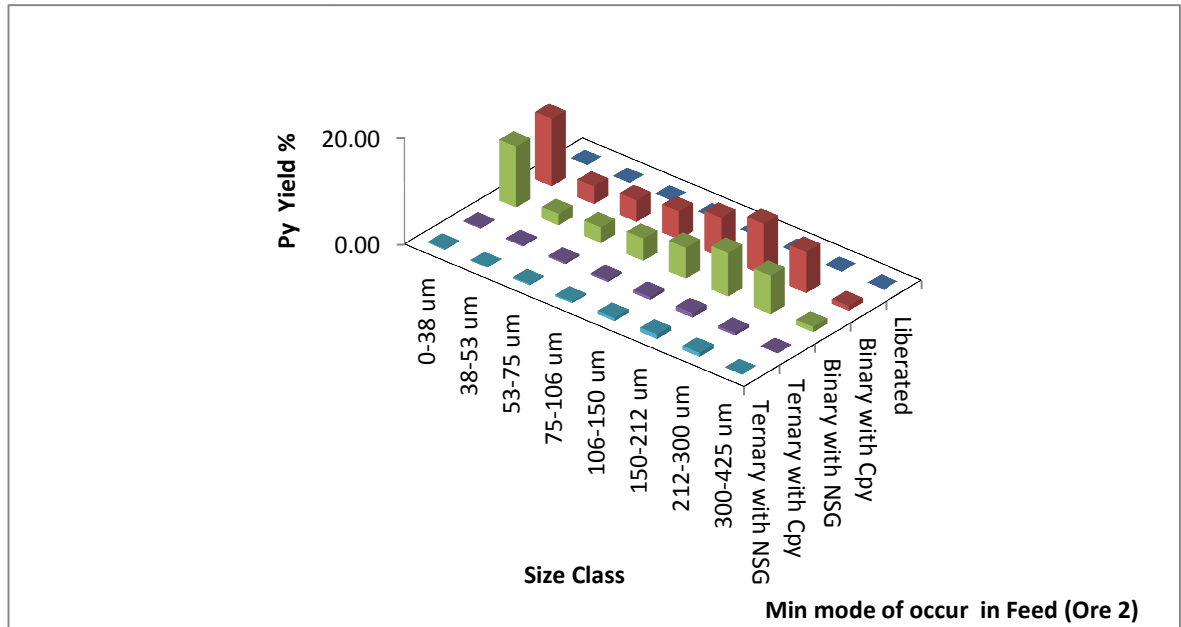


Figure 4-18: Pyrite mineral mode of occurrence in fictional Ore 2 artificial feed ore with a P₇₀ grind size of 120 µm.

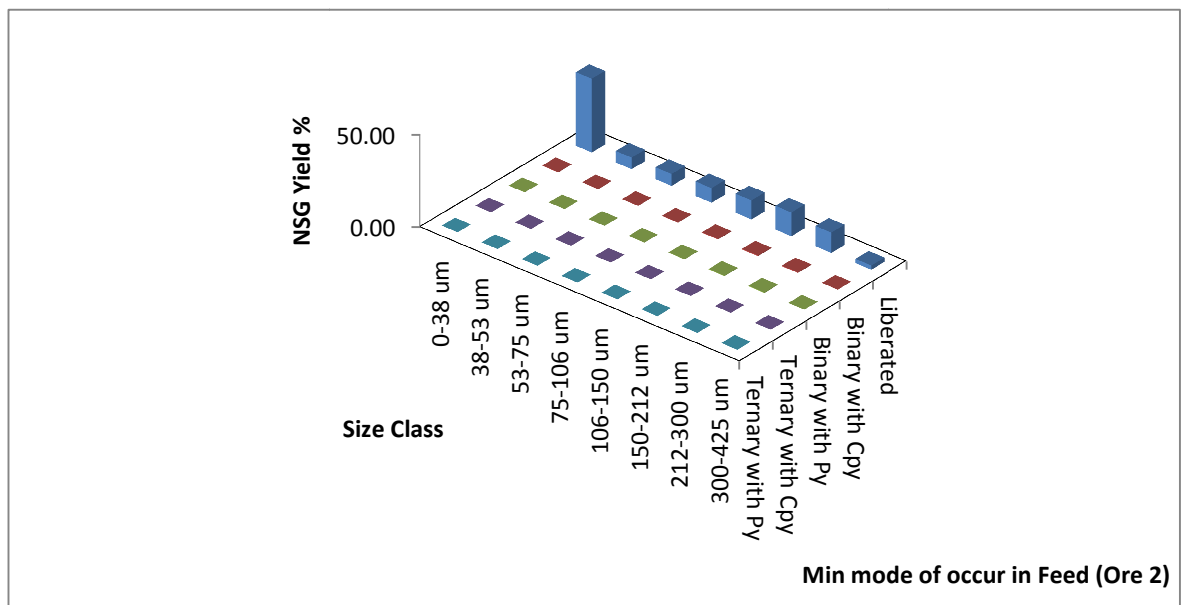


Figure 4-19: NSG mineral mode of occurrence in fictional Ore artificial feed ore with a P₇₀ grind size of 120 µm.

4.3.2.5. Ore 3

Ore 3 was created by redistributing 100% of the fully liberated NSG classes in the BC to the existing NSg+Py and NSG+Cpy binary liberated classes in each size fraction.

Table 4-10: Differences in liberation classes' weights in Ore 3 artificial ore expressed as a percentage of Copper 1 base case feed ore liberation classes.

Relative weight % of binary and ternary particles in Ore 3 compared to that of BC ore			
Size class	CpyNSG	PyNSG	CpyPyNSG
0-38 μm	5938%	13592%	100%
38-53 μm	1911%	5111%	100%
53-75 μm	1764%	4422%	100%
75-106 μm	1721%	3123%	100%
106-150 μm	1402%	2113%	100%
150-212 μm	1273%	1630%	100%
212-300 μm	1347%	1328%	100%
300-425 μm	1732%	1423%	100%

The major difference between the BC and Ore 1 was the absence of fully liberated NSG mineral classes in Ore 3. The relative percentage of binary and ternary liberated particle classes weight in Ore 3 compared to the BC is presented in Table 4-10 above. Appendix H shows the bulk particle weight for BC compared with Ore 3 for all the particle liberation classes in a size class (see Table H.1-1 to Table H.1-8). Ore 3 is expected to give less recovery of the value mineral than the BC ore due to the greater occurrence of the value mineral in association with NSG in the binary liberation class (see Figure 4-20).

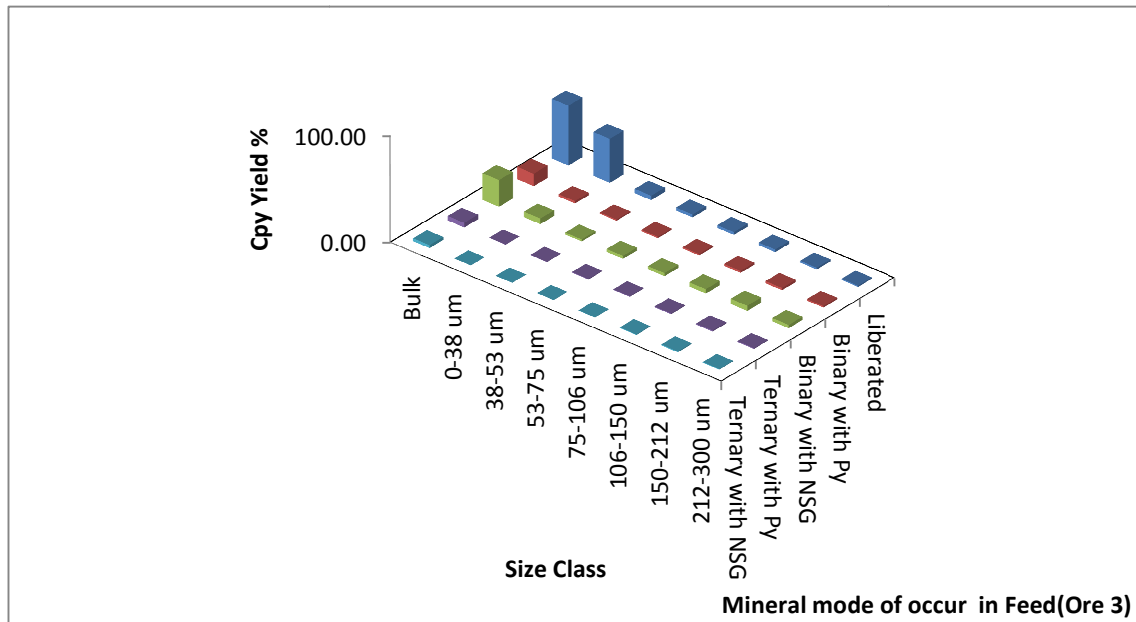


Figure 4-20: Chalcopyrite mineral mode of occurrence in Ore 3 artificial feed ore with a P₇₀ grind size of 120 µm.

Figure 4-21 and Figure 4-22 shows the mineral mode of occurrence of Py and NSG in the ore.

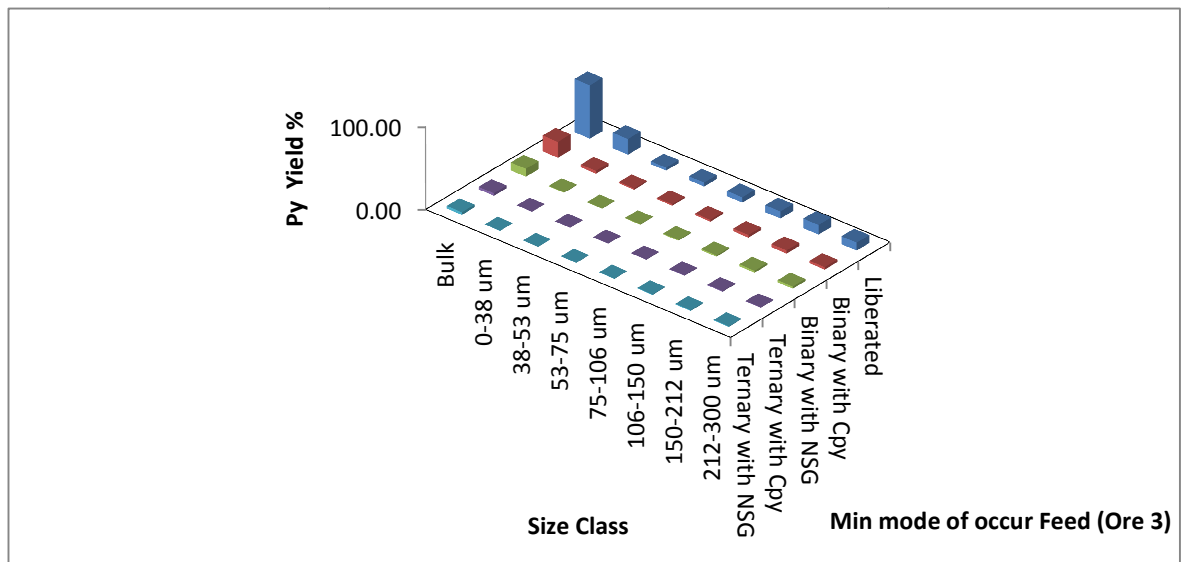


Figure 4-21: Pyrite mineral mode of occurrence in Ore 3 artificial feed ore with a P₇₀ grind size of 120 µm.

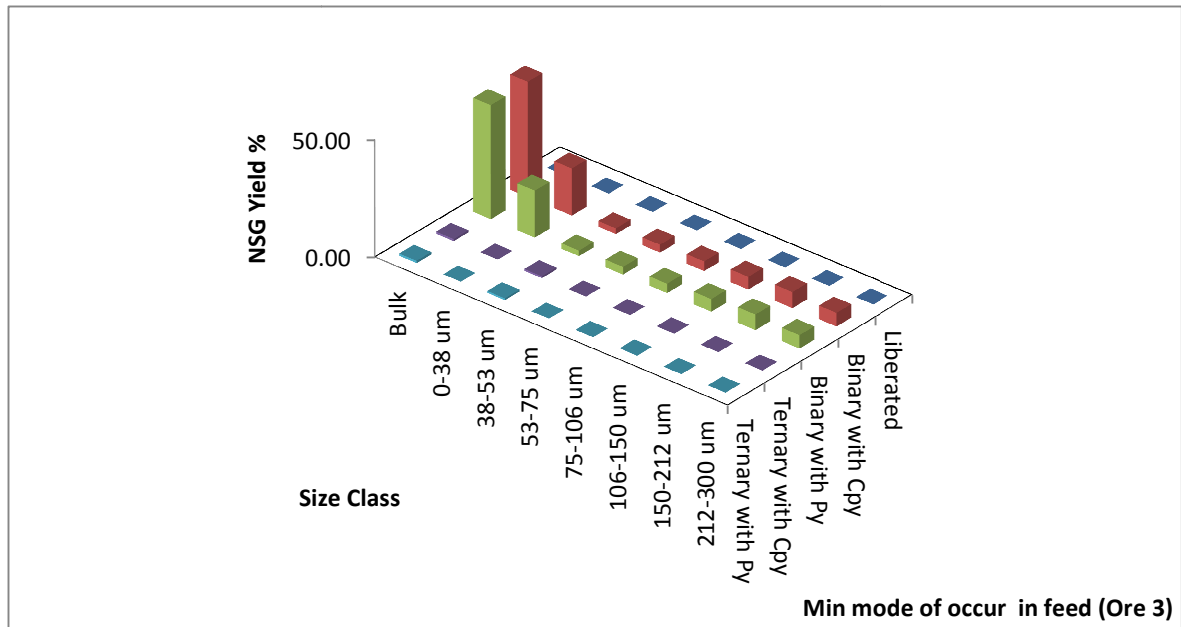


Figure 4-22: NSG mineral mode of occurrence in Ore 3 artificial feed ore with a P₇₀ grind size of 120 μm.

4.3.3. Copper 2 artificial ores

Similar artificial ores were created utilising Copper 2 base case feed with a P₇₀ grind size of 180μm, thus creating two groups of artificial feeds at different grind sizes. Methods similar to those described above in creating Copper 1 artificial ores were also applied in creating Copper 2 artificial ores. The resulting artificial feeds are presented below. The mineral modes of occurrence graphs for each ore are presented in Appendix A. Appendix H shows the bulk particle weight for all the particle liberation classes in a size class, for Copper 2 flotation feed ores (see Table H.2-1 to Table H.2-9).

4.3.3.1. Fully liberated ore

The differences between the base case and fully liberated ore were similar to those obtained for FL ore created from Copper 1 ore with a P₇₀ grind size of 120 μm (see Table 4-11). Appendix H shows the bulk particle weight for BC compared with FL for all the particle liberation classes in a size class (see Table H.2-1 to Table H.2-9).

Similar methods for creating FL liberated ore as described in section 4.3.2.1 were used in creating FL artificial ore from Copper 2 base case feed ore. Graphs of the mineral mode of occurrence for Chalcopyrite, Pyrite and NSG in FL liberated ore at a P₇₀ grind size of 180 µm are shown in Appendix A Figure A.1-1 to Figure A.1-3.

Table 4-11: Differences in liberation classes' weights in FL liberated artificial ore expressed as a percentage of Copper 2 base case feed ore liberation classes .

Relative weight % of minerals in fully liberated class of FL ore compared to that of BC ore			
Size Class	Cpy	Py	NSG
0-38 µm	129%	585%	101%
38-53 µm	181%	148%	101%
53-75 µm	254%	168%	102%
75-106 µm	249%	149%	103%
106-150 µm	394%	160%	105%
150-212 µm	632%	182%	106%
212-300 µm	600%	182%	107%
300-425 µm	2130%	174%	108%
425-600 µm	1160%	172%	108%

4.3.3.2. Fully locked ore (LC)

Similar methods for creating LC liberated ore as described in section 4.3.2.2 for LC created from Copper 1 base case feed were applied in creating LC artificial ore from Copper 2 base case feed ore. The differences between the base case and LC liberated ore at a P₇₀ grind size of 180 µm were similar to those obtained for LC ore created from Copper 1 ore with a P₇₀ grind size of 120µm (see Table 4-12). Appendix H shows the bulk particle weight for BC compared with LC for all the particle liberation classes in a size class (see Table H.2-1 to Table H.2-9). Graphs of the mineral mode of occurrence for Chalcopyrite, Pyrite and NSG in LC liberated ore at a P₇₀ grind size of 180 µm are shown in Appendix A, Figure A.1-4 to Figure A.1-6.

Table 4-12: Differences in liberation classes' weights in LC liberated artificial ore expressed as a percentage of Copper 2 base case feed ore liberation classes .

Relative weight % of binary particles in Fully locked ore(LC) compared to that of BC ore			
Size Class	CpyPy	CpyNSG	PyNSG
0-38 µm	526%	3849%	9029%
38-53 µm	263%	2702%	7080%
53-75 µm	212%	1899%	4653%
75-106 µm	271%	1752%	3668%
106-150 µm	239%	1321%	2154%
150-212 µm	210%	1226%	1564%
212-300 µm	225%	1199%	1269%
300-425 µm	275%	1262%	1089%
425-600 µm	304%	1499%	985%

4.3.3.3. Ore 1

Similar methods for creating Ore 1 artificial ore as described in section 4.3.2.3 for Ore artificial feed ore created from Copper 1 base case feed were applied in creating Ore 1 artificial ore from Copper 2 base case feed ore. The differences between the base case and Ore 1 liberated ore at a P₇₀ grind size of 180 µm were also similar to those obtained for Ore 1 artificial ore created from Copper 1 ore with a P₇₀ grind size of 120 µm (see Table 4-13). Appendix H shows the bulk particle weight for BC compared with Ore 1 for all the particle liberation classes in a size class (see Table H.2-1 to Table H.2-9). Graphs of the mineral mode of occurrence for Chalcopyrite, Pyrite and NSG in Ore 1 artificial ore at a P₇₀ grind size of 180µm are shown in Appendix A Figure A.1-7 to Figure A.1-9

Table 4-13: Differences in liberation classes' weights in Ore 1 liberated artificial ore expressed as a percentage of Copper 2 base case feed ore liberation classes.

Relative weight % of minerals in Ore 1 compared to that of BC ore			
Size Class	Cpy	Py	NSG
0-38 μm	129%	585%	101%
38-53 μm	181%	148%	101%
53-75 μm	254%	168%	102%
75-106 μm	249%	149%	103%
106-150 μm	394%	160%	105%
150-212 μm	632%	182%	106%
212-300 μm	600%	182%	107%
300-425 μm	2130%	174%	108%
425-600 μm	1160%	172%	108%

4.3.3.4. Ore 2

Similar methods for creating Ore 2 artificial ore as described in section 4.3.2.4 for Ore artificial feed ore created from Copper 1 base case feed were applied in creating Ore 2 artificial ore from Copper 2 base case feed ore.

Table 4-14: Differences in liberation classes' weights in Ore 2 liberated artificial ore expressed as a percentage of Copper 2 base case feed ore liberation classes .

Relative weight % of binary particles in Ore 2 compared to that of BC ore			
Size Class	CpyPy	CpyNSG	PyNSG
0-38 μm	526%	224%	331%
38-53 μm	263%	160%	444%
53-75 μm	212%	131%	325%
75-106 μm	271%	124%	305%
106-150 μm	239%	113%	232%
150-212 μm	210%	108%	197%
212-300 μm	225%	108%	168%
300-425 μm	275%	103%	152%
425-600 μm	304%	107%	137%

The differences between the Base case and Ore 2 liberated ore at a P₇₀ grind size of 180 µm were also similar to those obtained for Ore 2 artificial ore created from Copper 1 ore with a P₇₀ grind size of 120 µm (see Table 4-14). Appendix H shows the bulk particle weight for BC compared with Ore 2 for all the particle liberation classes in a size class (see Table H.2-1 to Table H.2-9). Graphs of the mineral mode of occurrence for Chalcopyrite, Pyrite and NSG in Ore 2 artificial ore at a P₇₀ grind size of 180 µm are shown in Appendix A, Figure A.1-10 to Figure A.1-12.

4.3.3.5. Ore 3

Similar methods for creating Ore 3 artificial ore as described in section 4.3.2.5 for Ore 3 artificial feed ore created from Copper 1 base case feed were applied in creating Ore 3 artificial ore from Copper 2 base case feed ore. The differences between the Base case and Ore 3 liberated ore at a P₇₀ grind size of 180µm were also similar to those obtained for Ore 3 artificial ore created from Copper 1 ore with a P₇₀ grind size of 120 µm (see Table 4-15). Appendix H shows the bulk particle weight for Ore 3 compared with FL for all the particle liberation classes in a size class (see Table H.2-1 to Table H.2-9). Graphs of the mineral mode of occurrence for Chalcopyrite, Pyrite and NSG in Ore 3 artificial ore at a P₇₀ grind size of 180µm are shown in Appendix A, Figure A.1-13 to Figure A.1-15.

Table 4-15: Differences in liberation classes' weights in Ore 3 liberated artificial ore expressed as a percentage of Cu 2 base case feed ore liberation

Relative weight % of binary particles in Ore 3 compared to that of BC ore		
Size Class	CpyNSG	PyNSG
0-38 µm	3725%	8798%
38-53 µm	2642%	6736%
53-75 µm	1868%	4427%
75-106 µm	1728%	3463%
106-150 µm	1308%	2022%
150-212 µm	1218%	1467%
212-300 µm	1191%	1201%
300-425 µm	1258%	1037%
425-600 µm	1492%	948%

4.4. Contact angle calculations Method

Mineral particle liberation in HSC Chemistry 7 is defined as either mineral weight composition percent or as surface area percent, of mineral as a fraction of other minerals that constitute the particle. In calculating the particle contact angle utilising the Cassie's equation for composite particles, surface area values of each mineral phase should be used according to the definition of the Cassie's equation (see equation 3.33). However, Ralston et al. (2007) utilised the weight composition percent definition of liberation in predicting the contact angle of composite particles in his work. Due to the methodology used in producing artificial ore feed in this work, where liberation was defined as weight composition percentage, the mineral weight composition definition of liberation was therefore used in calculating the contact angle.

Before this could be done, investigations had to be carried out to determine the relative error associated with utilising the weight percentage definition of liberation in calculating the composite particle contact angle utilising the Cassie's equation. Using the base case Copper 1 ore feed liberation data, contact angle values were calculated for each particle utilising both definitions of particle liberations in HSC Chemistry 7. The values of the contact angles that were obtained were then used in the general flotation model to predict flotation recovery in a single unit flotation cell. The recovery results obtained from the use of each contact angle definition were then compared in order to determine the differences in the values. A pure sulphide mineral contact angle value of 78° was used in the calculations.

4.4.1. Contact angle calculation results and discussion

Figure 4-23 shows a comparison of contact angle values calculated using surface area and weight % definitions of particle liberation in HSC Chemistry simulations in a single size class (0-38 μm). Appendix B Figure B.1-1 to Figure B.1-3 represent typical values of the contact angles for each particle in a specific size fraction calculated utilising Cassie's equation in the simulations.

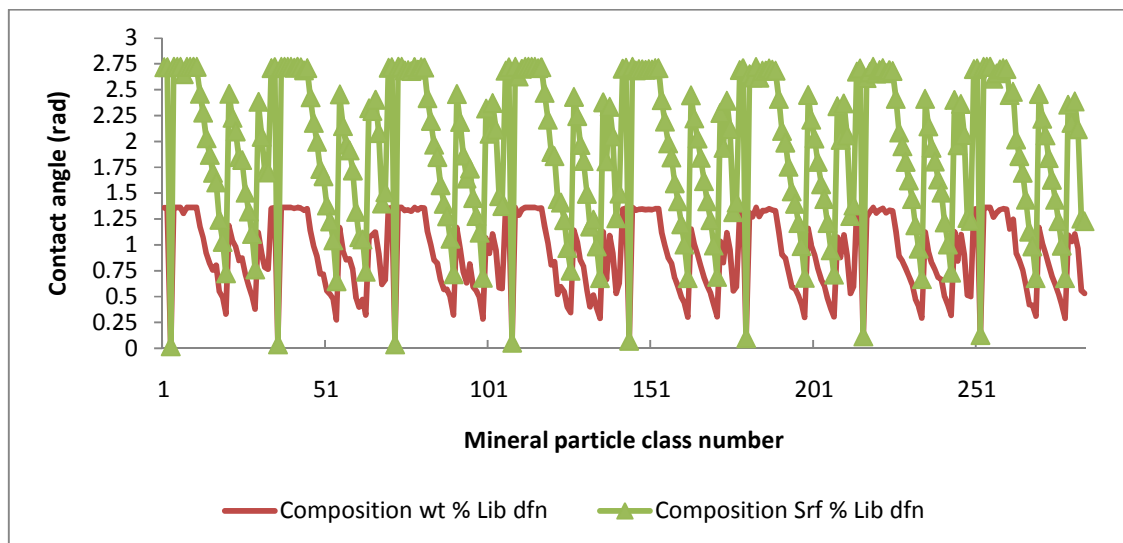


Figure 4-23: Comparison of contact angle values calculated using the weight composition % against those calculated utilising the surface area %.

It can be seen from Figure 4-24 that there is similar trends of contact angle values for particles in different size fractions.

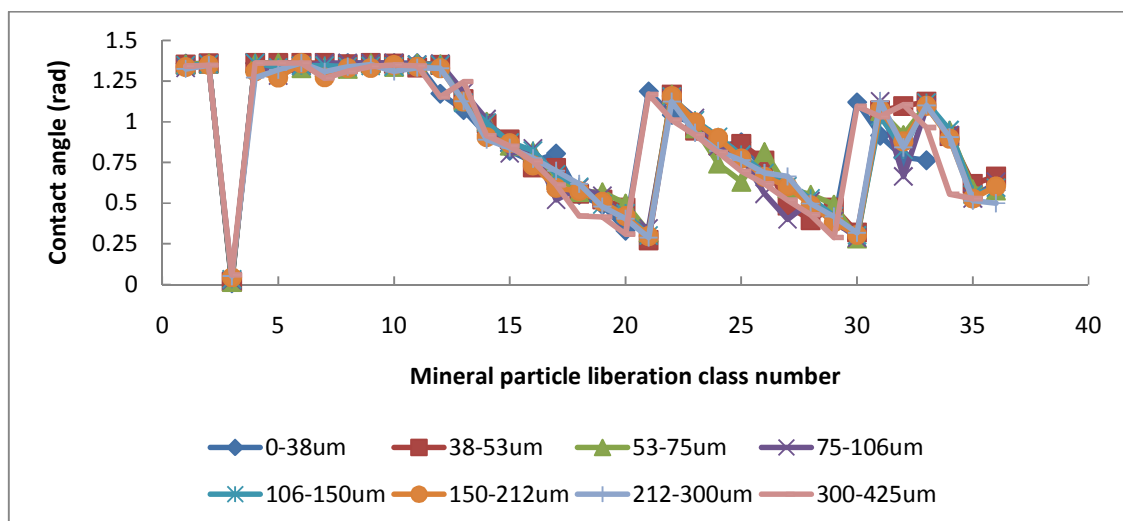


Figure 4-24: Contact angle variation with mineral particles liberation class for all feed particle size fractions

The recovery results in Figure 4-25 show a large difference in recovery at coarse sizes for chalcopyrite between simulated mineral recovery values obtained utilising liberation wt% calculated contact angles and that obtained by utilising surface area %.

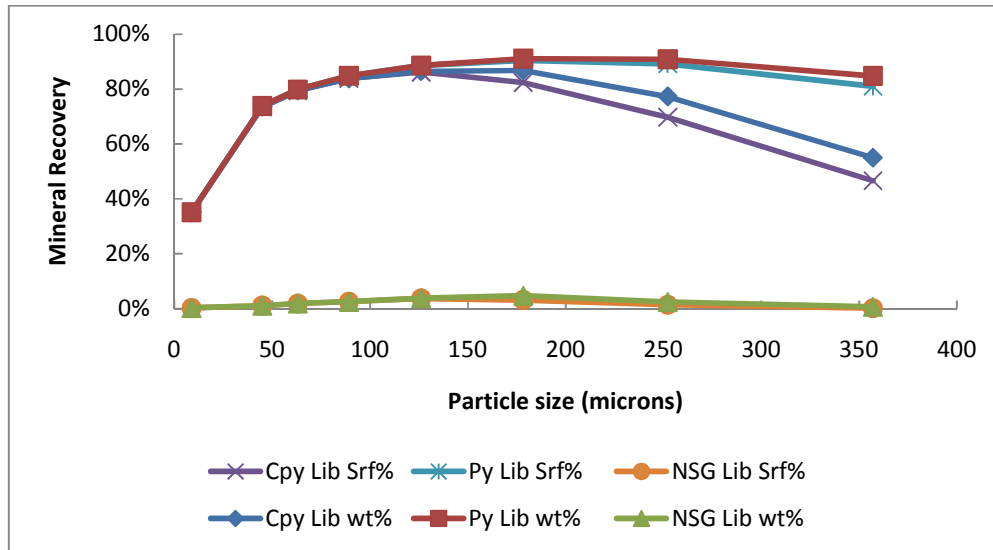


Figure 4-25: Comparison mineral recovery values obtained using the weight composition % calculated contact angles in the flotation model against those calculated utilising the surface area % calculated contact angles.

The weight percentage definition of liberation was used throughout this study in calculating particle contact angles.

4.5. Conclusion

This Chapter has provided a detailed description of the feed ores that were used in this study. A detailed methodology of how artificial ores were created from the two base case feed ore feeds MLA data that was available in this study has been given. These artificial ores are appropriate for use in carrying out investigations on the effect of feed ore liberation variation on flotation recovery. These artificial ores have varying liberation profiles which could represent the potential changes in feed ore liberation expected from microwave assisted comminution. The next Chapter will discuss the simulation studies that were carried utilising these artificial ores.

CHAPTER FIVE

5. SINGLE CELL FLOWSHEET SIMULATION

This Chapter will present and discuss the results of single cell flotation simulations that were carried out by incorporating the fundamental property based model into HSC Chemistry 7 simulation software. Firstly, preliminary flotation cell simulation results that were carried out in order to compare the general trend predicted by the fundamental flotation model with results obtained from experimental batch flotation tests will be presented. This will be followed by a presentation of the results of simulations of a continuous single flotation cell that were carried out in order to explore HSC Chemistry 7 simulation software particle tracking capability and to further test the flotation model's suitability for use in true particle modelling in HSC Chemistry 7. A description of the investigations that were carried out in order to determine the effects of feed ore liberation on single cell flotation value mineral recovery will be given. Lastly details of simulation results from investigations into the effect of grind size variation on value mineral recovery and their analysis will be given.

5.1. Comparison of simulated recovery trends with experimental trends

The mineral recovery values obtained from batch flotation experiments carried out on Copper 1 BC feed in a previous study (AMIRA:P879A, 2009), were compared with those calculated using the fundamental property based model. Details of the batch experimental flotation tests procedures from the previous study on Copper 1 BC feed are provided in Appendix F. No attempt was made to fit the actual experimental recovery values with model values due to lack of some of the hydrodynamic parameter values that characterised the experimental batch flotation conditions when the study was carried out. Where such values were not available, suitable values from literature were substituted into the model. This analysis was done as a way of determining the model's appropriateness for use in true particle modelling.

Table 5-1 shows the input parameter values that were used in simulating the experimental batch flotation test carried out on the Copper 1 BC feed, along with literature values of parameters that were not measured in the experiments.

Table 5-1: Summary of input parameter values used in simulating experimental batch flotation test carried out on the Copper 1BC feed .

Operating Parameter	Batch Experiments	Literature Data (Pyke et al., 2003)
Cell volume	0.004 m ³	
Energy dissipation (ϵ)	n.m	20 m ² /s ³
Bubble diameter (d _b)	n.m	0.0012 m
Bubble rise velocity (v _b)	n.m	0.18 m/s
Apparent viscosity of slurry (ϑ)	n.m	0.000891 kg/ms
Gas flow rate (G _{fr})	0.004 m ³ /min	
Sulphide mineral contact angle (θ)	n.m	78° (Ralston et al., 2007)
NSG contact angle (θ)	n.m	0° (Ralston et al., 2007)

Note that n.a refers to values that were not measured.

From Figures 5-1 and 5-2, it can be seen that the general trends in mineral recovery obtained from the model were fairly similar to those obtained experimentally.

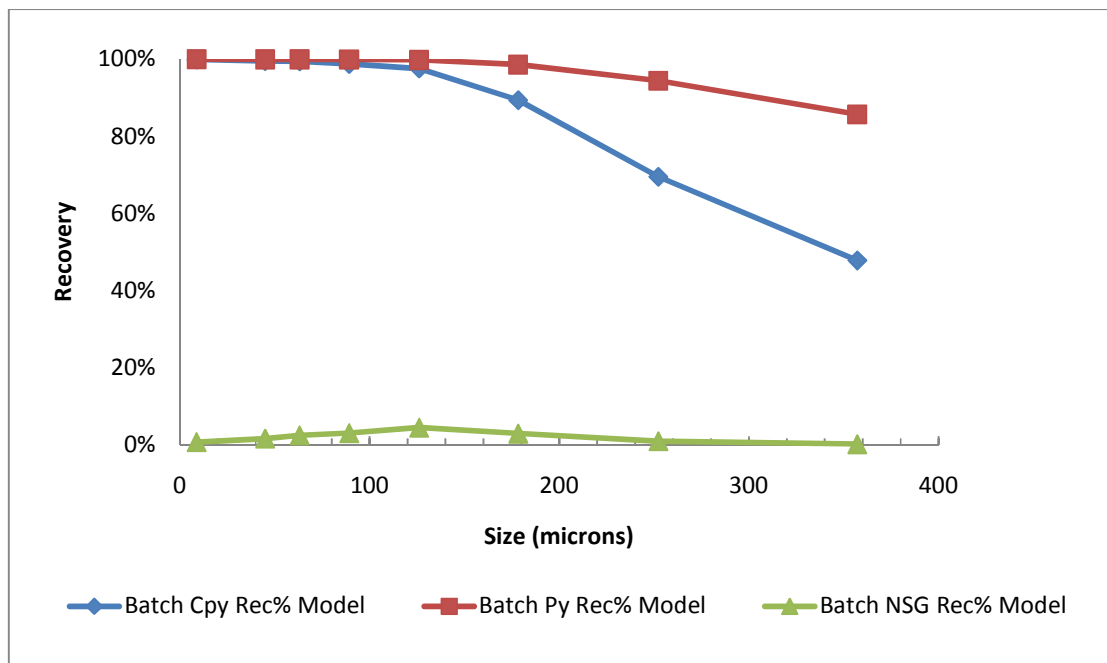


Figure 5-1: Simulated batch flotation mineral recovery for Copper 1 BC feed

The recovery values obtained from the model were higher than the experimental values, (see Figure 5-1). The higher simulated recovery values (see Figure 5-1) as compared to experimentally determined recovery values (Figure 5-2) were attributed to the first order rate expression model that was used in simulating the recovery values which assumes an ultimate recovery of 100%. This assumption, although widely used, is generally accepted to be an overestimation of the flotation ultimate recovery value (Wills and Napier-Munn, 2005). Greater recovery of NSG was observed from the experimental results compared to the flotation model prediction. This difference can be attributed to the effects of entrainment during the batch flotation experimental runs which contributed to high experimental NSG recovery. This high degree of entrainment observed during the batch experiments was higher than the entrainment values predicted by the flotation model. The results showed that the model could predict batch flotation recovery trends similar to those obtained experimentally. It was concluded that the model was appropriate for use in true particle modelling in HSC Chemistry 7 simulation software.

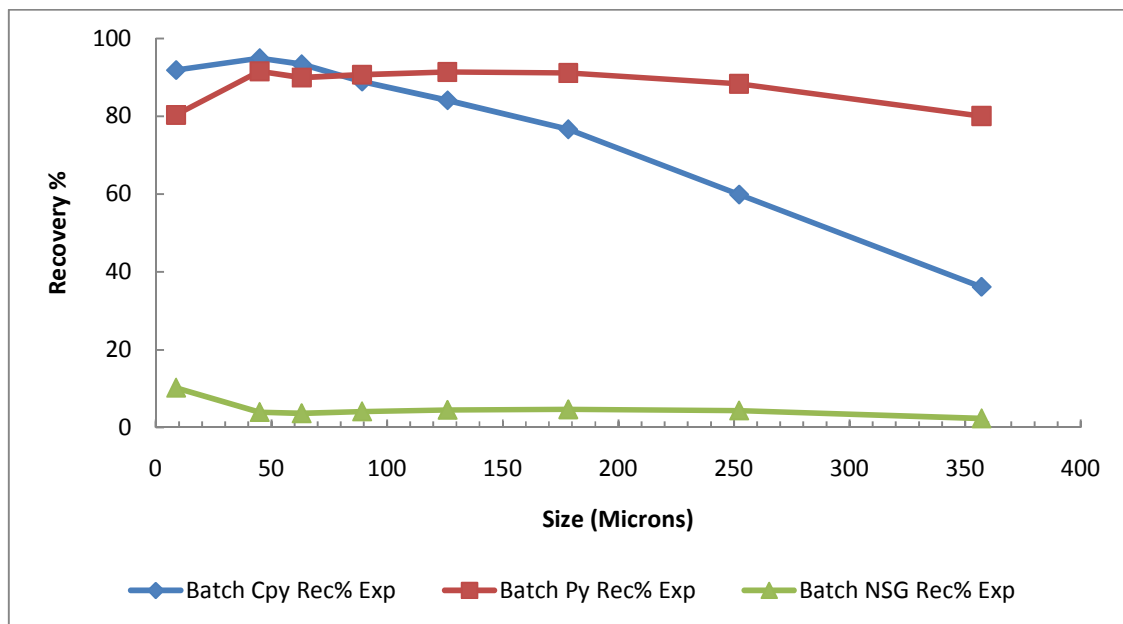


Figure 5-2: Experimentally determined batch flotation cell mineral recovery for Copper 1.

5.2. Continuous single cell flow sheet simulation

Single cell flotation simulation utilising Copper 1 base case feed data with a $P_{70} = 120 \mu\text{m}$ was carried out, after which the trends in flotation rate constant and mineral recovery were analysed. This was done in order to test the modelling framework developed in this study utilising HSC Chemistry 7 simulation software for the purpose of investigating the effects of feed ore liberation on value mineral recovery. These single cell simulation runs allowed for the various flotation simulation outputs to be analysed and for the particle tracking capability of HSC Chemistry 7 software to be explored. Table 5-2 is summary of the variables that were used in simulating a single flotation cell. The single cell flotation flow sheet designed in HSC Chemistry 7, consisted of a 85 m^3 flotation cell with feed solids input feed rate of 890 tph. These values that were used are equivalent to those that appear in a similar study by Ralston et al. (2007) for which flotation cell hydrodynamic parameter values required for model calibration used in this study were adapted from.

Table 5-2: Feed and literature hydrodynamic variables that were used in simulating a Single flotation cell flow sheet operation.

Variable	Parameter	Literature Parameter (Ralston et al.,2007)
Feed Ore	Porphyry Copper Ore	
P_{70}	120 μm	
Cell volume	85 m^3	85 m^3
Solids feed rate	890 tph	890tph
Solids weight % in feed		40.8%
Sulphide mineral contact angle (θ)		78°
NSG contact angle (θ)		0°
Energy dissipation (ϵ)		11 m^2/s^3
Bubble diameter (d_b)		0.0013 m
Bubble rise velocity (v_b)		0.18 m/s
Apparent viscosity of slurry (ϑ)		0.2 kg/ms
Gas flow rate (G_{fr})		4 m^3/min

Figure 5-3 shows the single cell flow sheet that was created in HSC Chemistry Simulation software and used for the simulations.

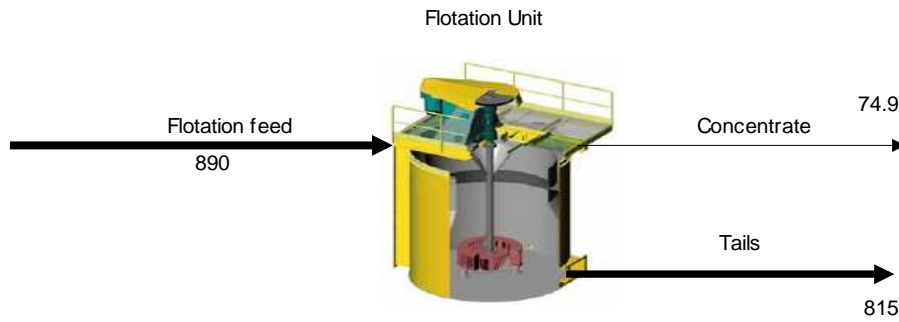


Figure 5-3: Single unit flotation cell flow sheet simulation layout in HSC Chemistry 7 Simulation software.

The following variables were selected to be indicators of the measure of the performance of the flotation cell; Cu recovery (%), Cu grade in the concentrate, mass pull and the enrichment ratio. Values of these variables from the simulations were compared with those from literature, as shown in Table 5-3.

Simulation results obtained were comparable with those reported in literature for a single cell operation, Table 5-3. The results show that the simulated flotation cell recovery values are within range of literature values for typical industrial single copper flotation cells. It can be concluded from the results that the fundamental property based flotation model has been successfully integrated into HSC Chemistry 7 simulation software.

Table 5-3: Summary of Single flotation cell flow sheet simulation grade recovery and mass full performance indicators results.

Parameter	Simulated value	Typical literature value (Yianatos et al., 2006)
Cu Recovery	56.3%	54.9%
Cu% grade in concentrate	7.43%	n.a ¹
Mass pull	8.00%	n.a
Enrichment ratio	6.69	7.20

¹ Note that the abbreviation n.a was used to indicate data that was not available for a single cell operation in literature

5.3. Analysis of simulation results using the Particle analysis tool in HSC Chemistry Simulation Software

The following stream properties and performance parameters of the single flotation cell were analysed using HSC Chemistry 7 simulation software particle tracking tool;

- I. Mineral mode of occurrence in the streams around the cell
- II. Value mineral recovery in concentrate and tail streams
- III. Cumulative liberation of minerals in the streams
- IV. Particle recovery in each stream

The following sections will present and discuss the results of each of the stream properties that were analysed.

Mineral mode of occurrence in the streams around the cell

Figures 5-4 to 5-6 are graphs showing the mineral mode of occurrence of Chalcopyrite in the feed concentrate and tail streams around the simulated single cell flotation unit flow sheet.

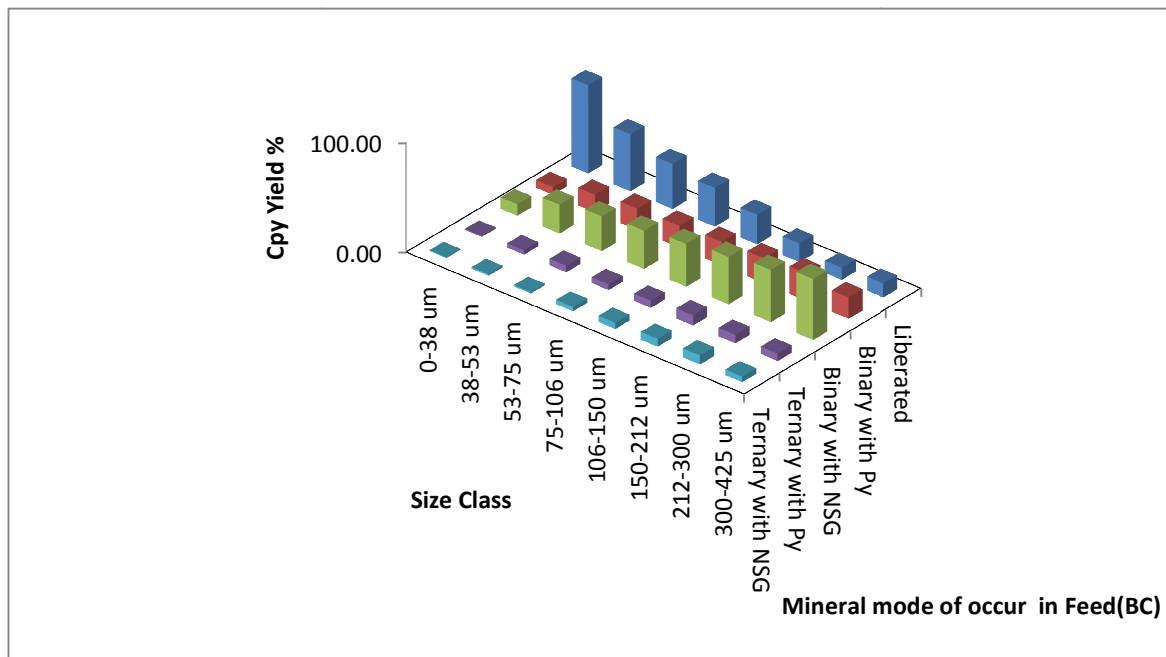


Figure 5-4: Chalcopyrite mineral mode of occurrence in Copper 1 base case feed ore stream to the single flotation cell flow sheet simulation. From Figure 5-4 it can be observed that most of the fully liberated Chalcopyrite in the Copper 1 ground ore feed is found between the 0 to 75 μm size fractions.

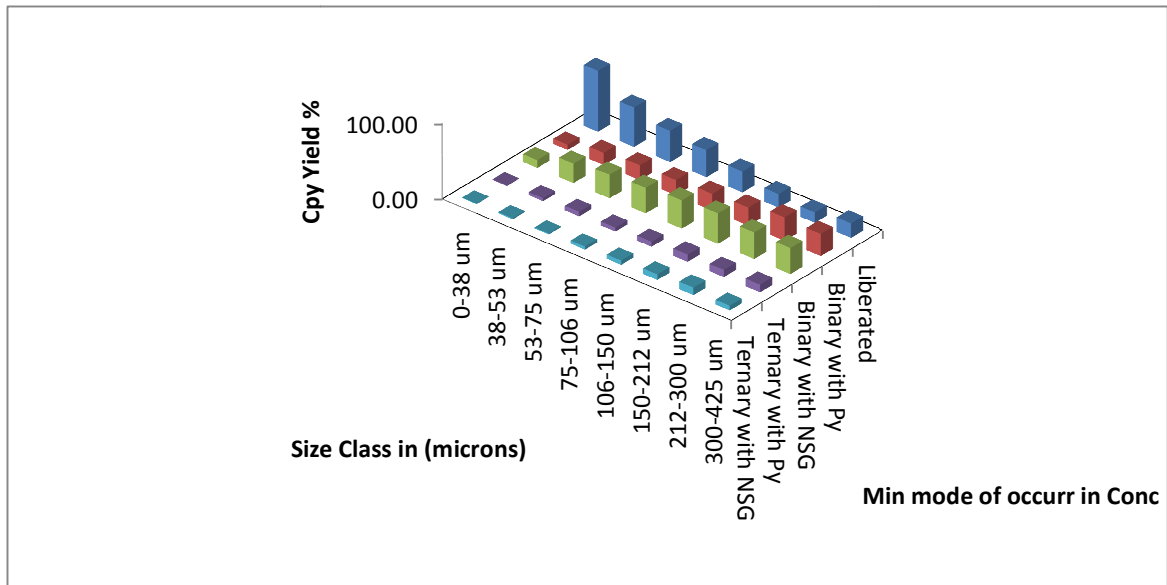


Figure 5-5: Chalcopyrite mineral mode of occurrence in Copper 1 base case concentrate product stream from the single flotation cell flow sheet simulation.

The mode of occurrence of mineral particles in the 0 to 75 μm fine size fraction range that report to the tails (see Figure 5-6), can be seen to be similar to mineral particles in the same size fraction range that report to the concentrate (see Figure 5-5).

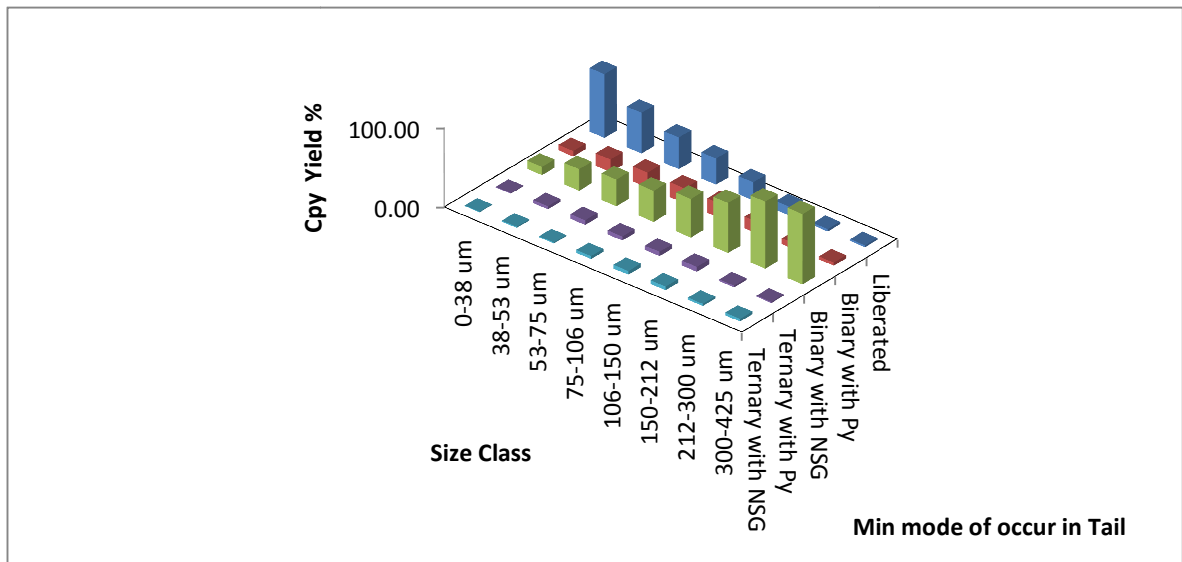


Figure 5-6: Chalcopyrite mineral mode of occurrence in Copper 1 base case ore tails product stream from the Single flotation cell flow sheet simulation.

Value mineral recovery in concentrate and tail streams

Analysis of the value mineral recovery against particle size shows a decrease in mineral recovery with increasing particle size above the 100 μm particle size, Figure 5-7. This trend compares well with that found in literature for the variation of mineral recovery with particle size (Pyke et al., 2003). As particle size increases the stability and attachment efficiencies also decrease, resulting in the value mineral particles detaching from the bubbles in the froth zone back into the pulp (see equation 3.28). A lower recovery is observed for fine particles below 100 μm particle size, as they have smaller size compared to the bubbles hence lower collection zone efficiency. Most of the NSG reports to the tails stream due to low floatability.

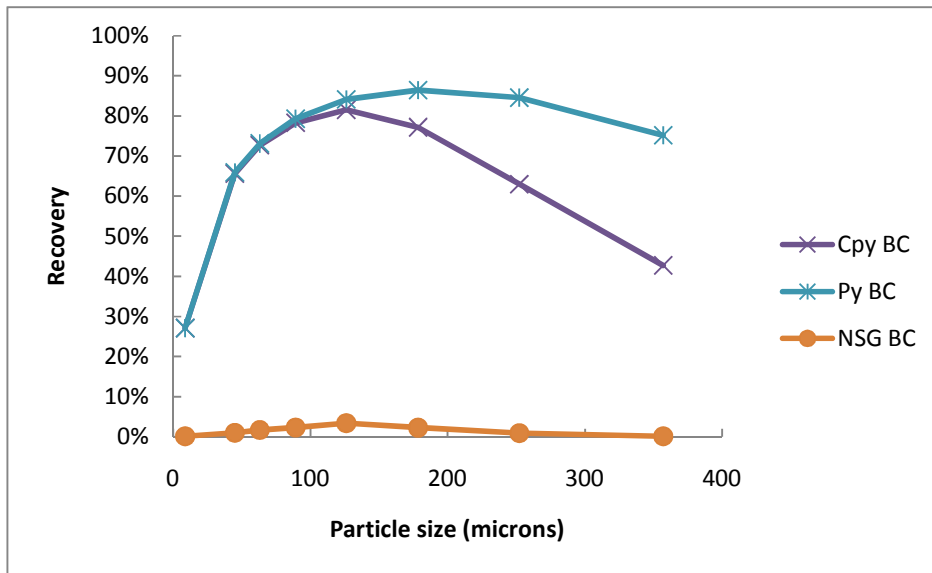


Figure 5-7: Mineral recovery against particle size for a Single flotation Cell simulation (Copper 1 BC feed).

Analysis of Particle recovery in streams around the Single cell flow sheet

Analysis of mineral particle recovery into the concentrate and tail streams of the simulated flotation cell operation showed a high recovery of coarse Chalcopyrite associated particles into the concentrate stream (see Figure 5-8). The fine sized particles in the 0 to 38 μm size fraction are poorly recovered into the concentrate stream despite being more liberated as compared to the coarser sized fractions (see Figure 5-9).

In practice the flotation rate of hydrophobic value minerals decreases with decreasing particle size due to the fact that as the particle size decreases the lower collision efficiency decreases as well (Ralston et al., 2007). This explains the poor recovery of fully liberated fine sized value mineral particles observed in the simulations (see Figure 5-8 and Figure 5-9).

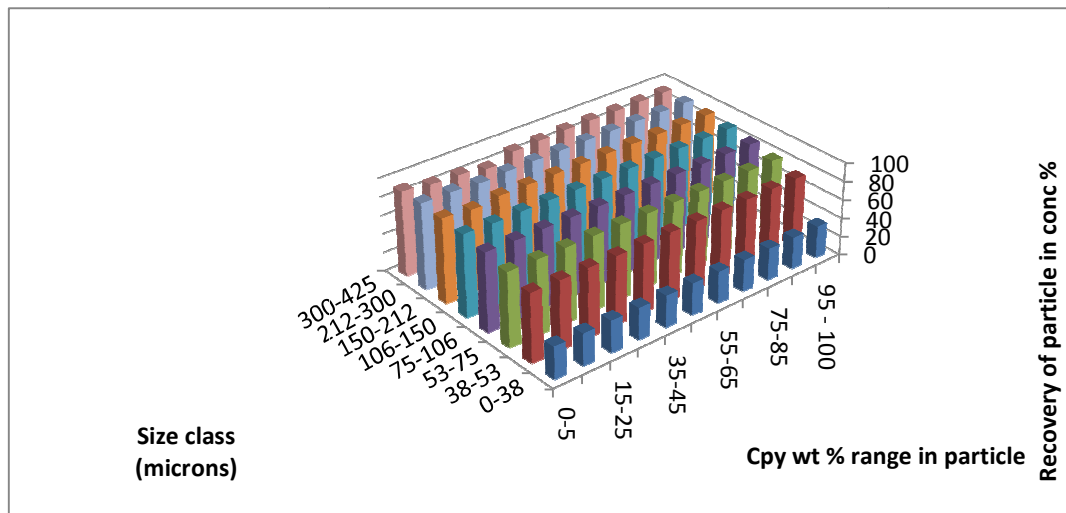


Figure5-8: Particle class recovery per size fraction in the concentrate stream against Cpy wt %.

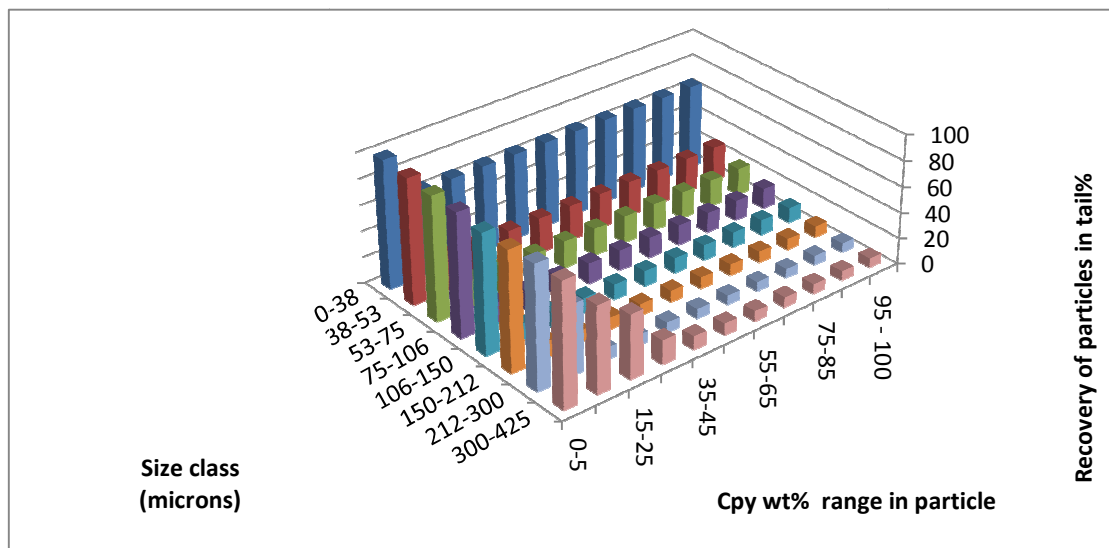


Figure 5-9: Particle class recovery per size fraction in the tails stream against Chalcopyrite wt % range in particle classes.

Analysis of Cumulative liberation of minerals in the flow streams

The feed stream liberation profile shows a greater liberation of particles in the 0 to 38 μm size fraction Figure 5-10.

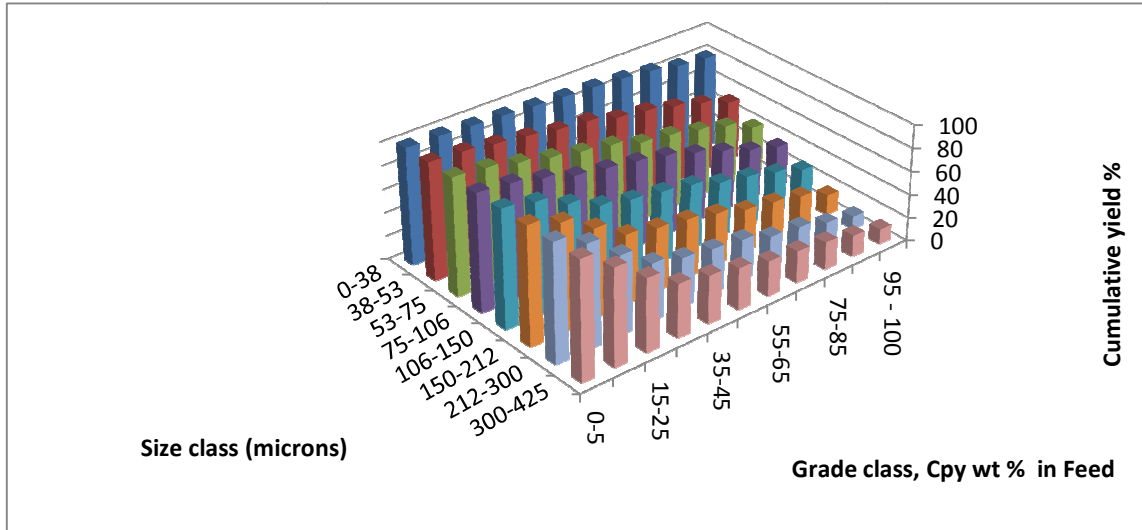


Figure 5-10: Cumulative liberation of Chalcopyrite in feed stream to the Single Unit flotation Cell flow sheet simulation.

There is a decrease in the cumulative liberation of particles from the fine sized fractions (0-38 μm) to the coarse sizes (300-425 μm) (see Figure 5-10).

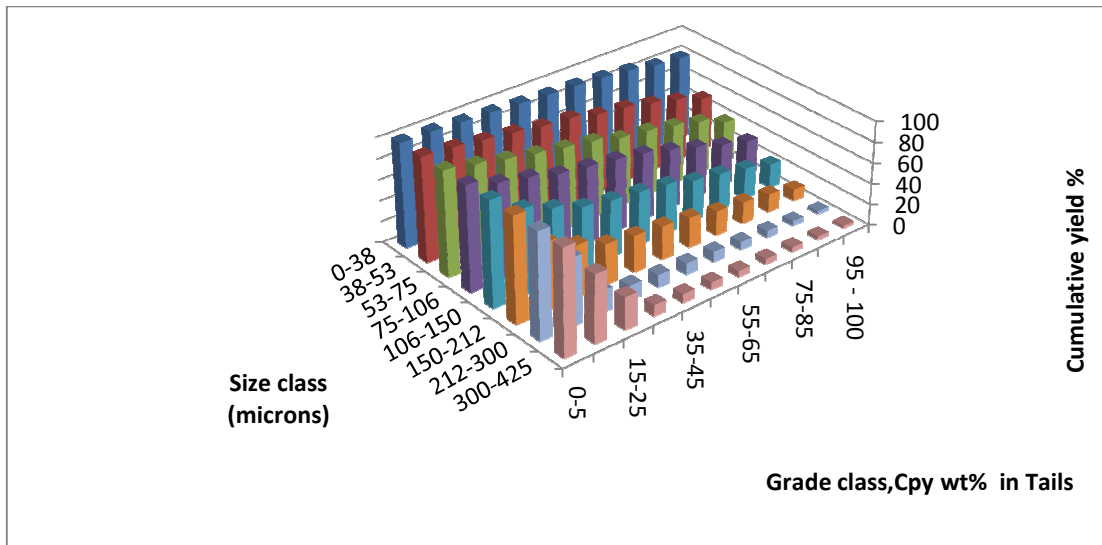


Figure 5-11: Cumulative liberation of Chalcopyrite in the output tail stream from the Single Unit flotation Cell flow sheet simulation.

Figures 5-11 and 5-12 show that fully liberated Chalcopyrite in the fine sized fractions (0-75 μm) mostly reported to the tails as was explained earlier fine sized particles have a lower probability of colliding with bubble hence they recover poorly.

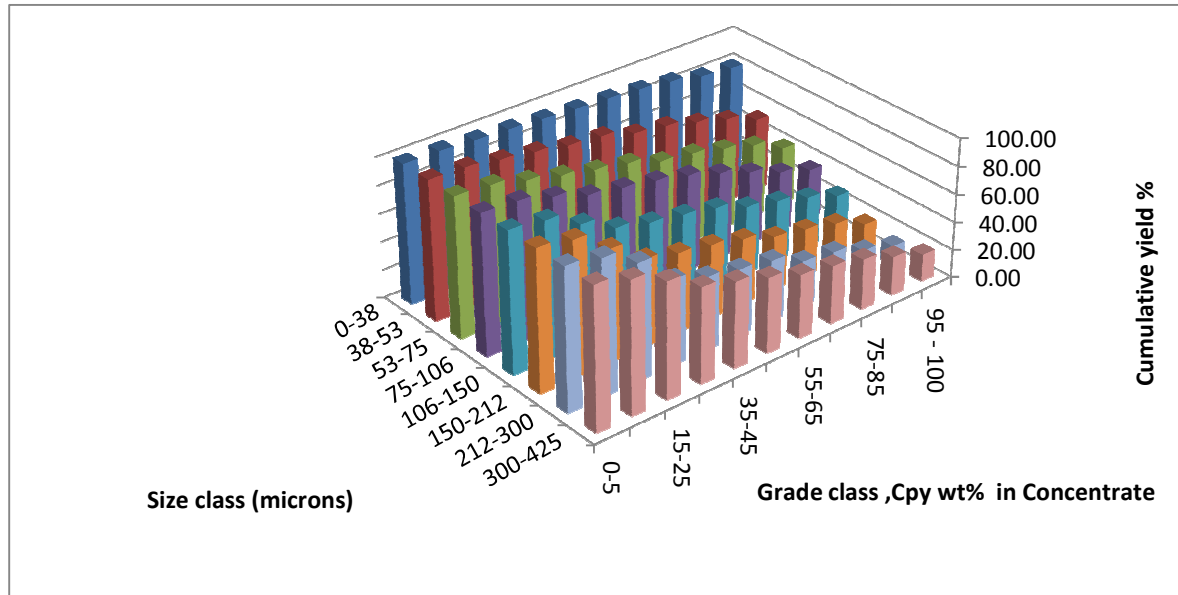


Figure 5-12: Cumulative liberation of Chalcopyrite in the output concentrate stream from the Single Unit flotation Cell flow sheet simulation.

5.4. Effects of changes in feed ore liberation on single Cell recovery

In order to understand fully the effects of microwave treatment on the downstream processing of ores, there is first a need to study the effects of feed ore liberation variation on the flotation process. This section presents the results of single flotation cell operation simulation work that was carried out to investigate the effects of feed ore liberation on value mineral recovery. The feed ore scenarios that were considered in the investigation are summarised in Table 4-5 Chapter 4. A detailed description of the feed ores has been provided in Chapter 4, section 4.3. Two ore groups representing flotation feeds at different grind sizes were utilised in the investigations, namely Copper 1 ($P_{70}=120 \mu\text{m}$) and Copper 2 ($P_{70}=180 \mu\text{m}$) flotation feed ores. A brief description of the method that was used in obtaining the simulation results for Copper 1 base case ore and artificial ores derived from it will be presented first followed by Copper 2 base case ore and its associated artificial ores. This will be followed by the presentation and discussion of the simulation results that were obtained for each feed ore group.

5.4.1. Methodology

A single flotation cell flow sheet was created in HSC Chemistry simulation software. A fundamental property based model wizard created for the purpose of this study and described in Chapter 3, section 3.3 was used to model the flotation process on the simulated flow sheet. The simulated flotation cell hydrodynamic conditions were described by utilising literature data from a previous study carried out by Ralston et al. (2007) on an industrial copper plant (see Table 5-4 and Appendix G Table G.1-1). These literature operating and hydrodynamic conditions were used to calibrate the fundamental property based model in all the simulations that were carried out. Six single cell flow sheet simulations representing the six different feed ore liberation scenarios considered in the study were carried out. The following flotation performance measurement parameters that are calculated from the model simulation output values were selected as key output parameters for investigating the effects of feed ore liberation changes;

1. Value mineral recovery by size (Chalcopyrite),
2. Cell enrichment ratio per feed ore
3. Cell mass pull per feed ore

Results that were obtained for both Copper 1 and Copper 2 feed ore groups were then analysed in order to determine the values of the key output parameters that have been listed above.

Table 5-4: Feed and literature hydrodynamic variables that were used in simulating a Single flotation cell flow sheet operation.

Variable	Parameter	Literature Parameter (Ralston et al., 2007)
Feed ore Type	Copper 1/ Copper 2 feeds	
P ₇₀	120 μm/180μm	
Cell volume	85 m ³	85 m ³
Feed rate	890 tph	890 tph
Sulphide mineral contact angle (θ)		78°
NSG contact angle (θ)		0°
Energy dissipation (ε)		11 m ² /s ³
Bubble diameter (d _b)		0.0013 m
Bubble rise velocity (v _b)		0.18 m/s
Apparent viscosity of slurry (ϑ)		0.2 kg/ms
Gas flow rate (G _{fr})		4 m ³ /min
Surface tension (γ)		70 N/m

5.4.2. Copper 1 feed ore (P₇₀ = 120 μm): Results and discussion

Figures 5-13 to 5-15 are graphical representation of the flotation simulation model's mineral recovery against particle size for all the feed ore scenarios that were considered. The differences in mineral recovery between the ores can be attributed to the differences in liberation profiles of the feed ore and hence the mineral particle hydrophobicity as described by the particle surface contact angle.

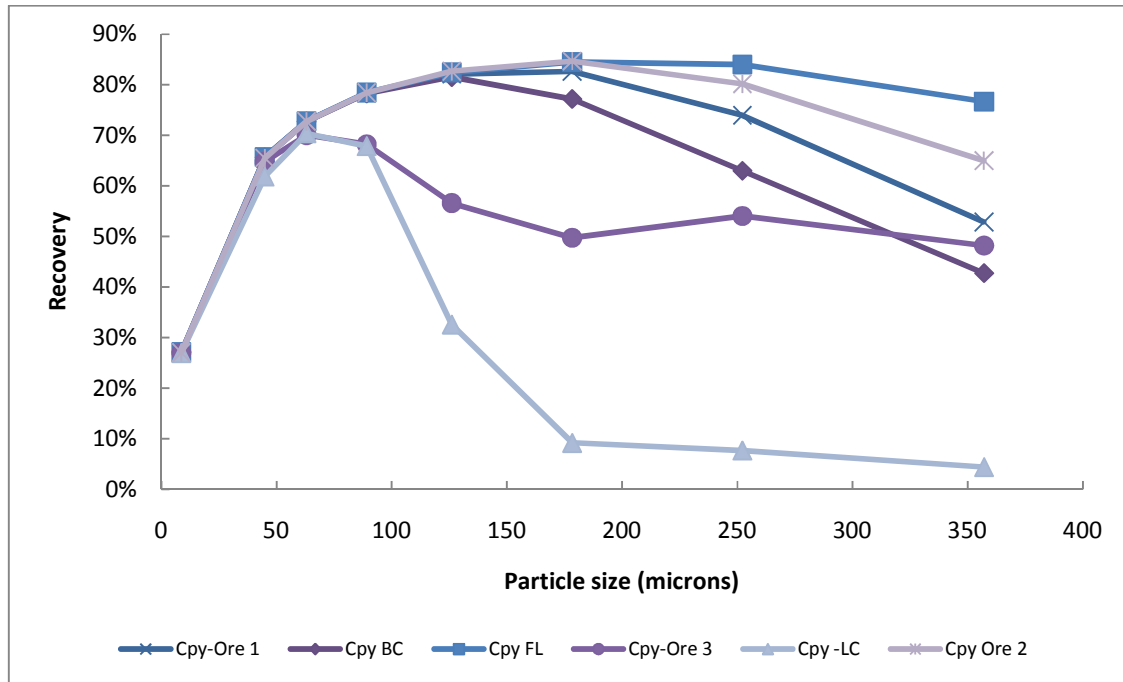


Figure 5-13: Chalcopyrite recovery against particle size for a single flotation Cell simulation for all the feed ore liberation scenarios considered in the simulations ($P_{70}=120 \mu\text{m}$).

Figure 5-13 and 5-14 show a decrease in value mineral recovery with increasing particle size. It is understood from literature that value mineral recovery decreases with increasing particle size (Pyke et al., 2003). There is no significant difference in value mineral recovery between the ores in the fine particle size classes Figure 5-13 and 5-14. As particle sizes increases there is a drop in recovery of the poorly liberated ores first (LC and Ore 3). As size increases and especially between the 120 μm to 150 μm particle size fractions, a significant difference in value mineral recovery is observed between the four well liberated ore feeds, which becomes quite pronounced at the very coarse particle sizes (see Figure 5-13 and Figure 5-14) .

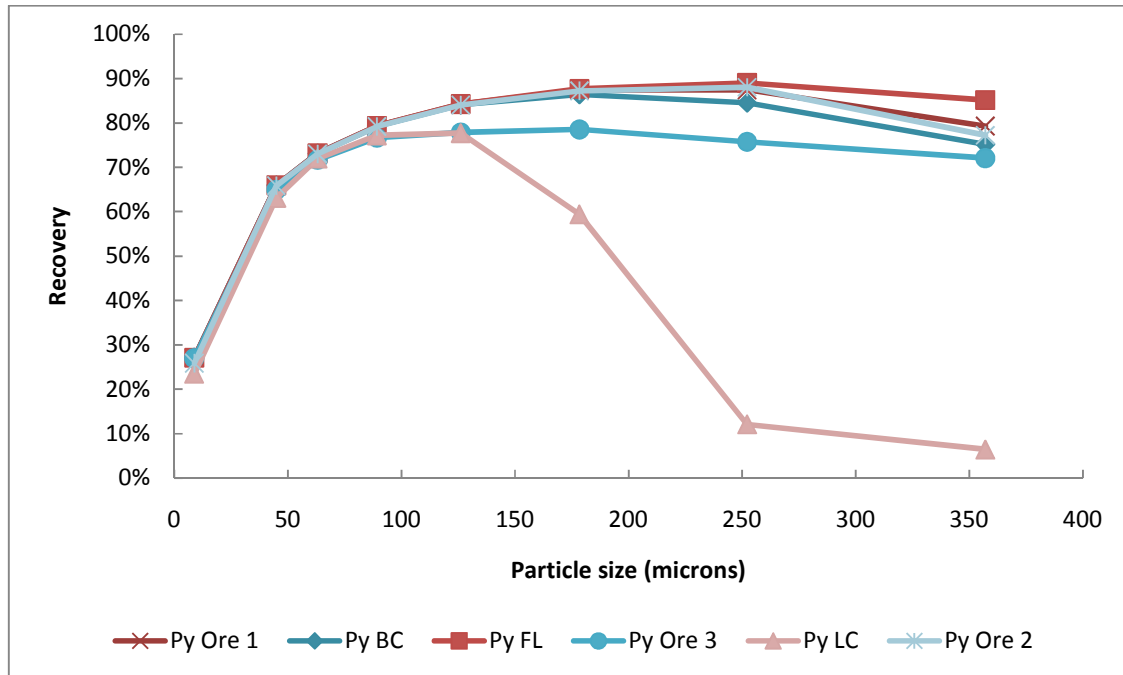


Figure 5-14: Pyrite recovery against particle size for a Single flotation Cell simulation for all the feed ore liberation scenarios considered in the simulations, ($P_{70}=120\mu\text{m}$).

Figure 5-14 shows similar Pyrite mineral recovery trend as that observed for Chalcopyrite. This can be attributed to the fact that a fully liberated Pyrite mineral particle was assumed to have the same hydrophobicity (contact angle) as a fully liberated Chalcopyrite value mineral in the simulations. For Pyrite value mineral recovery above the 150 μm particle size the percentage Pyrite recovery values for BC, Ore 1 and Ore 2 feed are of similar magnitude. This is mostly due to the fact that Pyrite in the BC feed is well liberated (see Figure 4-3). Thus the improvement in the recovery of Pyrite in FL, Ore 1 and Ore 2 feed compared with the BC feed Pyrite recovery is smaller than that observed for Cpy recovery (see Figure 5-13 and Figure 5-14).

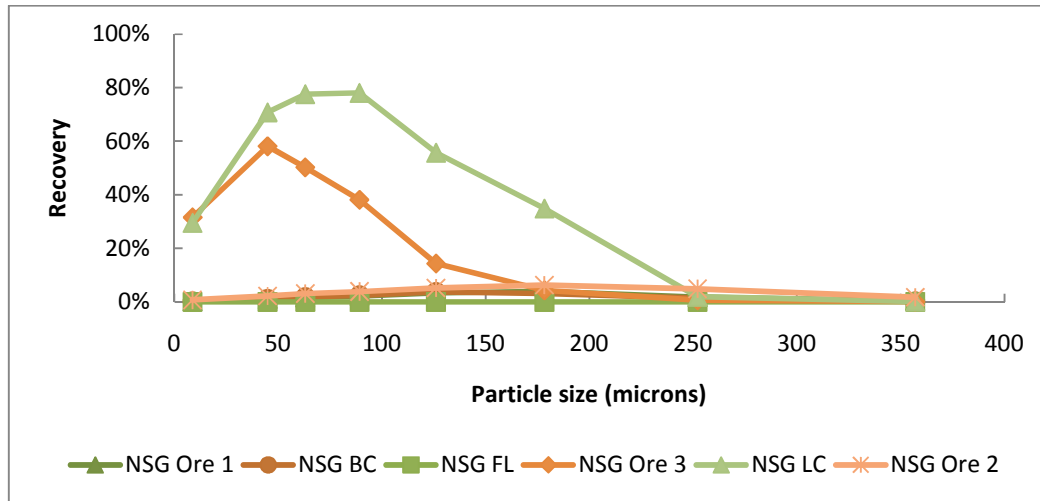


Figure 5-15: Pyrite recovery against particle size for a Single flotation Cell simulation for all the feed ore liberation scenarios considered in the simulations, ($P_{70}=120\ \mu\text{m}$).

The high NSG recovery reported for LC and Ore 3 feed ore shown in Figure 5-15 was due to the bulk of the NSG in these feed ores occurring in association with Chalcopyrite and Pyrite minerals as binary or ternary composite particles. Most of the NSG associated with the floating mineral therefore reported to the concentrate, hence high NSG recovery values were obtained for these ores.

Table 5-5 below summarises the results of the simulated flotation process key performance parameters for the six feed ore scenarios that were considered for Copper 1 group ores with a grind size P_{70} of $120\ \mu\text{m}$. From the table it can be observed that the FL and LC feed ore are the two extreme feed ore liberation scenarios in this study. FL ore describes an ideal fully liberated ore which gives maximum value mineral recovery, enrichment ratio and a very low mass pull as shown in Table 5-5. LC on the other hand is the complete opposite of FL feed ore as can be seen from the results in Table 5-5 below. Ore 1 and 2 feed ores have flotation performance values that are better than the BC feed ore (see Table 5-5). This is because Ore 1 has more fully liberated value minerals per size fraction compared to the BC feed; hence it gives better value mineral recovery (see Table 4-8). Ore 2 feed has more ChalcopyritePyrite (CpyPy) binary particles per size fraction compared with the BC feed and Ore 1 (see Figure 4-5, Figure 4-14 and Figure 4-17).

The CpyPy binary particles have composite contact angle values that are equivalent to fully liberated sulphide value mineral particles. Therefore Ore 2 feed ore recovers better than the BC and Ore 1 feed ores (Table 5-5).

Table 5-5: Simulated flotation process key performance parameters for the six feed ore scenarios that were considered for the base case grind size $P_{70}=120$ microns

Feed ore type	Mass pull %	Enrichment ratio	Cu Rec %	Cu % grade
BC	7.4	6.2	46.2	6.9
FL	6.2	7.9	48.8	8.8
Ore 1	7.2	6.8	47.0	7.2
Ore 2	7.4	6.3	46.3	6.7
Ore 3	13.8	2.8	38.4	3.0
LC	28.6	1.3	35.9	1.4

The simulation results above indicate the existence of maximum particle size below which changes in feed ore liberation have no effect on mineral recovery. An improvement in BC feed Cu recovery of 5.6% and an improvement in concentrate Cu grade of 27.5% can be achieved by improving the BC feed value mineral liberation to that of FL feed (see Table 5-5). Following on these results a further analysis of the sub-process bubble-particle interaction efficiency values for the different ores used in the simulations was carried out.

5.4.2.1. Sub-process bubble-particle interaction efficiency values

From the simulation results only an analysis of the trend in the stability and attachment sub-process efficiency was carried out, as the collision efficiency is not dependent on particle liberation. The following calculation steps were carried out in order to obtain the weighted mean sub-process efficiency values. For each feed ore within a given size class the product of the sub-process efficiency value and chalcopyrite weight percent of each particle class in the size class was summed up to determine the weighted sub-process efficiency. Equation 5.1 below summarises the calculation steps that were used in calculating the weighted mean sub-process efficiency per size fraction in the study.

$$\sum_{i=1}^n E_{zi} \times \text{Cpy wt\%}_{ij} = E_{zj} \quad 5.1$$

E_{zj} - weighted mean sub-process efficiency for size fraction j

Cpy wt% -chalcopyrite composition in each particle class i in size fraction j

z - Stability or attachment sub-process

n -number of particle liberation classes in j size fraction

i -particle liberation class

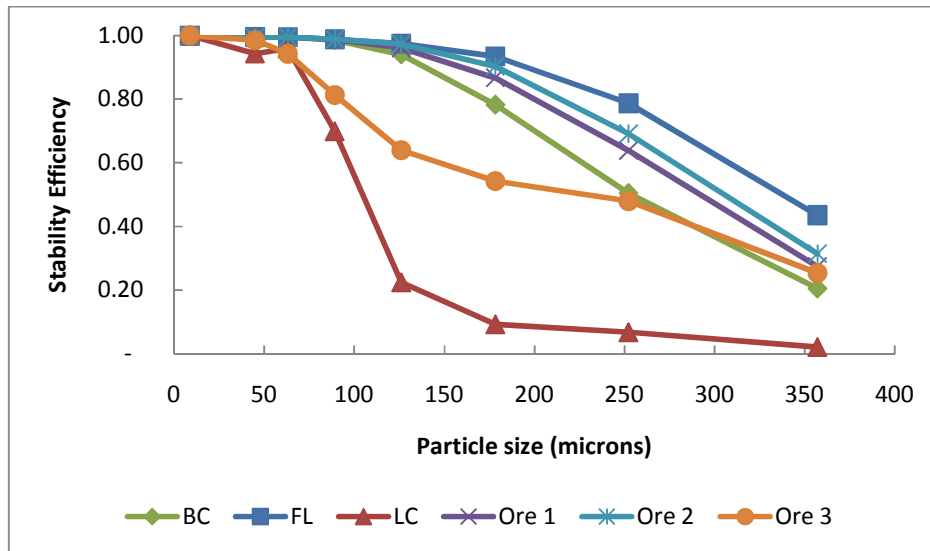


Figure 5-16: Mean Stability efficiency against mean particle size for feed ore with a $P_{70} = 120\mu\text{m}$

Figure 5-16 shows a decreasing trend in stability efficiency with increasing particle size. This is due to the effects of detachment forces acting on the bubble-particle aggregate which become predominantly large with increasing particle size (see equation 3.28). As particle size increases a higher particle contact angle value is required to float mineral particles with large particles sizes. There is no significant difference in stability efficiency at fine particle sizes below $75\mu\text{m}$, Figure 5-16. This explains the trend in mineral recovery that was observed in the simulations.

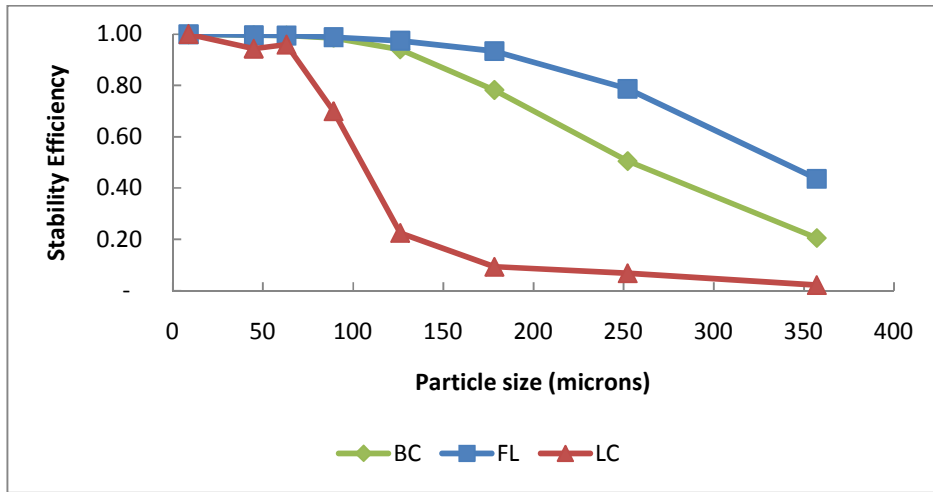


Figure 5-17: Mean Stability efficiency against mean particle size for Base Case ore and the two extreme liberation cases (FL and LC), for feed ore with a $P_{70} = 120 \mu\text{m}$.

Analysing the stability efficiency of the extreme liberated feed ore cases (i.e. LC and FL feed ores) clearly shows that there is a maximum particle size above which stability efficiency becomes a strong function of feed ore liberation profile (see Figure 5-17). This maximum particle size is greater for well-liberated feed ores for example BC and FL feed ores compared with poorly liberated ores such as LC feed ore (see Figure 5-17). This trend in particle stability efficiency with varying feed ore liberation explains the trends observed in mineral recovery.

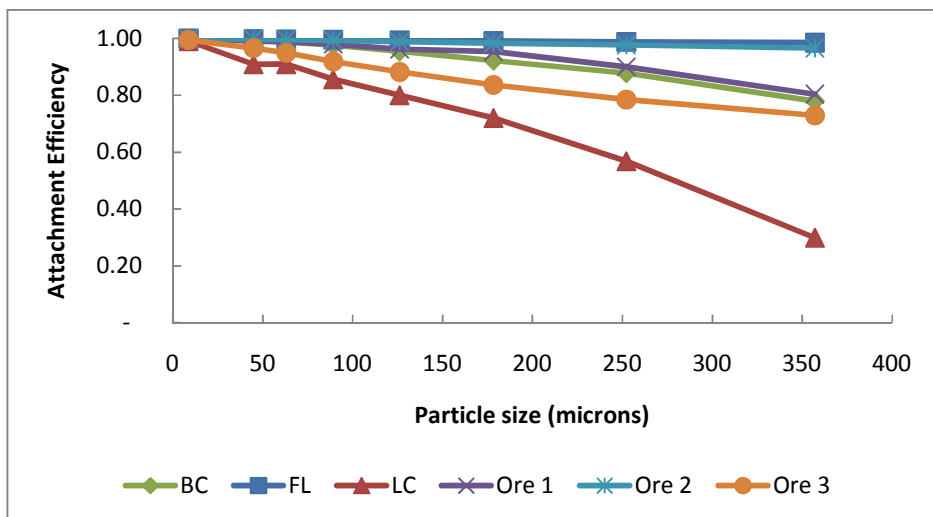


Figure 5-18: Mean attachment efficiency against mean particle size for feed ore with a $P_{70} = 120 \mu\text{m}$.

Figure 5-18 shows a decreasing trend in attachment efficiency with increasing particle size. This is because an increase in particle size results in a decrease in sliding time and an increase in the induction time hence decreases the attachment efficiency (see equation 3.24 and 3.25). Figure 5-19 below shows that the difference in stability efficiency is more pronounced at coarse particle sizes.

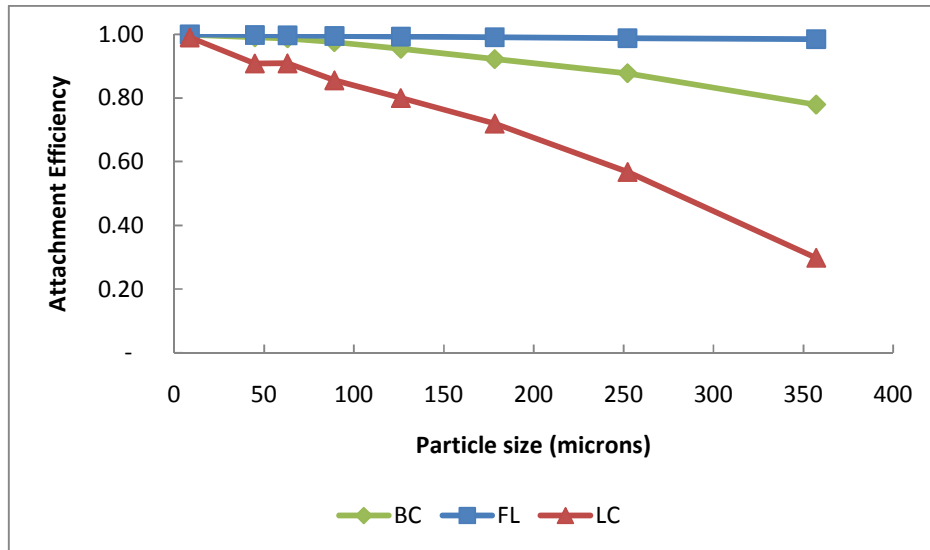


Figure 5-19: Mean Attachment efficiency against mean particle size for Base Case ore and the two extreme liberation cases (FL and LC), for feed ore with a $P70 = 120 \mu\text{m}$.

The differences in recovery, which were mostly observed at coarse particle sizes, with varying feed ore liberation can be attributed to the variation of stability and attachment efficiency values at coarse sizes. Since the feed ores used in the simulation have similar mineralogy, the differences in stability and attachment efficiency trends are due to a variation in particle contact angle, hence feed ore particles liberation properties. The results indicate the existence of a maximum particle size below which any improvement in mineral liberation as expected from the application of microwave technology does not result in an increase in value mineral recovery and that this maximum particle size is a strong function of the flotation feed ore liberation profile.

5.4.3. Copper 2 feed ore ($P_{70} = 180 \mu\text{m}$): Results and discussion

Copper 2 group feed ores with a grind size of $P_{70} = 180 \mu\text{m}$ represented coarse feed ore in the study. Figure 5-20 shows a decreasing trend in Chalcopyrite mineral recovery with increasing particle size above $120 \mu\text{m}$ particle size and a significant difference in mineral recovery at coarse sizes for the different ores mostly for FL feed above the $180 \mu\text{m}$ particle size.

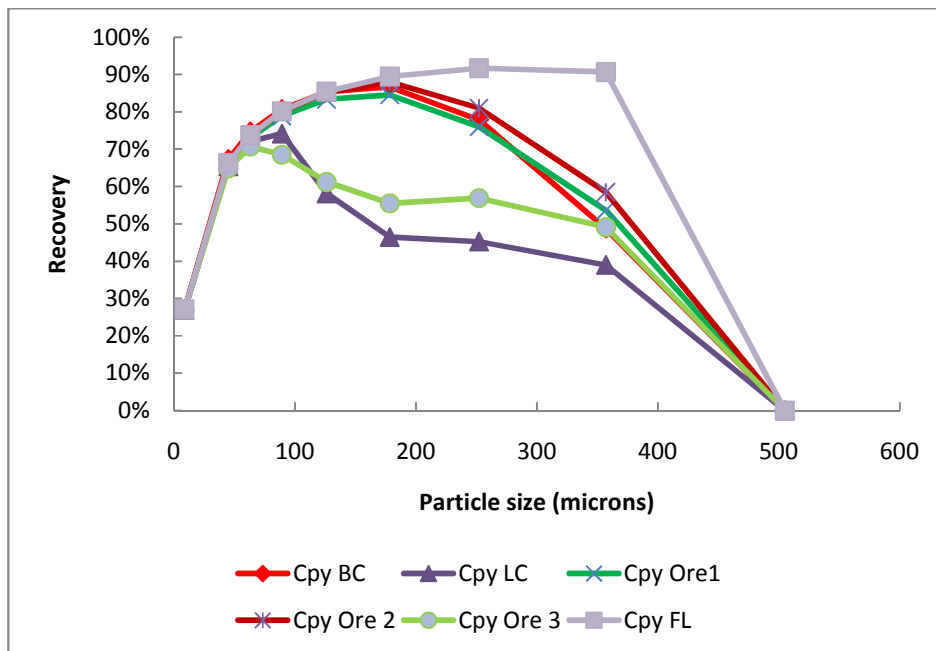


Figure 5-20: Chalcopyrite recovery against particle size for a Single flotation Cell simulation for all the feed ore liberation scenarios considered in the simulations, ($P_{70}=180 \mu\text{m}$).

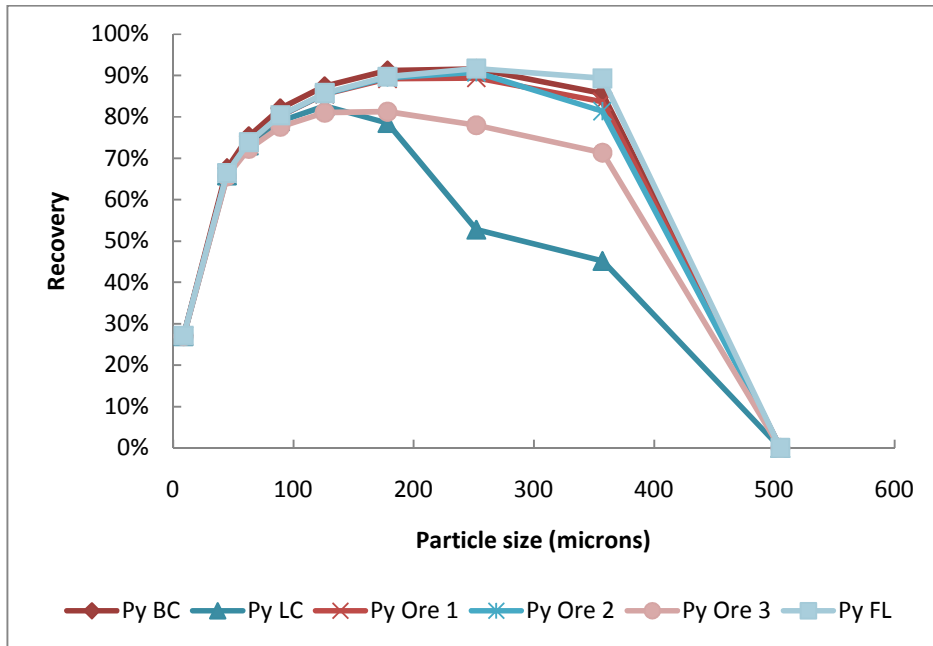


Figure 5-21: Pyrite recovery against particle size for a Single flotation Cell simulation for all the feed ore liberation scenarios considered in the simulations, ($P_{70}=180 \mu\text{m}$).

Figure 5-21 shows a decreasing trend in Pyrite mineral recovery with increasing particle size. There is little difference in mineral recovery at coarse sizes between the BC, Ore 1, Ore 2 and FL feed. Little improvement in pyrite recovery was observed between the BC and fully liberated feed ores in (see Figure 5-21). This was due to high pyrite liberation in the base case feed that was used in creating the fully liberated artificial ore (see Figure 4-6). Consequently further improvements in liberation of the BC feed yielded small improvements in Pyrite recovery (see Figure 5-21).

Table 5-6 below summarises the results of the simulated flotation process key performance parameters for the six feed ore scenarios that were considered for this ore. Better results were obtained for Copper 2 ore compared to those obtained for Copper 1 ore Table 5-6. An improvement in BC feed Cu recovery of 11.0% and an improvement in concentrate Cu grade of 31.3% can be achieved by improving the BC feed value mineral liberation to that of FL feed (see Table 5-6).

Table 5-6: Simulated flotation process key performance parameters for the six feed ore scenarios that were considered for the base case grind size $P_{70}=180$ microns

Feed ore type	Mass pull %	Enrichment ratio	Cu Rec %	Cu % grade
BC	7.0	6.3	44.5	6.7
FL	6.0	8.2	49.4	8.8
Ore 1	6.8	6.7	46.0	7.1
Ore 2	7.4	6.3	46.3	6.7
Ore 3	13.8	2.8	38.4	3.0
LC	24.1	1.5	35.7	1.6

5.4.3.1. Sub-process efficiency values

The stability and attachment efficiency values that were calculated in the simulation for the various feed ores in the simulations are shown to below in Figure 5-22 and Figure 5-23.

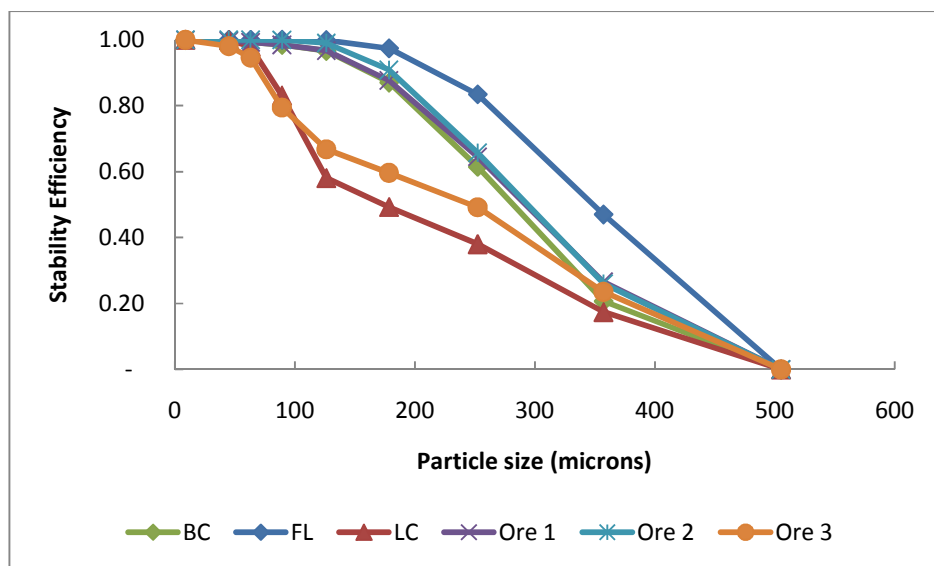


Figure 5-22: Mean Stability efficiency against mean particle size for feed ore with a $P_{70} = 180\mu\text{m}$.

Figure 5-22 shows a similar decreasing trend in stability efficiency with increasing particles size as was observed earlier for Copper 1 feed ores.

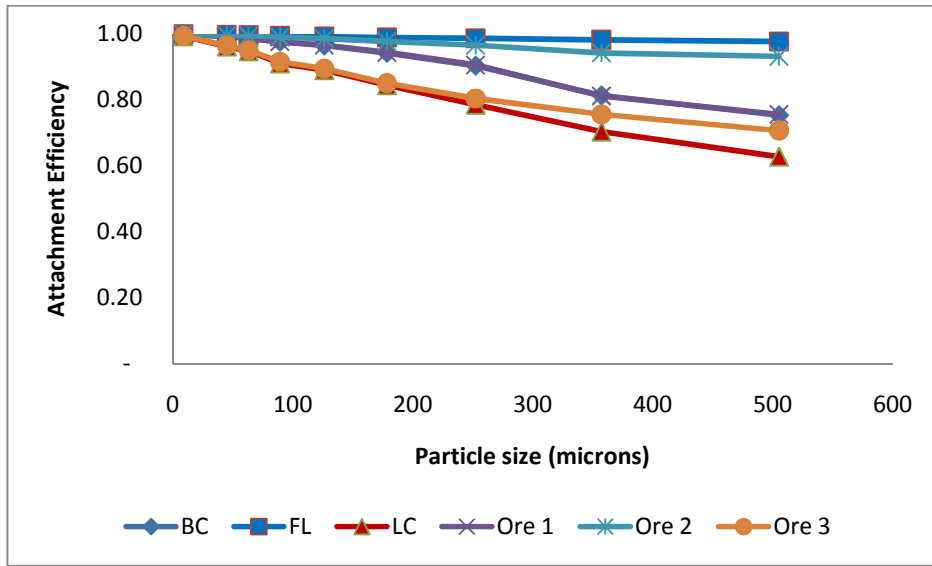


Figure 5-23: Mean attachment efficiency against mean particle size for feed ore with a $P_{70} = 180 \mu\text{m}$

Figure 5-23 shows decreasing attachment efficiency with increasing particle size. The results that were obtained for coarse ground feed ores stability and attachment efficiency further confirmed the significant variation in sub-process efficiency values at coarse size.

5.4.3.2. Feed ore Particle size sensitivity analysis

A particle size sensitivity analysis study was carried out on the Copper 2 group ores to verify the sensitivity of the flotation process as described by the fundamental property based model to particle size, for feed ores with the same mineralogy but with different particle size distributions. This was aimed at showing that there is a maximum particle size below which mineral recovery was not a strong function of feed ore liberation. Two sets of fictional mean particle size fractions were used describing very fine feed ores ($P_{70} = 63 \mu\text{m}$) and a very coarse ground ore ($P_{70} = 250 \mu\text{m}$). No changes were made to the feed ore particle weight distribution per size class of the original Copper 2 group ores described in Table 4-1, Chapter 4, section 4.2. Simulations similar to the ones described above were then carried out. Table 5-7 shows the fictional average mean particle sizes that were considered in investigating the fundamental property based model sensitivity in simulating flotation recovery for a very fine ground ore.

Table 5-7: Fictional average fine particle sizes and used in the sensitivity analysis investigations ($P_{70} = 63 \mu\text{m}$)

Average Size (μm)	Particle weight distribution, wt%
8.72	38.17
19.16	4.64
26.10	4.83
48.33	5.46
55.00	7.01
65.00	8.83
85.00	12.71
110.00	13.48
126.10	4.87

Figure 5-24 is the value mineral recovery results that were obtained using the particle size classes shown in Table 5-7. The results confirm the existence of a maximum particle size above which mineral recovery begins to drop in response to differences in feed ore liberation properties. This maximum particle size is lower for poorly liberated ores such as Ore 3 and LC (see Figure 5-24). This point is very important in the application of microwave technology in mineral processing as it indicates that little benefit from microwave enhanced liberation will be realised at fine flotation feed grind sizes.

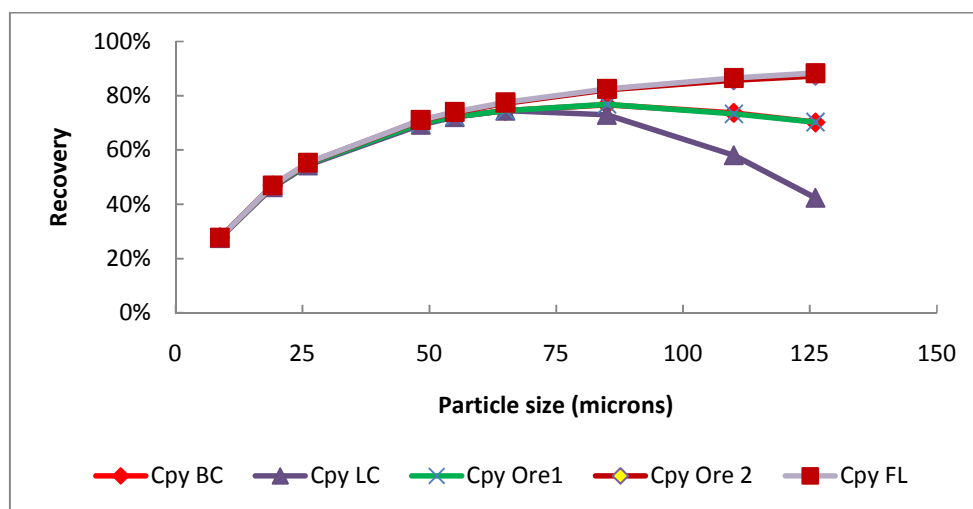


Figure 5-24: Chalcopyrite recovery against particle size for a Single flotation Cell ($P_{70}=63 \mu\text{m}$).

Table 5-8 shows the fictional average mean coarse particle sizes that were considered in investigating the fundamental property based model sensitivity in simulating flotation recovery for a very coarse ground ore along with the original bulk particle weight distribution for Copper 2 ores.

Table 5-8: Fictional average coarse particle size distribution ($P_{70} = 250\mu\text{m}$)

Average Size (μm)	Particle weight distribution, wt%
63.05	38.17
89.16	4.64
126.10	4.83
178.33	5.46
200.00	7.01
252.19	8.83
300.00	12.71
357.07	13.48
504.98	4.87

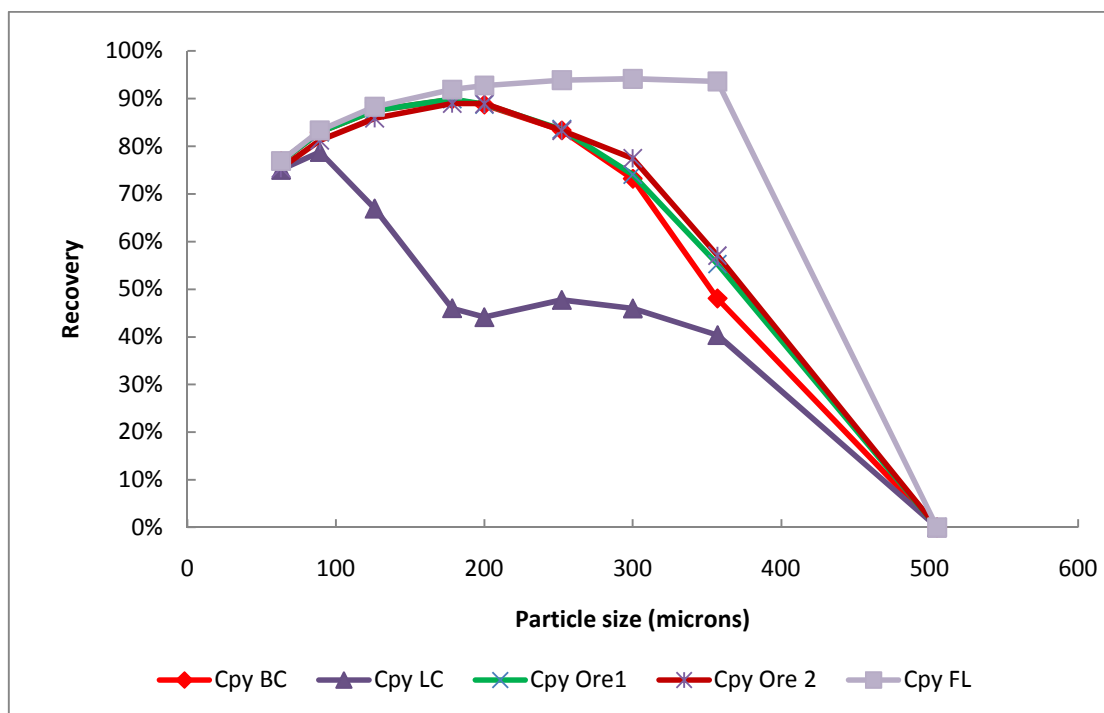


Figure 5-25 : Chalcopyrite recovery against particle size for a Single flotation Cell simulation ($P_{70}=250\mu\text{m}$).

Figure 5-25 further supports the results observed so far, which indicate that at coarse particle sizes the variation in feed ore liberation has a significant effect on value mineral recovery. From the sensitivity analysis results it appears that feed ore particle recovery is not a strong function of particle liberation at fine particle sizes, as shown in Figure 5-24. Maximum benefits from enhanced liberation due to microwave assisted comminution can thus be achieved by optimising feed ore grinding, Figure 5-25.

5.5. The effects of feed ore particle size distribution on value mineral recovery

Based on the results of investigations into the effects of varying feed ore liberation on value mineral recovery presented above, where a significant difference in value mineral recovery at coarser grind sizes with variation in liberation was observed, a feed ore grind size sensitivity study was carried out in order to investigate further the effects of grind size variation on value mineral recovery. The study was undertaken by using three feed ore liberation scenarios. These were LC feed ore representing the worst liberation case scenario, FL feed ore representing the maximum possible feed ore particle liberation scenario and a base case scenario, representing feed ore with a liberation spectrum from experimentally ground flotation feed. A brief outline of the methodology that was used will be described below followed by a presentation of the results and their discussion.

5.5.1. Methodology

Feed ore with varying grind size was created by varying the particle distribution of the Copper 2 group feed ores. The feed ore grind sizes that were used in the investigation are shown in (see Table 5-9).

Table 5-9: Particle cumulative weight distribution of the different feed ores considered in carrying out the feed particle weight distribution sensitivity analysis

Mean Size fraction	P ₇₀ Grind size				
	89 μm	129 μm	252 μm	300 μm	430 μm
8.72	37.17	25.6	10.17	8.12	0.87
44.88	47.71	38.14	17.81	14.76	2.42
63.05	60.54	53.65	26.64	22.59	5.25
89.16	69.99	63.1	36.1	31.05	7.39
126.10	77	70.11	46.11	43.06	10.11
178.33	85.83	78.94	57.94	51.92	17.97
252.19	93.69	86.65	70.65	62.66	26.79
357.07	97.13	95.13	89.13	79.2	44.2
504.98	100	100	100	100	100

Figure 5-26 is a cumulative weight distribution plot of the grind sizes considered in the sensitivity analysis. The graph shows a clear difference in particle weight distributions at different grind sizes.

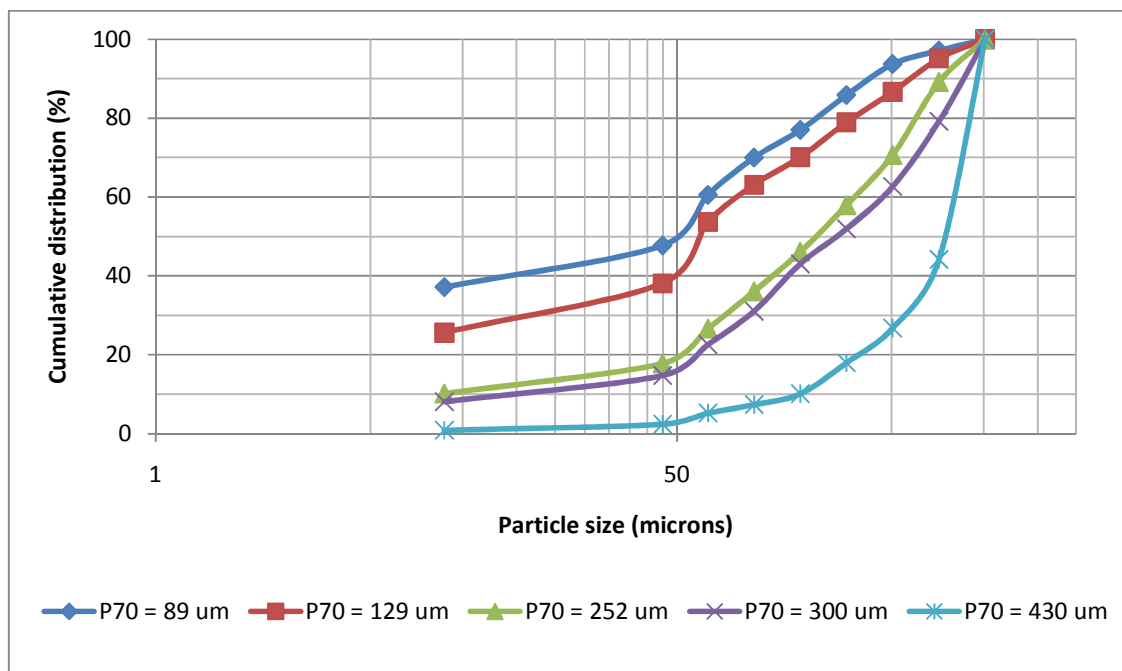


Figure 5-26: Cumulative particle weight distribution plot of the various P₇₀ grind sizes that were considered in the simulations.

Stream files were created for each particle size with the weight distribution that was considered shown in Table 5-9. By manipulating the feed particle size weight distribution in creating feeds with different grind sizes, feeds with different copper feed grades was produced (see Table 5-10). It was therefore not possible to create artificial ores with the same head grade since the liberation spectrum in each class was fixed. In practice this difference in head grade has a significant effect on feed ore recovery with feed ores with higher head grades having high value mineral recovery. However in this study the difference in final feed ore recovery due to the variation in feed ore head grade was assumed to be insignificant.

The resultant feed ores had different grind sizes and grade, but the same mineral composition per size fraction as Copper 2 BC feed which was used as a basis for creating the different grind size feeds by manipulating its size fraction weight distribution. All the feed ores had a particle liberation spectrum per size class that was the same as Copper 2 feed ores, since the mineral composition per size class for all the ores was the same. It was therefore not possible to create artificial ores with the same head grade since the liberation spectrum in each class was fixed. In practice this difference in head grade has a significant effect on feed ore recovery with feed ores with higher head grades having high value mineral recovery. However in this study the difference in final feed ore recovery due to the variation in feed ore head grade in was assumed to be insignificant (see Table 5-10).

Table 5-10: Cu% feed grades at different feed grind sizes

Mean Size fraction	P₇₀ Grind size				
	89 µm	129 µm	252 µm	300 µm	430 µm
Cu% feed grade	1.17	1.10	0.92	0.86	0.60

For each grind size shown in Table 5-9, three single cell simulations were carried out for the three feed ore liberation scenarios (i.e. BC, LC and FL) that were considered for each feed grind size. Similar cell operating and hydrodynamic conditions similar to those described in the previous simulations (see Table 5-4) were used in carrying out the simulations.

5.5.2. Grind size sensitivity analysis results

An increase in overall recovery was observed within a P_{70} feed ore grind size range of 89 to 250 μm (Figure 5-27). This trend in overall recovery is consistent with literature where an improvement in overall value mineral recovery is expected for relatively coarse ground feed ore (Gupta and Yan, 2006). Above the optimum grind size the overall recovery begins to drop with increasing particle grind size. The overall recovery for all the feeds decreased with increasing particle size over the 250 μm to 430 μm feed ore grind sizes.

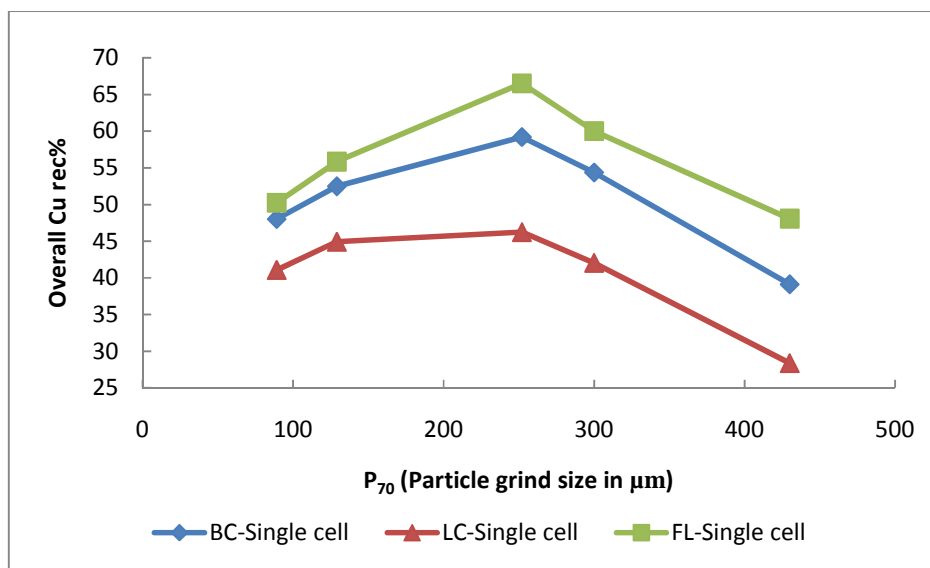


Figure 5-27: Overall single cell unit recovery against particle size for feed ore with varying size distributions.

The results indicate that there is a drop in overall copper recovery with increasing particle size above $P_{70} = 250 \mu\text{m}$.

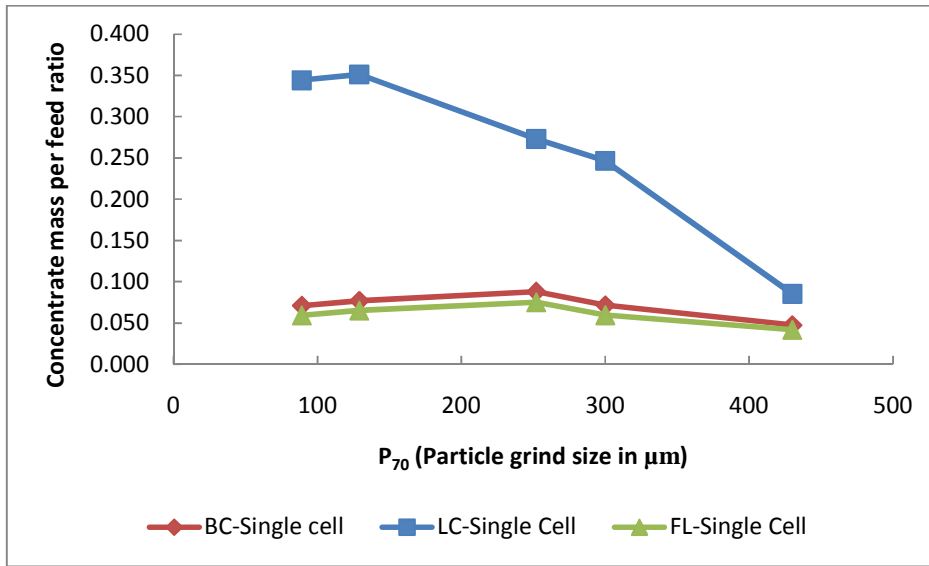


Figure 5-28: Concentrate mass recovery in a Single cell plotted against feed ore into the cell with varying size distributions.

Analysis of concentrate mass recovery as shown in Figure 5-28 indicates a low concentrate mass recovery above the 250 μm feed ore particle grind sizes for fully liberated and base case feed ores.

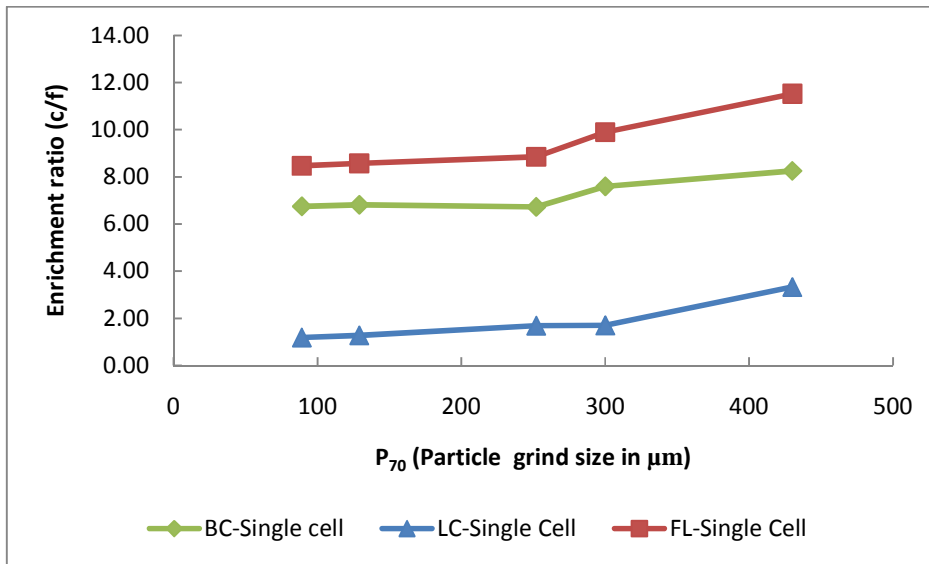


Figure 5-29: Enrichment ratio in a Single cell plotted against feed ore into the cell with varying size distributions.

Figure 5-30 shows an increase in enrichment ratio above the 250 μm P_{70} grind sizes. This increase is more pronounced for fully liberated ore. The results of the feed ore grind size sensitivity analysis study indicate that possible improvements in mineral recovery due to microwave treatment can be obtained for the particular ores considered in this study, if it is ground at size between a $P_{70} = 200 \mu\text{m}$ to $300 \mu\text{m}$. There is a limit to coarse particle flotation of $500 \mu\text{m}$ above which it becomes increasingly difficult to float coarse particles (Gontijo et al., 2007).

5.6. Conclusion

Simulations that were carried out using the fundamental property based model showed that mineral recovery trends obtained using the property based model were comparable to experimental batch flotation recovery trends obtained from a previous study for the same ore (AMIRA:P879A, 2009). The fundamental property based model has been successfully integrated into the simulation software and can be used for true particle modelling based on the results from the continuous single flotation cell simulations. Investigations into the effects of feed ore liberation variation on single cell flotation value mineral recovery showed that there exists a minimum particle size below which any variation in feed ore liberation has no effect on mineral recovery. Significant differences in value mineral recovery were only observed at coarse particle sizes. The results of the feed ore grind size sensitivity analysis indicate that maximum benefit from the application of microwave technology can best be obtained by utilising coarse grinding at sizes between $200 \mu\text{m}$ to $300 \mu\text{m}$ for the ores considered in this study

CHAPTER SIX

6. SIMULATION OF FLOTATION PLANTS

After successfully investigating the effects of feed ore liberation and particle size on value mineral recovery using a single flotation cell, work was carried out to determine these effects when a typical plant flow sheet is employed. A typical operating plant flotation flow sheet was developed for the purpose of investigating these effects in HSC Chemistry 7 simulation software. This section will describe the simulations that were carried out in investigating the effects of feed ore liberation and grind size by utilising rougher flotation section flow sheet. This will be followed by a presentation and discussion of the results from these simulations.

6.1. Rougher bank in series configuration simulation

The rougher flotation section flow sheet configuration, which was considered in this study, consisted of nine rougher cells in series with no recycle stream. Figure .D.1-1, Appendix D shows the rougher cell configuration that was used in the study. This flow sheet configuration is similar to the one at Escondida Leguna Seca copper plant (Yianatos et al., 2006). Flow sheet simulation results were compared with literature values for a similar cell configuration rougher plant. Flotation cell operating and hydrodynamic conditions that were used in the single cell simulations were also used to calibrate the fundamental property based model in each of the nine cells making up the rougher section flow sheet. The values describing the hydrodynamic conditions that were used in the model calibration were from a previous study in literature that was carried out by Ralston et al. (2007) on an industrial copper ore mineral processing plant. The values of the hydrodynamic and flotation cell operating condition parameters that were used in the investigations are shown in

Table 5-4 Chapter 5 (see also Appendix G). All flotation cells in the rougher bank were assumed to be operating at identical hydrodynamic and operating conditions, thus the froth depth in all the nine cells was assumed to be equal. Furthermore, the particle surface contact angle of the fully liberated value minerals was also assumed to be the same throughout the rougher bank.

The observed trend in simulated value mineral recovery (see Figure 6-1) was similar to that obtained from literature for a flow sheet of similar configuration treating a different copper ore feed (see Figure 6-2).

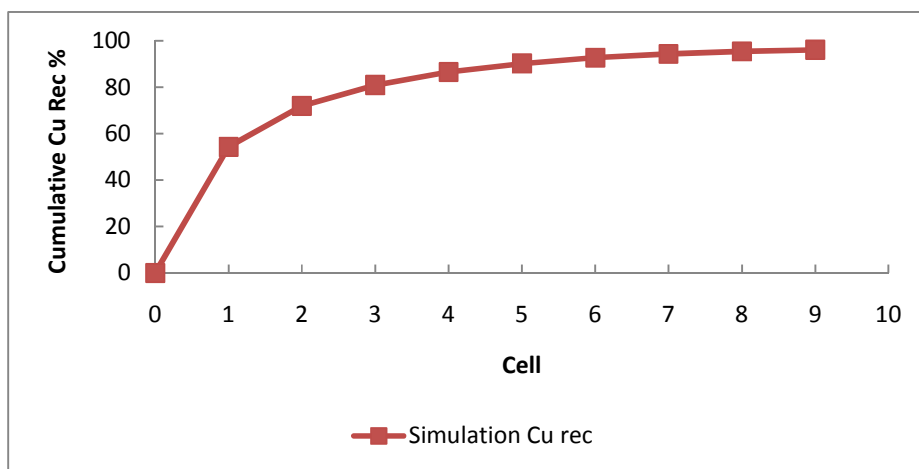


Figure 6-1: Cumulative value Copper recovery as a function of cell number in the rougher flotation section of a Simulated fictional plant.

From Figure 6-1 and Figure 6-2, it can be observed that there is a progressive decrease in local recovery per unit cell across the bank of rougher cells. A high stage recovery is observed for the first rougher cell; this is due to the presence of large amounts of floatable solids in the feed to the first rougher cell.

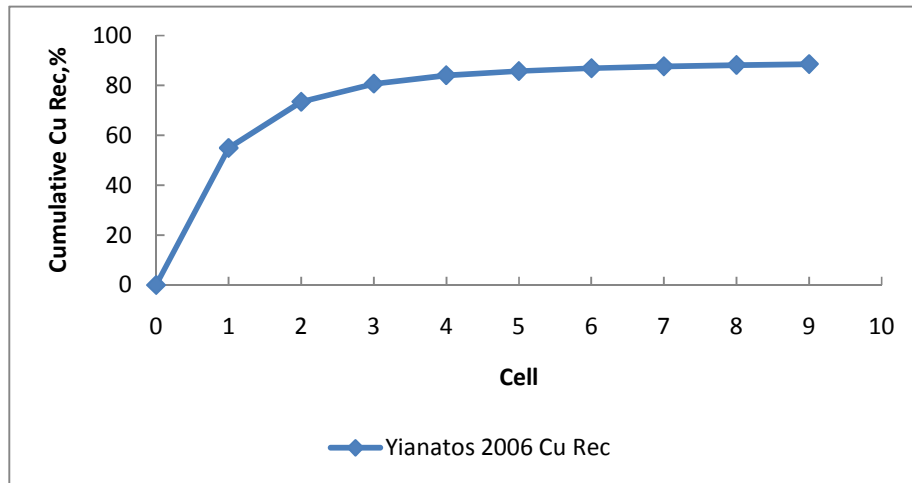


Figure 6-2: Cumulative value Copper recovery as a function of cell number in the rougher flotation section of an operating plant (Yianatos et al., 2006).

The amount of floatable solids in the feeds to subsequent cells progressively decreases along the rougher bank, as more of the floatable particles have already been recovered as concentrate.

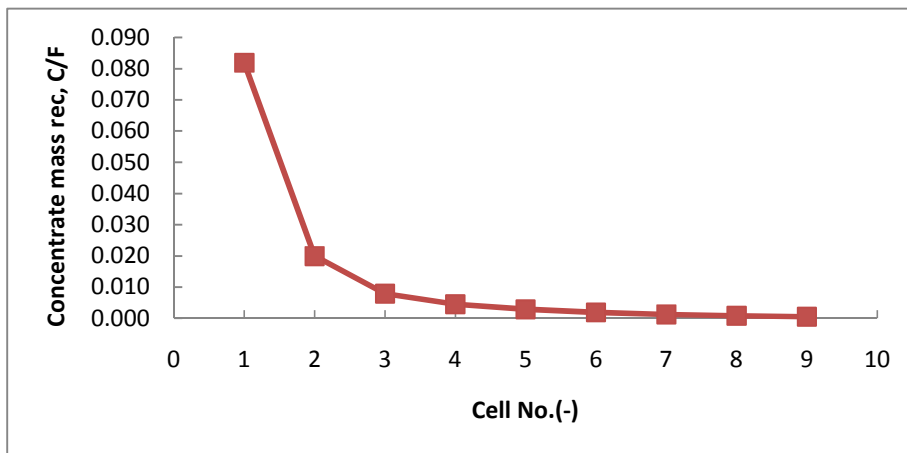


Figure 6-3: Concentrate mass recovery as a function of cell number in the rougher flotation section of simulated fictional plant.

The trends in concentrate mass recovery obtained from the simulation (see Figure 6-3) were comparable with those reported in literature for a similar rougher section flow sheet configuration (see Figure 6-4).

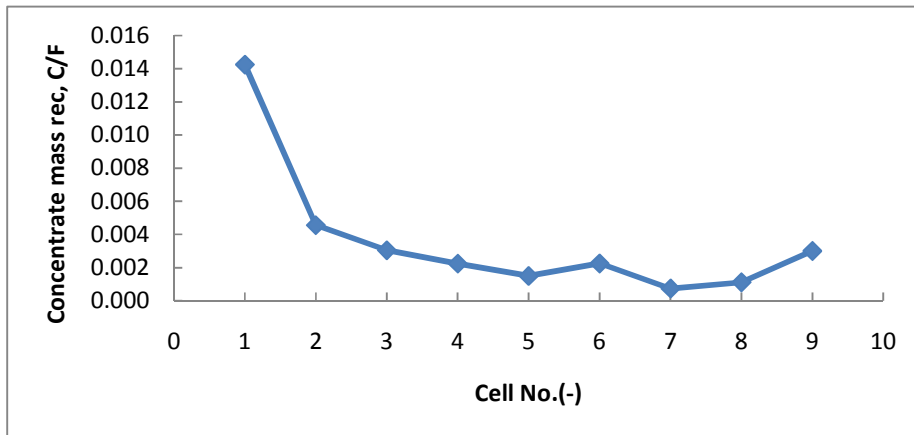


Figure 6-4: Concentrate mass recovery as a function of cell number in the rougher flotation section of an operating plant (Yianatos et al., 2006)

Lower concentrate mass recovery values were obtained for the third up to the ninth rougher cells (see Figure 6-3).

This was due to the assumptions that were made in describing the flotation process in the downstream flotation cell, where the same flotation selectivity was assumed for all the cells in the rougher bank. In typical industrial operation there is a difference in both the operational and hydrodynamic conditions that exist around each rougher flotation cell in the rougher bank (Yianatos et al., 2006).

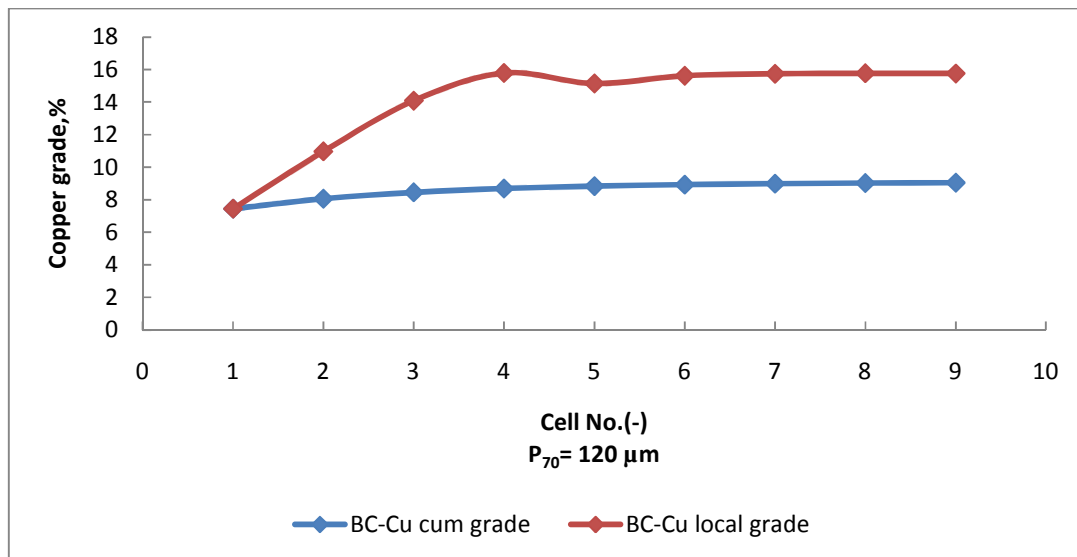


Figure 6-5: Local and cumulative copper grade profile as a function of cell number for a fictional copper plant

The local copper concentrate grade was expected to decrease downwards along the bank reaching a value closer to the feed (Wills and Napier-Munn, 2005); this was not the observed trend for the simulated grade profile (see Figure 6-5). This was due to pyrite and chalcopyrite being assumed to have similar contact angles in the simulations, because of this there was no significant difference in the chalcopyrite to pyrite ratio down the bank of rougher cells. Thus pyrite controlled the copper grade hence there was no drop in copper grade across the bank as is expected from literature. Contact angle values that were reported in literature were those for sulphide bearing mineral particles, no contact angle values were available for pyrite and chalcopyrite separately from the study by Ralston et al. (2007). In actual operations the value of the pyrite contact angle is lower than that of chalcopyrite due to the use of modifiers and depressants as the object of flotation is to recover more of the chalcopyrite.

However, for these simulations this assumption was deemed appropriate, as the cell conditions and the flotation feed ore sulphide contact angles were kept constant throughout all the simulations that were carried out, thus allowing for comparison of the various simulated results for different ore feeds.

6.2. Effect of Feed ore liberation

This section presents the results of the simulations carried out, of a nine rougher cells in series flotation flow sheet in order to investigate the effects of feed ore liberation on value mineral recovery.

6.2.1. Methodology

The feed ore scenarios that were considered for investigating the effects of feed ore liberation using a single flotation cell in Chapter 5 were also used here in this investigation. These consist of two ore groups which represent flotation feed ore at different grind sizes namely Copper 1 ($P_{70}=120\ \mu\text{m}$) and Copper 2 ($P_{70}=180\ \mu\text{m}$). The fundamental property based model was applied to model the flotation process in each individual cell. Six rougher section flow sheet simulations, representing the six different feed ore liberation scenarios (see

Table 5-4, Chapter 5), were run for each ore group. Comparative plots of the following feed ore scenario simulation results were then plotted and analysed for Copper 1 and Copper 2 feed ore groups. These were:

- I. Cumulative value mineral recovery per unit cell,
- II. Overall enrichment ratio across the bank of rougher section,
- III. Concentrate mass recovery per unit cell,
- IV. Local copper grade in concentrate per unit cell,
- V. Cumulative copper grade in concentrate per unit cell,

6.2.2. Copper 1 feed ore ($P_{70} = 120 \mu\text{m}$): Simulation results and discussion

Figure 6-6 below shows the simulation results obtained for different ores. As can be seen, a spread in cumulative recovery values of the various feed ores, which was attributed to the differences in liberation profiles between the ores, was observed.

However, there was only a slight improvement (about 2.5 percentage points) in final cumulative value mineral recovery between the BC and fully liberated ore. The improvement in recovery is even more reduced between the BC ore and Ore 1 or Ore 2 artificial ores as the number of cells increases.

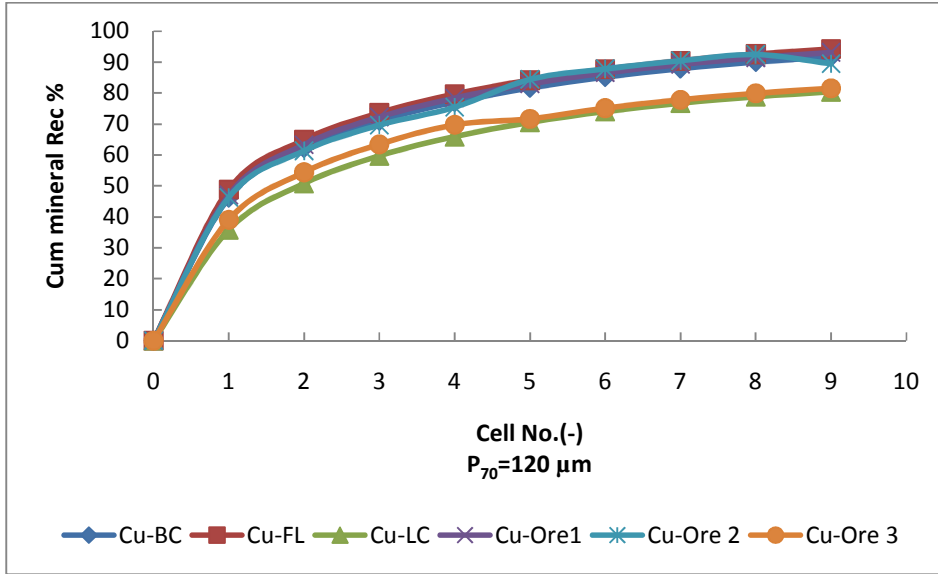


Figure 6-6: Comparison of Cu cumulative recovery per cell in a Rougher bank for different feed ore scenarios.

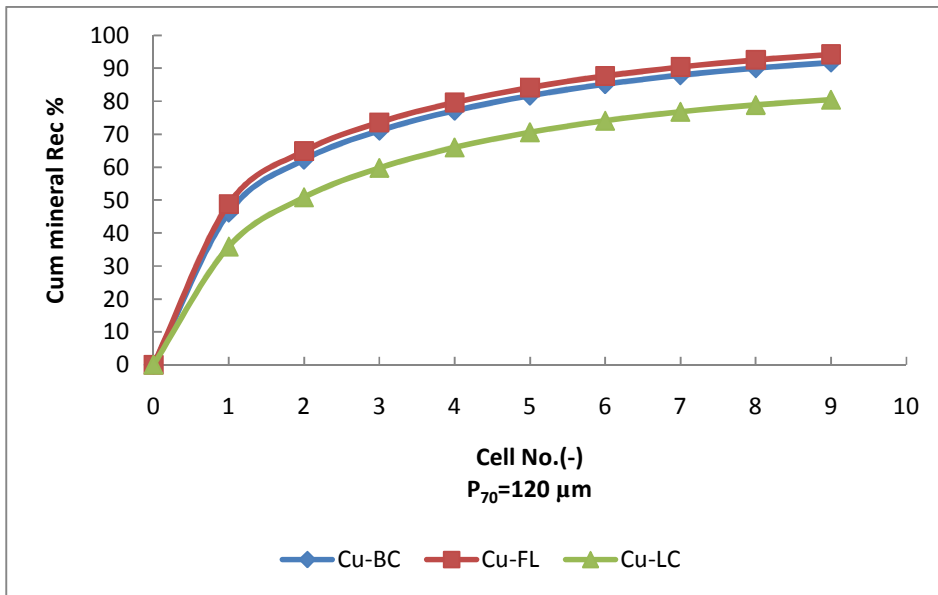


Figure 6-7: Comparison of Cu cumulative recovery per cell in a Rougher bank for the base case and extreme feed ore scenarios.

Figure 6-7 shows the cumulative recovery per unit cell values for the extreme feed ore liberation scenarios. As can be seen, a high cumulative copper recovery of about 94.2% for FL ore, 91.7% for BC and 80.4% for LC feed ore after the ninth rougher cell were obtained. There is an overall 13.8 percentage point spread in recovery between LC and

FL feed. The small difference in recovery between the BC feed ore and FL ore indicates that at a fine feed ore grind size of $P_{70} = 120 \mu\text{m}$ only a slight change in recovery would be expected from improving feed ore liberation through the application of microwave technology.

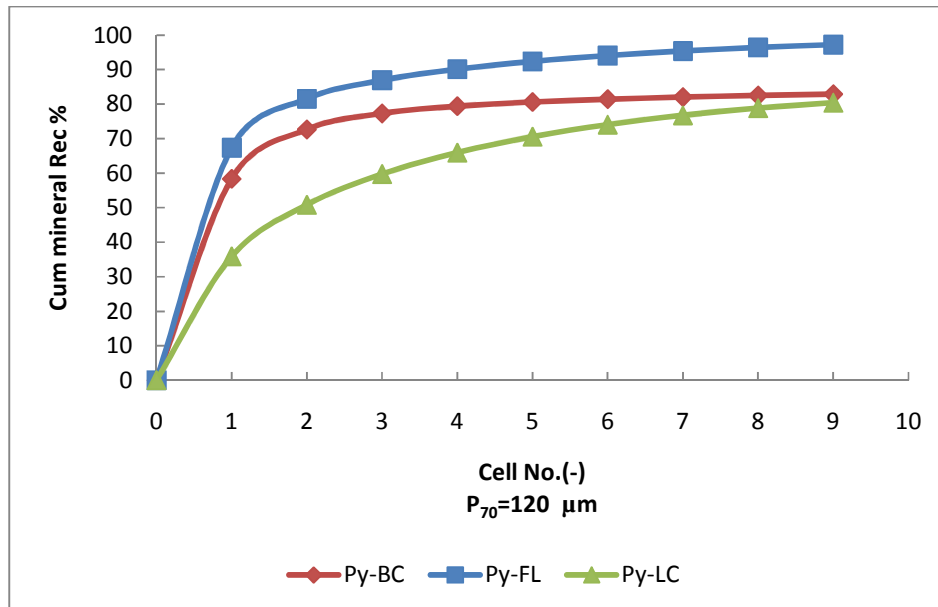


Figure 6-8: Comparison of Pyrite cumulative recovery per cell in a Rougher bank for the base case and extreme feed ore scenarios.

Figure 6-8 shows the pyrite cumulative recoveries obtained for the three cases (FL, BC, and LC). Compared with Copper cumulative recovery, significant improvement in the final cumulative mineral recovery between the BC and fully liberated ore of about 10 percentage points was observed. From analysis of the mineral mode of occurrence graphs for Pyrite in the BC feed at this grind size, Figure 4-2 (see Chapter 4, section 4.2), it can be observed that a greater amount of Pyrite exists in the binary and ternary classes in association with NSG compared with Cpy in the coarse size fractions.

When assuming that all the Pyrite exists as fully liberated particles in the FL feed, a higher improvement in recovery is expected between the BC and FL feed for Py recovery compared with that of Copper recovery after making similar assumptions for Cpy (see Figure 6-8).

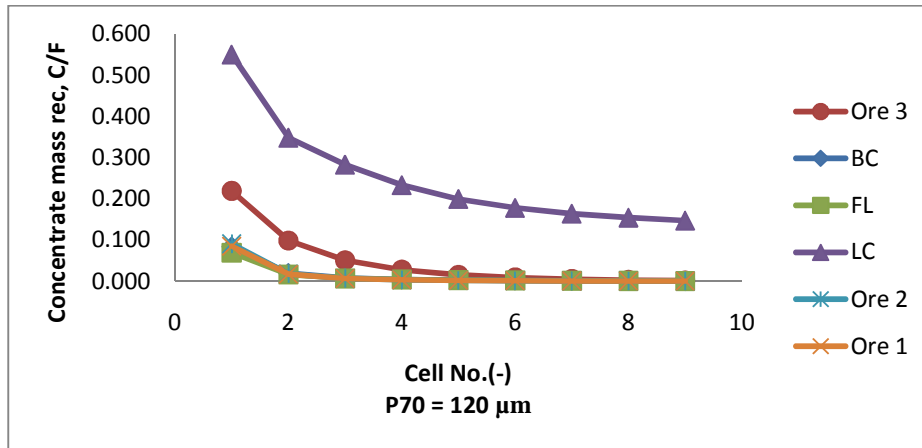


Figure 6-9: Comparison of concentrate mass recovery per unit cell in a Rougher bank for different feed ore scenarios.

It should be noted that in this study an equal froth depth was assumed for all the flotation cells in the rougher bank of cells. Thus, as shown in Figure 6-9, a progressive decrease in concentrate mass flow rates across the rougher bank was observed for all ores as expected. As can be seen, a significant variation of the concentrate mass recovery per unit cell was obtained for the different feed ores. LC feed ore has the highest concentrate mass recovery ratio per unit cell; this is followed by Ore 3 artificial ore feed. LC and Ore 3 are poorly liberated ores. The value mineral in these ores occurs as binary or ternary particles with non floating NSG which constitutes the bulk weight of the feed. Thus the bulk of the recovered concentrate contains value particles, explaining the high concentrate mass pull that was observed for the ores. There is no significant difference in concentrate mass recovery trends obtained for BC, FL, Ore 1 and Ore 2 feed ore across the rougher bank of cells. These feed ores represent relatively well liberated ore, hence there is greater amount of floatable solids in these ores.

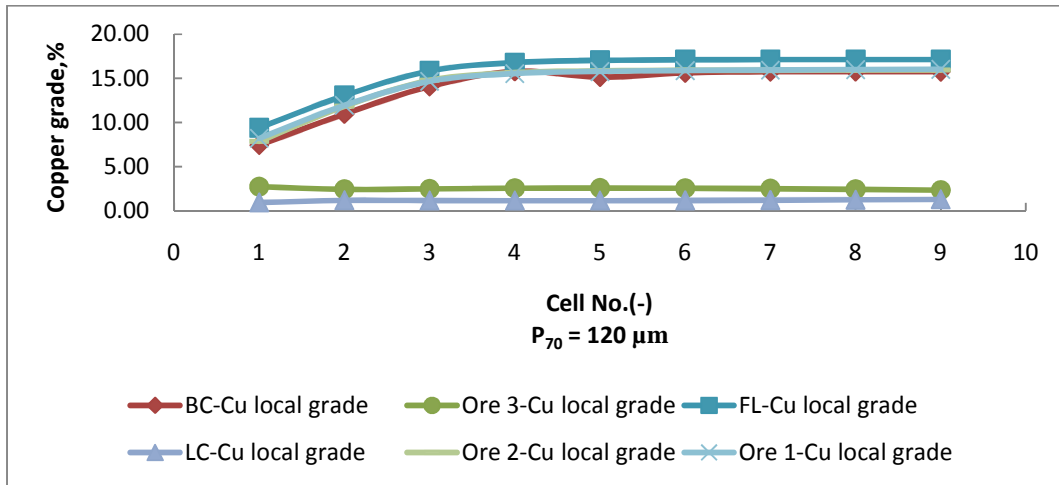


Figure 6-10: Comparison of Cu local grade per unit cell in a Rougher bank for different feed ore scenarios

Figure 6-10 shows the local copper grade obtained for each ore. The local copper concentrate grade was expected to decrease downwards along the bank, reaching a value closer to the feed (Wills and Napier-Munn, 2005). However, due to the assumption of constant flotation conditions for all the cells, all the rougher cells in the bank had high flotation selectivity. Thus, as shown in Figure 6-10, the recovered concentrate mass downwards along the bank had an increasing value mineral grade due to a decreasing concentrate mass pull (see Figure 6-9).

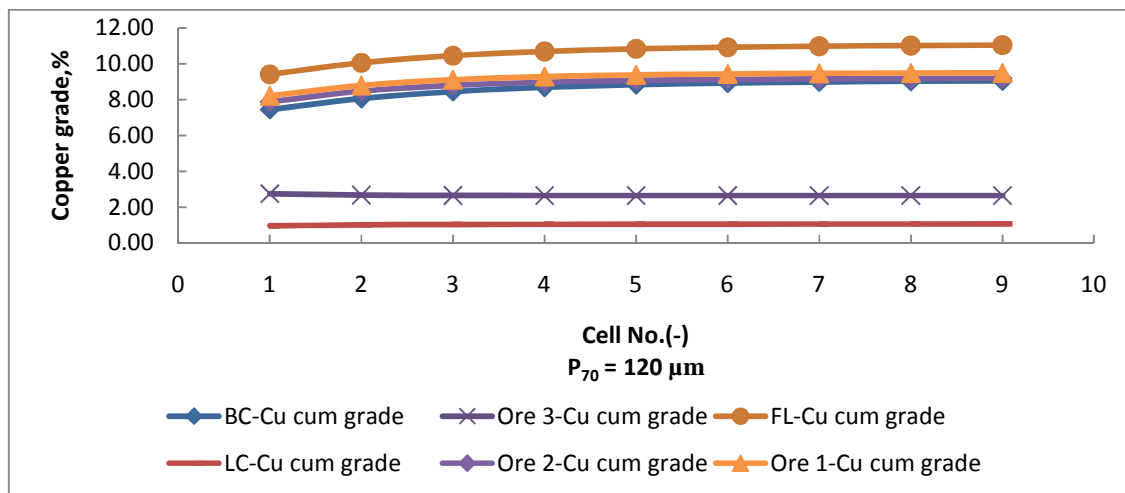


Figure 6-11: Comparison of Cu cumulative grade per unit cell in a Rougher bank for different feed ore scenarios

The cumulative copper grade plots show a low cumulative grade for LC and Ore 3 feed ores (see Figure 6-11). Similar cumulative copper grade values were observed for BC, Ore 1 and Ore 2. FL feed ore has a higher cumulative concentrate copper grade compared to the other feed ores. An increase in cumulative copper grade between the base case feed ore and the FL ore of about 1.9 percentage points was observed (see Figure 6-11). This shows that there is potential to improve final concentrate copper grade through increasing feed ore value mineral liberation.

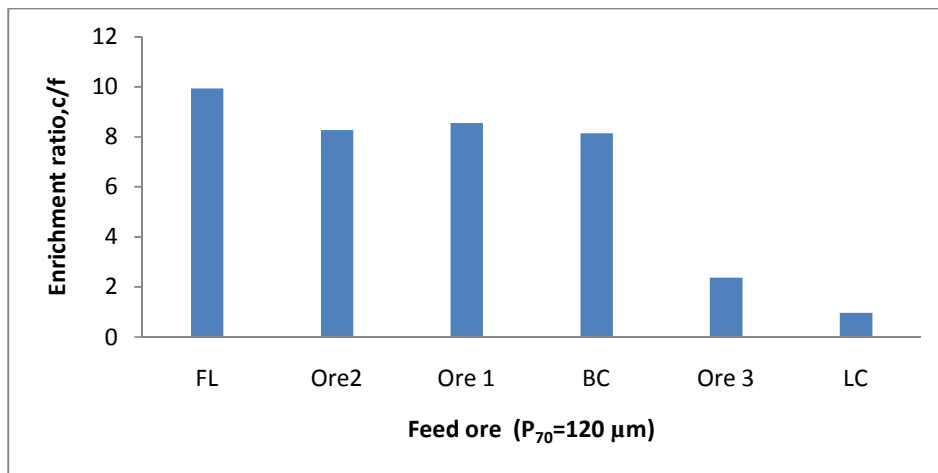


Figure 6-12: Comparison of overall rougher bank value mineral enrichment ratio for different feed ore scenarios.

Figure 6-12 shows the overall rougher bank value mineral enrichment ratio obtained for different feed ore scenarios. As can be seen, higher enrichment ratios were observed for the FL, Ore 1 and Ore 2 compared with the base case feed ore. Thus improved liberation has the effect of improving the overall rougher bank enrichment ratio. The poorly liberated ores gave very low enrichment ratio values this was due to low copper grade of the final concentrate for the two ores.

6.2.3. Copper 2 feed ore (P₇₀ = 180 μm): Results and discussion

Trends in value mineral cumulative recovery observed for various feed ores for P₇₀ grind size of 180 μm were similar to those reported in section 6.2.1 for the P₇₀ grind size of 120 μm (see Figure 6-6 and Figure 6-13).

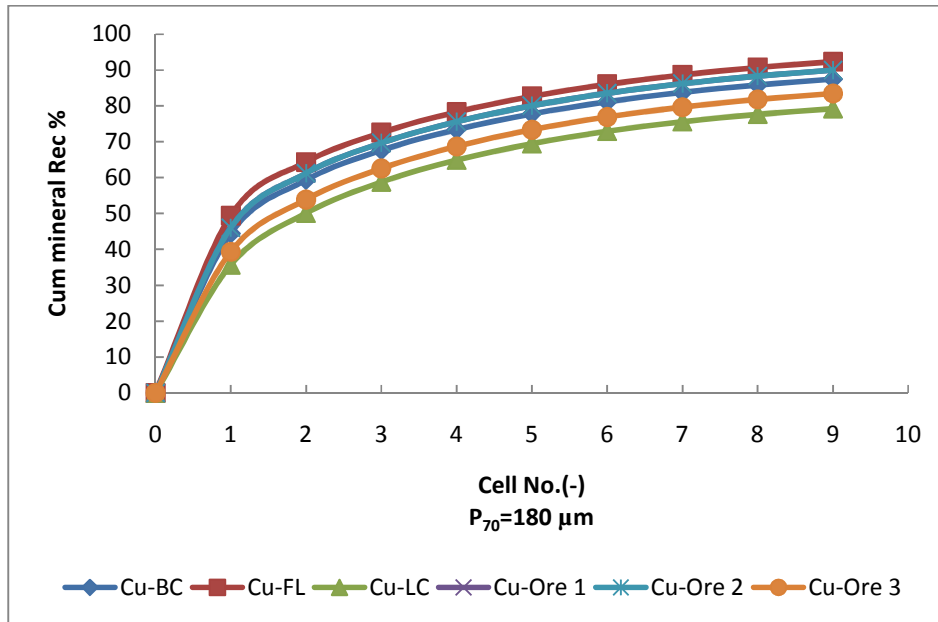


Figure 6-13: Comparison of Cu cumulative recovery per cell in a Rougher bank for different feed ore scenarios.

The cumulative recovery per unit cell values obtained for the base case and the extreme feed ore scenarios are shown in Figure 6-14. It can be seen that cumulative copper recovery of about 92.3% for FL ore ,87.5% for BC and 79.2% for LC feed ore after the ninth rougher cell were obtained. A 13.1 percentage point spread in Cu cumulative recovery after the ninth rougher cell was observed between Copper 2, LC and FL artificial feed ores, this spread in cumulative recovery is less than that which was obtained for Copper 1 LC and FL feeds. As the grind size becomes coarser, the spread in cumulative recovery becomes larger.

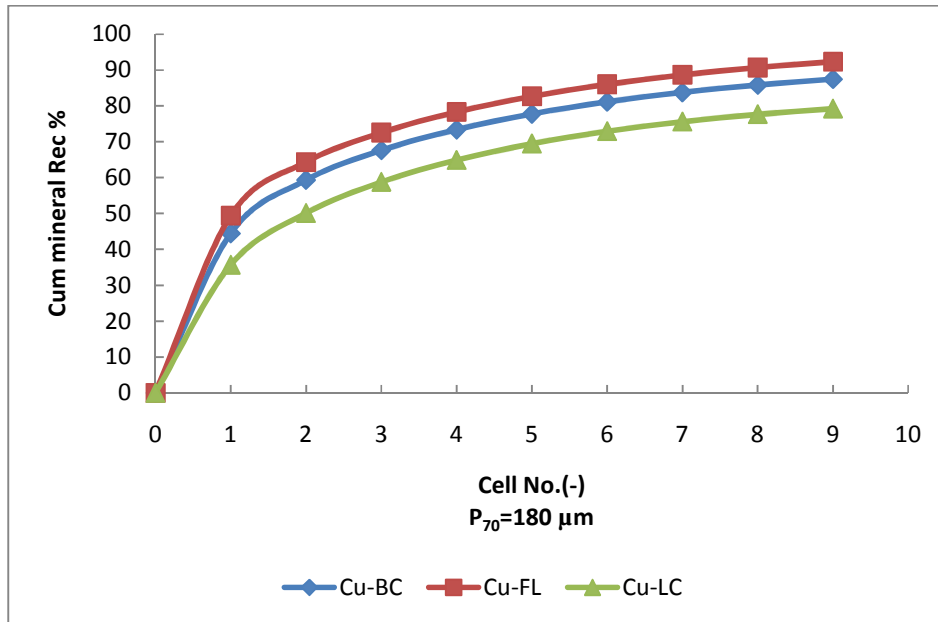


Figure 6-14: Comparison of Cu cumulative recovery per cell in a rougher bank for the base case and extreme feed ore scenarios

There was a noticeable improvement in final Cu cumulative value mineral recovery between the BC and FL ore of about 4.8 percentage points (see Figure 6-14). This improvement in Cu cumulative recovery was greater than the 2.5 percentage point improvement that was observed for a P_{70} grind size of $120\ \mu\text{m}$ (see Figure 6-7). As shown earlier in Chapter 5, section 5.4 there is a greater improvement in value mineral recovery at coarser sizes as feed ore liberation increases. Copper 2 artificial BC and FL feed ores at a P_{70} grind size of $180\ \mu\text{m}$ are coarser than Copper 1 artificial BC and FL feed ores. This explains the greater improvement in cumulative Cu recovery between the BC and FL Copper 2 feed ores compared to that between similar Copper 1 artificial feed ores.

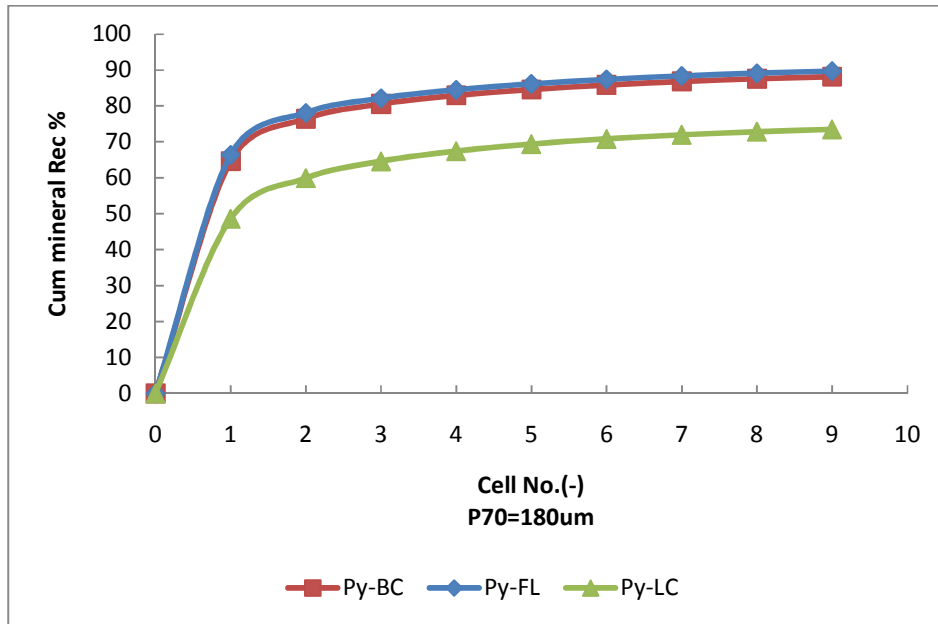


Figure 6-15: Comparison of Pyrite cumulative recovery per cell in a Rougher bank for the base case and extreme feed ore scenarios.

No significant difference in Pyrite cumulative recovery between the base case and the fully liberated case was observed, (see Figure 6-16). This might be due to the Pyrite mode of occurrence in the ore (see Figure 4-6, Chapter 4 Sections 4.2). Pyrite in the base case feed ore was observed to appear primarily as fully liberated particles or in association with Chalcopyrite. There was no room for improved liberation. Thus the cumulative recovery of BC and FL ores were similar.

The concentrate mass recovery obtained for LC feed ore with a P70 grind size of 180 μm was significantly less than that obtained at a P₇₀ grind size of 120 μm (see Figure 6-16 and Figure 6-9). At coarser feed ore grind sizes there is a particle size limit to flotation recovery. This is due to a decreasing stability and attachment efficiency at coarse sizes as was observed in Chapter 5 Section 5.2 (see

Figure 5-16 and Figure 5-18). Similar trends in concentrate mass recovery were observed for the other ores as seen at a P₇₀ grind size of 120 μm (see Figure 6-9).

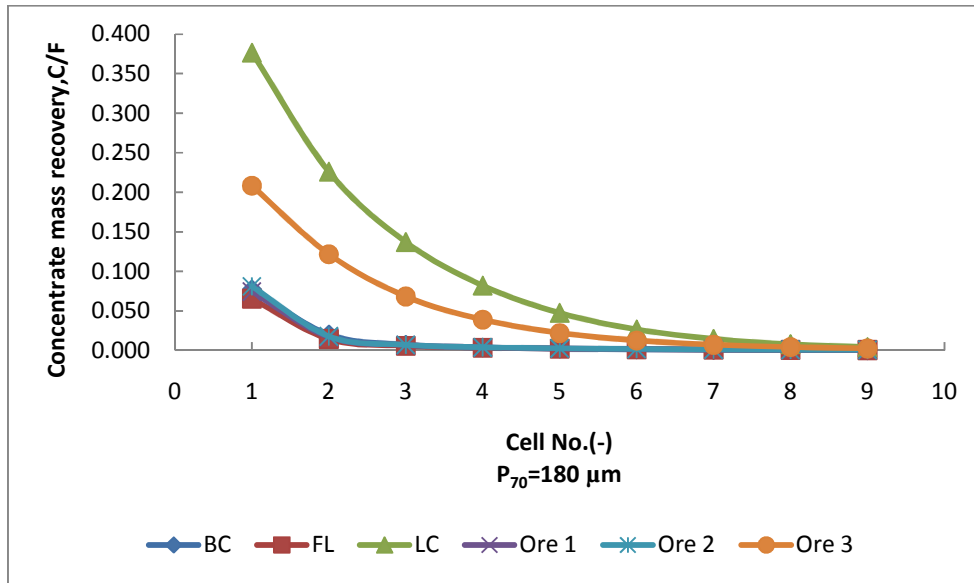


Figure 6-16: Comparison of concentrate mass recovery per unit cell in a Rougher bank for different feed ore scenarios

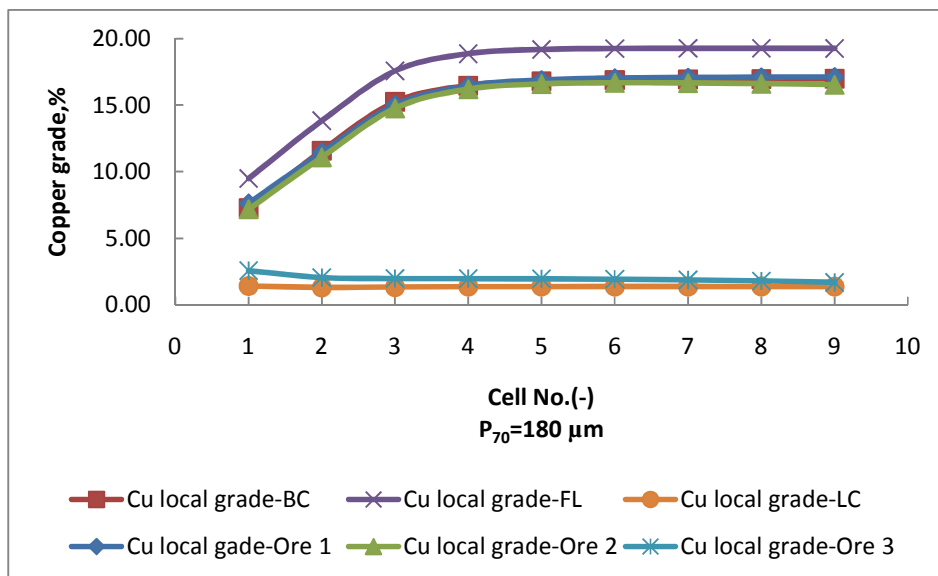


Figure 6-17: Comparison of Cu local grade per unit cell in a Rougher bank for different feed ore scenarios

Slightly higher local copper concentrate grades were observed for the FL, Ore 1, Ore 2 and BC feed ores at a P_{70} grind size of $180 \mu\text{m}$ compared with that observed at a P_{70} grind size of $120 \mu\text{m}$ (see Figure 6-11 and Figure 6-18).

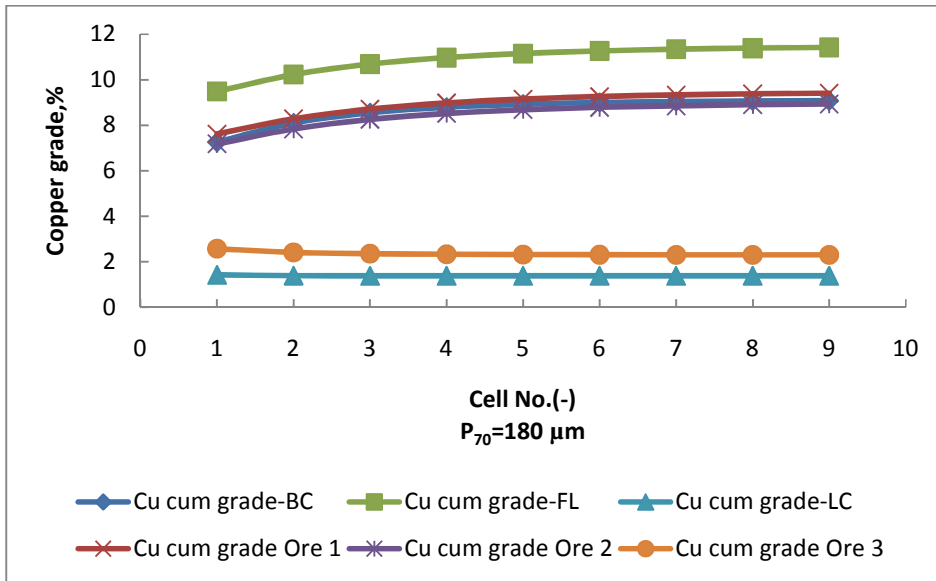


Figure 6-18 : Comparison of Cu Cumulative grade per unit cell in a Rougher bank for different feed ore scenarios (P₇₀ = 180 μm).

The trends in cumulative copper grade per unit cell were similar to those that were observed for feed ore at P₇₀ grind size of 120 μm (see Figure 6-19). An improvement in cumulative copper grade between the base case feed ore and the FL ore of about 2.35 percentage points was observed at a P₇₀ grind size of 180 μm.

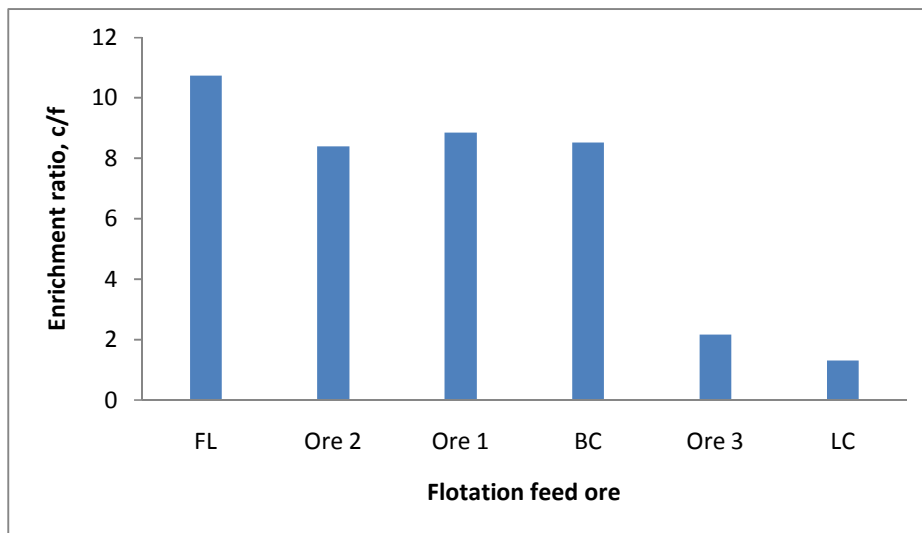


Figure 6-19: Comparison of overall rougher bank value mineral enrichment ratio for different feed ore scenarios.

The trends in overall enrichment ratio across the rougher bank flotation section for the various feed ores that were considered were similar to those observed for Copper 1 feed ore group at a P₇₀ grind size of 120 µm (see Figure 6-20).

6.3. Effect of Particle size distribution of the feed

Feed ore grind size sensitivity analysis was carried out in order to investigate further the effects of grind size of the feed on value mineral recovery for a typical operating plant rougher section. A brief outline of the methodology that was used will be described below followed by a presentation of the results and their discussion.

6.3.1. Methodology

The same feed ore grind sizes described earlier in Chapter 5, Table 5-9 were used in the investigations. For each grind size that was considered, three operating rougher concentrator section plant simulations were carried out, representing the three feed ore liberation scenarios that were considered to represent the base case and the two extreme liberation scenario cases. The LC and FL feeds represent the bounding cases. A base case scenario was included as a reference point representing the current flotation practice feed ore liberation scenario. The same flotation cell operating and hydrodynamic conditions as used in the previous simulations (see Table 5-1) were used in the investigations.

The overall rougher bank flotation section value mineral recovery, concentrate mass recovery and enrichment ratio values were analysed. This was followed by a cell by cell analysis of;

- I. Cumulative value mineral recovery per unit cell,
- II. Local copper grade in concentrate per unit cell,
- III. Concentrate mass recovery per unit cell,
- IV. Unit cell enrichment ratio per unit cell,
- V. Cumulative copper grade in concentrate per unit cell,

The results and their discussion are presented in the next section.

6.3.2. Operating plant Grind size sensitivity analysis results

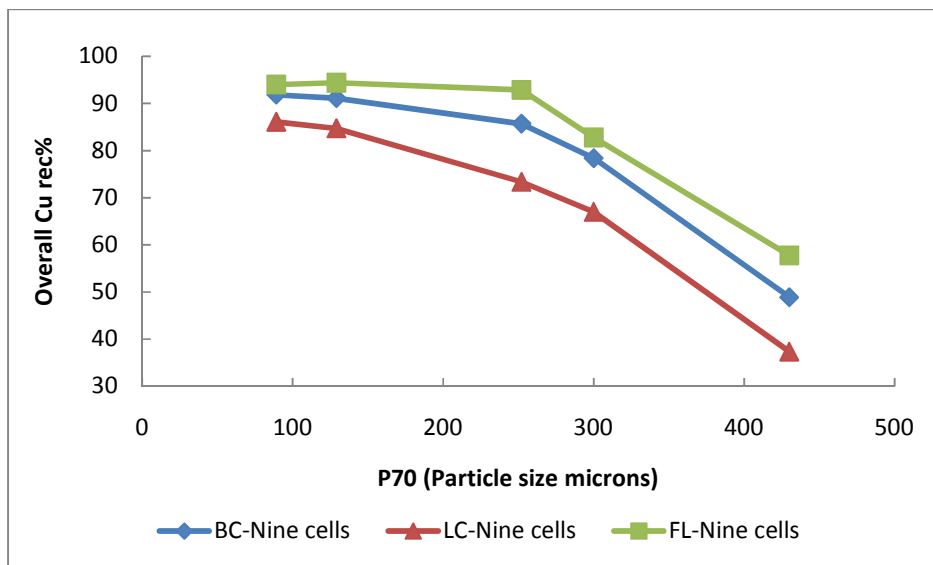


Figure 6-20: Overall a nine cell in series rougher bank recovery against particle size for feed ore grind size.

Figure 6-20 shows a decreasing trend in overall recovery for all feed ores with increasing P_{70} particle grind size. It is well known that flotation recovery decreases at very coarse sizes due to an increase in detachment forces (Gontijo et al., 2007). High contact angle values are required to float very coarse particles; fully liberated ore particles have high contact angle values hence their recovery is better than that of BC and LC feed ore. An increase in improvement in recovery between the base case and fully liberated ore feed was observed at P_{70} grind sizes greater than 250 μm .

Below a $P_{70}=120 \mu\text{m}$ grind size an improvement in overall recovery between the BC and FL liberated feed ore of around 3 percentage points is observed compared to an improvement in recovery of about 7 percentage points above the 250 μm grind size (see Figure 6-20). This shows that enhancement of feed ore value mineral liberation has more effect on value mineral recovery for coarser ground feeds.

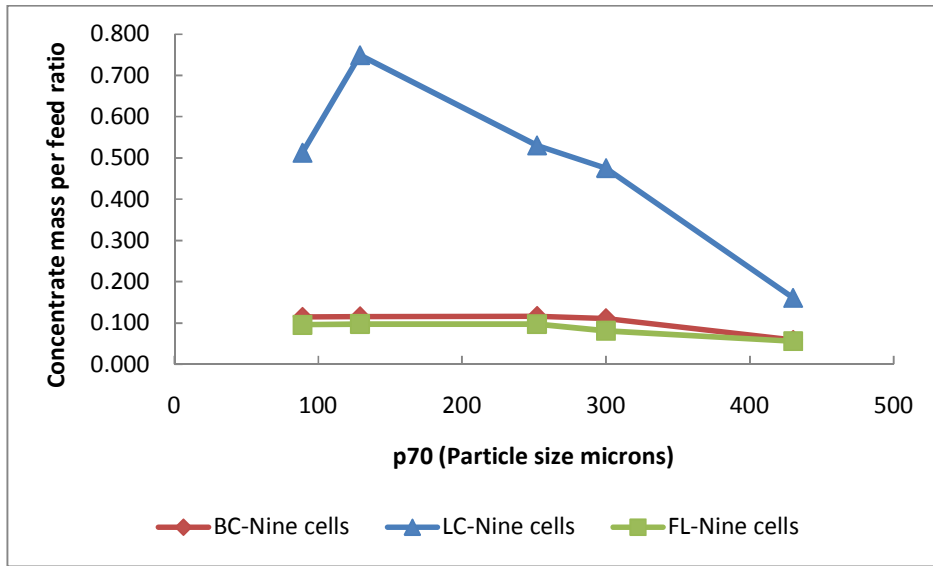


Figure 6-21: Concentrate mass recovery for a nine cell in series Rougher bank plotted against feed ore into the rougher section with varying feed grind size.

Analysis of concentrate mass recovery indicates a low concentrate mass recovery for fully liberated and base case feed ores (see Figure 6-21). The concentrate mass recovery for LC feed ore shows an increasing trend in the fine particle grind size range between 89 μm and 129 μm and decreases with particle size over a P_{70} grind size of 129 μm . Due to the composite nature of LC feed, a higher concentrate mass flow rate is observed at fine grind sizes which decrease with increasing grind size due to poor recovery of very coarse, locked particles.

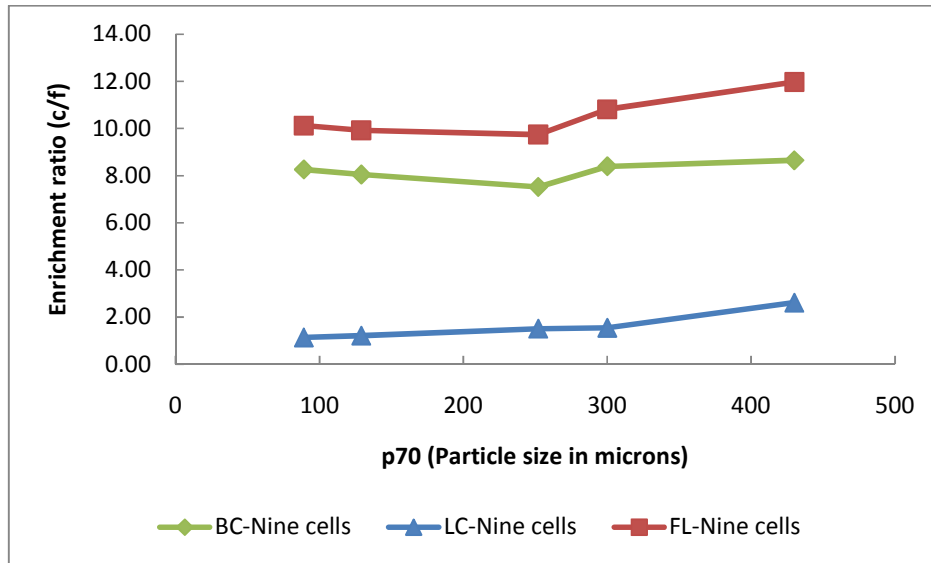


Figure 6-22: Enrichment ratio for a nine cell in series rougher bank plotted against feed ore into the rougher section with varying size distributions.

Figure 6-22 shows an increase in enrichment ratio above the 250 μm P_{70} grind sizes for all feeds. The increase is more pronounced for fully liberated ore. However, there are limits to coarse particle recovery at these coarse particle sizes especially where the particles are poorly liberated. This explains why the increase in BC and LC feed enrichment ratio is not as pronounced as that of FL feed above the 250 μm P_{70} grind sizes.

Analysis of cumulative copper value mineral recovery per unit cell for a feed ore grind size P_{70} of 89 μm showed a 2.1 percentage point improvement in cumulative copper recovery between the BC and fully liberated feed (see Figure 6-23). This improvement was observed after nine flotation cells. This supports the observation made earlier in Chapter 5 Section 5.4 that at fine grind sizes differences in value mineral liberation have no significant effect on value mineral particle flotation recovery (see Figure 5-20).

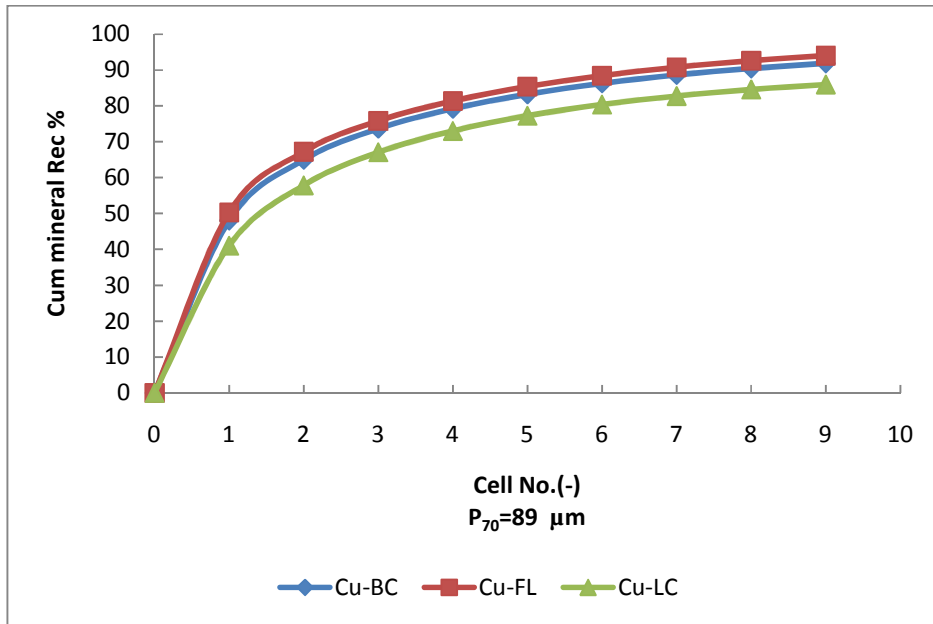


Figure 6-23: Cumulative Cu value mineral recovery as a function of cell number for a rougher bank processing BC, FL and LC feed ores.

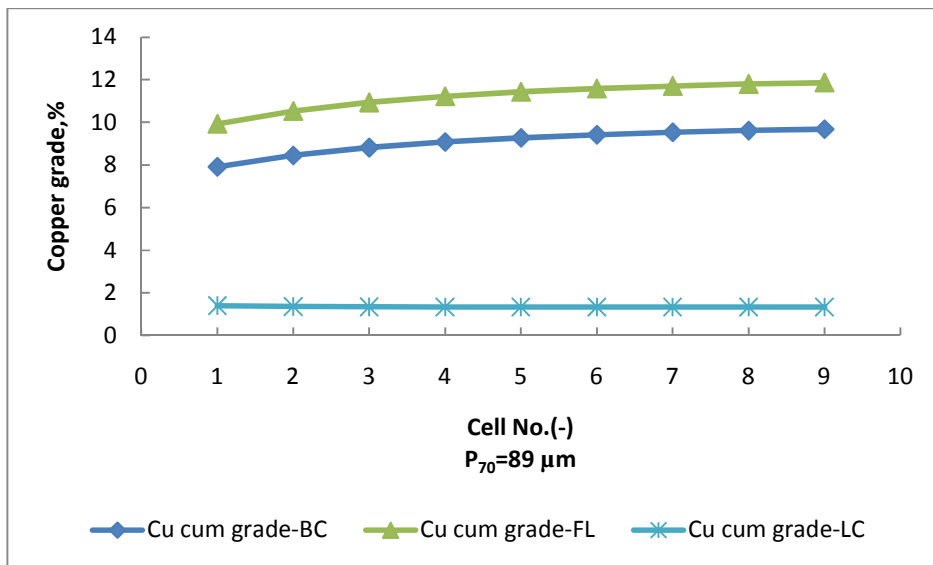


Figure 6-24: Cumulative copper grade profiles as a function of cell for a rougher bank processing BC, FL and LC feed ores.

A difference in cumulative copper grade between the base case and fully liberated ore was observed to be around 2 percentage points at grind size of $P_{70} = 89\mu\text{m}$ (see Figure 6-24).

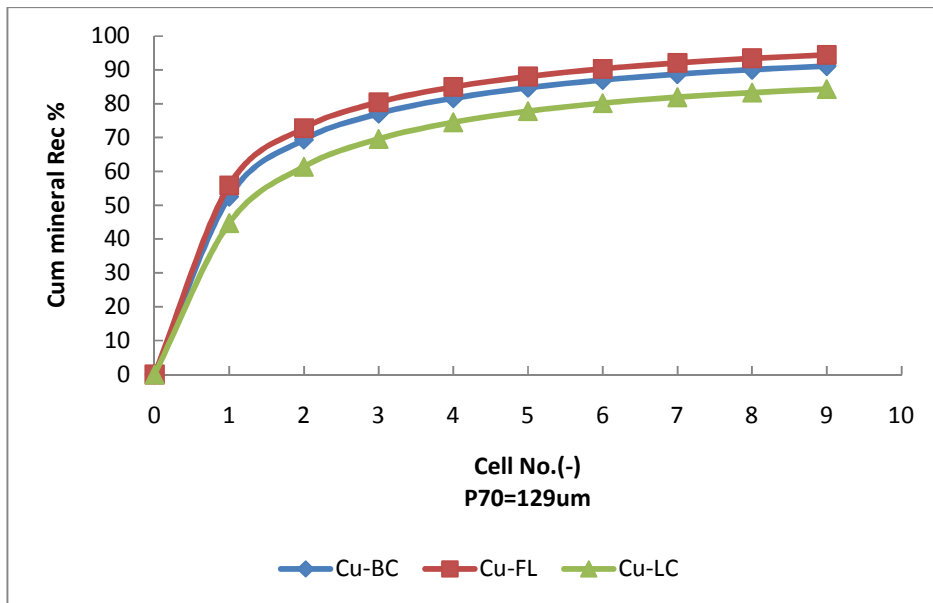


Figure 6-25: Cumulative Cu value mineral recovery as a function of cell number for a rougher bank processing BC, FL and LC feed ores.

Analysis of cumulative copper value mineral recovery per unit cell at a feed ore grind size of $P_{70}=129\mu\text{m}$ showed an improvement in cumulative copper recovery between the BC and fully liberated feed of 3.3 percentage points (see Figure 6-25).

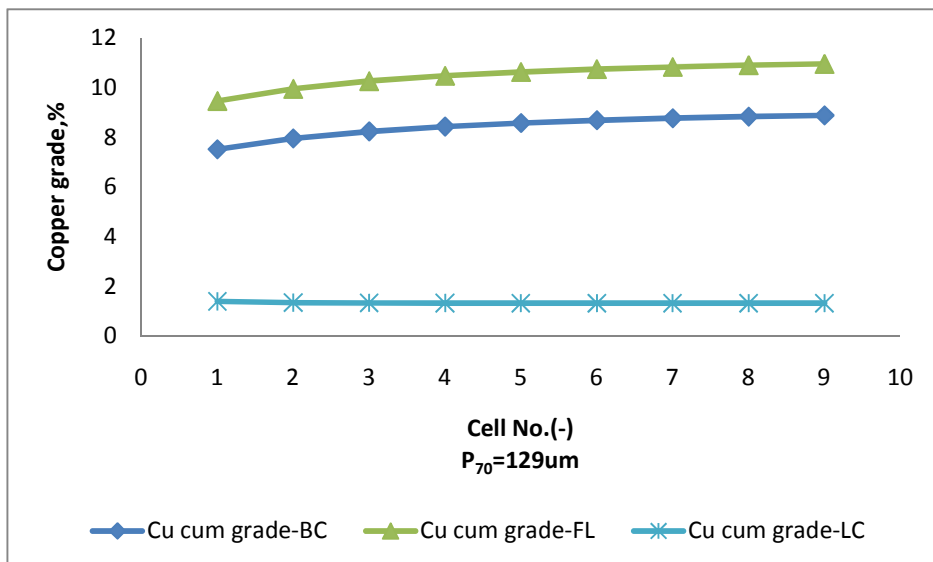


Figure 6-26: Cumulative copper grade profiles as a function of cell number for a rougher bank processing BC, FL and LC feed ores.

The difference in cumulative copper grade between the base case and fully liberated ore that was observed at a P_{70} grind size of 89 μm was around 2 percentage points (see Figure 6-26). There was a progressive decrease in Copper grade as the particle grind size increased hence the final cumulative grade for FL ore at a P_{70} grind size of 129 μm was lower than that at P_{70} grind size of 89 μm .

The results indicate a high value mineral cumulative recovery at a P_{70} grind sizes of 89 to 129 μm for the base case feed. However there are operational problems associated with fine grinding of flotation feeds such as slimes build up which would result in lower value mineral recoveries than those predicted from the simulation (Tabosa and Rubio, 2010). Grinding feed ore at P_{70} grind sizes of 89 μm increases the probability of producing progeny feed particles with sizes below 10 μm . These ultra fine mineral particles are usually called slimes (Sondir et al., 2002). Slimes worsen the selectivity of collector reaction with the desired value mineral as the slime may coat the mineral surface (Sondir et al., 2002; Tabosa and Rubio, 2010). This in turn results in a decrease in the contact angle of the value mineral, thus reducing the value mineral recovery. The effect of slimes was not considered in this study. It is therefore possible that the recovery values predicted from the simulations could be lower in practice.

The cumulative copper value mineral recovery per unit cell obtained at a feed ore grind size P_{70} of 252 μm showed a significant improvement in cumulative copper recovery between the BC and fully liberated ore (7.2 percentage points)(see Figure 6-27). This further supports the observation that at coarser particle sizes, a change in feed ore liberation has a significant effect on flotation recovery.

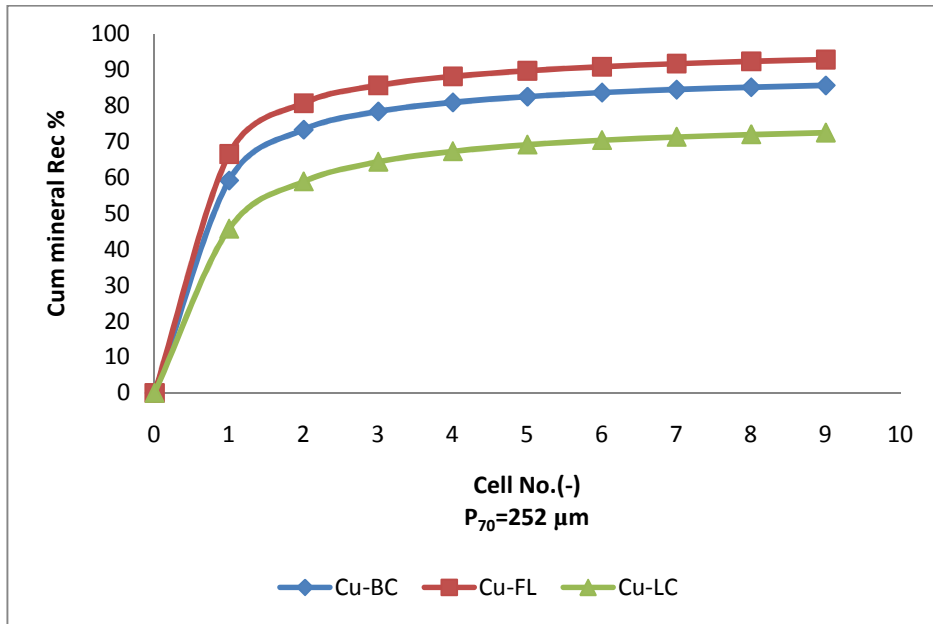


Figure 6-27: Cumulative Cu value mineral recovery as a function of cell number in the rougher section of a fictional simulated nine cell in series flotation plant processing BC, FL and LC feed ore with a P_{70} grind size of 252 μ m.

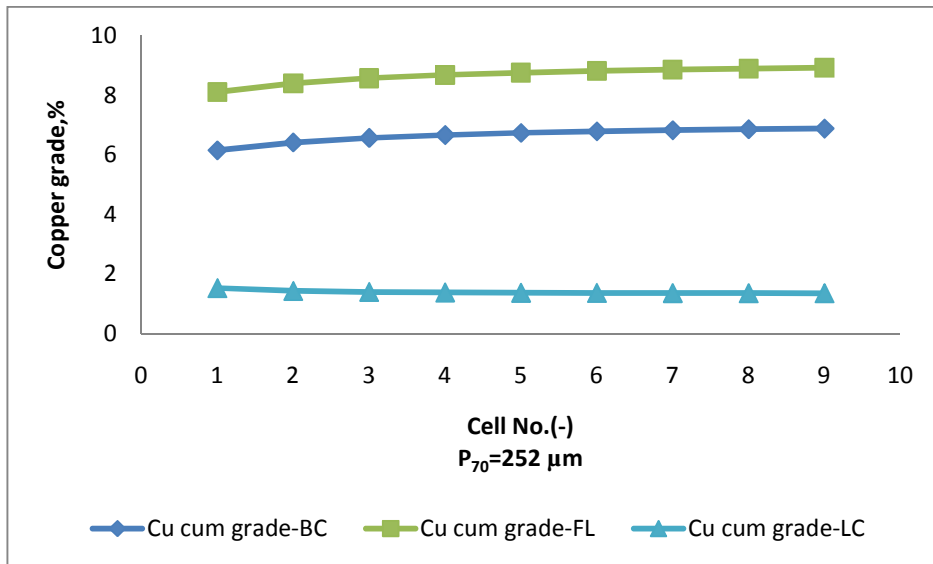


Figure 6-28: Cumulative copper grade profiles as a function of cell for a rougher bank processing BC, FL and LC feed ores.

Figure 6-28 shows a difference in cumulative copper grade of 2 percentage points between the base case and the fully liberated case at grind size of $P_{70} = 252 \mu$ m.

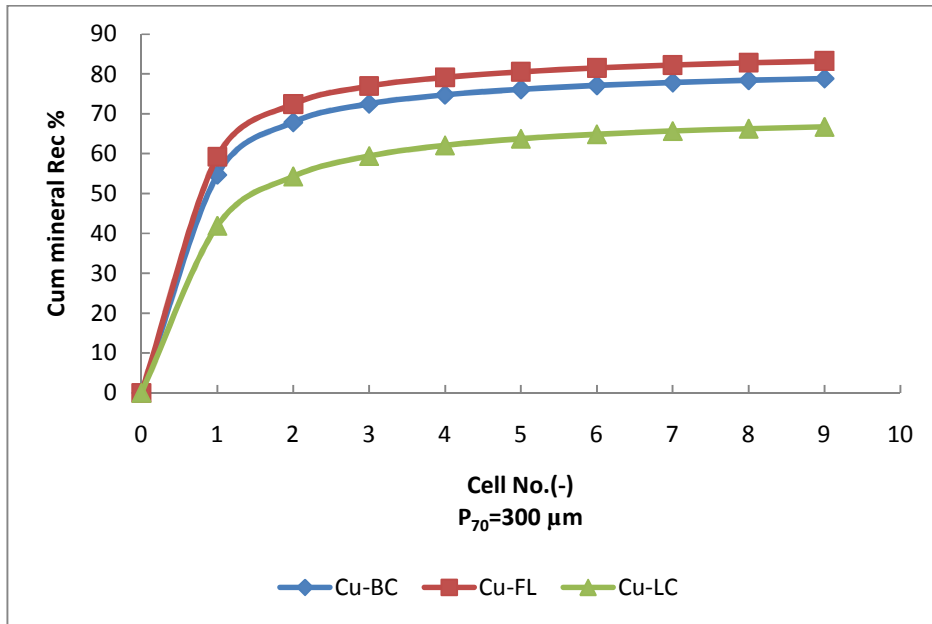


Figure 6-29: Cumulative Cu value mineral recovery as a function of cell number for a rougher bank processing BC, FL and LC feed ores.

At a feed ore grind size of $P_{70} = 300 \mu\text{m}$, the difference in value mineral recovery between the BC and fully liberated ore was less than that which was observed at a P_{70} grind size of $252 \mu\text{m}$ (see Figure 6-29). The difference was in the range of about 4.5 percentage points. A decrease in overall cumulative recovery is observed at this grind size compared with that at a P_{70} grind size of $252 \mu\text{m}$. As explained earlier overall cumulative recovery decreases with increasing particle sizes. A grind size of $252 \mu\text{m}$ is the optimum grind size where overall value mineral flotation recovery difference between the BC and FL feed is at its highest before it progressively decreases with increasing particle size.

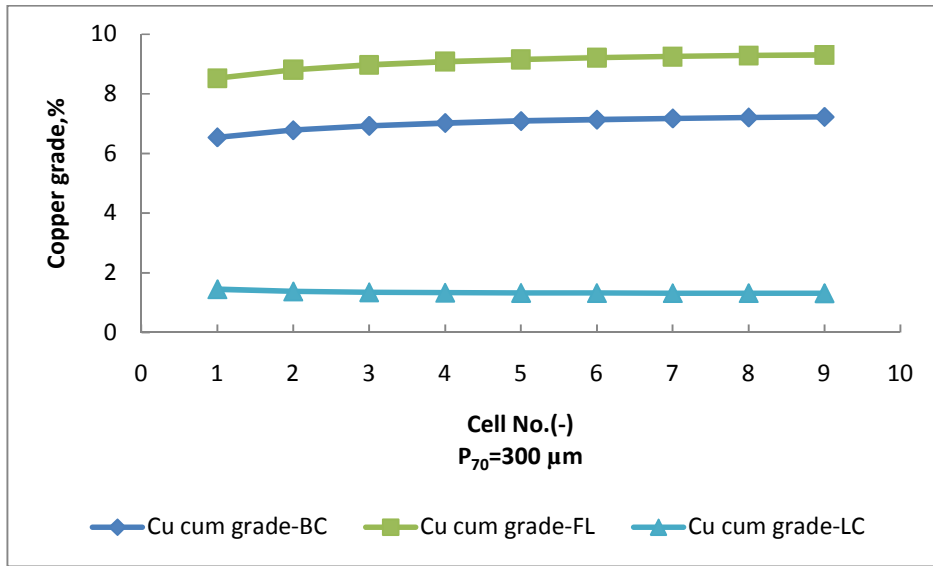


Figure 6-30: Cumulative copper grade profiles as a function of cell number for a rougher bank processing BC, FL and LC feed ore.

Figure 6-30 shows a difference in cumulative recovery of 2 percentage points for a feed ore grind size of P_{70} of 300 μm between the base case ore and fully liberated ore.

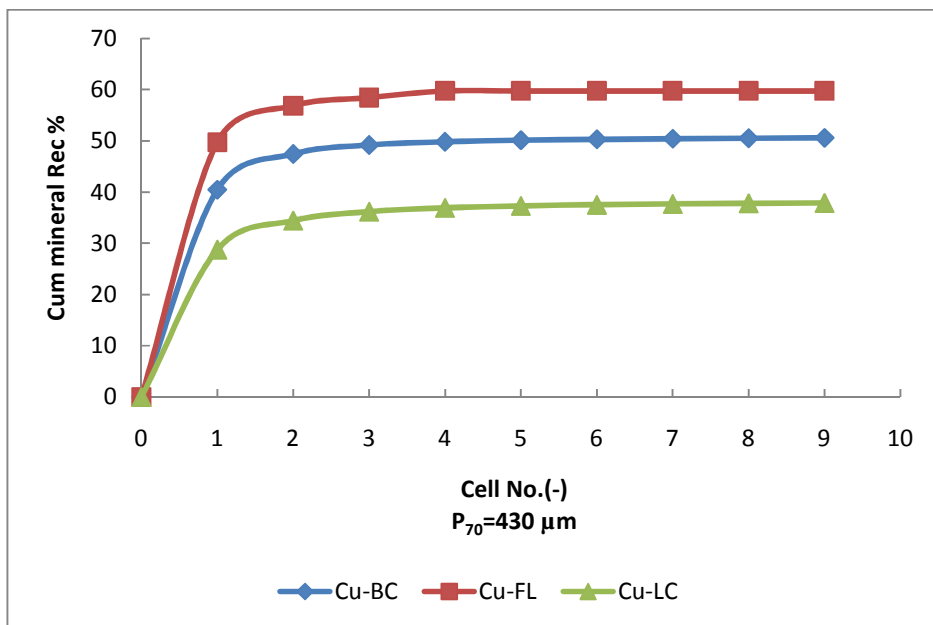


Figure 6-31: Cumulative Cu value mineral recovery as a function of cell number for a rougher bank processing BC, FL and LC feed ores.

At a coarser P_{70} grind size of $430\ \mu\text{m}$ an improvement in overall cumulative value mineral recovery of 9.4 percentage points between the BC and the fully liberated feed is observed (see Figure 6-31). Although the particle size effects of flotation recovery lowers the cumulative recovery of the all the feed ores, the high contact angle of the fully liberated ore allows for the coarse size particles to be recovered, hence a greater difference in overall cumulative recovery is observed at this grind size between the BC, FL and LC feed. Flotation circuits do not effectively recover very coarse particles (Mull and Sarich, 2002). The optimum particle size for flotation ranges between $38\ \mu\text{m}$ and $150\ \mu\text{m}$ (Sondir et al., 2002).

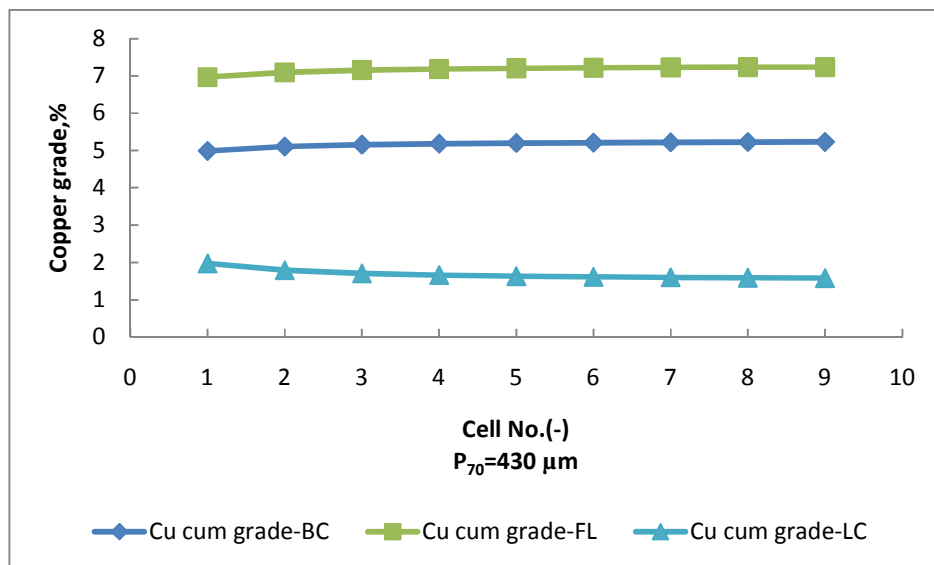


Figure 6-32: Local and cumulative copper grade profiles as a function of cell number for a rougher bank processing BC, FL and LC feed ores.

A cumulative grade difference of 2 percentage points at grind size of $P_{70} = 430\ \mu\text{m}$ was observed between the base case and fully liberated ores (see Figure 6-32). Analysis of the cumulative copper grade profile plots across the nine flotation cells for all feed grind sizes showed a 2 percentage point improvement in grade for all grind sizes. As explained earlier all the feed had similar liberation spectrum per size class, hence the same improvement in grade was observed between the BC and FL feed at different grind sizes.

6.4. Conclusion

A continuous plant rougher flotation flow sheet has been successfully developed that utilises the property based model for predicting flotation recovery. Results from applying the model in investigating the effects of feed ore liberation variation on flotation recovery indicate a greater variation in flotation recovery and final concentrate grade at coarse grind sizes of above 250 μm . The results presented in this Chapter have shown that a feed ore grind size of 252 μm gives the best value mineral recovery results for FL feed compared to the BC feed. At this grind size the overall difference in value mineral recovery between the BC and FL feed is at its highest before it progressively decreases with increasing particle size. This appears to be the best grind size result for exploiting improvements in flotation feed liberation due to microwave assisted comminution as there is a higher cumulative recovery difference between the BC and FL ore at this grind size.

CHAPTER SEVEN

7. CONCLUSIONS AND FUTURE WORK

Future commercialisation of microwave technology for mineral processing will depend on the determination and quantification of all the downstream processing benefits associated with the technology. Due to the limitations associated with such an exercise such as the costs of carrying out investigations on an operating plant, flow sheet modelling presents the best option for preliminary determination of the optimal value proposition for microwave assisted processing of ores.

In view of this, a modelling framework for investigating the downstream flotation processing effects of microwave treatment has been developed. The modelling framework is made up of a simulation flow sheet modelling tool in HSC Chemistry Software utilising MLA data and a fundamental property based flotation model that accounts for feed ore liberation in modelling flotation cell operation. The fundamental property model has been successfully integrated into the simulation software and can be used for true particle modelling based on the results from the continuous single flotation cell simulations (see Chapter 5).

A downstream flotation flow sheet simulation utilising the developed tool and MLA data from a previous study was then carried out in order to investigate the downstream processing effects of changes in feed ore liberation as expected from microwave treatment. Artificial feed with varying degrees of liberation were created and used to simulate the changes in feed ore liberation. From the single cell flotation results it has been found that below a certain size (120 μm) changes in feed ore liberation have no effect on value mineral recovery. Significant differences in value mineral recovery were only observed at sizes above 120 μm . From this result, it can be concluded that increasing recovery of value minerals due to improved liberation from applying microwave technology has size limits and is dependent on the feed ore grind size.

Feed ore grind size sensitivity analysis was then carried on the same single cell flow sheet utilising different ores with liberation properties and grind sizes. The results indicated that maximum benefits from the application of microwave technology would

best be obtained by utilising coarse grinding at sizes between $P_{70} = 200 \mu\text{m}$ and $P_{70} = 300 \mu\text{m}$ for the ores considered in this study. Coarse grinding appears to be the best way to exploit improved liberation in downstream processing of ores.

Investigations similar to those carried out on a single cell flotation flow sheet were then carried out on a continuous plant rougher flotation flow sheet. The results indicate no significant differences in final rougher bank overall cumulative recovery and grade at fine grind sizes for different flotation feeds. Feed ore grind size sensitivity analysis showed a greater difference in recovery at coarse grind sizes of above $P_{70} = 250 \mu\text{m}$ between the BC and FL feed. From the results it can be concluded that microwave technology application will offer greater benefits in downstream processing of coarse ground ores.

This study has produced a modelling framework for investigating the downstream processing effects of microwave treated flotation feed ore. Through the use of this modelling framework, it is now possible to investigate how differing degrees of mineral liberation, such as might be achieved through microwave treatment, affect the grade and recovery achieved in flotation. This is a significant contribution in the mineral processing field, particularly in the study of application of microwave assisted comminution. Most of the investigations that have been reported in literature on the study of the effects of downstream processing on microwave treated ore have been based on batch flotation results of microwave treated flotation feed. This study presents one of the few attempts at trying to determine the value proposition of microwave treated ore on an operating plant scale.

Using the development modelling framework and analysing the results from the simulations it has been shown in this study that mechanically agitated froth flotation cells can best exploit well-liberated material only if the material is coarser than a critical size. This important finding will direct investigations on how to best exploit the benefits of microwave induced grain boundary fracture towards the area of concentration of coarse flotation feeds. One possible suggestion would be to investigate the use of coarse grinding (as can be achieved in high pressure grinding rolls - HPGRs) following microwave treatment, followed by flash flotation of the coarsely liberated material.

The major limitations of such an investigation would be that no model exists in the open literature that allows prediction of liberation from coarse grinding in HPGRs. Further, no model exists in the open literature which allows fundamental modelling of particles behaviour in flash flotation. Future work should possibly look at the development of such types of models. Developing of these models and incorporating them into a flow sheet simulator such as the one used in this study will allow for a better assessment of the value proposition for microwave treatment.

The modelling framework developed in this study can be further improved on. Methods such as the creation of artificial flotation feeds and the fundamental models that have been used to describe the flotation process in this study can be developed further. It will also be essential to validate the flow sheet simulation results with experimental or plant data in the future, this will allow for a more accurate estimate of the potential benefits of microwave assisted processing of ores to be made. This study only focused on the downstream rougher bank flotation process, a study of a complete mineral processing flow sheet circuit that incorporates the comminution processes as well as the final cleaner stages will provide more information on the downstream processing benefits of microwave assisted processing of ores. Such a study would allow for the optimum grind size for microwave treated ore to be determined for a traditional processing flow sheet.

8. REFERENCES

- ABRAHAMSON, J. (1975) Collision rates of small particles in a vigorously turbulent fluid. *Chemical Engineering Science*, 30, 1371-1379.
- AKTAS, Z., CILLIERS, J. J. & BANFORD, A. W. (2008) Dynamic froth stability: Particle size, airflow rate and conditioning time effects. *International Journal of Mineral Processing*, 87, 65-71.
- ALBIJANIC, B., OZDEMIR, O., NGUYEN, A. V. & BRADSHAW, D. (2010) A review of induction and attachment times of wetting thin films between air bubbles and particles and its relevance in the separation of particles by flotation. *Advances in Colloid and Interface Science*, 159, 1-21.
- ALEXANDER, D. J., FRANZIDIS, J. P. & MANLAPIG, E. V. (2003) Froth recovery measurement in plant scale flotation cells. *Minerals Engineering*, 16, 1197-1203.
- ALEXANDER, D. J. & MORRISON, R. D. (1998) Rapid estimation of floatability components in industrial flotation plants. *Minerals Engineering*, 11, 133-143.
- ALI, A. Y. & BRADSHAW, S. M. (2009) Quantifying damage around grain boundaries in microwave treated ores. *Chemical Engineering and Processing: Process Intensification*, 48, 1566-1573.
- ALI, A. Y. & BRADSHAW, S. M. (2010) Bonded-particle modelling of microwave-induced damage in ore particles. *Minerals Engineering*, 23, 780-790.
- AMANKWAH, R. K., PICKLES, C. A. & YEN, W. T. (2005) Gold recovery by microwave augmented ashing of waste activated carbon. *Minerals Engineering*, 18, 517-526.
- AMIRA:P879A (2009) AMIRA P879A :PROGRESS REPORT.
- ATA, S., AHMED, N. & JAMESON, G. J. (2002) Collection of hydrophobic particles in the froth phase. *International Journal of Mineral Processing*, 64, 101-122.
- ATA, S., AHMED, N. & JAMESON, G. J. (2004) The effect of hydrophobicity on the drainage of gangue minerals in flotation froths. *Minerals Engineering*, 17, 897-901.
- ATA, S., PIGRAM, S. & JAMESON, G. J. (2006) Tracking of particles in the froth phase: An experimental technique. *Minerals Engineering*, 19, 824-830.
- BANFORD, A. W., AKTAS, Z. & WOODBURN, E. T. (1998) Interpretation of the effect of froth structure on the performance of froth flotation using image analysis. *Powder Technology*, 98, 61-73.
- BLOOM, F. & HEINDEL, T. J. (1997) Mathematical modelling of the flotation deinking process. *Mathematical and Computer Modelling*, 25, 13-58.
- BLOOM, F. & HEINDEL, T. J. (2002) On the structure of collision and detachment frequencies in flotation models. *Chemical Engineering Science*, 57, 2467-2473.
- BLOOM, F. & HEINDEL, T. J. (2003) Modeling flotation separation in a semi-batch process. *Chemical Engineering Science*, 58, 353-365.
- BORMASHENKO, E. (2008) Why does the Cassie-Baxter equation apply? *Colloids and Surfaces A: Physicochemical and Engineering Aspects*, 324, 47-50.
- BRADSHAW, D. J. & CONNOR, C. T. (1996) Measurement of the sub-process of bubble loadin in flotation. *Minerals Engineering*, 9, 443-448.

- BRADSHAW, D. J., OOSTENDORP, B. & HARRIS, P. J. (2005) Development of methodologies to improve the assessment of reagent behaviour in flotation with particular reference to collectors and depressants. *Minerals Engineering*, 18, 239-246.
- BRADY, M. R., TELIONIS, D. P., VLACHOS, P. P. & YOON, R.-H. (2006) Evaluation of multiphase flotation models in grid turbulence via Particle Image Velocimetry. *International Journal of Mineral Processing*, 80, 133-143.
- BULATOVIC, S. M. (2007) Summary of the Theoretical Aspects of Flotation. *Handbook of Flotation Reagents*. Amsterdam, Elsevier.
- CHAU, T. T. (2009) A review of techniques for measurement of contact angles and their applicability on mineral surfaces. *Minerals Engineering*, 22, 213-219.
- CHAU, T. T., BRUCKARD, W. J., KOH, P. T. L. & NGUYEN, A. V. (2009) A review of factors that affect contact angle and implications for flotation practice. *Advances in Colloid and Interface Science*, 150, 106-115.
- CHEBBI, R. (2003) Deformation of advancing gas-liquid interfaces in capillary tubes. *Journal of Colloid and Interface Science*, 265, 166-173.
- CHIBOWSKI, E. (2007) On some relations between advancing, receding and Young's contact angles. *Advances in Colloid and Interface Science*, 133, 51-59.
- CILEK, E. C. (2009) The effect of hydrodynamic conditions on true flotation and entrainment in flotation of a complex sulphide ore. *International Journal of Mineral Processing*, 90, 35-44.
- ÇILEK, E. C. & UMUCU, Y. (2001) A statistical model for gangue entrainment into froths in flotation of sulphide ores. *Minerals Engineering*, 14, 1055-1066.
- ÇILEK, E. C. & YILMAZER, B. Z. (2003) Effects of hydrodynamic parameters on entrainment and flotation performance. *Minerals Engineering*, 16, 745-756.
- CRAWFORD, R. & RALSTON, J. (1988) The influence of particle size and contact angle in mineral flotation. *International Journal of Mineral Processing*, 23, 1-24.
- CUTTING, G. W., BARBER, S. P. & NEWTON, S. (1986) Effects of froth structure and mobility on the performance and simulation of continuously operated flotation cells. *International Journal of Mineral Processing*, 16, 43-61.
- DAI, Z. (1998) PARTICLE-BUBBLE HETERO COAGULATION. *Ian Wark Research Institute Faculty of Health and Biomedical Science*. South Australia, University of South Australia.
- DAI, Z., DUKHIN, S., FORNASIERO, D. & RALSTON, J. (1998) The Inertial Hydrodynamic Interaction of Particles and Rising Bubbles with Mobile Surfaces. *Journal of Colloid and Interface Science*, 197, 275-292.
- DAI, Z., FORNASIERO, D. & RALSTON, J. (1999) Particle-Bubble Attachment in Mineral Flotation. *Journal of Colloid and Interface Science*, 217, 70-76.
- DAI, Z., FORNASIERO, D. & RALSTON, J. (2000) Particle-bubble collision models -- a review. *Advances in Colloid and Interface Science*, 85, 231-256.
- DOBBY, G. S. & FINCH, J. A. (1986) A model of particle sliding time for flotation size bubbles. *Journal of Colloid and Interface Science*, 109, 493-498.
- DOBBY, G. S. & FINCH, J. A. (1987) Particle size dependence in flotation derived from a fundamental model of the capture process. *International Journal of Mineral Processing*, 21, 241-260.

- DUAN, J.,FORNASIERO, D. & RALSTON, J. (2003) Calculation of the flotation rate constant of chalcopyrite particles in an ore. *International Journal of Mineral Processing*, 72, 227-237.
- FALUTSU, M. & DOBBY, G. S. (1992) Froth performance in commercial sized flotation columns. *Minerals Engineering*, 5, 1207-1223.
- FAN, M.,TAO, D.,HONAKER, R. & LUO, Z. (2010a) Nanobubble generation and its application in froth flotation (part I): nanobubble generation and its effects on properties of microbubble and millimeter scale bubble solutions. *Mining Science and Technology (China)*, 20, 1-19.
- FAN, M.,TAO, D.,HONAKER, R. & LUO, Z. (2010b) Nanobubble generation and its applications in froth flotation (part II): fundamental study and theoretical analysis. *Mining Science and Technology (China)*, 20, 159-177.
- FERREIRA, J. P. & LOVEDAY, B. K. (2000) An improved model for simulation of flotation circuits. *Minerals Engineering*, 13, 1441-1453.
- FETERIS, S. M.,FREW, J. A. & JOWETT, A. (1987) Modelling the effect of froth depth in flotation. *International Journal of Mineral Processing*, 20, 121-135.
- GEORGE, P.,NGUYEN, A. V. & JAMESON, G. J. (2004) Assessment of true flotation and entrainment in the flotation of submicron particles by fine bubbles. *Minerals Engineering*, 17, 847-853.
- GONTIJO, C.,FORNASIERO, D. & RALSTON, J. (2007) The limits of fine and coarse particle flotation. *The Canadian Journal of Chemical Engineering*, 85, 739-747.
- GORAIN, B. K.,HARRIS, M. C.,FRANZIDIS, J. P. & MANLAPIG, E. V. (1998) The effect of froth residence time on the kinetics of flotation. *Minerals Engineering*, 11, 627-638.
- GRANO, S. (2006) Effect of impeller rotational speed on the size dependent flotation rate of galena in full scale plant cells. *Minerals Engineering*, 19, 1307-1318.
- GRAU, R. A. & HEISKANEN, K. (2002) Visual technique for measuring bubble size in flotation machines. *Minerals Engineering*, 15, 507-513.
- GRAU, R. A. & HEISKANEN, K. (2003) Gas dispersion measurements in a flotation cell. *Minerals Engineering*, 16, 1081-1089.
- GROVES, L. (2007) Selective Heating of minerals and Ores using Microwave Energy. *School of Chemical and Environmental Engineering Nottingham, University of Nottingham*.
- GUPTA, A. & YAN, D. S. (2006) Flotation. *Mineral Processing Design and Operation*. Amsterdam, Elsevier Science.
- HAQUE, K. E. (1999) Microwave energy for mineral treatment processes--a brief review. *International Journal of Mineral Processing*, 57, 1-24.
- HERNANDEZ-AGUILAR, J. R.,COLEMAN, R. G.,GOMEZ, C. O. & FINCH, J. A. (2004) A comparison between capillary and imaging techniques for sizing bubbles in flotation systems. *Minerals Engineering*, 17, 53-61.
- HEWITT, D.,FORNASIERO, D. & RALSTON, J. (1994) Bubble particle attachment efficiency. *Minerals Engineering*, 7, 657-665.
- HONAKER, R. Q. & OZSEVER, A. V. (2003) Evaluation of the selective detachment process in flotation froth. *Minerals Engineering*, 16, 975-982.
- HONAKER, R. Q.,OZSEVER, A. V. & PAREKH, B. K. (2006) Selective detachment process in column flotation froth. *Minerals Engineering*, 19, 687-695.

- IRELAND, P., CUNNINGHAM, R. & JAMESON, G. J. (2007) The behaviour of wash water injected into a froth. *International Journal of Mineral Processing*, 84, 99-107.
- IRELAND, P. M. & JAMESON, G. J. (2007) Liquid transport in a multi-layer froth. *Journal of Colloid and Interface Science*, 314, 207-213.
- IVESON, S. M., HOLT, S. & BIGGS, S. (2004) Advancing contact angle of iron ores as a function of their hematite and goethite content: implications for pelletising and sintering. *International Journal of Mineral Processing*, 74, 281-287.
- IWAMATSU, M. (2006) The validity of Cassie's law: A simple exercise using a simplified model. *Journal of Colloid and Interface Science*, 294, 176-181.
- JONES, D. A., KINGMAN, S. W., WHITTLES, D. N. & LOWNDES, I. S. (2005) Understanding microwave assisted breakage. *Minerals Engineering*, 18, 659-669.
- KELLER, A. A., BROJE, V. & SETTY, K. (2007) Effect of advancing velocity and fluid viscosity on the dynamic contact angle of petroleum hydrocarbons. *Journal of Petroleum Science and Engineering*, 58, 201-206.
- KING, R. P. (1993) Comminution and liberation of minerals. *Minerals Engineering*, 7, 129-140.
- KINGMAN, S. (2006) Recent development in microwave processing of minerals. *International Materials Reviews*, 51, 1-12.
- KINGMAN, S., BRADSHAW, S., ROWSON, N. A., JACKSON, K., CUMBANE, A. & GREENWOOD, R. (2004a) Development of microwave assisted comminution. *International Journal of Mineral Processing*, 74, 71-83.
- KINGMAN, S., VORSTER, W. & ROWSON, N. A. (2000a) 'The effect of microwave radiation on the processing of Palabora copper ore'. *J. S. Afr. Inst. Min. Metall.*, 197-204.
- KINGMAN, S. W., JACKSON, K., BRADSHAW, S. M., ROWSON, N. A. & GREENWOOD, R. (2004b) An investigation into the influence of microwave treatment on mineral ore comminution. *Powder Technology*, 146, 176-184.
- KINGMAN, S. W., JACKSON, K., CUMBANE, A., BRADSHAW, S. M., ROWSON, N. A. & GREENWOOD, R. (2004c) Recent developments in microwave-assisted comminution. *International Journal of Mineral Processing*, 74, 71-83.
- KINGMAN, S. W. & ROWSON, N. A. (1998) Microwave treatment of minerals-a review. *Minerals Engineering*, 11, 1081-1087.
- KINGMAN, S. W., VORSTER, W. & ROWSON, N. A. (2000b) The influence of mineralogy on microwave assisted grinding. *Minerals Engineering*, 13, 313-327.
- KIRJAVAINEN, V. M. (1996) Review and analysis of factors controlling the mechanical flotation of gangue minerals. *International Journal of Mineral Processing*, 46, 21-34.
- KOBUSHESHE, J. (2010) Microwave enhanced processing of ores. *Department of Chemical and Environmental Engineering*. Nottingham, University of Nottingham.
- KOH, P. T. L. & SCHWARZ, M. P. (2006) CFD modelling of bubble-particle attachments in flotation cells. *Minerals Engineering*, 19, 619-626.
- KOH, P. T. L. & SCHWARZ, M. P. (2008) Modelling attachment rates of multi-sized bubbles with particles in a flotation cell. *Minerals Engineering*, 21, 989-993.

- LAM, C. N. C., KO, R. H. Y., YU, L. M. Y., NG, A., LI, D., HAIR, M. L. & NEUMANN, A. W. (2001) Dynamic Cycling Contact Angle Measurements: Study of Advancing and Receding Contact Angles. *Journal of Colloid and Interface Science*, 243, 208-218.
- LAM, C. N. C., WU, R., LI, D., HAIR, M. L. & NEUMANN, A. W. (2002) Study of the advancing and receding contact angles: liquid sorption as a cause of contact angle hysteresis. *Advances in Colloid and Interface Science*, 96, 169-191.
- LEIVA, J., VINNETT, L., CONTRERAS, F. & YIANATOS, J. (2010) Estimation of the actual bubble surface area flux in flotation. *Minerals Engineering*, In Press, Corrected Proof.
- LIU, T. Y. & SCHWARZ, M. P. (2009a) CFD-based modelling of bubble-particle collision efficiency with mobile bubble surface in a turbulent environment. *International Journal of Mineral Processing*, 90, 45-55.
- LIU, T. Y. & SCHWARZ, M. P. (2009b) CFD-based multiscale modelling of bubble-particle collision efficiency in a turbulent flotation cell. *Chemical Engineering Science*, 64, 5287-5301.
- LUTTRELL, G. H. & YOON, R. H. (1992) A hydrodynamic model for bubble--particle attachment. *Journal of Colloid and Interface Science*, 154, 129-137.
- MAO, L. & YOON, R.-H. (1997) Predicting flotation rates using a rate equation derived from first principles. *International Journal of Mineral Processing*, 51, 171-181.
- MASSINAEI, M., KOLAHDOOZAN, M., NOAPARAST, M., OLIAZADEH, M., YIANATOS, J., SHAMSADINI, R. & YARAHMADI, M. (2009a) Froth zone characterization of an industrial flotation column in rougher circuit. *Minerals Engineering*, 22, 272-278.
- MASSINAEI, M., KOLAHDOOZAN, M., NOAPARAST, M., OLIAZADEH, M., YIANATOS, J., SHAMSADINI, R. & YARAHMADI, M. (2009b) Hydrodynamic and kinetic characterization of industrial columns in rougher circuit. *Minerals Engineering*, 22, 357-365.
- MATHE, Z. T., HARRIS, M. C., O'CONNOR, C. T. & FRANZIDIS, J. P. (1998) Review of froth modelling in steady state flotation systems. *Minerals Engineering*, 11, 397-421.
- MELOY, J. R., NEETHLING, S. J. & CILLIERS, J. J. (2007) Modelling the axial dispersion of particles in froths. *International Journal of Mineral Processing*, 84, 185-191.
- MENDEZ, D. A., GÁLVEZ, E. D. & CISTERNAS, L. A. (2009) State of the art in the conceptual design of flotation circuits. *International Journal of Mineral Processing*, 90, 1-15.
- MIETTINEN, T., RALSTON, J. & FORNASIERO, D. (2009) The limits of fine particle flotation. *Minerals Engineering*, 23, 420-437.
- MOYS, M. H. (1978) A study of a plug-flow model for flotation froth behaviour. *International Journal of Mineral Processing*, 5, 21-38.
- MOYS, M. H. (1984) Residence time distributions and mass transport in the froth phase of the flotation process. *International Journal of Mineral Processing*, 13, 117-142.
- MOYS, M. H., YIANATOS, J. & LARENAS, J. (2009) Measurement of particle loading on bubbles in the flotation process. *Minerals Engineering*, 23, 131-136.

- MULL, T. & SARICH, S. (2002) Development of a mineral processing flowsheet- Case History, Batu Hijou. *Mineral processing plant design practice and control proceedings*, 12, 2211-2237.
- NAPIER-MUNN, T. (2005) Preface to 7th Edition. *Wills' Mineral Processing Technology (Seventh Edition)*. Oxford, Butterworth-Heinemann.
- NEETHLING, S. J. (2008) Simple approximations for estimating froth recovery. *International Journal of Mineral Processing*, 89, 44-52.
- NEETHLING, S. J. & CILLIERS, J. J. (2003) Modelling flotation froths. *International Journal of Mineral Processing*, 72, 267-287.
- NEETHLING, S. J. & CILLIERS, J. J. (2009) The entrainment factor in froth flotation: Model for particle size and other operating parameter effects. *International Journal of Mineral Processing*, 93, 141-148.
- NEETHLING, S. J., CILLIERS, J. J. & WOODBURN, E. T. (2000) Prediction of the water distribution in a flowing foam. *Chemical Engineering Science*, 55, 4021-4028.
- NEETHLING, S. J., LEE, H. T. & CILLIERS, J. J. (2003) Simple relationships for predicting the recovery of liquid from flowing foams and froths. *Minerals Engineering*, 16, 1123-1130.
- NEWELL, R. & GRANO, S. (2006) Hydrodynamics and scale up in Rushton turbine flotation cells: Part 2. Flotation scale-up for laboratory and pilot cells. *International Journal of Mineral Processing*, 81, 65-78.
- NEWELL, R. & GRANO, S. (2007) Hydrodynamics and scale up in Rushton turbine flotation cells: Part 1 -- Cell hydrodynamics. *International Journal of Mineral Processing*, 81, 224-236.
- NGUYEN-VAN, A. & KMET, S. (1994) Probability of collision between particles and bubbles in flotation: the theoretical inertialess model involving a swarm of bubbles in pulp phase. *International Journal of Mineral Processing*, 40, 155-169.
- NGUYEN, A. V., RALSTON, J. & SCHULZE, H. J. (1998) On modelling of bubble-particle attachment probability in flotation. *International Journal of Mineral Processing*, 53, 225-249.
- NGUYEN, A. V., SCHULZE, H. J. & RALSTON, J. (1997a) Elementary steps in particle-bubble attachment. *International Journal of Mineral Processing*, 51, 183-195.
- NGUYEN, A. V., SCHULZE, H. J., STECHEMESSER, H. & ZOBEL, G. (1997b) Contact time during impact of a spherical particle against a plane gas-liquid interface: theory. *International Journal of Mineral Processing*, 50, 97-111.
- NGUYEN, C. M., NGUYEN, A. V. & MILLER, J. D. (2006) Computational validation of the Generalized Sutherland Equation for bubble-particle encounter efficiency in flotation. *International Journal of Mineral Processing*, 81, 141-148.
- NGUYEN, P. T. & NGUYEN, A. V. (2009) Validation of the generalised Sutherland equation for bubble-particle encounter efficiency in flotation: Effect of particle density. *Minerals Engineering*, 22, 176-181.
- NGUYEN VAN, A. & KMET, S. (1992) Collision efficiency for fine mineral particles with single bubble in a countercurrent flow regime. *International Journal of Mineral Processing*, 35, 205-223.

- NIEMI, A. J. (1995) Role of kinetics in modelling and control of flotation plants. *Powder Technology*, 82, 69-77.
- PHAN, C. M., NGUYEN, A. V., MILLER, J. D., EVANS, G. M. & JAMESON, G. J. (2003) Investigations of bubble-particle interactions. *International Journal of Mineral Processing*, 72, 239-254.
- POLAT, M. & CHANDER, S. (2000) First-order flotation kinetics models and methods for estimation of the true distribution of flotation rate constants. *International Journal of Mineral Processing*, 58, 145-166.
- PRESTIDGE, C. A. & RALSTON, J. (1996) Contact angle studies of particulate sulphide minerals. *Minerals Engineering*, 9, 85-102.
- PYKE, B., FORNASIERO, D. & RALSTON, J. (2003) Bubble particle heterocoagulation under turbulent conditions. *Journal of Colloid and Interface Science*, 265, 141-151.
- RALSTON, J. & DUKHIN, S. S. (1999) The interaction between particles and bubbles. *Colloids and Surfaces A: Physicochemical and Engineering Aspects*, 151, 3-14.
- RALSTON, J., FORNASIERO, D., GRANO, S., DUAN, J. & AKROYD, T. (2007) Reducing uncertainty in mineral flotation--flotation rate constant prediction for particles in an operating plant ore. *International Journal of Mineral Processing*, 84, 89-98.
- RALSTON, J., FORNASIERO, D. & HAYES, R. (1999) Bubble-particle attachment and detachment in flotation. *International Journal of Mineral Processing*, 56, 133-164.
- RALSTON, J. & IAN, D. W. (2000) FLOTATION | Bubble-Particle Capture. *Encyclopedia of Separation Science*. Oxford, Academic Press.
- RODRÍGUEZ-VALVERDE, M. A. (2008) Mechanical derivation of the Wenzel and Cassie equations using a statistical interpretation of drop dispensation. *Journal of Colloid and Interface Science*, 327, 477-479.
- ROINE, A. (2010) *HSC Chemistry 7.0*, Outotec Research Oy.
- ROSS, V. E. (1991a) The behaviour of particles in flotation froths. *Minerals Engineering*, 4, 959-974.
- ROSS, V. E. (1991b) An investigation of sub-processes in equilibrium froths (I): the mechanisms of detachment and drainage. *International Journal of Mineral Processing*, 31, 37-50.
- SAM, A., GOMEZ, C. O. & FINCH, J. A. (1996) Axial velocity profiles of single bubbles in water/frother solutions. *International Journal of Mineral Processing*, 47, 177-196.
- SARROT, V., GUIRAUD, P. & LEGENDRE, D. (2005) Determination of the collision frequency between bubbles and particles in flotation. *Chemical Engineering Science*, 60, 6107-6117.
- SAVASSI, O. N. (2005) A compartment model for the mass transfer inside a conventional flotation cell. *International Journal of Mineral Processing*, 77, 65-79.
- SAVASSI, O. N., ALEXANDER, D. J., FRANZIDIS, J. P. & MANLAPIG, E. V. (1998) An empirical model for entrainment in industrial flotation plants. *Minerals Engineering*, 11, 243-256.

- SCHUBERT, H. (1999) On the turbulence-controlled microprocesses in flotation machines. *International Journal of Mineral Processing*, 56, 257-276.
- SCHUBERT, H. (2008) On the optimization of hydrodynamics in fine particle flotation. *Minerals Engineering*, 21, 930-936.
- SCHUBERT, H. & BISCHOFBERGER, C. (1998) On the microprocesses air dispersion and particle-bubble attachment in flotation machines as well as consequences for the scale-up of macroprocesses. *International Journal of Mineral Processing*, 52, 245-259.
- SCHULZE, H. J. (1977) New theoretical and experimental investigations on stability of bubble/particle aggregates in flotation: A theory on the upper particle size of floatability. *International Journal of Mineral Processing*, 4, 241-259.
- SCHULZE, H. J. (1992) Probability of particle attachment on gas bubbles by sliding. *Advances in Colloid and Interface Science*, 40, 283-305.
- SCHULZE, H. J., RADOEV, B., GEIDEL, T., STECHEMESSER, H. & TÖPFER, E. (1989a) Investigations of the collision process between particles and gas bubbles in flotation -- A theoretical analysis. *International Journal of Mineral Processing*, 27, 263-278.
- SCHULZE, H. J., WAHL, B. & GOTTSCHALK, G. (1989b) Determination of adhesive strength of particles within the liquid/gas interface in flotation by means of a centrifuge method. *Journal of Colloid and Interface Science*, 128, 57-65.
- SCHWARZ, S. & ALEXANDER, D. (2006) Gas dispersion measurements in industrial flotation cells. *Minerals Engineering*, 19, 554-560.
- SCHWARZ, S. & GRANO, S. (2005) Effect of particle hydrophobicity on particle and water transport across a flotation froth. *Colloids and Surfaces A: Physicochemical and Engineering Aspects*, 256, 157-164.
- SCOTT, G., BRADSHAW, S. M. & EKSTEEN, J. J. (2008) The effect of microwave pretreatment on the liberation of a copper carbonatite ore after milling. *International Journal of Mineral Processing*, 85, 121-128.
- SEAMAN, D. R., FRANZIDIS, J. P. & MANLAPIG, E. V. (2004) Bubble load measurement in the pulp zone of industrial flotation machines--a new device for determining the froth recovery of attached particles. *International Journal of Mineral Processing*, 74, 1-13.
- SEAMAN, D. R., MANLAPIG, E. V. & FRANZIDIS, J. P. (2006) Selective transport of attached particles across the pulp-froth interface. *Minerals Engineering*, 19, 841-851.
- SHAHBAZI, B., REZAI, B. & JAVAD KOLEINI, S. M. (2009) The effect of hydrodynamic parameters on probability of bubble-particle collision and attachment. *Minerals Engineering*, 22, 57-63.
- SHAHBAZI, B., REZAI, B. & JAVAD KOLEINI, S. M. (2010) Bubble-particle collision and attachment probability on fine particles flotation. *Chemical Engineering and Processing: Process Intensification*, In Press, Corrected Proof.
- SHERRELL, I. (2004) Development of a Flotation Rate Equation from First Principles under Turbulent Flow Conditions. *Mining and Minerals Engineering Department*. Blacksburg, Virginia, Virginia Polytechnic Institute and State University.
- SONDIR, I., PRAVDIC, V. & BOSKOVIC, R. (2002) Electrokinetics of clay mineral surfaces. *Encyclopedia of surface and colloid science*, 2, 1887-2241.

- STEVENSON, P. (2007) Comments on "An evaluation of different models of water recovery in flotation" by X. Zheng, J.P. Franzidis and N.W. Johnson. *Minerals Engineering*, 20, 207-209.
- STEVENSON, P.,ATA, S. & EVANS, G. M. (2007) Convective-dispersive gangue transport in flotation froth. *Chemical Engineering Science*, 62, 5736-5744.
- SUAZO, C. J.,KRACHT, W. & ALRUIZ, O. M. (2009) Geometallurgical modelling of the Collahuasi flotation circuit. *Minerals Engineering*, 23, 137-142.
- SUBRAHMANYAM, T. V. & FORSSBERG, E. (1988) Froth stability, particle entrainment and drainage in flotation -- A review. *International Journal of Mineral Processing*, 23, 33-53.
- TABOSA, E. & RUBIO, J. (2010) Flotation of copper sulphides assisted by high intensity conditioning (HIC) and concentrate recirculation. *Minerals Engineering*, 23, 1198-1206.
- TROMANS, D. (2008) Mineral comminution: Energy efficiency considerations. *Minerals Engineering*, 21, 613-620.
- TSATOUHAS, G.,GRANO, S. R. & VERA, M. (2006) Case studies on the performance and characterisation of the froth phase in industrial flotation circuits. *Minerals Engineering*, 19, 774-783.
- URIBE, S. A.,VÁZQUEZ, V. D.,PÉREZ, G. R. & NAVA, A. F. (1999) A statistical model for the concentrate water in flotation columns. *Minerals Engineering*, 12, 937-948.
- VAN DEVENTER, J. S. J.,FENG, D. & BURGER, A. J. (2001) The use of bubble loads to interpret transport phenomena at the pulp-froth interface in a flotation column. *Chemical Engineering Science*, 56, 6313-6319.
- VAN DEVENTER, J. S. J.,FENG, D. & BURGER, A. J. (2004a) Transport phenomena at the pulp-froth interface in a flotation column: I. Recovery profiles. *International Journal of Mineral Processing*, 74, 201-215.
- VAN DEVENTER, J. S. J.,FENG, D. & BURGER, A. J. (2004b) Transport phenomena at the pulp-froth interface in a flotation column: II. Detachment. *International Journal of Mineral Processing*, 74, 217-231.
- VERA, M. A.,FRANZIDIS, J. P. & MANLAPIG, E. V. (1999a) The JKMRC high bubble surface area flux flotation cell. *Minerals Engineering*, 12, 477-484.
- VERA, M. A.,FRANZIDIS, J. P. & MANLAPIG, E. V. (1999b) Simultaneous determination of collection zone rate constant and froth zone recovery in a mechanical flotation environment. *Minerals Engineering*, 12, 1163-1176.
- VERA, M. A.,MATHE, Z. T.,FRANZIDIS, J. P.,HARRIS, M. C.,MANLAPIG, E. V. & O'CONNOR, C. T. (2002) The modelling of froth zone recovery in batch and continuously operated laboratory flotation cells. *International Journal of Mineral Processing*, 64, 135-151.
- WEBER, M. E. & PADDOCK, D. (1983) Interceptional and gravitational collision efficiencies for single collectors at intermediate Reynolds numbers. *Journal of Colloid and Interface Science*, 94, 328-335.
- WHITTLES, D. N.,KINGMAN, S. W. & REDDISH, D. J. (2003) Application of numerical modelling for prediction of the influence of power density on microwave-assisted breakage. *International Journal of Mineral Processing*, 68, 71-91.

- WHYMAN, G., BORMASHENKO, E. & STEIN, T. (2008) The rigorous derivation of Young, Cassie-Baxter and Wenzel equations and the analysis of the contact angle hysteresis phenomenon. *Chemical Physics Letters*, 450, 355-359.
- WILLS, B. A. & NAPIER-MUNN, T. (2005) Froth flotation. *Wills' Mineral Processing Technology (Seventh Edition)*. Oxford, Butterworth-Heinemann.
- WU, H. & PATTERSON, G. K. (1989) Laser-Doppler measurements of turbulent-flow parameters in a stirred mixer. *Chemical Engineering Science*, 44, 2207-2221.
- YANG, S. Y., HIRASAKI, G. J., BASU, S. & VAIDYA, R. (1999) Mechanisms for contact angle hysteresis and advancing contact angles. *Journal of Petroleum Science and Engineering*, 24, 63-73.
- YIANATOS, J. & CONTRERAS, F. (2009) Particle entrainment model for industrial flotation cells. *Powder Technology*, 197, 260-267.
- YIANATOS, J., CONTRERAS, F., DÍAZ, F. & VILLANUEVA, A. (2009) Direct measurement of entrainment in large flotation cells. *Powder Technology*, 189, 42-47.
- YIANATOS, J., CONTRERAS, F., MORALES, P., CODDOU, F., ELGUETA, H. & ORTÍZ, J. (2010) A novel scale-up approach for mechanical flotation cells. *Minerals Engineering*, In Press, Corrected Proof.
- YIANATOS, J. B. (2007) Fluid Flow and Kinetic Modelling in Flotation Related Processes: Columns and Mechanically Agitated Cells--A Review. *Chemical Engineering Research and Design*, 85, 1591-1603.
- YIANATOS, J. B., BERGH, L. G. & AGUILERA, J. (2003) Flotation scale up: use of separability curves. *Minerals Engineering*, 16, 347-352.
- YIANATOS, J. B., BERGH, L. G. & CORTÉS, G. A. (1998) Froth zone modelling of an industrial flotation column. *Minerals Engineering*, 11, 423-435.
- YIANATOS, J. B., FINCH, J. A. & LAPLANTE, A. R. (1988) Selectivity in column flotation froths. *International Journal of Mineral Processing*, 23, 279-292.
- YIANATOS, J. B., HENRÍQUEZ, F. H. & OROZ, A. G. (2006) Characterization of large size flotation cells. *Minerals Engineering*, 19, 531-538.
- YIANATOS, J. B., MOYS, M. H., CONTRERAS, F. & VILLANUEVA, A. (2008) Froth recovery of industrial flotation cells. *Minerals Engineering*, 21, 817-825.
- YOON, R.-H. & MAO, L. (1996) Application of Extended DLVO Theory, IV: Derivation of Flotation Rate Equation from First Principles. *Journal of Colloid and Interface Science*, 181, 613-626.
- ZAWALA, J., DRZYMALA, J. & MALYSA, K. (2008) An investigation into the mechanism of the three-phase contact formation at fluorite surface by colliding bubble. *International Journal of Mineral Processing*, 88, 72-79.
- ZHANG, J. & KWOK, D. Y. (2005) On the validity of the Cassie equation via a mean-field free-energy lattice Boltzmann approach. *Journal of Colloid and Interface Science*, 282, 434-438.
- ZHENG, X., FRANZIDIS, J. P. & JOHNSON, N. W. (2006a) An evaluation of different models of water recovery in flotation. *Minerals Engineering*, 19, 871-882.
- ZHENG, X., FRANZIDIS, J. P., JOHNSON, N. W. & MANLAPIG, E. V. (2005) Modelling of entrainment in industrial flotation cells: the effect of solids suspension. *Minerals Engineering*, 18, 51-58.

ZHENG, X., JOHNSON, N. W. & FRANZIDIS, J. P. (2006b) Modelling of entrainment in industrial flotation cells: Water recovery and degree of entrainment. *Minerals Engineering*, 19, 1191-1203.

APPENDIX A MINERAL MODE OF OCCURRENCE FOR COPPER 2 ORE FEED

A.1.

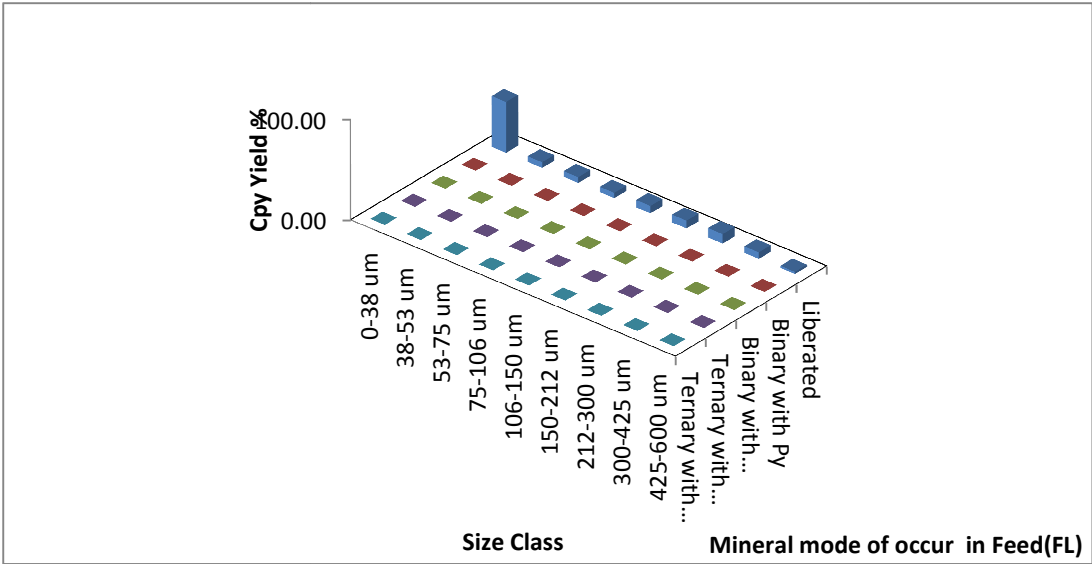


Figure A.1-1: Chalcopyrite mineral mode of occurrence in FL feed ore ($P_{70}=180 \mu\text{m}$) used in the simulations.

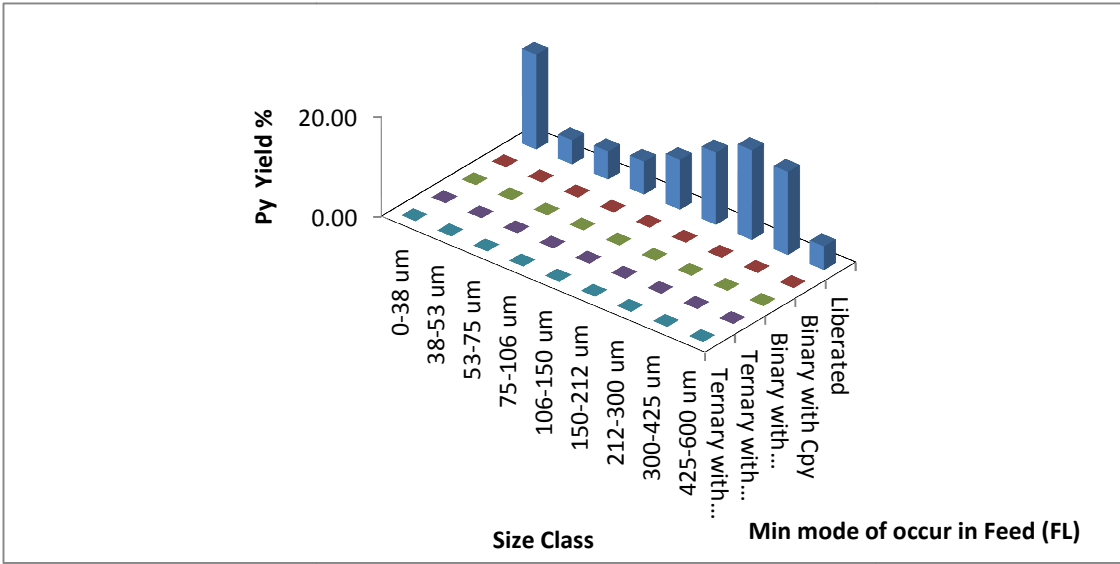


Figure A.1-2: Pyrite mineral mode of occurrence in FL feed ore ($P_{70}=180 \mu\text{m}$) used in the simulations.

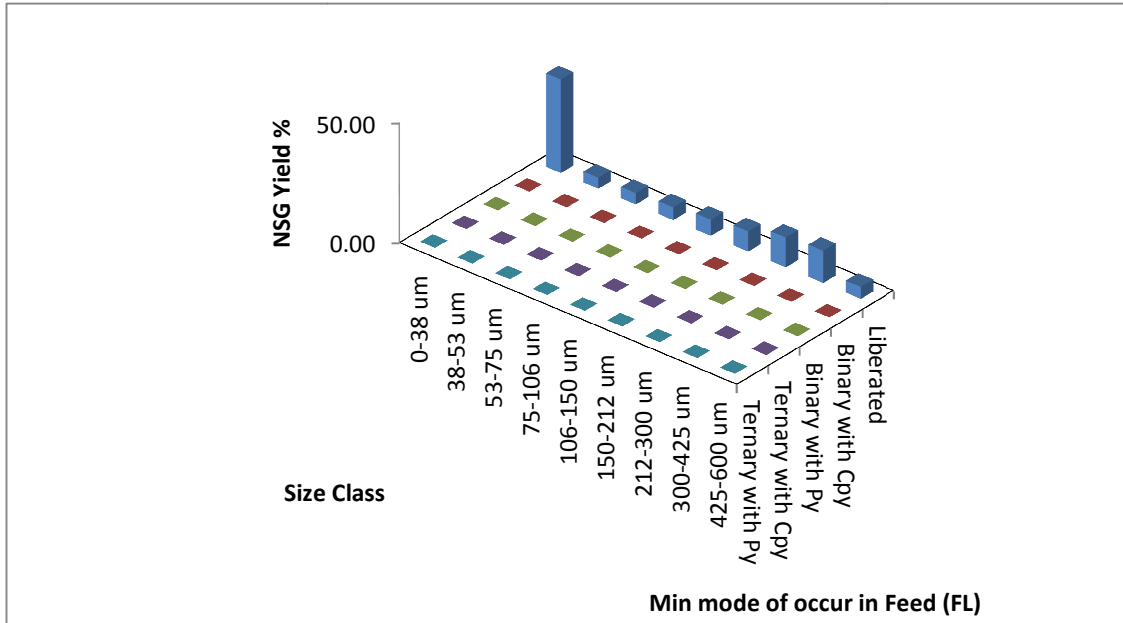


Figure A.1-3: NSG mineral mode of occurrence in FL feed ore ($P_{70}=180 \mu\text{m}$) in the simulations.

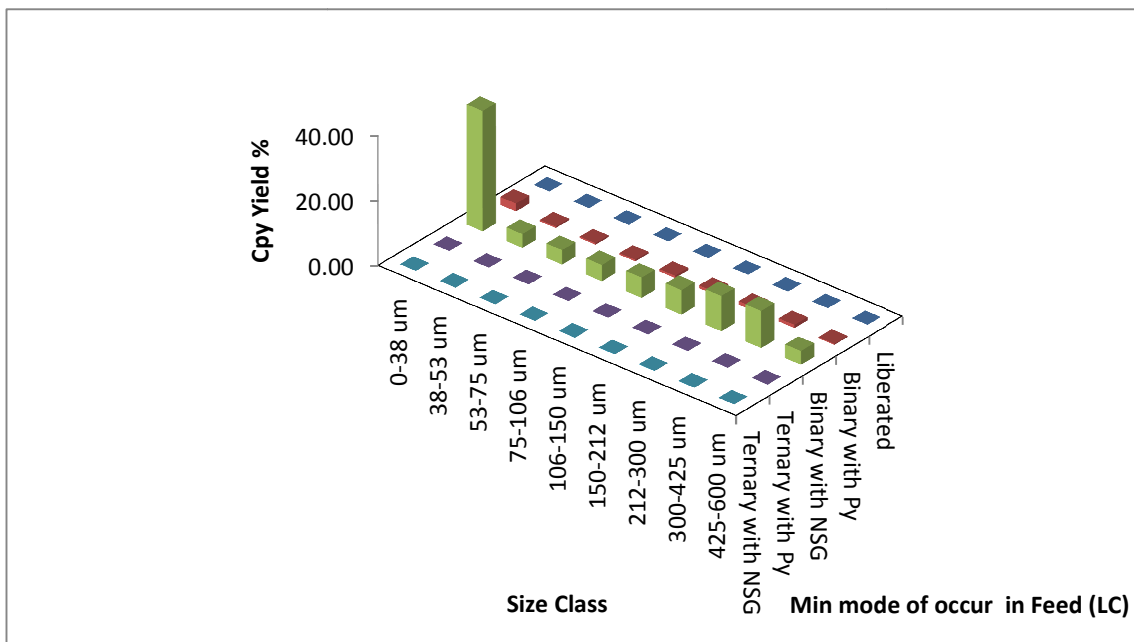


Figure A.1-4: Chalcopyrite mineral mode of occurrence in LC feed ore ($P_{70}=180 \mu\text{m}$) used in the simulations.

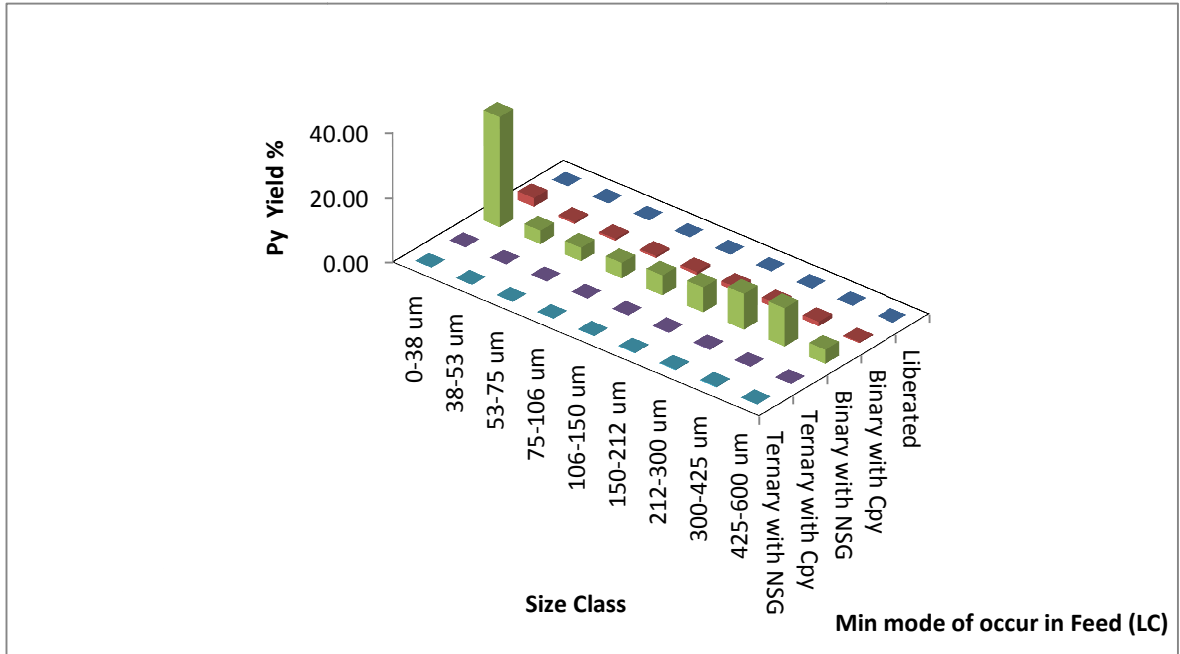


Figure A.1-5: Pyrite mineral mode of occurrence in LC feed ore ($P_{70}=180 \mu\text{m}$) used in the simulations.

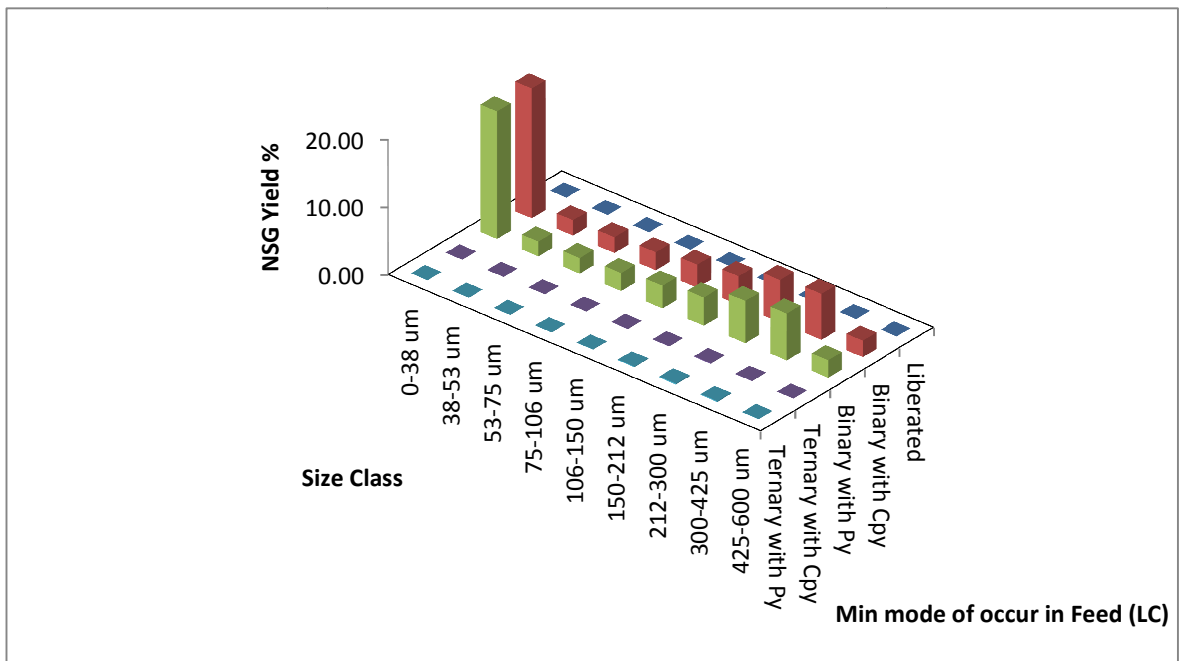


Figure A.1-6: NSG mineral mode of occurrence in LC feed ore ($P_{70}=180 \mu\text{m}$) used in the simulations.

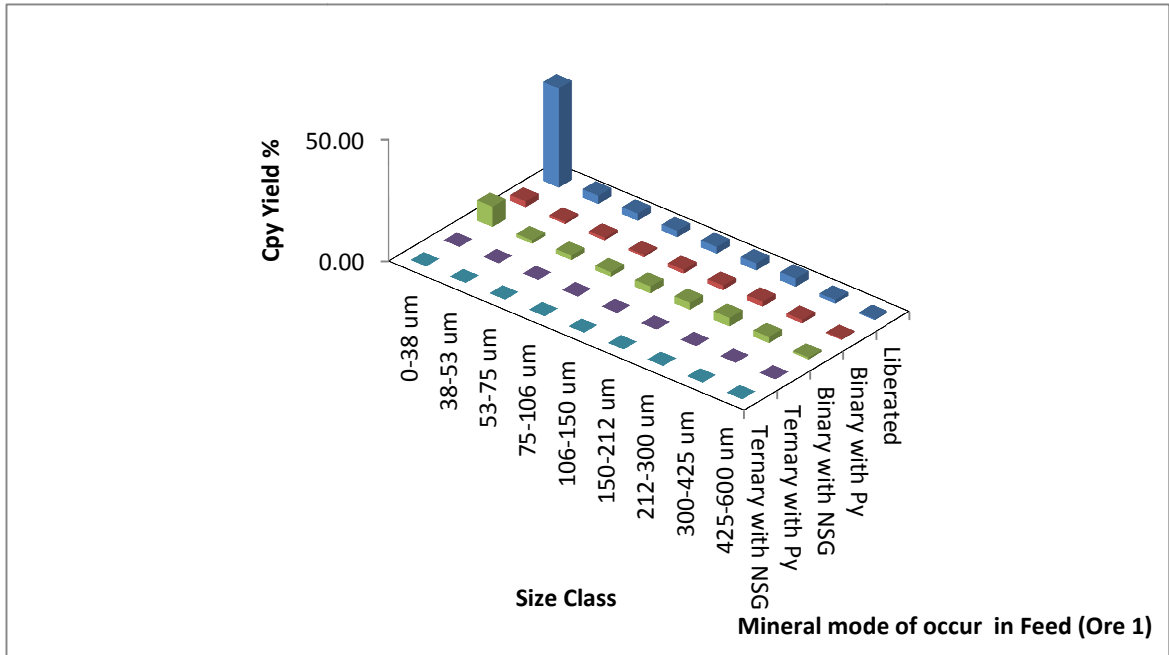


Figure A.1-7: Chalcopyrite mineral mode of occurrence in Ore 1 feed ore ($P_{70}=180 \mu\text{m}$).

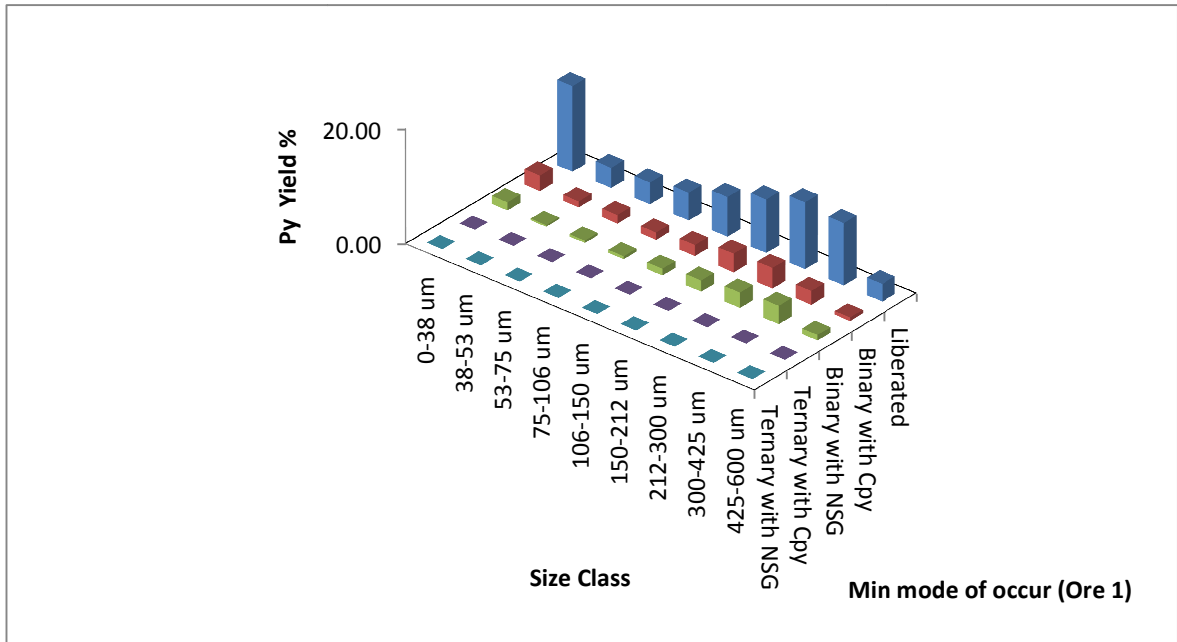


Figure A.1-8: Pyrite mineral mode of occurrence in Ore 1 feed ore ($P_{70}=180 \mu\text{m}$).

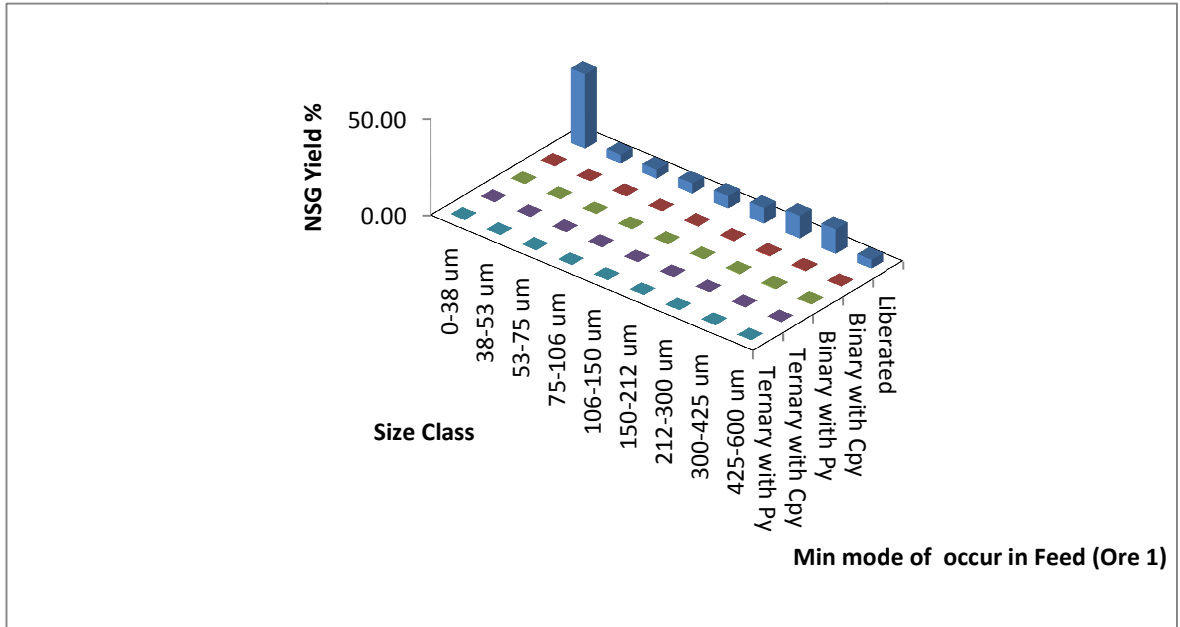


Figure A.1-9: NSG mineral mode of occurrence in Ore 1 feed ore (P₇₀=180 μm).

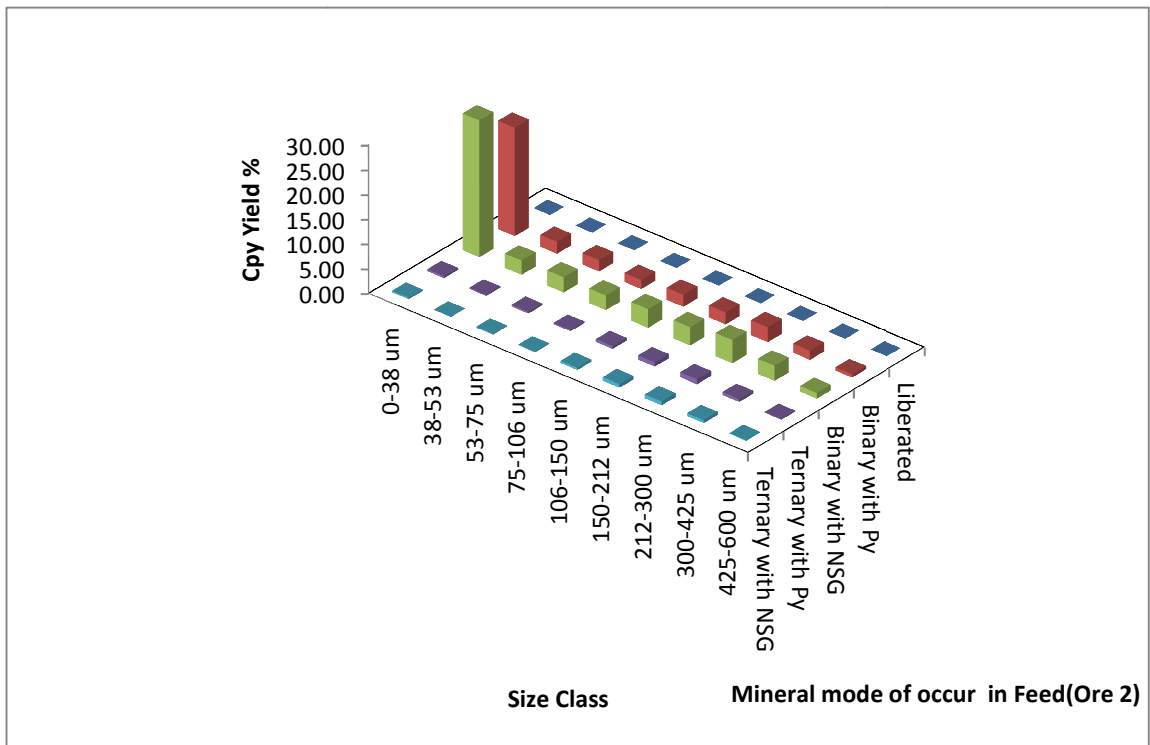


Figure A.1-10: Chalcopyrite mineral mode of occurrence in Ore 2 feed ore (P₇₀=180 μm)

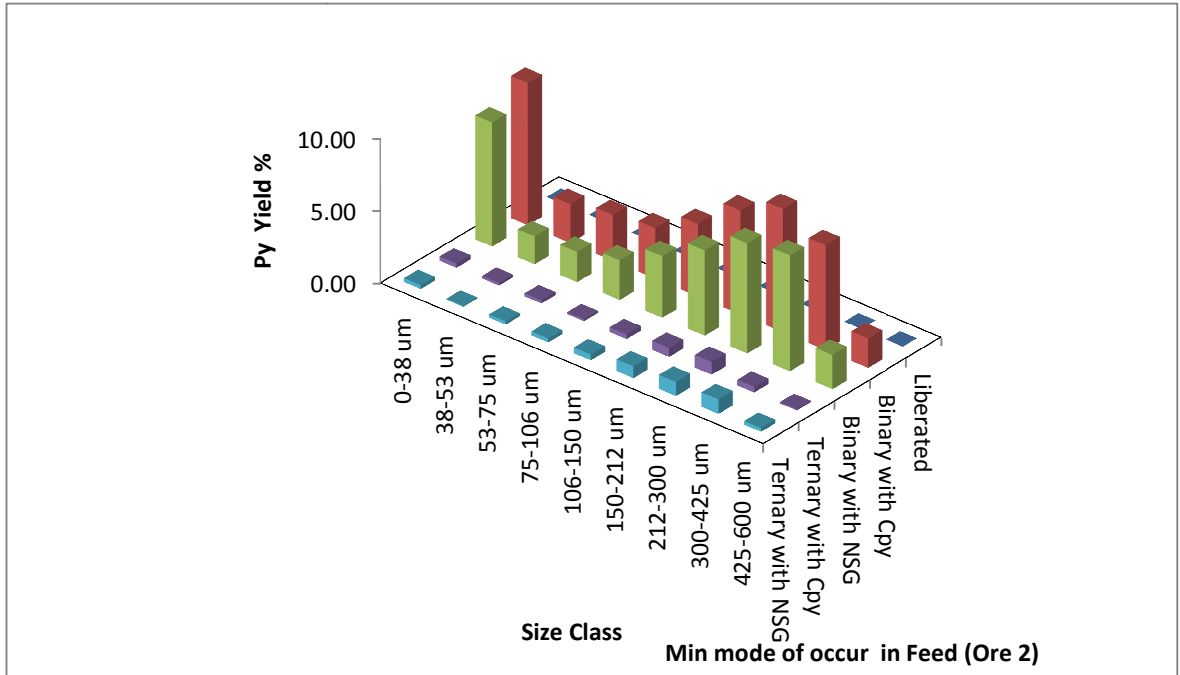


Figure A.1-11: Pyrite mineral mode of occurrence in Ore 2 feed ore (P₇₀=180 μm).

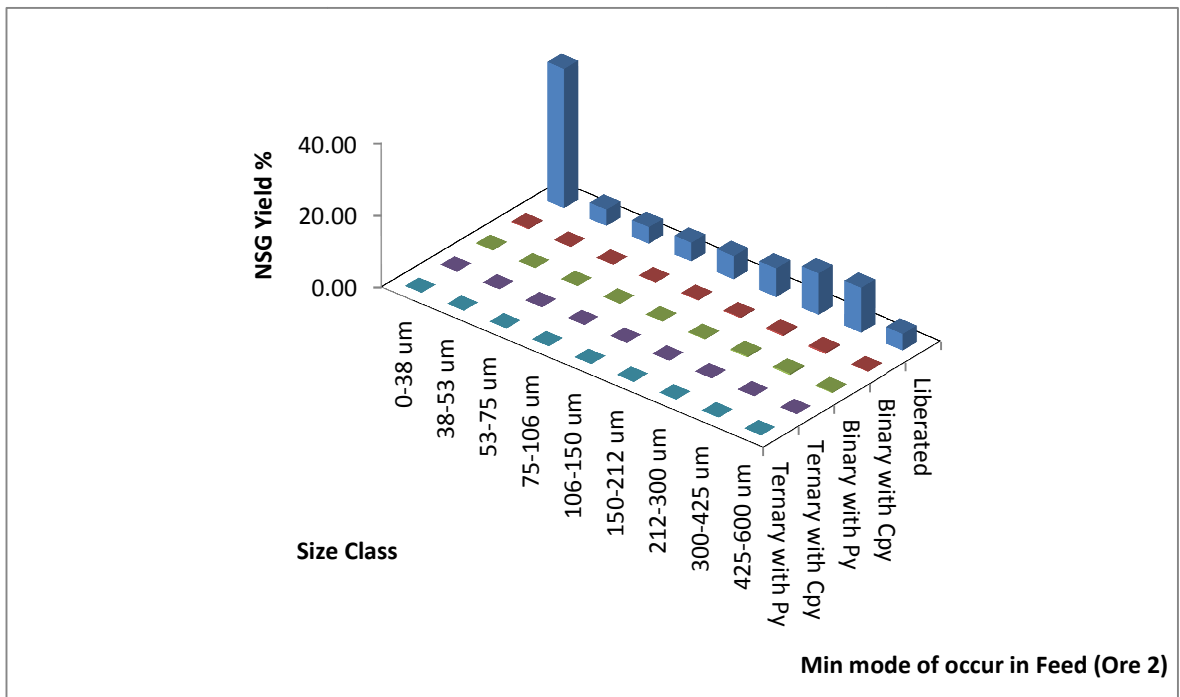


Figure A.1-12: NSG mineral mode of occurrence in Ore 2 feed ore (P₇₀=180 μm).

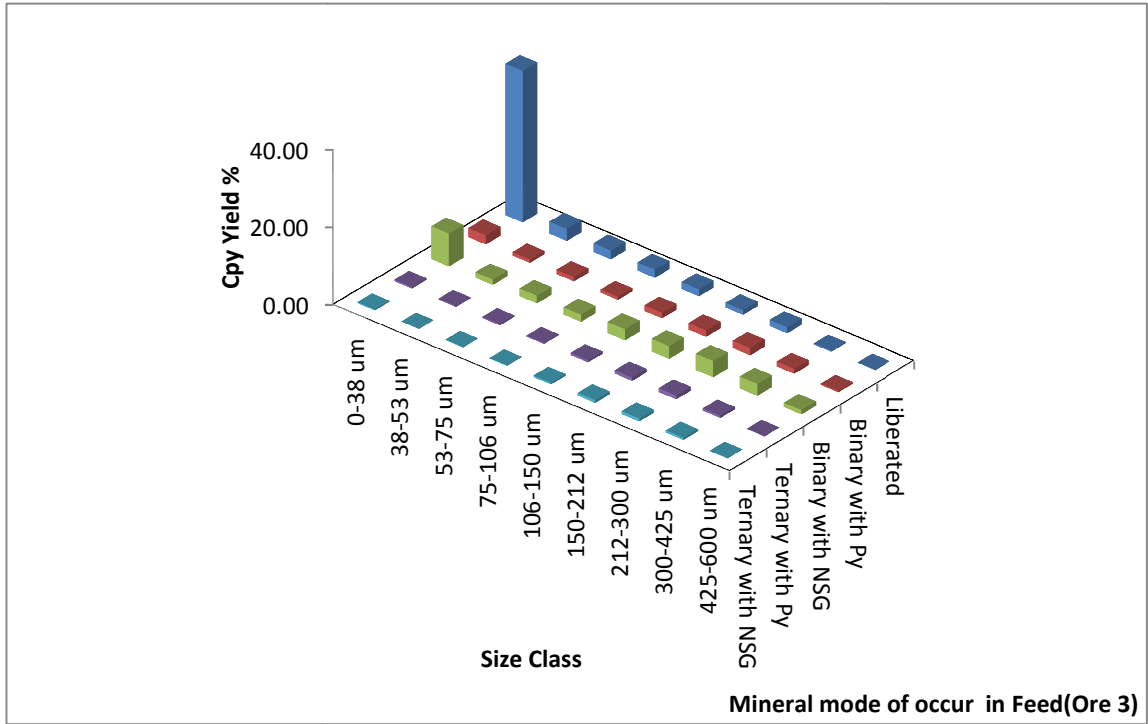


Figure A.1-13: Chalcopyrite mineral mode of occurrence in Ore 3 feed ore ($P_{70}=180 \mu\text{m}$).

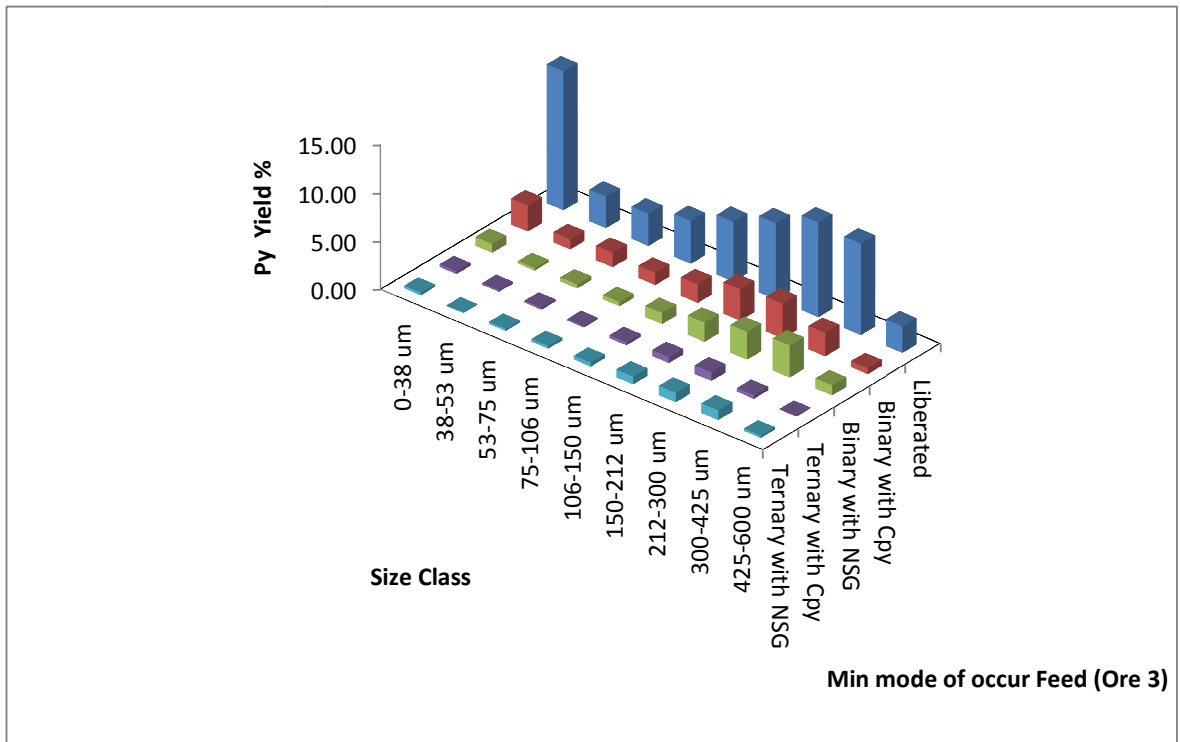


Figure A.1-14: Pyrite mineral mode of occurrence in Ore 3 feed ore ($P_{70}=180 \mu\text{m}$).

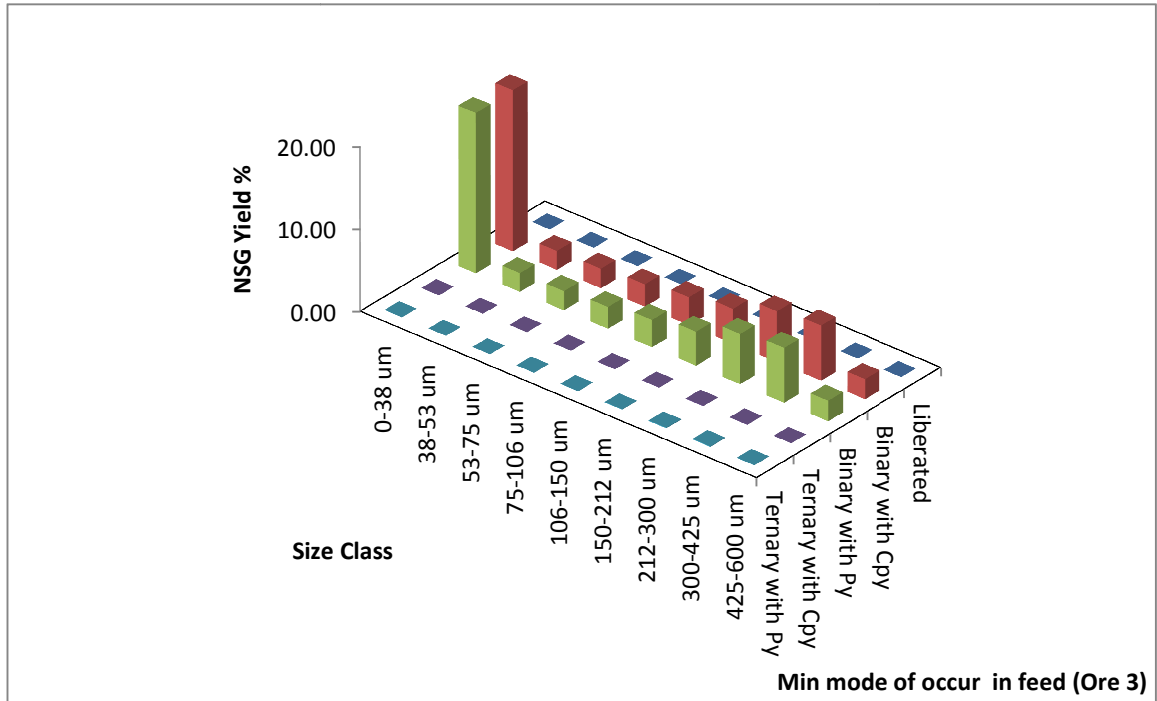


Figure A.1-15: NSG mineral mode of occurrence in Ore 3 feed ore (P₇₀=180 μm).

APPENDIX B CALCULATED PARTICLE CONTACT ANGLE VALUES IN FEED ORE PER SIZE FRACTION

B.1.

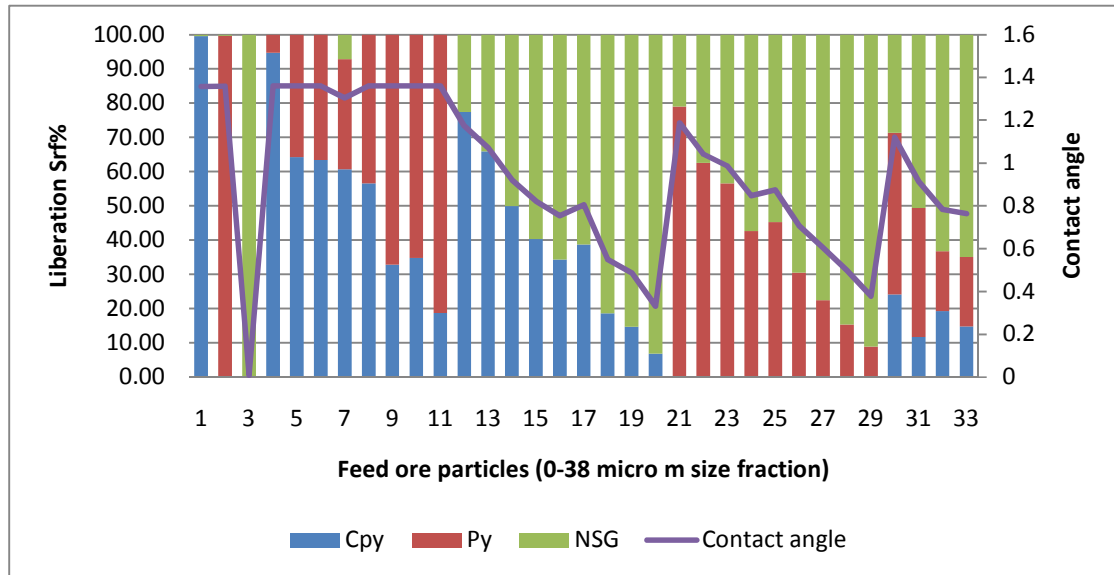


Figure B.1-1: Contact angle variation with particle liberation class for liberation particle classes in the 0-38 μm size fraction.

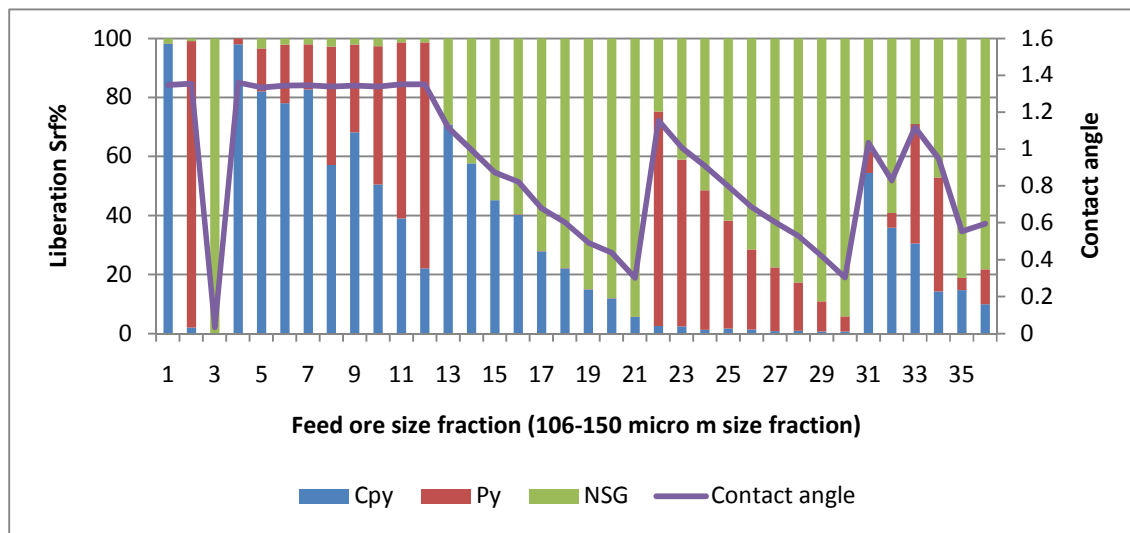


Figure B.1-2: Contact angle variation with particle liberation class for liberation particle classes in the 106-150 μm size fractions.

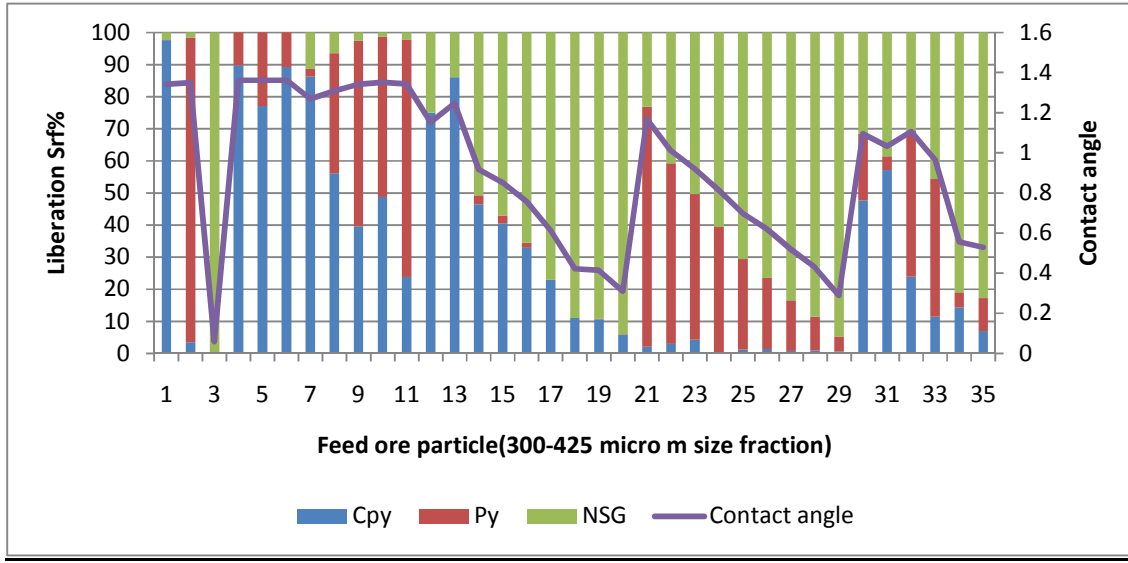


Figure B.1-3: Contact angle variation with particle liberation class for liberation particle classes in the 300-425 micron size fraction.

APPENDIX C : MINERAL GROUPS IN COPPER FEED ORE

C.1.

Table C.1-1: Main mineral groups in feed ores and their grouping

Cu bearing minerals	Non Cu bearing sulphides	Gangue minerals
<ul style="list-style-type: none"> • Chalcopyrite • Digenite • Covellite • Chalcocite • Anilite • Bornite • Enargite 	<ul style="list-style-type: none"> • Pyrite • Sphalerite 	<ul style="list-style-type: none"> • Illite (NSG) • All other minerals non sulphur minerals

Table C.1-2: Mineral groups in feed ores

	Mineral	Wt%	Formula	Mineral
1	Epi wt%	0.05	Ca ₂ (Al,Fe) ₃ Si ₃ O ₁₂ OH	Epidote
2	Titan wt%	0.05	CaTiSiO ₅	Titanite
3	Ort wt%	2.57	KAlSi ₃ O ₈	Orthoclase
4	Cal wt%	0.01	CaCO ₃	Calcite
5	Horn wt%	0.41	(Ca ₂ ,Na)(Mg ₂ FeAl)Si ₆ O ₂₂ (OH) ₂	Hornblende
6	Viv wt%	0.01	Fe ₃ (PO ₄) ₂ .8(H ₂ O)	Vivianite
7	Plum wt%	0.07	PbAl ₃ (PO ₄) ₂ (OH) ₅ .(H ₂ O)	Plumbogummite
8	Eng wt%	0.30	Cu ₃ AsS ₄	Enargite
9	Py wt%	6.25	FeS ₂	Pyrite
10	Dig wt%	0.21	Cu ₉ S ₅	Digenite
11	Iser wt%	0.06	FeTi ₂ O ₅	Iserite
12	Ilmen wt%	0.07	FeTiO ₃	Ilmenite
13	Hem wt%	0.67	Fe ₂ O ₃	Hematite
14	Cov wt%	0.04	CuS	Covellite
15	Cpy wt%	0.47	CuFeS ₂	Chalcopyrite
16	Chal wt%	0.91	Cu ₂ S	Chalcocite
17	Anil wt%	0.16	Cu ₇ S ₄	Anilite
18	Born wt%	0.77	Cu ₅ FeS ₄	Bornite
19	Mol wt%	0.01	MoS ₂	Molybdenite
20	Sph wt%	0.01	ZnS	Sphalerite
21	Alb wt%	2.31	NaAlSi ₃ O ₈	Albite
22	Chl wt%	8.59	(Mg ₃ ,Fe ₂)Al(AlSi ₃)O ₁₀ (OH) ₈	Chlorite
23	Gyp wt%	0.01	(Ca ₂ ,Na)(Mg ₂ FeAl)Si ₆ O ₂₂ (OH) ₂	Gypsum
24	Ill wt%	25.65	KAl ₂ (AlSi ₃ O ₁₀)(OH) ₂	Illite
25	Kao wt%	3.08	Al ₂ Si ₂ O ₅ (OH) ₄	Kaolinite
26	Kemm wt%	0.06	(Sr,Ce)Al ₃ (AsO ₄)(SO ₄)(OH) ₆	Kemmlitzite
27	Mon wt%	0.02	(La,Ce)PO ₄	Monazite
28	Olig wt%	0.78	(Na,Ca)(Al,Si) ₄ O ₈	Oligoclase
29	Pyro wt%	2.48	Al ₂ Si ₄ O ₁₀ (OH) ₂	Pyrophyllite
30	Qtz wt%	42.89	SiO ₂	Quartz
31	Goe wt%	0.06	FeOOH	Goethite
32	Rut wt%	0.25	TiO ₂	Rutile

APPENDIX D : ROUGHER CELLS IN SERIES PLANT FLOWSHEET CONFIGURATION

D.1.

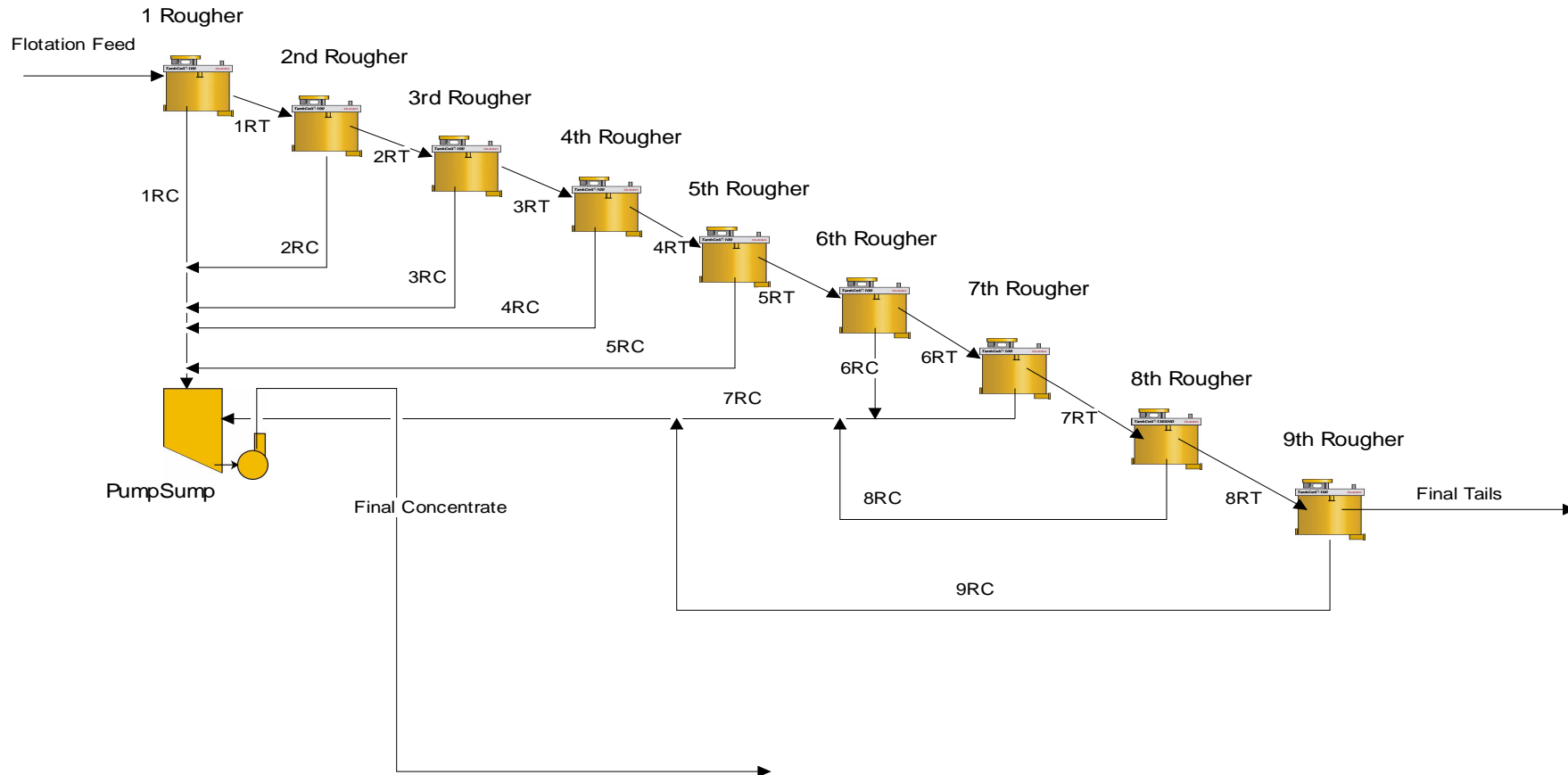


Figure D.1-1: Rougher cell flow sheet configuration that was used in the study.

APPENDIX E : FILE STRUCTURE IN HSC CHEMISTRY 7

E.1.

Global mineral settings in HSC are stored in the MinSetup.xls file while the composition of each input stream is stored in the Mineralogy_Stream.xls file. Each process unit is presented by an individual MS Excel file with the name of the unit. Figure 3-1 below summarises the file structure in HSC Sim. The properties of individual streams in HSC Sim in a mineral processing flow sheet are calculated from particle flow rates, particle composition and mineral properties. Mineral elements in the streams do not therefore behave independently in the process but with other associated mineral elements that are bound with them in the same particle (Roine, 2010).

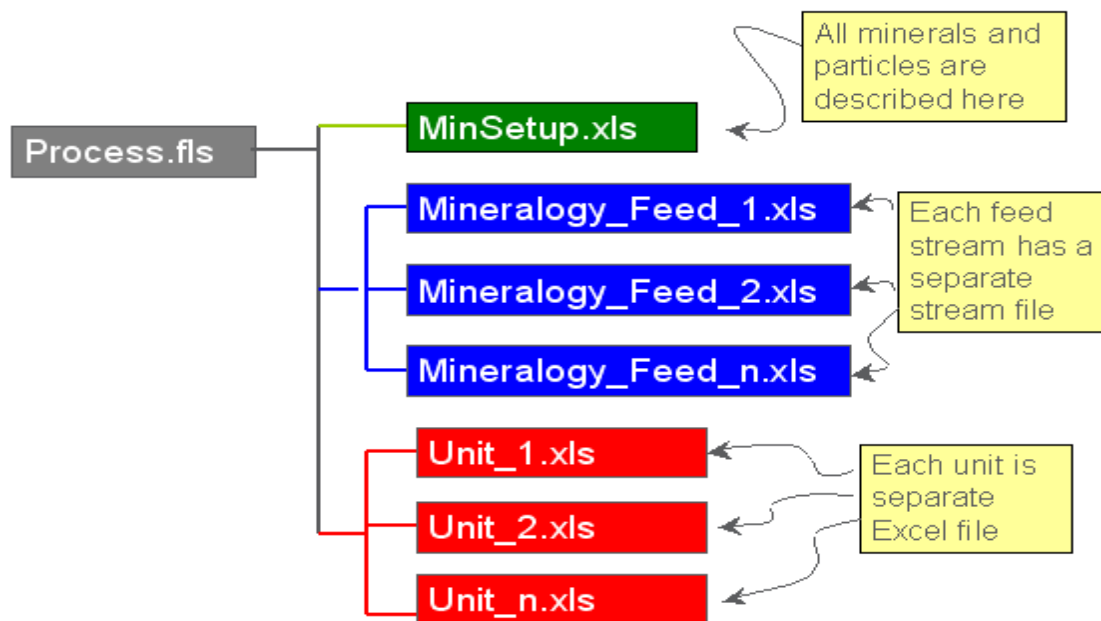


Figure E.1-1: File structure in HSC Sim in the Particle (Minerals) Mode adapted from HSC Chemistry 7 manual (Roine, 2010).

APPENDIX F : COPPER 1 BATCH FLOTATION EXPERIMENTAL PROCEDURE

F.1.

Porphyry copper ore was crushed in a Laboratory Rod mill at two grind sizes $P_{70} = 120 \mu\text{m}$ and $P_{70} = 180 \mu\text{m}$. A standard flotation procedure for obtaining flotation recovery by size data was used. The method involved floating the ore in a standard batch flotation cell designed for this purpose. Concentrate from the flotation cell was collected at timed intervals of 0.5, 1, 4, 9, 15 minutes. Flotation was carried out in a Denver D12 flotation machine was used to float the ore feed at an impeller speed of 1000 to 1100rpm. The flotation cell size was 4L and air was fed at a flow rate of 0.5L/min. In order to obtain recovery by size data the timed concentrates were combined and the following measurements were taken.

1. Solids % in the combined concentrate.
2. The size distribution of the combined concentrate.
3. Assay of each size class in the combined concentrate.

APPENDIX G : FLOTATION CELL SIMULATION INPUT VARIABLES

G.1.

Table G.1-1: Input variables used in calibrating the fundamental property based model in simulating the flotation process.

Variable	Parameter	Literature input parameter (Ralston et al., 2007)
Feed ore Type	Copper 1 base case feed	
P ₇₀ grind size	120 μm	
Cell volume (V)	85 m ³	85 m ³
Feed rate	890 tph	890 tph
Sulphide mineral contact angle (θ)		78°
NSG contact angle (θ)		0°
Energy dissipation (ε)		11 m ² /s ³
Bubble diameter (d _b)		0.0013 m
Bubble rise velocity (v _b)		0.18 m/s
Apparent viscosity of slurry (ϑ)		0.2 kg/ms
Gas flow rate (G _{fr})		4 m ³ /min
Surface tension (γ)		70 N/m
Fluid density (ρ _{fl})	1263 kg/ m ³	
Bubble density (ρ _b)	0.5 ρ _{fl} (Koh and Schwarz, 2006)	
Acceleration due to gravity	9.81 m/s ²	
Fluid velocity v _{fl}	0.1724 m/s	

APPENDIX H : COPPER 1 AND COPPER 2 FLOTATION FEED ORE BULK PARTICLE WEIGHT DISTRIBUTION.

H.1.

Table H.1-1: 0-38 μm bulk particle size class weight % for Copper 1 flotation feed ores (P_{70} = 120 μm)

Size Class	ParticleType	Bulk particle weight %					
		BC	FL	LC	Ore 1	Ore 2	Ore3
0-38 μm	Cpy	1.36	1.56	0.00	1.39	0.00	1.36
0-38 μm	Py	1.35	1.52	0.00	1.38	0.00	1.35
0-38 μm	NSG	35.87	36.34	0.00	35.90	35.87	0.00
0-38 μm	Cpy-Py	0.36	0.00	1.71	0.36	1.71	0.36
0-38 μm	Cpy-NSG	0.36	0.00	18.97	0.36	1.04	18.29
0-38 μm	Py-NSG	0.14	0.00	18.74	0.14	0.81	18.07
0-38 μm	NSG+	0.09	0.00	0.09	0.00	0.09	0.09

Table H.1-2: 38-53 μm bulk particle size class weight % for Copper 1 flotation feed ores (P_{70} = 120 μm)

Size Class	Cpy-Py	Bulk particle weight %					
		BC	FL	LC	Ore 1	Ore 2	Ore3
38-53 μm	Cpy	0.12	0.24	0.00	0.13	0.00	0.12
38-53 μm	Py	0.25	0.38	0.00	0.27	0.00	0.25
38-53 μm	NSG	5.62	5.75	0.00	5.63	5.62	0.00
38-53 μm	Cpy-Py	0.13	0.00	0.31	0.13	0.31	0.13
38-53 μm	Cpy-NSG	0.12	0.00	2.98	0.12	0.17	2.92
38-53 μm	Py-NSG	0.03	0.00	2.97	0.03	0.16	2.84
38-53 μm	NSG+	0.04	0.00	0.04	0.00	0.04	0.04

Table H.1-3: 53-75 μm bulk particle size class weight % for Copper 1 flotation feed ores (P_{70} = 120 μm)

Size Class	Cpy-NSG	Bulk particle weight %					
		BC	FL	LC	Ore 1	Ore 2	Ore3
53-75 μm	Cpy	0.09	0.24	0.00	0.10	0.00	0.09
53-75 μm	Py	0.34	0.50	0.00	0.37	0.00	0.34
53-75 μm	NSG	5.81	6.03	0.00	5.83	5.81	0.00
53-75 μm	Cpy-Py	0.17	0.00	0.38	0.17	0.38	0.17
53-75 μm	Cpy-NSG	0.13	0.00	3.09	0.13	0.18	3.04
53-75 μm	Py-NSG	0.07	0.00	3.14	0.07	0.24	2.97
53-75 μm	NSG+	0.07	0.00	0.07	0.00	0.07	0.07

Table H.1-4: 75-106 µm bulk particle size class weight % for Copper 1 flotation feed ores

(P₇₀ = 120 µm)

Size Class	Py-NSG	Bulk particle weight %					
		BC	FL	LC	Ore 1	Ore 2	Ore3
75-106 um	Cpy	0.09	0.24	0.00	0.11	0.00	0.09
75-106 um	Py	0.38	0.66	0.00	0.41	0.00	0.38
75-106 um	NSG	7.03	7.36	0.00	7.06	7.03	0.00
75-106 um	Cpy-Py	0.19	0.00	0.42	0.19	0.42	0.19
75-106 um	Cpy-NSG	0.21	0.00	3.77	0.21	0.26	3.72
75-106 um	Py-NSG	0.11	0.00	3.81	0.11	0.30	3.63
75-106 um	NSG+	0.09	0.00	0.09	0.00	0.09	0.09

Table H.1-5: 106-150 µm bulk particle size class weight % for Copper 1 flotation feed ores

(P₇₀ = 120 µm)

Size Class	Cpy-Py-NSG	Bulk particle weight %					
		BC	FL	LC	Ore 1	Ore 2	Ore3
106-150 um	Cpy	0.08	0.30	0.00	0.12	0.00	0.08
106-150 um	Py	0.70	0.94	0.00	0.78	0.00	0.70
106-150 um	NSG	8.99	9.82	0.00	9.05	8.98	0.01
106-150 um	Cpy-Py	0.29	0.00	0.68	0.29	0.68	0.29
106-150 um	Cpy-NSG	0.34	0.00	4.88	0.34	0.39	4.83
106-150 um	Py-NSG	0.25	0.00	5.09	0.25	0.60	4.74
106-150 um	NSG+	0.17	0.00	0.17	0.00	0.17	0.17

Table H.1-6: 150-212 µm bulk particle size class weight % for Copper 1 flotation feed ores

(P₇₀ = 120 µm)

Size Class	Cpy-Py	Bulk particle weight %					
		BC	FL	LC	Ore 1	Ore 2	Ore3
150-212 um	Cpy	0.05	0.34	0.00	0.10	0.00	0.05
150-212 um	Py	0.80	1.27	0.00	0.89	0.00	0.79
150-212 um	NSG	11.50	12.32	0.00	11.58	11.49	0.02
150-212 um	Cpy-Py	0.30	0.00	0.73	0.30	0.73	0.30
150-212 um	Cpy-NSG	0.45	0.00	6.23	0.45	0.48	6.19
150-212 um	Py-NSG	0.39	0.00	6.53	0.39	0.79	6.14
150-212 um	NSG+	0.23	0.00	0.23	0.00	0.23	0.23

Table H.1-7: 212-300 µm bulk particle size class weight % for Copper 1 flotation feed ores
(P₇₀ = 120 µm)

Size Class	Cpy-NSG	Bulk particle weight %					
		BC	FL	LC	Ore 1	Ore 2	Ore3
212-300 um	Cpy	0.02	0.24	0.00	0.06	0.00	0.02
212-300 um	Py	0.55	1.06	0.00	0.63	0.00	0.55
212-300 um	NSG	10.42	10.59	0.00	10.49	10.39	0.03
212-300 um	Cpy-Py	0.27	0.00	0.57	0.27	0.57	0.27
212-300 um	Cpy-NSG	0.40	0.00	5.62	0.40	0.43	5.60
212-300 um	Py-NSG	0.41	0.00	5.88	0.41	0.68	5.60
212-300 um	NSG+	0.18	0.00	0.18	0.00	0.18	0.18

Table H.1-8: 300-425 µm bulk particle size class weight % for Copper 1 flotation feed ores
(P₇₀ = 120 µm)

Size Class	Py-NSG	Bulk particle weight %					
		BC	FL	LC	Ore 1	Ore 2	Ore3
300-425 um	Cpy	0.00	0.03	0.00	0.01	0.00	0.00
300-425 um	Py	0.13	0.13	0.00	0.14	0.00	0.13
300-425 um	NSG	2.28	2.15	0.00	2.29	2.27	0.01
300-425 um	Cpy-Py	0.03	0.00	0.10	0.03	0.10	0.03
300-425 um	Cpy-NSG	0.08	0.00	1.22	0.08	0.08	1.21
300-425 um	Py-NSG	0.08	0.00	1.29	0.08	0.15	1.22
300-425 um	NSG+	0.03	0.00	0.03	0.00	0.03	0.03

H.2.

Table H.2-1: 0-38 μm bulk particle size class weight % for Copper 2 flotation feed ores (P_{70} = 180 μm)

Size Class	ParticleType	Bulk particle weight %					
		BC	FL	LC	Ore 1	Ore 2	Ore3
0-38 μm	Cpy	1.20	1.55	0.00	1.22	0.00	1.20
0-38 μm	Py	0.93	1.23	0.00	0.97	0.00	0.93
0-38 μm	NSG	35.02	35.39	0.00	35.05	35.02	0.00
0-38 μm	Cpy-Py	0.25	0.00	1.32	0.25	1.32	0.25
0-38 μm	Cpy-NSG	0.48	0.00	18.60	0.48	1.08	18.00
0-38 μm	Py-NSG	0.20	0.00	18.18	0.20	0.67	17.71
0-38 μm	NSG+	0.08	0.00	0.08	0.00	0.08	0.08

Table H.2-2: 38-53 μm bulk particle size class weight % for Copper 1 flotation feed ores (P_{70} = 180 μm)

Size Class	Cpy-Py	Bulk particle weight %					
		BC	FL	LC	Ore 1	Ore 2	Ore3
38-53 μm	Cpy	0.10	0.17	0.00	0.11	0.00	0.10
38-53 μm	Py	0.21	0.32	0.00	0.23	0.00	0.21
38-53 μm	NSG	4.09	4.15	0.00	4.10	4.09	0.00
38-53 μm	Cpy-Py	0.09	0.00	0.25	0.09	0.25	0.09
38-53 μm	Cpy-NSG	0.08	0.00	2.18	0.08	0.13	2.13
38-53 μm	Py-NSG	0.03	0.00	2.18	0.03	0.14	2.08
38-53 μm	NSG+	0.03	0.00	0.03	0.00	0.03	0.03

Table H.2-3: 53-75 μm bulk particle size class weight % for Copper 1 flotation feed ores (P_{70} = 180 μm)

Size Class	Cpy-NSG	Bulk particle weight %					
		BC	FL	LC	Ore 1	Ore 2	Ore3
53-75 μm	Cpy	0.07	0.18	0.00	0.09	0.00	0.07
53-75 μm	Py	0.22	0.37	0.00	0.25	0.00	0.22
53-75 μm	NSG	4.18	4.28	0.00	4.20	4.18	0.00
53-75 μm	Cpy-Py	0.13	0.00	0.28	0.13	0.28	0.13
53-75 μm	Cpy-NSG	0.12	0.00	2.25	0.12	0.16	2.21
53-75 μm	Py-NSG	0.05	0.00	2.25	0.05	0.16	2.14
53-75 μm	NSG+	0.06	0.00	0.06	0.00	0.06	0.06

Table H.2-4: 75-106 µm bulk particle size class weight % for Copper 1 flotation feed ores

(P₇₀ = 180 µm)

Size Class	Py-NSG	Bulk particle weight %					
		BC	FL	LC	Ore 1	Ore 2	Ore3
75-106 um	Cpy	0.06	0.16	0.00	0.08	0.00	0.06
75-106 um	Py	0.29	0.43	0.00	0.32	0.00	0.29
75-106 um	NSG	4.73	4.87	0.00	4.74	4.72	0.00
75-106 um	Cpy-Py	0.10	0.00	0.28	0.10	0.28	0.10
75-106 um	Cpy-NSG	0.15	0.00	2.54	0.15	0.18	2.51
75-106 um	Py-NSG	0.07	0.00	2.58	0.07	0.21	2.43
75-106 um	NSG+	0.06	0.00	0.06	0.00	0.06	0.06

Table H.2-5: 106-150 µm bulk particle size class weight % for Copper 1 flotation feed ores

(P₇₀ = 180 µm)

Size Class	Cpy-Py-NSG	Bulk particle weight %					
		BC	FL	LC	Ore 1	Ore 2	Ore3
106-150 um	Cpy	0.06	0.22	0.00	0.09	0.00	0.06
106-150 um	Py	0.41	0.65	0.00	0.45	0.00	0.40
106-150 um	NSG	5.87	6.14	0.00	5.91	5.86	0.01
106-150 um	Cpy-Py	0.17	0.00	0.40	0.17	0.40	0.17
106-150 um	Cpy-NSG	0.24	0.00	3.21	0.24	0.27	3.17
106-150 um	Py-NSG	0.15	0.00	3.28	0.15	0.35	3.08
106-150 um	NSG+	0.12	0.00	0.12	0.00	0.12	0.12

Table H.2-6: 150-212 µm bulk particle size class weight % for Copper 1 flotation feed ores

(P₇₀ = 180 µm)

Size Class	Cpy-Py	Bulk particle weight %					
		BC	FL	LC	Ore 1	Ore 2	Ore3
150-212 um	Cpy	0.04	0.24	0.00	0.09	0.00	0.04
150-212 um	Py	0.52	0.94	0.00	0.61	0.00	0.52
150-212 um	NSG	7.22	7.65	0.00	7.29	7.21	0.01
150-212 um	Cpy-Py	0.26	0.00	0.54	0.26	0.54	0.26
150-212 um	Cpy-NSG	0.32	0.00	3.95	0.32	0.35	3.93
150-212 um	Py-NSG	0.26	0.00	4.13	0.26	0.52	3.87
150-212 um	NSG+	0.21	0.00	0.21	0.00	0.21	0.21

Table H.2-7: 212-300 µm bulk particle size class weight % for Copper 1 flotation feed ores

(P₇₀ = 180 µm)

Size Class	Cpy-NSG	Bulk particle weight %					
		BC	FL	LC	Ore 1	Ore 2	Ore3
212-300 um	Cpy	0.05	0.29	0.00	0.11	0.00	0.05
212-300 um	Py	0.64	1.17	0.00	0.76	0.00	0.64
212-300 um	NSG	10.48	11.25	0.00	10.60	10.46	0.03
212-300 um	Cpy-Py	0.29	0.00	0.64	0.29	0.64	0.29
212-300 um	Cpy-NSG	0.48	0.00	5.75	0.48	0.52	5.71
212-300 um	Py-NSG	0.47	0.00	6.03	0.47	0.80	5.70
212-300 um	NSG+	0.29	0.00	0.29	0.00	0.29	0.29

Table H.2-8: 300-425 µm bulk particle size class weight % for Copper 1 flotation feed ores

(P₇₀ = 180 µm)

Size Class	Py-NSG	Bulk particle weight %					
		BC	FL	LC	Ore 1	Ore 2	Ore3
300-425 um	Cpy	0.01	0.19	0.00	0.05	0.00	0.01
300-425 um	Py	0.62	1.08	0.00	0.71	0.00	0.62
300-425 um	NSG	11.35	12.20	0.00	11.44	11.31	0.04
300-425 um	Cpy-Py	0.19	0.00	0.53	0.19	0.53	0.19
300-425 um	Cpy-NSG	0.49	0.00	6.16	0.48	0.50	6.14
300-425 um	Py-NSG	0.60	0.00	6.57	0.60	0.92	6.26
300-425 um	NSG+	0.22	0.00	0.22	0.00	0.22	0.22

Table H.2-9: 425-850 µm bulk particle size class weight % for Copper 1 flotation feed ores

(P₇₀ = 180 µm)

Size Class	Cpy-Py-NSG	Bulk particle weight %					
		BC	FL	LC	Ore 1	Ore 2	Ore3
425-850 um	Cpy	0.01	0.06	0.00	0.01	0.00	0.01
425-850 um	Py	0.18	0.31	0.00	0.20	0.00	0.18
425-850 um	NSG	4.18	4.50	0.00	4.21	4.16	0.02
425-850 um	Cpy-Py	0.05	0.00	0.15	0.05	0.15	0.05
425-850 um	Cpy-NSG	0.15	0.00	2.24	0.15	0.16	2.23
425-850 um	Py-NSG	0.25	0.00	2.42	0.25	0.34	2.33
425-850 um	NSG+	0.06	0.00	0.06	0.00	0.06	0.06

APPENDIX I SAMPLE MODEL WIZARD SCREEN CAPTURE IN HSC CHEMISTRY 7

I.1.

	A	B	C	D	E	F	G	H	I	J	K	L	M	N	O	P	
1	MODEL:	Fundamental Property based model				To apply wizard select 'Run Excel Wizard...' on the 'Wizard' menu											
2	WIZARD FILE:	HSC_Sim_S_1_Particle_Wizards.xls															
3	WIZARD SHEET:	Flotation property based model															
4	AUTHOR:	Edson Charikinya, Stellenbosch University				Use this model for flotation, using kinetic equation according to: <i>Causes (i.e. taking into account entrainment and both minerals)</i>											
5	VERSION:	21 May 2010 for Mineralogical Treatment of Materials Group															
6	Material divided between the products according to mineral composition and size class					Blue text indicates user check input											
7						Red text is calculated value which should not be touched, or it is an error message											
8																	
9	Basic info		Guides to fill in the parameters: (check and fill all fields with blue text)														
10	Minerals	0															
11	Size fractions	1															
12	Particles																
13	Input streams																
14	Output streams																
15																	
16	Cell Operating parameters		Advancing water Contact angles in Radians for fully liberated minerals														
17	Total volume m3	85															
18	Input pulp m3/h	1500															
19	Residence time, min	3.4															
20	Scale-up factor	1															
21	Eff. residence time, min	3.4															
22	σ	1.2															
23	Gas flowrate (Q) m3/min	4															
24	Mean Bubble diameter (m)	0.0013															
25	Fluid velocity (m/s)	0.01															
26	Bubble velocity (m/s)	0.01															
27	Fluid density (kg/m3)	1400															
28	Bubble density (kg/m3)	4100															
29	Density Diff (kg/m3)	2700															
30	Dissipation energy (m2/s3)	11															
31	viscosity (Pas)	0.2															
32	Kinematic Viscosity (m2/s)	0.00014208															
33	Surface tension	0.072															
34	Concentrate is	1	Stream1														
35																	
36	Number of collision per unit volume		Advancing water COS(Contact angles)-contact angles in Radians for fully liberated minerals														
37	Mechanical Term(m/min)	85.52															
38	Primary turbulence term (m)	0.16															
39	Water Recovery %	1.2%															
40																	
		Entrainment calculation parameters															
		Ent Parameter		0.00003													
		Drainage		1													
		Adj		1													
		induction time constant		0.6													

Figure I.1-1: Sample screen capture of model wizard screen as it would appear in HSC Chemistry 7.

COMMANDS (the area below contains HSC Sim macro commands which are run when initializing the model, please do not touch!)

Destination	A-column	B-column	Rows	Cols	Source Sheet	A-column	B-column	Rows	Cols	Formula	Function	Comment	Prompt	Comments
Sheet				4										
Input	M.P.*	*		4						=SUM(\$D:\$D)				Sums everything to column 4
Output	M.P.*	*		4						=SUM(\$D:\$D)				Sums everything to column 4
Model			10	3							nMinerals			Get number of minerals
Wizard			10	3							nMinerals			
Model			11	3							nSizeFractions			Number of size fractions
Model			12	3							nParticles			Number of particles
Model			13	3							nInputStreams			Number of input streams
Model			14	3							nOutputStreams			Number of output streams
Model			15	3	Input			10	4					
Model			16	3	Input			12	4					
Model			17	3				5	4		@*1000			Get the name of the stream
Model			18	3	Output			5	4					
Model			19	3	Model			34	3		OFFSET(R1C1,0)			
Model			11	12								HorizontalArray(nMinerals)		Copy down the size file
Model			12	12								HorizontalArray(nMinerals)		Copy down the size file
Model			17	12								HorizontalArray(nMinerals)		Copy down the size file
Model			18	12								HorizontalArray(nMinerals)		Copy down the size file
Model			19	11								VerticalArray(nSizeClasses)		
Model			19	12								VerticalArray(nSizeClasses)		
Model			19	12								TableRC(nSizeClasses,nMinerals)		Create table (size rows, 2 mineral co)
Cell	M.P.*		8	1	Cell			*	1					
Cell	M.P.*		8	6										
Model			45	6	Cell	M.P.*		*	6			ParticleRec(1:Model\$D\$10:\$D\$40)		Particle recovery according to size file
Cell	M.P.*		9	1	Cell	M.P.*		*	1					
Cell	M.P.*		9	9										
Model			45	4	Cell	M.P.*		*	9			ParticleC(1:SizeClass(1))		
Cell	M.P.*		10	1	Cell			*	1					
Cell	M.P.*		10	10	Cell			*	1			ParticleC(1:Size(1))		
Cell	M.P.*		11	1	Cell			*	1					
Cell	M.P.*		11	11	Cell			*	1			ParticleC(1:Size(1))		
Model			45	6	Cell	M.P.*		*	11					
Model			45	3								VerticalArray(nParticles)		Copy down the FORMULAS
Model			45	3								VerticalArray(nParticles)		Copy down the FORMULAS
Model			45	4								VerticalArray(nParticles)		Copy down the FORMULAS
Model			45	5								VerticalArray(nParticles)		Copy down the FORMULAS
Model			45	6								VerticalArray(nParticles)		Copy down the FORMULAS
Model			45	7								VerticalArray(nParticles)		Copy down the FORMULAS
Model			45	8								VerticalArray(nParticles)		Copy down the FORMULAS
Model			45	9								VerticalArray(nParticles)		Copy down the FORMULAS
Model			45	10								VerticalArray(nParticles)		Copy down the FORMULAS
Model			45	11								VerticalArray(nParticles)		Copy down the FORMULAS
Model			45	12								VerticalArray(nParticles)		Copy down the FORMULAS
Model			45	13								VerticalArray(nParticles)		Copy down the FORMULAS
Model			45	14								VerticalArray(nParticles)		Copy down the FORMULAS
Model			45	15								VerticalArray(nParticles)		Copy down the FORMULAS
Model			45	16								VerticalArray(nParticles)		Copy down the FORMULAS
Model			45	17								VerticalArray(nParticles)		Copy down the FORMULAS
Model			45	18								VerticalArray(nParticles)		Copy down the FORMULAS
Model			45	19								VerticalArray(nParticles)		Copy down the FORMULAS
Model			45	20								VerticalArray(nParticles)		Copy down the FORMULAS
Model			45	21								VerticalArray(nParticles)		Copy down the FORMULAS
Model			45	22								VerticalArray(nParticles)		Copy down the FORMULAS
Model			45	23								VerticalArray(nParticles)		Copy down the FORMULAS
Model			45	24								VerticalArray(nParticles)		Copy down the FORMULAS
Model			45	25								VerticalArray(nParticles)		Copy down the FORMULAS
Model			45	26								VerticalArray(nParticles)		Copy down the FORMULAS
Model			45	27								VerticalArray(nParticles)		Copy down the FORMULAS
Model			45	28								VerticalArray(nParticles)		Copy down the FORMULAS
Model			45	29								VerticalArray(nParticles)		Copy down the FORMULAS
Model			45	30								VerticalArray(nParticles)		Copy down the FORMULAS
Model			45	31								VerticalArray(nParticles)		Copy down the FORMULAS
Model			45	32								VerticalArray(nParticles)		Copy down the FORMULAS
Cell	M.P.*		5	32	Model			45	32					Particle ref reference
Cell	M.P.*		5	5								VerticalArray(nParticles)		Particle recovery according to particle
Output	M.P.*		5	5	Input			*	5					
Output	M.P.*		5	5	Cell			*	5					Dir formula
Output	M.P.*		5	5	Input			*	5					Out of ref
Output	M.P.*		5	5	Output			*	5					Output formula
Output			5	5	Model			39	13					
Output			5	5	Input			5	4					
Output			5	5	Input			5	4					
Model			43	32	Input			5	4			Input(\$D\$4:\$D\$30)		

Figure I.1-2: Sample HSC Chemistry Simulation macro commands in HSC Chemistry 7 that form part of the model wizard.

